

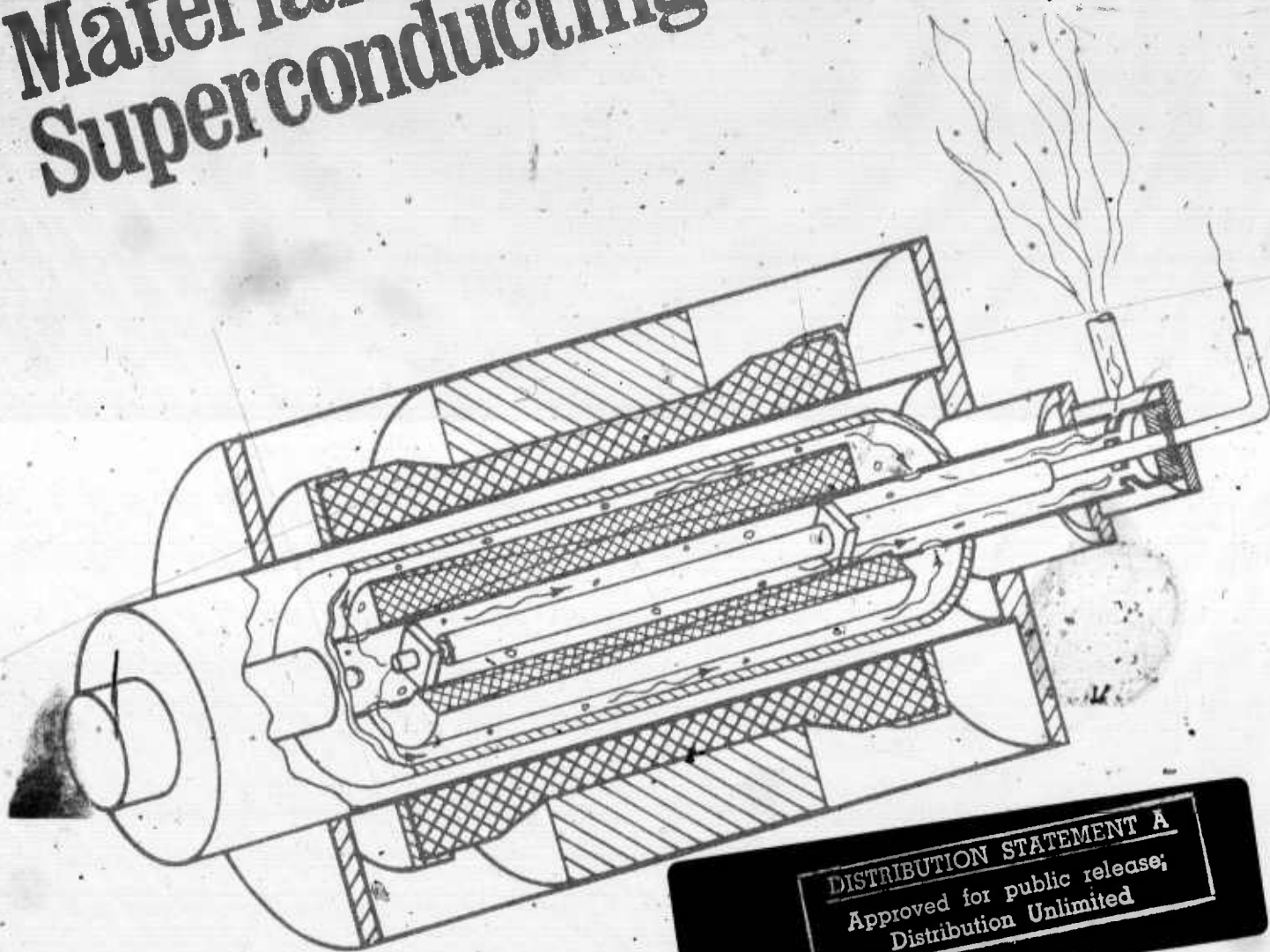
AD A 030170

NBS - ARPA



Materials Research for Superconducting Machinery

V



DISTRIBUTION STATEMENT A
Approved for public release;
Distribution Unlimited



SEMI-ANNUAL
TECHNICAL REPORT
APRIL 1976

SEMI-ANNUAL TECHNICAL REPORTS ON MATERIALS
RESEARCH IN SUPPORT OF SUPERCONDUCTING MACHINERY-V.

FOR

9 Semi-annual technical rept.
1 September 1975 to 1 March 1976

Edited by

11 Apr 76 10 Richard P. Reed and H. M. Ledbetter
National Bureau of Standards

and

Edward C. van Reuth
Advanced Research Projects Agency

Sponsored by

12 426p. 15 Advanced Research Projects Agency
1400 Wilson Boulevard, Arlington, VA 22209
ARPA Order No. 2569 - Program Code 5D10

Contracted for 11 September 1975

by

Cryogenics Division, Institute for Basic Standards
National Bureau of Standards, Boulder, CO 80302

Subcontracts to:

Battelle, Columbus Laboratories
National Bureau of Standards, Cryogenics Division
Westinghouse Electric Research & Development Center

D D C
RECEIVED
AUG 18 1976
A

DISTRIBUTION STATEMENT A

Approved for public release;
Distribution Unlimited

DISCLAIMER

The views and conclusions contained in this document are those of the authors and should not be interpreted as necessarily representing the official policies, either expressed or implied, of the Advanced Research Projects Agency or the U.S. Government.

400 992

LB

DISCLAIMER NOTICE

THIS DOCUMENT IS THE BEST
QUALITY AVAILABLE.

COPY FURNISHED CONTAINED
A SIGNIFICANT NUMBER OF
PAGES WHICH DO NOT
REPRODUCE LEGIBLY.

SUMMARY

The fifth semi-annual technical reports are collected from three subcontractors of an AFPA-sponsored program to study the very low-temperature properties of structural materials in support of the development of superconducting machinery. The program is outlined and new research results are reported. Low-temperature results are given for the following properties: elastic, tensile, fatigue and fracture, thermal expansion, specific heat, thermal and magnetothermal conductivity, electrical and magnetic. Effects of processing and fabrication are also considered for some properties; weld and braze-joint properties are included. Tensile and compressive properties at 4 K of selected composite materials are presented.

SECTION 1	
NTIS	White Section
WDC	Grey Section
RESEARCHER	
INSTITUTION	
<i>Letter of Title</i>	
BY	
ORIGINATOR/AVAILABILITY CODES	
AVAIL. CODE OR SPECIAL	
<i>[Signature]</i>	

	Page
ORGANIZATIONAL CONTACTS	iv
INTRODUCTION	1
PROGRAM DESCRIPTION	1
OUTLINE OF THIRD-YEAR PROGRAM	2
HIGHLIGHTS OF RESULTS	5
HANDBOOK	6
TECHNICAL REPORTS BY SUBCONTRACTORS	ff

BATTELLE, COLUMB LABORATORIES

Preparation of a Handbook on Mechanical, Thermal, Electrical, and
Magnetic properties of Materials for Superconducting Machinery.

Wilkes, K. E.
Thompson, J. K.
Hanby, K. R.

Low-Temperature Thermal Expansion and Specific Heat
Properties of Structural Materials

Jelinek, F. J.
Collings, E. W.

NATIONAL BUREAU OF STANDARDS

Advanced Composites

Kasen, M. B.
Schramm, P. E.

Elastic Properties

Ledbetter, H. M.
Read, D. T.

Fracture Mechanics Parameters

Read, D. T.
Reed, R. P.
Tobler, R. L.

Magnetothermal Conductivity

Sparks, L. L.

Thermal Conductivity

Hust, J. H.

WESTINGHOUSE ELECTRIC CORPORATION

Structural Materials for Cryogenic Applications

Wells, J. M.
Daniel, M. R.
Kossowsky, R.
Logsdon, W. A.

[Handwritten notes and scribbles]

SEARCHED		INDEXED	
SERIALIZED		FILED	
JUN 1964			
FBI - NEW YORK			
BY <i>Letter on file</i>			
DISTRIBUTION/AVAILABILITY CODE			
Dist.	AVAIL.	ORD.	SPEC.
A			

Table 1. Organizational Contacts, ARPA Low-Temperature
Properties of Structural Materials

Advanced Research Projects Agency, 1400 Wilson Blvd., Arlington, Virginia 22209

Program Director	Edward C. van Reuth	202-694-4750 694-4750 (FTS)
------------------	---------------------	--------------------------------

National Bureau of Standards, Cryogenics Division, Boulder, Colorado 80302

Program Manager	Richard P. Reed		Ext. 3870
Fracture, Fatigue	Ralph L. Tober	303-499-1000	Ext. 3421
Elastic	Hassell M. Ledbetter	323-ext. (FTS)	Ext. 3443
Thermal Conductivity	Jerome G. Hust		Ext. 3733
Magnetothermal Conductivity	L. L. Sparks		Ext. 3612
Composites	Maurice B. Kasen		Ext. 3558

Battelle, Columbus Laboratories, 505 King Avenue, Columbus, Ohio 43201

Program Manager	Kenneth R. Hanby		Ext. 1784
Mechanical Properties Data	Kenneth R. Hanby		Ext. 1784
Thermal Properties Data	Kenneth E. Wilkes	614-424-6424	Ext. 3489
Magnetic Properties Data	J. Ken Thompson	941-8045 (FTS)	Ext. 2612
Physical Properties Meas't.	Frank Jelinek		Ext. 1735

Westinghouse Electric Corporation, Research & Development Center, Beulah Road,
Pittsburgh, Pennsylvania 15235

Program Manager	Joseph M. Wells	412-256-7000	Ext. 3467
Joining & Processing	Joseph M. Wells	412-256-7000	Ext. 3633
Fracture Mechanics	William A. Logsdon	412-256-7000	Ext. 3652
Magnetic Measurements	Michael R. Daniels	412-256-7000	Ext. 7267
Metallurgy-Fractography	Ram Kossowsky	412-256-7000	Ext. 3684

INTRODUCTION

This report contains results of a research program designed to fill the need for materials properties data to facilitate design and development of superconducting machinery. The program was conceived and developed jointly by the staffs of the Materials Science Group at the Advanced Research Projects Agency and the Cryogenics Division of the National Bureau of Standards. This ARPA - sponsored program on "Materials Research in Support of Superconducting Machinery" is managed by NBS, with subcontracts to two other laboratories.

PROGRAM DESCRIPTION

The program's objectives are: (1) to evaluate candidate structural materials for use in superconducting electrical machinery by determining their mechanical and physical properties between 4 and 300 K and the effects of processing and joining on these properties; (2) to explore new materials, such as composites, for potential innovative design applications by performing screening tests on their low-temperature properties; (3) to assist the information transfer of the available low-temperature properties data into design use by compiling and publishing existing data; and (4) to assess which materials and properties need further study.

The third-year program plan to meet these objectives is shown in Tables 2 and 3. The research efforts at three research laboratories are described briefly in Table 2. As shown in the Tables, the major thrust has been fatigue and fracture measurements at low temperatures where virtually no data have existed previously. Major material categories include: structural alloys, composites, ferromagnetic alloys, and high-strength high-conductivity alloys.

Two workshops were held, and a third is planned for Vail, Colorado, April 5-7, 1976. These workshops have brought together research personnel Department of Defense project staff members. Design-materials interfacing problems were discussed and emphasis was placed on meeting Department of Defense materials needs.

A major new materials conference, the International Cryogenic Materials Conference, was held at Kingston, Ontario, in July, 1975. Over 60 technical papers (14 from this program) were presented and the proceedings will appear as a bound volume.

Table 2. Outline of Third-Year ARPA-Sponsored Program on
Materials Research for Superconducting Machinery

<u>Program Area</u>	<u>Organization</u>	<u>Program Description</u>
A. Mechanical Properties		
1. Fracture and Fatigue	NBS,Cryogenics	Fracture toughness, fatigue crack-growth rate, fatigue sustained-load crack-growth rate tests from 4-300 K on structural alloys, effects of stress level and frequency.
	Westinghouse	Mechanical, magnetic, electrical loss characterization of alloys proposed for use in DOD-sponsored programs. Mechanical tests include tensile, fracture toughness, fatigue.
2. Effects of Processing and Joining		
a. Processing	Westinghouse	Identification of effects of fabrication and processing techniques on mechanical properties of selected alloys. Variables include industrial melting practices, powder metallurgy techniques, cold working, grain size, and inhomogeneities.
b. Joining	Westinghouse	Mechanical properties of fabricated metal joints, including welding (GTAW, EB, GMAW), brazing, and soldering from 4-300 K. Properties include tensile, notched tensile, fracture toughness, and fatigue crack growth rate in the fused and heat affected zones and the base metal.
3. Elastic Properties	NBS,Cryogenics	Young's shear, bulk moduli; Poisson's ratio; dynamic tests; 4-300 K; structural alloys and composite materials.

<u>Program Area</u>	<u>Organization</u>	<u>Program Description</u>
B. Thermal Properties		
4. Thermal Expansion, Specific Heat	Battelle	Thermal expansion and specific heat measurements on selected insulations and structural alloys and composites.
5. Thermal-Magnetothermal Conductivity	NBS, Cryogenics	Thermal conductivity and thermal conductivity in magnetic fields up to 50 kilogauss from 4-300 K of structural alloys and composites.
C. Composites		
6. Evaluation of Advanced Composites	NBS, Cryogenics	Screening tests (tensile, fatigue at 4 K) on selected candidate metal and non-metal base composites, including B-epoxy, C-epoxy and polyimide, PRD 49-epoxy, borsic-Al, steel-Al.
D. Data Compilation and Evaluation		
7. Handbook	Battelle	Publication of Handbook containing recommended best value data and complete set of references for over 80 additional materials (structural alloys, superconductors, electrical materials, and polymers). Data presented in graphical and tabular formats; mechanical, thermal, electromagnetic properties from 0-300 K.
8. Workshop Meeting	NBS, Cryogenics	Organization of meeting for mutual data sharing and interaction with service agencies and their contractors.

Table 3. Materials Objectives

PROPERTIES	STRUCTURAL	COMPOSITES	FERROMAGNETIC	SUPERCONDUCTING MAGNET	HIGH STRENGTH HIGH CONDUCTIVITY
Fracture Toughness, Fatigue Crack Growth Rate, Tensile	21-6-9(NBS,W) Inc 718(W) AISI 310(NBS) Low Expan Fe-Ni (W) Al 2014, 2219(NBS) A286(W)		Fe-49Ni(NBS) Fe-Ni-Co(NBS)		PD-135(W)
Fatigue	AISI 304(M)	B/epoxy(NBS) B/Al(NBS) C/epoxy(NBS) K-49/epoxy(NBS) S-glass/epoxy(NBS)			
Elastic	21-6-9(NBS) Al 2014, 2219(NBS)	B/Al(NBS)	Fe-49Ni(NBS) Fe-Ni-Co(NBS)		
Thermal Conductivity		B/Al(NBS) G/Al(NBS)	Fe-Ni-Co(NBS) Fe-49Ni(NBS)		
Thermal Expansion and Specific Heat	Ti-6Al-4V(B) Ti-5Al-2.5Sn(B) Inconel 600,706(B) Hastelloy B,C(B) Pyromet 680,860(B) Invar(B)	S-glass/epoxy(B) C/epoxy(B) Kevlar/epoxy(B) B/Al(B)		Potting Compds (B)	
Magneto-Thermal Conductivity	AISI 304(NBS) Ti-6Al-4V(NBS) 1100 Al(NBS)		Fe-49Ni(NBS)	NbTi(NBS) CuSn(NBS) CuNi(NBS)	
Magnetic	Inc 718(W) Low Expan Fe-Ni(W)		AISI 410(W) Fe-9Ni(W) Fe-78Ni(W) Fe-3Si(W) Armco Fe(W)		PD-135(W)

HIGHLIGHTS OF RESULTS

A general overview of the program is best obtained by examining the individual technical reports contained herein. A summary of materials studied during the third year of the program is given in table 3. The major technical accomplishments to date are briefly as follows:

The Handbook on Materials for Superconducting Machinery was published in 1974. The second edition of the Handbook was published in December of 1975. It included approximately eighty materials and approximately thirty mechanical and physical properties.

A variety of mechanical properties have been studied for six different composite materials at low temperatures.

Thermal expansion data at low-temperatures have now been obtained for about thirty materials, and low-temperature specific heats have been obtained for eight materials.

Elastic constants at low-temperatures have been determined for about thirty engineering alloys and a composite.

Magnetothermal conductivities, including thermal conductivities have been measured at low temperatures for ten materials, and the electrical conductivities of some of these materials have also been measured.

Thermal conductivity measurements on six additional structural materials, including a boron-epoxy composite, have also been made.

Fatigue-crack growth-rate data and fracture toughness data have been determined for about twenty-five important structural alloys and weldments. Also, conventional fatigue data were obtained for five alloys. For most of these materials, the usual tensile properties--elongation, reduction in area, yield strength and ultimate strength -- were also obtained.

A new major material conference, the International Cryogenic Materials Conference (ICMC) was held in Kingston, Ontario during July, 1975. Over sixty contributed papers were presented at the conference, and these will appear in a forthcoming book.

To facilitate information exchange, especially between researchers and designers, a third workshop will be held in Vail, Colorado in April, 1976.

HANDBOOK

One of the important outputs of this program is the Handbook. In one volume, it collects information, including data generated by this program, on the low-temperature properties of structural materials of possible use in superconducting machinery. The Handbook project is directed by K. R. Hanby at Battelle (Columbus Laboratories). It presents in loose-leaf format the mechanical, elastic, thermal, electrical, and magnetic properties of materials for superconducting machinery. Best-value data are presented either graphically and/or tabularly together with original data and test conditions. It contains data on about seventy metals, alloys, and polymers in various conditions: and it contains about 1000 references to the experimental literature. The principal reference sources were the Materials and Ceramics Information Center (MCIC), the Defense Documentation Center (DDC), and the Cryogenic Information Center (CIC).

Handbooks can be ordered from the National Technical Information Service (NTIS), Operation Division, Springfield, Virginia 22151 by requesting: Handbook on Materials for Superconducting Machinery (November 1974) MCIC - HB - 04 and its supplements.

SEMIANNUAL TECHNICAL REPORT

on

PREPARATION OF A HANDBOOK ON MECHANICAL,
THERMAL, ELECTRICAL, AND MAGNETIC PROPERTIES OF
MATERIALS FOR SUPERCONDUCTING MACHINERY

Sponsored by
Advanced Research Projects Agency
ARPA Order No. 2569
Program Code 4D10
Contract No. CST-8303

Contract Monitor
Cryogenics Division
National Bureau of Standards
Boulder, Colorado 80302

April 1, 1976

METALS AND CERAMICS INFORMATION CENTER
A Department of Defense Information Analysis Center
BATTELLE
Columbus Laboratories
505 King Avenue
Columbus, Ohio 43201
Telephone (614) 424-6424

FOREWORD

This research was supported by the Advanced Research Projects Agency of the Department of Defense with Dr. Edward C. VanReuth as Project Monitor. The handbook preparation task was subcontracted to Battelle-Columbus by the Cryogenics Division, National Bureau of Standards under Contract No. CST-8303 with Dr. Richard P. Reed as Program Manager and Contract Monitor.

The research described in this report was carried out under ARPA Order No. 2569 and Program Code 4D10 by the Metals and Ceramics Information Center (MCIC) with K. R. Hanby (614, 424-6424, Extension 1784) as the Program Coordinator, and K. E. Wilkes (614, 424-6424, Extension 3489), and J. K. Thompson (614, 424-6424, Extension 2612) as Principal Investigators. Contract No. CST-8303 includes two tasks. Task I of the current program provides for a compilation of low-temperature property data on an expanded series of selected materials for structural applications in superconducting machinery. These data compilations will be produced as the second Revision of the "Handbook on Materials for Superconducting Machinery". Task II provides for determination of thermal expansion and specific heat values at cryogenic temperatures for selected structural alloys. The Semiannual Technical Report on the latter program is presented under separate cover. Overall contract funding was \$90,000 with \$60,000 for the handbook program and \$30,000 for the laboratory study. The effective date of the current contract period was September 10, 1975, and the contract expiration date November 15, 1976.

DISCLAIMER

The views and conclusions contained in this document are those of the authors and should not be interpreted as necessarily representing the official policies, either expressed or implied, of the Advanced Research Projects Agency or the U. S. Government.

PREPARATION OF A HANDBOOK ON MECHANICAL, THERMAL, ELECTRICAL, AND MAGNETIC PROPERTIES OF MATERIALS FOR SUPERCONDUCTING MACHINERY

INTRODUCTION

This report describes the task of preparing the second revision (for producing the third edition) of the handbook and the progress made to date on that task. The end product of this task is a series of new or modified pages which, added to or replacing existing pages in the second edition, will produce an up-to-date handbook covering the materials scope shown in Table 1. Preparation of a first draft of those pages is scheduled for September 1976, and the published version, to be distributed by MCIC, is expected to be available by November 15, 1976.

SUMMARY

The specific properties that are included in the handbook are listed in Table 2. Data covering all of the properties in Table 2 are being sought for all of the materials of Table 1. The search for data includes all forms of the materials, including sheet, plate, forgings, extrusions, bar, rod, and weldments. All conditions of heat treatment are included. The types of sources that are being exploited are listed in Table 3. Table 4 indicates the information centers and indexing and abstracting services that are being used in attempts to retrieve pertinent data. In addition, the reference lists in all documents screened on this project, including those accessioned during previous contract periods, are being exploited systematically to maximize the recovery of data.

QUALITY CONTROL

The all-source search is turning up data of varying reliability with respect to precision, accuracy, pertinence, and validity. For convenience, each document screened on this project is evaluated and put into one of the three categories listed in Table 5.

Quality is being maintained initially by using only data from Category I sources. After Category I sources have all been exhausted, remaining information gaps will be filled insofar as possible with data from Category II sources (including handbooks). The latter will be identified explicitly in the handbook as lower quality data. Throughout, great pains are being taken to insure that primarily original data are used in the handbook. Average values are taken in lieu of original data only when there is reasonable assurance that the values are not based on original data which are already incorporated. When average values are used, they are weighted commensurate with the number of specimens each represents.

NEW FORMATS

The second revision of the handbook contains data on two types of material or component requiring small modifications of format — composite materials and weldments.

The format for presenting mechanical properties of composite materials was devised by Dr. M. B. Kasen of NBS — Boulder, who is responsible for the data search and presentation on composite materials for the current contract period. The heading for the composites format includes:

Composite Class — fiber and matrix material classes, such as Glass-Epoxy, Boron-Aluminum, etc.

Type — specific fiber and matrix materials

Layup

Fiber — particulars, including brand names

Matrix — essentially as given in type.

Nominal fiber volume fraction

Nominal ply thickness

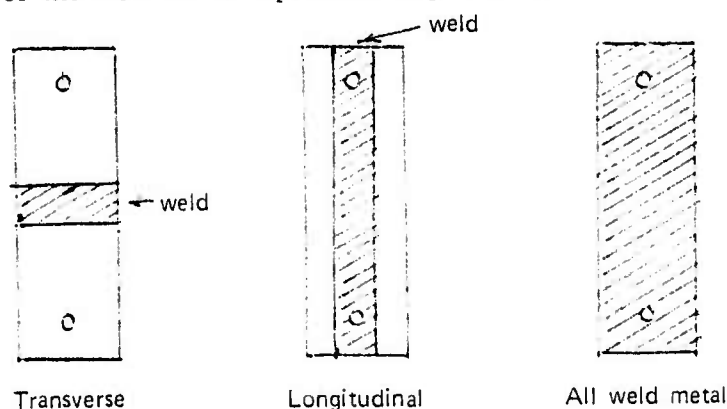
Nominal density

Comments — includes condition for metal matrix composites.

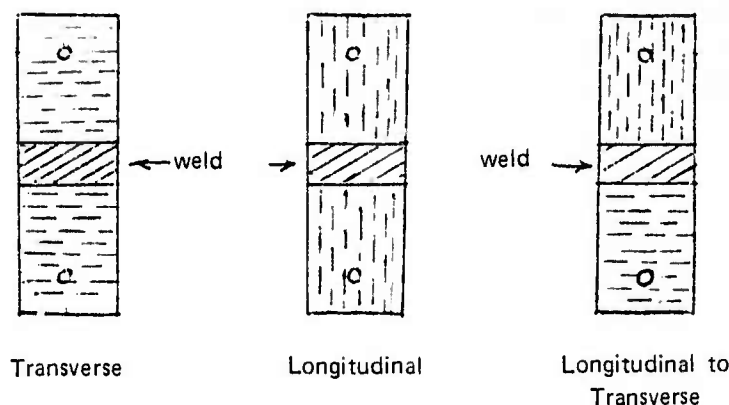
The format for presenting the properties of composites covered is similar to that for the monolithic materials, with the following modifications:

- Tensile proportional limit replaces yield stress
- Two moduli are included for each fiber orientation (E_1 and E_2)
- Stress level at which modulus changes from E_1 to E_2 is given
- Compressive, impact, thermal, and electrical properties for sheet normal are included
- Shear properties are given for both in-plane and interlaminar cases.

Data for weldments can be accommodated by the existing format; however, a few additional parameters must be specified over those required for parent metal only. Type of weld (TIG, MIG, electron beam) and filler material, if any, are specified on the line for "Form", in addition to the usual indication of sheet, plate, etc. "Thickness", specified on the next line, refers then to that of the plate, sheet, or bar from which the weldment is made. On the line for "Condition", the temper of the sheet, plate or bar prior to welding is given. In addition, the condition of the test specimen, "as welded", or specifications of postweld heat treatment, are given. Finally, to the far right of the same line, the orientation of the weld on the specimen is given:



For the transverse weld orientation only, the data in the table will be given for one or more of the following grain orientations:



For the other two weld orientations, the grain orientation is not of significance, and the "longitudinal" section of the tensile data format will be used.

PROGRESS

All of the documents already accessioned for this program during previous contract periods have been re-examined for data applicable to the present contract period. Reference lists in them have exploited systematically, new sources identified, and documents ordered. Many of the items cited previously in the bibliography have, on re-examination, been rejected. Secondary data have been identified for possible later use in filling gaps.

Computer printouts from previous searches are being looked at again in light of known information gaps, and some items previously rejected are being retrieved. A computer run has been completed by NBS-Cryogenic Data Center covering update of searches on materials previously in the scope and comprehensive searches for data on the materials added this contract period.

The following handbooks, or data collections, have been examined, and secondary data useful for filling gaps identified:

Cryogenic Materials Handbook - Aug. 1968
 Damage Tolerant Design Handbook (MCIC)
 Alloy 718 Processes and Properties Handbook (DMIC)
 DMIC Data Sheets
 Structural Alloys Handbook (MPDC)
 Aerospace Structural Alloys Handbook (MPDC)
 NBS Monograph 13 (1960)

The latest semiannual report for this program has been examined, and pertinent data extracted.

Presently, the process of evaluating data tentatively selected for incorporation in the third edition by careful comparison with data already in the handbook is underway. A few data sheets for actual inclusion have been completed.

Dr. Kasen has already completed and forwarded to Battelle data sheets for incorporation in the handbook covering eight specific composite types, as follows:

<u>Class</u>	<u>Type</u>
Glass - Epoxy	181/Epon 828(CL)
Glass - Epoxy	1581/E-787 (58-68R)
Glass - Epoxy	S-901/NASA Resin 2
Boron - Epoxy	4.0 mil Boron/2387
Boron - Epoxy	5.6 mil Boron/2387
Graphite - Epoxy	AS/NASA Resin 2
Graphite - Epoxy	HT-S/X-904
Boron - Aluminum	5.6 mil Boron/6061

HANDBOOK ON MATERIALS FOR SUPERCONDUCTING MACHINERY—
3rd Edition (2nd Revision)

TABLE 1. MATERIALS SCOPE

Aluminum and Magnesium Alloys

99.9% aluminum
E C aluminum
1050
1100
2014
2024
2219
5083
5456
6061
7005
7006
7039

AZ31B

Copper and Copper Alloys

99.96% Cu
Electrolytic tough pitch
OFHC
Phosphorized
90Cu-10Zn
80Cu-20Zn
70Cu-30Zn
90Cu-10Ni
80Cu-20Ni
70Cu-30Ni
Cu-Be (1.6-1.8)
Cu-Be (1.8-2.0)
95Cu-5Sn
92Cu-8Sn
90Cu-10Sn
Cu-0.2Zr (Amzirc)
Cu-0.4Cr-0.4Cd (PD-135)
Cu + 0.2Al₂O₃
Cu + 0.7Al₂O₃
Cu + 1.1Al₂O₃
Aluminum Bronze

Nickel and Cobalt and Their Alloys

High purity nickel
Nickel "A"
K Monel
Inconel 600
Inconel X-750
Alloy 718
Inconel 706
Invar 36
Ni-Span C
unnamed Inco LEA alloy

Steels and Iron Alloys

3Ni Steel
5Ni Steel
9Ni Steel
18Ni (200) Maraging Steel
Transformer Steel
1010 Steel
Armco Iron
Fe(47-50)-Ni

Stainless Steels

AISI 301
AISI 303
AISI 304
AISI 304L
AISI 310
AISI 310S
AISI 316
AISI 321
AISI 347
AISI 410
AISI 416
A-286
Kromarc-58
Armco 21-6-9
Armco 22-13-5

Materials Scope (cont.)Titanium and Titanium Alloys

Ti-65A
Ti-75A
Ti-5Al-2.5Sn
Ti-5Al-2.5Sn (ELI)
Ti-6Al-4V
Ti-6Al-4V (ELI)

Special Metals and Alloys

Niobium
Nb₃Sn
Nb-Zr alloys
Nb-Ti alloys
Nb-Ti+Cu composites
V₃Ga

Composites

Glass/Epoxy
Boron/Epoxy
Graphite/Epoxy
Boron/Aluminum

Polymers

Polyethylene
Polychlorotrifluoroethylene
Polytetrafluoroethylene
Polymethylmethacrylate
Polystyrene
Polyvinylacetate

TABLE 2. PROPERTY SCOPEMechanical Properties

Tensile

Ultimate, yield, elongation, reduction in area

Elastic modulus, Poisson's ratio

Notch tensile strength

Compressive

Ultimate, yield

Elastic modulus

Shear

Ultimate

Shear modulus

Impact

Charpy V-Notch

Izod (polymers only)

Fracture Toughness

 K_{Ic} , K_{IIc} , J_{Ic}

Fatigue (Axial and Flexure)

S-N Curves

da/dN Curves

Flexure

Ultimate, yield

Elastic moduli

} polymers only

Thermal and Electrical Properties

Thermal Conductivity

Magnetothermal Conductivity

Thermal Expansion

Specific Heat

Electrical Resistivity

Magnetic Properties

Susceptibility

Permeability

TABLE 3. SOURCES OF DATA

Reports of Government-sponsored R&D
(including semiannual reports of this ARPA contract)

Open published literature
(including handbooks, state-of-the-art reports, and conference proceedings)

Private communication

TABLE 4. ACCESS TO DATA

Information Centers

- NBS Cryogenic Information Center
- Metals and Ceramics Information Center (MCIC)
- Defense Documentation Center (DDC)
- Thermophysical and Electronic Properties Information Analysis Center (TEPIAC)
- Copper Data Center
- Iron Information Center
- Plastics Technical Evaluation Center (Plastec)
- Mechanical Properties Data Center (MPDC)

Indexing and Abstracting Services

Chemical Abstracts	}	Machine searchable through MCIC
Metallurgical Abstracts		
Engineering Index		
Nuclear Abstracts		

TABLE 5. CATEGORIES OF SOURCE DOCUMENTS

- I contains data that meet precision, accuracy, pertinence, and validity criteria as specified below
- II a review (IIR); or contains data not meeting the criteria as specified for category I — (IID)
- III contains no pertinent data — reject

Criterion	Category I	Category II
Precision	Tabular data on properties other than fatigue and graphical S/N or da/dN data	Graphical data (except fatigue data)
Accuracy	Data for which form, condition, specimen thickness and number of specimens per value are given	Data for which any of the parameters required for Category I are not specified*
Pertinence	All tabular data for room temperature and below, where lowest test temperature was 77 K or below. Data from references not older than 1950	**
Validity	Valid K_{Ic} data. J_{Ic} data based on compact specimens	Invalid K_{Ic} data. J_{Ic} data based on other than compact specimens

*—This criterion is not inviolate. It has been overlooked occasionally for mechanical properties and regularly for thermal and magnetic properties data.

**—References containing no data for temperatures below 77 K and pre-1950 references are put in Category III — reject.

SEMIANNUAL TECHNICAL REPORT

on

LOW-TEMPERATURE THERMAL EXPANSION AND SPECIFIC HEAT
PROPERTIES OF STRUCTURAL MATERIALS

Sponsored by

ADVANCED RESEARCH PROJECTS AGENCY
ARPA Order No. 2569
Program Code 4D10
Contract No. CST-8303

Contract Monitor

CRYOGENICS DIVISION
NATIONAL BUREAU OF STANDARDS
Boulder, Colorado 80302

by

F. J. Jelinek and E. W. Collings

April 30, 1976

BATTELLE
Columbus Laboratories
505 King Avenue
Columbus, Ohio 43201

SEMIANNUAL TECHNICAL REPORT

on

LOW-TEMPERATURE THERMAL EXPANSION AND SPECIFIC HEAT
PROPERTIES OF STRUCTURAL MATERIALS

Sponsored by

ADVANCED RESEARCH PROJECTS AGENCY
ARPA Order No. 2569
Program Code 4D10
Contract No. CST-8303

from

BATTELLE
Columbus Laboratories

F. J. Jelinek and E. W. Collings

April 30, 1976

FOREWORD

This research was supported by the Advanced Research Projects Agency of the Department of Defense and was monitored by the Cryogenics Division, National Bureau of Standards under Contract No. CST-8303. Dr. Richard P. Reed serves as Program Manager and Contract Monitor.

The research was carried out under ARPA Order No. 2569 and Program Code 4D10 by the Materials Technology and Metal Science Sections of Battelle-Columbus Laboratories with F. J. Jelinek (614-424-6424, Extension 1735) and E. W. Collings (614-424-6424, Extension 1664) as Principal Investigators. Contract CST-8303, under the overall coordination of K. R. Hanby, covers both the handbook program and the property measurement program. Only the property measurement program is presented here. Effective date of the contract was September 10, 1975, and the contract expiration date is September 10, 1976.

DISCLAIMER

The views and conclusions contained in this document are those of the authors and should not be interpreted as necessarily representing the official policies, either expressed or implied, of the Advanced Research Projects Agency or the U.S. Government.

TECHNICAL REPORT SUMMARY

The development of superconducting electrical machinery requires the suitable engineering property characterization of all candidate materials at cryogenic temperatures. This program involves the determination of thermal expansion and specific heat for several structural materials in the cryogenic temperature region (4.2 to 300 K).

Materials selected for this study period were supplied through the cooperation of Westinghouse R&D and the National Bureau of Standards. Additional materials were secured from within Battelle-Columbus Laboratories or purchased from an appropriate vendor. All materials are appropriately labeled in the text of the report.

Thermal expansion measurements were performed utilizing a fused silica dilatometer with a linear differential transducer as the dilatometer head. The accuracy of the measurement is 1 percent. Specific heat at low temperatures is measured to 1 percent by adiabatic calorimetry from a method developed by Nernst. In this method, small increments of heat are supplied to a thermally insulated sample, and the accompanying temperature increase is measured.

In this reporting period, thermal expansion characteristics of eight materials were determined in the temperature range 77 to 300 K. The specific heats of two new materials were also measured.

PROGRAM PROGRESS

PART I. THERMAL EXPANSION

Introduction

Low-temperature thermal expansion results are reported for eight materials in the temperature range 77 to 300 K. The technique used to perform the measurements was a fused silica dilatometer which has been previously described.

In addition to the two materials furnished by Westinghouse for this study, we have included four composite materials furnished by NBS and two alloys supplied by Battelle-Columbus Laboratories. Table 1 lists these materials with a brief description and/or heat treatment used.

TABLE 1. LIST OF THERMAL EXPANSION SPECIMENS
INCLUDED IN THIS REPORT

COMPOSITES

5.6 Mil Boron/5505 Epoxy	- Fiber Vol. Frac. 50 %
Type "AS" Graphite/NASA Resin 2	- Fiber Vol. Frac. 60 %
5.6 Mil Boron/6061 Aluminum	- 6061-F Temper
S-901 Glass (20 End)/NASA Resin 2	- Fiber Vol. Frac. 60 %

ALLOYS

NITRONIC 33	- ST/FC
NITRONIC 33	- STQ
Ti-6Al-4V	- ANNEALED
A-286	- ST

Data Presentation

The results reported in this work are shown as percent contraction versus temperature (K) with all data normalized at the ice point (273 K).

Figures 1 through 8 illustrate the initial results in graphic form. The results in the liquid helium range have been completed, but were not available for inclusion in this report. The complete data in tabular and graphic form will be presented in the final semiannual report in October, 1976.

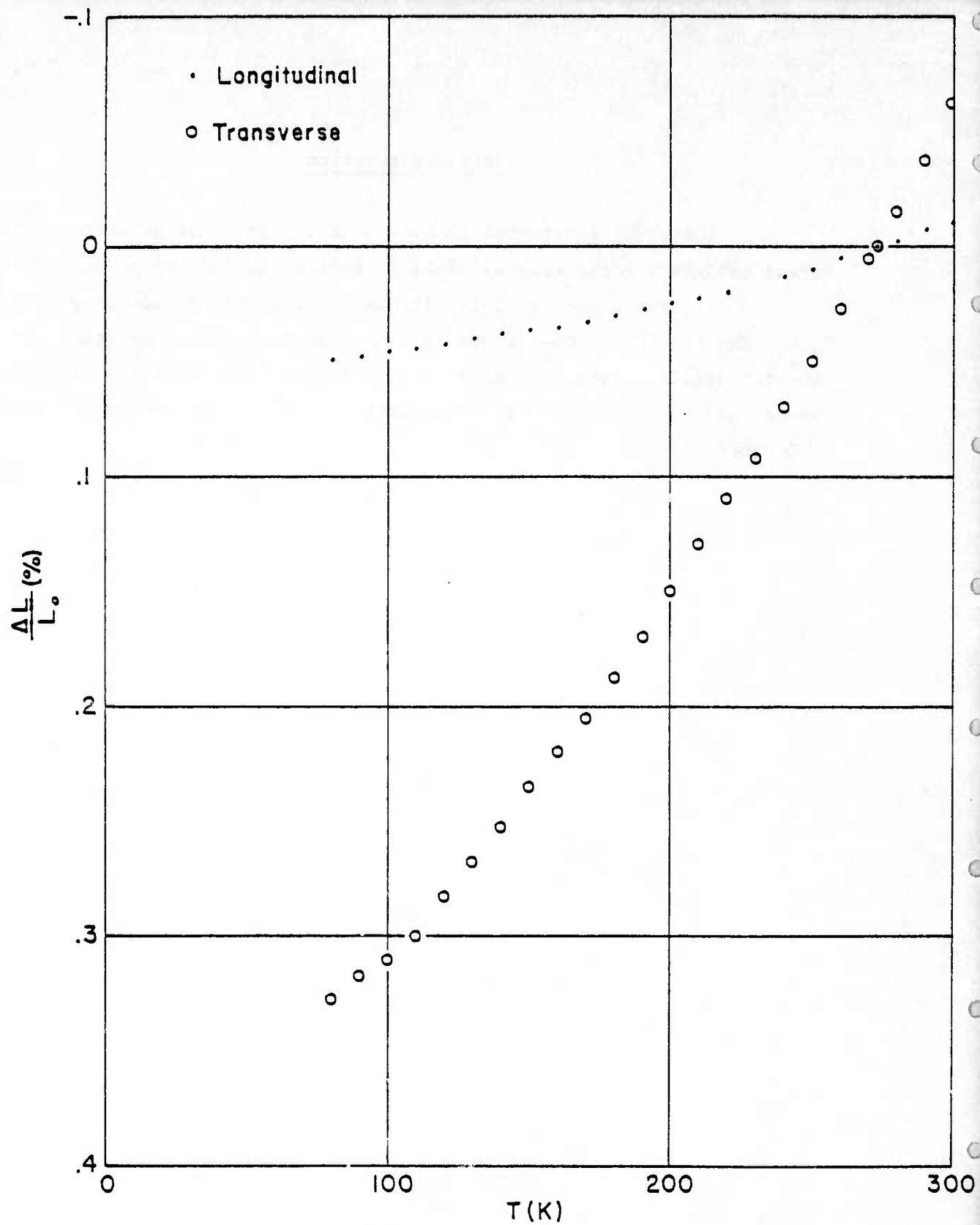


FIGURE 1. THERMAL EXPANSION BEHAVIOR OF 5.6 MIL BORON-5505 EPOXY, NOMINAL FIBER VOLUME FRACTION ABOUT 50 %

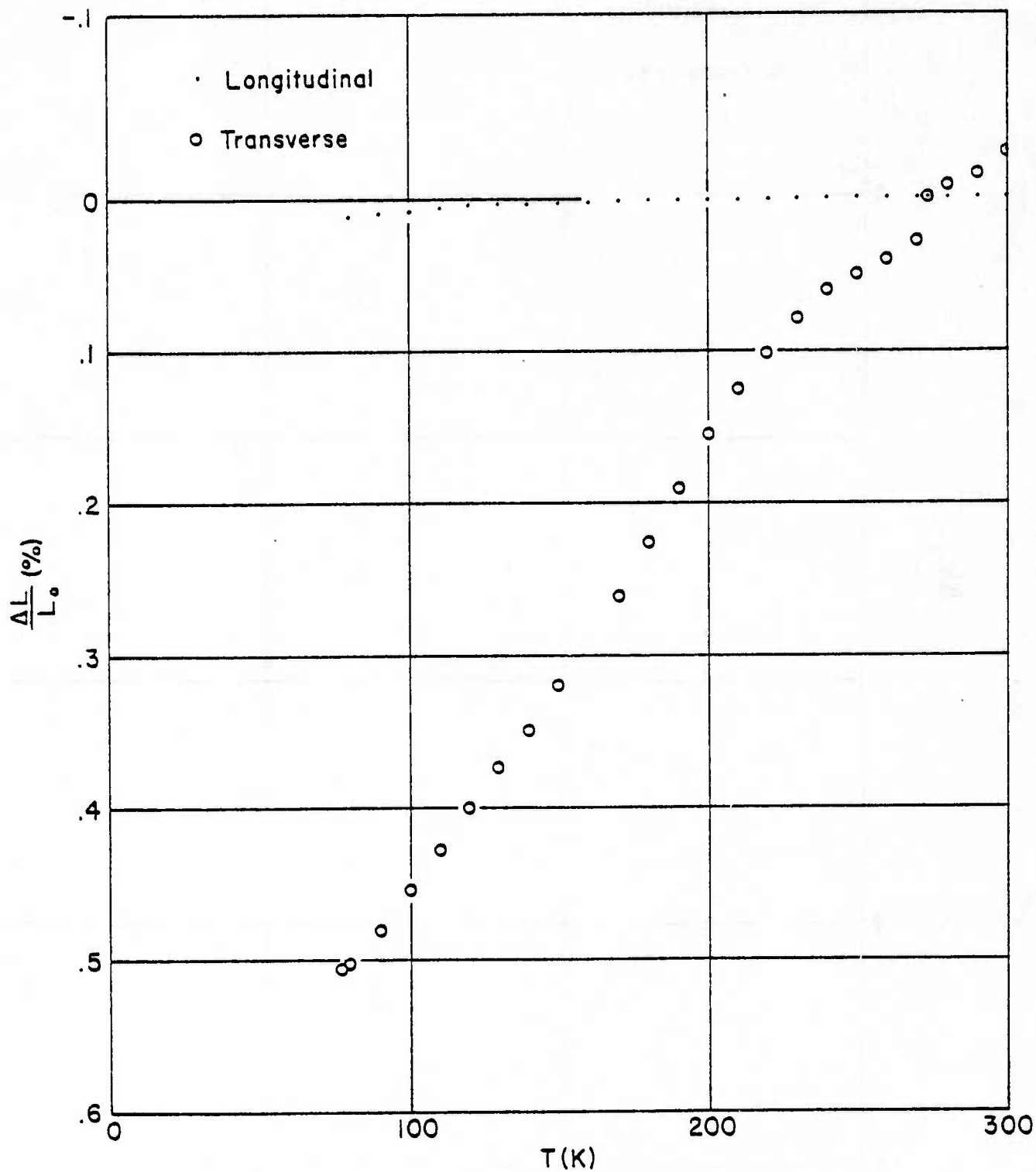


FIGURE 2. THERMAL EXPANSION BEHAVIOR OF TYPE AS GRAPHITE-NASA RESIN 2, NOMINAL FIBER VOLUME FRACTION ABOUT 60 %

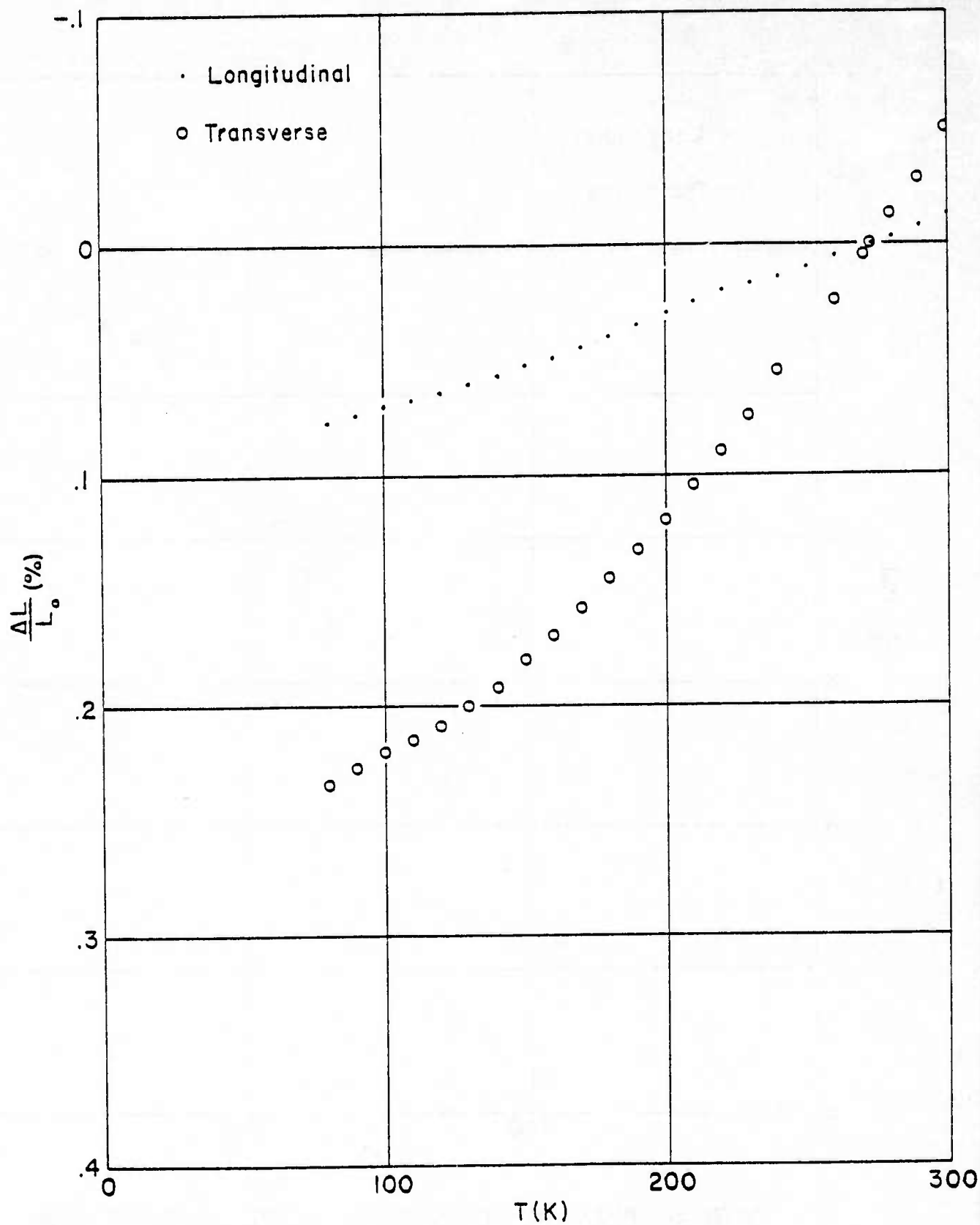


FIGURE 3. THERMAL EXPANSION BEHAVIOR OF 5.6 MIL BORON-6061 ALUMINUM, F TEMPER

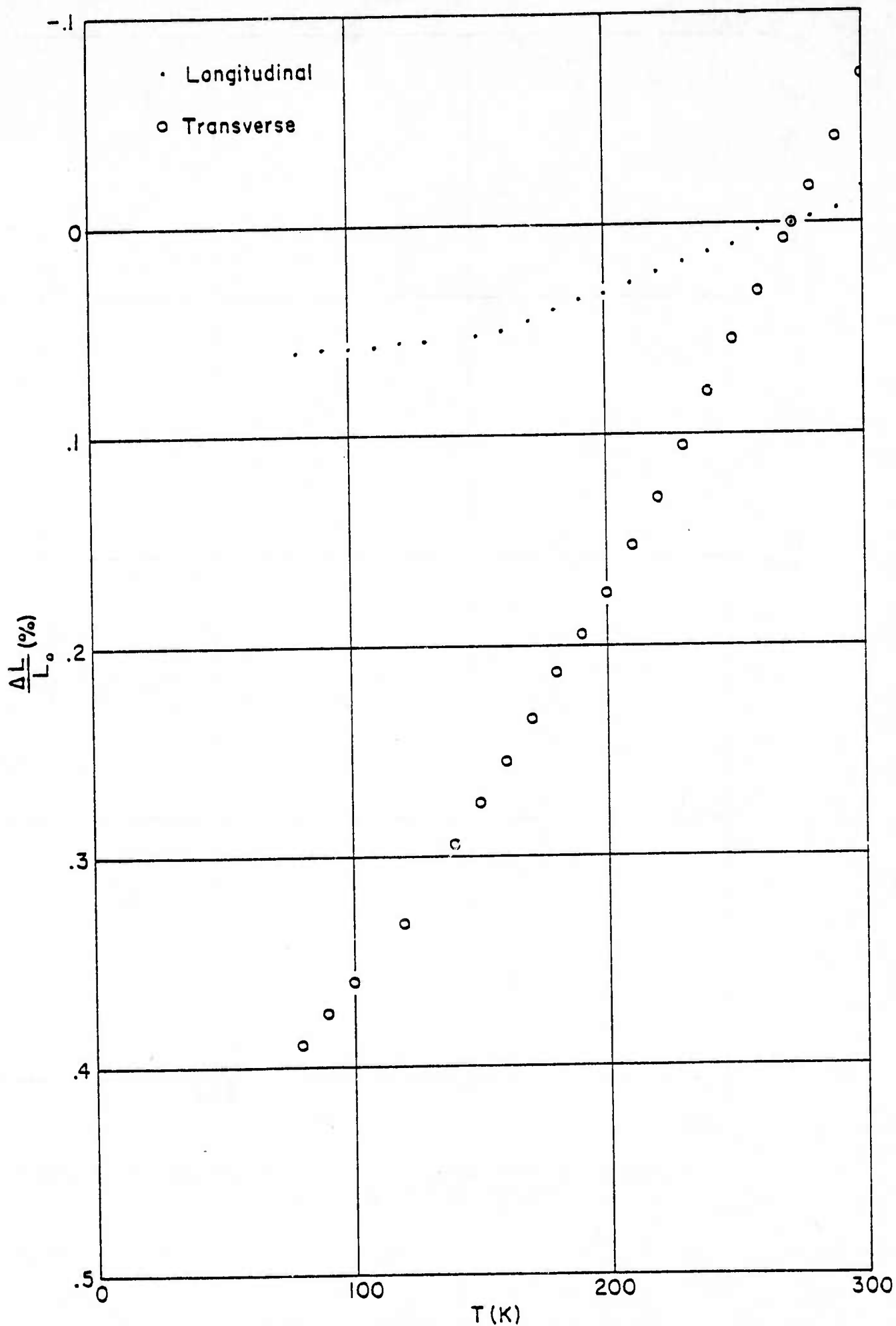


FIGURE 4. THERMAL EXPANSION BEHAVIOR OF S-901 GLASS, 20 END - NASA RESIN 2, NOMINAL FIBER VOLUME FRACTION ABOUT 60 %

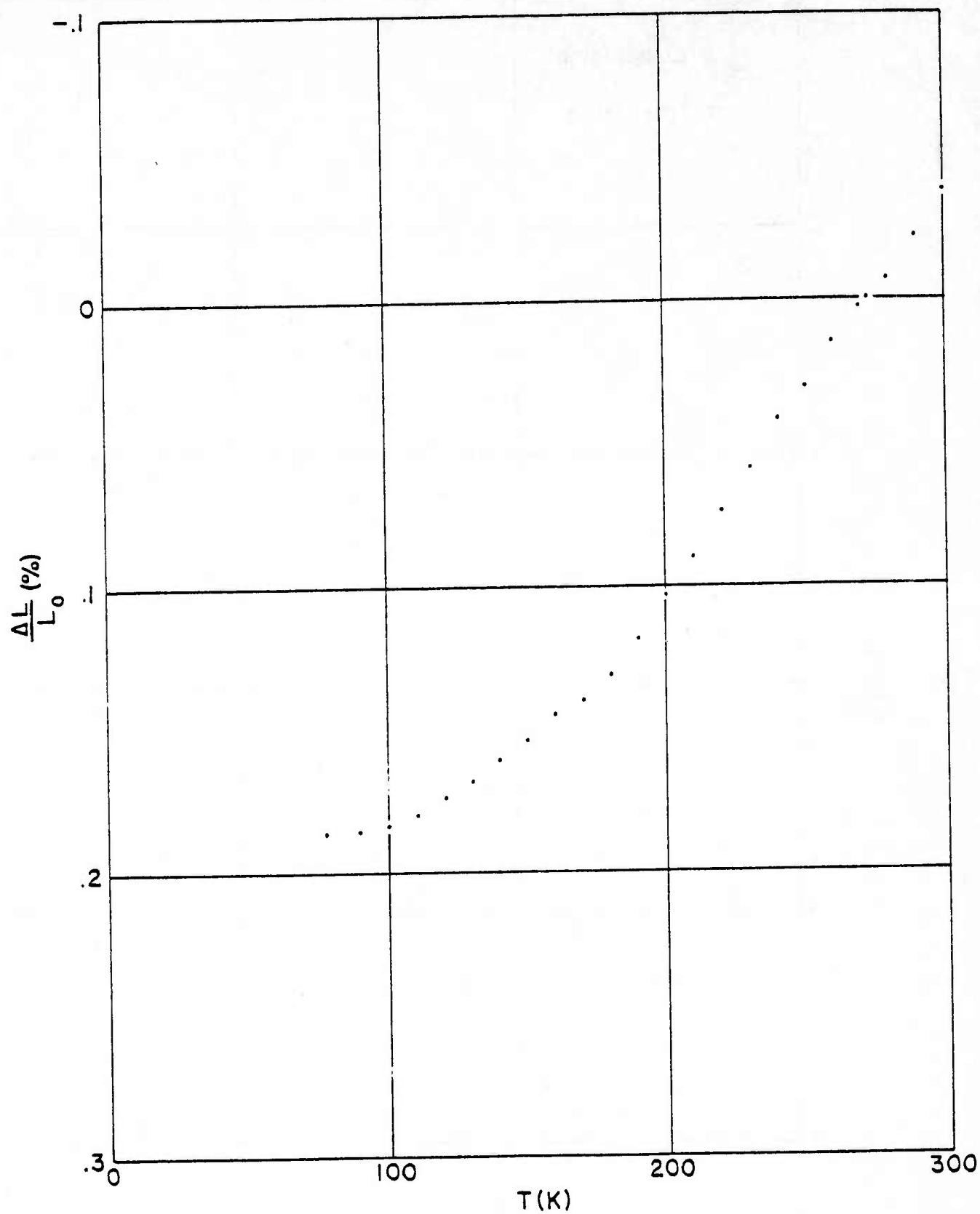


FIGURE 5. THERMAL EXPANSION BEHAVIOR OF NITRONIC 33, SOLUTION TREATED AND FURNACE COOLED

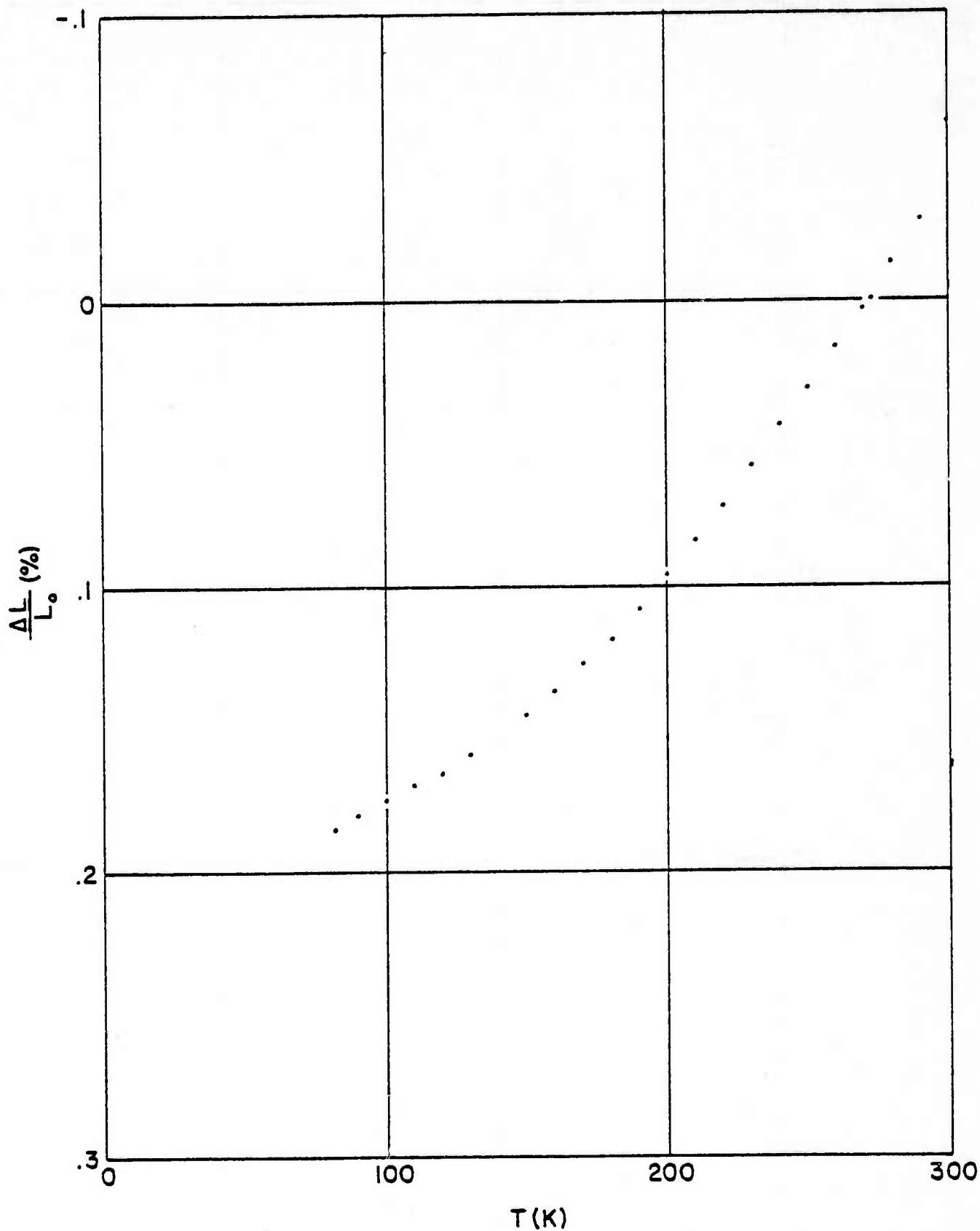


FIGURE 6. THERMAL EXPANSION BEHAVIOR OF NITRONIC 33, SOLUTION TREATED AND QUENCHED

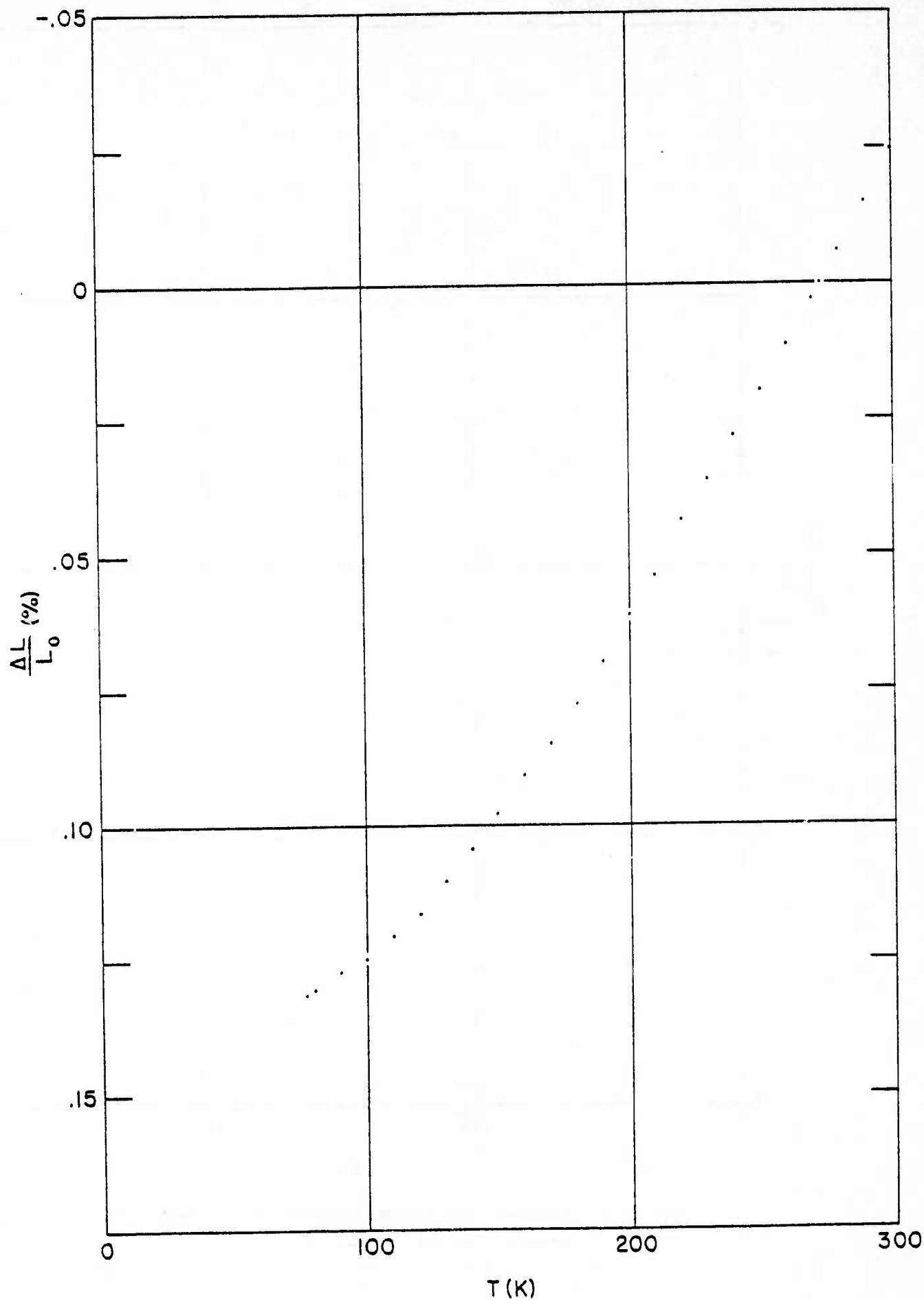


FIGURE 7. THERMAL EXPANSION BEHAVIOR OF Ti-6Al-4V IN THE ANNEALED CONDITION

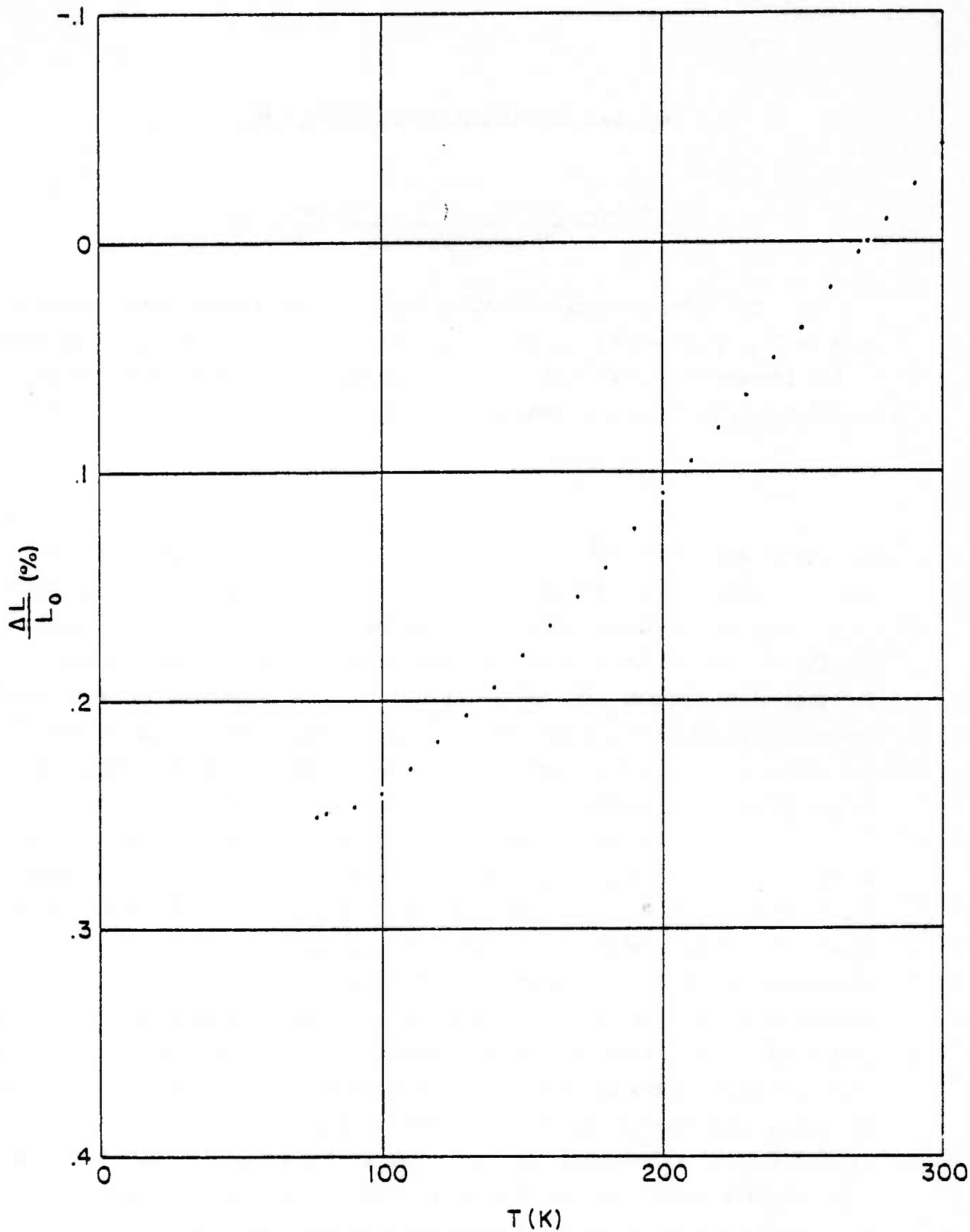


FIGURE 8. THERMAL EXPANSION BEHAVIOR OF ALLOY A-286 SOLUTION TREATED

PART II. LOW-TEMPERATURE SPECIFIC HEAT

Least-Squares Fitting of Low-Temperature Specific Heat Data

The lattice specific heat of solids at low temperature generally goes as T^3 . With metals, an additional term, proportional to T , is important at low temperatures. Thus, to a first approximation, the low-temperature specific heat of metals is usually written

$$C = \gamma T + \beta T^3 .$$

In fitting the experimental data, however, improvements of fit have been obtained by extending the above equation as a Taylor expansion in odd powers of T . Care must be used in carrying out such a procedure since, although the fit may get better with the addition of more and more terms, their physical significances tend to become obscured as the goodness of fit exceeds the precision of the experimental data. For example, we have noted for stainless steel data that fits out to T^5 and T^7 have resulted in negative values of β and consequently, θ_D .

There seems no a priori reason why an odd-power expansion should be selected over an expansion in both odd and even powers of T . Accordingly, for a metallic sample we experimented with both odd-power and odd-and-even power fits to the specific heat data. The results of this procedure are summarized in Table 2. Inspection of Table 2 reveals the competition between terms that occur as the expansion is carried out to higher and higher powers of T . When both odd and even powers of T are used, large positive and negative coefficients are generated. Using the terms in T and T^3 as references, we notice large variations in the coefficients occurring until the odd-power expansion to T^7 is reached. At this point it seems that the odd-power, four-term expansion merely serves as a correction to the simple two-term expression. As sources of γ and θ_D either the two-term or the four-term odd-power expansion could be used in this particular case.

In analyzing the data each alloy class is treated individually and the decision on the number of terms to be used is made on the basis of goodness of fit and physical reality.

TABLE 2. EXAMPLE OF MULTI-TERM LEAST SQUARES FITTING OF SPECIFIC HEAT DATA FOR A METALLIC SAMPLE (IN THIS CASE A BORON-ALUMINUM COMPOSITE)

$$C = \alpha_1 T + \alpha_3 T^3 + \alpha_4 T^4 + \alpha_5 T^5 + \alpha_6 T^6 + \alpha_7 T^7$$

(J/kg-degⁿ)

$10^2 \alpha_1$	$10^4 \alpha_3$	$10^6 \alpha_4$	$10^8 \alpha_5$	$10^8 \alpha_6$	$10^{10} \alpha_7$
2.65	4.98				
2.83	4.40	2.99			
2.58	6.01	-15.49	54.47		
2.80	4.64		9.35		
2.73	4.37	14.15	-131.45	3.90	
2.61	6.39	-36.44	369.14	-18.28	36.53
2.67	5.06		-19.28		4.90

Low Temperature Specific Heat of
Metallic Alloys

In October, 1975, we reported on the low temperature specific heats of the following alloys, fitting the results to a three-term expression of the form $C = A + \gamma T + \beta T^3$.

Inconel X750 HIP
Inconel X750 HIP STDA
Inconel X706 VIM-VAR ST
Inconel X706 VIM-VAR STDA
Inconel X760 VIM-EFR ST

During the current reporting period we added one more alloy to this list (Inconel X706 VIM-EFR STDA) and with the aid of the published chemical compositions shown in Table 3 (Westinghouse contribution to NBS-ARPA reports, I and IV), have calculated average molar weights and hence Debye temperatures (from the measured lattice specific heats) for all the above alloys.

The complete set of low temperature specific heat coefficient data are listed in Table 4, while specific heat values fitted to a set of selected temperatures are listed in Table 5 (in the 4-20 K range).

Low-Temperature Specific Heat of
A Glass-Epoxy Composite

The specimen studied here was a sample of a glass-epoxy potting material used in the fabrication of an assembly of multifilamentary Nb-Ti-Cu wires. The assembled superconductive bus is used in the Navy superconducting motor.

The experimental data were fitted to numerous polynomial expansions, after which it was decided that the four-term expression

$$C = \alpha_1 \left(\frac{T}{10}\right) + \alpha_2 \left(\frac{T}{10}\right)^2 + \alpha_3 \left(\frac{T}{10}\right)^3 + \alpha_4 \left(\frac{T}{10}\right)^4$$

gave the best description. The values of the polynomial coefficients are listed in Table 6. It is necessary to use the two columns presented because of the higher precision of the data above 10 K in this case.

TABLE 3. PRINCIPAL COMPONENTS AND CALCULATED MOLAR WEIGHT OF THE STAINLESS STEELS
AND INCONELS USED IN THIS PROGRAM

Alloy Name	Melting Practice (MP)	Compositions (wt. percent)			Molar Weight (MP)
		Ni	Cr	Fe	
Stainless Steel 310S	Base metal	19.66	24.40	53.09	55.21
	Weld plate	20.80	25.00	51.58	
Inconel X750	VIM-VAR (MP-1)	73.0	15.2	6.47	57.10
	AAM-VAR (MP-2)	74.82	14.19	6.22	56.74
	VIM (MP-3)	73.02	15.40	6.87	56.64
	HIP [pre-HIP, see MP-1]				
Inconel 706	VIM-EFR	41.49	16.09	37.27	56.65
	VIM-VAR	41.80	16.33	36.64	56.71

TABLE 4. LOW-TEMPERATURE SPECIFIC HEAT PARAMETERS FOR SIX INCONEL ALLOYS

$$C = A + \gamma T + \beta T^3$$

Parameter	Alloy and Parameter Value*				
	Inconel X750 (HIP) as-HIP	Inconel X750 (HIP) STDA	Inconel 706 VIM-VAR ST	Inconel 706 VIM-VAR STDA	Inconel 706 VIM-EFR ST Inconel 706 VIM-EFR STDA
$A, 10^{-1} \text{ J/kg-deg}$	1.88 ± 0.08	1.63 ± 0.08	2.33 ± 0.07	2.35 ± 0.08	2.21 ± 0.06 3.63 ± 0.10
$\gamma, 10^{-1} \text{ J/kg-deg}^2$	2.36 ± 0.02	2.30 ± 0.02	3.08 ± 0.02	3.13 ± 0.02	3.10 ± 0.02 2.91 ± 0.02
$\beta, 10^{-4} \text{ J/kg-deg}^4$	3.16 ± 0.07	3.17 ± 0.06	3.99 ± 0.06	3.45 ± 0.09	4.10 ± 0.05 4.29 ± 0.06
$\theta_D, \text{ K}$	476 ± 4	475 ± 3	441 ± 3	463 ± 4	437 ± 2 431 ± 2

* The standard errors are indicated.

TABLE 5. LOW-TEMPERATURE SPECIFIC HEATS (FITTED VALUES) FOR SIX INCONEL ALLOYS AT SPECIFIED TEMPERATURES

Temperature (K)	Alloy and Specific Heat, C (J/kg-deg)*							
	Inconel X750 (HIP) as-HIP	Inconel X750 (HIP) STDA	Inconel 706 VIM-VAR ST	Inconel 706 VIM-VAR STDA	Inconel 706 VIM-EFR ST	Inconel 706 VIM-EFR STDA	Inconel 706 VIM-EFR STDA	
4.0	1.15 ± 0.02	1.10 ± 0.02	1.49 ± 0.02	1.51 ± 0.02	1.49 ± 0.01	1.55 ± 0.02		
5.0	1.41 ± 0.02	1.35 ± 0.02	1.82 ± 0.02	1.84 ± 0.02	1.82 ± 0.02	1.87 ± 0.02		
10.0	2.86 ± 0.04	2.78 ± 0.03	3.71 ± 0.04	3.71 ± 0.04	3.72 ± 0.03	3.70 ± 0.04		
15.0	4.80 ± 0.06	4.68 ± 0.06	6.20 ± 0.06	6.09 ± 0.07	6.22 ± 0.06	6.18 ± 0.06		
20.0	7.44 ± 0.10	7.30 ± 0.10	9.59 ± 0.09	9.26 ± 0.12	9.63 ± 0.09	9.62 ± 0.09		

* The standard errors are indicated.

TABLE 6. LOW-TEMPERATURE SPECIFIC HEAT COEFFICIENTS FOR
A GLASS-EPOXY COMPOSITE

$$C = \alpha_1 \left(\frac{T}{10} \right) + \alpha_2 \left(\frac{T}{10} \right)^2 + \alpha_3 \left(\frac{T}{10} \right)^3 + \alpha_4 \left(\frac{T}{10} \right)^4$$

Coefficient	Value (J/kg-deg ⁿ)	
	below 10K	above 10K
α_1	-1.81 ± 0.14	-1.81 ± 0.05
α_2	9.48 ± 0.46	9.48 ± 0.15
α_3	1.99 ± 0.45	1.99 ± 0.15
α_4	-1.05 ± 0.13	-1.05 ± 0.04

As indicated in Table 6 the quadratic term is dominant. Usually this term is absent in the expression for specific heat of a solid, as dictated by the physics of the three-dimensional model. The presence of a dominant quadratic term indicates the presence of two-dimensional, rather than three-dimensional, arrays of atomic oscillators. It would be interesting to correlate this observation with further research into the chemical physics of polymers such as epoxy resins.

Table 7 is a list of fitted specific heat values for a sample of fiberglass reinforced resin at a set of selected temperatures.

TABLE 7. LOW-TEMPERATURE SPECIFIC HEAT OF A GLASS-EPOXY COMPOSITE AT SPECIFIED TEMPERATURES

Temperature (K)	Specific Heat, C (J/kg-deg)
4.0	0.89 \pm 0.15
5.0	1.65 \pm 0.25
10.0	8.6 \pm 1.2
15.0	20.0 \pm 2.2
20.0	33.4 \pm 5.1

Specific Heat of A Boron Reinforced
Aluminum Composite

Low-Temperature Specific Heat

Low-temperature specific heat data for a boron-reinforced aluminum composite were fitted to the following expressions

$$C = \alpha_1 T + \alpha_3 T^3$$

and
$$C = \alpha_1 T + \alpha_3 T^3 + \alpha_5 T^5 + \alpha_7 T^7$$

The results of so doing, expressed in terms of the regression coefficients, α_1 , are summarized in Table 8. Finally, in Table 9, are presented lists of actual specific heat values fitted at selected temperatures in the range 4.0 to 20.0 K. The four-term expression gives a better fit to the data (as indicated by the standard deviations listed) but no appreciable change (about 1-2%) in the fitted specific heat values.

Intermediate-Temperature Specific Heat

Specific heat data for temperatures near 80 K and 300 K, respectively, are presented in Table 10. Straight lines fitted to each cluster of three (C,T) datum points were extrapolated to 80.0 K and 300.0 K, respectively. The scatters of the specific heat values about the fitted line (temperatures being assumed free from error) were used to determine the standard error. The results of carrying out this procedure are presented in Table 11.

TABLE 8. LOW-TEMPERATURE SPECIFIC HEAT COEFFICIENTS
FOR BORON-ALUMINUM

$$C = \alpha_1 T + \alpha_3 T^3 + \alpha_5 T^5 + \alpha_7 T^7$$

Coefficient	Value (J/kg-deg ⁿ)	
	2-term fit	4-term fit
α_1	$(2.65 \pm 0.02) \times 10^{-2}$	$(2.67 \pm 0.03) \times 10^{-2}$
α_3	$(4.98 \pm 0.02) \times 10^{-4}$	$(5.06 \pm 0.07) \times 10^{-4}$
α_5		$(-1.93 \pm 0.45) \times 10^{-7}$
α_7		$(4.90 \pm 0.75) \times 10^{-10}$

TABLE 9. FITTED LOW-TEMPERATURE SPECIFIC HEAT OF BORON-ALUMINUM
AT SPECIFIED TEMPERATURES

Temperature (K)	Specific Heat, C (J/kg-deg)	
	2-term fit	4-term fit
4.0	0.138 ± 0.002	0.139 ± 0.002
5.0	0.195 ± 0.005	0.196 ± 0.003
10.0	0.763 ± 0.046	0.759 ± 0.015
15.0	2.08 ± 0.16	2.05 ± 0.08
20.0	4.51 ± 0.38	4.59 ± 0.30

TABLE 10. MEASURED SPECIFIC HEATS OF A BORON-ALUMINUM COMPOSITE
AT TEMPERATURES NEAR 80K AND 300 K RESPECTIVELY

Temperature (K)	Specific Heat (J/Kg-deg.)
78.71	200
79.26	200
79.81	206
296.61	944
297.01	962
297.46	977

TABLE 11. SPECIFIC HEAT OF BORON-ALUMINUM COMPOSITE ADJUSTED BY
LINEAR FITTING TO TEMPERATURES OF 80.0 K AND 300.0 K*

Temperature (K)	Specific Heat (J/kg-deg.)
80.0	206 \pm 2
300.0	1076 \pm 1

* Standard errors are indicated.

Discussion of the Boron-Aluminum Data

In order to determine the applicability of the law of mixtures to the specific heat of a fiber-reinforced composite, the sample was chemically analyzed for aluminum content and the assumption was made that the remainder of the specimen could be regarded as boron (the presence of the tungsten core, or its reaction product with the surrounding boron was neglected).

Low-Temperature Specific Heat. No low-temperature specific heat data exist for boron; however, measurements in the temperature range 60 to 150 K have yielded a Debye temperature, Θ_D , of 1219 K⁽¹⁾. Another reported value is 1220 K⁽²⁾, and this we will use in the following analysis.

The input data to be used in the synthesis (law of mixtures) of a lattice specific heat coefficient for boron-aluminum are listed in Table 12.

TABLE 12. INPUT DATA - B AND Al VALUES

	γ J/Kg-deg ²	Θ_D K	M	10 ⁴ β	wgt % Present (100 f)
Al	0.0504	426	26.9815	9.320	49.1
B	Unknown	1220	10.811	0.990	Assume balance

The average specific heat coefficient ($\langle\beta\rangle$) is expected to be

$$\begin{aligned}\langle\beta\rangle &= f\beta_{Al} + (1-f)\beta_B \\ &= 5.08 \times 10^{-4} \text{ J/kg-deg}^4\end{aligned}$$

in excellent agreement with the measured value (4-term fit, Table 8) of $5.06 \times 10^{-4} \text{ J/kg-deg}^4$. In addition, a γ for boron may be derived from γ_{Al} and $\langle\gamma\rangle$ (measured) using the expression:

- (1) H. L. Johnston, et al., J. Amer. Chem. Soc., 73, 1112 (1951)
- (2) E.S.R. Gopal, "Specific Heat at Low Temperatures", Plenum N.Y., p 33, (1966)

$$\begin{aligned}\gamma_B &= \frac{\langle \gamma \rangle - f\gamma_{Al}}{(1-f)} \\ &= 0.38 \times 10^{-2} \text{ J/kg-deg}^2\end{aligned}$$

This value of γ_B , less than one-tenth that of aluminum, is not inappropriate to a heavily doped semiconductor.

Room Temperature Specific Heat. At room temperature (RT) and 300 K, we have the following data:

<u>Metal</u>	<u>Temperature</u>	<u>C_p J/kg-deg</u>
Al	RT	904.1
B	300 K	1032.2

from which an average specific heat of 969.3 may be calculated. This is in reasonable agreement with the directly measured value of 1076 J/kg-deg.

We conclude that the laws of mixtures are valid for computing the specific heats of composite materials from the values appropriate to the individual constituents.

NBSIR 76-839

SEMI-ANNUAL REPORT ON MATERIALS RESEARCH IN SUPPORT OF SUPERCONDUCTING MACHINERY

R. P. Reed, J. G. Hust, M. B. Kasen, H. M. Ledbetter,
D. T. Read, R. E. Schramm, L. L. Sparks, and R. L. Tobler

Cryogenics Division
Institute for Basic Standards
National Bureau of Standards
Boulder, Colorado 80302

April 1976

Prepared for :
Advanced Research Projects Agency
1400 Wilson Boulevard
Arlington, Virginia 22209



U.S. DEPARTMENT OF COMMERCE, Elliot L. Richardson, Secretary
James A. Baker, III, Under Secretary
Dr. Betsy Ancker-Johnson, Assistant Secretary for Science and Technology
NATIONAL BUREAU OF STANDARDS, Ernest Ambler, Acting Director

SEMI-ANNUAL REPORT ON MATERIALS RESEARCH
IN SUPPORT OF SUPERCONDUCTING MACHINERY

Sponsored by
Advanced Research Projects Agency
ARPA Order No. 2569
Program Code 4D10
August 10, 1975 - October 1, 1976

Program Director
Dr. E. C. van Reuth
Materials Sciences
Advanced Research Projects Agency
1400 Wilson Boulevard
Arlington, Virginia 22209

Program Manager
Dr. R. P. Reed
Cryogenics Division
Institute for Basic Standards
National Bureau of Standards
Boulder, Colorado 80302

The views and conclusions contained in this document are those of the authors and should not be interpreted as necessarily representing the official policies, either expressed or implied, of the Advanced Research Projects Agency or of the U.S. Government.

Abstract

Results are reported of a six-month study, ending March 1976, on candidate materials for superconducting machinery. The results cover five areas--advanced composites, elastic properties, fatigue resistance and fracture toughness, magnetothermal conductivity, and thermal conductivity. Material properties were studied over the temperature range 4 to 300 K. Materials studied include: aluminum alloys 1100, 2014, 2219; a nickel-chromium-iron alloy; iron-47.5 nickel; and the composite materials boron/aluminum, boron/epoxy, S-glass/epoxy; graphite/epoxy. Some notable results of the study are: first reports of compressive mechanical testing on composite materials at 4 K; regular temperature behavior of the elastic constants of aluminum 2014 and 2219 and of iron-47.5 nickel, which is magnetic; none of the mechanical properties of the nickel-chromium-iron alloy tested were affected deleteriously by cryogenic temperatures; in aluminum alloy 2219, J_{Ic} and K_{Ic} are not equivalent because of sub-critical crack extension; both electrical and thermal conductivities of aluminum alloy 1100 are reduced by magnetic fields.

This work was supported by the Advanced Research Projects Agency of the U.S. Department of Defense.

Keywords: Aluminum alloys; composites; elastic properties; engineering materials; fatigue; fracture; iron alloys; cryogenic temperatures; mechanical properties; nickel alloys; superconducting machinery; thermal conductivity.

Report Contents

	Page
ADVANCED COMPOSITES	
R. E. Schramm and M. B. Kasen	1
Reprint: Mechanical and Thermal Properties of Filamentary-Reinforced Structural Composites at Cryogenic Temperatures. 2: Advanced Composites; M. B. Kasen; Cryogenics <u>15</u> (1975) 701-22	19
ELASTIC PROPERTIES OF ENGINEERING MATERIALS AT CRYOGENIC TEMPERATURES	
H. M. Ledbetter and D. T. Read	41
Low-Temperature Elastic Constants of Precipitation-Hardened Aluminum Alloys 2014 and 2219 D. T. Read and H. M. Ledbetter	43
Low-Temperature Elastic Properties of an Iron-47.5 Nickel Alloy H. M. Ledbetter and D. T. Read	58
Reprint: Low-Temperature Elastic Properties of a Nickel-Chromium- Iron Alloy; W. F. Weston and H. M. Ledbetter; Mater. Sci. Eng <u>20</u> (1975) 287-90	66
Reprint: Low-Temperature Elastic Properties of Four Wrought and Annealed Aluminum Alloys; E. R. Naimon, H. M. Ledbetter and W. F. Weston; J. Mater. Sci. <u>10</u> (1975) 1309-16	70
Reprint: Low-Temperature Elastic Constants of a Superconducting Coil Composite; W. F. Weston; J. Appl. Phys. <u>46</u> (1975) 4458-65	78
FRACTURE MECHANICS PARAMETERS OF ENGINEERING MATERIALS AT CRYOGENIC TEMPERATURES	
R. L. Tobler, D. T. Read, and R. P. Reed	87
Low-Temperature Effects on the Fracture Behavior of Inconel 718 R. L. Tobler	89
Effects of Specimen Thickness on Fracture Toughness of Some Aluminum Alloys D. T. Read and R. P. Reed	110
MAGNETOTHERMAL CONDUCTIVITY	
L. L. Sparks	139
THERMAL CONDUCTIVITY	
J. G. Hust	149

Disclaimer

Tradenames of equipment and materials are used in this report for clarity and to conform with standard usage in the scientific and engineering literature. Selection of materials for discussion and examination with regard to application in superconducting machinery is based on properties reported in the literature, and must be regarded as preliminary and tentative. In no case does such selection imply recommendation or endorsement by the National Bureau of Standards. It does not imply that the material or equipment is necessarily the best available for the purpose.

SEMI-ANNUAL REPORT ON MATERIALS RESEARCH
IN SUPPORT OF SUPERCONDUCTING MACHINERY

ADVANCED COMPOSITES

R. E. Schramm and M. B. Kasen

Cryogenics Division
Institute for Basic Standards
National Bureau of Standards
Boulder, Colorado 80302

April 1976

Summary: Advanced Composites

Phase II of the experimental program has been completed. This report contains 295 K, 76 K and 4 K uniaxial compressive laminate mechanical property data on the following commercial composites: 5.6 mil boron/6061 aluminum, 5.6 mil boron/5505 epoxy*, S-901 glass/NASA Resin 2 epoxy, and type AS graphite/NASA Resin 2 epoxy. A reprint of a review of the literature on the mechanical and thermal properties of advanced composites at cryogenic temperatures is also included.

Contents: Advanced Composites

	Page
1.0 Review	3
2.0 Phase II (Continued): Static Mechanical Properties of Uniaxial Composites at Cryogenic Temperatures	3
2.1 Introduction	3
2.2 Experimental Procedures	4
2.3 Results and Discussion	5
2.3.1 Compressive Modulus	5
2.3.2 Compressive Strength	5
2.4 Conclusions	6
3.0 Future Work	7
4.0 References	7
5.0 List of Figures	7
6.0 List of Tables	8
Appendix I: Calculation of Compressive Moduli	18
Appendix II: M. B. Kasen, "Mechanical and thermal properties of filamentary-reinforced structural composites at cryogenic temperatures. II: Advanced composites," Cryogenics <u>15</u> (12), pp. 701-722 (1975)	19

* The use of trade names or designations in this paper is essential to proper understanding of the work presented. Their use in no way implies approval, endorsement, or recommendation by NBS.

1.0 Review

Work on this project was initiated by preparing state-of-the-art reviews on the mechanical and thermal properties of structural composites at cryogenic temperatures. A general review has been published(1). More comprehensive reviews of glass-reinforced composites and of advanced-fiber (high-modulus) composites have been published(2,3). A reprint of Ref. 3 is included in the present report. Reprints of Refs. 1 and 2 have appeared in a previous Semi-Annual Report(4).

The reviews suggested that boron-aluminum, boron-epoxy, graphite-epoxy, glass-epoxy and Kevlar 49-epoxy composites warranted further study to characterize key static mechanical properties at cryogenic temperatures. Key properties are those required for a prediction of strength or stiffness limits in complex crossply layups using macromechanical composite theory. The properties are obtained from uniaxial composite laminates, and consist of strengths and elastic moduli in tension and compression in the longitudinal and transverse directions plus in-plane elastic shear moduli.

Phase I of the experimental work was the development of apparatus and procedures for obtaining these data at cryogenic temperatures. Results have been reported previously(5,6). Phase II encompassed the static characterization work. The tensile and in-plane shear portion of this Phase was reported previously(4). The static compressive mechanical properties of these composites are presented and discussed in the present report.

In Phase III of this work, the performance of boron-epoxy and boron-aluminum composites in tensile-tensile fatigue will be examined at cryogenic temperatures. This work is presently under way and will be reported subsequently.

2.0 Phase II (Continued): Static Mechanical Properties of Uniaxial Composites at Cryogenic Temperatures

2.1 Introduction

This report presents compressive static mechanical property data for the composites listed in Table 1, all of which had previously been characterized in tension and in-plane shear. The boron-reinforced composites were fabricated from state-of-the-art commercial preimpregnated tape materials, not optimized for cryogenic use. The cryogenic properties reported for these materials in the present work are believed representative of the properties of boron-reinforced aluminum or epoxy composites as a class, independent of the specific manufacturer.

NASA Resin 2 is a non-proprietary formulation, developed for cryogenic filament-wound pressure vessels(7). It consists of Epon 828, DSA/Empol 1040/BDMA in proportions of 100/115.9/20/1 by weight.

The Kevlar 49/NASA Resin 2 composite, previously included in the tensile evaluation, was not included in the compressive test program. The very low transverse strength of the material obtained for this program suggested that the composite was not representative of good production quality.

Key compressive static mechanical properties include uniaxial longitudinal and transverse ultimate strengths, elastic moduli, and ultimate failure strains. Where possible, the stresses at the proportional limit and the 0.2% offset yield strengths were also determined.

The present data have been obtained from rod or bar type specimens

designed to fail in approximately 45° shear. This is believed to best approximate compressive failure in bulk composite structures in the absence of significant column bending or end brooming. The reader should be aware that compressive properties obtained by the sandwich beam method may differ somewhat from those reported in the present work.

2.2 Experimental Procedures

The compression fixture shown in Figure 1 converts pull rod separation into compression by means of interlocking yokes. Specimen (A) with its end caps is inserted into compression blocks (B). Alignment is maintained by sleeve (C), which slips around the blocks. The compression blocks are anodized to minimize friction. Additionally, MoS_2 lubricant sprayed on the fixture during assembly serves as both a release agent for the end caps and as a lubricant between the compression blocks and alignment tube. Extraneous frictional forces are typically 5-10 N (1-2 lb).

The split compression blocks are joined by stainless steel bolts, facilitating removal of the end caps after testing. Fixture dimensions and construction materials are detailed in Figure 2.

The compression fixture was designed to interchange with the tensile fixture in the cryostat previously described(5). Helium consumption was typically 5-6 liters per specimen test.

The desired 45° shear failure mode was reliably obtained after several iterations of specimen design. The two final configurations are shown in Figure 3. Specimens of square cross section, embedded in 6061-T6 aluminum end caps, proved satisfactory for most materials and orientations (Figure 3(a)). However, the very high compressive strengths developed by the boron-reinforced materials when tested along the fiber direction required round specimens and stainless steel end caps (Figure 3 (b)). Both specimen types were diamond ground to finished dimensions of Figure 3.

A longitudinally-slitted tube, having an i.d. matching the o.d. of the end caps, was used to align and support the specimens during room temperature curing of the epoxy used to bond the specimens into the end caps. Several conventional types of epoxy proved satisfactory for this application.

All polymer-matrix composites were environmentally conditioned for a minimum of 40 hours at $23 \pm 1^\circ \text{C}$ in $50 \pm 10\%$ relative humidity prior to testing. The boron/6061 aluminum was tested in the as-fabricated condition (F temper) without additional conditioning.

A universal testing machine was used for all tests. The crosshead speed was $0.10\text{-}0.13 \text{ cm min}^{-1}$ ($0.04\text{-}0.05 \text{ in min}^{-1}$), providing a strain rate of $0.06\text{-}0.08 \text{ min}^{-1}$.

Specimens of square cross-section were instrumented with a single longitudinal strain gage. On transverse specimens, the gage was always on the side parallel to the fiber reinforcement. The initial tangent modulus was obtained from load-displacement traces recorded at high sensitivity on an x-y plotter; maximum stress was limited to less than 25% of the ultimate strength. Specimens were subsequently compressed to failure while recording load and strain at lower sensitivity. The strain gage typically failed prior to specimen fracture. However, simultaneous load-time traces on a strip-chart recorder permitted calculation of overall failure strain.

Strain gages were not used with specimens of round cross section. However, the compressive moduli of these specimens were calculated from the load-time trace of the strip chart recorder using the procedure described in Appendix I.

2.3 Results and Discussion

Individual specimen data appear in Tables 2-5. Table 6 presents average values, omitting data from invalid fractures when calculating ultimate strain and strength. The inaccuracy of the data is estimated at + 3% for ultimate strength, + 10% for modulus and ultimate strain, and + 20% for proportional limits and yield strengths.

The maxima of the compressive ultimate strengths and elongations are presented in Table 7. It is probable that the values in this Table are a better reflection of the true ultimate properties of the bulk composites than are the average values of Table 6. Particularly when testing in the uniaxial longitudinal direction, values obtained from relatively small cross section rod specimens are probably lower due to premature failure in other than pure compression.

The desired shear mode of compressive failure is evident in the fractures of the various materials illustrated in Figure 4.

2.3.1 Compressive Modulus

The compressive moduli of the boron-epoxy, glass-epoxy and graphite-epoxy materials are very close to their tensile moduli in both the longitudinal and transverse directions. In contrast, the longitudinal compressive moduli of the boron-aluminum composite was computed to be 30-80% higher than the tensile value, while the transverse compressive moduli was computed to be 10-30% less than the corresponding tensile value.

The authors do not believe that the compressive moduli calculated for the boron-aluminum composite represent valid material properties. An average longitudinal compressive modulus of 359 GN/m^2 ($52.1 \times 10^6 \text{ psi}$) is hardly realistic for a composite reinforced with 50 v/o of boron which itself has a modulus of about 379 GN/m^2 ($55 \times 10^6 \text{ psi}$). Furthermore, preliminary studies of the elastic constants of the same boron-aluminum composite using dynamic resonance techniques indicate that the average of the tensile and compressive moduli is about 234 GN/m^2 ($34 \times 10^6 \text{ psi}$), with a small temperature sensitivity on cooling to cryogenic temperatures(8). It therefore appears that the method used to obtain compressive moduli in the present work is invalid for boron-aluminum composites. We do not know the reason for this discrepancy. However, until the problem is resolved, the authors suggest that tensile moduli values be used to approximate compressive moduli when working with boron-aluminum composites.

The longitudinal compressive moduli of the boron-epoxy and glass-epoxy composites increased about 20% on cooling to 4 K, while that of the graphite-epoxy composite remained relatively unchanged. A much larger temperature dependence of modulus was observed in the transverse direction, with increases of 67%, 108% and 178% being observed for the graphite-epoxy, boron-epoxy, and glass-epoxy, respectively. Similar temperature dependences had been previously observed for the tensile moduli of these materials.

2.3.2 Compressive Strength

Present data suggest that boron-reinforced composites are capable of providing longitudinal compressive strengths approaching 3.4 GN/m^2 ($50 \times 10^4 \text{ psi}$) at 4 K in the absence of column bending. This is twice the tensile strength at that temperature. Conversely, the 4 K longitudinal compressive strengths of the glass and graphite-epoxy composites were 30-50% lower than their 4 K longitudinal tensile strengths. The superior ability of the boron fibers to sustain compressive loads is clear.

The transverse compressive strength of all four composite types are substantially higher than their transverse tensile strengths. This is

particularly noticeable in the graphite-epoxy composite.

The compressive strength of the boron-reinforced composites in the longitudinal direction appears to be relatively independent of temperature, although present data are incomplete. However, the longitudinal compressive strengths of the glass-epoxy material is very temperature dependent, increasing by 180% on cooling. A 25% increase in strength was observed for the graphite-epoxy on cooling. In the transverse direction, the compressive ultimate strength of the boron-aluminum, boron-epoxy, and glass-epoxy increased by 100-170% on cooling. However, cooling to cryogenic temperatures decreased the transverse compressive strength of the graphite-epoxy composite by about 30%.

2.4 Conclusions

Commercial, state-of-the-art boron-6061 aluminum and boron-epoxy composites have excellent static compressive properties at cryogenic temperatures. The compressive strength is particularly outstanding, approaching 3.4 GN/m^2 ($50 \times 10^4 \text{ psi}$) in the uniaxial longitudinal direction at 4 K. Transverse compressive strengths of 620 MN/m^2 ($90 \times 10^3 \text{ psi}$) for boron-aluminum and 427 MN/m^2 ($62 \times 10^3 \text{ psi}$) for boron-epoxy at 4 K are substantially higher than in other composite systems. The compressive strength properties of the boron-reinforced materials are superior to the already high tensile strength properties at all cryogenic temperatures. With a modulus of $206\text{-}240 \text{ GN/m}^2$ ($30\text{-}35 \times 10^6 \text{ psi}$), the boron-reinforced composites appear to be excellent cryogenic structural materials.

At 4 K, NASA Resin 2 epoxy reinforced with S-901 glass fibers has about half the compression strength of the boron materials in both the longitudinal and transverse directions. The longitudinal compressive strength of this composite is 30-60% lower than the corresponding tensile strength, while the transverse compression strength is 100-200% greater than in tension. Compressive moduli increase with cooling, attaining about 62 GN/m^2 ($9 \times 10^6 \text{ psi}$) longitudinally and about 31 GN/m^2 ($4.5 \times 10^6 \text{ psi}$) in the transverse direction at 4 K.

NASA Resin 2 reinforced with Type AS graphite fiber had the lowest compressive strength of the composites tested. Uniaxial longitudinal strengths at 4 K were about 25% of that of the boron materials, while transverse strengths averaged about 130 MN/m^2 ($19 \times 10^3 \text{ psi}$). The longitudinal compression modulus of about 117 GN/m^2 ($17 \times 10^6 \text{ psi}$) was about the same as the tensile modulus.

The comparatively poor performance of the graphite-epoxy composite in the present work should not be construed as indicating a general inferiority of this type of composite for cryogenic applications. The data suggest that an incompatibility may exist between the fiber and matrix in the AS/NASA Resin 2 composite selected for this study.

Present data indicate that the compressive and tensile moduli of the boron-epoxy, graphite-epoxy and glass-epoxy composites are substantially the same from 295 K to 4 K. In view of the experimental difficulty, there appears to be little justification for a separate determination of compressive moduli if tensile moduli are available.

We conclude from this study that the compressive moduli of uniaxial boron-6061 aluminum composites cannot be reliably measured by the procedures used in this study, even though such procedures were satisfactory for the epoxy-matrix composites.

3.0 Future Work

Phase III of this program will examine the extent to which cryogenic temperatures affect the wear-out rate of boron-aluminum and boron-epoxy composites under tension-tension fatigue. Criteria will be changes in specimen modulus and damping. This study is presently under way using composites of [0/+ 45/0]s orientation and stacking.

4.0 References

1. Kasen, M. B., "Properties of Filamentary-Reinforced Composites at Cryogenic Temperatures," Composite Reliability, ASTM STP 580, American Society for Testing and Materials, 1975, pp. 586-611.
2. Kasen, M. B., "Mechanical and Thermal Properties of Filamentary-Reinforced Structural Composites at Cryogenic Temperatures. I: Glass-Reinforced Composites," Cryogenics, 15 (6), 1975, pp. 327-349.
3. Kasen, M. B., "Mechanical and Thermal Properties of Filamentary-Reinforced Structural Composites at Cryogenic Temperatures. II: Advanced Composites," Cryogenics, 15 (12), 1975, pp. 701-722.
4. Schramm, R. E. and Kasen, M. B., "Advanced Composites," in Semi-Annual Technical Reports on Materials Research in Support of Superconducting Machinery - IV; R. P. Reed, A. F. Clark, E. C. van Reuth (Eds.); Nat. Bur. Stds., Boulder, CO; October 1975; ADA019230.
5. Kasen, M. B., "Advanced Composites," in Semi-Annual Technical Reports on Materials Research in Support of Superconducting Machinery; R. P. Reed, A. F. Clark, E. C. van Reuth (Eds.); Nat. Bur. Stds., Boulder, CO; March 1974; AD780596.
6. Kasen, M. B. and Schramm, R. E., "Advanced Composites," in Semi-Annual Technical Reports on Materials Research in Support of Superconducting Machinery - II; R. P. Reed, A. F. Clark, E. C. van Reuth (Eds.); Nat. Bur. Stds., Boulder, CO; October 1974; ADA004586.
7. Soffer, L. M. and Molho, R., "Cryogenic Resins for Glass Filament-wound Composites," NASA CR-72114 (Final), 1967, N67-25076.
8. Read, D. T. and Ledbetter, H. M., NBS-Boulder, personal communication (March 1976).

5.0 List of Figures

1. Fixture for compression testing of composites at cryogenic temperatures.
 - (a) Specimen with end caps
 - (b) Anodized aluminum compression blocks
 - (c) Aluminum alignment sleeve
2. Drawing of fixture for compression testing of composites at cryogenic temperatures.
3. Specimen configurations used in determining static compressive properties of composites at cryogenic temperatures.
 - (a) Square specimen for glass-epoxy, graphite-epoxy and transverse boron-aluminum and boron-epoxy
 - (b) Round specimen for longitudinal boron-aluminum and boron-epoxy

4. Typical composite compressive fractures.
 - (a) Glass-epoxy, longitudinal, 295 K
 - (b) Glass-epoxy, transverse, 295 K
 - (c) Glass-epoxy, longitudinal, 4 K
 - (d) Boron-aluminum, longitudinal, 4 K
 - (e) Boron-epoxy, longitudinal, 4 K
 - (f) Boron-epoxy, transverse, 4 K
 - (g) Graphite-epoxy, longitudinal, 295 K
 - (h) Graphite-epoxy, longitudinal, 4 K

6.0 List of Tables

1. Composites Tested in Compression
2. Compression Properties of 5.6-mil Boron-6061 Aluminum Composite (Individual Specimens)
3. Compression Properties of 5.6-mil Boron-5505 Epoxy Composite (Individual Specimens)
4. Compression Properties of S Glass-NASA Resin 2 Composite (Individual Specimens)
5. Compression Properties of Type AS Graphite-NASA Resin 2 Composite (Individual Specimens)
6. Compressive Properties of Composites (Averages of Specimens Tested)
7. Compressive Properties of Composites (Maxima of Ultimate Strength Values)

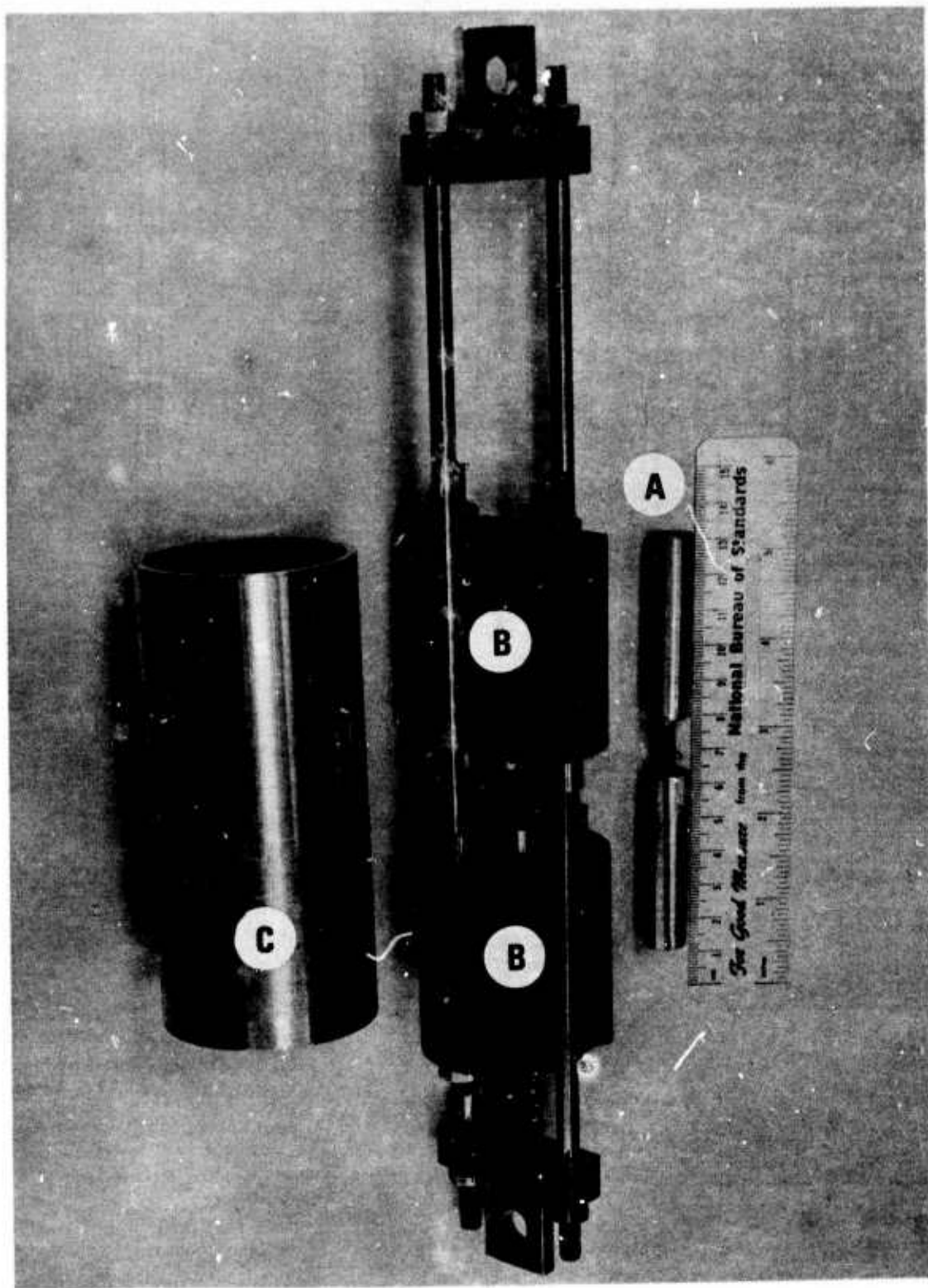
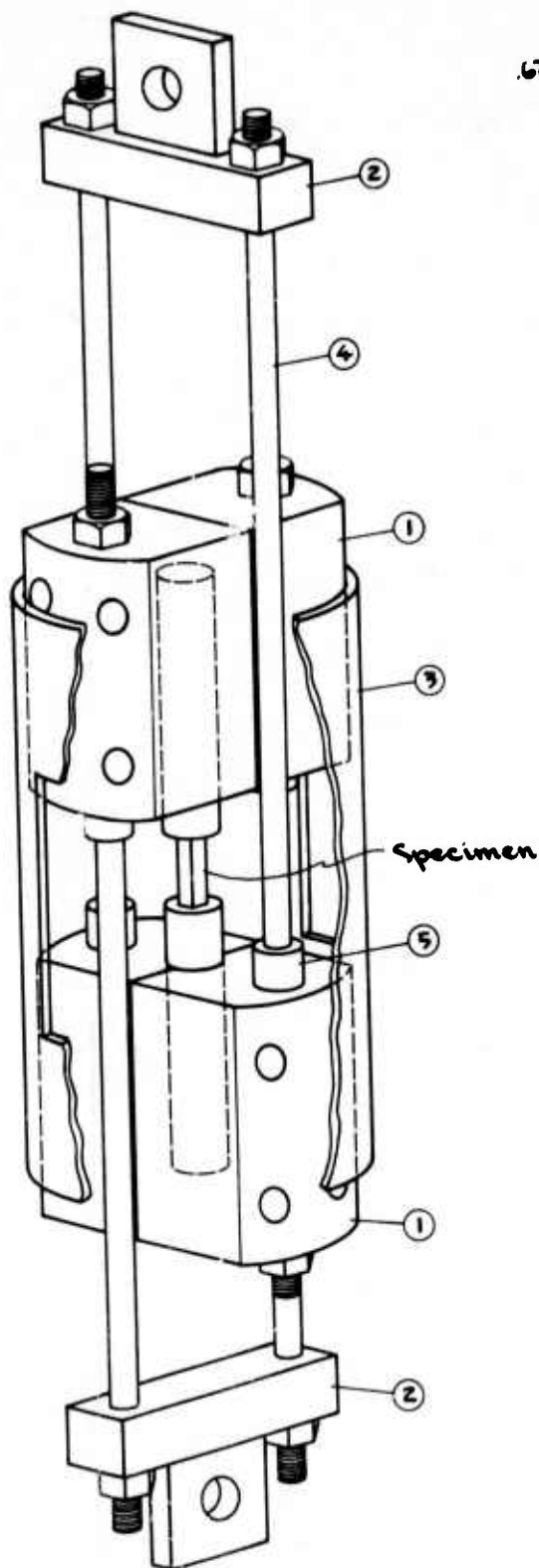


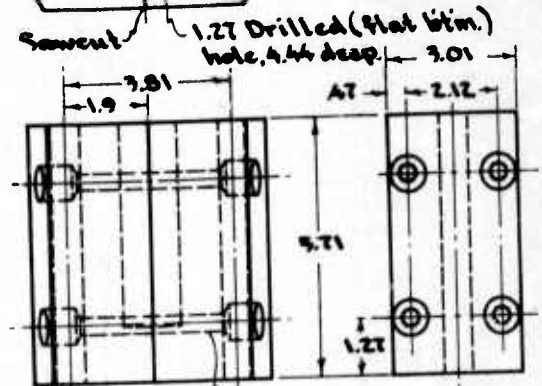
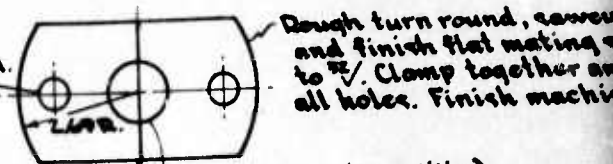
Fig. 1. Fixture for compression testing of composites at cryogenic temperatures

- (a) Specimen with end caps
- (b) Anodized aluminum compression blocks
- (c) Aluminum alignment sleeve



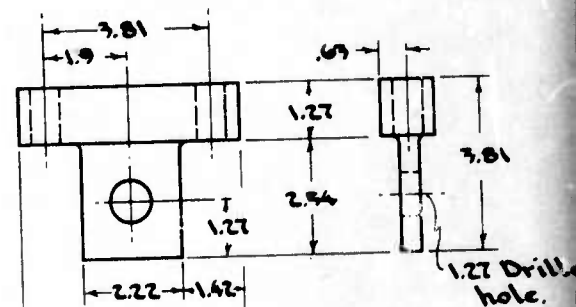
ASSEMBLY

.67 Dia. drill, thru.
2 Places.



.33 Dia. drill, thru.
.79 countersink, ~.79 deep.
4 Places as shown. Use
stainless steel bolts.

MATERIAL: 6061-T6 ALUMINUM
(2) Two Required
Anodized after completion

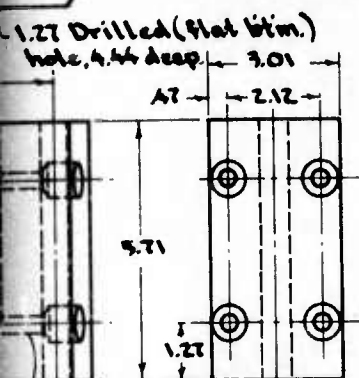


.67 Dia. drill, thru.
2 Places.

(2)
MATERIAL: AISI 304 STAINLESS STEEL
(2) Two Required

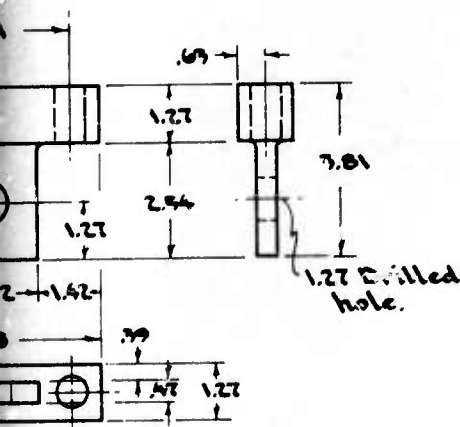
All dimensions shown in cm.

Dough turn round, sawout and finish flat mating surfaces to $\frac{1}{32}$ ". Clamp together and drill all holes. Finish machining.



$\frac{3}{32}$ Drilled hole, thru. .79 countersink, ~.79 deep. 4 Places as shown. Use stainless steel bolts.

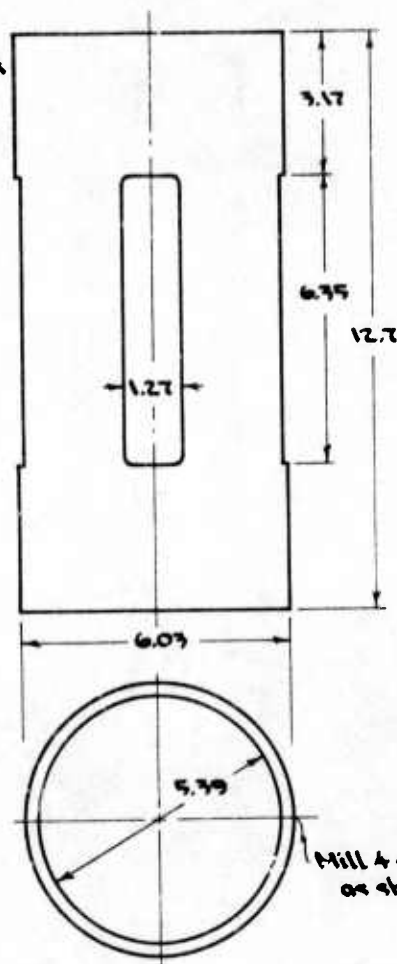
MATERIAL - 6061-T6 ALUMINUM
(2) Two Required
after completion



(2)

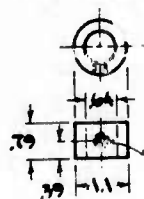
MATERIAL - AISI 304 STAINLESS STEEL
(2) Two Required

one shown in cm.



(3)

MATERIAL - 6061-T6 ALUMINUM
(1) One Required



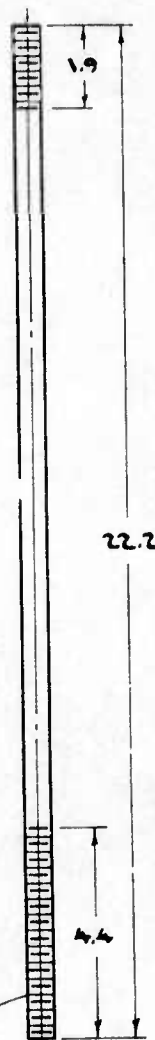
(5)

MATERIAL - AISI 304 STAINLESS STEEL
(4) Four Required

Drill & tap for #5-40 NC set screw.

Mill 4 slots @ 90° as shown.

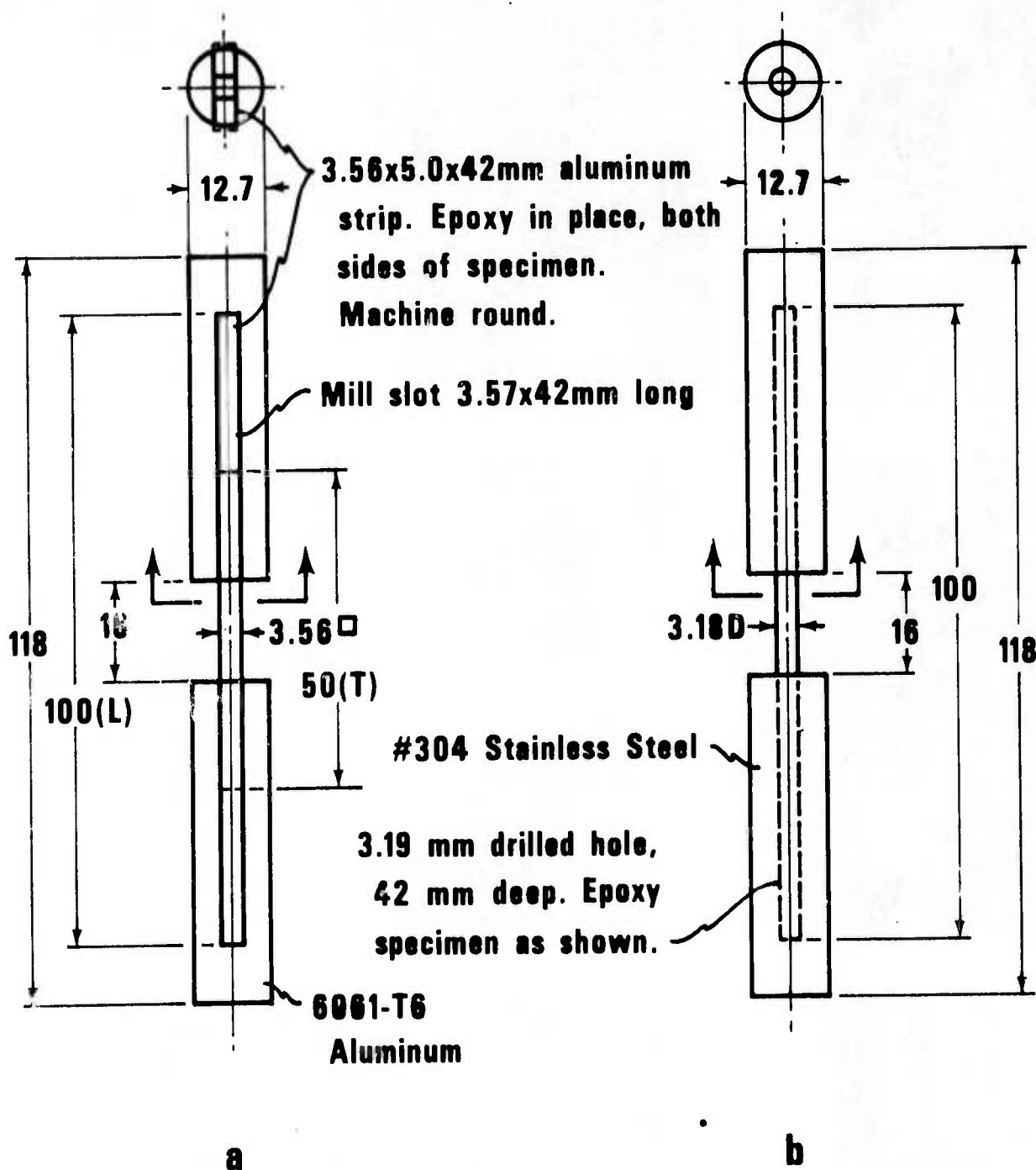
$\frac{1}{4}$ -20 NC 2. both ends.



(4)

MATERIAL - .63 DIA.
Ti-6Al-4V
(2) Req'd. as shown
(2) Req'd. 27.3 long.

Fig. 2. Drawing of fixture for compression testing of composites at cryogenic temperatures.

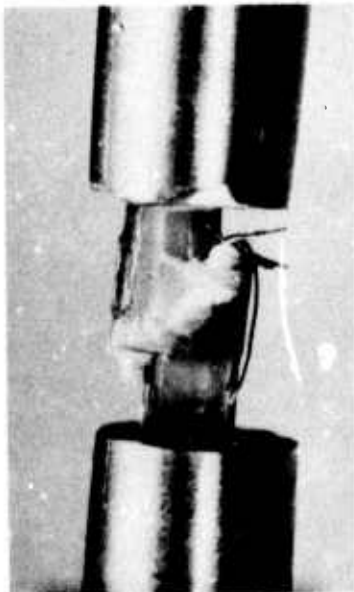


All dimensions shown in mm.

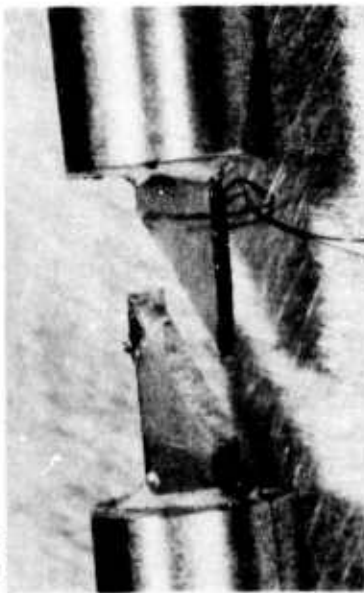
Fig. 3. Specimen configurations used in determining static compressive properties of composites at cryogenic temperatures.

(a) Square specimens for glass-epoxy, graphite-epoxy and transverse boron-aluminum and boron-epoxy.

(b) Round specimen for longitudinal boron-aluminum and boron-epoxy.



(a) Glass-epoxy, longitudinal, 295K



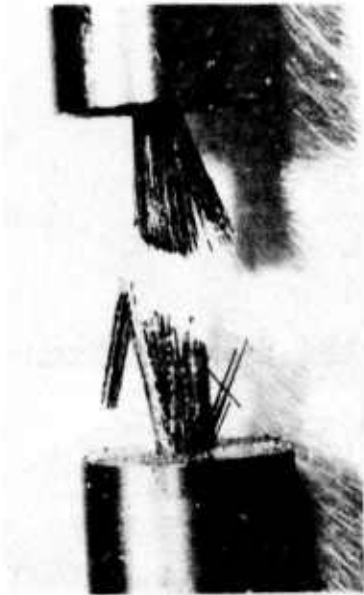
(b) Glass-epoxy, transverse, 295K



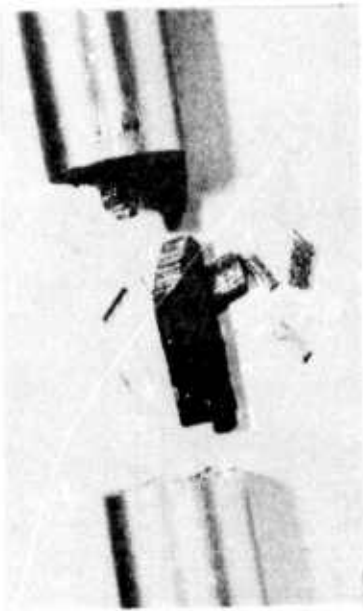
(c) Glass-epoxy, longitudinal, 4K



(d) Boron-alum., longitudinal, 4K



(e) Boron-epoxy, longitudinal, 4K



(f) Boron-epoxy, transverse, 4K



(g) Graphite-epoxy, longitudinal, 295K



(h) Graphite-epoxy, longitudinal, 4K

Fig. 4. Typical composite compressive fractures.

Table 1. Composites Tested in Compression

Composite Type	Plate Thickness (cm)	Plate Thickness (in)	Nominal Ply Thickness (cm)	Nominal Ply Thickness (in)	Average Fiber Volume Percent*
5.6 mil Boron-6061 Aluminum (condition F)	0.373	0.147	0.0175	0.0069	47
5.6 mil Boron-5505 Epoxy	0.345	0.137	0.0170	0.0067	52
S-901 Glass-NASA Resin 2 Epoxy	0.462	0.182	0.0206	0.0081	66
Type AS Graphite-NASA Resin 2 Epoxy	0.366	0.144	0.0193	0.0076	64

* Plate-to-plate variation was $\pm 2\%$.

Table 2. Compressive Properties of 5.6 mil Boron-6061 Aluminum Composite^a (Individual Specimens)

Temperature (K)	Young's Modulus (10 ⁹ N/m ²)	Modulus (10 ⁶ psi)	Proportional Limit, σ^{Pl} (10 ⁸ N/m ²) (10 ³ psi)		0.2% Yield Strength, σ^{cy} (10 ⁸ N/m ²) (10 ³ psi)		Ultimate Strength, σ^{cu} (10 ⁸ N/m ²) (10 ³ psi)		Ultimate Strain, ϵ^{cu} (%)
Longitudinal (0°)									
295	221	32.0					19.2	8	1.8
295	293	42.5					15.2	224	0.7
76	311	45.1					21.7	314	1.0
76 ^b	407 ^c *	59.0 ^c *					28.7	416	0.5 ^c
4 ^b	335 ^c	48.6 ^c					28.5	413	0.6 ^c
4 ^b	337 ^c	48.8 ^c					26.0	377	0.5 ^c
4 ^b	302 ^c	43.8 ^c					32.6	473	0.7 ^c
Transverse (90°)									
295 ^d	150	21.2	0.588	8.53	1.43	20.8	2.60	37.7	0.4 ^c
295	186	27.0	0.545	7.97	1.43	20.7	2.54	36.8	0.4 ^c
295	107	15.5	0.594	8.61	1.03	15.0	2.59	37.5	0.5 ^c
76	101	14.7	0.833	12.1	1.95	28.4	4.56	66.2	0.6 ^c
76	89 *	12.9 *	0.818	11.9	2.06	30.0	4.45	64.6	0.8 ^c
76	101	14.6	0.967	14.0	1.99	28.9	4.50	65.3	0.9 ^c
4	123	17.8	1.13	16.4	2.82	40.9	6.56	95.1	0.7 ^c
4	90	13.0	1.11	16.0	2.44	35.3	6.29	91.2	1.2 ^c
4	90	13.1	1.01	14.6	2.39	34.7	5.83	84.5	1.0 ^c

^aSquare specimens except as marked.

^bRound specimen.

^cEstimated from strip-chart recording.

^dThis is the only boron-aluminum specimen that was load cycled.

Underlined values represent invalid fractures.

* See text discussion on validity of these values.

Table 3. Compressive Properties of 5.6 mil Boron-3503 Epoxy Composite (Individual Specimens)

Temperature (K)	Elastic Modulus, E^c (10^9 N/m ²) (10 ⁶ psi)		Proportional Limit, σ^{pl} (10^8 N/m ²) (10 ³ psi)		0.2% Yield Strength, σ^{cy} (10^8 N/m ²) (10 ³ psi)		Ultimate Strength, σ^{cu} (10^8 N/m ²) (10 ³ psi)		Ultimate Strain, ϵ^{cu} (%)
					Longitudinal (0°)				
295 ^a	186	27.0					11.8	171	0.7
295 ^a	190	27.6					12.9	186	0.8
295 ^b	260	37.7					14.1	204	0.6
76 ^a	225	32.6					22.8	331	1.1
76 ^a	234	33.9					18.7	263	0.8
4 ^a	239	34.7					13.0	188	0.6
4 ^c	257 ^d	37.3 ^d					25.9	375	0.4 ^d
4 ^c	233 ^d	33.7 ^d					19.2	278	0.3 ^d
4 ^c	291 ^d	42.2 ^d					36.6	531	0.6 ^d
					Transverse (90°)				
295 ^a	20.9	3.03	0.395	5.7	1.78	25.8	2.27	32.3	1.6
295 ^a	13.3	2.02	0.975	14.1	--	--	1.41	20.5	1.6
295 ^b	20.0	2.90	0.715	10.4	1.79	25.9	2.10	30.5	1.2
295 ^b	22.4	3.24	0.790	11.4	1.80	26.1	1.96	28.4	1.4
76 ^a	38.7	5.62	2.31	33.6			4.23	61.4	1.2
76 ^a	39.0	5.64	1.98	28.6			3.84	55.6	0.5
76 ^a	37.7	5.46	1.66	24.1			1.80	26.1	0.5
76 ^b	39.5	5.74	2.72	39.5			4.56	66.2	1.5
76 ^b	41.4	5.99	3.38	49.0			4.36	63.1	1.1
4 ^b	42.8	6.20					4.24	61.4	1.1
4 ^b	37.8	5.49					1.67	24.2	0.4
4 ^b	41.3	5.98					4.52	65.5	1.1
4 ^b	39.4	5.71					4.08	59.2	0.9

^a Rectangular specimen.^b Square specimen.^c Round specimen.^d Estimated from strip-chart recording.

Underlined values represent invalid fractures.

Table 4. Compressive Properties of S Glass-NASA Resin 2 Composite (Individual Specimens)

Temperature (K)	Elastic Modulus, E ^c (10 ⁹ N/m ²) (10 ⁶ psi)		Proportional Limit, σ ^{pl} (10 ⁸ N/m ²) (10 ³ psi)		0.2% Yield Strength, σ ^{cy} (10 ⁸ N/m ²) (10 ³ psi)		Ultimate Strength, σ ^{cu} (10 ⁸ N/m ²) (10 ³ psi)		Ultimate Strain, ε ^{cu} (%)
				Longitudinal (0°)					
295	40.4	5.87	1.36	19.8			4.72	68.5	1.2
295	59.2	8.44	0.93	13.5			5.62	81.6	1.3
295	53.2	7.71	3.14	45.6			4.75	68.8	0.9
76	69.7	10.1	1.78	25.8	7.32	106	16.5	239	3.0
76	64.2	9.3	3.24	47.0	9.87	143	13.4	195	2.5
76	72.5	10.5	3.07	44.4	--	--	10.3	150	1.5
76	48.6	7.0	4.47	64.8	7.03	102	14.0	203	2.5 ^a
4	53.8	7.81	2.44	35.3	9.08	132	14.1	204	1.5
4	63.0	9.13	3.81	55.2	7.56	110	15.4	224	2.6 ^a
4	64.7	9.38	3.11	45.1	--	--	13.1	190	1.8 ^a
				Transverse (90°)					
295	11.7	1.70	0.550	7.97	0.733	10.6	0.962	13.9	3.4
295	12.3	1.78	0.380	5.51	0.753	10.9	0.935	13.6	2.6
295	9.8	1.42	0.422	6.12	0.703	10.2	1.052	15.3	3.4
76	19.8	2.87	0.92	13.4			2.35	34.0	0.7
76	26.0	3.77	1.31	19.0			2.84	41.2	1.1
76	22.7	3.29	1.19	17.2			3.11	45.1	0.9
4	27.2	3.95					2.76	40.0	1.1
4	39.4	5.71					2.99	43.4	0.8
4	27.3	3.96					2.13	30.9	0.7

^a Estimated from strip chart recording.

All square specimens

Table 5. Compressive Properties of Type AS Graphite-NASA Resin 2 Composite (Individual Specimens)

Temperature (K)	Elastic Modulus, E^c		Proportional Limit, σ^{pl}		0.2% Yield Strength, σ^{cy}		Ultimate Strength, σ^{cu}		Ultimate Strain, ϵ^{cu} (%)
	(10^9 N/m ²)	(10^6 psi)	(10^8 N/m ²)	(10^3 psi)	(10^8 N/m ²)	(10^3 psi)	(10^8 N/m ²)	(10^3 psi)	
Longitudinal (0°)									
295	137	19.9	2.25	32.6			5.61	81.2	0.5
295	125	18.1	2.66	38.6			4.96	71.9	0.4
295	125	18.2	3.55	51.5			5.38	78.0	0.4
76	115	16.7	4.54	65.9			7.95	115	0.8
76	97	14.1	--	--			4.75	69	0.5
76	110	16.0	3.95	57.3			6.72	97	0.7
76	141	20.4	5.04	73.1			12.29	178	1.0
4	109 ^a	15.8 ^a	--	--			8.83	128	0.7 ^a
4	124	18.0	3.70	53.7			5.87	85	0.6
4	125	18.2	3.77	54.7			5.99	87	0.8
Transverse (90°)									
295	9.09 ^a	1.32 ^a	0.90 ^a	13.0 ^a			1.04	15.1	0.8 ^a
295	9.99 ^a	1.45 ^a	0.58 ^a	8.4 ^a			0.91	13.2	0.8 ^a
295	9.91 ^a	1.44 ^a	--	--			0.71	10.3	0.6 ^a
76	16.6	2.41	1.16	16.8			1.51	21.9	1.1
76	13.1	1.89	0.80	11.5			1.25	18.1	1.0
76	16.1	2.34	0.90	13.1			1.33	19.3	0.9
4	18.8	2.72	0.660	9.58			1.00	14.4	0.5
4	14.4	2.09	0.723	10.48			1.50	21.8	1.0
4	15.3	2.22	0.647	9.39			1.43	20.7	0.9

^a Estimated from strip-chart recording.

All square specimens

Table b. Compressive Properties of Composites (Averages of Specimens Tested^a)

Temperature (K)	Elastic Modulus, E ^c (10 ⁹ N/m ²)		CV(%)	Proportional Limit, σ _{PL} (10 ³ psi)		CV(%)	0.2% Yield Strength, σ _{0.2} (10 ⁸ N/m ²)		CV(%)	Ultimate Strength, σ _{cu} (10 ⁸ N/m ²)		CV(%)	Ultimate Strain, ε _{cu} (%)		Number of Specimens Tested	Valid Fractures
	(10 ⁹ N/m ²)	(10 ⁶ psi)		(10 ³ psi)	(10 ³ psi)		(10 ⁸ N/m ²)	(10 ⁸ N/m ²)		(10 ⁸ N/m ²)	(10 ⁸ N/m ²)		(%)	(%)		
295 76 4	5.6 mil Boron-6061 Aluminum			Longitudinal (0°)												
				Transverse (90°)												
	257 (51)	37.2 (7.4)	20.0	8.4 (0.3)	4.6		1.30 (0.23)	18.8 (3.3)	17.8	2.58 (0.03)	37.3 (0.5)	1.3	0.4 (0.1)	13.4	3	0
295 76 4	5.6 mil Boron-5505 Epoxy			Longitudinal (0°)												
				Transverse (90°)												
	148 (40)	21.2 (5.8)	27.1	12.7 (1.2)	9.9		2.00 (0.06)	29.1 (0.8)	2.8	4.50 (0.06)	66.4 (0.8)	1.2	0.8 (0.2)	19.6	3	1
295 76 4	S Glass-NASA Resin 2			Longitudinal (0°)												
				Transverse (90°)												
	212 (42)	30.8 (6.0)	19.6	10.4 (3.5)	33.7		1.79 (0.01)	25.9 (0.2)	0.6	2.11 (0.16)	30.6 (2.3)	7.5	1.5 (0.2)	13.2	4	4
295 76 4	Type AS Graphite-NASA Resin 2			Longitudinal (0°)												
				Transverse (90°)												
	19.1 (4.0)	2.80 (0.54)	20.9	35.0 (9.7)	27.8		8.07 (1.56)	117 (23)	19.3	4.25 (0.30)	61.6 (4.5)	7.2	1.1 (0.5)	43.3	5	5
295 76 4	Type AS Graphite-NASA Resin 2			Longitudinal (0°)												
				Transverse (90°)												
	50.9 (9.6)	7.34 (1.32)	18.9	6.53 (1.28)	19.6		0.730 (0.025)	10.6 (0.4)	3.5	5.03 (0.51)	73.0 (7.5)	10.2	1.1 (0.2)	18.4	3	3
295 76 4	Type AS Graphite-NASA Resin 2			Longitudinal (0°)												
				Transverse (90°)												
	63.8 (10.7)	9.23 (1.56)	17.0	16.5 (2.9)	17.5		0.451 (0.089)	11.7 (2.3)	13.2	13.6 (2.5)	197 (36)	18.8	2.4 (0.6)	26.5	4	4
295 76 4	Type AS Graphite-NASA Resin 2			Longitudinal (0°)												
				Transverse (90°)												
	60.5 (5.9)	8.77 (0.84)	9.7	45.2 (10.0)	22.0		8.32 (1.07)	121 (16)	13.2	14.2 (1.2)	206 (17)	8.3	2.0 (0.6)	28.9	3	3
295 76 4	Type AS Graphite-NASA Resin 2			Longitudinal (0°)												
				Transverse (90°)												
	11.3 (1.3)	1.63 (0.19)	11.6	6.53 (1.28)	19.6		0.730 (0.025)	10.6 (0.4)	3.5	0.983 (0.061)	14.3 (0.91)	6.4	3.1 (0.5)	14.7	3	3
295 76 4	Type AS Graphite-NASA Resin 2			Longitudinal (0°)												
				Transverse (90°)												
	22.8 (3.1)	3.31 (0.45)	13.6	16.5 (2.9)	17.5		0.451 (0.089)	11.7 (2.3)	13.2	2.77 (0.39)	40.1 (5.63)	14.0	0.9 (0.2)	22.2	3	3
295 76 4	Type AS Graphite-NASA Resin 2			Longitudinal (0°)												
				Transverse (90°)												
	31.3 (7.0)	4.54 (1.01)	22.4	6.53 (1.28)	19.6		0.730 (0.025)	10.6 (0.4)	3.5	2.73 (0.45)	38.1 (6.5)	17.0	0.9 (0.2)	24.0	3	3
295 76 4	Type AS Graphite-NASA Resin 2			Longitudinal (0°)												
				Transverse (90°)												
	129 (7)	18.7 (1.0)	5.4	40.9 (9.7)	23.6		0.730 (0.025)	10.6 (0.4)	3.5	5.49 (0.16)	79.6 (2.3)	2.9	0.4 (0.1)	13.3	3	3
295 76 4	Type AS Graphite-NASA Resin 2			Longitudinal (0°)												
				Transverse (90°)												
	116 (18)	16.8 (2.6)	15.9	65.4 (7.9)	12.1		0.730 (0.025)	10.6 (0.4)	3.5	7.93 (3.19)	115 (46)	40.3	0.8 (0.2)	27.8	4	4
295 76 4	Type AS Graphite-NASA Resin 2			Longitudinal (0°)												
				Transverse (90°)												
	120 (8)	17.4 (1.3)	7.3	51.2 (0.7)	1.3		0.730 (0.025)	10.6 (0.4)	3.5	6.90 (1.68)	100 (24)	24.3	0.7 (0.1)	14.3	3	3
295 76 4	Type AS Graphite-NASA Resin 2			Longitudinal (0°)												
				Transverse (90°)												
	9.7 (0.2)	1.40 (0.07)	5.2	10.7 (3.3)	30.6		0.730 (0.025)	10.6 (0.4)	3.5	0.89 (0.17)	12.9 (2.4)	18.8	0.7 (0.1)	15.8	3	3
295 76 4	Type AS Graphite-NASA Resin 2			Longitudinal (0°)												
				Transverse (90°)												
	15.3 (1.9)	2.21 (0.28)	12.8	13.8 (2.7)	19.7		0.730 (0.025)	10.6 (0.4)	3.5	1.36 (0.13)	19.8 (1.9)	9.8	1.0 (0.1)	10.0	3	3
295 76 4	Type AS Graphite-NASA Resin 2			Longitudinal (0°)												
				Transverse (90°)												
	16.2 (2.3)	2.36 (0.33)	14.3	9.82 (0.58)	6.0		0.730 (0.025)	10.6 (0.4)	3.5	1.31 (0.27)	19.0 (4.0)	21.0	0.8 (0.3)	33.1	3	3

^a Standard deviations are in parentheses. CV is the coefficient of variation. Data from specimens showing an invalid fracture are not included in the calculations of ultimate strength or elongation.
^b See text discussion on validity of these values.

Table 7. Compressive Properties of Composites (Maxima of Ultimate Strength Values)

Temperature (K)	Ultimate Strength, σ^{cu} (10^8 N/m ²) (10 ³ psi)		Ultimate Compression, ϵ^{cu} (%)	Number of Specimens
<u>5.6 mil Boron-6061 Aluminum</u>				
Longitudinal (0°)				
295	--	--	--	
76	28.7	416	0.5	1
4	32.6	473	0.7	3
Transverse (90°)				
295	2.60	37.7	0.5	3
76	4.56	66.2	0.9	3
4	6.56	95.1	1.2	3
<u>5.6 mil Boron-5505 Epoxy</u>				
Longitudinal (0°)				
295	--	--	--	
76	--	--	--	
4	36.6	531	0.6	3
Transverse (90°)				
295	2.27	32.3	1.6	4
76	4.56	66.2	1.5	5
4	4.52	65.5	1.1	3
<u>5 Glass-NASA Resin 2</u>				
Longitudinal (0°)				
295	5.62	81.6	1.3	3
76	16.5	239	3.0	4
4	15.4	224	2.6	3
Transverse (90°)				
295	1.05	15.3	3.4	3
76	3.11	45.1	1.1	3
4	2.99	43.4	1.1	3
<u>Type AS Graphite-NASA Resin 2</u>				
Longitudinal (0°)				
295	5.61	81.2	0.5	3
76	12.3	178	1.0	4
4	8.83	128	0.8	3
Transverse (90°)				
295	1.04	15.1	0.8	3
76	1.51	21.9	1.1	3
4	1.50	21.8	1.0	3

Appendix I: Calculation of Compressive Moduli

The elastic (Young's) modulus, E , is determined from a stress-strain curve by the relationship:

$$E = \frac{L}{A\epsilon} \quad (1)$$

where L = load, A = specimen cross-sectional area and ϵ = specimen strain. If the only available record of the test is a strip chart trace of load as a function of time, the time axis must be calibrated in units of strain.

For an infinitely rigid test machine, the strain would be given by the product of time and crosshead speed divided by the specimen gage length. In reality, a fraction of the crosshead motion causes strain in various components of the load train other than the specimen. This extraneous strain may be accounted for if one knows the functional relationship between incremental specimen strain, $\Delta\epsilon$, and incremental strip-chart time, Δt :

$$\Delta\epsilon = f(\Delta t) \quad (2)$$

The factor f is a function of both the spring constant of the loading system and of specimen stiffness, $E \cdot A$. It is uniquely defined for a given specimen and load train, and may be determined by comparing a strip-chart trace with a load-strain trace recorded concomitantly from a strain-gaged specimen. Specimens of differing stiffness yield differing f factors, reflecting differences in the distribution of overall strain between the specimen and the load train. However, if f factors are calculated from a large number of specimens which vary in modulus and cross-sectional area (but are of identical gage length), a plot of f versus the $E \cdot A$ product provides a calibration curve for the test system.

Combining Eqs. (1) and (2) yields:

$$E = \frac{\Delta L}{A \cdot f(\Delta t)} \quad (3)$$

Since ΔL , Δt and A are known, an iterative process is used to find the correct value of the factor f . An estimate is made of the modulus, the $E \cdot A$ product is calculated, and the corresponding f value is determined from the calibration chart. This value is substituted in Eq. (3). A few iterations suffice to narrow estimated and calculated moduli to within $\pm 10\%$, which appears to be a reasonable limit of accuracy for this method.

The same f value may be used to estimate the fracture strain from the time scale of a load-time trace.

It is also possible to estimate the ultimate strain from the total test time using Eq. (2). In those cases where a strain gage was applied but failed before specimen fracture, a comparison of the initial linear portion of the load time curve with the modulus from the load-strain curve yields an f value from Eq. (3) without recourse to the calibration curve or any iterations.

The low temperature mechanical and thermal properties of advanced-fibre reinforced structural composites are reviewed. The magnitude and range of particular properties are discussed with respect to composite type and temperature. A property-material cross reference is given with a 128-entry bibliography. This is Part 2 of a two-part series. Part 1 considered glass-reinforced composites.

Mechanical and thermal properties of filamentary-reinforced structural composites at cryogenic temperatures

2: Advanced composites

M. B. Kasen

Nomenclature

σ^{tu}	tensile ultimate strength
E_1^t	initial tensile modulus
E_2^t	secondary tensile modulus
ϵ^{tu}	tensile ultimate strain
σ^{fu}	flexural ultimate strength
E_1^f	initial flexural modulus
E_2^f	secondary flexural modulus
σ^{cu}	compressive ultimate strength
E^c	compressive modulus
ϵ^{cu}	compressive ultimate strain
σ^{si}	interlaminar shear strength
η^f	fatigue strength
σ^{by}	bearing yield strength
σ^{bu}	bearing ultimate strength
σ^i	impact strength
λ	thermal conductivity
$\Delta L/L$	thermal contraction (expansion)
C_p	specific heat at constant pressure
ρ	density

This review has four main objectives: (a) to give the designer some idea of the general magnitude of property values which can reasonably be expected from a given category and class of advanced-fibre composites within the cryogenic range; (b) to provide insight into the ranking of specific composite classes with regard to a specific property; and (c) to allow him to assess whether the property of interest is likely to increase, remain unaffected, or decrease with lowering of temperature. Readers with more specific interests are referred to the Bibliography and Bibliography-Property Cross Reference for retrieval of specific documents. The Bibliography in this report is similar to that in Part 1 and

includes references to both the glass and advanced-fibre reinforced composite literature. The scope of the literature survey has already been described in Part 1 (*CRYOGENICS* Vol 15, No 6 (June 1975) pp 327-49).

We define a composite *category* by the general reinforcement type, for example, glass-fibre or advanced-fibre (graphite, boron, etc). We subdivide the category into composite *classes* by the general matrix type, for example, glass-polyester or graphite-epoxy. We subdivide the class by referring to a composite *type* when a specific reinforcement/matrix combination is specified, for example, HT-S/X-904 epoxy.

The term 'advanced-fibre' is used to distinguish fibres having high modulus ($20-70 \times 10^6$ lb in⁻², 138-483 GPa) in contrast to the relatively low modulus of glass fibre (10×10^6 lb in⁻², 69 GPa). Fibres of boron, graphite or proprietary organic type dominate the advanced-fibre field.

Several differences will be noted between the presentation of the data in this work and in Part 1. First, because of the wide variation in properties among the advanced fibres (and, therefore, among the composites in which they are used), separate data are presented on each specific reinforcement type.

Secondly, as no data were available on woven-cloth advanced-fibre composites at cryogenic temperatures, present data are restricted to uniaxial longitudinal and uniaxial transverse layups. Thirdly, the overwhelming majority of the relevant data for advanced-fibre polymeric systems are reported for epoxy matrices, in contrast to the variety of polymeric matrices for which data were available in glass-reinforced systems. Finally, data are presented for advanced-fibre reinforcement of a metal matrix (aluminium).

A more subtle difference in the present work is the separation of static mechanical properties into primary and secondary categories. The former category distinguishes those properties useful in design calculations, while the latter discusses properties more qualitative in nature, which are primarily useful in quality control or for comparative performance screening of composites.

In other respects, the data presentation follows that used in Part 1, that is, literature property values are presented in graphical form as a function of temperatures at 295 K, 200 K, 77 K, 20 K, and 4 K. The absence of a data point for a given temperature indicates failure to find significant data. References are given for each plotted curve.

The author is in the Cryogenics Division, NBS Institute for Basic Standards, Boulder, Colorado 80302, USA. Received 16 June 1975.

Curves presenting data averaged from several sources may have a considerable scatter band associated with them. We discuss the range of values associated with such curves and emphasize those specific types for which the best values were reported.

The complexity of the subject and the necessity of a cut-off data for data acquisition makes it unavoidable that some data worthy of inclusion have been inadvertently overlooked. The author would appreciate having such omissions brought to his attention. The author also wishes to emphasize that the data presented in this review reflect the published results of the cited authors. These data have not been experimentally verified by NBS, and the conclusions and evaluations presented herein do not imply approval, endorsement, or recommendation of any commercial product by NBS.

There exists no universally accepted method of determining many of the reported properties. It is not easy to obtain valid uniaxial longitudinal tensile fracture because of the difficulty of transferring the tensile load from the specimen grips into the fibres of the specimen without introducing excessive localized stress concentrations. Problems also arise in uniaxial longitudinal compression testing where an unsupported specimen may fail by the 'brooming' of its ends or by column buckling. However, such premature failures result in property values lower than the true values and tend to bias the data accordingly.

The discussion of properties of the composites included in this review does not take into consideration the effect of variations in fibre resin ratio among specific types of composites and test specimens. Boron-reinforced composites normally contain an 0.45–0.50 fibre resin ratio volume, while composites reinforced with graphite or organic fibre conventionally have an 0.50–0.65 ratio. Composite properties are strongly influenced by this ratio. Controlled variations in many of the properties are obtainable in practice by specific variation of the fibre content of the composites. The property data discussed in this paper reflect values and trends reported for composites containing of the order of 50% fibre volume. However, the reader must refer to the literature for specific composite data.

Finally, the reader should be aware that composite technology is developing so rapidly that some of the data presented in this review may not reflect the current state of the art. Recent introduction of new reinforcing fibres, improvements in composite fabrication techniques and refinement of test methods have resulted in overall improvement in both the level and the consistency of composite mechanical properties.

For the reader unfamiliar with the development of advanced composite technology, it will be useful to establish a perspective on the field. The two primary reinforcement systems are boron filaments produced by vapour deposition of boron on a very fine tungsten wire substrate and graphite fibre produced by graphitization (pyrolysis) of an organic precursor fibre. Additionally, a proprietary aromatic polyamide organic fibre commercially called Kevlar 49 (PRD 49) is currently receiving attention. The boron filaments were initially produced at 4 mil (1 mil = 25.4 μ m) diameter; however, 5.6 mil diameter filaments are now widely used. Boron fibre coated with a thin layer of silicon carbide, produced under the trade name of Borsic, is reported to have improved interfacial bonding to certain matrix types. The graphite fibre is much more complex, as it is not only possible to

produce such fibres from different precursor materials (the two most common being rayon and polyacrylonitrile (PAN)), but it is also possible to vary the production process to produce fibres differing greatly in modulus and strength. As the properties obtainable with graphite reinforcement may approach those with boron reinforcement at a somewhat lower cost, development of graphite fibres has proceeded at a very rapid rate. Today the user is confronted with an abundance of fibre choices, many of which are not well characterized and many of which will disappear to be replaced by newer types. At the present time, the potential user of these materials would be wise to restrict his interest to those types whose behaviour is reasonably well known, barring compelling reasons for doing otherwise.

Graphite fibres may be produced with elastic moduli varying from 25–75 $\times 10^6$ lb in⁻² (170–500 GPa), with strengths varying inversely to moduli. In the present report, these fibres are classified according to low, medium or high modulus, the differentiation being < 40, 40–60 and > 60 $\times 10^6$ lb in⁻², respectively (< 275, 275–415, and > 415 GPa).

As composites are frequently used where weight is critical or where high specific strengths are required, typical composite densities have been summarized in Table 1.

Primary static mechanical properties

The key static mechanical properties required for preliminary design calculations with composites are: uniaxial longitudinal and transverse tensile and compressive ultimate strengths; uniaxial in-plane shear ultimate strength; and ultimate strains in the uniaxial longitudinal and transverse directions. Key elastic properties are uniaxial tensile and compressive moduli in the longitudinal and transverse direction, uniaxial in-plane shear moduli and Poisson's ratios in the longitudinal and transverse uniaxial direction (see reference 124, Vol 1, Design). The literature data available on these key properties for composites within the cryogenic range are far from complete, and in some cases, non-existent. Nevertheless, available data provide a feel for the magnitude and temperature dependence of many key properties and serve to define areas in which further data are required.

For most mechanical properties, the data for the graphite-reinforced composites have been separated from that of the other advanced composites, that is, those reinforced with boron or PRD 49 (Kevlar 49). This reflects the larger amount of available data on the graphite-reinforced materials

Table 1. Typical composite densities

Composite system	Fibre/resin ratio	Density, lb in ⁻³ (g cm ⁻³)
s-glass-epoxy	0.60–0.67	0.068–0.074 (1.87–2.04)
Kevlar 49-epoxy	0.60–0.65	0.047–0.050 (1.3–1.38)
Boron-epoxy	0.55	0.070–0.074 (1.93–2.04)
Graphite-epoxy	0.55–0.60	0.050–0.055 (1.38–1.52)
Boron-aluminum (4 mil)	0.50	0.10 (2.62)

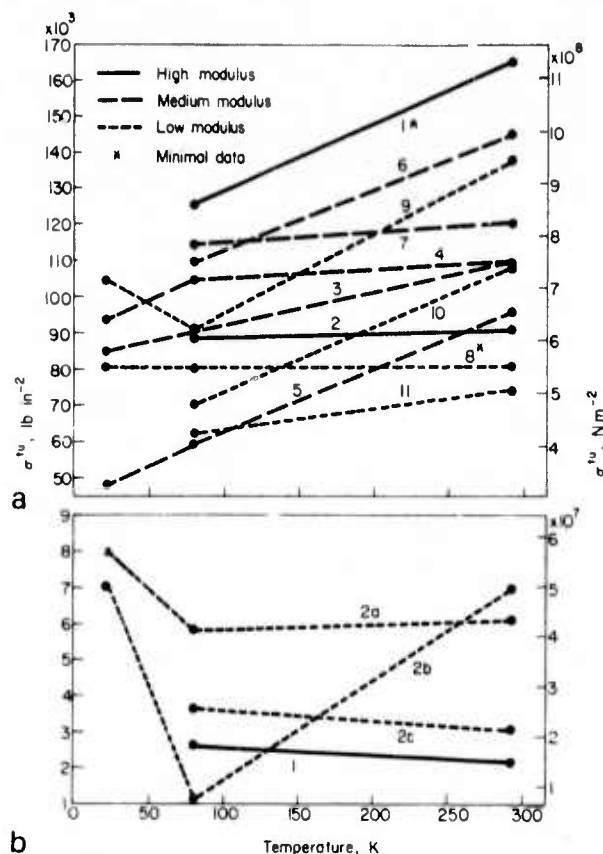


Fig.1 Ultimate tensile strength, σ^{tu} , of graphite-epoxy composites
 a - Uniaxial longitudinal: 1 - Thornel 75⁵¹; 2 - GY-70¹³; 3 - Thornel 50^{8,10}; 4 - HMG-50¹⁰; 5 - MH-S¹⁰; 6 - Modmor I⁸; 7 - Samco 320⁸; 8 - Thornel 25⁴⁷; 9 - HT-S^{9,10,13,13.2,58}; 10 - Modmor II⁸; 11 - HMG-25⁸
 b - Uniaxial transverse: 1 - Thornel 75/ERLB 4617⁵¹; 2a - HT-S/NASA Resin 2¹⁰; 2b - HT-S/4617 (modified)¹⁰; 2c - HT-S/X-904¹³

and the large variety of graphite fibres for which data have been published.

Composite tensile strength

Fig.1 summarizes the available data on the temperature dependence of the ultimate tensile strength of graphite-reinforced epoxy composites from room temperature into the cryogenic temperature range for the uniaxial longitudinal and uniaxial transverse orientations. A surprisingly large amount of cryogenic data were found in the literature for graphite-reinforced materials - 58 separate reports of test data, each report being the average of several tests on a given composite. Undoubtedly, this large effort reflects the desire to exploit the relatively low cost of graphite fibres.

The available data summarized on Fig.1 indicate that graphite-reinforced epoxy composites may suffer significant strength losses upon cooling to 77 K, and as was observed with the glass-reinforced materials in Part 1, the strength behaviour below 77 K appears to become erratic.

Fig.1a indicates that the uniaxial tensile strength obtainable in graphite-reinforced composites is about 30% of that obtainable with glass-fibre reinforcement in the cryogenic range. The ultimate tensile strength of composites tested in the uniaxial longitudinal mode should be fibre controlled; hence,

the tensile strengths should inversely follow the modulus of the fibre. This trend is not reflected in the data of Fig.1a - indeed the averaged data indicate the converse; higher strengths are associated with higher modulus fibres and lower strengths with lower modulus fibres. However, a more detailed examination of the data averaged into these curves shows that the expected correlation does exist if one considers only the highest strength values reported for each modulus range. Thus, the highest overall ultimate strength at 77 K was $147 \times 10^3 \text{ lb in}^{-2}$ (1.01 GPa) reported for the low modulus HT-S graphite fibre in X-904 resin.¹³ The next highest was $130 \times 10^3 \text{ lb in}^{-2}$ (0.90 GPa) reported for HMG-50 in a flexibilized epoxy matrix¹⁰ for Modmor I and for Samco 360 in modified ERL 1156,⁸ all medium modulus fibres, while $126 \times 10^3 \text{ lb in}^{-2}$ (0.87 GPa) was the maximum reported for the high-modulus Thornel 75 fibre in ERLB 4617.⁵¹ This suggests that the higher strengths normally associated with the lower modulus fibres may have been lost in the averaging process due to variations in composite quality or perhaps due to difficulties in obtaining valid tensile fractures. Additional evidence that the test method is capable of affecting the results is found in the work of Larsen and Simon¹⁰ who report almost diametrically opposite temperature dependence of the ultimate tensile strength for NASA Resin 2 and ERLB 4617 epoxy reinforced with HT-S fibre when each was tested, first as flat tensile coupons and subsequently as NOL (Naval Ordnance Laboratory) ring specimens. NASA 2 resin is a bisphenol A epoxy system modified for low temperature flexibility by means of a long-chain anhydride and a high molecular weight tricarboxy acid. This resin, consisting of Epon 828/DSA/Empol 1040/BDMA in proportions 100/115.9/20/1 pbw, was developed by Soffer and Molho⁵ under NASA Sponsorship.

The uniaxial longitudinal tensile strength data for other types of advanced composites are presented in Fig.2a. The data for PRD 49-epoxy, boron-epoxy, boron (Borsic)-aluminium, stainless steel-aluminium, and the hybrid Borsic-steel-aluminium and Borsic-titanium-aluminium composites all have higher absolute values of tensile strength and retain their strength to lower temperatures than do the graphite-reinforced composites. Data for Borsic and boron-fibre composites have been combined except where differences in reported values justified separating the data. The hybrid Borsic-steel-aluminium (6061) composite contained 4.2 mil Borsic fibres in the tensile direction and stainless wires in the transverse direction. The hybrid Borsic-titanium-aluminium (6061) composite contained 4.2 mil Borsic fibres in the tensile direction with β -3Ti foil interleaved between the boron lamellae.¹³ While the latter two composites are not strictly uniaxial, they have been included to illustrate the interesting possibilities of hybrids.

The magnitude and temperature dependence of the ultimate tensile strength of the graphite HT-S/polyimide (Skybond 703) material were comparable to that of the graphite-epoxies. A very sharp rise in strength on cooling was reported for the HT-S/epoxy-phenolic (HT-424 Primer).

The stainless steel reinforced composite contained NS-355 stainless wires in a 2024 aluminium alloy matrix. This type of composite is available commercially on special order; however, it has not received wide acceptance in view of the wider availability of boron-reinforced aluminium, which has similar strength properties.

Boron-aluminium composites are available commercially with

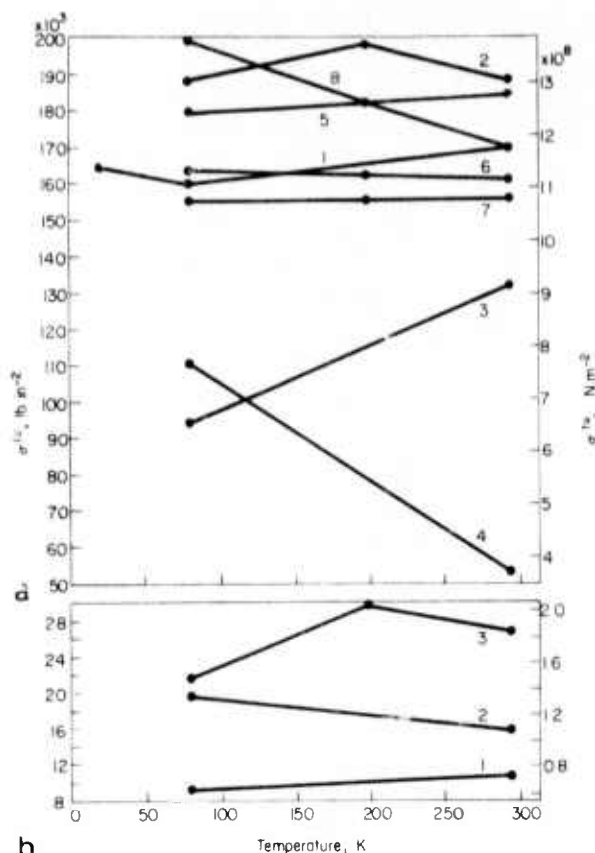


Fig.2 Ultimate tensile strength, σ^{tu} , of miscellaneous advanced composites

a — Uniaxial longitudinal: 1 — PRD 49-1/epoxy^{59,60}; 2 — boron-epoxy^{13,22,47,53,58,61}; 3 — HT-S/polymide¹³; 4 — HT-S/epoxy-phenolic⁵⁸; 5 — boron-aluminium (6061)¹³; 6 — Borsic-steel-aluminium (6061)¹³; 7 — Borsic-titanium-aluminium (6061)¹³; 8 — stainless steel-aluminium (2024)^{7,74}
 b — Uniaxial transverse: 1 — boron-epoxy^{13,81}; 2 — boron-aluminium (6061)¹³; 3 — Borsic-titanium-aluminium¹³

either 4 or 5.6 mil boron or Borsic reinforcement, while 8 mil boron fibers are currently being studied. Available literature values of uniaxial tensile strength at 77 K ranged from $163\text{--}202 \times 10^3 \text{ lb in}^{-2}$ ($1.12\text{--}1.39 \text{ GPa}$), with highest values reported for 5.6 mil Borsic/6061.¹³ Data were not available for any other aluminium alloy matrix. Boron-epoxy composites containing either 4 mil or 5.6 mil fibre are commercially available in the form of prepreg tape, that is, with the plastic matrix partially cured to facilitate component fabrication and to improve composite quality. The literature values for boron-epoxy composites tested in the longitudinal direction at 77 K varied from $167\text{--}226 \times 10^3 \text{ lb in}^{-2}$ ($1.15\text{--}1.56 \text{ GPa}$), the highest value being reported for the commercial SP-272 product.¹³

PRD 49 (Kevlar 49) is a relatively new type of organic fibre. Present data indicate that this fibre in an epoxy matrix is capable of developing tensile strengths at cryogenic temperatures comparable to that developed with the graphite fibres. Hoggatt⁵⁹ reports NOL ring ultimate strengths of $146 \times 10^3 \text{ lb in}^{-2}$ (1.0 GPa) for PRD 49-1 in a NASA Resin 2 matrix and $183 \times 10^3 \text{ lb in}^{-2}$ (1.26 GPa) in an ERLB 4617 matrix at 20 K. There is some evidence of a slight decrease in strength on cooling to 77 K; however, available data indicate that the ultimate tensile strength of this

material is relatively independent of temperature within the cryogenic range.

The hybrids Borsic-steel-aluminium and Borsic-titanium-aluminium complete the group of advanced composites that has reasonably high strength in uniaxial tension. The somewhat lower strength of these hybrids, compared to the conventional boron-aluminium composite, reflects the reduced density of boron fibres in the loading direction.

Metal-matrix composites are clearly superior to polymer-matrix composites in transverse mechanical properties. As seen in Fig.2(b), the ultimate uniaxial transverse tensile strength of boron/6061 aluminium is about 50% higher than that of boron-epoxy. Addition of titanium foil to the boron-aluminium further increases the transverse strength at 295 K and 200 K; however, the effect appears to diminish rapidly as the material is cooled to 77 K. While the transverse strength of the conventional boron-epoxy composite is much lower than that of the metal-matrix materials, values are still in excess of those developed with the graphite fibre reinforcement.

The boron/6061 aluminium data reviewed here reflects the as-fabricated (F) condition. Solution-treating and aging the composite increase the transverse ultimate strength by about 30%, with a slight decrease in transverse ductility.¹³

The literature reported a 77 K transverse ultimate strength of $14.2 \times 10^3 \text{ lb in}^{-2}$ (97 MPa) for 4.2 mil Borsic/6061 aluminium and a somewhat higher value of $24.9 \times 10^3 \text{ lb in}^{-2}$ (172 MPa) for 5.6 mil boron reinforcement.¹³ It is also probable that this strength difference is real; however, available data^{13,126} also indicate that the observed difference may be due to residual stresses inherent in the small diameter fibre rather than to the presence or absence of a silicon carbide coating. The reader is referred to the section on ultimate tensile strain for further discussion of this subject.

Composite tensile modulus

The primary reason for development of advanced composites is the high modulus obtainable with the newer types of fibre reinforcement. In contrast to a maximum of about $10 \times 10^6 \text{ lb in}^{-2}$ (69 GPa) for glass-reinforced composites in the fibre direction, Figs 3a and 4a show that moduli ranging from $30\text{--}40 \times 10^6 \text{ lb in}^{-2}$ ($207\text{--}276 \text{ GPa}$) are obtainable with several of the advanced fibre composites. Thus, while glass-reinforced composites may at their best equal the modulus of aluminium, the modulus of composites using advanced fibres may at their best equal and often exceed that of steel.

Looking first at the graphite-epoxy composites, Fig.3a shows that the uniaxial longitudinal modulus of the composite does, on the average, reflect the modulus of the fibre when tested in the uniaxial longitudinal mode. The available data indicate that the modulus of the Thornel 75 composite (the only representative of the high modulus fibres) declines to about that of the medium modulus fibres at 77 K. With this exception, the average data indicate that the moduli in the fibre direction slightly increase on cooling to 77 K. No correlation is observed between fibre modulus and transverse composite moduli in Fig.3b; indeed, none is expected, as the latter is controlled by the properties of the matrix and by the fibre-matrix interfacial bond strength.

A comparison of Figs 3a and 4a shows that the uniaxial longitudinal modulus of graphite-epoxy composites may exceed that of any other type of advanced composite when certain graph-

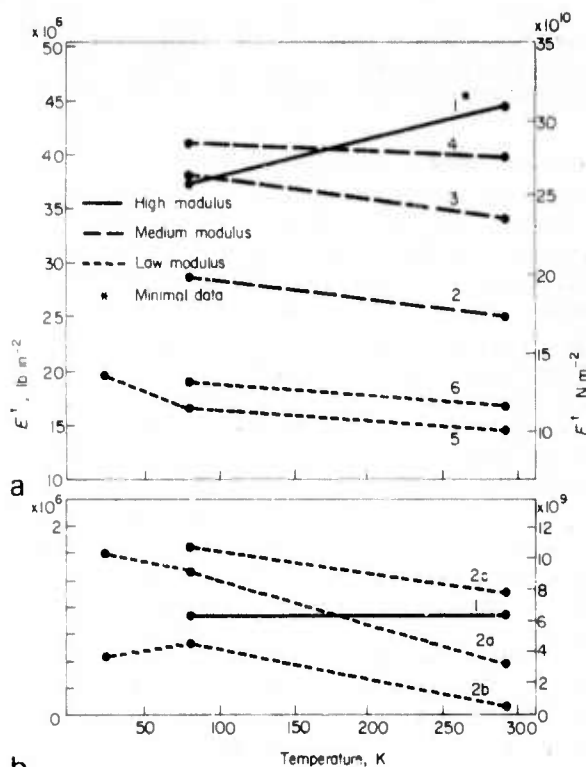


Fig.3 Initial tensile modulus, E_1 , of graphite-epoxy composites
a — Uniaxial longitudinal: 1 — Thornel 75⁵¹; 2 — Thornel 50⁸; 3 — Modmor 1⁸; 4 — Sancom 320⁸; 5 — HT-S^{8,10,13}; 6 — HMG-25⁸
b — Uniaxial transverse: 1 — Thornel 75/ERLB 4617⁵¹; 2a — HT-S/NASA Resin 2¹⁰; 2b — HT-S/4617 (Modified); 2c — HT-S/X-904¹³

ite fibres are used. However, a comparison of Figs 3b and 4b shows that the uniaxial transverse tensile moduli of graphite-epoxy composites are much lower than that developed by the other advanced composites over the entire cryogenic temperature range.

A closer look at the literature data from which Fig.3a was prepared revealed that among the medium modulus fibres, the modulus at 77 K was $39\text{--}43 \times 10^6 \text{ lb/in}^2$ (269–297 GPa) for Samco 360; the highest value being reported with a modified ERL 2256 resin.⁸ The Modmor 1 fibre produced almost as high moduli, ranging from $32\text{--}42 \times 10^6 \text{ lb/in}^2$ (221–290 GPa), with the highest values reported for a NASA Resin 2 composite.⁸ (Note that these same fibres developed high uniaxial tensile strengths). A distinctly lower range of $26\text{--}33 \times 10^6 \text{ lb/in}^2$ (179–228 GPa) was reported for Thornel 50; the highest values were for a modified ERL 2256 composite.⁸ among the low modulus fibres, HT-S (the most tested fibre) produced $15\text{--}20 \times 10^6 \text{ lb/in}^2$ (103–138 GPa), the highest value being reported with X-904 resin,¹³ while $17\text{--}22 \times 10^6 \text{ lb/in}^2$ (117–152 GPa) was the reported range for HMG-25, the highest values being obtained in a NASA Resin 2 matrix.⁸

As the transverse modulus properties are matrix dominated, Fig.3b shows significant differences for the same HT-S fibre in different epoxies. The illustrated data are for the same composites as appear in Fig.1b. Here the lower moduli of the HT-S/NASA Resin 2 and the HT-S/4617 (modified) are due to the additions of flexibilizers and elastomers to the

epoxy resin, while the highest modulus was developed with the conventional X-904 matrix. In general, the transverse modulus increases with decreasing temperature. A lower composite modulus value was reported for the high-modulus Thornel 75 fibre in ERLB 4617 resin than for the HT-S/X-904 combination.

Leaving the graphite-reinforced composites and turning to those reinforced with other advanced fibres, we observe in Fig.4a that the uniaxial longitudinal moduli reported for the boron-epoxy, the boron-aluminium and the hybrid Borsic-titanium-aluminium and Borsic-steel-aluminium composites all cluster around $30\text{--}35 \times 10^6 \text{ lb/in}^2$ (207–242 GPa) with little temperature dependence. The PRD 49/epoxy modulus is reported to be significantly lower, at $16\text{--}18 \times 10^6 \text{ lb/in}^2$ (110–124 GPa), but undergoing a significant rise between 77 K and 20 K. In general, these uniaxial longitudinal moduli values compare favourably with those of the graphite-epoxies.

The uniaxial transverse moduli are another matter. As seen in Fig.4b, the transverse moduli of the aluminium-matrix materials are far higher than those of the graphite-epoxies and are, in fact, almost twice as high as that of unreinforced 6061 aluminium. The transverse moduli of the boron-epoxy is much lower than that for the same fibre in an aluminium matrix, but is still almost twice that of the graphite-epoxy materials. These data reflect the contribution made by fibre-matrix interface to the transverse modulus.

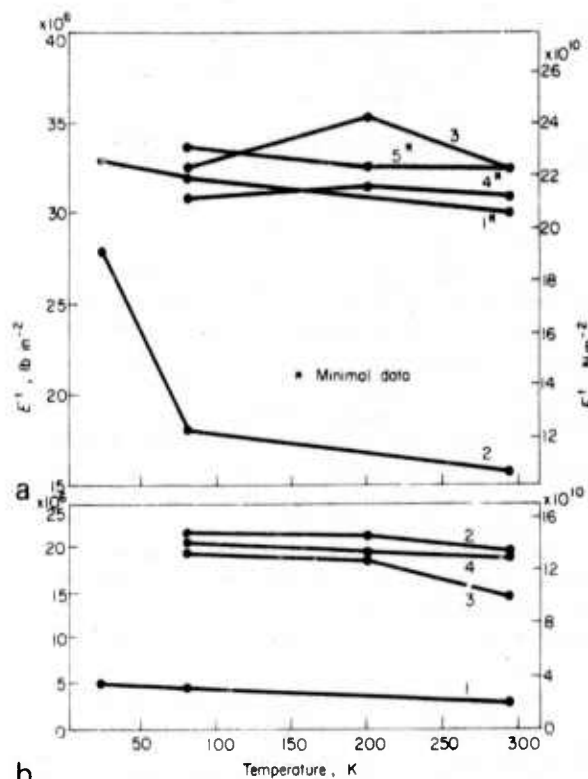


Fig.4 Initial tensile modulus, E_1 , of miscellaneous advanced composites
a — Uniaxial longitudinal: 1 — boron-epoxy⁸¹; 2 — PRD 49-1/epoxy^{59,60}; 3 — boron-aluminium (6061)¹³; 4 — Borsic-titanium-aluminium (6061)¹³; 5 — Borsic-steel-aluminium (6061)¹³
b — Uniaxial transverse: 1 — boron-epoxy (SP-272, Narmco 5505)⁶¹; 2 — boron-aluminium (6061)¹³; 3 — Borsic-titanium-aluminium (6061)¹³; 4 — Borsic-steel-aluminium (6061)¹³

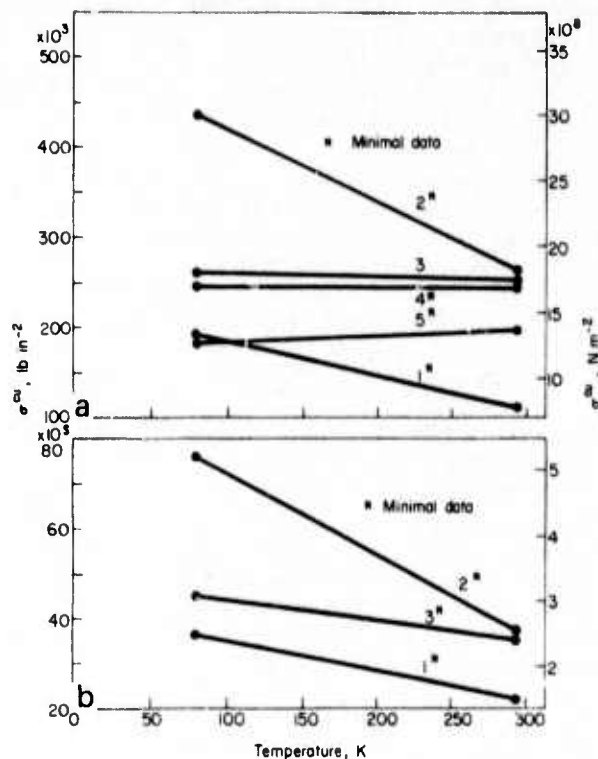


Fig.5 Ultimate compressive strength, σ_{CU} , of advanced composites
 a — Uniaxial longitudinal: 1 — HT-S/X-904¹³; 2 — boron-epoxy⁸¹ (SP-272, Narmco 5505); 3 — boron-aluminium¹³ (6061); 4 — Borsic-titanium-aluminium (6061)¹³; 5 — Borsic-steel-aluminium (6061)¹³
 b — Uniaxial longitudinal: 1 — HT-S/X-904¹³; 2 — boron-epoxy⁸¹ (Narmco 5505, SP-272)⁸¹; 3 — boron-aluminium¹³

Looking in more detail at the uniaxial longitudinal data, we find that the boron (Borsic)-aluminium data ranged from $30.4\text{--}36.2 \times 10^6 \text{ lb/in}^2$ (210–250 GPa) with little temperature dependence. These data combine values obtained from fibres of 4 mil and 5.6 mil diameter in the two production variants, as no significant difference was reported for these materials. The boron-epoxy data represent average results reported by Nadler et al⁸¹ on SP-272 and Narmco 5505 (data range was not available). The hybrids, Borsic-titanium-aluminium, and Borsic-steel-aluminium, were the same composites discussed in reference to the tensile data of Fig.2a. The slightly lower uniaxial tensile modulus of the hybrids compared to that of the conventional boron-aluminium reflects the lower density of fibres in the stress direction in the hybrids.

The PRD 49 data reflect input from both an ERLB 4617 and a NASA Resin 2 matrix.^{59,60} The ERLB 4617 composite produced a slightly increased tensile modulus at all temperatures, its value being $18.5 \times 10^6 \text{ lb/in}^2$ (128 GPa) at 77 K compared to $17.5 \times 10^6 \text{ lb/in}^2$ (121 GPa) for the NASA Resin 2. A large rise in modulus between 77 K and 20 K was reported for both matrices.

Considering the transverse data of Fig.4b in more detail, we observe that the three aluminium-matrix composites have similar moduli, about $20 \times 10^6 \text{ lb/in}^2$ (138 GPa). The boron-aluminium data was again the average of data obtained from 4.2 mil Borsic and 5.6 mil boron, similar

values being reported for each variant. The boron-epoxy data of Fig.4b again reflect the average values obtained from the commercial SP-272 and Narmco 5505 materials.⁸¹

Composite compressive strength and modulus

Data on the compressive properties of advanced composites at cryogenic temperatures were also relatively sparse. Those which were available appear in Figs 5 and 6, combining the graphite-epoxy data with those of the other composite types.

These data show that the advanced composites have significantly higher compressive strengths and moduli than those of the glass-reinforced composites. Comparison of Fig.5 with Figs 1 and 2 also shows that the compressive strengths are 100–200% higher than the tensile strengths for the same composites.

The highest uniaxial longitudinal compressive strength, more than 200% above that obtainable with glass reinforcement, was reported for the commercial boron-epoxy types SP 272 and Narmco 5505.⁸¹ The compressive strength of this composite class was observed to increase on cooling to 77 K. Boron-aluminium reportedly has a comparatively lower uniaxial compressive strength. The latter data reflect input from both 4.2 mil Borsic and 5.6 mil boron-fibre composites.¹³ A slightly higher strength was reported for the 5.6 mil composite, but not sufficiently to justify a separate plot. Again, the Borsic-titanium-aluminium and Borsic-steel-aluminium hybrids developed strengths some-

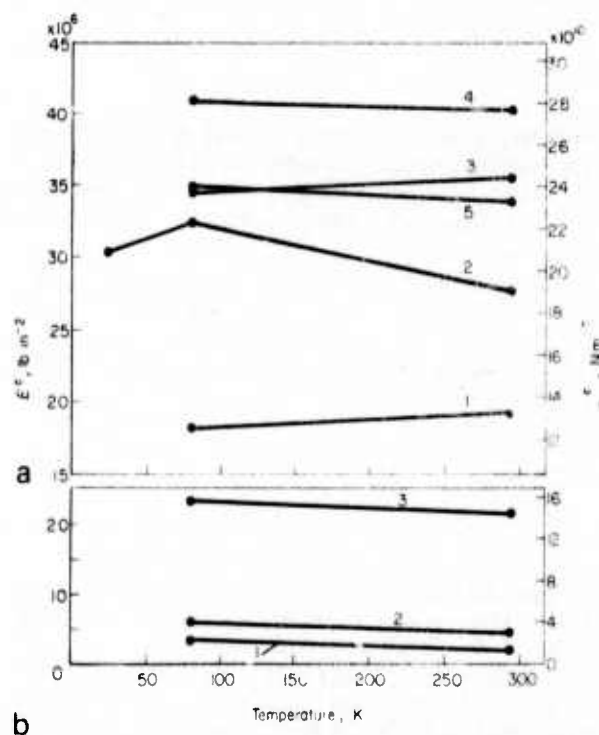


Fig.6 Compressive modulus, E^c , of advanced composites
 a — Uniaxial longitudinal: 1 — HT-S/X-904¹³; 2 — boron-epoxy (Narmco 5505, SP-272)⁸¹; 3 — boron-aluminium (6061)¹³; 4 — Borsic-titanium-aluminium (6061)¹³; 5 — Borsic-steel-aluminium (6061)¹³
 b — Uniaxial transverse: 1 — HT-S/X-904¹³; 2 — boron-epoxy (Narmco 5505, SP-272)⁸¹; 3 — boron-aluminium (6061)¹³

what below that of the conventional boron-aluminium, reflecting the decreased density of boron fibres in the stress direction. Lowest uniaxial longitudinal compressive strengths were reported for the HT-S/X-904 graphite-epoxy composite; however, this composite developed a compressive strength about twice that developed in tension and about 40% higher than that available with glass reinforcement. The compressive strength of the graphite-epoxy composite was reported to increase with cooling, in contrast to the tensile behaviour.

The available data on the transverse compressive strengths of boron-epoxy, boron-aluminium, and graphite-epoxy composites are compared on Fig. 5b. These composites appear in the same relative order of strength as in the longitudinal test mode. The commercial SP-272 and Narmco 5505 boron-epoxy products display substantial increases in compressive strength on cooling. Lesser increases are observed in the boron/aluminium and in the HT-S/X-904 graphite-epoxy composite.

The compressive modulus of a given composite is expected to be the same as the tensile modulus. This is found to be generally true for the HT-S/X-904 graphite-reinforced material, for the boron-epoxy, for the Borsic-aluminium composites, and for the Borsic-steel-aluminium hybrid, as may be seen by comparing the compressive moduli of Fig. 6a with the tensile moduli of the same composites on Fig. 3 and 4. The Borsic-titanium-aluminium data are at variance with this principle, as the reported compressive modulus is about 30% higher than in tension. The boron-aluminium and the boron-aluminium hybrids again show the highest longitudinal moduli, with the boron-epoxy only slightly lower. The modulus of the HT-S/X-904 graphite-reinforced composite is again much lower than that of the boron-reinforced materials. There does not appear to be a significant temperature sensitivity of this parameter. Also, as in the tensile case, the boron-aluminium is found to have a higher transverse compressive modulus than either the boron-epoxy or the graphite-epoxy composite.

Composite failure strain

Available data on the temperature dependence of ultimate tensile strain for advanced composites are minimal; all of that which has been published reflects the work of Hertz et al.¹³ Nevertheless, these data suffice to illustrate that: (a) the strain at tensile fracture is very low for the advanced composites, being of the order of $1-9 \times 10^{-3}$ in the longitudinal uniaxial direction; and (b) the strain at tensile fracture is relatively independent of temperature within the cryogenic range. These data are summarized on Fig. 7. These strains are about an order of magnitude lower than those obtained with glass-reinforced composites, reflecting the negligible fracture strain of the advanced fibres.

Fig. 7 includes data on one graphite-reinforced composite (HT-S/X-904), on two conventional boron-aluminium composites (4.2 mil Borsic and 5.6 mil boron, both in 6061 aluminium) and on the two Borsic-aluminium hybrids discussed previously with reference to the other properties. Both longitudinal and transverse ultimate fracture strains appear on Fig. 7.

Fig. 7 indicates that the transverse fracture strain of the HT-S/X-904 graphite-epoxy composite will be about 2×10^{-3} , or about 25% of the longitudinal strain. By comparison, the transverse fracture strain for the commercial HT-S/3002

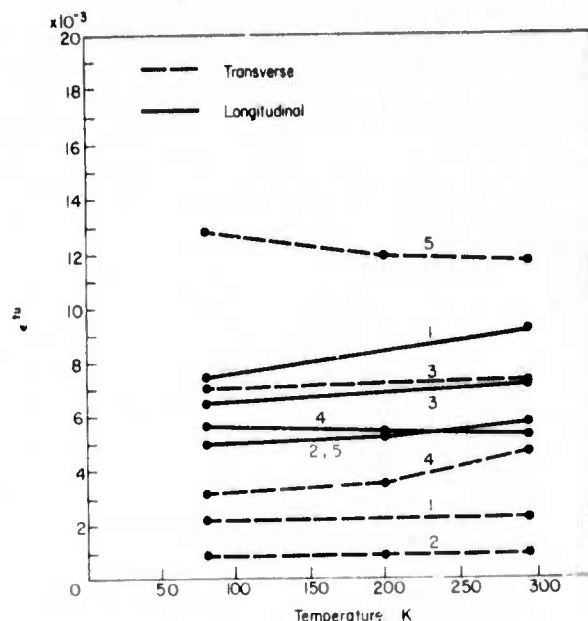


Fig. 7 Ultimate tensile strain, ϵ^{10} , of advanced composites (uniaxial tensile) ¹³; 1 - HT-S/X-904 ¹³; 2 - 4.2 mil Borsic-aluminium (6061) ¹³; 3 - 5.6 mil boron-aluminium (6061) ¹³; 4 - 4.2 mil Borsic-titanium-aluminium (6061) ¹³; 5 - 4.2 mil Borsic-steel-aluminium (6061) ¹³

graphite-epoxy composite is reported¹² to be 7.8×10^{-3} , only slightly less than its longitudinal fracture strain of 8.6×10^{-3} . The interfacial-bond strength between the fibre and matrix in the HT-S/3002 composite was undoubtedly superior to that existing in the HT-S/X-904 composite.

Fig. 7 shows that a 5.6 mil boron/6061 aluminium composite is expected to fail at about the same strain in both the longitudinal and transverse directions. The 4.2 mil Borsic/6061 composite is expected to fail at a much lower strain when tested in the transverse direction. Hertz et al.¹³ found that the 4.2 mil Borsic fibre was failing by longitudinal fibre splitting during transverse testing, while such splitting did not occur in the larger diameter fibre. The authors concluded that the problem was related to the use of plasma-sprayed tape. Higher transverse strains were observed in the same type of composite when diffusion-bonded tape was used to make the test specimens. They concluded that diffusion-bonded boron-aluminium tape was superior for oriented-ply applications. Kreider and Prewo^{12s} has proposed an alternative explanation for longitudinal splitting of the small diameter boron fibres, citing results of diametral compression tests of individual fibres, which indicate that such splitting reflects strength anisotropy in the small fibres due to residual stresses retained from the original fibre manufacturing process and from pre-existing flaws in the fibres. Such anisotropy was not observed in the larger fibres. Fibre splitting was not directly related to the presence or absence of a silicon carbide coating on the fibres. (Manufacturers of boron-aluminium tape report that current fabrication technology has overcome the problem of fibre splitting)

The Borsic-titanium-aluminium hybrid reportedly developed higher strain values in both directions than did the conventional 4.2 mil Borsic-aluminium, but lower values than that of the composite reinforced with 5.6 mil boron. The borsic-

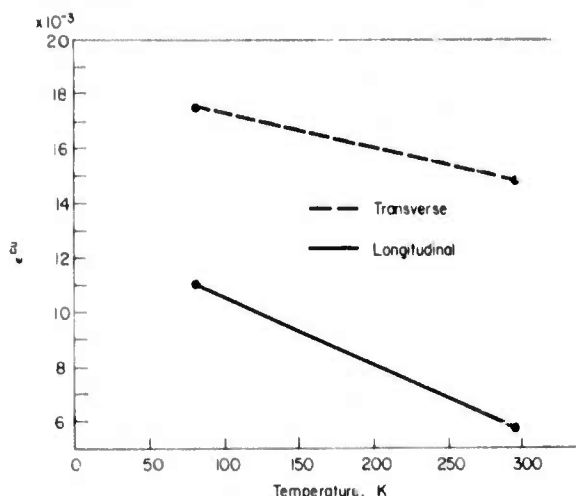


Fig.8 Ultimate compressive strain, ϵ_{cu} , of graphite-epoxy composites: uniaxial compression HT-S/X 904¹³

steel-aluminium hybrid shows clearly the increase in transverse strain capability due to the presence of stainless wires oriented in this direction. The longitudinal strain of this hybrid did not appear to be significantly affected by the transverse reinforcement.

The only data available on the temperature dependence of compressive strain within the cryogenic temperature range was for the HT-S/X 904 graphite-epoxy composite, again reflecting the work of Hertz et al.¹³ These data, Fig.8, indicate an increasing compressive strain capability for this composite type as the temperature is lowered, with a substantially higher strain capability in the transverse direction. As in the tensile case, these strain values are substantially lower than those reported for an HT-S/3002 graphite-reinforced composite.¹²⁴

Composite in-plane shear strength and modulus

The key shear properties are the in-plane ultimate strength and modulus, sometimes referred to as the intralaminar or longitudinal shear properties. The requirements for obtaining valid shear property data are the same as for metals, that is, values must reflect pure shear resolved onto a 45° shear plane with respect to the tensile axis without significant compressive or tensile forces normal to the shear plane. Three shears may be defined in a bulk, uniaxial composite laminate. Most important are the two longitudinal shears represented by shear between parallel fibres in the plane of the fibres. For example, taking the x axis parallel to the fibres, longitudinal shear strengths may be defined as σ_{yx}^{su} or σ_{zx}^{su} ; however, in thin laminates, only one such in-plane shear is of consequence. A third shear, which is transverse or cross-fibre, is not an important composite design parameter.

It is important to distinguish between in-plane or intralaminar shear defined as above and *interlaminar* shear, which refers to shear between adjacent layers in a layered composite. The latter, sometimes called horizontal shear, is *not* a basic material property and is used primarily as an adjunct to quality control or in material screening tests. Because the test is simple and inexpensive, a large amount of interlaminar shear data have been reported.

In-plane shear is a difficult property to measure accurately because of the necessity of avoiding extraneous compressive

or tensile stresses on the shear plane. The torque tube (torsion) method works well but is expensive. Consequently, somewhat simpler methods such as the 'rail shear' or the '± 45° laminate' test have been devised. The interested reader can find discussions of the relative merits of these latter methods in ASTM STP Vols 460, 497, and 546.

Few data are available on the in-plane shear properties of composites at cryogenic temperatures. Hertz et al.¹³ report a decrease in the shear strength of HT-S/X-904 graphite-epoxy from 8 592 lb in⁻² (60 MPa) at 295 K to 7 378 lb in⁻² (51 MPa) at 77 K, using the torsion tube test method. A concomitant shear modulus increase from 7.27 × 10⁵ lb in⁻² (10.5 GPa) was reported. Obviously, much additional in-plane shear data are required before trends in the cryogenic temperature dependence of shear properties can be defined. Room temperature values of shear strengths and moduli are reportedly about 18 × 10³ lb in⁻² (124 MPa) and 9.5 × 10⁶ lb in⁻² (65 GPa), respectively, for boron-aluminium, while values for boron-epoxy are about 15 × 10³ lb in⁻² (124 MPa) and 7 × 10⁵ lb in⁻² (0.48 GPa), respectively.¹²⁴ Reported room temperature values for the shear strength of graphite-epoxy composites vary from 9–13 × 10³ lb in⁻² (62 MPa) with a modulus of about 6.5 × 10⁵ lb in⁻² (0.45 GPa), the variation in strength reflecting variation in properties of the graphite fibre used in the composite. As most of the other mechanical properties of boron-aluminium and boron-epoxy composites either remain unaffected or increase upon cooling to cryogenic temperatures, these room temperature values likely represent conservative values for such materials at the lower temperatures. However, confirmation must await further testing at the cryogenic temperatures.

Secondary static mechanical properties

The properties discussed in this section are classified as secondary only in that they are not generally useful in a predictive design analysis using macromechanics composite theory. However, such secondary properties are important in other ways. Because composites are largely fabricated *in situ*, a large number of options are available among fibre (or combinations of fibres) and matrix materials. Options are also available in fabrication procedure. It is necessary to efficiently evaluate various combinations in a meaningful comparative manner in order to optimize the final selection. Furthermore, having made a selection, it is necessary to have viable techniques for measuring the consistency of composite quality over a production run. For such objectives, the flexure test and the interlaminar shear test (usually also performed in flexure) are relatively inexpensive and informative. Additionally, there are properties that are classed as secondary only in that the results are specific to a given geometry as, for example, bearing yield strength.

Composite flexural strength and modulus

The flexure test requires that a bar or plate specimen be supported near its ends while deflected by a moving ram at its centre, providing symmetrical three-point loading. Dimensions of the fixture and specimen are proportioned to develop maximum stress in the outer (tension) fibres as flexure progresses. Fibres run lengthwise along the specimen, that is, between the supports, in uniaxial longitudinal flexure and across the specimen in uniaxial transverse flexure.

Fewer data were available on the temperature dependence of

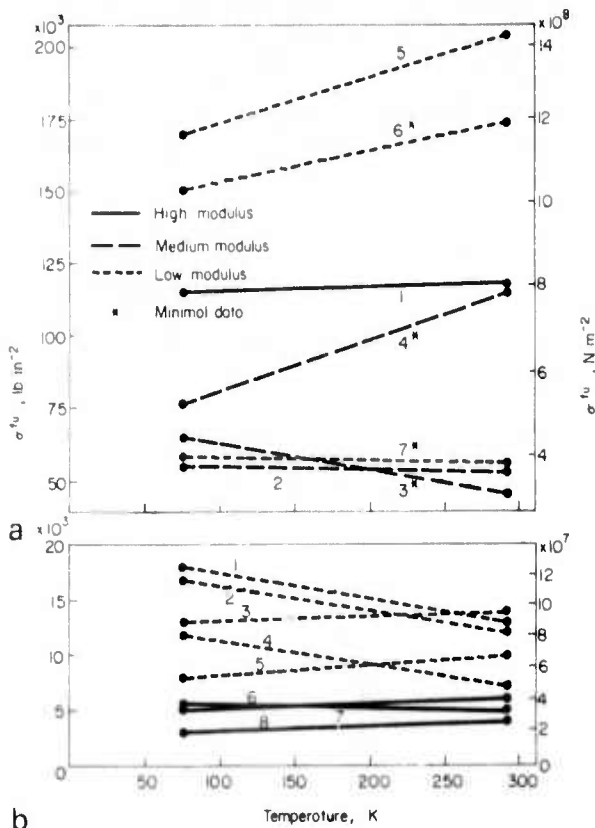


Fig.9 Ultimate flexural strength, σ_f , of graphite-epoxy composites
a - Uniaxial longitudinal: 1 - GY-70^{11,13}; 2 - Thornel 50⁸; 3 - Courtaulds HM⁸; 4 - Fibraltex 300¹³; 5 - HT-S^{11,12,13,58}; 6 - Modmor II¹³; 7 - HMG-25⁸;
b - Uniaxial transverse: 1 - Modmor II/1004¹³; 2 - HT-S/1004¹³; 3 - HT-S/BSP-2401¹³; 4 - HT-S/X-904^{11,13}; 5 - HT-S/3002^{11,13}; 6 - GY-70/1004¹³; 7 - GY-70/E-350A¹³; 8 - GY-70/X-904^{11,13}

the flexural strength and elastic modulus than for tensile properties; furthermore, most of those available were reported for graphite-epoxy composites. Fig.9 summarizes the flexural strength data for the latter, while Fig.10 summarizes the available data for other types of reinforcements or matrices. The minimal available data on flexural modulus properties appear in Fig.11.

Comparison of Fig.9 with Fig.1 shows that the graphite-epoxy flexural strength data span a much greater range of values than does the tensile strength data in both the longitudinal and transverse directions. The expected higher strength of the lower modulus fibres is more in evidence for the flexural test than it was for the tensile test mode.

By far the largest amount of data was available for HT-S/epoxy composites. Furthermore, such composites had the highest longitudinal flexural strength of all the graphite-reinforced materials for which data were available. Strengths were reported over a $113-234 \times 10^3 \text{ lb in}^{-2}$ (0.78-1.61 GPa) range at 77 K. This is significantly lower than the $325-470 \times 10^3 \text{ lb in}^{-2}$ (2.24-3.24 GPa) range reported for uniaxial glass-epoxies in Part 1. These data included test series designed to investigate cure cycles, aging effects, and environmental effects.^{12,13,58} Most of the work was done with E-350, X-915, or X-904 matrices, for which the average flexural strengths at 77 K were reported to be very similar, varying only from $167-178 \times 10^3 \text{ lb in}^{-2}$ (1.15-1.23 GPa).¹³

The available data on the HT-S fibre composites remind us that processing variables are important; in particular, those variables that affect the void content. Detailed examination of the available data showed that in 84 of the 89 reported test series, the flexural strength of composites made with HT-S fibre declined markedly on cooling to 77 K. The five series for which strength increases were noted were reported by Scheck¹² to have occurred concomitantly with a change to a vacuum-bagging method of fabrication. This suggests that at least a part of the observed drop in flexural strength on cooling might have been due to the presence of voids in the composites.

Continuing this with the other fibres, we observe on Fig.9a that the order of decreasing strength is Modmor II, GY-70, and Fibraltex 300, arriving finally at a group comprising the lowest reported strengths and consisting of Courtaulds HM, HMG-25, and Thornel 50 fibres. The flexure strength of this latter group is only about a third that of the HT-S fibre composites. Among these other fibres, most data were available for the high-modulus GY-70, for which the spread of values at 77 K was $85-133 \times 10^3 \text{ lb in}^{-2}$ (586-917 MPa); the highest being reported in X-904 epoxy resin.¹³

The clear separation between the transverse flexural strengths of the low modulus HT-S composites and the high modulus GY-70 composites in Fig.9b suggests that there are

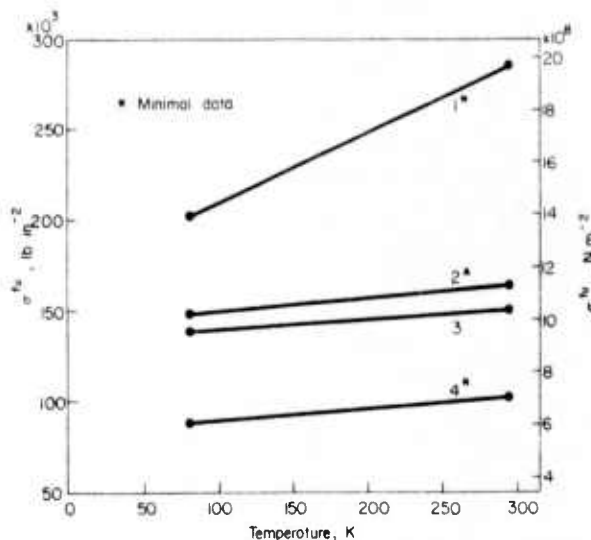


Fig.10 Ultimate flexural strength, σ_f , of miscellaneous advanced composites
1 - boron-epoxy (SP-272)⁵⁷; 2 - HT-S/polyimide^{11,58}; 3 - HT-S/epoxy-phenolic⁵⁸; 4 - GY-70/polyimide¹¹

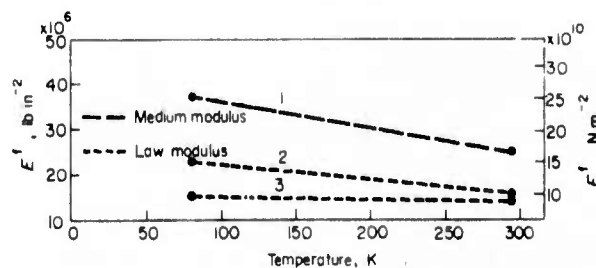


Fig.11 Initial flexural modulus, E_f , of advanced composites: uniaxial longitudinal
1 - Thornel 50; 2 - HMG-25; 3 - Modmor II (all reference 8)

Table 2. Comparison of ranking of specific uniaxial graphite-epoxy composites by longitudinal flexure strength and by longitudinal tensile strength (77 K)

Composite	σ^u , 10^3 lb in $^{-2}$	Rank	σ^t , 10^3 lb in $^{-2}$	Rank
A	178	1	147	1
B	172	2	87	6
C	167	3	103	2
D	146	4	45	8
E	117	5	92	4
F	58	6	91	5
G	55	7	71	7
H	5 ^a	8	93	3

differences in the fibre-matrix bond strength between these two fibre types, the high modulus fibre having the poorer bonding. Note that X-904 and 1004 epoxies were used with both fibre types.

Before leaving the data of Fig.9, it is of interest to consider whether or not the literature data support the contention that the relatively inexpensive flexure test may be used to obtain comparative ranking of composite strength in lieu of the more expensive tensile test. A visual comparison of the data on Fig.9a with that of Fig.1a is hardly convincing. However, such a comparison is nebulous because these graphs present data from different composite types. To clarify this question, the literature data were examined more closely and a comparison of ranking of strength in longitudinal tension versus longitudinal flexure was made at 77 K for eight specific composite types (same fibre and matrix) for which data were available. The data are summarized in Table 2. Results suggest that the flexure test results are not a very good measure of the relative tensile strengths of graphite/epoxy composites at 77 K. Insufficient data existed for similar comparisons with other mechanical properties.

Flexure data on other types of advanced composites were somewhat meagre. Fig.10 does indicate that the uniaxial longitudinal flexural strength of boron-epoxy in the form of the commercial SP-272 product is much higher than that of the graphite-epoxies, although still lower than that developed with glass reinforcement. A quite rapidly declining strength is observed on cooling to 77 K. The latter effect was not observed in the comparable tensile data (see Fig.2a). Data were available for two polyimide composites, one with the high modulus GY-70 fibre and one with the low modulus HT-S fibre. Of these, the HT-S composite developed the higher strength. A small decrease in flexure strength is evidenced in these composites at 77 K, but the magnitude of the decrease is less than that reported for the uniaxial tensile strength. Finally, the HT-S/epoxy-phenolic (HT-424 Primer) appears to possess acceptable flexure strength with little temperature dependence, in contrast to the comparatively low strength and significant temperature dependence reported for the same composite in longitudinal tension (see Fig.2a).

Very little data were available on the flexural modulus. Data for the longitudinal mode appearing on Fig.11 reflect the modulus of the reinforcing fibres and appear to agree reasonably well with the moduli of the same composites in tension. The Thornel 50 data are an average of data from two matrix types, a modified ERL 2256 epoxy and NASA

Resin 2.⁸ A slightly higher modulus was reported for the latter at both 295 K and 77 K.

Composite interlaminar shear strength

Interlaminar shear strength is the resistance to failure between layers in a layered laminate along the plane of their interface. Interlaminar shear is sometimes measured by the guillotine method, in which shear is forced by the imposition of opposing but offset cuts across the width of a flat tensile specimen. Alternatively, the short-beam method may be used. Here, the specimen resembles a flat flexural specimen but is proportioned to fail by shear on the central layers of the composite. The guillotine method is reputed to produce less scatter. However, the values obtained are usually higher than those obtained with the short-beam method. The latter method is the most widely used. A modification of the short-beam test is used with filament-wound NOL ring specimens. Here, a short section of the

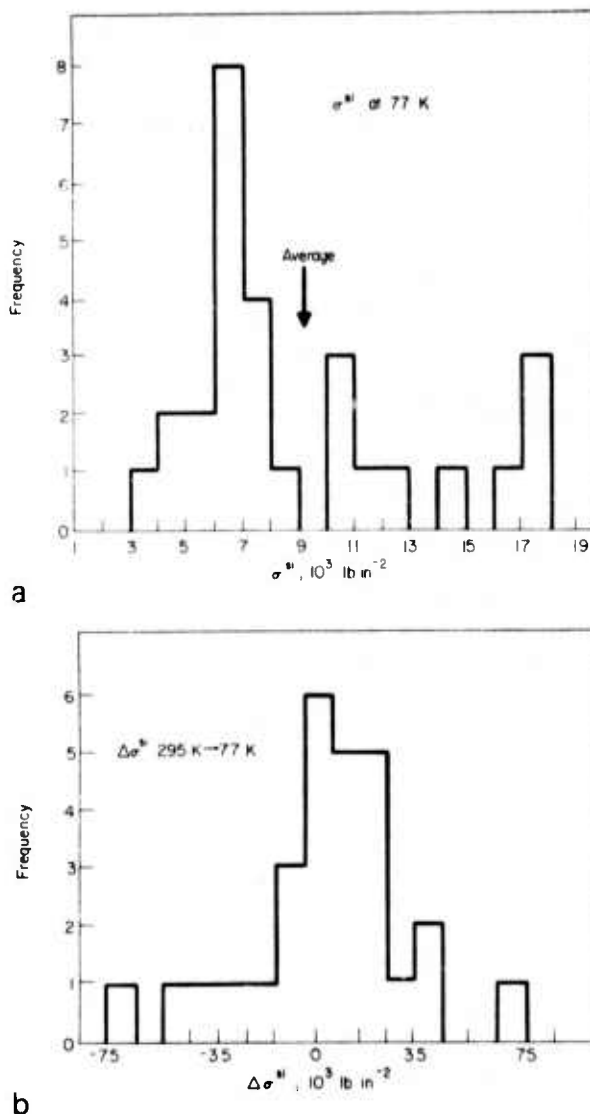


Fig.12 Histograms illustrating the reported range of longitudinal interlaminar shear strength, σ^u
a — as reported for HT-S/X-304 graphite-epoxy at 77 K and
b — the reported changes in interlaminar shear strength in the same composite upon cooling from 295 K to 77 K

ring (concave downward) is substituted for the flat specimen. Results of the NOL segment and the flat short-beam tests are not equivalent.

A wide range of interlaminar shear strength values may be obtained with a single composite type. Fig. 12a is a frequency histogram illustrating the range of longitudinal interlaminar shear strength reported in the literature for the graphite-reinforced composite HT-S/X-904 at 77 K. The substantial amount of data available for this composite reflects a comprehensive study of the effect of processing variables by Maximovich and Scheck.¹² These data suggest that the maximum interlaminar shear strength obtainable with this type composite is on the order of $17-18 \times 10^3 \text{ lb in}^{-2}$ (117–124 MPa).

The data of Maximovich and Scheck may be analysed further to determine what this relatively large body of data can tell statistically about the temperature dependence of interlaminar shear strength. From the frequency histogram of Fig. 12b, we observe that the reported change in this parameter upon cooling from 295 K to 77 K approximates a normal distribution around zero change, suggesting that interlaminar shear strength is relatively independent of temperature for this composite over this temperature range. However, a more detailed look at the data shows that those composites at the high end of the strength range increased their interlaminar shear strength by about 4000 lb in^{-2} (27 MPa) between 295 K and 77 K, suggesting that the temperature dependence is affected by composite quality.

Cryogenic interlaminar shear strength data have been published for other graphite-epoxy composites and for boron-epoxy, PRD 49-epoxy, and for boron-aluminium.^{8,10,13,47,58} However, available data are insufficient for statistical examination. One finds that the reported 77 K interlaminar shear strengths for graphite-epoxy composites made with ten fibre types other than HT-S range from about $4-18 \times 10^3 \text{ lb in}^{-2}$ (27–124 MPa), that is, covering about the same range covered by the HT-S data of Fig. 12a.

Somewhat surprisingly, available data on boron-epoxy^{13,58} and boron-aluminium¹³ composites suggest that the maximum interlaminar shear strengths of these composites are almost the same as for the best of the graphite-epoxy composites, that is, about $18 \times 10^3 \text{ lb in}^{-2}$ (124 MPa) at 77 K with about a 4000 lb in^{-2} (27 MPa) increase between 295 K and 77 K.

The only data on the interlaminar shear strength of PRD 49-epoxy composites are those of Hoggatt^{59,60} who reported NOL-ring segment values of approximately 400 lb in^{-2} (27 MPa) in both ERLB 4617 and NASA Resin 2 matrices. Values obtained with the latter of these were found to be consistently higher by 40–70%. Very little temperature dependence was observed. It is perhaps noteworthy that the highest shear strengths reported for the graphite-epoxy composites, $21 \times 10^6 \text{ lb in}^{-2}$ (145 MPa), was also obtained with NASA Resin 2 epoxy.¹⁰

Composite bearing strength

The only data found in the literature on the temperature dependence of bearing properties of advanced composites in the cryogenic range were published by Hertz et al.¹³ for boron and Borsic-reinforced 6061 aluminium, including the steel and titanium-reinforced hybrids. These data, appearing

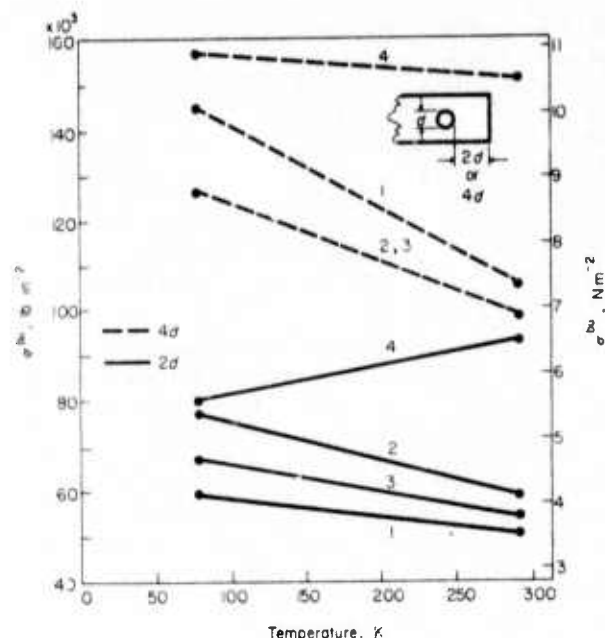


Fig. 13 Ultimate bearing strength, σ^{bu} , of boron-aluminium composites, uniaxial longitudinal direction
1 – 4.2 mil Borsic-aluminium (6061); 2 – 5.6 mil Boron-aluminium (6061); 3 – 4.2 mil Borsic-steel-aluminium (6061); 4 – 4.2 mil Borsic-titanium-aluminium (6061) (all reference 13)

on Fig. 13, are for bearing strength in the uniaxial longitudinal direction, that is, the stress required for bearing pull-out, rather than the more conventional bearing yield strength. The data on Fig. 13 refer to material hole-to-free surface dimensions two and four times the diameter of a No 10 steel pin ($\sim 4.8 \text{ mm}$). An increase in bearing strength with decreasing temperature is observed for both conventional boron and Borsic-reinforced materials, the effect being more pronounced in the 4D tests. The Borsic-steel-aluminium hybrid performed much like the conventional materials, while the Borsic-titanium-aluminium hybrid performed somewhat erratically, although the highest strengths were developed with this latter composite.

Dynamic mechanical properties

Composite fatigue

The only available data on the temperature dependence of the fatigue properties of advanced composites were generated during cyclic pressure testing of filament-wound pressure vessels. As the composites in these vessels were cross plied and subjected to biaxial stressing, the data are of value only in a comparative sense.

Hanson⁴⁵ has studied the cyclic fatigue performance of pressure vessels overwrapped with Thornel 50 graphite fibre using an ERL 2256/ZL 0820 epoxy resin. The fatigue life at 77 K was found to be similar to that at 295 K, with 90% of the relevant single-cycle strength being retained after 10 000 cycles. This compares to a retention of only about 45% of the single-cycle strength for glass-fibre reinforced vessels. Hanson concluded that, on the basis of specific strength, graphite-fibre reinforced vessels would have fatigue performance superior to that of glass-fibre reinforced vessels after only 80 cycles.

Allring et al.²⁰ have reported cryogenic cyclic fatigue data on pressure vessels filament-wound with 4 mil boron in a Polaris-resin matrix. Polaris resin consists of Epon 828/Epon 1031/NMA/BDMA in proportions 50/50/90/0.55 phw. Commercial designations are E-787 and 58-68R. The results were again reported to be independent of temperature (down to 20 K). However, the fatigue life of the boron-reinforced vessels was found to be relatively low, with residual strengths falling to 40–50% of single-cycle values after 10 000 cycles. This is about the same as for glass reinforcement.

These results suggest that graphite may be superior to boron as a reinforcement fibre for composite structures subject to fatigue at cryogenic temperatures. However, these data must be considered very tentative in view of the aforementioned tendency for the 4 mil boron fibre to split longitudinally when subjected to transverse stresses such as are present in biaxially-loaded pressure vessels. The fatigue performance at cryogenic temperatures of composites reinforced with 5.6 mil boron fibre should be substantially better than with the 4 mil fibre, if fibre splitting is a factor in the smaller diameter fibre.

Composite impact strength

Few data were available on the impact strength of advanced composites at cryogenic temperatures. The Advanced Composites Design Guide¹²⁴ includes some unpublished data on the Charpy V-notch impact values of commercial 5505-4 boron-epoxy material tested transverse to the uniaxial longitudinal direction. These data indicate a slight increase in impact strength from 22.8 ft lb in⁻¹ (121.7 N m m⁻¹) at 295 K to 27.0 ft lb in⁻¹ (144 N m m⁻¹) at 20 K. Concomitantly, a slight decrease from 46.3 to 39.5 ft lb in⁻¹ (247 to 211 N m m⁻¹) was reported for unnotched specimens over this temperature range. The notched/unnotched ratios of about 0.49 at 295 K and about 0.68 at 20 K indicate some notch sensitivity. Sumner and Davis⁷ have reported a 12 ft lb in⁻¹ (64 N m m⁻¹) Charpy V-notch strength at 295 K for 25 v/o stainless steel wire reinforced 2024 aluminium, this value increasing to 18 ft lb in⁻¹ (96 N m m⁻¹) at 77 K. Cryogenic impact strength data were not available for the other types of advanced composites. However, room temperature data indicate that the graphite-reinforced composites have substantially lower impact strengths than boron-reinforced types. There is no *a priori* reason to expect this relationship to change at cryogenic temperatures. Such impact strengths are substantially lower than those discussed in Part I for glass-reinforcement, where notched values transverse to the uniaxial longitudinal direction were seen to range from 67–162 ft lb in⁻¹ (357–865 N m m⁻¹) at 77 K.⁴ The critical factor has been identified as the stress-strain behaviour of the fibre reinforcement, higher impact values being associated with higher failure strains of the fibre whenever tests are made in the longitudinal (cross-fibre fracture) mode.^{125,127}

Impact strengths of uniaxial composites tested in the transverse direction (anvil impact parallel to the fibres) are essentially matrix controlled. Since composite structures are usually of crossply construction and subjected to complex stresses, an improvement in the impact strength of the matrix offers the possibility of an overall improvement of composite toughness. Larsen⁹ has reported efforts to improve

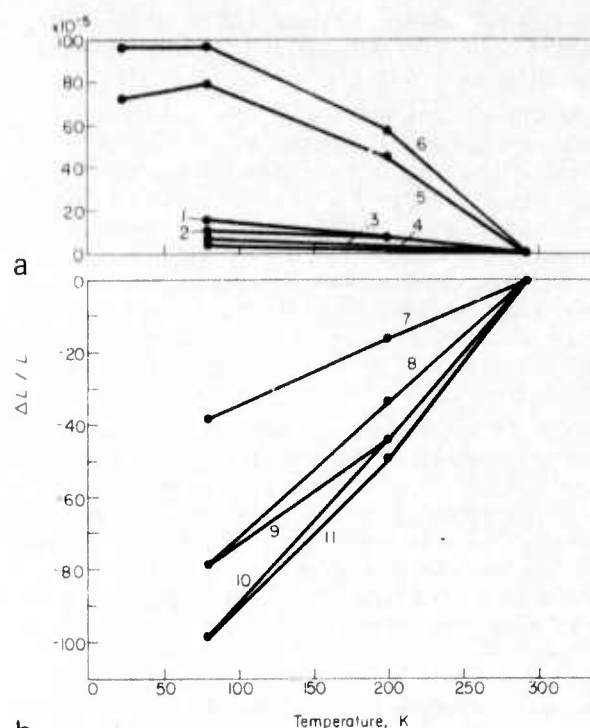


Fig.14 Longitudinal thermal expansion, $\Delta L/L$, of uniaxial advanced composites
1 — Thornel 75/ERLB 4617⁵¹; 2 — GY-70/X-904¹³; 3 — Fibrallloy 300/X-904¹³; 4 — HT-S/X-904¹³; 5 — PRD49-1/ERLA 4617^{59,60}; 6 — PRD49-1/NASA Resin 2^{59,60}; 7 — boron/epoxy SP-272; 8 — 5.6 mil boron/aluminium 6061; 9 — 4.2 mil Borsic-titanium-aluminium 6061; 10 — 4.2 mil Borsic-steel-aluminium (6061); 11 — 4.2 mil Borsic/aluminium (6061) (all reference 13)

the impact properties of crossplied HT-S/epoxy materials at cryogenic temperatures by addition of elastomeric components to the matrix. Results of this work were reported in terms of energy density, that is, the area under the force-deflection curve, using a cleavage-type specimen. This work showed that some improvement was indeed possible with CBTN-modified ERLB 4617 epoxy. However, the benefit gained was negated by a significant lowering of the room temperature impact properties and by unpredictable performance at cryogenic temperatures. Larsen concluded that improved overall cryogenic properties would be obtained by use of the NASA Resin 2 epoxy formulation with graphite-reinforced composites.

It appears at this time that substantial improvement of impact strength of the advanced composites will require development of hybrids, possibly combining glass with the advanced fibres.

Thermal properties

Composite thermal expansion and contraction

Unlike the glass-reinforced composites, some advanced-fibre composites expand in the fibre direction when cooled to cryogenic temperatures. Available data for the temperature dependence of dimensional changes in the uniaxial longitudinal direction are summarized in Fig.14, while comparable data for the uniaxial transverse direction appear in Fig.15.

The graphite-reinforced composites display a very small longitudinal expansion on cooling, slightly larger expansions being reported for the high modulus Thornel 75 and GY-70 fibre composites than for composites made with the medium-modulus Fibrallloy 300 and the low-modulus HT-S fibres. The PRD 49 (Kevlar 49) composites undergo a comparatively large longitudinal expansion on cooling, reportedly reaching a maximum of about $8-10 \times 10^{-4}$ at about 77 K.^{59,60} Slightly larger expansion was reported with a NASA Resin 2 matrix than with ERLA 4617. The other advanced composites undergo linear contraction on cooling. The least longitudinal contraction was reported for the commercial SP-272 boron-epoxy product, while boron-aluminium undergoes the largest contraction. The matrix contraction properties appear to be dominating in the latter composites, as relatively little difference is seen among the four variants, including the hybrids. The 5.6 mil composite displays a slightly lower contraction than does the 4 mil product. The longitudinal thermal contractions of these boron-aluminium composites are about 25% of that of an unreinforced 6061 aluminium alloy.

Dimensional changes in the transverse direction are strongly influenced by the matrix; all advanced composites showing contraction in this direction on cooling. These contractions are large compared to changes observed in the fibre direction, as witnessed by the necessity to change the ordinate scale on Fig. 15. The data indicate that boron-epoxy composites have the least transverse contraction of the group, yet even this relatively low value is three times larger than its longitudinal change. The graphite-reinforced composites appear to under-

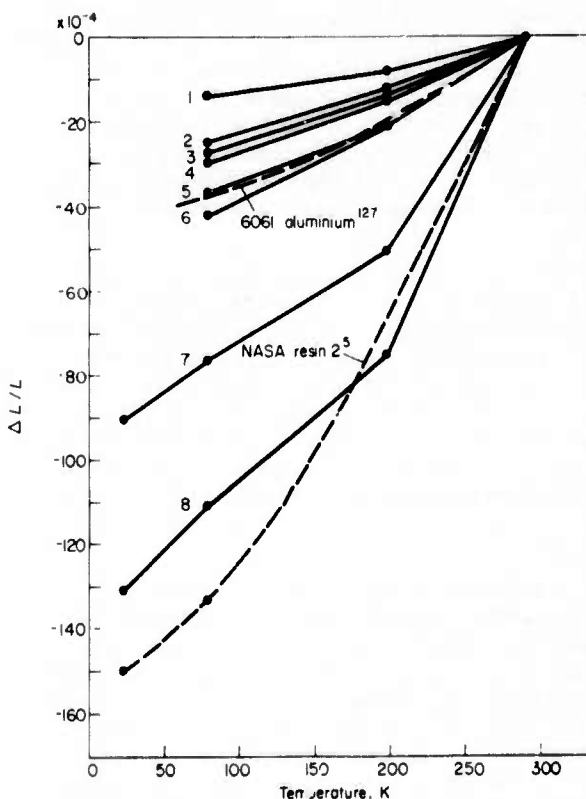
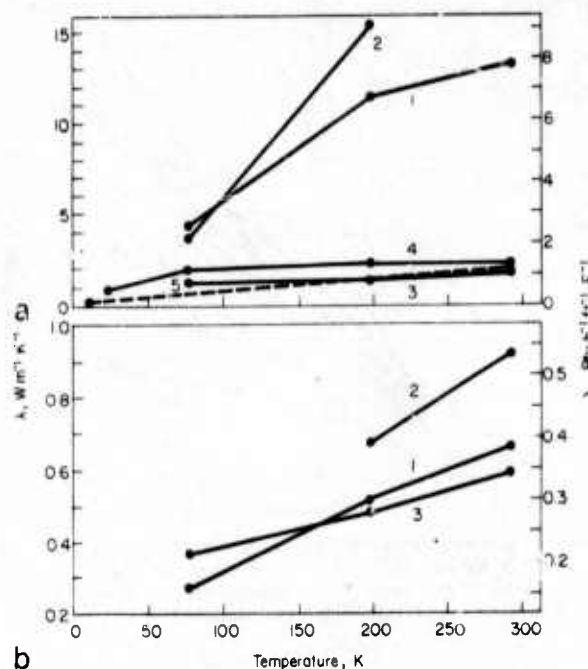


Fig. 15 Transverse thermal expansion, $\Delta L/L$, of uniaxial advanced composites: 1 - boron/epoxy (SP-272)¹³; 2 - Fibrallloy 300/ERLA 4617 HT-S/X-904¹³; 3 - 4.2 mil Borsic-titanium/aluminium 6061¹³; 4 - GY-70/X-904¹³; 5 - boron/aluminium 6061¹³; 6 - 4.2 mil Borsic-steel/aluminium (6061)¹³; 7 - PRD 49-1/ERLA 4617^{59,60}



b
Fig. 16 Thermal conductivities, λ , of advanced composites: a - Uniaxial longitudinal; 1 - HTS/X-904¹³; 2 - Thornel 50-Polaris³⁸; 3 - B-epoxy, SP-272¹³; 4 - B-epoxy, 4.0 B-on-Polaris¹⁸; 5 - PRD 49-epoxy⁶¹; b - Uniaxial transverse; 1 - HT-5/X-904¹³; 2 - Thornel 50 - Polaris³⁸; 3 - B-epoxy, SP-272¹³

go about twice the transverse thermal contraction of the boron-reinforced composites, reflecting the lesser constraint provided in this direction by the small graphite fibres. A slightly higher transverse contraction is reported for the high-modulus GY-70/X-904 composite than for the low modulus HT-S/X-904 material. However, such a small difference could easily be accounted for by variations in fibre volume fraction. The conventional boron/6061 aluminium composites have the next largest transverse contraction. By comparison with the contraction of unreinforced 6061 alloy (dashed curve), it is seen that the transverse contraction of the boron-aluminium composite is almost completely matrix dominated. No significant difference in thermal contraction were reported for 4.2 mil Borsic and 5.6 mil boron fibre composites.

The PRD 49-epoxy composites undergo the largest transverse thermal contraction. Comparing the temperature dependence of PRD 49-1/NASA Resin 2 (curve 8) with that reported by Soffer and Molho⁵ for NASA Resin 2 alone (dashed curve), indicates that the matrix is also dominating the transverse dimensional changes in this composite. The PRD 49 fibres do not offer appreciable restraint to transverse contraction of the matrix because, as seen in Fig. 14, this fibre expands significantly in the longitudinal direction during cooling. Of necessity, this is accompanied by significant transverse fibre contraction. Cooling to cryogenic temperatures would be expected to produce sizable interfacial shear forces between the PRD 49 fibre and matrix, with lesser forces normal to the fibres.

Composite thermal conductivity

Few data were available on the temperature dependence of uniaxial longitudinal and uniaxial transverse thermal conductivity of advanced composites. Those which were available are plotted in Fig. 16. When considering these data, the

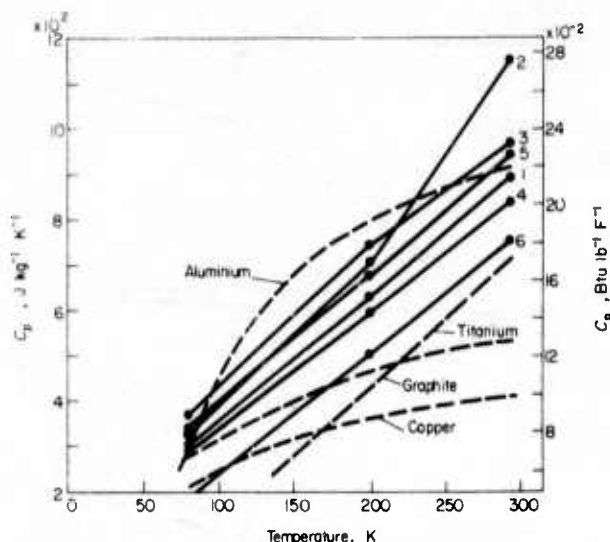


Fig. 17 Specific heat, C_p , of advanced composites
 1 - HT-S/X 904, GY-70/X 904¹³; 2 - B-epoxy (SP-292)¹³;
 3 - boron/6061 aluminium¹³; 4 - Borsic-titanium/aluminium¹³;
 5 - Borsic-steel/aluminium¹³; 6 - graphite/phenolic¹⁵

reader should be aware of the difficulties and potential sources of error in determining thermal conductivity within the cryogenic range. The comments made in Part 1 of this paper on this subject apply equally well here. Furthermore, the volume fraction of fibre will influence the conductivities, particularly in graphite-reinforced composites. For these reasons, the data on Fig. 16 should be considered as only indicating trends.

The graphite-reinforced composites have relatively high thermal conductivities in the fibre direction, reflecting relatively high conductivity of the graphite fibres compared to epoxy. Longitudinal conductivity in these materials is highly temperature dependent. The boron-reinforced composites have much lower conductivities than do the graphite-reinforced composites in the fibre direction and show a comparatively small temperature dependence of thermal conductivity. Data were not available for boron-reinforced aluminium; however, the thermal conductivity of such materials will certainly be much higher than that of a polymeric-matrix composite. The conductivity should be approximately half that of unreinforced aluminium in a typical 50 volume % boron-aluminium composite. Transverse thermal conductivities are matrix dominated and very low for both the graphite and boron-reinforced epoxy materials.

The only available data for PRD 49 indicate a longitudinal thermal conductivity approximately the same as that for boron-epoxy within the cryogenic range.

These data suffice to show that the thermal conductivities of the epoxy-matrix advanced composites, particularly boron-reinforced, are low enough to make them attractive for cryogenic structural components.

Composite specific heat

Fig. 17 shows the specific heat of the advanced composites to be similar to those of the glass-reinforced composites discussed in Part 1 of this paper. Again, an almost linear temperature dependence of C_p is observed from 295 K to 77 K. As a group, the specific heats of the composites are

slightly lower than that of aluminium for much of the region between 295 K and 77 K, but substantially higher than that for copper and most other metals. The temperature dependence of C_p for aluminium, copper and titanium are included on Fig. 17 for comparative purposes.

The highest specific heat at cryogenic temperatures was reported for boron-aluminium, the aluminium matrix undoubtedly contributing significantly to this relatively high value. The depicted curve is the average of data reported by Hertz et al.¹³ for 4.2 mil Borsic/6061 and 5.6 mil boron/6061. Slightly higher values were reported at 295 K and 200 K for the larger filament size, falling to slightly lower at 77 K. The data indicate that the Borsic-aluminium hybrids had slightly lower specific heats, probably reflecting the contributions from the steel and titanium reinforcements. The specific heat of the boron-epoxy composite lies between that of the boron-aluminium and the graphite-epoxy. The specific heat of the latter has undoubtedly been lowered by the graphite which, as shown by the dashed curve on Fig. 17, has itself a relatively low specific heat.

The data indicate that boron-epoxy has a comparatively high specific heat at room temperature. This is not unreasonable, as boron has a room temperature specific heat of about $12.9 \times 10^2 \text{ J kg}^{-1} \text{ K}^{-1}$. No cryogenic specific heat data were available for boron or epoxy; however, the composite data suggest a rapidly decreasing value of C_p for boron as temperature decreases, while indicating that the specific heat of epoxy probably lies between the curves for boron-epoxy and graphite-epoxy.

Comments on advanced composites

The purpose of this review is to give the reader an understanding of the present state of knowledge as to the magnitude and temperature dependence of the properties of advanced fibre composites at cryogenic temperatures. It is apparent that present knowledge is incomplete in many respects; nevertheless, the available data justify considerable optimism as to the future applicability of these materials as structural components operating at cryogenic temperatures.

Available data indicate that commercial state-of-the-art boron-reinforced epoxy and aluminium perform well at cryogenic temperatures. The high tensile and compressive strengths and elastic moduli of these materials remain constant or improve as the temperature is lowered. Equally impressive is the relatively small scatter in the data, suggesting a high degree of reliability for components made from boron-reinforced composites. The data suggest that the commercial products may be used effectively at cryogenic temperatures without optimization of the composite matrix.

Although actual data are not available, boron-aluminium composites are certain to have a much higher thermal conductivity than any polymer-matrix composite (approximately half that of the unreinforced alloy). This is a distinct disadvantage in many cryogenic applications. On the other hand, the transverse strength and modulus of boron-aluminium is much higher than that of polymer-matrix composites. The latter is a distinct advantage of metal-matrix composites, simplifying composite design and increasing component reliability.

Available data on the cryogenic performance of the graphite-reinforced epoxy class of composites are less convincing.

These materials can be produced with moduli higher than those obtainable with boron-reinforced materials. Graphite-epoxies have the highest thermal stability of any composite class, which is an advantage for many cryogenic applications. However, the ultimate tensile strengths of the graphite-epoxies are substantially lower than for composites with boron reinforcement, and the strength tends to decrease upon cooling to cryogenic temperatures. Mechanical property test results are frequently unpredictable and contradictory. It is not at present known how much of the erratic behaviour is due to problems in testing and how much is an inherent characteristic of the material. Certainly, the overall performance of graphite-fibre overwrapped pressure vessels reported by Larsen and Simon¹⁰ was much better than would have been predicted from their basic test data. We therefore conclude that graphite-reinforced composites have potential for structural use at cryogenic temperatures, in particular, for applications requiring dimensional stability. However, further development and testing are required.

PRD 49 (Kevlar 49)-reinforced epoxies also appear promising for cryogenic applications, due to the relatively low cost of the fibre and the improved modulus compared to glass. However, present data on this material are minimal, and further investigation must be undertaken before this material can be applied with confidence in a cryogenic environment. PRD 49 is unusual in that it undergoes a significant expansion in the fibre direction during cooling to cryogenic temperatures. Large residual stresses between the fibre and the epoxy matrix might be expected to adversely affect the mechanical properties of composites made with this material. Nevertheless, the work of Hoggatt^{59,60} has shown that, with proper design, PRD 49-epoxy composites can be used to good advantage in some cryogenic applications. As no compressive strength data were available at cryogenic temperatures, the potential user should investigate this parameter in applications where compressive loading is a factor.

In contrast to the boron-reinforced materials, the available data suggest that both graphite and PRD 49-reinforced composites may benefit from matrix optimization when used at cryogenic temperatures. Larsen and Simon¹⁰ have recommended NASA Resin 2 for both uniaxial and crossply graphite-reinforced composites. The work of Hoggatt suggests that this type of matrix is also satisfactory for PRD 49 reinforcement.^{59,60} When considering the use of NASA Resin 2, the reader should be aware that this resin has been optimized for cryogenic use by the addition of flexibilizers, which significantly reduce the strength at elevated temperatures. In particular, care must be taken to properly support components made with this resin whenever elevated temperature baking of a component is required.

The foregoing is not intended to imply that the NASA Resin 2 formulation is clearly the best resin for all cryogenic applications. Composite manufacturers may well recommend other types of epoxies for cryogenic applications. The present report is not intended to be prejudicial to such recommendations. However, the purchaser is advised to request documentation that the recommended resin has shown itself to be suitable for the intended cryogenic application. In particular, the suitability of various resins for crossply composites subjected to fatigue loading under cryogenic conditions has not been adequately investigated.

Summary of primary property trends in uniaxial advanced composites upon cooling to cryogenic temperatures

Tensile strength

Boron-epoxy and boron-aluminium show little temperature dependence of strength. The same appears to be true for PRD 49 (Kevlar 49)-epoxy, although data are minimal. The graphite-epoxies tend toward decreased strength on cooling, 77 K values being of the order of $20 \times 10^3 \text{ lb in}^{-2}$ (138 MPa) lower than at room temperature.

Tensile modulus

Boron-epoxy, boron-aluminium, and graphite-epoxy composites appear to retain their room-temperature moduli when cooled to 77 K. Minimal available data indicate that PRD 49 (Kevlar 49)-epoxy composites undergo a substantial modulus increase on cooling below 77 K.

Compressive strength

Compressive strengths of the advanced composites tend to either increase (boron-epoxy, graphite-epoxy) or to remain essentially unchanged (boron-aluminium) during cooling to 77 K. Compressive strength data were not available for PRD 49 (Kevlar 49)-epoxy composites.

Compressive modulus

Compressive moduli generally remain unchanged upon cooling to cryogenic temperatures, except for a small moduli increase reported for boron-epoxy. Data were not available for PRD 49 (Kevlar 49)-epoxy.

Ultimate tensile strain

Available data indicate a small (5–15%) decrease in longitudinal strain at failure on cooling boron-aluminium and graphite-epoxy to 77 K; the latter being the more temperature sensitive. Transverse failure strain appears almost independent of temperature in these composites. Data were not available for PRD 49 (Kevlar 49) or boron-epoxy.

In-plane shear strength and modulus

Insufficient data are available to indicate trends in these properties. One reference cited about a 14% drop in shear strength, concomitant with about a 50% shear modulus increase, for a graphite-epoxy composite upon cooling to 77 K; however, variations in fibre type and matrix composition will undoubtedly affect the temperature sensitivity of these properties. No data were available for other advanced composites.

Thermal expansion and contraction

Graphite-epoxy is the most dimensionally stable of the advanced composites, undergoing a very slight expansion longitudinally (fibre direction) and moderate transverse contraction on cooling. Boron-epoxy is the next most stable, showing moderate contraction in both directions on cooling. Boron-aluminium contracts about twice as much as boron-epoxy longitudinally; however, the contraction is only about 20% of that of the unreinforced metal. Transverse contraction of boron-aluminium is al-

most the same as that of the unreinforced metal. PRD 49 (Kevlar 49)-epoxy composites are the least dimensionally stable, expanding substantially in the longitudinal direction and contracting substantially in the transverse direction.

Thermal conductivity

Boron-epoxy and PRD 49 (Kevlar 49)-epoxy have substantially lower longitudinal thermal conductivity than graphite-epoxy composites. Differences in conductivity decrease as temperature decreases. Conductivity in the transverse direction is approximately the same for graphite and boron-epoxy, being much lower in this direction. Data were not available for PRD 49 (Kevlar 49)-epoxy and for boron-aluminium.

Specific heat

The specific heat of the advanced composites appear to be almost linear from 295 K to 77 K. As a group, the values are slightly lower than that of aluminium, but substantially above that of titanium or copper. The specific heat of boron-aluminium is slightly higher than that of boron-epoxy or graphite-epoxy. No data were available for PRD 49 (Kevlar 49)-epoxy.

The author thanks Dr R. P. Reed for consultation and review of the completed manuscript. Many thanks are also due to the NBS-NOAA library staff of the Boulder Laboratories for their assistance in retrieving the documents on which this work depended. This research was supported by the Advanced Research Projects Agency.

The use in this paper of trade names of specific products is essential to the proper understanding of the work presented. Their use in no way implies approval, endorsement or recommendation by NBS. Generic names have been substituted whenever it was possible to do so without sacrificing clarity. Manufacturers of the trade named materials are listed in the Appendix.

Appendix

The following materials are referred to in this report:

Fibres

Graphite

IIT-S, HM-S	Courtaulds Ltd
HMG-25, HMG-50	Hitco Corp
Modmor I, II	Morganite Ltd
Thornel 25, 50	Union Carbide Corp
Samco 320	Samco Corp
Fibralloy 300	Monsanto Corp
GY-70	Celanese Corp

Boron

Borsic	Hamilton Standard Corp
--------	------------------------

Others

PRD 49 (Kevlar 49)	E. I. DuPont de Nemours, Inc
--------------------	------------------------------

Resins

Epoxies

X-904, X-915	Fiberite Corp
ERL 2256, ERLB 4617	Union Carbide Plastics Co
Epon 828, 1031, 58-68R	Shell Chemical Corp,

E-350, E-787
Ciba 8183/137, 3002

Plastics & Resin Div
US Polymeric Corp
Hercules Corp

Others

Skybond 703 (polyimide)	Monsanto Corp
IHT-424 (epoxy-phenolic)	American Cyanamid

Flexibilizers, Hardeners

ZZL 0820	Union Carbide Plastics Co
Empol 1040	Emery Industries, Inc
DSA — dodecenyl succinic anhydride	
BDMA — benzyl dimethylamine	
NMA — nadic methyl anhydride	

Boron Composite Products

SP-272	Minnesota Mining & Manufacturing Co
5505	AVCO Corporation

Bibliography

Mechanical properties

Contract AF-33 (616)- 3289

Contractor: Directorate of Materials and Processes, Aeronautical Systems Division, Air Force Systems Command, Wright-Patterson Air Force Base, Ohio

Research Facility: Narmco Research and Development, San Diego, California

- 1 Brink, N. O. 'Determination of the performance of plastic laminates under cryogenic temperatures' ASD TDR 62-794 (1962) (AD 288 944)
- 1.1 Brink, N. O. 'Mechanical behaviour of reinforced plastics at cryogenic temperatures', Technical Papers, 20th Annual Technical Conference, Society of Plastics Engineers, Vol 10, Section XV-2 (1964) 1-19
- 1.2 Brink, N. O. 'Mechanical behaviour of reinforced plastics at cryogenic temperatures', *Society of Plastics Engineers Journal* 20 (1964) 1123
- 1.3 Brink, N. O. 'Mechanical behaviour of reinforced plastics at cryogenic temperatures', Narmco Research and Development Report, Code No 105-4 (1964)
- 2 Chamberlain, D. W., Lloyd, B. R., Tennant, R. L. 'Determination of the performance of plastic laminates at cryogenic temperatures', ASD-TDR-62-794, Part II (1964) (N64-24212)
- 2.1 Chamberlain, D. W. 'Tensile fatigue testing at temperatures down to 20 K', *Advances in Cryogenic Engineering* 9 (1964) 131
- 2.2 Chamberlain, D. W. 'Mechanical properties testing of plastic laminate materials down to 20 K', *Advances in Cryogenic Engineering* 10 (1965) 117

Contract NAS 8-11070

Contractor: National Aeronautics and Space Administration, George C. Marshall Space Flight Center, Huntsville, Alabama

Research Facility: Goodyear Aerospace Corporation, Akron, Ohio

- 3 Toth, L. W., Boller, T. J., Butcher, I. R., Kariotis, A. H., Yoder, F. D. 'Programme for the evaluation of structural reinforced plastic materials at cryogenic temperatures', NASA CR-80061 (Final) (1966) (N67-12051)
- 3.1 Toth, L. W. 'Properties testing of reinforced plastic laminates through the 20 degree K range', Technical Papers, 20th Annual Technical Conference, Society of the Plastics Industry, Section 7-C (1965) 1

- 3.2 Toth, L. W., Kariotis, A. H. 'An assessment of test specimens and test techniques useful to the evaluation of structural reinforced plastic materials at cryogenic temperatures', *Advances in Cryogenic Engineering* 10 (1965) 126
- 3.3 Toth, L. W. 'Properties of glass-reinforced epoxy through the 20 K range', *Modern Plastics* 42 (1965) 123
- 3.4 Toth, L. W., Burkley, R. A. 'Mechanical response at cryogenic temperatures of selected reinforced plastic composite systems', Goodyear Aerospace Report GER-13169, Paper No 16, Seventieth Annual Meeting of the American Society for Testing and Materials (1967)
- 3.5 Toth, L. W., Boller, T. J., Kariotis, A. H., Yoder, F. D. 'Programme for the evaluation of structural reinforced plastic materials at cryogenic temperatures', NASA CR-64005 (1963-64) (N65-29724)

Contract NAS 3-6297

Contractor: National Aeronautics and Space Administration, Lewis Research Center, Cleveland, Ohio

Research Facility: Aerojet General Corporation, Azusa, California

- 4 Lewis, A., Bush, G. E. 'Improved cryogenic resin-glass filament wound composites', NASA CR-72163 (Final) (1967) (N67-31856)
- 4.1 Lewis, A., Bush, G. E., Creedon, J. 'Improved cryogenic resin glass filament-wound composites', NASA Interim Report CR-54867 (1966) (N66-28040)

Contract NAS 6-6287

Contractor: National Aeronautics and Space Administration, Research Center, Cleveland, Ohio

Research Facility: Aerojet General Corporation, Azusa, California

- 5 Soffer, L. M., Molho, R. 'Cryogenic resins for glass filament-wound composites', NASA CR-72114 (Final) (1967) (N67-25076)
- 5.1 Soffer, L. M., Molho, R. 'Mechanical properties of epoxy resins and glass epoxy composites at cryogenic temperatures', *Cryogenic Properties of Polymers* (J. L. Koenig (ed)) (Marcel Dekker, New York, 1968) 87 (Identical to NASA CR-84451, 1967, (N66-27217))

Contract FO4701-69-C-0059

Contractor: Space and Missiles Systems Organization, Air Force Systems Command, Los Angeles Air Force Station, Los Angeles, California

Research Facility: The Aerospace Corporation, El Segundo, California

- 6 Pepper, R. Y., Rossi, R. E., Upp, U. W., Riley, W. E. 'Development of an aluminum-graphite composite' SAMSO-TR-70-301 (1970) (AD 718 469)
- 6.1 Pepper, R. T., Upp, J. W., Rossi, R. C., Kendall, E. G. 'Aluminum graphite composites' SAMSO-TR-70-174 (1970) (AD 706 883). (Identical to *Metalurgical Trans* 2 (1971) 117)
- 6.2 Rossi, R. C., Pepper, R. T., Upp, J. W., Riley, W. C. 'Development of aluminum-graphite composites' *Ceramic Bull* 50 (1971) 484

Contract NAS 8-11508

Contractor: National Aeronautics and Space Administration, George C. Marshall Space Flight Center, Huntsville, Alabama

Research Facility: Harvey Engineering Laboratories, Torrance, California

- 7 Summer, E. V., Davis, L. W. 'Development of ultrahigh strength, low density aluminum sheet and plate composites', NASA CR-85863 (Final) (1966) (N67-1181)

- 7.1 Davis, L. W. 'Composites at low temperature', Paper No. 15, Seventieth Annual Meeting of the American Society for Testing Materials (1967)

Contract NASA DPR C 10360-B

Contractor: National Aeronautics and Space Administration, Lewis Research Center, Cleveland, Ohio

Research Facility: Naval Ordnance Laboratory, Silver Springs, Maryland

- 8 Simon, R. A., Alfiring, R. 'Properties of graphite fiber composites at cryogenic temperatures', NASA CR-72652 (NOLTR 69-183) (1970) Tasks I and II (AD 746 885)
- 9 Larsen, J. V. 'Properties of graphite fiber composites at cryogenic temperatures - effect of elastomeric additions to resin systems', NASA CR-72804 (NOLTR 70-195) (1971) Task III (AD 882 972)
- 10 Larsen, J. V., Simon, R. A. 'Carbon fiber composites for cryogenic filament-wound vessels', NASA CR-120899 (NOLTR 71-201) (1972) Tasks IV, V, and VI (N73-11553)
- 10.2 Larsen, J. W. 'Fracture energy of CBN/epoxy-carbon fiber composites', Technical Papers, 26th Annual Technical Conference, Society of the Plastics Industry, Section 10-D (1971)

Contract NAS 8-26198

Contractor: George C. Marshall Space Flight Center, Huntsville, Alabama

Research Facility: General Dynamics Convair, San Diego, California

- 11 Scheck, W. G. 'Development of design data for graphite reinforced epoxy and polyimide composites', NASA TN-D2970, Report No GDC-DBG-70-005, Final National Aeronautics and Space Administration, Marshall Space Flight Center, Alabama (1974)
- 12 Scheck, W. G. 'Development of design data for graphite reinforced epoxy and polyimide composites', Report No GDC-DBG-70-005, General Dynamics Quarterly Report No 1 (1970) [see also Maxlmovich, M. and Scheck, W. G. Quarterly Report No 2, (1970)]
- 12.1 Stuckey, J. M., Scheck, W. G. 'Development of graphite/polyimide composites', National Technical Conference, Society of Aerospace Material and Process Engineers, Vol 3 (1971) 717

Contract F33615-70-1442

Contractor: Air Force Materials Laboratory, Wright-Patterson Air Force Base, Ohio

Research Facility: General Dynamics/Convair, San Diego, California

- 13 Hertz, J., Christian, J. L., Varlas, M. 'Advanced composite applications for spacecraft and missiles, Phase I Final Report, Volume II: Material Development', AFML-TR 71-186, Vol 2 (1972) (AD 893 715L)
- 13.1 Forest, J. D., Fujimoto, A. F., Foelsch, G. F. 'Advanced composite applications for spacecraft and missiles, Phase I Final Report, Volume I: Structural Development', AFML-TR-71-186, Vol 1, (1972)
- 13.2 Forest, J. D., Varlas, M. 'Advanced composite applications for spacecraft and missiles, Final Report, AFML-TR-72-278 (1973)
- 13.3 Christian, J. L., Campbell, M. D. 'Mechanical and physical properties of several advanced metal-matrix composite materials', *Advances in Cryogenic Engineering* 18 (1973) 175

2. Thermophysical properties

Contract AF-33 (66-)-9160

Contractor: Air Force Materials Laboratory, Wright-Patterson Air Force Base, Ohio

Research Facility: General Dynamics/Astronautics, San Diego, California

The following reports are in a series entitled 'Thermophysical properties of plastic materials and composites to liquid hydrogen temperature (-423°F)'

- 14 Haskins, J. F., Campbell, M. C., Hertz, J., Percy, J. L. ML-TDR-64-33, Part 1 (1964) (AD 601 337)
- 15 Campbell, M. D., Hertz, J., O'Barr, H. L., Haskins, J. F. ML-TDR-64-33, Part 2 (1965) (X65-18921)
- 16 Campbell, M. D., O'Barr, G. L., Haskins, J. F., Hertz, J. ML-TDR-64-33, Part 3 (1965) (AD 468 155)
- 16.1 Hertz, J., Haskins, J. F. 'Thermal conductivity of reinforced plastics at cryogenic temperatures', *Advances in Cryogenic Engineering* 10 (1965) 163
- 16.2 Campbell, M. D. 'Thermal expansion characteristics of some plastic materials and composites from room temperature to -253°C' *Advances in Cryogenic Engineering* 10 (1965) 154
- 16.3 Campbell, M. D., Haskins, J. F., O'Barr, G. L., Hertz, J. 'Thermophysical properties of reinforced plastics at cryogenic temperatures' *Journal of Spacecraft* 3 (1966) 596 (See also reference 13)

Contract F33615-73-C1388 (Work currently in progress)

Contractor: Air Force Materials Laboratory, Wright-Patterson Air Force Base, Ohio

Research Facility: General Dynamics/Convair, San Diego, California

- 17 Forest, J. D., Schaeffer, W. H. 'Advanced composite missile and space design data', General Dynamics Report GDCA-CHB72-001-1, Progress Report No 1 (1972)
- 18 Forest, J. D. 'Advanced composite missile and space design data', General Dynamics Report GDCA-CHB72-001-2, Progress Report No 2 (1973)

3. General bibliography

- 19 Aleck, B. 'Fibreglass-overwrapped 2219-T87 aluminium alloy low-pressure cryogenic tankage', Society of Aerospace Material and Process Engineers National Technical Conference, Space Shuttle Materials, Vol 3 (1971) 131
- 20 Alfring, R. J., Morris, E. E., Landes, R. E. 'Cycle-testing of boron filament-wound tanks', NASA CR-72899, National Aeronautics and Space Administration, Lewis Research Center A (1971) (N71-38023)
- 21 Barber, J. R. 'Design and fabrication of shadow shield systems for thermal protection of cryogenic propellants', NASA CR-72595, National Aeronautics and Space Administration, Lewis Research Center, Cleveland, Ohio (1969) (N70-25098)
- 22 Baucom, R. M. 'Tensile behaviour of boron filament-reinforced epoxy rings and belts', NASA TN D-5053, Langley Research Center, Hampton, Virginia (1969) (N69-19918)
- 23 Benton, W., Carr, R., Cohen, A., Gustafson, G., Lankton, C., Zeldin, B. 'Propellant storability in space', RPL-TDR-64-75 (Final), Air Force Systems Command, Edwards Air Force Base, California, (1964) (AD 603 215)
- 24 Brechna, H. 'Superconducting magnets for high energy physics applications', Proc ICECI (Heywood Temple Industrial Publishers Ltd, London, 1968) 119 (CFSCI N67-36009)
- 25 Bullard, B. R. 'Cryogenic tank support evaluation', NASA CR-72546, NASA Lewis Research Center, Cleveland, Ohio (1969) (N70-13085)
- 26 Campbell, M. D. 'Development of thermal expansion capabilities and the investigation of expansion characteristics of space vehicle materials', General Dynamics/Astronautics Report ERR-AN-251 (1962)
- 27 Campbell, M. D. 'Development of the thermal expansion capabilities and the investigation of the thermal expansion characteristics of space vehicle materials (II)', General Dynamics/Astronautics Report ERR-AN-450 (1963)
- 28 Caren, R. P., Costou, R. M., Holmes, A. M. C., Dubus, F. 'Low-temperature tensile, thermal contraction, and gaseous

- hydrogen permeability data on hydrogen-vapor barrier materials', *Advances in Cryogenic Engineering* 10 (1965) 171
- 29 Chiao, T. T., Moore, R. L. 'Tensile properties of PRD-49 fiber in epoxy matrix', *J Comp Mat* 6 (1972) 547
- 30 Cooper, G. A., Sillwood, J. M. 'Multiple fracture in a steel reinforced epoxy resin composite', *J Mat Sci* 7 (1972) 325
- 31 Darwish, F., Tetelman, A. S. 'Mechanical behaviour of S O₂-epoxy composite', Conference Proceedings No 63, Advisory Group for Aerospace Research and Development, Symposium on Composite Materials, Paper No 9, Paris, April 1970 (Hartford House, London)
- 32 Davis, J. G., Zender, G. W. 'Mechanical behaviour of carbon fiber reinforced-epoxy composites', 12th National Symposium Society of Aerospace Material and Process Engineers, Vol 12 (1967) section AC-10
- 33 Dervy, A. J. 'Reinforced plastics of high strength/weight ratio for space applications', Technical Papers, 17th Annual Technical Conference, Society of the Plastics Industry section 7-D, 1 (1962)
- 34 Fontana, M. G., Bishop, S. M., Spretnak, J. W. 'Investigation of mechanical properties and physical metallurgy of aircraft alloys at very low temperatures, Part 5 - Mechanical properties of metals and a plastic laminate at low temperatures', AF Technical Report 5662, Part 5, Materials Laboratory, Wright-Patterson Air Force Base, Ohio, (1953) (AD 27726)
- 35 Freeman, S. M. 'Properties of vapour barriers, adhesives and foams at cryogenic and elevated temperatures', Lockheed Aircraft Corporation Report ER-5687 (1962)
- 36 Freeman, W. T., Campbell, M. D. 'Thermal expansion characteristics of graphite reinforced composite materials', Composite Materials: Testing and Design (Second Conference), ASTM STP 497, American Society for Testing and Materials (1972) 121
- 37 Funk, C. W., Dixon, C. E. 'Cryogenic radiation damage in structural polymers', *Trans of the American Nuclear Society* 9 (1966) 406
- 38 Gille, J. P. 'Development of advanced materials for integrated tank insulation system for the long term storage of cryogens in space', NASA CR-102570 (Final), National Aeronautics and Space Administration, Huntsville, Alabama (1969) (N70-23348)
- 39 Gleich, D. 'Development of a filament-overwrapped cryoformed metal pressure vessel', NASA CR-72753, National Aeronautics and Space Administration, Lewis Research Center, Cleveland, Ohio (1971) (N71-22401)
- 40 Gray, P. D., Cornelius, G. K., O'Donnell, J. D., Howard, W. W. 'Rockets in space environment, Volume 1: The experimental programme', RID-TDR-63-1050, Aerojet General Corporation (1963) (N63-20999)
- 41 Greer, F. 'Flexural properties of Conolon 506 at room temperature -320°F and -423°F', Convair/Astronautics Report 55E 522 J (1971) (AD 677 565)
- 42 Hale, D. V. 'Study of thermal conductivity requirements: MSFC 20-inch and 105-inch cryogenic tank analyses', NASA CR-61288, National Aeronautics and Space Administration, Marshall Space Flight Center, Alabama (1969) (N69-35811)
- 43 Hall, J. 'Cryogenic tensile tests - epoxy fiberglass', Douglas Aircraft Company Report MP 1348 (1961)
- 44 Hanson, M. P. 'Effects of temperature and creep characteristics of PRD-49 fiber epoxy composites', NASA TN D-7120, National Aeronautics and Space Administration, Lewis Research Center, Cleveland, Ohio (1972) (N73-12607)
- 45 Hanson, M. P. 'Tensile and cyclic fatigue properties of graphite filament-wound pressure vessels at ambient and cryogenic temperatures', NASA TN D-5334, National Aeronautics and Space Administration, Lewis Research Center, Cleveland, Ohio (1969) (N69-31300) (Identical to SAMPE 15, 249)
- 46 Hanson, M. P., Richards, R. T., Hick, R. O. 'Preliminary investigation of filament-wound glass-reinforced plastics and liners for cryogenic pressure vessels', NASA TN D 2741, National Aeronautics and Space Administration, Lewis Research Center, Cleveland, Ohio (1965)
- 47 Hanson, M. P. 'Glass, boron, and graphite-filament-wound resin composites as liners for cryogenic pressure vessels', NASA TN D-4412, National Aeronautics and Space Administration, Lewis Research Center, Cleveland, Ohio (1968) (Identical to NASA TN X-57350, 1967)

- 48 Hanson, M. P. 'Static and dynamic fatigue behaviour of glass filament-wound pressure vessels at ambient and cryogenic temperatures', NASA TN D-5807, National Aeronautics and Space Administration, Lewis Research Center, Cleveland, Ohio (1970) (CFSTI-CSCL-20 K)
- 49 Haskins, J. F., Hertz, J. 'Thermal conductivity testing of coast P-224-6 phenolic-fiberglass laminate', General Dynamics/Convair Report No AR-592-1-482 (1963)
- 50 Haskins, J. F., Hurlich, A. 'Measured values for the coefficients of linear expansion of Plycel 420 and Conolon 506 at low temperatures', Convair/Astronautics Report MRG-154 (1960)
- 51 Haylett, J. W., Rottmayer, E., Butcher, I. 'Advanced composite material study for millimeter wavelength antennas', Technical Report AFML-TR-71-205, Vol 1, Air Force Materials Laboratory, Wright-Patterson Air Force Base, Ohio (1971) (AD 893 368)
- 52 Haylett, C. E. 'Advanced composite material study for millimeter wavelength antennas, Volume II, Environmental Tests', AFML-TR-71-205-Vol 2, Air Force Materials Laboratory, Wright-Patterson Air Force Base, Ohio (1971) (AD 893 358 L)
- 53 Herring, H. W., Baucom, R. M., Pride, R. A. 'Research on boron filaments and boron reinforced composites', 10th National Symposium, Society of Aerospace Material and Process Engineers, Vol 10 (1966) B-21 to B-34
- 54 Hertz, J. 'Tensile testing of Conolon 506 at room and sub-zero temperatures', Convair/Astronautics Report MRG-120
- 55 Hertz, J. 'Tensile testing of Adlock 851, Adlock PG-LA and Adlock EG-11A-81A from -423°F to 78°F', Convair/Astronautics Report MRG 237 (1961)
- 56 Hertz, J. 'Investigation of potential low temperature insulations' General Dynamics/Astronautics Report GS/A-ERR-AN-668 (1964)
- 57 Hertz, J. 'The effect of cryogenic temperatures on the mechanical properties of reinforced plastic laminates', General Dynamics Report AR-592-1-415 (1963) (AD 405 170)
- 58 Hertz, J. 'Investigation into the high-temperature strength degradation of fiber-reinforced resin composite during ambient aging', General Dynamics/Convair Report No GDCA-DBG73-005 (Final Contract NAS 8-27435) (1973)
- 59 Hoggatt, J. T. 'Development of cryogenic PRD-49-1 filament-wound tanks', NASA CR-120835, National Aeronautics and Space Administration, Lewis Research Center, Cleveland, Ohio (1971) (N72-24941)
- 60 Hoggatt, J. T. 'High performance filament wound composites for pressure vessel applications', Society of Aerospace Material and Process Engineers National Technical Conference, Space Shuttle Materials, Vol 3 (1971) 157
- 61 Hust, J. G. 'Low temperature thermal conductivity of two fibre-epoxy composites' *Cryogenics* 15 (1975) 126
- 62 Johnston, H. L., Brooks, H. E. 'Impact strength of various metals at temperatures down to 20° absolute', Ohio State University Cryogenic Laboratory Report TR 264-17 (1952)
- 63 Keller, C. W. 'Fiberglass supports for cryogenic tanks', NASA CR-120937 (Final), National Aeronautics and Space Administration, Lewis Research Center, Cleveland, Ohio (1972) (N72-33564)
- 64 Kerlin, E. E., Smith, E. T. 'Measured effects of the various combinations of nuclear radiation, vacuum and cryotemperatures on engineering Materials: Biennial report', NASA CR-77772, National Aeronautics and Space Administration, George C. Marshall Space Flight Center, Huntsville, Alabama (1966) (N66-35963)
- 65 Kerlin, E. E., Smith, E. T. 'Measured effects of the various combinations of nuclear radiation, vacuum and cryotemperatures on engineering materials: Annual report', NASA CR-58830, National Aeronautics and Space Administration, George C. Marshall Space Flight Center, Huntsville, Alabama (1964) (N64-33043)
- 66 Keys, R. D., Kiefer, T. F., Schwartzberg, F. R. 'Cryogenic properties of high-strength glass-reinforced plastics', *Advances in Cryogenic Engineering* 11 (1966) 470
- 67 Krause, D. R. 'Development of lightweight material composites to insulate cryogenic tanks for 30-day storage in outer space', NASA CR-123797, National Aeronautics and Space Administration, George C. Marshall Space Flight Center, Huntsville, Alabama (1972) (N72-30755)
- 68 Krause, D. R., Fredrickson, G. O., Klevatt, P. L. 'Effects of cyclindrical environments on high-performance multi-layer insulation materials', Society of Aerospace Material and Process Engineers National Technical Conference, Space Shuttle Materials, Vol 3 (1971) 639
- 69 Lantz, R. B. 'Materials for filament wound cryogenic pressure vessels', 5th National Symposium, Society of Aerospace Materials and Process Engineers, Vol 2, Engineering Paper No 1750
- 70 Lavengood, R. E., Anderson, R. M. 'Matrix properties controlling torsional fatigue life of fiber reinforced composites', Technical Papers, 24th Annual Technical Conference, Society of the Plastics Industry, section 11-E (1969)
- 71 Levin, V. A., Naumenkov, P. G., Shchitov, M. V. 'Some properties of plastics at low temperatures', *Plasticheskaia Massy* 11 (1966) 64
- 72 Luikov, A. V., Vasiliev, L. L., Shashkov, A. G. 'A method for the simultaneous determination of all thermal properties of poor heat conductors over the temperature range 80 to 500 K', Proceedings Third American Society of Mechanical Engineers Symposium, Purdue University (1965) 314
- 73 Lyon, D. N., Parrish, W. R. 'Low temperature thermal conductivities of two high compressive strength materials', *Cryogenics* 7 (1967) 21
- 74 Maher, L. E. 'Some problems arising from the use of hydrogen-fuelled propulsion systems', *J Royal Aeronautical Society* 68 (1964) 765
- 75 McKannon, E. C., Gause, R. L. 'Effects of nuclear radiation and cryogenic temperatures on non-metallic engineering materials', *J of Spacecraft* 2 (1965) 558
- 76 Morris, E. E. 'Glass-fiber-reinforced metallic tanks for cryogenic service', 12th National Symposium, Society of Aerospace Materials and Process Engineers, Vol 12 (1967) section AS-4 (also NASA CR-72224)
- 77 Morris, E. E. 'The performance of glass-filament-wound pressure vessels with metal liners at cryogenic temperatures' *J of Mat* 4 (1969) 970
- 78 Morris, E. E., Alfring, R. J. 'Cryogenic boron-filament-wound pressure vessels', Composite Materials: Testing and Design, ASTM STP 460, American Society for Testing and Materials (1969) 430
- 79 Morris, E. E., Landes, R. E. 'Cryogenic glass-filament-wound tank evaluation', NASA CR-72948 (Final), National Aeronautics and Space Administration, NASA Lewis Research Center, Cleveland, Ohio (1971) (N72-14696)
- 80 Mowers, R. E., Leib, J. H., Sherman, S. 'Programme of testing nonmetallic materials at cryogenic temperatures', Rocketdyne Corporation Report R-3498, Rocket Propulsion Laboratories, Edwards, California (1962) (AD 294 772)
- 81 Nadler, M. A., Yoshino, S. Y., Darms, F. J. 'Boron/epoxy support strut for non-integral cryogenic tankage', North American Rockwell Space Division Report SD 68-99501 (1969) (see also 15th National Symposium SAMPE April 1969 and North American Rockwell Report SD 995 2, 1968)
- 82 Nelson, L. F. 'Compressive strength of Conolon 506 at +75°F and -320°F', Convair/Astronautics Report No 27E 1336 (1962)
- 83 Nelson, L. R. 'Mechanical properties of Adlock 851 at room temperature, 1000°, -320° and -423°F', Convair/Astronautics Report No 55E 812 (1961)
- 84 Nelson, P. T., Archer, J. S. 'Graphite reinforced plastic EHF antenna', TRW Systems Group, Redondo Beach, California Report No 99900-7128-RO-11 (1969)
- 85 Patten, P. M. 'Internal insulation liner alteration', Douglas Aircraft Company Report No SM 45975 (1964)
- 86 Perkins-Elmer Optical Group, Norwalk, Connecticut, Work-In-Progress on Contract No F33615-72-C-2033, Air Force Systems Command, Wright-Patterson Air Force Base, Ohio
- 87 Pink, E., Campbell, J. D. 'The effect of strain rate and temperature on the deformation behaviour of reinforced and unreinforced epoxy resin', Oxford University Department of Engineering Report No 1040/72, Oxford, England (1972) (N73-10568)
- 88 Pirgon, O., Wostenholm, G. H., Yates, B. 'Thermal expansion at elevated temperatures, IV. Carbon-fibre composites', *J Physics D: Appl Phys* 6 (1973) 309
- 89 Pride, R. A., Stein, B. A., Schmidt, F. W. 'Mechanical properties of polyimide-resin/glass-fiber laminates for various time, temperature and pressure exposures', Technical Papers, 23rd Annual Reinforced Plastics Technical and Management Conference, Washington, DC (1968) section 17-c, 1

- 90 Ratcliffe, E. H. 'Thermal conductivities of plastics with glass, asbestos and cellulosic fiber reinforcements', *Appl Mat Res* 5 (1966) 200
- 91 Roseland, L. M. 'Materials for cryogenic usage', Technical Papers, 21st Annual Technical Conference, Society of the Plastics Industry (1966) section 4-C, 1
- 92 Roseland, L. M. 'Investigation of structural properties at cryogenic temperatures of filament-wound pressure vessels containing both organic and glass filaments', Douglas Aircraft Corporation Report No SM-48409 (1966)
- 93 Ross, J. E. 'Fiberglass laminate - ultimate tensile and flexural strength tests at room temperature, -100°F and 320°F', Convair Astronautics Report No 7E 1687 (1959) (AD 830 230)
- 94 Sanders, R. H., Weleff, W. 'Final report on GTR-17 effects of radiation on organic materials irradiated in liquid hydrogen', Aerojet-General Corporation Report No RN-S-0317 (1967)
- 95 Sanger, M. J., Molho, R., Howard, W. W. 'Exploratory evaluation of filament-wound composites for tankage of rocket oxidizers and fuels', AFML-TR-65-381, Air Force Materials Laboratory, Wright-Patterson Air Force Base, Ohio (1966) (AD 477 455)
- 96 Sanger, M. J., Reinhardt, T. J. 'Development of filament-wound tankage for rocket oxidizers and fuels', Technical Papers, 12th National Symposium, Society of Aerospace Material and Process Engineers (1967) section AS-7
- 97 Sewell, J. J., Kuno, J. K. 'Aerospace use of plastic hardware and thermal insulation', Technical Papers, 17th Annual Technical Conference, Society of the Plastics Industry (1962) section 7-A
- 98 Shriver, C. B. 'Design and fabrication of an internally insulated filament wound liquid hydrogen propellant tank', NASA CR-127, National Aeronautics and Space Administration, Washington DC (1964) (N65-10775)
- 99 Soltysiak, D. J., Toth, J. M. 'Static fatigue of fiber glass pressure vessels from ambient to cryogenic temperatures', Technical Papers, 22nd Annual Technical Conference, Society of the Plastics Industry (1967) section 14-E
- 100 Speare, J. C. 'Preliminary sizing of filament-wound RNS tanks', Report No TOR-0066 (5759-07)-13, Space and Missile Systems Organization, Air Force Systems Command, Los Angeles Air Force Station, Los Angeles, California (1970) (AD 872 626)
- 101 Steinhauer, R. A. 'Linear thermal expansion of 828CL 181 cloth laminate', Douglas Aircraft Company Report No MP 11 979 (1961)
- 102 Stinnett, W. D. 'Cryogenic tensile properties of selected materials', NASA CR-71751, AEC-NASA Space Nuclear Propulsion Office, Report No 2712 (1964) (N66-22816)
- 103 Suezawa, Y., Hojo, H., Nakamura, K. 'Impact characteristics of fiberglass reinforced plastics at low temperatures', *Kagaku Kagaku (Chemical Engineering, Japan)* 33 (1969) 1051
- 104 Toth, J. M. 'Barrier films for filament-wound fiberglass cryogenic vessels', *Advances in Cryogenic Engineering* 1 (1964) 537
- 105 Toth, J. M., Soltysiak, D. J. 'Investigation of smooth-bonded metal liners for glass fiber filament-wound pressure vessels', NASA CR-72165 (Final), National Aeronautics and Space Administration, Lewis Research Center, Cleveland, Ohio (1967) (N67-25070)
- 106 Toth, J. M., Sherman, W. C., Soltysiak, D. J. 'Investigation of smooth-bonded metal liners for glass fiber filament-wound pressure vessels', Douglas Missile and Space Systems Division Report No SM-49384, Quarterly Report No 3, Contract No NAS 3 6193, NASA Lewis Research Center, Cleveland, Ohio (1966)
- 107 Toth, J. M., Sherman, W. C., Soltysiak, D. J. 'Investigation of structural properties of fiber-glass filament-wound pressure vessels at cryogenic temperatures', NASA CR-54393, National Aeronautics and Space Administration, Lewis Research Center, Cleveland, Ohio (1965) (N65-35392)
- 108 Toth, J. M., Barber, J. R. 'Structural properties of glass-fiber filament-wound cryogenic pressure vessels', *Advances in Cryogenic Engineering* 10 (1965) 134
- 109 Voloshenko-Klimovitskii, Yu. Ya., Belyaev, Yu. A., L'vov, B. S., Schpakovskaya, E. I. 'Strength of cold-hardening GRPs based on PN-1 resin under impact tension at normal (20°C) and low (-196°C) temperatures', *Plasticheski Massy* 6 (1964) 39
- 110 Voloshenko-Klimovitskii, Yu. Ya., Belyaev, Yu. A., Korenkov, Yu. A. 'Impact tensile tests on glass-fibre reinforced plastics at normal and low temperatures', *Plasticheski Massy* No 5 (1963) 51
- 111 Watson, J. F., Christian, J. L., Hertz, J. 'Selection of materials for cryogenic applications in missiles and aerospace vehicles', Convair/Astronautics Report No MRG 132-1 (1960)
- 112 Weleff, W. 'Effect of nuclear radiation and liquid hydrogen on mechanical properties of three phenolic materials', *Advances in Cryogenic Engineering* 11 (1966) 486
- 113 Weleff, W. 'Final report, GTR-16 radiation effects test on structural materials at -423°F', Aerojet-General Corporation Report No RN-S-0290 (1966)

4. Handbooks and reviews

- 114 Coston, R. M. 'Handbook of thermal design data for multilayer insulation systems', LMSC-A847882, Vol 2 (Final), George C. Marshall Space Flight Center, Huntsville, Alabama (1967) (N67-34910)
- 115 Hertz, J. 'The effect of cryogenic temperatures on the mechanical properties of reinforced plastic laminates', *Society of Plastics Engineers* 1 21 (1965) 181
- 116 Hertz, J., Knowles, D. 'Survey of thermal properties of selected materials', General Dynamics/Convair Report AAL-65-008 (AR-504-1-553) (1965) (N65-31775)
- 117 Jurevic, W. G., Rittenhouse, J. B. 'Structural applications handbook', AFML TR-67-332, Air Force Materials Laboratory, Wright-Patterson Air Force Base, Ohio (1968) (AD 804 585)
- 118 Landrock, A. H. 'Properties of plastics and related materials at cryogenic temperatures', Plastec Report No 20, Plastics Technical Evaluation Center, Picatinny Arsenal, Dover, New Jersey (1965) (AD 469 126)
- 119 Maximovich, M., Scheck, W. G. 'Data summary and reference file for graphite and boron reinforced composite materials', General Dynamics/Convair Report No GDCA-1DBG71-006 (1971) (Contract NAS 8-26198, George C. Marshall Space Flight Center, Huntsville, Alabama)
- 120 Nored, D. L., Hennings, G., Sinclair, D. H., Smith, G. T., Smolak, G. R., Stefan, A. J. 'Storage and handling of cryogenic fluids', NASA Special Publication SP-5053, Proceedings of Conference on Selected Technology for the Petroleum Industry, Lewis Research Center, Cleveland, Ohio (1965) (N66-33674)
- 121 'Plastics for aerospace vehicles, Part 1. Reinforced plastics', MIL-HDBK-17A, Department of Defense, Washington, DC (1971)
- 122 Rittenhouse, J. B., Singletary, J. B. 'Space materials handbook', 3rd edn, NASA Special Publication SP-3051, National Aeronautics and Space Administration, Washington, DC (1969) (Limited publication as AFML-TR-68-205)
- 123 Schwartzberg, F. R., Hertz, R. G., Osgood, S. H. et al. 'Cryogenic materials data handbook (revised), Volume 2', AFML-TOR-64-280-Vol II (Revised), Air Force Materials Laboratory, Wright-Patterson Air Force Base, Ohio (1970) (AD 713 620)

5. Miscellaneous references

- 124 'Advanced composites design guide', 3rd edn, Vol 4: Materials, Air Force Materials Laboratory, Wright-Patterson Air Force Base, Ohio (1973)
- 125 Kreider, K. G., Prew, K. M. 'The transverse strength of boron fibers', Composite Materials, Testing and Design, ASTM STP 497 (1972) 539
- 126 Arp, V., Wilson, J. H., Windich, L., Sikora, P. 'Thermal expansion of some engineering materials from 20 to 293 K', *Cryogenics* 2 (1962) 230
- 127 Novak, R. C., DeCrescente, M. D. 'Impact behaviour of unidirectional resin matrix composites tested in the fiber direction', Composite Materials, Testing and Design, ASTM STP 497 (1972) 311
- 128 Kastelic, J. R., Hiltner, A., Baer, E. 'Crazing, yielding and fracture in polycarbonate and polyethylene terephthalate at low temperatures', *J of Macro Molecular Science-Physics* B7 (4) (1973) 679

Bibliography — property cross reference

Property	Glass-Epoxy	Glass-Polyester	Glass-Phenolic	Glass-Teflon	Glass-Silicone	Glass-Polyurethane	Glass-Phenyl Silene	Glass-PBI**
σ_{tu}	1-1.3, 2-2.2, 3-3.5, 4, 5, 5.1, 22, 24, 28, 33, 35, 40, 43, 46, 47, 52, 54, 55, 57, 66, 71, 87	1-1.3, 2-2.2, 3-3.2, 3-4, 3.5, 34, 40, 55, 57, 63, 64, 66, 75, 109	1-1.3, 2-2.2, 40, 54, 55, 57, 64-66, 71, 75, 83, 93, 97, 111, 112	2-2.2, 37, 67, 68, 80, 94, 102, 113	1-1.3, 2-2.2, 24, 40, 57, 64, 66, 68, 97	2-2.2, 85	2-2.2, 57, 66,	2-2.2
E_1^f	1-1.3, 2-2.2, 3-3.5, 4.5, 5.1, 24, 28, 35, 55, 56, 57, 66, 87	1-1.3, 2-2.2, 3, 34, 55, 57,	1-1.3, 2-2.2, 54, 55, 57, 97, 111	2-2.2, 80	1-1.3, 2-2.2, 24, 57	2-2.2	2-2.2, 57, 66	2-2.2, 24
E_2^f	1-1.3, 2, 3-3.5, 28, 55, 56, 57	1-1.3, 2, 55, 57	1-1.3, 55, 57		1-1.3, 2, 57	2	2, 57	2
ϵ^t	3-3.5, 4, 5, 5.1, 35, 64, 85	3-3.5, 64	64, 65, 112	80, 89, 102	64	85		
σ_{fu}	1-1.3, 2-2.2, 3-3.5, 4, 40, 57, 66, 71	1-1.3, 2-2.2, 3-3.3, 3.5, 40, 57, 66	1-1.3, 2-2.2, 40, 41, 57, 71, 83, 93, 97	2-2.2, 80	1-1.3, 2-2.2, 40, 57, 97	2-2.2	2-2.2	2-2.2
E_1^f	1-1.3, 2, 3-3.2, 3.4, 3.5, 57	1-1.3, 2, 2.2, 57	1-1.3, 2-2.2, 57, 83, 93, 97	2-2.2, 80	1-1.3, 2-2.2, 57	2-2.2	2-2.2	2-2.2
E_2^f	1-1.3, 2	1-1.3, 2	1-1.3, 2	1-1.3, 2		1-1.3, 2	2	2
σ_{cu}	1-1.3, 2, 2.2, 3-3.2, 3.4, 3.5, 24, 57, 66	1-1.3, 2, 2.2, 3-3.5, 34, 57	1-1.3, 2-2.2, 57, 82, 97	2-2.2, 80	1-1.3, 2-2.2, 24, 57	2-2.2	2-2.2, 57	2-2.2, 24
E^c	1, 1.2, 1.3, 2, 2.2, 57	1-1.3, 2, 2.2, 57, 66	1-1.3, 2-2.2, 57, 82, 97	2-2.2, 80	1-1.3, 2-2.2, 57	2-2.2	2-2.2	2-2.2
σ_{si}	3-3.2, 3.4, 3.5, 4, 4.1, 5, 5.1, 22, 47, 71	3-3.5	71					
η^t	1, 1.3, 2, 2.1, 2.2, 66, 70, 99	1-1.3, 2-2.2, 34, 70	1-1.3, 2-2.2		1-1.3, 2	2	2	2
σ_{by}	2-2.2, 3-3.2, 3.4, 3.5				2	2	2	2
σ_{l^*}	4, 71, 103	62, 109	71, 97	80				
λ	3, 4.1, 14, 16-16.3, 21, 23-25, 38, 42, 56, 61, 63, 90, 114	3, 14, 16-16.3, 90	14, 16-16.3, 49	14, 16-16.3	14, 16-16.3,		14, 16-16.3	16, 24
$\Delta L/L$	3, 5, 14, 16, 16.2, 16.3, 28, 69, 85, 91, 100, 101, 104, 114	3, 14, 16-16.3	14, 16-16.3, 26, 27, 50, 111	14, 16-16.3, 80	14, 16-16.3, 67	5, 85, 91	14, 16-16.3	16, 16.2
c_p	15, 16, 16.2, 16.3, 24, 114	15, 16-16.3	15, 16-16.3, 64	15, 16-16.3	15, 16-16.3, 24		15, 16-16.3	16-16.3, 24

* includes fracture toughness

** polybenzimidazole

Bibliography—property cross reference (contd)

Property	Graphite-Epoxy	Boron-Epoxy	Boron-Aluminium	PRD-49 Epoxy
σ^{tu}	8, 9, 10, 10.2, 13, 13.2, 32, 47, 51, 58	13, 20, 22, 47, 53, 58, 81	13, 13.3	29, 44, 59, 60
E^t	8, 9, 10, 10.1, 13, 51	13, 81	13, 13.3	44, 59, 60
ϵ^t	13	20	13	
σ^{fu}	8, 10, 10.1, 11, 12, 13, 13.2, 58	58		
E^f	8, 10.1			
σ^{cu}	13		13, 13.3	
E^c	13	13, 81	13, 13.3	
σ^{si}	8, 9, 10, 10.1, 10.2, 12, 13, 13.2, 47, 58	13, 22, 47, 58, 81	13, 13.3	59, 60
η^t	45	20		
σ^{by}			13, 13.3	
σ^{I^*}	9, 10.2	81		
λ	13, 17, 18, 38	13, 38, 63, 81		
$\Delta L/L$	10, 13, 13.2, 17, 18, 36, 51, 52, 84, 88	13	13, 13.3	59, 60
c_p	13	13	13, 13.3	

* includes fracture toughness

Miscellaneous properties

Notch tensile strength Glass-Epoxy (3–3.2, 3.4, 3.5, 43, 46)

Vapour permeability Glass-Epoxy (28)

Modulus of rigidity Glass-Epoxy (53), Glass-Teflon (80), Boron-Epoxy (53)

Poissons ratio Glass-Epoxy (53), Boron-Epoxy (53)

Proportional limit in tension Glass-Epoxy (55, 56), Glass-Polyester (1–1.3, 55, 56)

Static fatigue Glass-Epoxy (66, 99), PRD 49-Epoxy (44)

Environmental effects Glass-Epoxy (4–4.4), Graphite-Epoxy (13, 13.2, 17, 58) Boron-Epoxy (13, 58), Boron-Aluminium (13, 36), PRD 49-Epoxy (44)

Electrical resistivity Graphite-Epoxy (13), Boron-Epoxy (13)

Thermo-optical effects Graphite-Epoxy (13, 84), Boron-Epoxy (13)

Density Glass-Epoxy, Polyester, Phenolic, Silicone, Phenyl Silane (14, 57), Glass-Teflon (14), Glass-Polybenzimidazole (16), Graphite-Epoxy (9, 13), Graphite-Phenolic (14), Graphite-Polyimide (12.1)

Radiation effects (13.2, 33, 37, 40, 51, 52, 64, 65, 75, 94, 112, 113)

Cryogen competability (33)

Miscellaneous composites

Glass-Polyimide σ^{tu} (24, 67, 68), σ^{fu} (89), σ^{si} (12.1, 89) $\Delta L/L$ (67)

Glass-Melamine σ^{tu} (65), ϵ^t (65), λ (90)

Glass-Viton σ^{tu} (68)

Glass-Phenyl formaldehyde σ^I (110), λ (72), c_p (72)

SiO₂-Epoxy σ^{tu} (31), $\Delta L/L$ (28)

Graphite-Aluminium σ^{tu} (thermal cycling effects 6–6.2)

Graphite-Polyimide σ (14, 16–16.3) $\Delta L/L$ (14, 16–16.3)

Steel-Aluminium σ^{tu} (7, 7.1), ϵ^t (7.1), σ^t (7, 7.1)

Steel-Epoxy σ^{tu} (2, 30), E^t (2, 30), σ^{fu} (2), σ^{cu} (2), E^c (2), n^t (2)

Boron/Steel-Aluminium σ^{tu} , E^t , σ^{cu} , E^c , σ^{by} , $\Delta L/L$, c_p
Boron/Titanium-Aluminium (13, 13.3), σ^{si} , ϵ^t , n^t (13)

Potassium titanate-epoxy λ (16), c_p (16)

Pressure vessel applications

Glass-filament (19, 20, 39, 42, 46–48, 53, 67, 69, 76, 77, 91, 92, 95, 96, 98–100, 104–108, 113)

Graphite-filament (8, 10, 10.1, 45, 47, 100)

Boron-filament (20, 47, 53, 78)

PRD 40-filament (59, 60)

SEMI-ANNUAL REPORT ON MATERIALS RESEARCH
IN SUPPORT OF SUPERCONDUCTING MACHINERY

ELASTIC PROPERTIES OF ENGINEERING MATERIALS
AT CRYOGENIC TEMPERATURES

H. M. Ledbetter and D. T. Read

Cryogenics Division
Institute for Basic Standards
National Bureau of Standards
Boulder, Colorado 80302

April 1976

Summary: Elastic Properties

During the six months preceding March 1976, the following studies were completed:

- (1) 2000-series aluminum alloys. Two alloys -- 2014 (Al-Cu-Si-Mg) and 2219 (Al-Cu) were studied in their precipitation-hardened conditions by a pulse-echo method between room temperature and liquid-helium temperature. These alloys exhibit similar elastic properties and regular behavior with respect to temperature. They are slightly stiffer elastically than some of the other aluminum alloys that were reported on previously in these reports. Results of the study are given in an accompanying manuscript "Low-temperature elastic properties of aluminum alloys 2014 and 2019" by D. T. Read and H. M. Ledbetter.
- (2) Face-centered-cubic, iron-nickel, high-permeability alloy. Iron-47.5 nickel was studied between room temperature and liquid-helium temperature by a pulse-echo method. Besides invar, iron-36 nickel, this is the only material of this type for which low-temperature elastic constants have been determined. Contrary to some previous reports, the room-temperature thermo-elastic coefficients are normal for this material. Results of the study are given in an accompanying manuscript "Low-temperature elastic properties of iron-47.5 nickel" by H. M. Ledbetter and D. T. Read.
- (3) Nickel-chromium-iron-molybdenum alloy. There is an accompanying reprint of our previously described results on Inconel 718: W. F. Weston and H. M. Ledbetter, "Low-temperature elastic properties of a nickel-chromium-iron-molybdenum alloy," Mater. Sci. Engg. 20 (1975) 287-90.
- (4) Aluminum alloys 1100, 5083, 7005, 7075. There is an accompanying reprint of our previously described results on four aluminum alloys: E. R. Naimon, H. M. Ledbetter, and W. F. Weston, "Low-temperature elastic properties of four wrought and annealed aluminum alloys," J. Mater. Sci. 10 (1975) 1309-16.
- (5) Copper-nickel alloys. Our study on copper, copper-10 nickel, and copper-30 nickel was published: H. M. Ledbetter and W. F. Weston, "Low-temperature elastic properties of some copper-nickel alloys," 1975 Ultrasonics Symp. Proc., IEEE Cat. No. 75 CHO 994-45U, 623-7. A reprint is not included here because it is indential to the preprint version given previously.
- (6) Superconducting-coil composite. There is an accompanying reprint of our previously described results on a niobium-titanium, copper-stabilized, epoxy-impregnated, superconducting-coil composite: W. F. Weston, "Low-temperature elastic constants of a superconducting coil composite," J. Appl. Phys. 46 (1975) 4458-65.

LOW-TEMPERATURE ELASTIC CONSTANTS OF PRECIPITATION-
HARDENED ALUMINUM ALLOYS 2014 and 2219⁺

D. T. Read* and H. M. Ledbetter

Cryogenics Division
Institute for Basic Standards
National Bureau of Standards
Boulder, Colorado 80302

+ Contribution of NBS, not subject to copyright. This work was partially supported by the Advanced Research Projects Agency of the U. S. Dept. of Defense.

* NRC-NBS Postdoctoral Research Associate, 1975-76.

Abstract

Elastic properties of aluminum alloys 2014 and 2219 were studied in their precipitation-hardened conditions between 4 and 300 K using an ultrasonic pulse-echo superposition technique. Results are given for longitudinal sound velocity, transverse sound velocity, Young's modulus, shear modulus, bulk modulus, and Poisson's ratio. The Young's moduli increase about eleven percent on cooling. The shear moduli are about ten percent higher than for unalloyed aluminum. All the elastic constants show regular temperature behavior.

Key words: Aluminum alloys; bulk modulus; compressibility; Debye temperature; Poisson's ratio; precipitation-hardening alloys; shear modulus; sound velocity; Young's modulus.

Introduction

The combination of a high ratio of strength to weight and high toughness at low temperatures makes many aluminum alloys attractive for cryogenic structural applications. In this report, the cryogenic elastic properties of two aluminum alloys, 2014 and 2219, used frequently at low temperatures, are described. All 2000-series alloys are precipitation hardenable, containing copper as the principal alloying element.

Alloy 2014 has better mechanical properties, but alloy 2219 has superior weldability. This is believed to be the first report of a complete set of low-temperature polycrystalline elastic constants for a series of 2000-type aluminum alloys.

Elastic constants are necessary parameters in the design of critical load-bearing members; they relate the stress applied to an object to its change in dimensions produced by the stress. Elastic constants are also used in analyzing the fracture properties of a material. The factor $E/(1 - \nu^2)$, where E is Young's modulus and ν is Poisson's ratio, occurs frequently when the strength properties of materials are considered.

Some elastic-property data on these alloys were reported previously[1]. However, the inaccuracies of those data were high, and the shear modulus was not reported. Thus, neither the bulk modulus nor Poisson's ratio, which are frequently of interest in engineering design, can be computed.

In the present study, an ultrasonic (10 MHz) pulse-superposition method[2] was used for determining the velocity v of an ultrasonic pulse propagated through the specimen. Appropriate moduli C were calculated using equations of the type $C = \rho v^2$, where ρ is the mass density. This indirect technique is more accurate than the more familiar direct

measurement of the change in length of a specimen under load where large errors can arise from mechanical misalignments. Ultrasonic methods have many advantages: small specimens are sufficient, so that ancillary equipment such as probes and dewars can also be small, and refrigeration costs are low; specimens can have a simple geometry and can be easily prepared; measurements can be made as nearly continuously as desired; relative imprecision is low, about one part in 10^5 for the velocities; laboratory-to-laboratory variations of the elastic constants are typically a few percent or less; and the relevant properties of the quartz transducer used to generate and detect ultrasonic pulses are affected only slightly by temperature.

Materials

Aluminum alloys 2014 and 2219 are precipitation-hardenable alloys containing copper and other alloy elements. Their chemical compositions are given in Table 1. The 2014 alloy was tested in the T652 condition: solution heat-treated, artificially aged, and stress relieved by rolling. The 2219 alloy was tested in the T87 condition: solution heat treated, cold worked, and artificially aged. The 2014-T652 and 2219-T87 alloys had Rockwell hardnesses of B 80.6 and B 81.1 and mass densities of 2.810 and 2.835 g/cm³, respectively. Metallographic examination of these alloys revealed severely elongated grains. Surfaces perpendicular to the rolling direction showed nearly equi-axed grains with diameters of about 0.02 cm in the 2014 alloy and 0.03 cm in the 2219 alloy. Surfaces parallel to the rolling direction showed grains so severely elongated that their dimensions could not be determined accurately.

Procedures

The specimen materials were obtained from commercial sources; the

2014 alloy was obtained as a 7.6-cm thick forging, and the 2219 alloy was received in the form of a 3.8-cm thick plate. The hardnesses were determined by a standard technique; the mass densities were determined by the method of Archimedes using distilled water as a standard.

Quartz transducers were bonded to the specimens with phenyl salicylate (salol) for room temperature measurements and with stopcock grease for the initial part of the low-temperature measurements. These bonds failed around 70 K, so that a silicone fluid (viscosity = 20 kPa·s at 25⁰ C) was used for bonding at very low temperatures. The low-temperature apparatus was described previously[3].

Elastic constants were determined from sound-velocity measurements between room temperature and liquid-helium temperature. The inaccuracy of the velocities is estimated to be less than $\pm 1\%$.

Transducer and bond effects were minimized by measuring the transit times for both the one-transducer (usual) case and the two-transducer case, using "identical" transducers and bonds. The corrections were about one percent.

Low-temperature data were obtained by a pulse-echo-superposition method[2], which gives the ratio of the low-temperature velocity to the room-temperature velocity with an imprecision of about 0.001%.

The main limitation on the usefulness of the present results is the batch-to-batch variation of commercial materials. Due to this factor, variations in the elastic constants as large as one percent could be expected, but temperature coefficients should be unaffected. Thus, measurements on similar alloys at room temperature should establish their elastic constants over the entire 0-300 K region.

Results and Discussion

The measured longitudinal moduli $C = \rho v_l^2$ for both alloys are shown in Fig. 1. The small steps between adjacent data points for the 2219 alloy at 80 K and 140 K are not representative of the material's elastic behavior, but are artifacts of the measurement process. They are due to the use of two different bonding agents to seal the quartz transducer to the specimen for the low temperature measurements. The temperature dependences of the longitudinal moduli of both the 2014 and the 2219 alloys are quite regular.

The measured transverse moduli are shown in Fig. 2. Again, the small step at 120 K in the modulus of the 2219 alloy is a measurement artifact. The temperature dependences of the transverse moduli of both alloys are also quite regular. The data shown in Figs. 1 and 2 were fitted to a function of temperature suggested by Varshni[4]:

$$C = C^0 - \frac{s}{\exp(t/T) - 1}, \quad (1)$$

where C is any elastic stiffness constant (C_l and C_t in this case), C^0 , s , and t are the fitting parameters, and T is the temperature. The fitted curves are shown along with the data in Figs. 1 and 2. Values of the fitting parameters are given in Table 2. Average differences between the measured moduli and the fitted curves were about 0.05%.

The elastic Debye temperatures for these alloys were calculated from their elastic constants at $T = 0$ K, and they are given in Table 2.

As expected from their higher shear moduli (discussed below), the alloys have higher Debye temperatures than "pure" aluminum where $\Theta = 431$ K.

Values of the longitudinal and transverse moduli calculated using the fitted Voigt parameters were used to calculate other elastic constants. The additional elastic constants reported here: the shear modulus G , the Young's modulus E , the bulk modulus B , and the Poisson's ratio ν , are given by the following formulas[5]:

$$G = C_t = \rho v_t^2, \quad (2)$$

$$E = 3G(C_l - 4/3 C_t)/(C_l - C_t), \quad (3)$$

$$B = C_l - 4/3 C_t, \quad (4)$$

and

$$\nu = 1/2(C_l - 2 C_t)/(C_l - C_t). \quad (5)$$

The four elastic constants obtained using these relations are shown as functions of temperature in Figs. 2-5. Values of these elastic constants at selected temperatures are given in Table 3, along with some previous results.

As shown by the data in Table 3, changes in the elastic constants of aluminum alloys 2014 and 2219 between 300 and 0 K are about 12% for E and G , and about 4% for B and ν . These changes are much larger than those

observed in alloys based on iron[6] and copper[7], two other common base metals. Most of the changes in the elastic constants of these aluminum alloys with temperature occur above liquid-nitrogen temperature, 77°K.

The outstanding feature of the data shown in Figs. 1-5 is the regular temperature dependence of all the elastic constants. These two aluminum alloys are good examples of materials with simple, ordinary elastic behavior with respect to temperature. This regular behavior was not evident from some previous reports on these alloys.

The bulk moduli of the 2014 and 2219 alloys differ by 0.3% and 3.9% from that of pure aluminum, while the shear moduli of these alloys differ by 8.5% and 11.9% from that of pure aluminum[8]. Thus, the alloying elements increase not only the yield strength but also the shear modulus of the base material. Alloying effects in these materials are complicated by the large number of alloying elements, but it is clear that the alloying raises the shear moduli much more than is expected from a simple rule of mixtures, while the bulk modulus is affected only slightly.

These alloys were not examined for anisotropic elastic behavior because aluminum single crystals are only slightly anisotropic[8]. Even strongly textured polycrystalline aggregates of aluminum should exhibit nearly isotropic elastic properties.

Compared to other aluminum alloys that were studied previously[9], 2000-series alloys have higher longitudinal and transverse moduli, resulting in higher Young's moduli and higher bulk moduli than the other alloys; but they have the same Poisson's ratio. The higher elastic moduli of the 2000-series alloys may be useful in critical design situations.

Conclusions

- (1) With respect to unalloyed aluminum, alloys 2014 and 2019 have

higher Young's moduli ($\sim 9\%$), higher shear moduli ($\sim 10\%$), higher bulk moduli ($\sim 2\%$), and lower Poisson ratios ($\sim 3\%$).

(2) These elastic moduli are also higher than those reported previously for 5000-series and 7000-series aluminum alloys.

(3) Alloy 2219 has a slightly higher shear modulus, but a slightly lower bulk modulus, than alloy 2014.

(5) The temperature behaviors of the two alloys are very similar. Between 300 and 0 K, B increases about 4%, E increases about 11%, G increases about 12%, and ν decreases about 3 %.

References

1. Christian, J. L. and Watson, J. F., "Mechanical Properties of Several 2000 and 6000 Series Aluminum Alloys," Advan. Cryo. Eng., Vol. 10, 1965, pp. 63-76.
2. McSkimin, H. J., "Pulse Superposition Method for Measuring Ultrasonic Wave Velocities in Solids," J. Acoust. Soc. Amer., Vol. 33, 1961, pp. 12-16.
3. Naimon, E. R., Weston, W. F., and Ledbetter, H. M., "Elastic Properties of Two Titanium Alloys at Low Temperatures," Cryogenics, Vol. 14, 1974, pp. 246-249.
4. Varshni, Y. P., "Temperature Dependence of the Elastic Constants," Phys. Rev. B, Vol. 2, pp. 3952-3958.
5. Landau, L. D. and Lifshitz, E. M., "Theory of Elasticity," Pergamon, London, 1959, pp. 13, 99.
6. Ledbetter, H. M. and Reed, R. P., "Elastic Properties of Metals and Alloys. I. Iron, Nickel, and Iron-Nickel Alloys," J. Phys. Chem. Ref. Data, Vol. 2, 1973, pp. 531-618.
7. Ledbetter, H. M. and Naimon, E. R., "Elastic Properties of Metals and Alloys. II. Copper," J. Phys. Chem. Ref. Data, Vol. 3, 1974, pp. 897-935.
8. Kamm, G. N. and Alers, G. A., "Low-Temperature Elastic Moduli of Aluminum," J. Appl. Phys., Vol. 35, 1964, pp. 327-330. Polycrystalline averages were calculated from the single-crystal data in this reference using the Voigt-Reuss-Hill-arithmetic method.
9. Naimon, E. R., Ledbetter, H. M., and Weston, W. F., "Low-Temperature Elastic Properties of Four Wrought and Annealed Aluminium Alloys," J. Mat. Sci., Vol. 10, 1975, pp. 1309-1316.

Table 1 Chemical compositions of studied
aluminum alloys, wt. %^a

Alloy	Cu	Fe	Mg	Mn	Sn	Ti	V	Zn	Zr	Al
2014	4.4		0.05	0.8	0.8					Bal
2219	6.4	0.20	0.01	0.26	0.15	0.16	0.12	0.09	0.16	Bal

^a For 2014, nominal composition. For 2219, plasma arc analysis.

Table 2 Varshni-function parameters determined from a least-squares
fit of the data (see equation 1) and elastic Debye temperature, Θ

Alloy	Mode	$C^0(10^{11} \text{ Nm}^{-2})$	$s(10^{11} \text{ Nm}^{-2})$	$t(K)$	$\Theta(K)$
2014	l	1.241	0.0781	217	439
	t	0.3152	0.0339	212	
2219	l	1.220	0.0859	230	443
	t	0.3250	0.0345	209	

Table 3 Values of the elastic constants of two aluminum alloys at selected temperatures in units of 10^{11} Nm⁻², except ν , which is dimensionless

Alloy	Temperature(K)	P r e s e n t R e s u l t s				Previous results ^a
		B	E	G	ν	E
2014	300	.791	.757	.282	.341	.73
	200	.805	.794	.297	.336	.74
	100	.817	.827	.311	.331	.76
	0	.821	.838	.315	.330	---
2219	300	.758	.774	.291	.330	.72
	200	.772	.812	.306	.325	.72
	100	.784	.845	.320	.320	.74
	0	.787	.857	.325	.318	---

^a 2014 alloy in the T-6 condition, average of longitudinal and transverse, interpolated data; 2219 alloy in the T-81 condition, average of longitudinal and transverse, interpolated data.

List of Figures

Fig. 1. Longitudinal modulus $C_1 = \rho v_l^2$ for two 2000-series aluminum alloys in precipitation-hardened condition as a function of temperature.

Fig. 2. Shear modulus $G = C_t = \rho v_t^2$ for two aluminum alloys.

Fig. 3. Young's modulus for two aluminum alloys.

Fig. 4. Bulk modulus for two aluminum alloys.

Fig. 5. Poisson's ratio for two aluminum alloys.

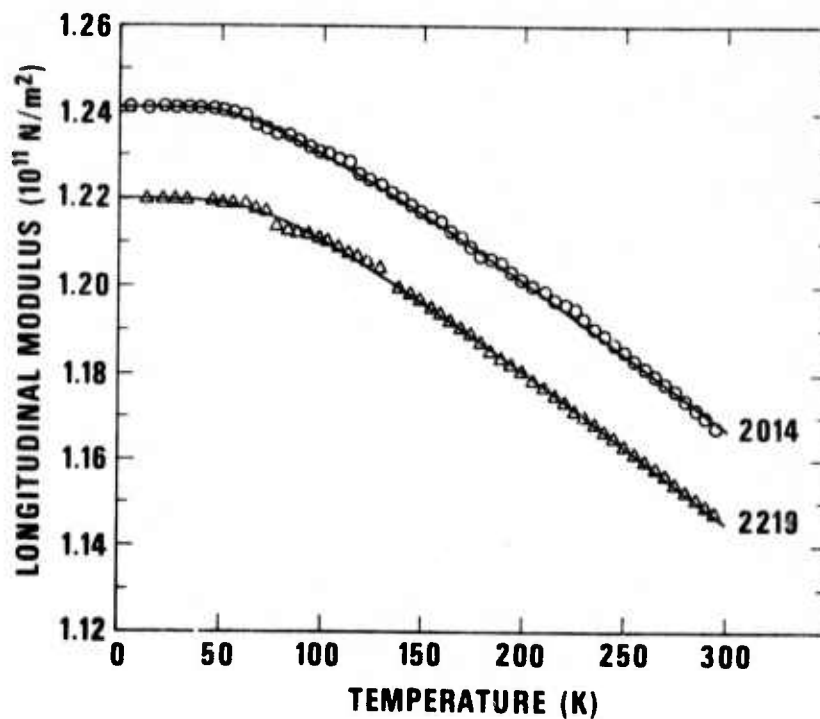


Fig. 1. Longitudinal modulus $C_l = \rho v_l^2$ for two 2000-series aluminum alloys in precipitation-hardened condition as a function of temperature.

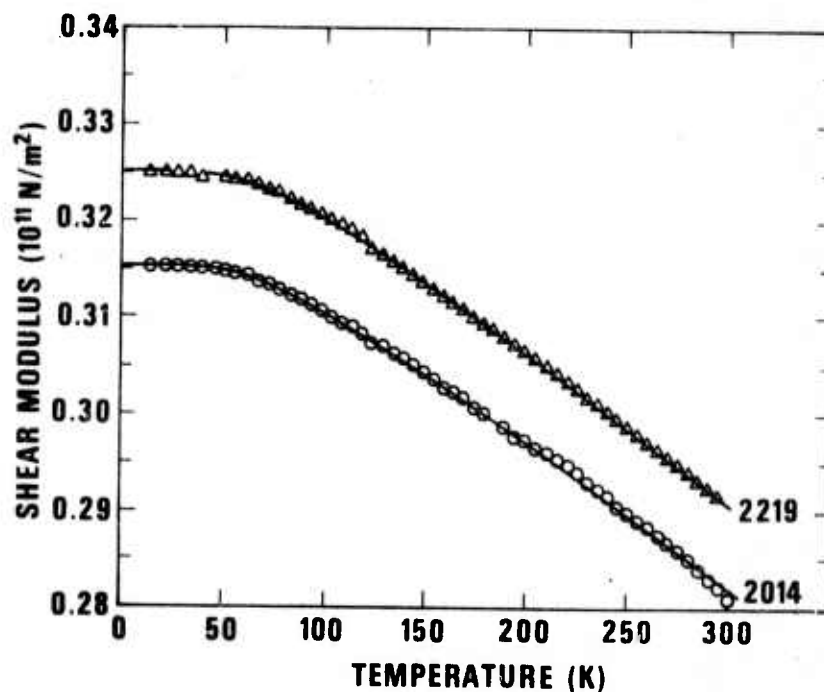


Fig. 2. Shear modulus $G = C_t = \rho v_t^2$ for two aluminum alloys.

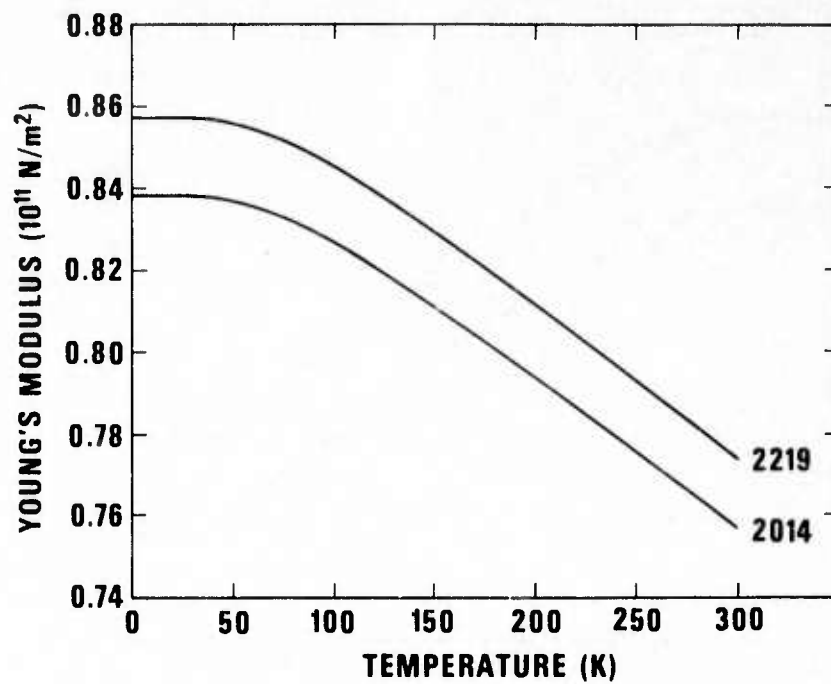


Fig. 3. Young's modulus for two aluminum alloys.

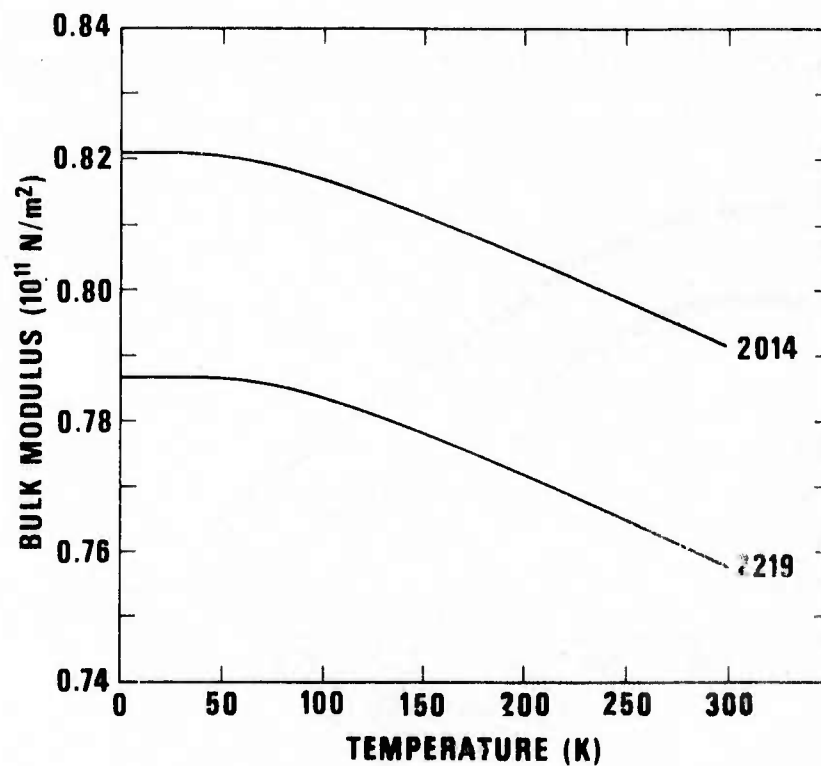


Fig. 4. Bulk modulus for two aluminum alloys.

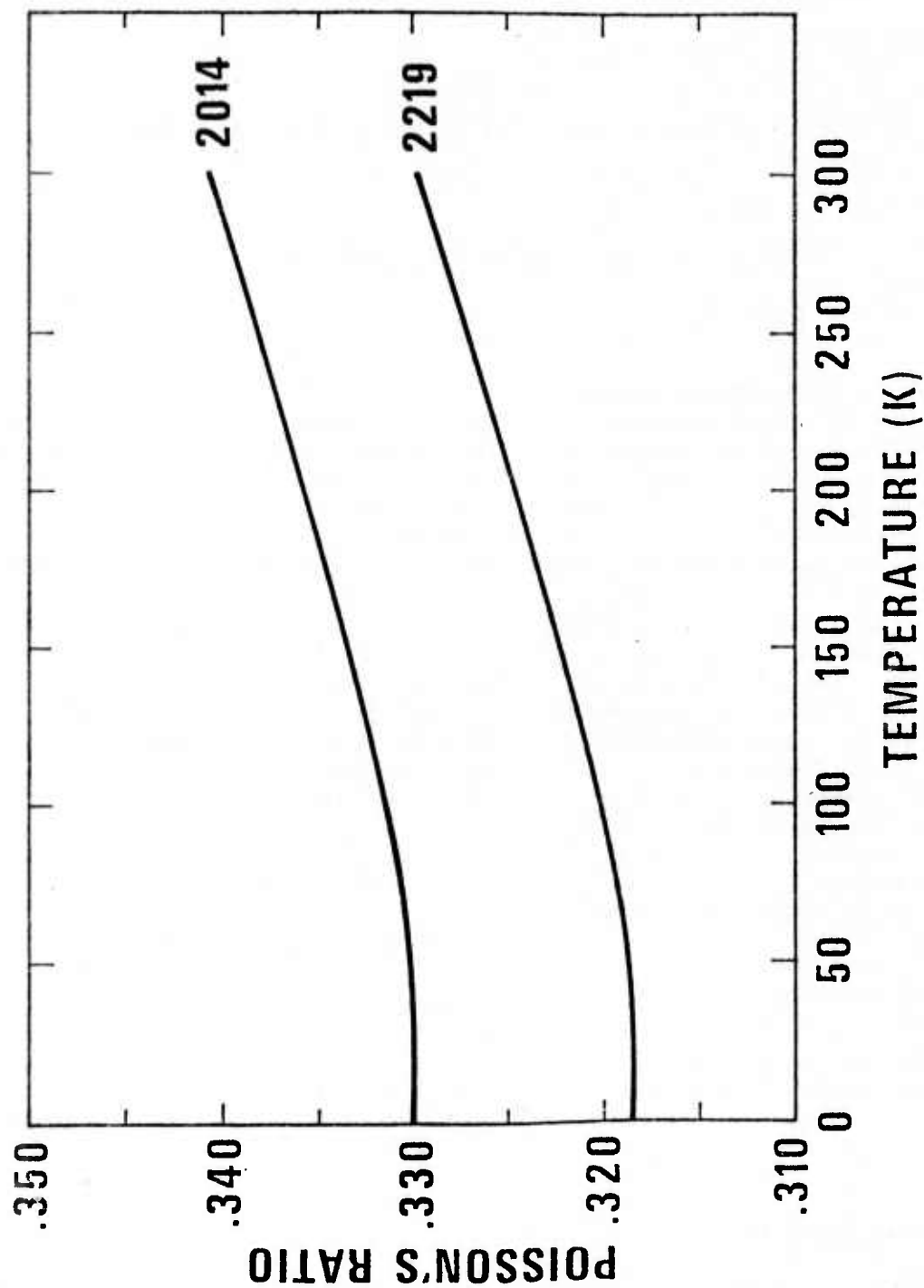


Fig. 5. Poisson's ratio for two aluminum alloys.

Note to readers: Pages 58-65 are omitted from this report. This material will be published in the future. Interested readers may consult the authors for pre-publication information on this subject.

Short Communication

Low-temperature Elastic Properties of a Nickel—Chromium—Iron—Molybdenum Alloy*

W.F. WESTON[†] and H.M. LEDBETTER

Cryogenics Division, Institute for Basic Standards, National Bureau of Standards, Boulder, Colorado 80302 (U.S.A.)

(Received in revised form May 12, 1975)

The low-temperature elastic properties of two nickel-chromium-iron alloys, Inconel 600** and Inconel X-750, were reported recently [1]. The same properties — the longitudinal modulus, Young's modulus, the shear modulus, the bulk modulus (reciprocal compressibility) and Poisson's ratio — are reported here for a nickel-chromium-iron-molybdenum alloy, Inconel 718. Except for being slightly softer elastically, it resembles Inconel X-750.

The low-temperature elastic properties of Inconel 718 are of interest mainly because it is a candidate material for cryogenic structural applications [2]. The elastic properties are important both for the design of structural components and for understanding the basic physical properties of a material. From the temperature-dependent elastic constants, deflections can be predicted for any combination

of stress and temperature. Also, the Debye characteristic temperature can be calculated from the elastic constants. The Debye temperature relates in turn to a wide variety of solid-state phenomena [3].

Inconel 718 is made precipitation hardenable by its niobium-plus-tantalum content. (Inconel X-750 is made precipitation hardenable by its aluminum-plus-titanium content.) It differs from the nickel-chromium-iron alloys in having superior mechanical properties such as yield, creep, rupture and fatigue strengths [2]. Its sluggish response to precipitation hardening permits annealing and welding without significant property changes.

EXPERIMENTAL METHODS

Ultrasonic (10 MHz) longitudinal and transverse sound-wave velocities were measured between room temperature and liquid-helium temperature (4 K) using a pulse-echo-superposition method [4]. Experimental procedures were identical with those reported previously [1] except that the material was obtained from

* Contribution of NBS, not subject to copyright.

[†] NRC-NBS Postdoctoral Research Associate, 1973-74.

** Tradenames are used to identify the materials tested; they are not NBS endorsements of particular products.

TABLE 1

Composition and properties of the alloy

Chemical composition, mill analysis (wt.%)						Hardness (DPH No., 1 kg load)	Mass density at 294 K (g/cm ³)	
Ni	Cr	Fe	Nb + Ta	Mo	Ti	425	8.229	
53.73	18.49	17.62	5.17	2.98	1.01			
Al	C	Mn	Si	S	Cu	Condition: As-received; hot-rolled		
0.58	0.05	0.08	0.17	0.007	0.04			

a commercial source in the form of 3/4-inch (1.9-cm) rods. Chemical and physical data on the material are given in Table 1.

RESULTS

The longitudinal modulus

$$C_1 = \rho v_l^2 \quad (1)$$

is shown *versus* temperature in Fig. 1, where ρ is the mass density and v_l is the longitudinal sound-wave velocity. The transverse modulus

$$C_t = \rho v_t^2 = G \quad (2)$$

is shown *versus* temperature in Fig. 2, where v_t is the transverse sound-wave velocity and G is the shear modulus. Young's modulus E , the bulk modulus B and Poisson's ratio ν were calculated from the formulas [5]:

$$E = 3C_t(C_1 - \frac{4}{3}C_t)/(C_1 - C_t), \quad (3)$$

$$B = C_1 - \frac{4}{3}C_t, \quad (4)$$

$$\nu = (1/2)(C_1 - 2C_t)/(C_1 - C_t); \quad (5)$$

and these elastic constants are shown *versus* temperature in Figs. 3 - 5. For comparison, Figs. 1 - 5 also show as dashed lines the elastic constants of Inconel X-750, which were reported previously [1].

The temperature dependences of both C_1 and C_t were fitted to a theoretical relationship suggested by Varshni [6]:

$$C = C^0 - s/(e^{t/T} - 1) \quad (6)$$

where C^0 , s , and t are adjustable parameters

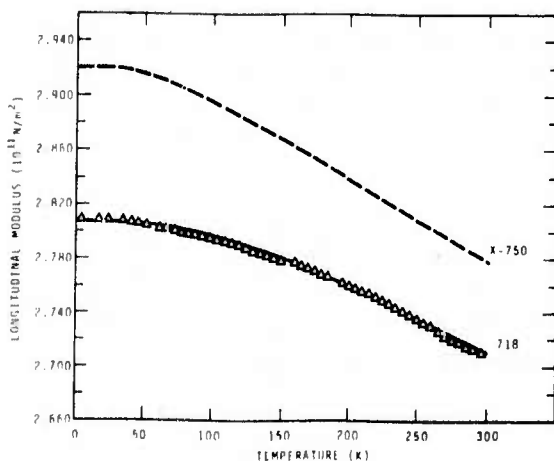


Fig. 1. Longitudinal modulus *vs.* temperature for two Inconel alloys.

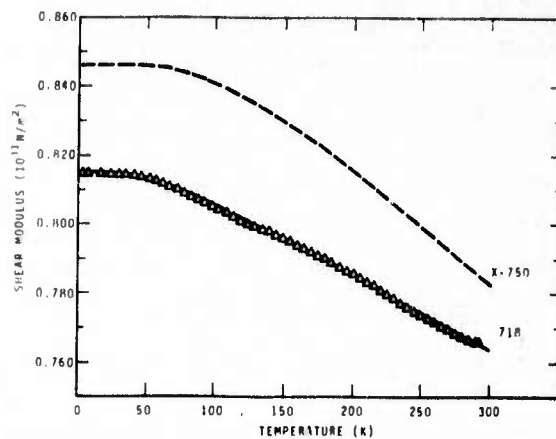


Fig. 2. Transverse (= shear) modulus *vs.* temperature for two Inconel alloys.

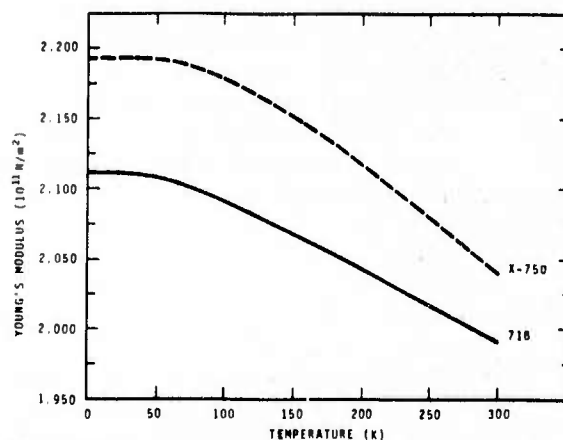


Fig. 3. Young's modulus *vs.* temperature for two Inconel alloys.

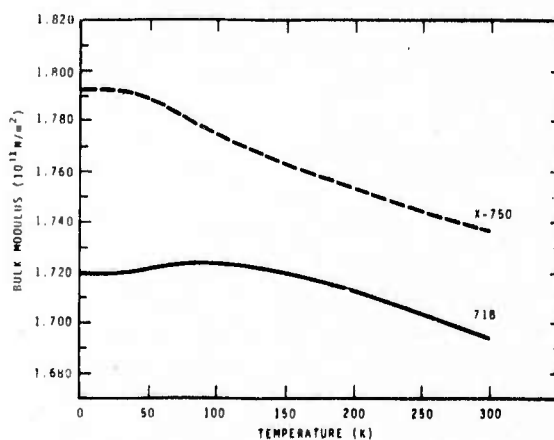


Fig. 4. Bulk modulus (reciprocal compressibility) *vs.* temperature for two Inconel alloys.

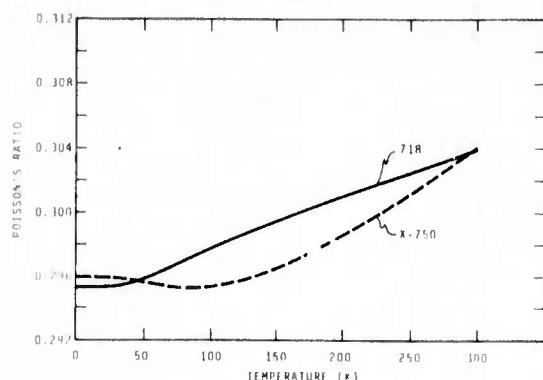


Fig. 5. Poisson's ratio vs. temperature for two Inconel alloys.

and T is temperature. The average difference between curve values and measured values was 0.06 and 0.05% for the transverse and the longitudinal modes, respectively.

The elastic Debye temperature was calculated from C_1 and C_t using standard formulas [1] and was found to be $\theta = 446$ K at absolute zero. For comparison, θ (nickel) = 476 K and θ (Inconel X-750) = 474 K.

DISCUSSION

Basically, the low-temperature elastic properties of Inconel 718 are very similar to those of Inconel X-750. The higher-iron, lower-nickel content of Inconel 718 accounts for its slightly lower elastic Debye temperature. Inconel 718 is also similar to Inconel X-750 in the temperature dependences of its elastic constants for the cases of E , G , and C_1 , which show regular behavior. By regular behavior is meant: continuously decreasing with increasing temperature, linear behavior at higher temperatures, relative flatness at low temperatures, and zero slope at $T = 0$ K. Both materials show slight anomalies in the temperature dependence of the bulk modulus. While Inconel X-750 shows a concavity upwards in the $B(T)$ curve, Inconel 718, as shown in Fig. 4, shows a maximum near 100 K in its $B(T)$ curve. Based on the previous experience of this laboratory, it is believed in this case that the imprecisions in both C_1 and C_t are a few parts in 10^4 . Thus, this anomaly (though small) is believed to be real and not a measurement-computational artifact.

The interpretation of the maximum in the $B(T)$ curve of Inconel 718 can only be speculative. Unlike Inconel X-750, it was verified during the present study that Inconel 718 is non-magnetic between room temperature and liquid-nitrogen temperature (77 K). In some respects, the low-temperature behavior of the bulk modulus of Inconel 718 resembles that of stainless steels AISI 304, 310 and 316 reported previously [7]. In those cases, the anomalous behavior was interpreted in terms of the Döring effect that results from a large volume magnetostriction accompanying a paramagnetic-to-antiferromagnetic transition. However, no evidence of a low-temperature magnetic transition in Inconel 718 seems to exist; and neither the longitudinal modulus nor Young's modulus shows any evidence of a dilatational anomaly. Thus, the nature of this anomaly, its magnitude and perhaps even the question of its existence deserve further study.

Comparisons with some previous results [8] show reasonable agreement for both the room-temperature elastic constants and the temperature derivatives of E and G . It is easy to verify that the temperature derivative of ν reported here is more reasonable than that obtained from data in ref. 8. Differentiation of the standard relationship

$$\nu = \frac{E}{2G} - 1 \quad (7)$$

gives

$$\frac{1}{\nu} \frac{d\nu}{dT} = \frac{E}{E - 2G} \left(\frac{1}{E} \frac{dE}{dT} - \frac{1}{G} \frac{dG}{dT} \right) \quad (8)$$

The present data satisfy eqn. (8) exactly, while the data from ref. 8 give a L.H.S./R.H.S. ratio of 2.6. Temperature derivatives of B have apparently not been reported previously. The only previously reported elastic constant at 4 K is Young's modulus [2]; this value, 2.11×10^{11} N/m², is identical with the present value.

This work was supported in part by the Advanced Research Projects Agency of the U.S. Department of Defense. Dr. E.R. Naimon of Dow Chemical (Rocky Flats Division) commented on the manuscript.

REFERENCES

- 1 W.F. Weston, H.M. Ledbetter and E.R. Naimon, Mater. Sci. Eng., to be published.

- 2 Handbook on Materials for Superconducting Machinery, Battelle Metals and Ceramics Information Center, Columbus, Ohio, 1974.
- 3 F.H. Herbstein, Adv. Phys., 10 (1961) 313.
- 4 H.J. McSkimin, J. Acoust. Soc. Am., 33 (1961) 12.
- 5 H.M. Ledbetter and R.P. Reed, J. Phys. Chem. Ref. Data, 2 (1974) 531.
- 6 Y.P. Varshni, Phys. Rev., B2 (1970) 3952.
- 7 H.M. Ledbetter, W.F. Weston and E.R. Naimon, J. Appl. Phys., to be published.
- 8 Huntington Alloys: Inconel Alloy 718, Intern. Nickel Co., Huntington, West Virginia.

Low-temperature elastic properties of four wrought and annealed aluminium alloys

E. R. NAIMON*, H. M. LEDBETTER, W. F. WESTON

Cryogenics Division, Institute for Basic Standards, National Bureau of Standards, Boulder, Colorado, USA

The elastic properties of four annealed polycrystalline commercial aluminium alloys were studied between 4 and 300 K using a pulse-superposition method. Results are given for longitudinal sound velocity, transverse sound velocity, Young's modulus, shear modulus, bulk modulus (reciprocal compressibility), Poisson's ratio, and elastic Debye temperature. The elastic stiffnesses of the alloys increase 4 to 13% on cooling from room temperature to liquid helium temperature. The elastic constant-temperature curves exhibit regular behaviour.

1. Introduction

Aluminium alloys are used extensively at cryogenic temperatures because of their favourable mechanical properties. These properties include increased strength without loss of ductility at lower temperatures, absence of a ductile-brittle fracture transition, and, for some alloys, high strength-to-weight ratios.

Knowledge of a material's elastic constants is essential for understanding its mechanical behaviour. Most mechanical behaviour is best described by a dislocation model, and the elastic constants (usually the shear modulus and Poisson's ratio) occur in most equations describing the stress-strain state of a dislocated solid.

In this paper, the elastic properties of four wrought aluminium alloys (commonly designated 1100, 5083, 7005, and 7075) are reported over the temperature range 300 to 4 K. These properties include the longitudinal modulus, Young's modulus, the shear modulus, the bulk modulus (reciprocal compressibility), and Poisson's ratio. While the changes of the elastic constants in this temperature range are only moderate (4 to 13%), exact values of the elastic constants are very useful design parameters, permitting accurate calculations of deflections for any combination of stress and temperature. Low-temperature elastic constants are also quite valuable theoretically; they permit the calculation of the Debye characteristic temperature, which is related in turn to a wide variety of solid-state phenomena that depends on the vibrational properties of solids.

An ultrasonic (10 MHz) pulse-superposition method was used for determining the velocity, v , of a sound pulse propagated through the specimen. The elastic modulus, C , is then given by $C = \rho v^2$, where ρ is the mass density. Different elastic constants were determined from different modes of ultrasonic excitation. This method has many advantages: small specimens are sufficient, thus ancillary equipment such as probes and dewars can also be small, and refrigeration costs are low; specimens can have a simple geometry and can be easily prepared; measurements can be made as nearly continuously as desired; relative precision is high, about one part in 10^5 for the velocities; laboratory-to-laboratory variations of the elastic constants are typically a few percent or less; and tests are completely non-destructive.

Low-temperature elastic data for aluminium alloys have two-fold interest. First, the elastic constants provide basic information about interatomic forces. Second, the same numbers are essential design parameters for stress-bearing members. Data given here permit the load-deflection behaviour of the alloys to be accurately predicted between room temperature and liquid helium temperature. Accurate elastic data

*Present address: Dow Chemical USA, Rocky Flats Division, Golden, Colorado, 80401

become especially important in applications involving high stresses, large structural parts, or precision parts.

2. Materials

Aluminium alloy 1100 is commercial quality aluminium. It has good corrosion resistance, high electrical and thermal conductivities, high ductility, but low strength properties. Strength can be improved somewhat by strain-hardening without significantly decreasing other properties. The main impurities in this alloy are usually iron and silicon.

Aluminium alloy 5083 is characterized by good welding properties and by good corrosion resistance in marine environment. Magnesium is the major alloying element and, along with manganese, produces a moderately strong, yet ductile alloy, which does not respond to heat-treatment. The strength properties of 5083 improve with lower temperatures. The main advantage of 5083 seems to be its weldability: welds as strong as the base metal can be obtained. Currently this alloy is being used in a number of applications involving the manufacture, transfer, and storage of liquefied natural gas; these applications require many millions of kilograms of material.

Aluminium alloy 7005 is a heat-treatable alloy containing zinc and magnesium, which are balanced to obtain a natural-ageing alloy. Chromium is added to reduce corrosion of the heat-affected weld zones, and zirconium is added to reduce weld cracking and to improve mechanical properties.

Aluminium alloy 7075 contains zinc as the major alloying element, together with a small

percentage of magnesium. This alloy can be precipitation-hardened to produce high strength. (However, the studies reported here were made on annealed alloys.)

Details of compositions, heat-treatments, mass densities, and hardnesses of the alloys are given in Tables I and II.

3. Experimental

Alloys were obtained from commercial sources: 1100 and 7075 in the form of 1.9 cm rods, 5083 and 7005 in the form of 1.9 cm thick plate. Cylindrical specimens 1.6 cm diameter and 1.6 cm long were prepared by grinding. Opposite faces were flat and parallel within 2.5 μ m. Specimens were annealed at a pressure of 5×10^{-6} Torr, or less, and cooled in the furnace. Hardnesses were determined by standard metallurgical methods, and mass densities were determined by Archimedes's method using distilled water as a standard.

Quartz transducers (10 MHz) were bonded to the specimens with phenyl salicylate for room-temperature measurements and with a stopcock grease for lower temperatures. In a few cases, failure of these bonds at very low temperatures required using a silicone fluid (viscosity = 2×10^3 P at 25 $^{\circ}$ C) for bonding. The low-temperature apparatus was described previously [1].

A pulse-superposition method was used to determine the sound-wave velocities over the temperature range 300 to 4 K. Details concerning this method were given elsewhere [2].

4. Results

Quantities that were measured directly are the longitudinal and the transverse sound-wave

TABLE I Compositions of the alloys, mill analyses, wt %

Alloy	Al	Cr	Cu	Fe	Mg	Mn	Ni	Si	Ti	V	Zn	Zr
1100	Bal		0.2	0.6				0.1				
5083	Bal	0.13	0.04	0.19	4.75	0.63	0.003	0.08	0.01	0.007	0.04	
7005	Bal	0.25	< 0.1	< 0.4	1.2	< 0.2		< 0.3	< 0.1		4.6	0.3
7075	Bal	0.3	1.6	0.7	2.5	0.3		0.5	0.2		5.6	

TABLE II Properties of the alloys

Alloy	Hardness (DPH no., 1 kg load)	Mass density at 294 K (g cm ⁻³)	Condition
1100	28	2.818	Annealed 345 $^{\circ}$ C; furnace cooled
5083	78	2.666	Annealed 413 $^{\circ}$ C, $\frac{1}{2}$ h; furnace cooled
7005	77	2.779	Annealed 400 $^{\circ}$ C, 3 h; furnace cooled
7075	67	2.721	Annealed 413 $^{\circ}$ C, 3 h; furnace cooled

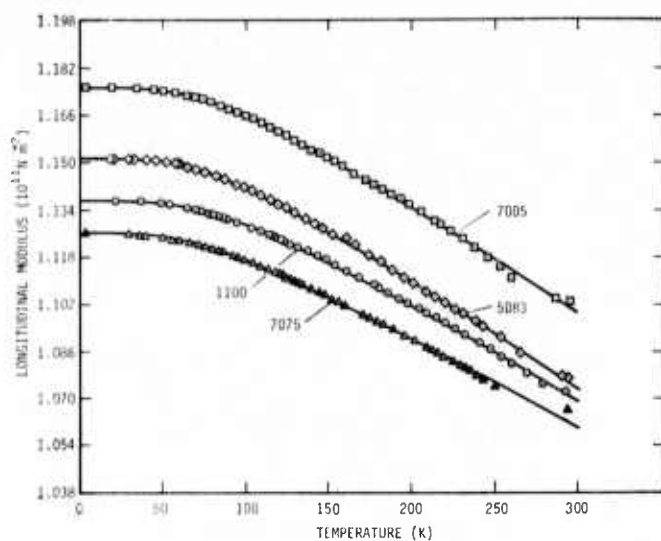


Figure 1 Temperature variation of the longitudinal modulus.

velocities v_l and v_t . From these, the longitudinal modulus, C_l , and the transverse modulus, C_t , were calculated according to

$$C_l = \rho v_l^2 \quad (1)$$

and

$$C_t = \rho v_t^2. \quad (2)$$

These moduli are shown in Figs. 1 and 2 for the temperature range studied. No corrections were made for the change of mass density with

temperature; for aluminium this introduces a maximum error, over 300 K, of 0.4%. Errors in the absolute velocities are believed to be about $\frac{1}{2}\%$ or less. All the other elastic constants that are used to describe polycrystalline aggregates are simply related to these two moduli. The moduli considered here – the shear modulus G , Young's modulus E , the bulk modulus B , and Poisson's ratio ν – are given by:

$$G = C_t, \quad (3)$$

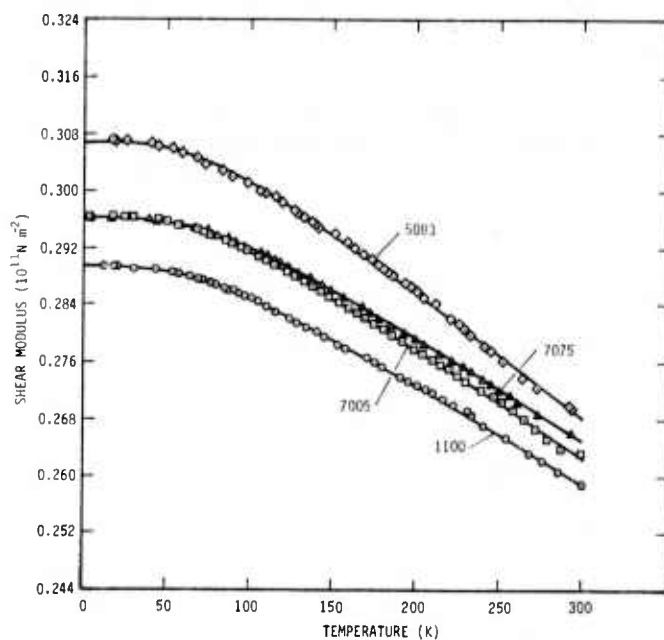


Figure 2 Temperature variation of the transverse or shear modulus.

$$E = 3G(C_1 - \frac{2}{3}C_t)/(C_1 - C_t), \quad (4)$$

$$B = C_1 - \frac{2}{3}C_t, \quad (5)$$

and

$$\nu = \frac{1}{2}(C_1 - 2C_t)/(C_1 - C_t). \quad (6)$$

The elastic constants obtained from these relationships are shown as functions of temperature in Figs. 3 to 5. Values of the elastic constants at selected temperatures are given in Table III.

The temperature variations of the elastic constants can be described mathematically in various ways. In this case, the temperature

dependences of both C_1 and C_t were fitted to a theoretical relationship suggested by Varshni [3]:

$$C = C^\circ - \frac{s}{e^{t/T} - 1}, \quad (7)$$

where C is any elastic constant (C_1 and C_t in this case), C° , s , and t are adjustable parameters and T is temperature. The value of C at $T = 0$ K is C° , and $-s/t$ is the high-temperature limit of the temperature derivative dC/dT . By invoking an Einstein oscillator model of solids, it can be shown (in the absence of electronic effects) that t is the Einstein characteristic temperature.

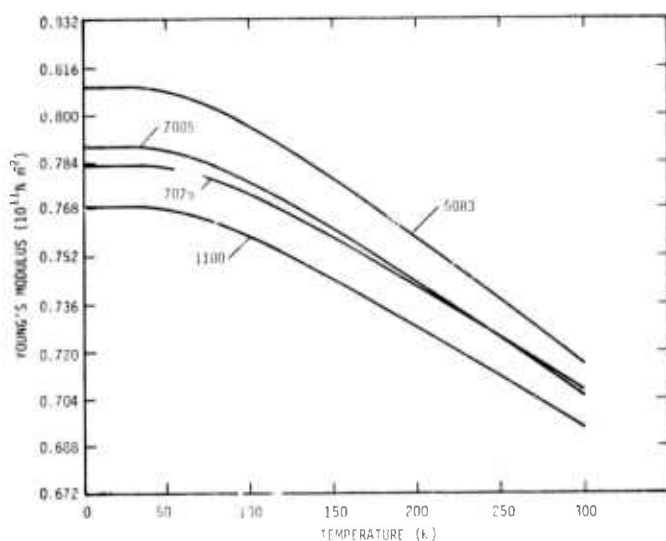


Figure 3 Temperature variation of Young's modulus.

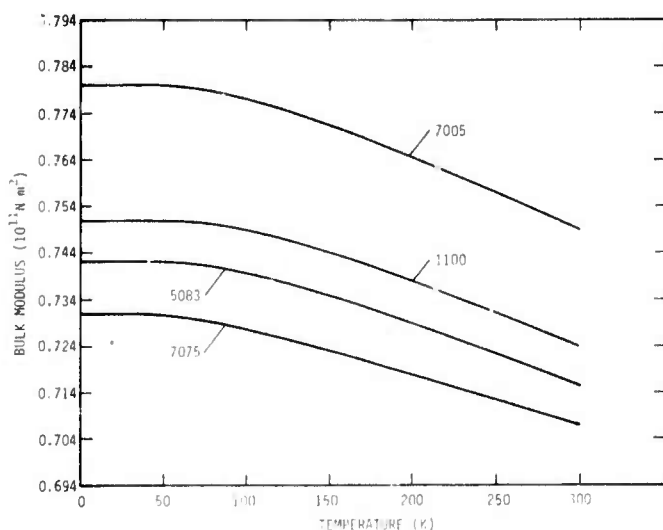


Figure 4 Temperature variation of the bulk modulus (reciprocal compressibility).

TABLE III Values of the elastic constants of aluminium alloys at selected temperatures in units of 10^{11} N m^{-2} except ν , which is dimensionless

Alloy	Present results					Previous results†					Reference
	Temperature (K)	B	E	G	ν	Temperature (K)	B	E	G	ν	
1100	300	0.724	0.694	0.259	0.340	300	(0.697)	0.689	0.258	0.33	[7]
	200	0.738	0.728	0.273	0.336						
	100	0.749	0.758	0.285	0.331						
5083	0	0.751	0.769	0.289	0.329						[7]
	300	0.716	0.715	0.268	0.333	300	(0.762)	0.710	0.264	0.33	
	200	0.729	0.758	0.286	0.327						
7005	100	0.739	0.796	0.301	0.321						[8]
	0	0.742	0.809	0.307	0.318						
	300	0.749	0.705	0.262	0.343	300	(0.635)	0.711	0.271	(0.313)	
7075	200	0.765	0.743	0.278	0.338	77	(0.735)	0.779	0.294	(0.323)	[9]
	100	0.777	0.777	0.291	0.333	20	(0.671)	0.792	0.304	(0.303)	
	0	0.780	0.789	0.296	0.331						
Alumin- ium*	300	0.707	0.707	0.265	0.333	298		0.731			
	200	0.718	0.742	0.279	0.328	200		0.786			
	100	0.728	0.773	0.292	0.323	20		0.786			
Alumin- ium*	0	0.731	0.783	0.296	0.321						
	300	0.761	0.701	0.260	0.347						
	200	0.777	0.738	0.275	0.342						
Alumin- ium*	100	0.790	0.771	0.288	0.337						
	0	0.794	0.784	0.293	0.336						

*Calculated from single-crystal data in [4].

†Entries in parentheses were derived using standard formulae.

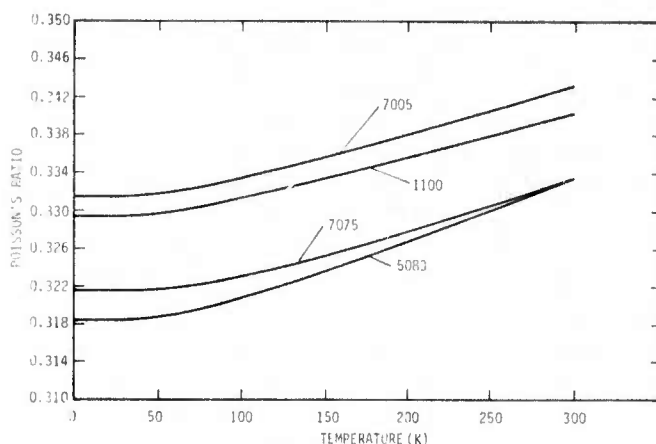


Figure 5 Temperature variation of Poisson's ratio.

Parameters C^c , s , and t (determined by a least-squares fit of Equation 7 to the data) are given in Table IV. Average differences between

TABLE IV Parameters in Equation 7

Alloy	Mode	C^c (10^{11} N m $^{-2}$)	s (10^{11} N m $^{-2}$)	t (K)
1100	l	1.136	0.0903	255.9
	t	0.2892	0.0301	206.9
5083	l	1.151	0.0926	235.3
	t	0.3067	0.0381	206.7
7005	l	1.175	0.0928	240.0
	t	0.2963	0.0327	203.4
7075	l	1.126	0.0707	219.6
	t	0.2961	0.0344	223.3

measured and curve values are 0.03% and 0.06% for the longitudinal and transverse moduli, respectively. Room-temperature values of the temperature coefficients of the elastic moduli are given in Table V; these values occur in the linear high-temperature region.

TABLE V Temperature coefficients of the elastic constants at room temperature (10^{-4} K $^{-1}$)

Alloy	$\frac{1}{B} \frac{dB}{dT}$	$\frac{1}{E} \frac{dE}{dT}$	$\frac{1}{G} \frac{dG}{dT}$	$\frac{1}{\nu} \frac{d\nu}{dT}$
1100	-2.01	-5.01	-5.37	1.41
5083	-1.92	-6.06	-6.58	2.08
7005	-2.13	-5.48	-5.88	1.54
7075	-1.58	-5.08	-5.52	1.75
Aluminium*	-1.97	-5.53	-5.77	1.80

*Derived from single-crystal data in [4].

The elastic Debye temperature, θ , can be calculated from the elastic wave velocities by [5]:

$$\theta = K \langle v \rangle, \quad (8)$$

where

$$K = \frac{h}{k} \left(\frac{3N\rho}{4\pi A} \right)^{1/3} \quad (9)$$

Here h is Planck's constant, k is Boltzmann's constant, N is Avogadro's constant, ρ is the mass density, and A is the effective atomic weight. The average velocity is given by

$$\langle v \rangle = \left(\frac{v_l^{-3} + 2v_t^{-3}}{3} \right)^{-1/3} \quad (10)$$

The elastic Debye temperatures for the four alloys at $T = 0$ K, and also for unalloyed aluminium are given in Table VI.

TABLE VI Elastic Debye temperatures at $T = 0$ K

Alloy	θ (K)
1100	426.2
5083	440.4
7005	425.9
7075	422.2
Aluminium	430.6*

*Calculated from single-crystal data in [4].

5. Discussion

As shown by the data in Table III, changes in the elastic constants of aluminium and its alloys between 300 and 4 K are about 4% for B and ν , and 12% for E and G . These changes are somewhat larger than those observed in alloys based on copper or iron, for example. Most of the changes occur above about 100 K. Below this temperature the elastic constants change only slightly with temperature. Thus, any changes in the mechanical behaviour of these

alloys in this temperature region probably cannot be ascribed to an elastic origin.

The temperature behaviour of the elastic constants of the aluminium alloys reported on here is quite regular. The moduli decrease regularly with increasing temperature and the modulus-temperature curves are relatively flat at low temperatures. Also, in accord with the third law of thermodynamics, the slopes dC/dT approach zero at zero temperature. A linear temperature dependence is exhibited above about 150 K, which is roughly one-third of the Debye temperature. Besides indicating the absence of magnetic or structural transitions, this ideal temperature behaviour suggests that the anharmonic properties of these alloys can probably be explained by a relatively simple model.

These alloys were not examined for texture. However, texture would have little effect on their elastic properties. Aluminium single crystals are only slightly anisotropic; the Zener anisotropy ratio for aluminium is 1.2; it is 1.0 for the isotropic case. Aluminium's isotropy is purely accidental since aluminium, because of its three valence electrons, has a large band-structure contribution to the elastic constants [10]. This contribution is usually anisotropic; the anisotropy is cancelled in the case of aluminium by other energy terms. Thus, since aluminium single crystals are only slightly anisotropic, even a strongly textured polycrystalline aggregate of aluminium would have nearly isotropic elastic behaviour.

It should be emphasized that the data reported here are dynamic (adiabatic) rather than static (isothermal); they apply strictly to rapid rather than slow loading. However, the differences between adiabatic and isothermal elastic constants are small. They become smaller at lower temperatures because of the diminishing thermal-expansion coefficient, and they vanish at zero temperature. Using formulae given by Landau and Lifshitz [6] it can be shown for aluminium at room temperature:

$$\frac{E_S - E_T}{E_T} = 0.005, \quad \frac{B_S - B_T}{B_T} = 0.045 \quad (11)$$

$$\frac{\nu_S - \nu_T}{\nu_T} = 0.020, \quad \text{and} \quad \frac{G_S - G_T}{G_S} = 0,$$

where subscripts S and T denote the adiabatic and the isothermal cases, respectively. For E , B , ν and G , these corrections are typically in the ratio 1:9:4:0 if ν has a value near $\frac{1}{3}$.

Effects of alloying on the elastic properties of aluminium cannot be accurately determined from the present study because of the large number of alloying elements and their interactions. Such effects have been considered elsewhere [11]. However, some general observations can be made concerning alloying. Disregarding alloy 1100, with respect to "pure" aluminium, the shear modulus and Young's modulus increased in all cases while the bulk modulus decreased, and by a larger percentage. Poisson's ratio decreased in all four alloys. The 1100 alloy, which contains only 1% of impurities, presents an interesting case. The data indicate that while the shear modulus of this alloy is identical to that of unalloyed aluminium, the bulk modulus is higher by about 5%. Since the bulk modulus is not measured directly, but is calculated from the difference of two velocities according to Equation 5, a compounding of errors may account for this discrepancy. If the effect is real, then it has important consequences for the problem of averaging single-crystal elastic coefficients to obtain the bulk modulus of a polycrystalline aggregate.

Finally, approximate relationships among the elastic constants are indicated. For all the alloys and for all temperatures, as a first approximation,

$$\nu \approx \frac{1}{3} \quad (12)$$

and

$$B \approx E \approx (8/3)G. \quad (13)$$

These should be useful for many engineering purposes where only rough numbers are needed and only one of the elastic constants is known.

6. Conclusions

From the results of this study the following conclusions are drawn:

(1) all the elastic properties of aluminium alloys 1100, 5083, 7005, and 7075 behave regularly with respect to temperature;

(2) for all alloys studied, the temperature behaviour of both C_1 and C_2 can be described accurately by a theoretical relationship suggested by Varshni;

(3) in this series of alloys, in the annealed condition, alloy 5083 has the highest Young's modulus, the highest shear (rigidity) modulus, and the lowest Poisson's ratio. Alloy 7005 has the highest bulk modulus.

Acknowledgement

This work was supported in part by the Advanced Research Projects Agency of the U.S. Department of Defense.

References

1. E. R. NAIMON, W. F. WESTON and H. M. LEDBETTER, *Cryogenics* **14** (1974) 246.
2. H. J. MCSKIMIN, *J. Acoust. Soc. Amer.* **33** (1961) 12.
3. Y. P. VARSHNI, *Phys. Rev.* **B2** (1970) 3952.
4. G. N. KAMM and G. A. ALERS, *J. Appl. Phys.* **35** (1964) 327.
5. P. DEBYE, *Ann. Phys. (Leipz.)* **39** (1912) 789.
6. L. D. LANDAU and E. M. LIFSHITZ, "Theory of Elasticity" (Pergamon, London, 1959) p. 17.
7. T. LYMAN, Ed., "Metals Handbook" (ASM, Metals Park, Ohio, 1961).
8. R. DEVELAY, A. FAURE, S. LEHONGRE, D. MUGNIER and D. SCHROETER, in "Advances in Cryogenic Engineering", Vol. 12, edited by K. Timmerhaus (Plenum, New York, 1967) p. 484.
9. J. L. CHRISTIAN and J. F. WATSON, *ibid*, Vol. 6, (1961) p. 604.
10. T. SUZUKI, *Phys. Rev.* **B3** (1971) 4007.
11. W. KÖSTER, *Z. Metallk.* **32** (1940) 282.

Received 11 December 1974 and accepted 28 January 1975.

Low-temperature elastic constants of a superconducting coil composite

W. F. Weston*

Cryogenics Division, Institute for Basic Standards, National Bureau of Standards, Boulder, Colorado 80302
(Received 27 February 1975; in final form 17 June 1975)

A resonant piezoelectric oscillator method for measuring elastic moduli was applied to composite materials. The complete set of elastic compliances of a superconducting coil composite was determined semicontinuously between 4 and 300 K. Also, two moduli of a layered fiber-glass-epoxy composite were determined; this composite is essentially the matrix material of the coil composite. The Young's moduli, shear moduli, Poisson ratios, and elastic stiffness coefficients are also reported. Results agree closely with elastic data obtained by conventional testing methods.

PACS numbers: 62.20.D, 74.50.

I. INTRODUCTION

The elastic properties of composite materials are currently of considerable interest. Many composites, because they have high mechanical strength and a high modulus-to-density ratio, are useful as strong lightweight structural materials. Some composites have been designed for use at low temperatures, for example, as superconducting coils for high-field magnets. However, few elastic data are available for composite materials, particularly at low temperatures. To the author's knowledge, no complete sets of elastic data are available for composite materials at 4 K. Some data are useful as design parameters, and elastic constants are among the most accurately known fundamental physical properties of solids.

Because composite materials are usually highly anisotropic, the determination of their elastic constants is much more difficult than for the more usual quasi-isotropic engineering materials. Conventional methods of measuring the elastic properties of solids have been applied to composites with only limited success. These methods usually require relatively large specimens and considerable time and effort, especially if a complete set of elastic constants is required.¹ These methods, as applied to composites, include vibrating^{2,3} or resonant-beam⁴⁻⁶ tests, tensile or compressive tests,^{1,7,8} torsion tests,^{1,9} bending tests,^{1,10} and pressure tests.¹¹⁻¹³ Generally, the elastic constants measured by these methods are less accurate than those acquired by ultrasonic tests.

Ultrasonic pulse techniques are limited by the necessity of using wavelengths that are large compared with fiber diameters and at the same time sufficiently small compared with the dimensions of the specimen so that true plane-wave conditions can exist. Since ultrasonic pulse methods are typically performed at megahertz frequencies, this condition cannot be met for many composites. If the wavelength is not larger than the fiber diameter, the wave is attenuated and scattered. Ultrasonic pulse-echo methods have been applied to some metal-matrix composites with extremely small fibers.¹⁴⁻¹⁶ Even in these cases the pulse-echo signals are poor because of high attenuation and dispersion.¹⁵ In fact, Achenbach and Herrman¹⁷ predicted large dispersive effects for shear waves propagated in the fiber direction, even when the wavelength is much larger

than fiber diameters. Zimmer and Cost¹⁸ verified this prediction by measuring sound velocities in a unidirectional glass-reinforced epoxy-fiber composite. For wavelength-to-fiber diameter ratios of roughly 50, dispersion increased some phase velocities by a factor of 2. Elastic constants of some carbon-fiber-reinforced plastics have also been measured by ultrasonic pulse-echo techniques.¹⁹⁻²¹

Attempts to use 10-MHz pulse-echo techniques on the composite studied herein were unsuccessful. Both longitudinal and shear waves were propagated along all orientations and produced no detectable echoes. This is understandable since the filament sizes for this composite, as described in the text, are larger than the sound wavelength. Larger specimens than are currently available would be needed for 1-5-MHz pulses, although it is doubtful that even these frequencies would produce useable echo patterns for this material.

The ultrasonic immersion technique, as described by Markham,²² is fast and accurate and offers the possibility of measuring all the elastic properties on one specimen. However, this technique is also limited by fiber size and by sample dimensions.^{23,24} The choice of ultrasonic modes that can be propagated in a given direction in a specimen is also limited, and the technique is inapplicable to low-temperature measurements.

Zecca and Hay²⁵ avoided the problems encountered with megahertz frequencies by using electrostatic transducers to generate and to detect resonant kilohertz frequencies of a metal-matrix composite. Electrostatic transducers, however, cannot be used with nonmetallic materials.

The most widely used ultrasonic technique, using kilohertz frequencies, is the resonant piezoelectric oscillator. This method is due principally to Quimby and associates.²⁶ Quimby thoroughly analyzed the vibrations of solid rods driven by a piezoelectric crystal, and Balamuth²⁷ first employed drivers and specimens of matching fundamental frequencies. Rose²⁸ extended this method to torsional oscillators. Basically, the piezoelectric properties of quartz are used to generate and to detect resonant frequencies of an oscillator consisting of one or two quartz crystals, a specimen, and perhaps a dummy rod, all cemented together. This method has been used to measure elastic moduli at both high^{29,30} and

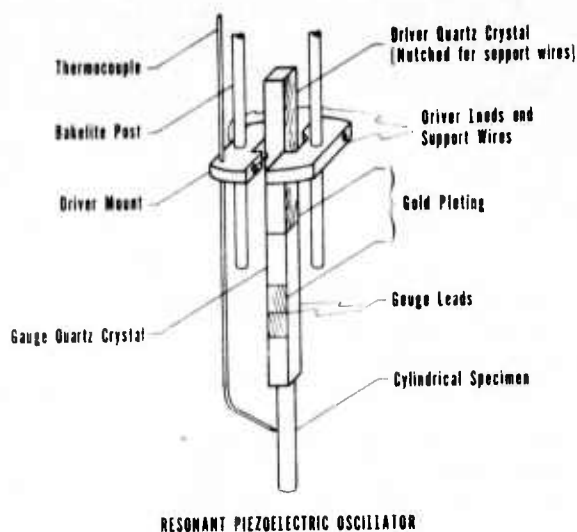


FIG. 1. Resonant piezoelectric oscillator apparatus.

low^{27, 28, 30, 31} temperatures, and has worked well with both metals^{32, 33} and nonmetals.²⁷⁻³¹ Thus, this technique is well understood both theoretically and practically, and it would seem to be well suited for testing composites. The long wavelengths used (typically on the order of centimeters in the kilohertz region) are much larger than fiber diameters, and, since the technique employs standing waves rather than traveling waves, specimen sizes can still be kept small.

In the present paper it is described how this resonance technique was used to measure the complete set of elastic compliances of a superconducting coil composite, which was essentially composed of an epoxy matrix and unidirectional copper-niobium-titanium fibers. The compliances were measured semicontinuously from 300 to 4 K. Results are given also for an epoxy-fiber-glass layered composite. The results generally agreed closely with the few existing static measurements on the same composite.

II. EXPERIMENTAL PROCEDURE

A. Resonant piezoelectric oscillator

The three-component resonant piezoelectric oscillator technique was originally described by Marx,³⁴ and was discussed in detail by Fine.³⁵ The technique consists of bonding quartz-driver and quartz-gauge piezoelectric crystals to a specimen to produce and to detect a standing longitudinal (or torsional) resonant wave. Each component's length is adjusted so that its resonant frequency is closely matched to that of the other components. The system is then driven by the driver transducer at its resonant frequency, which is monitored by the gauge crystal.

Longitudinal waves are excited by α -quartz bars of square cross section, excited into longitudinal vibration by an ac signal applied to full-length adherent electrodes (see Fig. 1). The driver quartz was fully gold plated on two parallel sides (z faces) with a shallow notch cut in the center of each electrode. Fine gold-

plated tungsten wires, seated in these notches, served to suspend the resonator assembly at displacement nodes and provided the necessary electrical contact. The gauge quartz was gold plated only over the center third of the two parallel faces and electrical contact was made through fine wires adhered into the notches with silver conducting paint. The electric axes of the driver and the gauge crystals were perpendicular to reduce electrical pickup.

The longitudinal oscillator apparatus is illustrated in Fig. 1. The driver-quartz crystal was suspended by 0.003 in. gold-plated tungsten wires. The driver mounts, which were aluminum, were removed during the torsional measurements, since the torsional driver crystal was suspended between the Bakelite posts by nylon threads. The specimens were cylindrical for all measurements. The chromel-constantan thermocouple was placed near, but not touching, the specimen. The entire apparatus was sealed in a thin-walled stainless-steel can. The can was partially evacuated, placed in the ullage of a helium Dewar, and lowered stepwise to achieve cooling.

The torsional quartz crystals were circular with their length in the x direction and with four gold-plated electrodes running the length of the crystal.³⁶ Opposite pairs of electrodes were electrically connected. The driver quartz was suspended vertically by means of fine nylon treads attached with varnish to opposite sides of the quartz near a displacement node of vibration.

The quartz crystals were bonded together with a semi-permanent adhesive, Eastman 910.³⁷ The specimens were right-circular cylinders and were also bonded to the gauge quartz with the same adhesive. For some torsional experiments, this cement occasionally failed at low temperatures; such experiments were repeated until successful. Other materials such as vacuum grease and epoxy resin have been used as low-temperature bonding agents.³⁸

The quartz crystals used had resonant frequencies of 60 and 100 kHz. Most of the measurements were done with the 60-kHz quartz crystals ($\frac{3}{16}$ -in. square cross for longitudinal, and $\frac{3}{16}$ in. in diameter for torsional), but some were done with the 100-kHz crystals ($\frac{1}{8}$ in. in diameter). The mass of each driver-gauge combination was noted and the resonant frequencies were monitored from 300 to 4 K. The length of each specimen was determined such that its resonant frequency for the entire temperature range was within approximately 5% of the oscillator assembly although in some cases the specimen frequency differed by as much as 10%. The mass, length, and diameter of each specimen were noted and its mass density was determined by Archimedes's method using distilled water as a standard. The specimen was then cemented to the quartz crystals and the resonant frequency of the oscillator was monitored from 300 to 4 K. No thermal contraction corrections were made; for the coil composite described below this introduces a maximum error (over a 300 K range) of about 0.5%.³⁹ Maximum uncertainties in the frequency measurements are estimated to be about one part in 10^5 .

B. Electronics

Most workers who have used the piezoelectric oscillator technique have employed electronics similar to those described by Marx.³¹ This system requires manual adjustment of the input frequency to the driver crystal to keep the oscillator at resonance. A less time-consuming and more accurate system is the regenerative system designed by Gerk⁴⁰ and slightly modified by Johnson.⁴¹

Gerk's system consists primarily of a closed loop containing an amplifier and the driver-gauge combination of piezoelectric crystals, which act as a resonant element, with a feedback circuit to control the gain of the amplifier. This system is based on the principles of an oscillator; that is, the output of an amplifier is fed into the input through a frequency-selective network (the quartz crystals). The phase shifts are corrected with a variable phase shifter. A more complete description of the system was given by Gerk.⁴⁰ This system locks onto the resonant frequency and automatically stays at the resonant frequency if this frequency changes, due to a change of the specimen's environment, for example.

C. Specimens

The superconducting coil composite is fully described elsewhere.³⁹ Basically, the coil is composed of a copper-stabilized niobium-titanium wire (0.56 × 0.72 mm cross section) coil impregnated with epoxy. The wire layers are separated by layers of dry fiber-glass cloth (0.1 mm thick). The copper-to-superconductor volume ratio of the wire is 1.8–1. The wire-to-epoxy cross-sectional area fraction is about 3 to 1. The coil dimensions were approximately 19 cm l.d., 24 cm o.d., and 10 cm long.

Coordinate axes were chosen to coincide with the specimen axes. The longitudinal axis (3 axis) coincides with the axis of the wire, which was assumed to have zero helix angle. The 1 and 2 axes lie along the radius and coil axes, respectively, and form an orthogonal set with the 3 axis. The symmetry of the coil (orthorhombic) requires nine elastic constants to characterize the material. By assuming the material to be transversely isotropic and by neglecting the effects of curvature, the number of independent elastic constants is reduced to five. An orthotropic body with transverse isotropy has the same symmetry as close-packed hexagonal crystals such as magnesium and zinc. Justification for equating the 1 and 2 axes is given elsewhere,³⁹ and additional experimental data show that the effect of curvature on the moduli is minor.⁴²

The masses, lengths, and angles between the specimen axes and the 3 axis are given in Table I. The density of the coil composite was found to be 6.000 g/cm³.

Besides the superconducting coil, some specimens composed only of the fiber-glass cloth and epoxy were available. The fiber-glass-to-epoxy volume ratio in these samples was approximately the same as in the coil composite. Measurements were made on two specimens of this material. Dimensions and orientations of these specimens are also reported in Table I, with the angle θ corresponding to the angle between the speci-

TABLE I. Dimensions and orientations of specimens.

Specimen No.	Diameter (in.)	Mass (g)	Length (cm)	θ (deg)
Superconducting coil composite specimens				
1	0.1250	0.540	1.1128	90
2	0.1250	0.925	1.9439	0
3	0.1863	1.081	1.0818	0
4	0.1890	1.248	1.1481	90
5	0.1875	1.874	1.7600	60
6	0.1851	1.327	1.2555	60
Epoxy-fiber-glass composite specimens				
1	0.1875	0.885	2.5387	0
2	0.1878	0.520	1.4862	0

men axis and the direction parallel to the layers of fiber-glass cloth. The density of this material was found to be 1.931 g/cm³. This material can also be considered transversely isotropic, if the fiber-glass is considered transversely isotropic. Thus, five constants are again needed to completely characterize the material elastically. Cylindrical specimens of only one orientation were available; thus, only two elastic constants of the fiber-glass-epoxy matrix material were determined.

III. RESULTS

The directly measured quantity in these measurements is f_0 , the frequency of the three-component piezoelectric resonator. For longitudinal resonance the frequency of the specimen (f_s) can be found from f_0 , the frequency of the driver-gauge quartz assembly (f_q), the mass of the specimen (m_s), and the mass of the quartz (m_q):⁴³

$$f_s^2 = f_0^2 + (f_0^2 - f_q^2)m_q/m_s. \quad (1)$$

This formula is more exact than the approximation

$$f_s = f_0 + (f_0 - f_q)m_q/m_s, \quad (2)$$

which is usually quoted and used for resonant oscillators.³⁴

The formula for the torsional oscillator is somewhat more complicated since the moments of inertia (rather than the masses) of the components are involved³⁸:

$$f_s^2 = f_0^2 + (f_0^2 - f_q^2)m_q r_q^2 / m_s r_s^2. \quad (3)$$

Here, r_q is the radius of the quartz and r_s is the radius of the specimen.

The Young's modulus E or shear modulus G for the particular orientation of the specimen is given by

$$E \text{ or } G = 4L^3 f_s^2 \rho. \quad (4)$$

E is found from the longitudinal-mode fundamental frequency and G is found from the torsional-mode fundamental frequency. In Eq. (4), L is the specimen length and ρ is the mass density.

Thus, the measured quantities are the Young's and shear moduli, which are directly related to the elastic compliances S_{ij} . However, if the wavelength is not much larger than the sample dimensions, a correction for the Poisson contraction (or lateral motion) must be

TABLE II. Experiments performed on superconducting coil composite.

Exp. No.	Spec. No.	Mode	θ	Measured quantity
1	1	L	90	$E_{11} = \frac{1}{S_{11}}$
2	2	L	0	$E_{33} = \frac{1}{S_{33}}$
3	3	T	0	$G_{13} = \frac{1}{S_{44}}$
4	4	T	90	$G' = \frac{2}{S_{44} + S_{66}}$
5	5	L	60	$E_{\theta=60^\circ} = \frac{16}{9S_{11} + S_{33} + 6S_{13} + 3S_{44}}$
6	6	T	60	$G_{\theta=60^\circ} = \frac{8}{3S_{11} + 3S_{33} - 6S_{13} + 2S_{44} + 3S_{66}}$

applied to Young's modulus.³⁵ When the length-to-diameter ratio is 10 to 1, this correction amounts to about one part in 10^3 .

The value of Young's modulus for an arbitrary direction in a specimen with transverse isotropy is given in terms of the elastic compliances by⁴⁴

$$1/E = S_{11} \sin^4 \theta + S_{33} \cos^4 \theta + (2S_{13} + S_{44}) \sin^2 \theta \cos^2 \theta, \quad (5)$$

where θ is the angle between the specimen axis and the unique axis. Similarly, the shear modulus is

$$1/G = S_{44} + (S_{11} - S_{12} - \frac{1}{2}S_{44}) \sin^2 \theta + 2(S_{11} + S_{33} - 2S_{13} - S_{44}) \sin^2 \theta \cos^2 \theta. \quad (6)$$

Most measurements were made during cooling. All experiments were performed at least twice, and any unusual behavior was examined on heating as well as cooling, for reversibility.

A. Superconducting coil composite

Measurements made on the coil composite are listed in Table II. Again, θ is the angle between the specimen axis and the 3 axis (longitudinal axis). The mode specifies either longitudinal or torsional oscillations. The

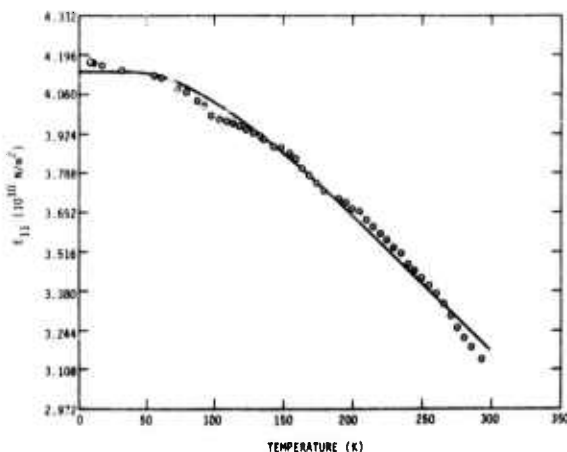


FIG. 2. Young's modulus of the superconducting coil composite, $\theta = 90^\circ$.

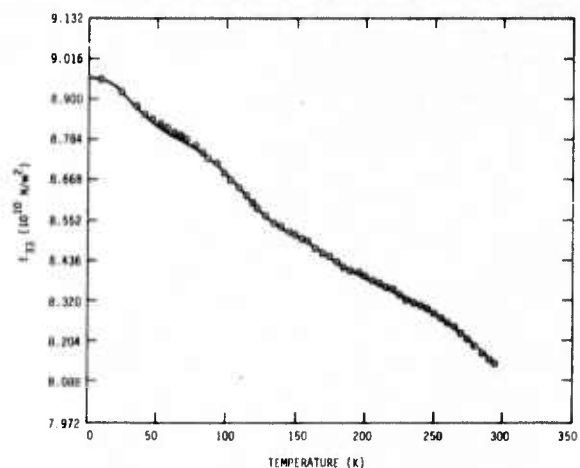


FIG. 3. Young's modulus of the superconducting coil composite, $\theta = 0^\circ$.

subscripts on E and G designate the direction of the force and the plane on which the force is applied, respectively. The compliances S_{11} , S_{33} , and S_{44} are found directly from experiments 1, 2, and 3, respectively. From experiment 4, S_{12} is found using the relation $2(S_{11} - S_{12}) = S_{66}$ and the value of S_{44} from experiment 3. Either specimen 5 or 6 can be used to determine S_{13} . This compliance must be determined from a measurement on a specimen with its axis at an angle to the longitudinal direction. As can be seen from Table II, however, the Young's or shear modulus measured on specimens with $0^\circ < \theta < 90^\circ$ is only partly dependent on S_{13} . Thus, S_{13} will be the least accurately determined compliance. The measurement of this compliance corresponds to the measurement of the elastic stiffness C_{13} by megahertz ultrasonic techniques. Zimmer and Cost¹⁷ encountered difficulty in measuring C_{13} for a composite material and their estimated uncertainty in this elastic constant (100%) was ascribed to dispersion as well as to the relatively high inaccuracy.

The experimental data are presented in Figs. 2-7. The smooth curves represent regular temperature be-

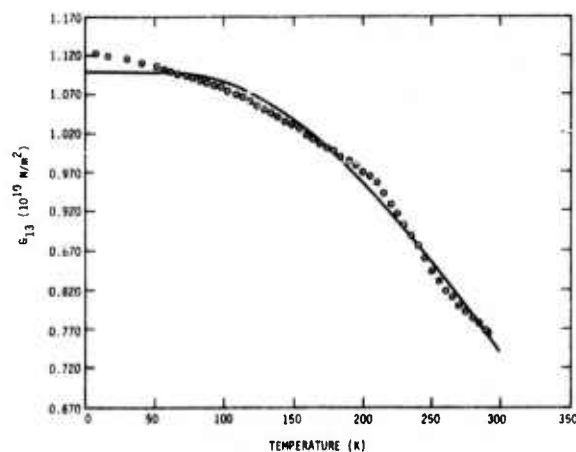


FIG. 4. Shear modulus of the superconducting coil composite, $\theta = 0^\circ$.

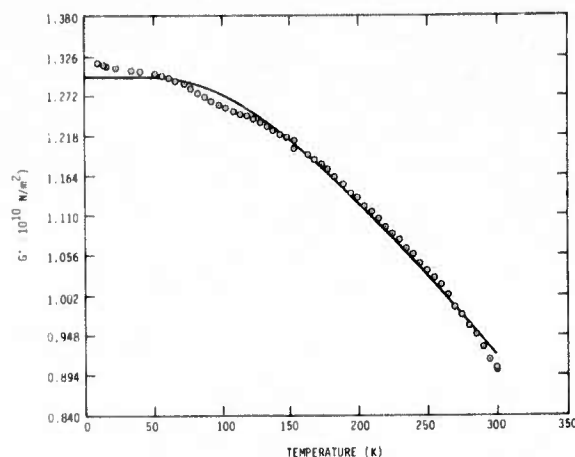


FIG. 5. Shear modulus of the superconducting coil composite, $\theta = 90^\circ$.

havior as given by a theoretical relationship suggested by Varshni⁴⁵ that has been used successfully to represent the temperature dependences of metals,⁴⁵ ionic solids,⁴⁵ and several alloys.⁴⁶ The over-all fit of this function to these data is not nearly as good as for other materials, and the data for E_{33} could not be fitted to the Varshni function because of its concave-upward curvature. A smooth curve was drawn through the data points and the actual point values were used in calculations. This modulus was measured several times to check its behavior, and data from different measurements agreed closely. These data had completely reversible temperature response.

The shear modulus corresponding to shearing the axial planes in the radial direction G_{12} , or vice versa, is shown in Fig. 8. This modulus was calculated from the curve values of G_{13} and G' , since $G_{12} = 1/S_{66}$.

Because of the difficulty in machining the specimens to small radii, the ratios of lengths to diameters were in some cases on the order of 4 or 5 to 1. The estimated correction to the Young's moduli in these cases is still only about 1%.

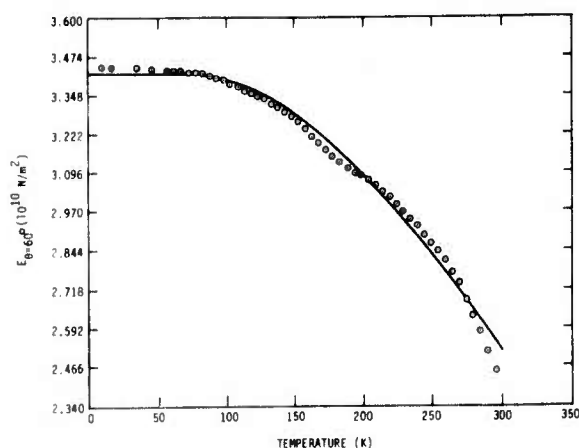


FIG. 6. Young's modulus of the superconducting coil composite, $\theta = 60^\circ$.

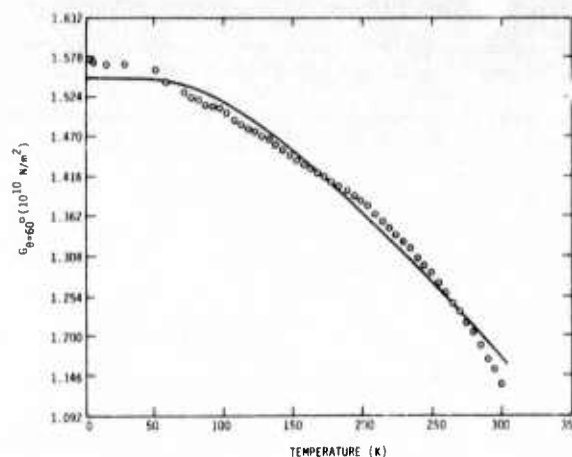


FIG. 7. Shear modulus of the superconducting coil composite, $\theta = 60^\circ$.

The elastic compliances as functions of temperature are given in Table III. The compliances S_{11} , S_{33} , and S_{44} are just reciprocals of E_{11} , E_{33} , and G_{13} , as mentioned previously. The error in the directly measured moduli is estimated to be about 1%; thus these compliances should be accurate to 1% also. The compliance S_{12} is found from combining the results of three measurements. Thus, S_{12} may be less accurately known. It was found that in solving for S_{13} from either Eq. (5) or (6), a 1% error in the measured modulus led to a 10–20% error in S_{13} . Thus, the error associated with S_{13} is considerable, perhaps as much as 100%. The values reported for S_{13} are the average of the values found from experiments 5 and 6, which are -0.110 and -0.058 , respectively. From the material available, it was not possible to machine specimens with $\theta < 60^\circ$ for other determinations of S_{13} . As expected, the material was found to be highly anisotropic with $s_{11} \approx 2s_{33}$.

It is emphasized that the data reported here are dynamic (adiabatic) rather than static (isothermal) and apply to rapid, rather than slow, loading. Conversion formulas are given in Landau and Litschitz,⁴⁷ for ex-

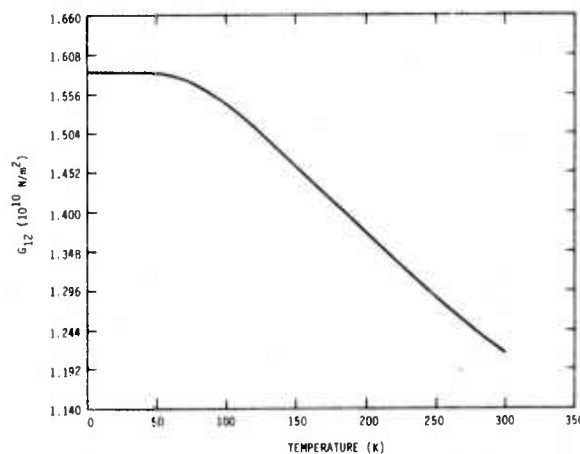


FIG. 8. Shear modulus G_{12} of the superconducting coil composite.

TABLE III. Elastic compliances of the superconducting coil composite at selected temperatures ($10^{-10} \text{ m}^2/\text{N}$) as determined by resonance oscillator techniques.

T (K)	S_{11}	S_{12}	S_{13}	S_{33}	S_{44}	S_{66}
0	0.242	-0.074	-0.061	0.112	0.910	0.631
50	0.242	-0.074	-0.061	0.113	0.910	0.632
100	0.248	-0.076	-0.066	0.115	0.920	0.648
150	0.260	-0.083	-0.073	0.118	0.964	0.684
200	0.275	-0.089	-0.079	0.119	1.046	0.728
250	0.294	-0.094	-0.082	0.121	1.170	0.776
300	0.316	-0.096	-0.084	0.123	1.350	0.823

ample; in most cases the differences between adiabatic and isothermal elastic constants are small. These formulas involve the thermal-expansion coefficients and the specific heat. The thermal-expansion coefficients are known for this composite,³⁹ but the specific heat has not yet been determined. If an estimate of the specific heats of the components, the difference between the adiabatic and isothermal Young's moduli is at most 0.5%. The adiabatic and isothermal shear moduli are, of course, equal.

B. Epoxy-fiber-glass composites

Measurements were also made on the epoxy-fiber-glass specimens listed in Table I. These specimens were oriented with the layers of fiber-glass cloth running the length of the specimen; these were the only orientations available. The Young's and shear moduli are shown in Figs. 9 and 10. The shear modulus is well represented by the Varshni function, and is seen to have normal temperature behavior. A smooth curve was drawn through the Young's modulus data, which could not be fitted to the Varshni function because of the low-temperature maximum.

IV. DISCUSSION

Some elastic data, taken by conventional static methods, were available for the superconducting coil composite and the epoxy-fiber-glass composite.³⁹ These data generally compared very favorably with the resonance data. For example, resonance values of E_{11} at room temperature and 4 K are 12 and 1% larger than

the static data taken at these temperatures. The inaccuracy of the static values is given as about 10%. Also, resonance values of E_{33} agree with the static data within 5–7%, and resonance values of G_{13} agree with the static values within 6–11%.

Other elastic constants of interest include the Poisson ratios:

$$\nu_{12} = -S_{12}/S_{11} \quad (7)$$

and

$$\nu_{13} = -S_{13}/S_{33}, \quad (8)$$

where ν_{ij} represents the negative ratio of strain in the j direction to strain in the i direction.

The value of ν_{12} at room temperature is 0.304. The reported³⁹ static value is 0.335, with the inaccuracy again believed to be about 10%. Thus, this result gives added confidence to the resonance value of S_{12} . However, the Poisson ratio ν_{13} , involves the compliance S_{13} , which has already been noted to be much more inaccurate than the other four compliances. In fact, if the room-temperature values of S_{13} and S_{33} are used, $\nu_{13} = 0.683$, whereas the static value is 0.333.³⁹ Since the other elastic constants are all in relatively good agreement with the static values, it is reasonable to expect that ν_{13} should be also. Thus, the value of S_{13} is highly suspect, especially since a value near $\frac{1}{3}$ seems more realistic for Poisson's ratio.

It is also of interest to consider the compressibilities. For a material with transverse isotropy, the linear compressibilities are

$$k_1 = S_{11} + S_{12} + S_{13} \quad (9)$$

and

$$k_3 = 2S_{13} + S_{33},$$

where the subscripts designate the axis. Also, the volume compressibility is

$$K = 2k_1 + k_3. \quad (10)$$

If the room-temperature values of the compliances, as given in Table III, are used, then $k_1 = 0.136 \times 10^{-10}$

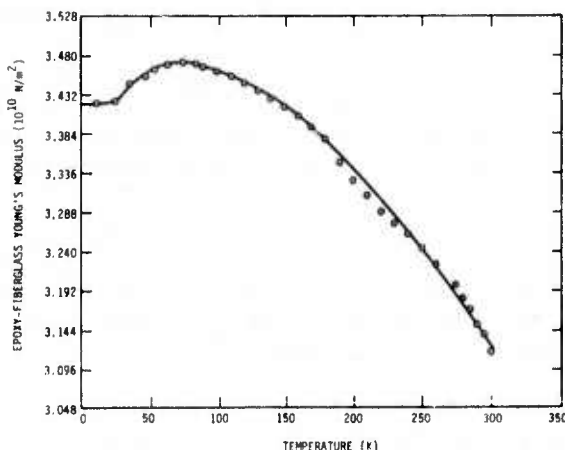


FIG. 9. Young's modulus of epoxy-fiber-glass, $\theta = 0^\circ$.

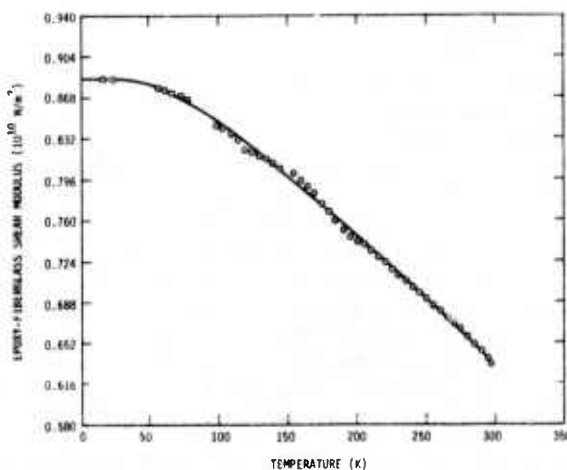


FIG. 10. Shear modulus of epoxy-fiber-glass, $\theta = 0^\circ$.

TABLE IV. Elastic stiffnesses of the superconducting coil composite at selected temperatures (10^{10} N/m²).

T (K)	C_{11} ^a	C_{12} ^a	C_{13} ^a	C_{33} ^a	C_{44}	C_{66}
0	5.10	1.94	2.39	10.59	1.10	1.58
50	5.10	1.93	2.39	10.46	1.10	1.58
100	4.99	1.90	2.34	10.27	1.09	1.54
150	4.80	1.87	2.27	10.05	1.04	1.46
200	4.54	1.79	2.15	9.86	0.96	1.37
250	4.21	1.63	1.99	9.64	0.85	1.29
300	3.82	1.39	1.77	9.35	0.74	1.22

^aThese constants are dependent on ν_{13} , and were calculated using the static value of ν_{13} , which was taken as independent of temperature.

m^2/N , $k_3 = -0.045 \times 10^{-10}$ m²/N, and $K = 0.027 \times 10^{-10}$ m²/N. However, if the Poisson ratio ν_{13} is taken as $\frac{1}{3}$, then $S_{13} = -0.041 \times 10^{-10}$ m²/N at room temperature, and $k_1 = 0.179 \times 10^{-10}$ m²/N, $k_3 = 0.041 \times 10^{-10}$ m²/N, and the volume compressibility $K = 0.399 \times 10^{-10}$ m²/N. The relatively large value for ν_{13} and the negative k_3 that result from the resonance S_{13} may not be unreasonable, considering the multicomponent material. The elastic stiffness coefficients, however, can be calculated from the compliances and indicate that the resonance value of S_{13} is in error.

The elastic stiffnesses (C_{ij}) can be directly calculated by inverting the S_{ij} matrix if all the compliances are known. The explicit relationships are⁴⁹

$$\begin{aligned} C_{11} &= \frac{S_{11}S_{33} - S_{13}^2}{(S_{11} - S_{12})\tilde{S}}, \\ C_{12} &= \frac{S_{13}^2 - S_{12}S_{33}}{(S_{11} - S_{12})\tilde{S}}, \\ C_{13} &= \frac{-S_{13}}{\tilde{S}}, \\ C_{33} &= \frac{S_{11} + S_{12}}{\tilde{S}}, \\ C_{44} &= \frac{1}{S_{44}}, \end{aligned} \quad (11)$$

and

$$C_{66} = \frac{1}{S_{66}},$$

where $\tilde{S} = S_{33}(S_{11} + S_{12}) - 2S_{13}^2$. Except for C_{44} and C_{66} , these relationships depend strongly on S_{13} . Using the resonance value of S_{13} , the elastic stiffnesses that depend on S_{13} are found to increase with increasing temperature, which is contrary to normal behavior. Since the Young's and shear moduli all behave fairly regularly with temperature, the resonance value of S_{13} seems unreasonable. In calculating the elastic stiffnesses, then, a value of $\frac{1}{3}$ for ν_{13} was used, and this Poisson's ratio was taken as constant with temperature.³⁹ It is believed that the elastic stiffnesses obtained this way are more accurate than those obtained using the resonance value of S_{13} . The elastic stiffnesses are given in Table IV.

As expected, the elastic properties of this composite are highly anisotropic. The anisotropy is best described by considering the percent elastic anisotropy as dis-

cussed by Chung and Buessem.⁴⁹ For transversely isotropic symmetry, this scheme involves using the conventional anisotropy ratios (the linear compressibility ratio $A_c = k_3/k_1$, and the shear anisotropy $A_s = C_{44}/C_{66}$) to calculate anisotropy parameters A_c^* and A_s^* with the following properties: A^* is zero for materials that are elastically isotropic, i.e., $A = 1$; A^* is always positive and a single-valued measure of the elastic anisotropy of a material regardless of whether $A < 1$ or $A > 1$; and A^* gives the relative magnitude of the elastic anisotropy present in the material. For this composite $A_c \approx 0.23$, $A_c^* \approx 8.4\%$, $A_s \approx 0.61$, and $A_s^* \approx 12.3\%$. For comparison, $A_c^* \approx 9.9\%$ and $A_s^* \approx 13.7\%$ for zinc,⁴⁹ which is one of the most anisotropic hexagonal metals.

The static value of Young's modulus of the fiber-glass-epoxy is also available.⁴⁰ This Young's modulus was measured on a specimen oriented like the one used for the resonance measurements. The resonance and static values differ by 4–10%. There was no evidence of a maximum in the static data, but it is believed that the maximum is real. This maximum was observed during several measurements and was completely reversible. No explanation for this behavior can be given at this time.

V. CONCLUSIONS

The resonant piezoelectric oscillator method used in this work is generally suitable for measuring the elastic properties of composite materials. This method is accurate, fast, and requires only small specimens. It is suitable for measurements at all temperatures from 0 K to greater than 1000 °C.^{29,30} The general techniques and theory of this method are well understood. This method does not appear to have the limitations of static and other ultrasonic techniques.

The elastic compliance data presented in this work generally agree well with existing data taken by conventional static methods, with the exception of S_{13} . It is believed, however, that if specimens with different orientations were available, a more accurate determination of S_{13} could be made. These data can be used to calculate other elastic properties, such as the elastic stiffness coefficients and compressibilities. However, many of these elastic properties depend on S_{13} , and their accuracies would also benefit from a better determination of S_{13} .

The superconducting coil composite was highly anisotropic, with elastic anisotropies similar to those of zinc. This high anisotropy, characteristic of many composite materials, necessitates careful measurements of elastic properties of these materials.

The measured elastic moduli of the composite are not as well represented by the Varshni function as they are for most metals and alloys; i.e., the elastic moduli of the superconducting coil composite are less regularly behaved with respect to temperature.

ACKNOWLEDGMENTS

The author would like to express his gratitude to D. L. Johnson for his considerable assistance with the piezoelectric oscillator techniques. He would also like to

thank A. F. Clark for supplying the specimens and static data on the coil composite, and H. Dickinson, who aided in the experiments. The author is also indebted to H. M. Ledbetter for many helpful discussions on elastic properties in general and for a critical reading of the manuscript. This work was supported in part by the Annapolis Laboratory of the Naval Ship Research and Development Center and in part by the Advanced Research Projects Agency of the U.S. Department of Defense.

*NRC-NBS Postdoctoral Research Associate, 1974-5.

- ¹P. R. Goggin, *J. Mater. Sci.* 8, 233 (1973).
- ²T. J. Dudek, *J. Compos. Mater.* 4, 232 (1970).
- ³T. Hirai and D. E. Kline, *J. Compos. Mater.* 7, 160 (1973).
- ⁴Albert B. Schultz and Stephen W. Tsai, *J. Compos. Mater.* 2, 368 (1968).
- ⁵R. C. Rossi, J. R. Cost, and K. R. Janowski, *J. Am. Ceram. Soc.* 55, 234 (1972).
- ⁶G. C. Wright, *J. Sound Vib.* 21, 205 (1972).
- ⁷R. E. Allred and W. R. Hoover, *J. Compos. Mater.* 8, 15 (1974).
- ⁸L. J. Cohen and O. Ishai, *J. Compos. Mater.* 1, 1030 (1967).
- ⁹N. L. Hancox, *J. Mater. Sci.* 7, 1030 (1972).
- ¹⁰T. R. Tauchert, *J. Compos. Mater.* 5, 456 (1971).
- ¹¹A. Smith, *J. Phys. E* 5, 274 (1972).
- ¹²A. Smith, W. N. Reynolds, and N. L. Hancox, *J. Compos. Mater.* 7, 138 (1973).
- ¹³A. Smith, S. J. Wilkinson, and W. N. Reynolds, *J. Mater. Sci.* 9, 547 (1974).
- ¹⁴J. V. Grabel and J. R. Cost, *Met. Trans.* 3, 1973 (1972).
- ¹⁵A. E. Lord and D. Robert Hay, *J. Compos. Mater.* 6, 275 (1972).
- ¹⁶W. Sachse, *J. Compos. Mater.* 8, 378 (1974).
- ¹⁷J. O. Achenbach and G. Hermann, *AIAA J.* 6, 1832 (1968).
- ¹⁸J. E. Zimmer and J. R. Cost, *J. Acoust. Soc. Am.* 47, 795 (1970).
- ¹⁹W. N. Reynolds and S. J. Wilkinson, *Ultrasonics* 12, 109 (1974).
- ²⁰S. J. Wilkinson and W. N. Reynolds, *J. Phys. D* 7, 50 (1974).
- ²¹T. R. Tauchert and A. N. Guzelsu, *Trans. ASME* 39, 98 (1972).
- ²²M. F. Markham, *Composites* 1, 145 (1970).
- ²³G. D. Dean and P. Turner, *Composites* 4, 174 (1973).
- ²⁴Robert S. Smith, *J. Appl. Phys.* 43, 2555 (1972).
- ²⁵A. R. Zecca and D. R. Hay, *J. Compos. Mater.* 4, 556 (1970).
- ²⁶S. L. Quimby, *Phys. Rev.* 25, 558 (1925).
- ²⁷L. Balamuth, *Phys. Rev.* 45, 715 (1934).
- ²⁸F. C. Rose, *Phys. Rev.* 40, 50 (1936).
- ²⁹L. Hunter and S. Siegel, *Phys. Rev.* 61, 84 (1942).
- ³⁰J. W. Marx and J. M. Slivertsen, *J. Appl. Phys.* 24, 81 (1953).
- ³¹M. E. Fine, *Rev. Sci. Instrum.* 25, 1188 (1954).
- ³²S. Siegel and S. L. Quimby, *Phys. Rev.* 49, 663 (1936).
- ³³J. Zacarias, *Phys. Rev.* 44, 116 (1933).
- ³⁴J. Marx, *Rev. Sci. Instrum.* 22, 503 (1951).
- ³⁵M. E. Fine, ASTM Special Technical Publication No. 129, 1952, p. 48 (unpublished).
- ³⁶W. H. Robinson, S. H. Carpenter, and J. L. Tallon, *J. Appl. Phys.* 45, 1975 (1974).
- ³⁷The use in this paper of trade names of specific products is essential to a proper understanding of the work presented. Their use in no way implies any approval, endorsement, or recommendation by NBS.
- ³⁸A. J. Matheson, *J. Phys. E* 4, 796 (1971).
- ³⁹C. W. Fowlkes, P. E. Angerhofer, P. N. Newton, and A. F. Clark, National Bureau of Standards Report No. NBSIR 73-349, 1973 (unpublished).
- ⁴⁰A. P. Gerk, *Rev. Sci. Instrum.* 43, 1786 (1972).
- ⁴¹D. L. Johnson (private communication).
- ⁴²A. F. Clark, V. D. Arp, W. F. Weston, and J. G. Hust, National Bureau of Standards Report No. NBSIR 74-399, 1974 (unpublished).
- ⁴³W. N. Robinson and A. Edgar, *IEEE Trans. Sonics Ultrason.* 21, 98 (1974).
- ⁴⁴W. Voigt, *Lehrbuch der Kristallphysik* (Teubner, Berlin, 1928), pp. 746-7.
- ⁴⁵Y. P. Varshni, *Phys. Rev. B* 2, 3952 (1970).
- ⁴⁶E. R. Naimon, W. F. Weston, and H. M. Ledbetter, *Cryogenics* 14, 721 (1973).
- ⁴⁷L. D. Landau and E. M. Lifshitz, *Theory of Elasticity* (Pergamon, London, 1959), p. 17.
- ⁴⁸R. F. S. Hearmon, *Rev. Mod. Phys.* 18, 409 (1946).
- ⁴⁹D. H. Chung and W. R. Buessem, *Anisotropy in Single-Crystal Compounds*, edited by F. W. Vahldiek and S. A. Mersol (Plenum, New York, 1968), Vol. 2, p. 217.

SEMI-ANNUAL REPORT ON MATERIALS RESEARCH
IN SUPPORT OF SUPERCONDUCTING MACHINERY

FRACTURE MECHANICS PARAMETERS OF ENGINEERING
MATERIALS AT CRYOGENIC TEMPERATURES

R. L. Tobler, D. T. Read, and R. P. Reed

Cryogenics Division
Institute for Basic Standards
National Bureau of Standards
Boulder, Colorado 80302

April 1976

Summary: Fracture Mechanics Parameters of Engineering
Materials at Cryogenic Temperatures

This section of the report contains two manuscripts. Fracture mechanics design data are presented for a nickel base superalloy, Inconel 718, and an aluminum base alloy, 2219-T6. The plane strain fracture toughness parameters (K_{IC} and J_{IC}), tensile, and fatigue crack growth rates (da/dN) were measured using state-of-the-art test procedures. The results are summarized as follows:

(1) The tensile, fatigue, and fracture properties of Inconel 718 alloy are nearly constant or slightly improved at decreasing temperatures between 295 and 4 K. The fracture toughness (K_{IC}) at 4 K is 16% higher than the room temperature value of $96.3 \text{ MPa}\cdot\text{m}^{1/2}$. This alloy is useful for cryogenic structural applications requiring an exceptional yield strength (1.172 GPa at 295 K) and moderate fracture toughness.

(2) J-integral resistance curves for three specimen thicknesses and valid (according to ASTM Method E 399) K_{IC} values at 76 K are reported for aluminum alloy 2219. The J-integral values were independent of thickness at small crack extensions, but at substantial crack extensions the values for the thin specimens were larger than those for the thick specimens. The measured J_{IC} values were less than those calculated from the measured K_{IC} values. The reason for this discrepancy was that crack extension occurred before the K_{IC} measurement point was reached.

LOW TEMPERATURE EFFECTS ON THE FRACTURE BEHAVIOR OF INCONEL 718[†]

R. L. Tobler

Cryogenics Division
Institute for Basic Standards
Boulder, Colorado 80302

ABSTRACT

The mechanical properties of a solution treated and double aged Inconel 718 forging were studied to assess its utility at temperatures in the ambient-to-cryogenic range. Uniaxial tensile property measurements using unnotched specimens at decreasing temperatures between 295 and 4 K show that yield and ultimate strengths increase by 20% and 29%, respectively, while ductility remains virtually constant. Fracture mechanics tests using 2.54 cm-thick compact specimens revealed that the fatigue crack growth resistance of this alloy improves slightly at extreme cryogenic temperatures, and its plane strain fracture toughness, K_{IC} , increases from $96.3 \text{ MPa}\cdot\text{m}^{1/2}$ at 295 K to $112.3 \text{ MPa}\cdot\text{m}^{1/2}$ at 4 K. These results are compared with similar data for Inconel 750 alloys.

Key words: Fatigue; fracture; low temperature tests; mechanical properties; nickel alloys; superalloys.

[†] Contribution of NBS, not subject to copyright.

INTRODUCTION

A precipitation hardenable nickel base superalloy known as Inconel 718* was first developed for elevated temperature service. Then, by virtue of its austenitic structure, high strength, and weldability, the alloy found applications in the ambient-to-cryogenic temperature region as well. Current applications at temperatures as low as 20 K include liquid oxygen and liquid hydrogen pressure vessels for spacecraft. Emerging applications related to superconducting machinery (torque tubes, damper shields) will probably further extend the utility of Inconel 718 to temperatures approaching absolute zero.

A need for reliable mechanical property data accompanies the expanded use of this alloy. Conventional tensile properties for the temperature range 295 to 4 K [1-14] are insufficient to characterize the load-carrying capability of large structures subject to fatigue. As demonstrated by this study, relatively brittle fractures may occur when fatigue cracks are located in thick sections of Inconel 718, despite the fact that this material exhibits appreciable ductility in the unnotched condition.

The existing fatigue crack growth and fracture toughness data [12-17] relate predominantly to thin sections and non-standard specimen geometries, or concentrate only on room temperature properties. The present study describes the mechanical behavior of Inconel 718 at several temperatures including 295, 195, 76, and 4 K. In addition to conventional tensile property determinations, fatigue crack growth resistance was evaluated, and the ASTM standard method of test for plane strain fracture toughness of metallic materials (ASTM E-399-74) [18] was applied to generate valid K_{Ic} data for this alloy.

MATERIAL

The Inconel 718 alloy was purchased in the form of a forged 7.7 cm x 7.7 cm square bar that had been annealed at 1200 K for 1h. As quoted from the mill sheet, the chemical composition in weight percent is: 53.4 Ni, 18.5 Fe, 18.1 Cr, 5.24 Nb + Ta, 2.95 Mo, 0.90 Ti, 0.49 Al, 0.17 Co, 0.10 Mn, 0.10 Cu, 0.10 Si, 0.05 C, 0.01 P, 0.003 B, 0.002 S. All test specimens were machined prior to precipitation hardening, which followed the standard heat treatment:

- 1) Solution treatment (1256 K for 3/4h, air cool);
- and 2) Double age (992 K for 8h, furnace cool to 894 K, hold 10h, and air cool).

PROCEDURES

Tensile

Tensile tests were conducted at room, liquid nitrogen, and liquid helium temperatures at a crosshead velocity of 0.008 mm per second. Reed [19] described the 44.5 kN screw-driven machine, cryostat, and low temperature techniques used here. The tensile specimens had a

* Tradenames are used in this report for clarity and in no way imply endorsement or recommendation by NBS.

reduced section 3.8 cm long and 0.51 cm in diameter. The tensile axis was transverse to the forging axis, such that the fracture plane orientation matched that of the compact specimens described below. The outputs of a commercial load cell and clip-on strain gage extensometer were recorded and analyzed as outlined in ASTM Method E8-72 [20].

Fracture

The compact specimens used for fatigue and fracture tests had a thickness, B , of 2.54 cm and a width, W , of 5.08 cm. These specimens were machined in the TS orientation [18], with their loading axis and crack propagation directions transverse to the original forging axis. Other specimen features were in accordance with the E-399-74 method, except that a modified notch was incorporated. As shown in Figure 1, the modified notch permits clip gage attachment at knife edges in the loadline.

Room temperature tests were conducted using a 100 kN servo-hydraulic test machine and cryostat in ambient air. Low temperature environments were achieved by immersing the load frame, specimen, and clip gage in alcohol and dry ice (195 K), liquid nitrogen (76 K) or liquid helium (4 K). The clip gage satisfied E-399-74 linearity requirements at each temperature. A detailed description of the low temperature apparatus and techniques was given by Fowlkes and Tobler [21].

Fracture toughness specimens were precracked at their K_{Ic} test temperatures and loaded to fracture at $1 \text{ MPa}\cdot\text{m}^{1/2}$ per second. Following the E-399-74 method, K_{Ic} was calculated from the solution for compact specimens:

$$K_{Ic} = P_Q B^{-1/2} W^{-1/2} [f(a/W)] \quad (1)$$

where

$$f(a/W) = 29.6 (a/W)^{1/2} - 185.5 (a/W)^{3/2} + 655.7 (a/W)^{5/2} - 1017.0 (a/W)^{7/2} + 638.9 (a/W)^{9/2} \quad (2)$$

In these equations, P_Q is the load defined by the secant offset procedure [18], and a is the average of three crack length measurements at 25, 50, and 75% of specimen thickness.

Fatigue

Fatigue crack growth rates were measured during the precracking of K_{Ic} specimens where the maximum stress intensity factor never exceeded $0.6 K_{Ic}$. Additional specimens were tested to obtain growth rates at higher stress intensities. Although most specimens were 2.54 cm thick ($W/B = 2$), four tests of a 0.508 cm thickness ($W/B = 10$) were also included. The fatigue operations were conducted using controlled load, a sinusoidal load cycle, and a cycle frequency of 20 Hz; the ratio, R , of minimum/maximum load was 0.1.

Crack growth was monitored indirectly by compliance measurements, as previously described [21]. Briefly, a correlation between crack length and specimen deflection per unit load (δ/P) was determined by measurements on fractured specimens. The fatigue tests were

interrupted periodically to record δ/P , from which crack lengths could be inferred and plotted as a function of fatigue cycles, N . A computer program was used to fit the a -versus- N curves with a third order polynomial, to differentiate the curves to obtain da/dN values, and to calculate the associated stress intensity factor ranges, ΔK , from the peak fatigue loads:

$$\Delta K = (P_{\max} - P_{\min}) B^{-1} W^{-1/2} [f(a/W)] \quad (3)$$

RESULTS

Tensile

Table 1 lists the yield and ultimate strengths, elongation, and reduction in area measurements for Inconel 718 at 295, 76, and 4 K. These data are plotted in Figures 2-4, along with data for other Inconel 718 forgings in the 1256 K solution treated and double aged condition. The temperature dependences of these tensile parameters illustrate what are considered to be classical trends for face centered cubic metals and alloys [22-24]: ductility remains nearly constant, there is a moderate increase of yield strength, and a larger increase of ultimate strength. The yield strength of the present alloy ranges from 1.172 to 1.408 GPa over the temperature interval investigated, showing good agreement with other results [9-13].

On the other hand, the heat-to-heat variations of ductility appear to be sizable. With reference to Figure 4, reduction in area measurements at room temperature range from 14 to 30%, but the values for our alloy are intermediate at 19%.

Handbooks [1-3] contain other low temperature tensile data for thin sheet and other Inconel 718 stock having thermal or mechanical treatments differing from the 1256 K solutioning and double aging treatment studied here. The comparisons above are sufficient to demonstrate that the present is representative of commercially available forgings.

Fracture

The load-deflection behavior and fracture surface of a compact specimen tested at 4 K are shown in Figure 5. "Type 1" test records [18] with slight nonlinearity prior to maximum load were observed at each temperature. The fracture surfaces displayed no shear portions but were flat and granular in appearance, and uninfluenced by test temperature.

The K_{Ic} calculations are itemized in Table 2. The 2.54 cm-thick specimens tested here amply satisfy the E-399-74 criterion for thickness, $B \geq 2.5 \left(\frac{K_{Ic}}{\sigma_y} \right)^2$, which requires a minimum thickness of 1.9 cm for this alloy at room temperature. Other information pertinent to assessing the validity of K_{Ic} measurements are included in Table 2. In three tests, a/W exceeded the 0.45 to 0.55 range. However, these three deviations are minor, and any effects on K_{Ic} results are considered negligible compared to the degree of scatter among specimens.

The average K_{Ic} value at each temperature is plotted in Figure 6. The data are mildly temperature dependent, showing a 16% increase from 96.3 to 112.3 $\text{MPa}\cdot\text{m}^{1/2}$ as temperature is lowered from 295 to 4 K. Logsdon, et al. [12] reported a 14% increase for compact specimens of an Inconel 718 alloy tested at 295 and 4 K. Note that their K_{Ic} values are lower (70 to

80 MPa·m^{1/2}) compared to the present results; They also reported lower tensile ductility, as shown in Figures 3 and 4. Note also that the temperature dependence of fracture toughness for Inconel 718 is opposite to that for Inconel 750 alloys: as temperature is lowered, Inconel 750 shows moderate decreases in K_{Ic} amounting to 8% between 295 and 76 K [26], and 11% between 295 and 4 K [25].

The literature [13-16] contains other fracture toughness data for Inconel 718 which were not obtained by the E-399-74 method. Those measurements were derived from tests of center-notched, single-edge-notched, or surface-flawed specimens. To their advantage, surface-flawed specimens simulate a flaw type that commonly occurs in pressure vessels, but the fracture toughness results are directly applicable only when the service conditions match the specifics of specimen flaw shape and thickness. Hall's experimental results indicate that surface flawed specimens produce high apparent fracture toughness values as compared with the true K_{Ic} values from standard compact or bend specimens [27]. Further difficulty arises from the fact that the Inconel 718 specimens tested by Witzell [13], Pettit, Feddersen, and Mindin [14] and Taylor [16], are too thin (1.6 to 3.5 mm) to avoid size effects according to the E-399-74 criterion. For these reasons, such data are of limited value to designers. On the other hand, the K_{Ic} data of Figure 6 are independent of specimen geometry and represent true material constants which are generally applicable in design.

Fatigue Crack Growth Rates

As demonstrated by Paris and Erdogan [28], fatigue crack growth rates can usually be described as power-law functions of the stress intensity factor range, ΔK :

$$\frac{da}{dN} = C(\Delta K)^n \quad (4)$$

where C and n are material constants that depend on environment and test variables. Logarithmic plots of da/dN -versus- ΔK measurements that are in agreement with Eq. (4) reveal linear trends from which n and C can be determined as the slope and ordinate intercept at $\Delta K = 1$, respectively.

The fatigue crack growth rates of Inconel 718 at 295, 195, 76, and 4 K are plotted on logarithmic coordinates in Figure 7. The data define a scatterband approximately 7 to 12 MPa·m^{1/2} wide. At equivalent ΔK values, the rates at cryogenic temperatures are slightly lower than at room temperature. However, the improvement in fatigue crack propagation resistance is modest, and barely distinguishable beyond the scatter of replicate tests unless the temperature differential exceeds 150 to 200 kelvins.

Linear segments representing two Paris equations were chosen to approximate the upper (295 K) and lower (4 K) extremes of data in Figure 7. Thus, at 295 K:

$$\frac{da}{dN} = 8 \times 10^{-11} (\Delta K)^4 \quad (5)$$

and at 4 K:

$$\frac{da}{dN} = 4.8 \times 10^{-11} (\Delta K)^4 \quad (6)$$

where ΔK is in $\text{MPa}\cdot\text{m}^{1/2}$ and da/dN is in mm/cycle . The exponent, $n = 4$, which some theories predict [29], provides a good approximation for these experimental results.

Figures 8 and 9 compare the fatigue crack propagation resistance of Inconel 718 with the available results for other nickel base alloys and stainless steels which could be considered material competitors for various applications. Note that the room temperature crack growth rates reported by Shahinian, Watson, and Smith [17] are in close agreement with the present data for Inconel 718. As shown in Figures 8 and 9, the fatigue crack propagation resistance of Inconel 718 is intermediate compared with other austenitic alloys.

DISCUSSION

The low temperature tensile properties of this Inconel 718 alloy were equivalent or superior to its properties at room temperature. Other studies of Inconel 718 alloys have shown that, as the temperature decreases to 4 K, Young's modulus increases by 6% [31], fatigue strength at 10^6 cycles increases by approximately 75% [8], and Charpy impact values show little change [11]. Since none of these parameters are deleteriously affected, the reliability of Inconel 718 structures will not be decreased at extreme cryogenic temperatures.

The attractive feature of a high yield strength which increases at cryogenic temperatures without sacrifice of tensile ductility justifies Inconel 718's selection for numerous applications. Nevertheless, this alloy is susceptible to brittle fracture in thick sections containing flaws. The fracture toughness at ambient and cryogenic temperatures is useful but moderate; therefore, accurate fracture mechanics evaluations seem necessary to assure structural safety and efficient design.

In the fracture mechanics approach, K is proportional to the magnitude of elastic stresses at the crack tip. Upon reaching a critical value, K_{IC} , the material fractures catastrophically, without significant plastic deformation. Using handbook [32] equations for various component geometries of known dimensions and loadings, the maximum flaw size that a structure will tolerate can be calculated based on the material's K_{IC} value. Fatigue crack growth rates enable a prediction of the total number of load cycles required to propagate an initial crack to critical proportions. Thus, the da/dN and K_{IC} data of this report can be used to assess the safe operating lifetimes of Inconel 718 structures.

The significant finding that Inconel 718's da/dN and K_{IC} parameters are nearly invariant at temperatures below 295 K should facilitate fracture mechanics analyses. For example, the performance of a component of this material at cryogenic temperatures could be conservatively predicted using room temperature data obtained from quality control tests of production material. Similarly, for convenience and economy, cryogenic structures might be proof-tested at room temperature.

An important question regarding alloy selection is whether Inconel 718 might supersede Inconel 750 as a construction material for some applications in superconducting generators.

Inconel 750 and 718 alloys possess a high resistance to fatigue crack propagation which seems to be a characteristic of austenitic alloys in general [30]. Figures 8-9 compared the fatigue crack growth rates of Inconel 750 and 718 with those reported for several austenitic stainless steels. Dismissing minor differences in the rates for Inconel 750 and 718, attention centers on yield strength and fracture toughness comparisons. At 4 K, the yield strengths of solution treated and double aged Inconel 750 alloys range from 0.736 to 1.194 GPa, depending on manufacturing process and heat treatment variations [25]; K_{IC} values for the same heats range from 102 to 239 $\text{MPa}\cdot\text{m}^{1/2}$. Based on the present study, Inconel 718 offers a higher yield strength, 1.408 GPa, but its K_{IC} value of 112 $\text{MPa}\cdot\text{m}^{1/2}$ is on the low side of the range for Inconel 750 alloys. This trade-off between yield strength and fracture toughness will determine alloy selection relative to the specific requirements of each application.

CONCLUSIONS

Uniaxial tensile properties and fracture mechanics data were obtained for a precipitation hardened Inconel 718 forging at temperatures in the ambient-to-cryogenic range. The temperature dependences of the mechanical properties of this alloy may be considered typical, qualitatively, of austenitic alloys in general. At 4 K, the yield strength of this Inconel 718 alloy was 20% greater than the room temperature value of 1.172 GPa. The K_{IC} values showed that fracture toughness varies from 96.3 to 112.3 $\text{MPa}\cdot\text{m}^{1/2}$ between 295 and 4 K, whereas tensile ductility and fatigue crack growth resistance remain nearly constant. Based on these data trends, the load-carrying capability of flawed or unflawed Inconel 718 structures is not expected to decrease at cryogenic temperatures.

ACKNOWLEDGEMENTS

This program was sponsored by the Advanced Research Projects Agency of the U.S. Department of Defense. The contributions of Dr. R. P. Mikesell and R. L. Durcholz in conducting the tensile tests are gratefully acknowledged.

REFERENCES

1. Handbook on Materials for Superconducting Machinery, MCIC-HB-04 (Battelle Columbus Laboratories, 1974).
2. Cryogenic Materials Data Handbook, AFML-TDR-64-280 (Martin Marietta Co., 1964).
3. Materials Data Handbook: Inconel Alloy 718, NASA-CR-123774 (Western Res. and Dev. Inc., 1972).
4. Inconel Alloy 718, Bulletin T-39 (Huntington Alloy Products Division, International Nickel Co., 1973).
5. Wagner, H. J., Hall, A. M., Physical Metallurgy of Alloy 718, Defense Metals Information Center Report 217 (Battelle Memorial Institute, 1968).
6. Christian, J. L., in Advances in Cryogenic Engineering 12 (1962) 520.
7. Nachtigall, A. J., in Properties of Materials for Liquefied Natural Gas Tankage, ASTM STP 579 (Amer. Soc. Test. Mater., Philadelphia, 1975) 378.
8. Nachtigall, A. J., Klima, S. J., Freche, J. C., J. Materials, JMLSA 3 (1968) 425.
9. Inouye, F. T., Hunt, V., Janser, G. R., Frick, V., NASA Tech. Rept. CR-788 (Aerojet General Corp., 1967).
10. Morgan, W. R., NASA Internal Note IN-P and VE-M-66-2 (George C. Marshall Space Flight Center, 1966).
11. Malin, C. O., NASA Tech. Brief MFS-18244 (George C. Marshall Space Flight Center, 1965).
12. Logsdon, W. A., Kossowsky, R., Daniel, M. R., Wells, J. M., in Materials Research for Superconducting Machinery IV, Reed, R. P., Clark, A. F., and van Reuth, E. C., Eds., Semi-Annual Tech. Rept., October 1975 (Advanced Research Projects Agency, 1975).
13. Witzell, W. E., Tech. Rept. AFML-TR-67-257 (General Dynamics-Convair, 1967).
14. Pettit, D. E., Feddersen, C. E., Mindin, H., NASA CR 101942 (Battelle Memorial Institute, 1969).
15. Forman, R. G., NASA Tech. Note TN D-7665 (National Aeronautics and Space Administration, 1974).
16. Taylor, J. L., in Proceedings of the Seventh Symposium on Nondestructive Evaluation of Components and Materials in Aerospace (Amer. Soc. Nondestructive Testing, San Antonio, 1969) 420.
17. Shahinian, P., Watson, H. E., Smith, H. H., J. Materials, JMLSA 7 (1972) 527.
18. Annual Book of ASTM Standards, Part 10 (Amer. Soc. Test. Mater. Philadelphia, 1974) 432.
19. Reed, R. P., in Advances in Cryogenic Engineering 7 (1962) 448.
20. Annual Book of ASTM Standards, Part 31 (Amer. Soc. Test. Mater., Philadelphia, 1973) 220.
21. Fowlkes, C. W., Tobler, R. L., Eng. Fract. Mech., to be published.
22. McLean, D., Mechanical Properties of Metals (Wiley, New York, 1962).
23. Conrad, H., in High Strength Materials (Wiley, New York, 1964).
24. Wigley, D. A., Mechanical Properties of Materials at Low Temperatures (Plenum, New York, 1971).
25. Logsdon, W. A., in International Cryogenic Materials Conference Proceedings (Plenum, New York, 1976) to be published.

26. Tobler, R. L., Mikesell, R. P., Durcholz, R. L., Reed, R. P., in Materials Research for Superconducting Machinery II, Clark, A. F., Reed, R. P., and van Reuth, E. C., Eds., Semi-Annual Tech. Rept., October 1974 (Advanced Research Projects Agency, 1974).
27. Hall, L. R., in Fracture Toughness Testing at Cryogenic Temperatures, ASTM STP 496 (Amer. Soc. Test. Mater., Philadelphia, 1970) 40.
28. Paris, P. C., Erdogan, F., J. Basic Engrg., Trans. ASME Series D, 85 (1963) 528.
29. Johnson, H. H., Paris, P. C., Eng. Fract. Mech. 1 (1968) 3.
30. Tobler, R. L., Reed, R. P., in International Cryogenic Materials Conference Proceedings (Plenum, New York, 1976) to be published.
31. Weston, W. F., Ledbetter, H. M., Mater. Sci. Eng. 20 (1975) 287.
32. Tada, H., Paris, P. C., Irwin, G. R., The Stress Analysis of Cracks Handbook (Del Research Corp., Hellertown, PA, 1973).

Table 1. Tensile property results for Inconel 718.

Temperature K	0.2% Yield Strength		Ultimate Strength		Elongation	Reduction in Area
	GPa	(ksi)	GPa	(ksi)	%	%
295	1.165		1.391		16.1	19.5
	---		1.396		14.3	18.4
	<u>1.178</u>		<u>1.425</u>		<u>15.8</u>	<u>16.8</u>
	Avg 1.172	(170.0)	1.404	(203.6)	15.4	18.2
76	1.326		1.649		20.2	20.6
	<u>1.359</u>		<u>1.649</u>		<u>20.9</u>	<u>18.9</u>
	Avg 1.342	(197.4)	1.649	(239.2)	20.6	19.8
4	1.371		1.802		21.7	24.0
	<u>1.445</u>		<u>1.830</u>		<u>19.5</u>	<u>16.3</u>
	1.408	(204.2)	1.816	(263.4)	20.6	20.2

Table 2. Fracture toughness results for Inconel 718.

Temperature K	Specimen Number	a/W	$K_f^{(a)}$ $MPa \cdot m^{1/2}$	$\frac{a_{edge}}{a}$ (b)	P_m/P_Q (c)	K_{Ic} $MPa \cdot m^{1/2}$	$(ksi \cdot in^{1/2})$
295	3	0.461	30	0.92	1.02	104	
	4	0.499	37.5	0.95	1.01	91.5	
	9	0.575	54	0.93	1.01	93.5	
					Avg	96.3	(87.8)
195	2	0.565	51	0.93	1.08	100	
	5	0.465	38	0.95	1.06	112	
					Avg	106	(96.5)
76	1	0.536	43.5	0.95	1.02	110	
	14	0.561	55	0.92	1.03	96.5	
	16	0.480	45	0.92	1.03	103	
					Avg	103.2	(94)
4	8	0.555	55	0.93	1.05	104	
	13	0.512	48	0.95	1.09	119	
	15	0.470	50	0.92	1.05	114	
					Avg	112.3	(102.3)

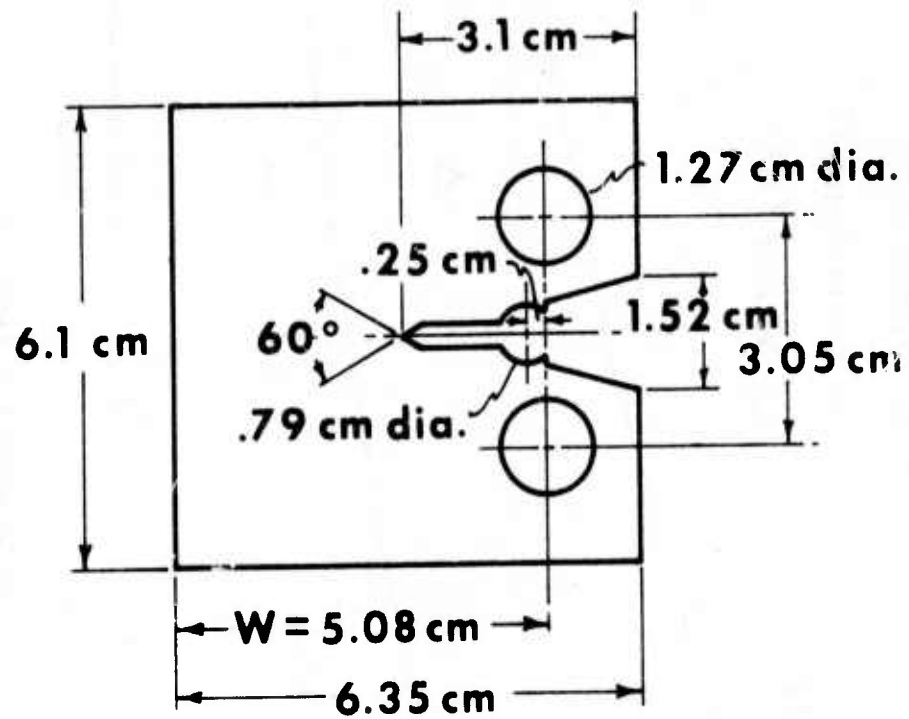
^a $K_f \leq 0.6 K_{Ic}$ is required by the E-399-74 method.

^b an edge-crack-to-average-crack-length ratio, $a_{edge}/a \geq .90$ is required.

^c $P_m/P_Q < 1.10$ is required.

LIST OF FIGURES

- Figure 1. Compact specimen used for fatigue and fracture tests.
- Figure 2. Yield and ultimate tensile strengths of Inconel 718 forgings in the solution treated (1225 to 1256 K) and double aged condition.
- Figure 3. Tensile elongation of Inconel 718 forgings in the solution treated and double aged condition.
- Figure 4. Reduction in area of Inconel 718 forgings in the solution treated and double aged condition.
- Figure 5. Fracture toughness test record for Inconel 718, showing fracture surface appearance.
- Figure 6. Temperature dependence of fracture toughness for two Inconel 718 alloys.
- Figure 7. Fatigue crack propagation rates for Inconel 718.
- Figure 8. Comparison of fatigue crack propagation rates of Inconel alloys 718 and 750.
- Figure 9. Comparison of fatigue crack propagation rates of Inconel 718, Inconel 750, and austenitic stainless steels at 4 K.



THICKNESS, $B = 2.54$ cm; $W/B = 2$

Figure 1. Compact specimen used for fatigue and fracture tests.

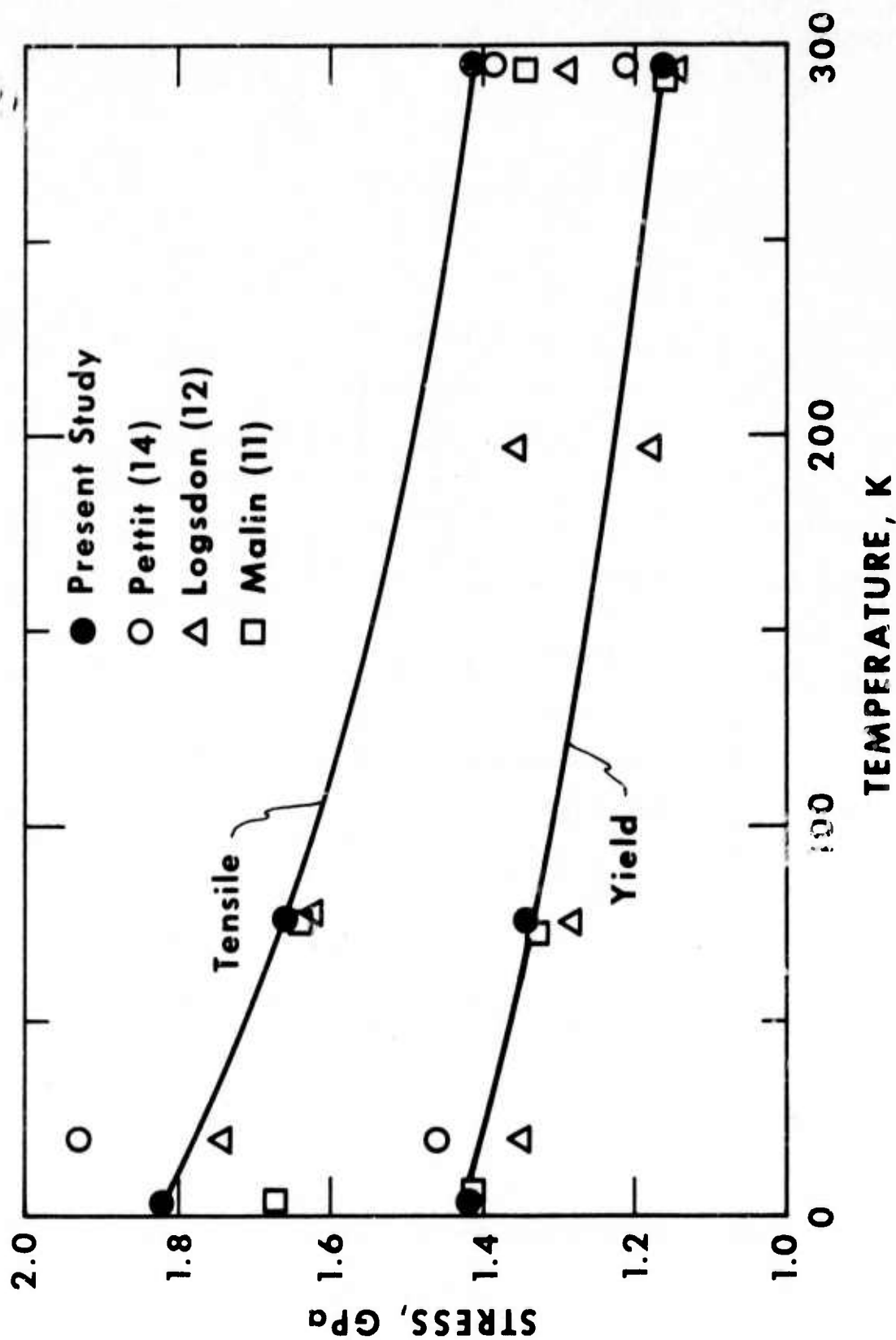


Figure 2. Yield and ultimate tensile strengths of Inconel 718 forgings in the solution treated (1225 to 1256 K) and double aged condition.

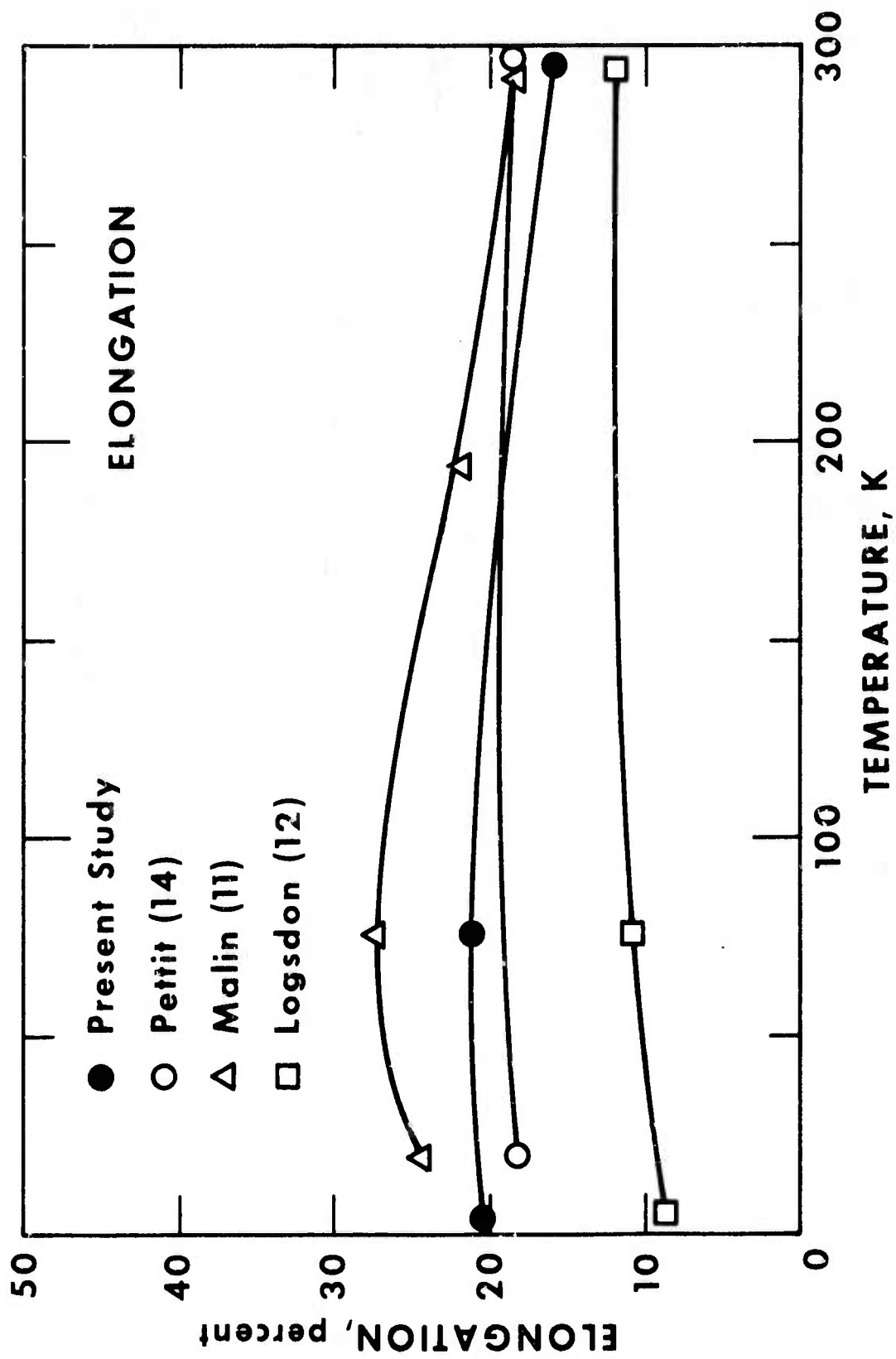


Figure 3. Tensile elongation of Inconel 718 forgings in the solution treated and double aged condition.

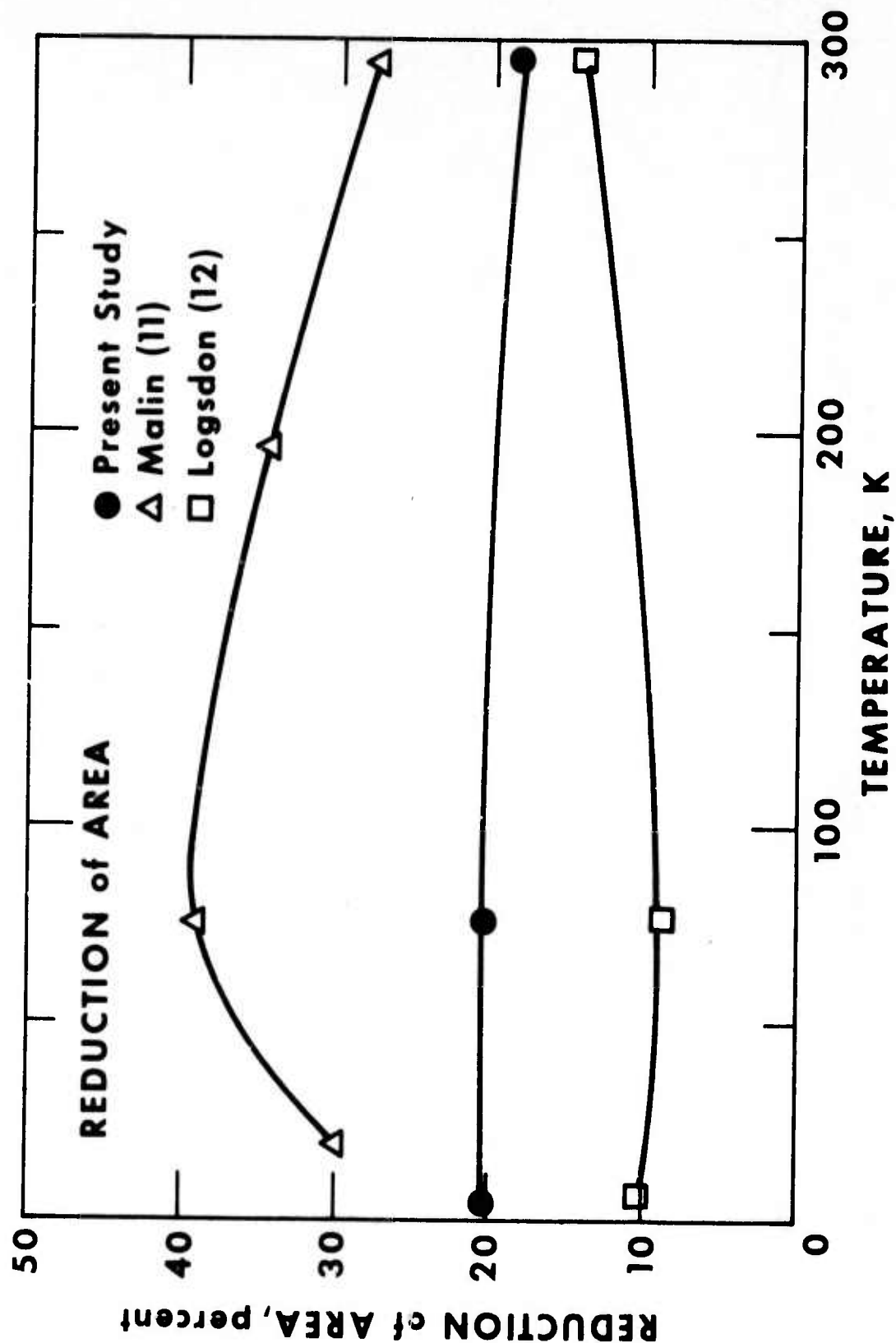


Figure 4. Reduction in area of Inconel 718 forgings in the solution treated and double aged condition.

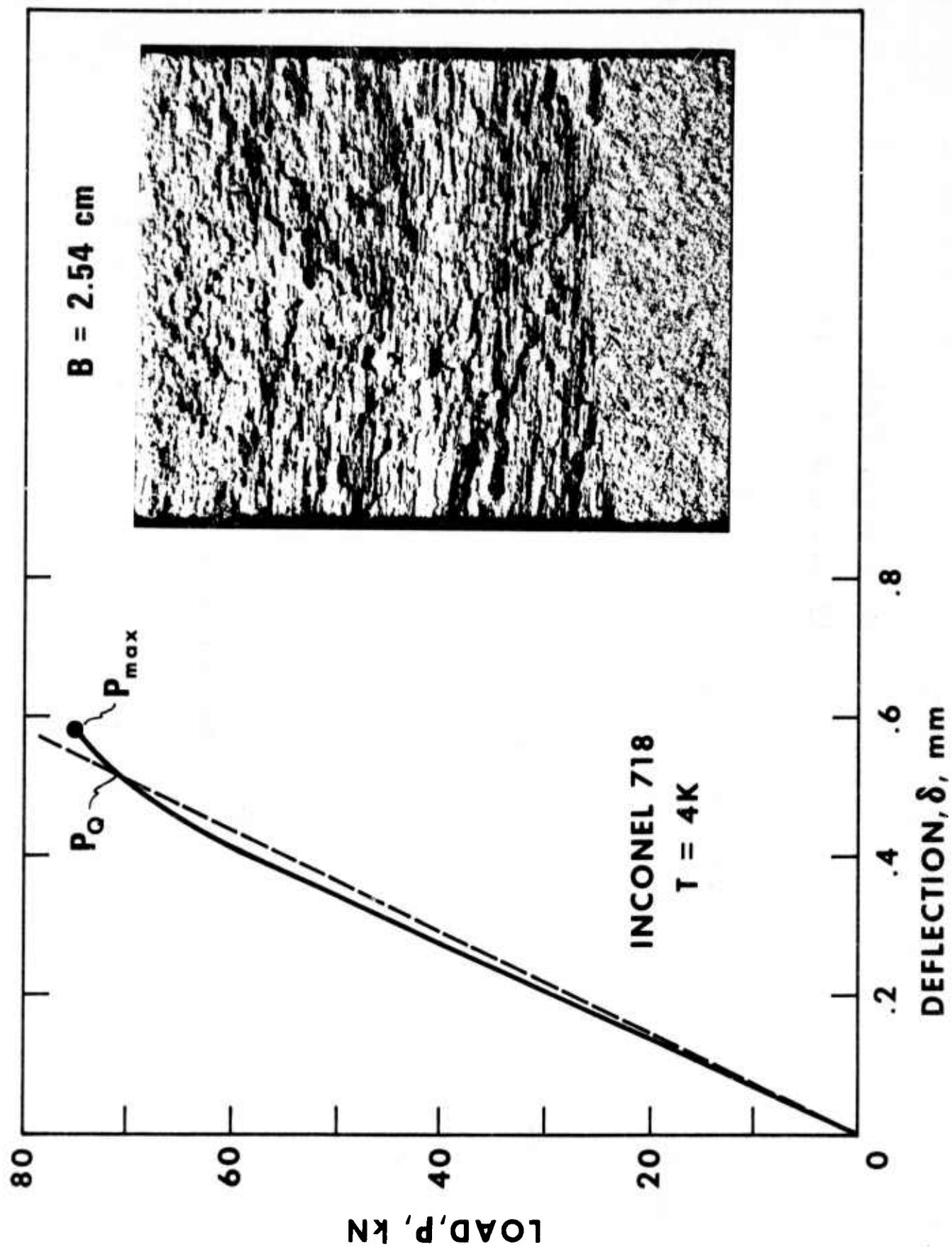


Figure 5. Fracture toughness test record for Inconel 718, showing fracture surface appearance.

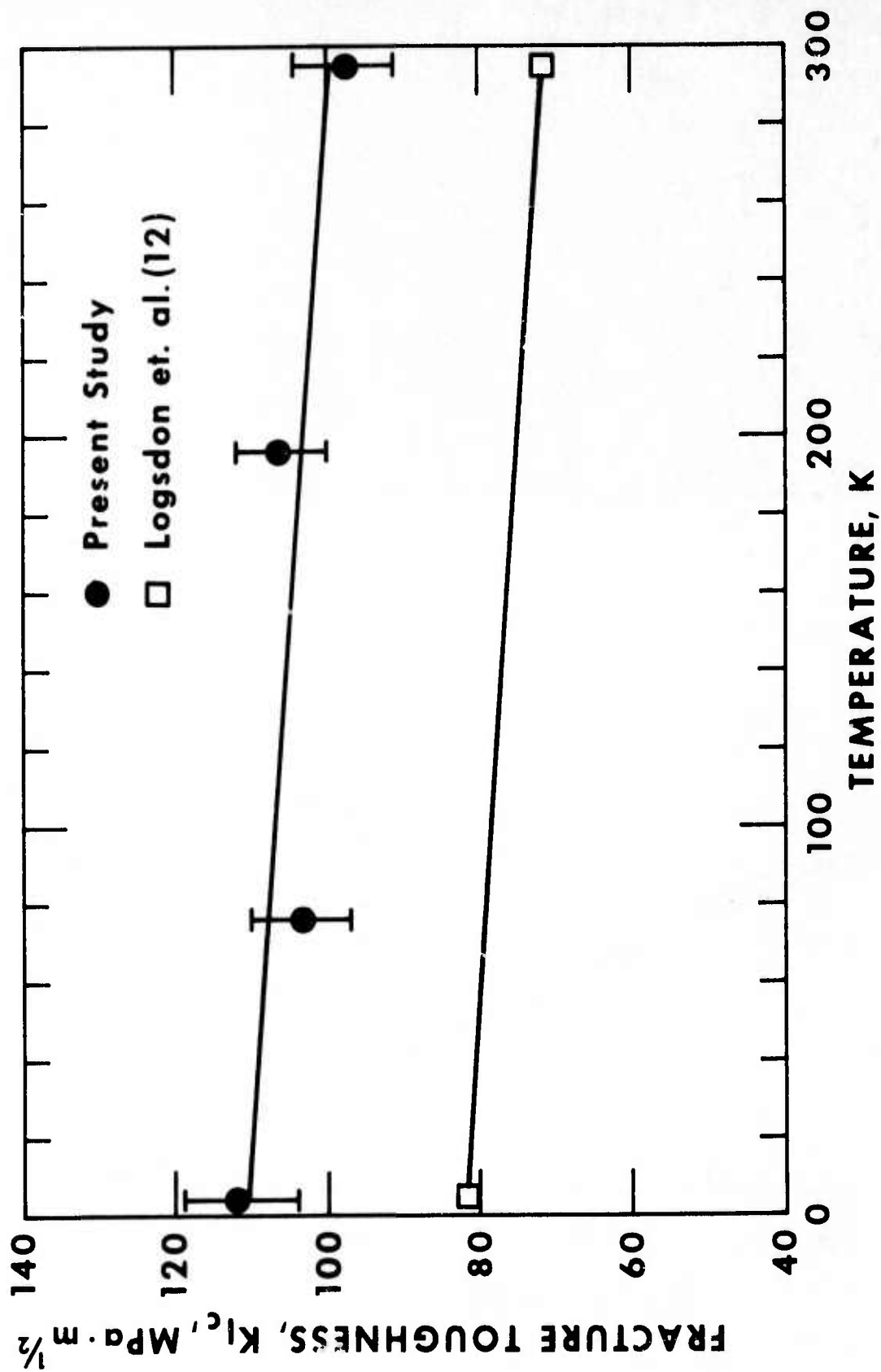


Figure 6. Temperature dependence of fracture toughness for two Inconel 718 alloys.

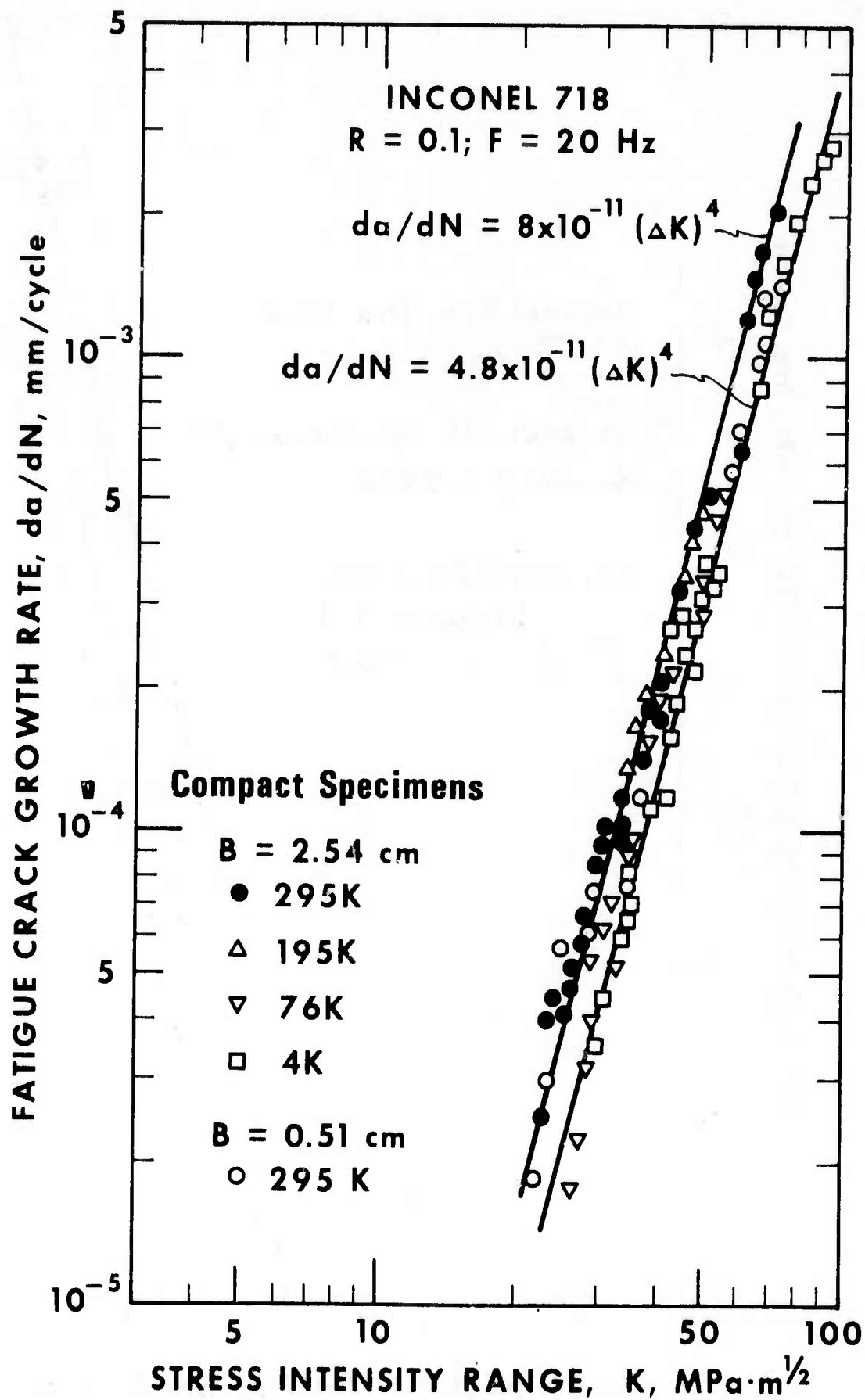


Figure 7. Fatigue crack propagation rates for Inconel 718.

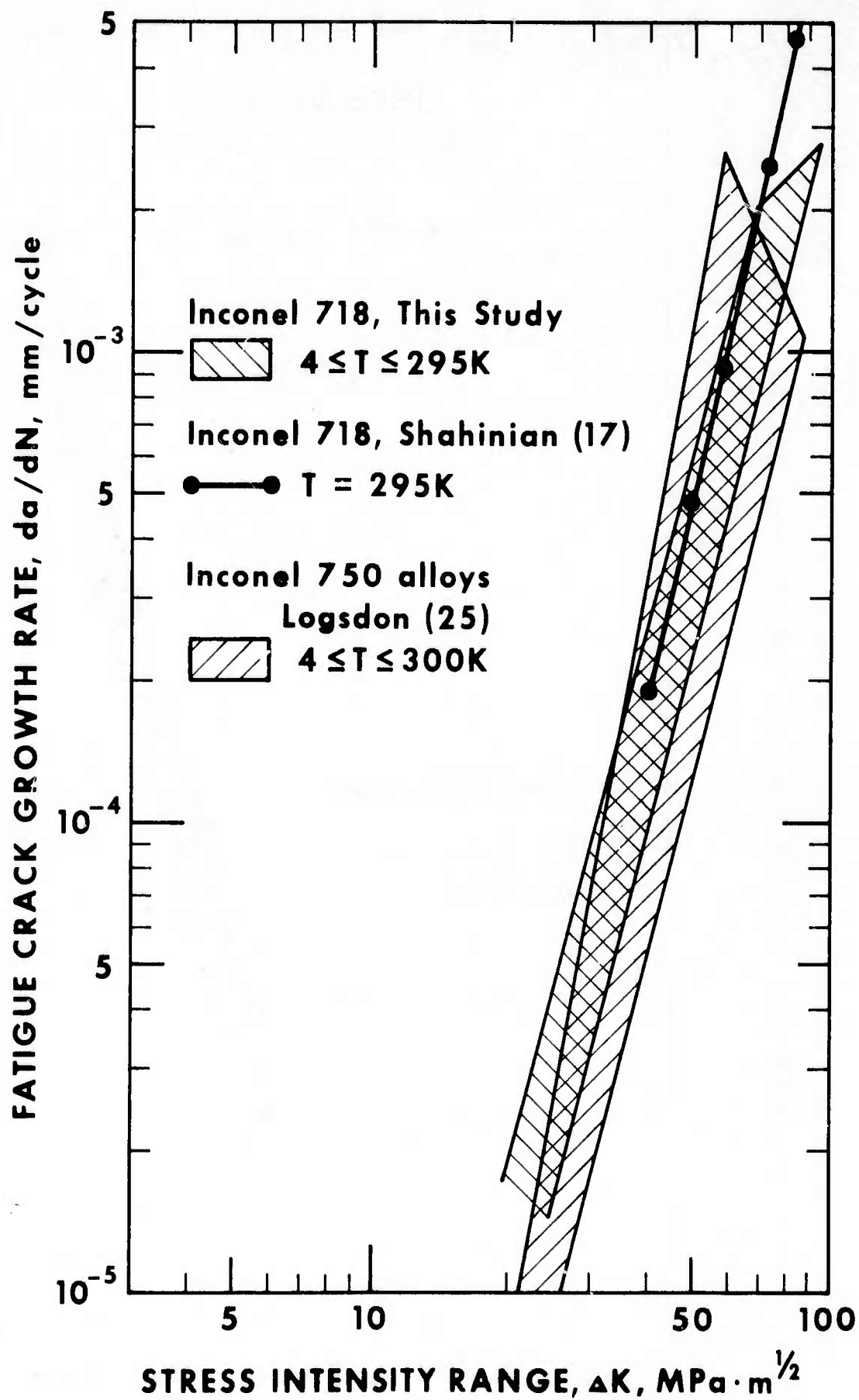


Figure 8. Comparison of fatigue crack propagation rates of Inconel alloys 718 and 750.

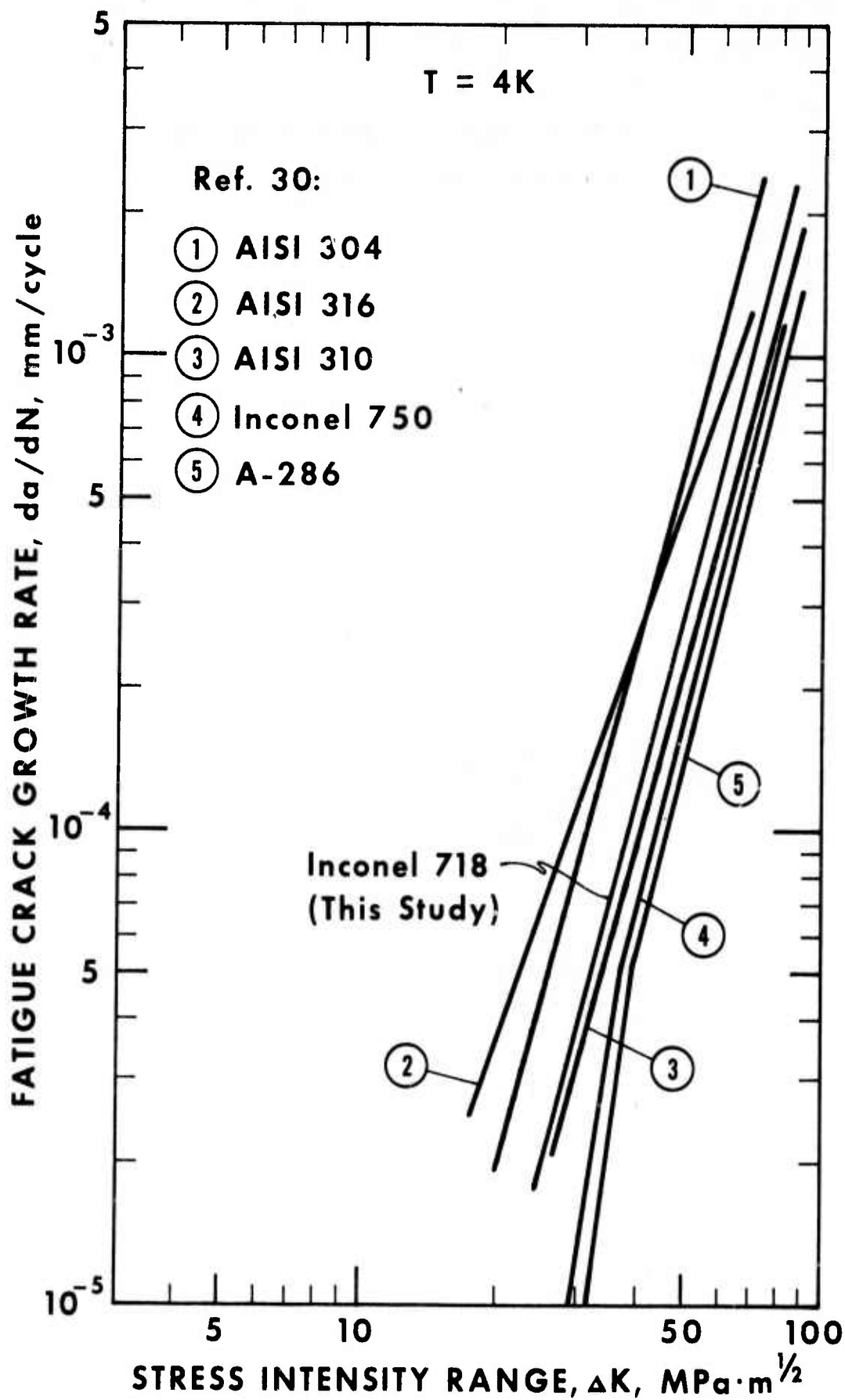


Figure 9. Comparison of fatigue crack propagation rates of Inconel 718, Inconel 750, and austenitic stainless steels at 4 K.

EFFECTS OF SPECIMEN THICKNESS ON FRACTURE
TOUGHNESS OF SOME ALUMINUM ALLOYS*

D. T. Read⁺ and R. P. Reed

Cryogenics Division
Institute for Basic Standards
National Bureau of Standards
Boulder, CO 80302

*This research was partially supported by the Advanced Research Projects Agency of the U. S. Department of Defense; it is a contribution of NBS, not subject to copyright.

⁺NRC-NBS Postdoctoral Research Associate, 1974-1975.

EFFECTS OF SPECIMEN THICKNESS ON FRACTURE
TOUGHNESS OF SOME ALUMINUM ALLOYS

J-integral resistance curves for three specimen thicknesses and valid (according to ASTM Method E 399) K_{IC} values at 76 K are reported for aluminum alloy 2219. The J-integral values were independent of thickness at small crack extensions, but at substantial crack extensions the values for the thin specimens were larger than those for the thick specimens. The measured J_{IC} values were less than those calculated from the measured K_{IC} values. The reason for this discrepancy was that crack extension occurred before the K_{IC} measurement point was reached.

Key words: Aluminum alloys; critical stress intensity, cryogenic temperature; fracture toughness; J-integral; sub-critical crack extension.

1. Introduction

The generally accepted measure of the fracture toughness of a metal is the plane strain fracture toughness, K_{IC} , as measured by ASTM Method E 399-74 (Ref. 1). However, the specimen size required for a valid measurement of K_{IC} may be so great that tests to obtain K_{IC} may be too difficult or too expensive to perform (Ref. 2). An alternative method of measuring plane strain fracture toughness known as the J-integral method (Refs. 3, 4) is being widely considered because of its less stringent requirements on specimen size. The results described in this report are of use in evaluating the J-integral method of fracture toughness testing.

The parameter characteristic of fracture toughness which is measured in a J-integral test is J_{IC} , the value of the J-integral at the onset of crack extension. In the linear elastic case, K_{IC} and J_{IC} are related as (Ref. 3):

$$J_{IC} = \frac{K_{IC}^2}{E} (1 - \nu^2) \quad (1)$$

where E is Young's modulus and ν is Poisson's ratio of the material.

The J-integral test can be traced back to the Griffith criterion (Refs. 5, 6) for crack extension and to the analytical work of Eshelby (Ref. 7). However, Rice (Ref. 8) and Begley and Landes (Refs. 3, 4) have been mainly responsible for the formulation of the current concept of the J-integral and its uses in fracture toughness testing. Landes and Begley (Ref. 4) have recently proposed a standard test method for determining J_{IC} .

There are two major obstacles to the successful implementation of the J-integral test method. The proposed test method is an attempt to resolve the first of these, namely, the choice of a measurement point. The basic procedure in a J-integral test is to determine experimentally a resistance curve consisting of a set of measured J-integral versus crack extension (J versus Δa) data points, and then to determine J_{IC} from this curve according to a rule which specifies the measurement point. In the proposed J-integral test method, the measurement point is chosen at a knee in the J- Δa curve, and thus the shape of this curve is critical to the measurement. It is asserted that if J_{IC} is chosen properly, Eq.(1) holds, and a measurement of J_{IC} is equivalent to a measurement of K_{IC} . The second major problem with the J-integral method is that the validity of Eq.(1) for useful structural materials has not been demonstrated theoretically (Ref. 9). The attempted extension of the equivalence of J_{IC} and K_{IC} from the linear elastic to the elastic plastic case has been supported by appeal to experimental results. There is evidence that for some materials J_{IC} and K_{IC} are equivalent (Ref. 4). However, J_{IC} and K_{IC} have been found not to be related by Eq. (1) in some other materials (Ref. 10).

The objectives of the present study were to determine experimentally:

- (1) J_{IC} as a function of specimen thickness for an aluminum alloy;
- (2) the relationship between J_{IC} and K_{IC} , when K_{IC} is determined according to ASTM Method E 399;
- (3) the effect of specimen thickness on the shape of the J- Δa curve.

Information of this kind is quite scarce, and is necessary before the J-integral method can be standardized as a reliable test method.

2. Materials

Two aluminum alloys, 2014-T652 and 2219-T87, were used as specimen materials. The chemical compositions of these alloys are given in Table 1. The 2014-T652 designation indicates that this material has been heat-treated, artificially aged, and stress relieved by compressing. The 2219-T87 designation indicates that this material has been solution heat-treated, cold-worked, and then artificially aged. After polishing and etching, the grains in both alloys were seen to be severely elongated. A section cut perpendicular to the rolling direction shows some grains about .02 cm (.008 inch) in diameter and some larger grains of various sizes in the 2014 alloy, while the same treatment reveals grains about .03 cm (.012 inch) in diameter in the 2219 alloy. On sections cut parallel to the rolling direction, only grain boundaries approximately parallel to the rolling direction, spaced .02 cm were seen in the 2014 alloy. The 2014-T652 and 2219-T87 alloys had Rockwell hardness of B 80.6 and B 81.1, respectively.

The yield strength σ_y , ultimate tensile strength σ_{uts} , Young's modulus E , Poisson's ratio ν , and plane strain fracture toughness K_{IC} values obtained for the two alloys tested are listed in Tables 2 and 3 (Ref. 11). For measurements of K_{IC} and J , the 2014 alloy specimens were machined in the L-T orientation, and the 2219 specimens were machined in the T-L orientation. For comparison, handbook (Ref. 12) values of K_{IC} are also shown. The unusually high K_{IC} of the 2014 alloy specimens is probably due to nonuniformities in the specimen material produced during forging. Metallographic evidence for such nonuniformities is discussed below. Originally, the 2014 alloy was chosen for its availability and the convenience of machining and testing the specimens. The 2014 alloy specimens were cut

from a 7.6 cm (3 inch) thick forged plate.

The J - Δa data for the 2014 alloy summarized in Table 4 exhibited an uneven dependence of J upon Δa . This scatter was attributed to variation of properties among the specimens. The specimens used in the tests were examined metallographically. On sections cut perpendicular to the rolling direction, some relatively large grains several millimeters in diameter were observed along with the small grains .02 cm in diameter. The fraction of the surface which was made up of small grains was recorded in Table 4 for the 2014 alloy specimens. Both the raw J - Δa data and the data classified by grain size for the 2014 alloy exhibited so much scatter that they were useless for the purposes of the present study. For this reason, a plate 3.8 cm (1.5 inch) thick of aluminum alloy 2219-T87 was obtained and tested. The remainder of this report is concerned with the results of measurements made on the 2219 alloy.

3. Procedures

The specimen geometry used was a modified compact specimen, as shown in Fig. 1. The normal dimensions of all the specimens tested are listed in Table 5. Tests were conducted in an electrohydraulic testing apparatus equipped with a stand-off and dewar for cryogenic service which has been described previously (Ref. 13). The specimens were mounted in the loading fixtures and cooled to 76 K by immersion in liquid nitrogen. Each specimen was precracked by loading in tension-tension fatigue at 20 Hz at a load which in most cases was 60% or less of the quasistatic load used in the J test. The precracking was continued to a nominal crack length of $a/W = .60$. Typically the precrack reached the desired length of about .5 cm (.2 inch) after approximately 60,000 fatigue cycles. After precracking, each specimen was loaded quasistatically to a stress

equal to or less than the maximum load used in the precracking procedure, and the load-displacement line was recorded. This line was extended to high loads, and a secant line deviating from this anticipated load line by a preselected amount was also drawn. After these preliminary steps, the quasistatic crack extension was accomplished by loading the specimen until the actual load-displacement curve intersected the pre-drawn secant line, and immediately unloaded. Then the specimen was refatigued, beginning with a load of about half the maximum load reached during the measurement of the load-displacement curve. After the refatigue crack had grown to several millimeters in length, the specimen was pulled apart so that the fracture surfaces were accessible for examination. The crack growth produced during the static load cycle was visible as a dark, rough band between the two bright, relatively smooth, fatigue surfaces.

Each value of the J-integral was computed from the load-displacement record obtained during the static load cycle, using the procedure recommended by Merkle and Corten (Ref 14). This procedure results in a value of the J-integral of

$$J = \frac{\lambda A}{Bb}, \quad (2)$$

where A is the area under the load displacement curve, B is the specimen thickness, b is the specimen ligament remaining after precracking, and λ is a function of the crack length and the nonlinearity of the load-displacement record. The value of λ was approximately 2.4 in all the tests performed in this study.

In the proposed standard method for determining J_{Ic} (Ref. 4) the crack extension Δa is defined to include both the stretch zone and the zone of material separation, if any. If the crack extension consists

only of a stretch zone, the J - Δa graph is expected to fall along the line given by

$$J = 2 \sigma_{flow} \Delta a \quad (3)$$

where σ_{flow} is the arithmetic mean of the yield strength and the ultimate tensile strength. J_{IC} is defined as the value of J at the intersection of the line given by Eq.(3) with the back-extrapolation of the J - Δa curve from the region where material separation does take place. According to the proposed method, the back-extrapolated J - Δ curve is expected to have a slope different from that of the line given by Eq.(3), so that the measured J - Δa curve ought to have a relatively sharp knee in it.

Because of the relatively high value of the yield and ultimate tensile stresses of the 2219-T87 alloy, J_{IC} as defined by this proposed standard occurs at a crack extension of less than .002 cm. Due to the difficulty of measuring extremely small values of crack extensions, and the apparent unreliability of extrapolating to zero crack extension, the initiation of crack extension was taken as the point of .005 cm crack extension for purposes of the present study. This point was determined by interpolation or extrapolation on graphs of J - Δa . The J_{IC} values obtained in this way were higher than those which could have been obtained by extrapolation according to the proposed standard, but they were less uncertain.

4. Results and Discussion

The J - Δa data for aluminum alloy 2219 are listed in Table 6 and plotted in Fig. 2. The J_{IC} values obtained from the J - Δa curves are listed in Table 7. The values of J_{IC} range from 9.5 to 10.3 kJ \cdot m⁻²

over a tenfold variation in specimen thickness. Thus, J_{IC} is indeed a thickness-independent measure of the fracture resistance of the material.

Using the measured value of K_{IC} and Eq. (1), one would expect a J_{IC} of $13.6 \text{ kJ} \cdot \text{m}^{-2}$, 38% larger than the values actually found. Thus, for aluminum alloy 2219, K_{IC} and J_{IC} are not related by Eq. (1). This finding was attributed to the difference in the measurement point for the two test methods; subsequent experimental measurements showed this to be the correct explanation for the observed discrepancy. The measurement point for determining J_{IC} was chosen as the initiation of crack extension, whereas the measurement point for determining K_{IC} was chosen as set forth in ASTM Method E 399, that is, at 2% apparent crack extension. The apparent crack extension includes the plastic zone, but the possibility exists that significant actual crack extension may occur before the K_{IC} measurement point is reached. If this is the case, the values of K_{IC} obtained may be characteristic of a somewhat extended crack, and not of crack initiation. This possibility is widely suspected (Ref. 15) as a cause of discrepancy between observed values of K_{IC} and J_{IC} as related by Eq. (1), and was used by Logsdon (Ref. 10) to explain some of his data. But it appears that this explanation has never been tested experimentally.

To determine the extent of crack extension in a valid K_{IC} test, three 3.8 cm (1.5 inch) thick compact tensile specimens, more than twice as thick as necessary to obtain valid K_{IC} data, were tested according to the J-procedure described in Section 3. In two tests, the specimen was unloaded prior to the intersection of the load line with the 5% offset secant, and in the other test the specimen was unloaded just after this intersection. The records of these tests were analyzed as follows. A

line was drawn through the origin of the test record and the point on the record at which unloading was begun. The percent difference between the slope of this secant line and the tangent to the initial linear portion of the load record, referred to as the percent secant deviation, was recorded. This procedure allowed a correlation of secant deviation with crack extension to be made. The data are listed in Table 8 and plotted in Fig. 3. These data clearly show that the critical point in the K_{IC} test of 2219 aluminum alloy, that is, the point of 5% secant deviation, occurs at a crack extension of about .064 cm (.025 inch) in specimens which satisfy the thickness requirements by a wide margin. As a double check, a similar plot for the 1.42 cm (.56 inch) thick specimens, which are almost exactly in the minimum thickness required in a K_{IC} test, shows the same characteristic; i.e., crack extension of about .064 cm (.025 inch) before the 5% secant offset is reached. If the J_{IC} evaluation point were chosen not at crack initiation but at .064 cm (.025 inch) crack extension in these specimens, good agreement could be found between K_{IC} and J_{IC} . Thus, the discrepancy between the measured values of K_{IC} and J_{IC} related by Eq. (1) is explained. However, because of the observed dependence of the J integral value at significant crack extensions on specimen thickness, the critical state for J_{IC} measurement cannot be chosen as a point of significant crack extension such as .064 cm (.025 inch) because this would defeat the purpose of J-integral testing, which is to obtain a parameter characteristic of the material tested independent of specimen thickness. Thus, in this alloy it is impossible to obtain agreement between K_{IC} and J_{IC} in Eq.(1) that is independent of thickness.

An obvious feature of the J-resistance curves of Fig. 2 is that the curves for the three different material thicknesses separate for

the larger values of crack extension but converge near zero crack extension. It can be seen for this material that the effect of increasing specimen thickness is to decrease the J values at sizable values of Δa while leaving them unchanged, within experimental uncertainties, near zero crack extension. A similar divergence in thickness was observed by Griffis and Yoder (Ref. 16) for 2024-T351 aluminum tested at room temperature using a three-point-bend specimen and thus may be a normal feature of J-integral behavior of many aluminum alloys. Thickness effects are discussed further in the Appendix below.

5. Conclusions

The following conclusions have been drawn from the present study:

(1) In specimens cut from a plate of 2219 aluminum alloy, crack extension was initiated at a constant value of the J-integral over a ten-fold range of specimen thickness, extending from well above to well below the minimum specimen thickness given in ASTM Method E 399 for valid K_{IC} measurement. This result supports the hypothesis that J_{IC} is a useable measure of material toughness.

(2) J_{IC} and K_{IC} (K_{IC} determined according to ASTM Method E 399) are not equivalent measurements of fracture toughness for 2219 aluminum because of subcritical crack growth in K_{IC} tests; the J_{IC} value anticipated from measurements of K_{IC} was 38% larger than the measured J_{IC} value.

(3) As crack extension increased, the J-integral value was significantly larger for thin specimens than for thick ones.

Appendix. Observations on Plane Stress Toughening

The specimen thickness B may be expressed in dimensionless form:

$$\gamma = \frac{B}{(K_{IC}/\sigma_y)^2} \quad (A1)$$

The parameter γ can be used as an index of the operative fracture mode. The possible modes are plane strain, mixed, and plane stress. According to Eq.(A1) and the measured values of the parameters K_{Ic} and σ_y , the samples used in the present study fall at $\gamma = .72, 1.34, 2.68$, and 7.19 . Values of γ equal to or greater than 2.5 correspond to the criteria of ASTM Method E-399 for plane strain testing. Thus, for values of γ below 2.5 , we may expect plane stress toughening effects, whereas for γ above 2.5 plane strain should dominate. A strong increase in apparent sample toughness is to be expected as the thickness is decreased (Ref. 17).

An experimental search for such a dependence of apparent toughness on specimen thickness may be made by observing the maximum stress intensity sustained by the samples as a function of thickness. Such stress intensities may be calculated using the maximum load sustained by the sample and the crack length present at the initiation of loading. Values of the maximum stress intensity measured in this manner are denoted K_M . K_M may be corrected for the plastic zone size as follows. First, the plastic zone radius is calculated from the uncorrected stress intensity according to (Ref. 18):

$$r_y = \frac{1}{2\pi} \left(\frac{K_{Ic}}{\sigma_y} \right)^2 \quad (A2)$$

Then the effective crack length $a_{eff} = a + r_y$ is used to find the first corrected stress intensity factor according to:

$$K_{Ic} = \frac{P f(a_{eff}/W)}{B W^{1/2}} \quad (A3)$$

where $f(\frac{a_{eff}}{W})$ is given by Newman (Ref. 19). This corrected stress intensity is used to calculate a new value of r_y , which is then used to calculate a new stress intensity, and the iteration continues in this manner. If this process converges, the final value of r_y is not too large and the plastic zone correction has been made successfully. An asterisk indicates a stress intensity value which includes the plastic zone correction. For instance, K_{M*} is the stress intensity at maximum load corrected for the plastic zone.

Measured values of K_M and K_{M*} are listed in Table A-1 and plotted versus thickness in Fig. A-1. The classic decrease of this measure of material toughness with increasing specimen thickness is emphasized by the plastic zone correction. The curve shown in this figure is given by

$$K_{M*} = K_{Ic} \sqrt{1.4 \gamma^{-2}} \quad (A4)$$

where γ was defined in Eq.(A1). This equation was used by Irwin et al. (Ref. 19) to curve-fit some fracture toughness data on aluminum. The qualitative agreement between this curve and the measured values of K_{M*} indicates that the anticipated strong increase in apparent sample toughness with decreasing thickness was indeed found in the present study. The increase of K_{M*} indicates that plane stress toughening occurs as the specimen thickness decreases. From these data, we may conclude that the border between plane strain and mixed modes occurs at about $\gamma = 2.5$; thus, the requirements of ASTM Method E-399 are adequate to insure plane strain conditions, but are not excessive. Due to limitations on the specimen size, the pure plane stress region was not attained in these tests. Nevertheless, the data are sufficient to show tendencies of the difference between plane strain and plane stress modes of fracture.

References

1. Standard Method of Test for Plane Strain Fracture Toughness of Metallic Materials (Designation E 399-74), 1974 Annual Book of ASTM Standards, Part 10, 1974, pp. 432-451.
2. Kaufman, J. G. and Kelsey, R. A., in: Properties of Materials for Liquefied Natural Gas Tankage, ASTM STP 579, American Society for Testing and Materials, Philadelphia, PA (1975), pp. 138-158.
3. Begley, J. A. and Landes, J. D., in: Fracture Toughness, Proceedings of the 1971 National Symposium on Fracture Mechanics, Part II, ASTM STP 514, American Society for Testing and Materials, Philadelphia, PA (1972), pp. 1-20.
4. Landes, J. D. and Begley, J. A., in: Fracture Analysis, ASTM STP 560, American Society for Testing and Materials, Philadelphia, PA (1974), pp. 170-186.
5. Griffith, A. A., Phil. Trans. Royal Soc. 221A, 163 (1920-21); Reprinted with corrections in Trans. Quart. ASM 61, 861 (1968).
6. Griffith, A. A., Proc. First International Congress on Applied Mechanics, Delft (1924), p. 55.
7. Eshelby, J. D., "The Force on an Elastic Singularity," Trans. Roy. Soc. Lond. A244, 87 (1951).
8. Rice, J. R., in: Fracture, Vol. II, H. Liebowitz, ed., Academic Press, New York (1968), p. 191.
9. Eftis, J. and Liebowitz, H., Engr. Fracture Mechanics 7, 101 (1975).
10. Logsdon, A. W., "Elastic Plastic (J_{IC}) Fracture Toughness Values: Their Experimental Determination and Comparison with Conventional Linear Elastic (K_{IC}) Fracture Toughness Values for Five Materials," Westinghouse Research Laboratories, Pittsburgh, PA, Scientific Paper 74-1E7-FMPWR-P1 (1974).

11. The yield strengths, ultimate tensile strengths, and fracture toughnesses were measured using standard techniques; Young's modulus and Poisson's ratio for the specimen materials were measured by an ultrasonic technique as described by D. T. Read and H. M. Ledbetter, to be published.
12. Matthews, W. T., "Plain Strain Fracture Toughness (K_{IC}) Data Handbook for Metals," Army Materials and Mechanics Research Center, AMMRC MS 73-6, Watertown, MA (1973).
13. Fowlkes, C. W. and Tobler, R. L., "Fracture Testing and Results for a Ti-6Al-4V Alloy at Liquid Helium Temperature," to be published in Engineering Fracture Mechanics.
14. Merkle, J. G. and Corten, H. T., "A J-Integral Analysis for the Compact Specimen, Considering Axial Force as Well as Bending Effects," presented at the Pressure Vessels and Piping Conference with Nuclear Engineering and Mechanical Divisions, American Society Mechanical Engineers, Paper No. 74-PVP-33 (1974).
15. Tobler, R., Sha, G. and Begley, J., personal communication.
16. Griffis, C. A. and Yoder, G. R., "Application of the J-Integral to Crack Initiation in a 2024-T351 Aluminum Alloy," Naval Research Report 7676, (1974), p. 21.
17. Srawley, J. E. and Brown, W. F., in: Fracture Toughness Testing and Its Applications, ASTM STP 381, American Society for Testing and Materials, Philadelphia, PA (1965), pp. 133-196.
18. Weiss, V. and Yukawa, S., in: Fracture Toughness Testing and Its Applications, ASTM STP 381, American Society for Testing and Materials, Philadelphia, PA (1965), pp. 1-22.

19. Newman, J. C., Jr., in: Fracture Analysis, ASTM STP 560, American Society for Testing and Materials, Philadelphia, PA (1974), pp. 105-121.
20. Irwin, G. R., Krafft, J. M., Paris, P. C., Wells, A. A., "Basic Aspects of Crack Growth and Fracture," Naval Research Laboratory Report No. 6598, 1967, p. 50.

LIST OF TABLES

- Table 1. Chemical compositions of the alloys, wt. %.
- Table 2. Tensile and fracture data for aluminum alloy 2014-T652 in the L-T orientation.
- Table 3. Tensile and fracture data for aluminum alloy 2219-T87 in the T-L orientation.
- Table 4. J-integral data for aluminum alloy 2014-T652 in the T-L orientation at 76 K.
- Table 5. Dimensions of specimens used in the present study.
- Table 6. J-integral data for aluminum alloy 2219-T87 in the L-T orientation at 76 K.
- Table 7. Measured and predicted (from K_{IC}) values of J_{IC} for four specimen thicknesses of aluminum alloy 2219-T87 at 76 K.
- Table 8. Measured values of crack extension and secant deviation for two specimen thicknesses of aluminum alloy 2219-T87 at 76 K.
- Table A1. Maximum stress intensity and maximum stress intensity corrected for the plastic zone for four specimen thicknesses of aluminum alloy 2219-T87 at 76K.

Table 1. Chemical compositions of the alloys, wt. %.^a

	Cu	Fe	Mg	Mn	Si	Ti	V	Zn	Zr
2014	4.4		0.5	0.8	0.8				
2219	6.4	0.20	<.01	0.26	0.15	0.16	0.12	0.09	0.16

^a For 2014, nominal composition. For 2219, plasma arc analysis.

Table 2. Tensile and fracture data for aluminum alloy 2014-T652 in the L-T orientation.

T(K)	300	76	4
σ_y (MPa)	405	442	561
	<u>402</u>	<u>436</u>	<u>534</u>
	Avg = 403.5	Avg = 439.	Avg = 547.
σ_y (ksi)	58.8	64.1	81.3
	<u>58.4</u>	<u>63.3</u>	<u>77.4</u>
	Avg = 58.6	Avg = 63.7	Avg = 79.4
σ_{uts} (MPa)	476	524	700
	<u>475</u>	<u>536</u>	<u>663</u>
	Avg = 475.5	Avg = 530.	Avg = 681.5
σ_{uts} (ksi)	69.1	76.0	101.5
	<u>68.9</u>	<u>77.7</u>	<u>96.2</u>
	Avg = 69.0	Avg = 76.8	Avg = 98.8
E(GPa)	75.6	83.3	83.8
E(Msi)	11.0	12.1	12.1
ν	.341	.331	.330
K_{Ic} (MPa $\cdot m^{1/2}$)	53.4	49.9	53.4
	<u>46.7</u>	53.4	
	Avg = 50.1	<u>51.3</u>	
		Avg = 51.5	
K_{Ic} (ksi $\cdot in^{1/2}$)	48.6	45.4	48.6
	<u>42.5</u>	48.6	
	Avg = 45.6	<u>46.7</u>	
		Avg = 46.9	
K_{Ic} (MPa $\cdot m^{1/2}$)	26.4	33.0	---
(handbook value)			
K_{Ic} (ksi $\cdot in^{1/2}$)	24	30	---
(handbook value)			

Table 3. Tensile and fracture data for aluminum alloy 2219-T87 in the T-L orientation.

T(K)	300	76	4
σ_y (MPa)	411	490	547
	<u>412</u>	<u>496</u>	<u>514</u>
	Avg = 411.5	Avg = 493.	Avg = 531.
σ_y (ksi)	59.6	71.1	79.4
	<u>59.7</u>	<u>72.0</u>	<u>74.6</u>
	Avg = 59.65	Avg = 71.6	Avg = 77.0
σ_{uts} (MPa)	509	630	734
	<u>503</u>	<u>630</u>	<u>706</u>
	Avg = 506.	Avg = 630.	Avg = 720.
σ_{uts} (ksi)	73.8	91.4	106.5
	<u>73.0</u>	<u>91.3</u>	<u>102.4</u>
	Avg = 73.4	Avg = 91.35	Avg = 104.4
E(GPa)	77.4	85.2	85.7
E(Msi)	11.2	12.4	12.4
ν	.330	.319	.318
K_{Ic} (MPa $\cdot m^{1/2}$)	31.0	37.2	---
	<u>30.6</u>	<u>33.5</u>	---
	Avg = 30.8	Avg = 35.9	
K_{Ic} (ksi $\cdot in^{1/2}$)	28.2	33.9	---
	<u>27.9</u>	<u>30.5</u>	---
	Avg = 28.1	Avg = 32.7	
K_{Ic} (MPa $\cdot m^{1/2}$) (handbook value) ¹⁴	33.0	---	---
K_{Ic} (ksi $\cdot in^{1/2}$) (handbook value) ¹⁴	30.0	---	----

Table 4. J-integral data for aluminum alloy 2014-T651 in the T-L orientation at 76 K.

Sample #	B(cm)	B(in)	b(cm)	b(in)	Δa (cm)	$\Delta a(10^{-3} \text{ in})$	$J(\frac{\text{kJ}}{\text{m}^2})$	$J(\frac{\text{in-lb}}{\text{in}^2})$	% small grains
A-6	.508	0.2	3.71	1.46	.011	4.3	33.6	191.9	10%
A-15	.508	0.2	3.56	1.40	.027	10.5	54.0	308.2	30%
A-1	.508	0.2	3.58	1.41	.036	14.2	29.6	169.2	100%
A-2	.508	0.2	3.62	1.42	.071	27.8	56.0	320.0	50%
A-3	.508	0.2	3.66	1.44	.116	45.2	100.5	573.7	50%
B-8	1.27	0.5	3.61	1.42	.009	3.4	13.4	76.8	100%
B-3	1.27	0.5	3.35	1.32	.009	3.5	26.7	152.3	20%
B-7	1.27	0.5	3.56	1.40	.010	4.0	17.1	97.8	60%
B-2	1.27	0.5	3.43	1.35	.033	13.0	27.3	156.0	100%
B-6	1.27	0.5	3.48	1.37	.045	17.9	24.9	142.0	100%
B-1	1.27	0.5	3.43	1.35	.054	21.2	34.7	197.9	40%
B-5	1.27	0.5	3.45	1.36	.057	22.5	46.2	264.1	0%
B-4	1.27	0.5	3.53	1.39	.141	55.5	37.5	214.2	50%
C-6	2.54	1.0	3.63	1.43	.008	3.1	13.2	75.1	50%
C-1	2.54	1.0	3.45	1.36	.017	6.6	21.1	120.5	100%
C-5	2.54	1.0	3.51	1.38	.018	7.0	30.2	172.7	20%
C-8	2.54	1.0	3.63	1.43	.036	14.1	28.6	162.9	60%
C-3	2.54	1.0	3.68	1.45	.056	22.0	33.0	188.7	25%
C-7	2.54	1.0	3.51	1.38	.067	26.5	40.3	230.3	50%
C-4	2.54	1.0	3.38	1.33	.129	50.9	37.6	215.0	50%
C-2	2.54	1.0	3.30	1.30	.218	86.0	59.2	338.3	100%

Table 5a. Dimensions of aluminum 2014 specimens used in the present study. B and W have the meanings indicated in Fig. 1.

B	W	a	Number of specimens tested
0.51 cm (0.2 in)	7.62 cm (3 in)	4.57 cm (1.8 in)	5
1.27 cm (0.5 in)	7.62 cm (3 in)	4.57 cm (1.8 in)	7
2.54 cm (1.0 in)	7.62 cm (3 in)	4.57 cm (1.8 in)	7
3.81 cm (1.5 in)	7.62 cm (3 in)	4.01 cm (1.58 in)	6

Table 5b. Dimensions of aluminum 2219 specimens used in the present study. B and W have the meanings indicated in Fig. 1.

B	W	a	Number of specimens tested
0.38 cm (.15 in)	5.08 cm (2 in)	3.05 cm (1.2 in)	5
0.72 cm (.28 in)	5.08 cm (2 in)	3.05 cm (1.2 in)	5
1.44 cm (.56 in)	5.08 cm (2 in)	3.05 cm (1.2 in)	5
3.81 cm (1.5 in)	7.62 cm (3 in)	4.19 cm (1.65 in)	7

Table 6. J-integral data for aluminum alloy 2219-T87 in the L-T orientation at 76 K.

Sample #	B(cm)	B(in)	b(cm)	b(in)	Δa (cm)	$\Delta a(10^{-3} \text{ in})$	$J(\frac{\text{kJ}}{\text{m}^2})$	$J(\frac{\text{in-lb}}{\text{in}^2})$
A-4	.38	.15	2.03	.80	0	0	10.0	57.2
A-5	.38	.15	2.04	.80	.013	5.1	12.6	72.1
A-3	.38	.15	2.03	.80	.033	12.8	16.7	95.4
A-1	.38	.15	2.04	.80	.074	29.0	21.8	124.6
A-2	.38	.15	2.02	.80	.130	51.0	33.7	192.3
B-4	.71	.28	2.03	.80	.001	0.4	9.6	54.7
B-5	.71	.28	2.09	.82	.008	3.4	10.9	62.2
B-3	.71	.28	2.06	.81	.024	9.3	13.1	74.8
B-1	.71	.28	2.11	.83	.097	38.1	12.5	105.5
B-2	.71	.28	2.06	.81	.183	71.9	27.3	155.8
C-3	1.42	.56	2.08	.82	.002	0.7	9.0	51.5
C-5	1.42	.56	2.02	.80	.013	5.1	11.7	66.8
C-1	1.42	.56	2.09	.82	.020	8.0	13.0	74.1
C-2	1.42	.56	1.99	.78	.076	30.0	16.6	94.6
C-7	1.42	.56	2.01	.79	.157	62.0	20.2	115.3
D-7	3.81	1.5	3.65	1.44	.009	3.8	10.0	56.9
D-6	3.81	1.5	3.47	1.37	.067	26.2	13.4	76.4
D-5	3.81	1.5	3.51	1.38	.072	28.5	14.8	84.8

Table 7. Measured and predicted (from K_{Ic}) values of J_{Ic} for four specimen thicknesses of aluminum alloy 2219-T87 at 76 K.

B(cm)	B(in)	J_{Ic} (kJ/m ²) ^{MEASURED}	J_{Ic} ($\frac{in-lb}{in^2}$) ^{MEASURED}	J_{Ic} (kJ/m ²) ^{PREDICTED}	J_{Ic} ($\frac{in-lb}{in^2}$) ^{PREDICTED}
.38	.15	10.3	59	13.6	77.5
.71	.28	10.0	57	13.6	77.5
1.42	.56	9.6	55	13.6	77.5
3.81	1.50	9.5	54	13.6	77.5

Table 8. Measured values of crack extension and secant deviation for two specimen thicknesses of aluminum alloy 2219-T87 at 76 K.

Sample #	B(cm)	B(in)	Δa (cm)	$\Delta a(10^{-3} \text{ in})$	secant deviation (per cent)
C-3	1.42	.56	.002	.7	0
C-5	1.42	.56	.013	5.1	0
C-1	1.42	.56	.020	8.0	2.1
C-2	1.42	.56	.076	30.0	7.1
C-7	1.42	.56	.157	62	14.0
D-7	3.81	1.5	.010	3.8	3.0
D-6	3.81	1.5	.067	26.2	4.0
D-5	3.81	1.5	.072	28.5	5.7

Table A1. Maximum stress intensity and maximum stress intensity corrected for the plastic zone for four specimen thicknesses of aluminum alloy 2219-T87 at 76 K.

Sample #	B(cm)	B(in)	K_M (MPa·m ^{1/2})	K_M (ksi·in ^{1/2})	K_M^* (MPa·m ^{1/2})	K_M^* (ksi·in ^{1/2})
A-4	.38	.15	46.2	42.0	57.6	52.4
B-4	.71	.28	38.1	34.7	42.3	30.5
C-4	1.42	.56	34.8	31.7	37.9	34.5
D-7	3.81	1.5	34.1	31.0	35.6	32.4
O-1	3.81	1.5	37.6	34.2	39.3	35.8
O-2	3.81	1.5	37.8	34.4	39.6	36.0

List of Figures

- Figure 1. Specimen configuration used in the present study.
- Figure 2. J- Δa data for aluminum alloy 2219.
- Figure 3. Secant deviation versus crack extension for aluminum alloy 2219.
- Figure A1. Observed maximum stress intensity versus specimen thickness.

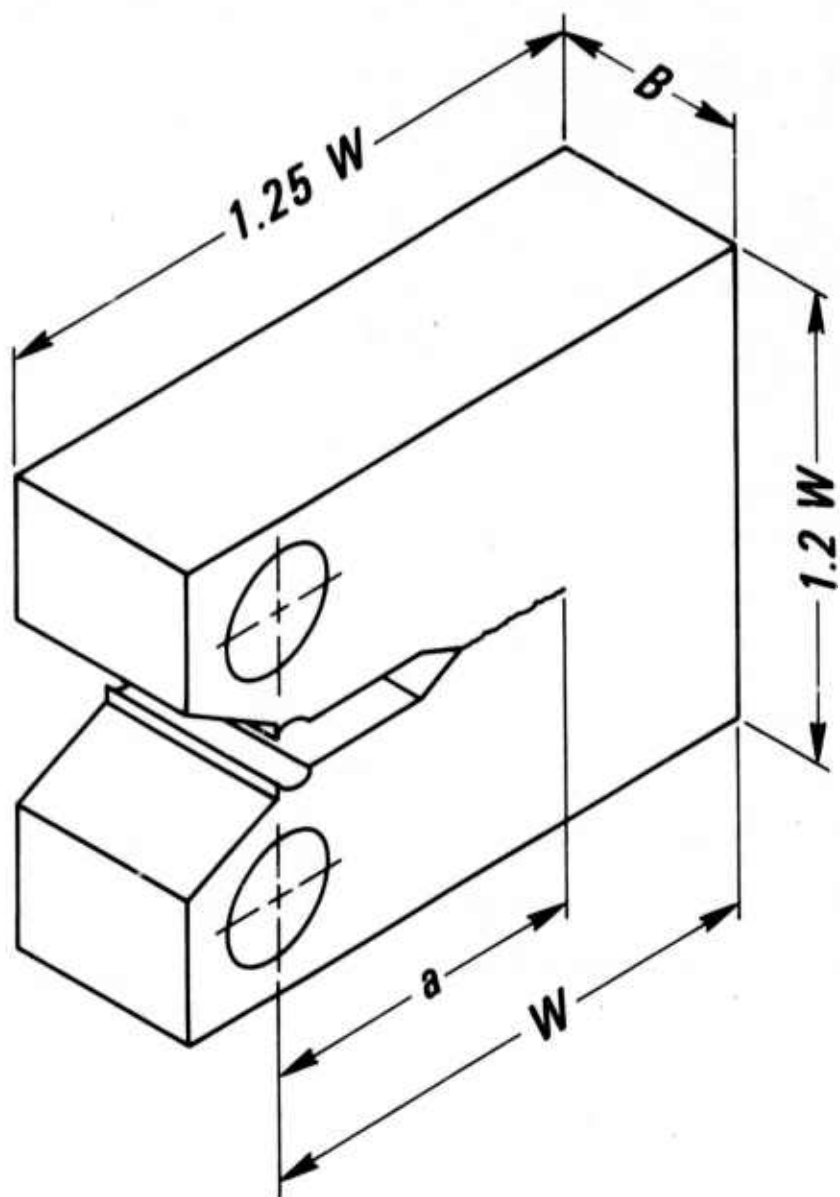


Figure 1. Specimen configuration used in the present study.

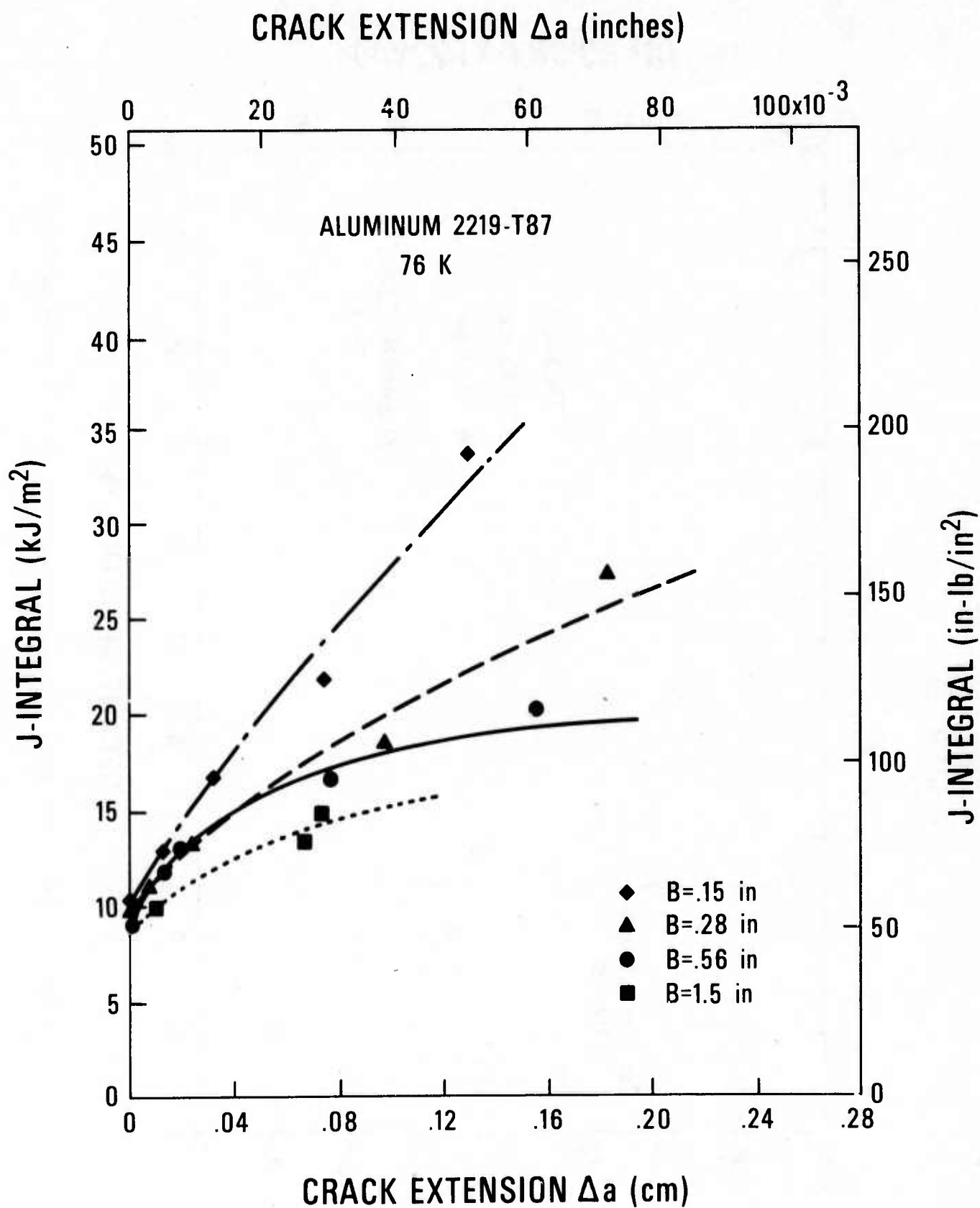


Figure 2. J- Δa data for aluminum alloy 2219.

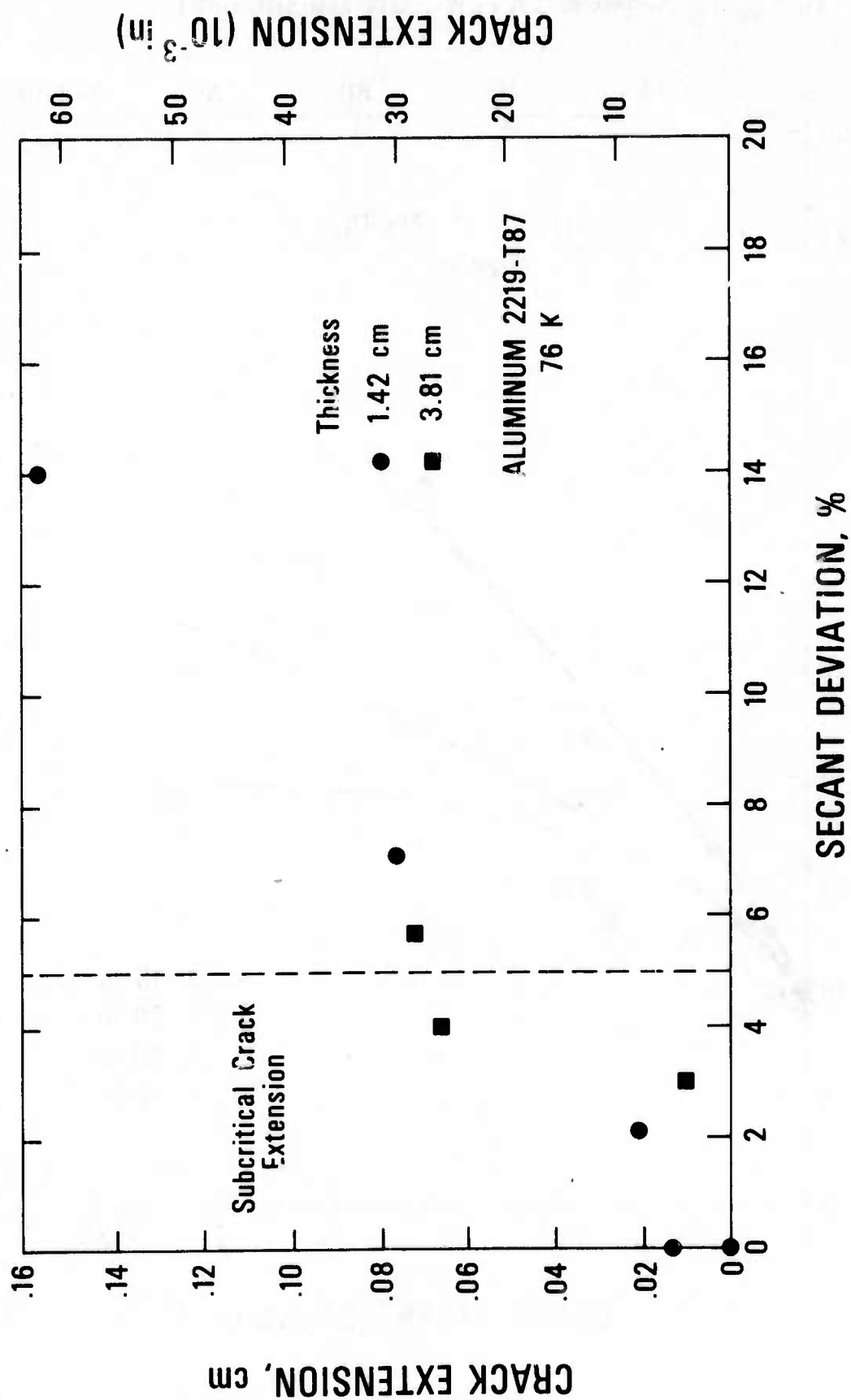


Figure 3. Secant deviation versus crack extension for aluminum alloy 2219.

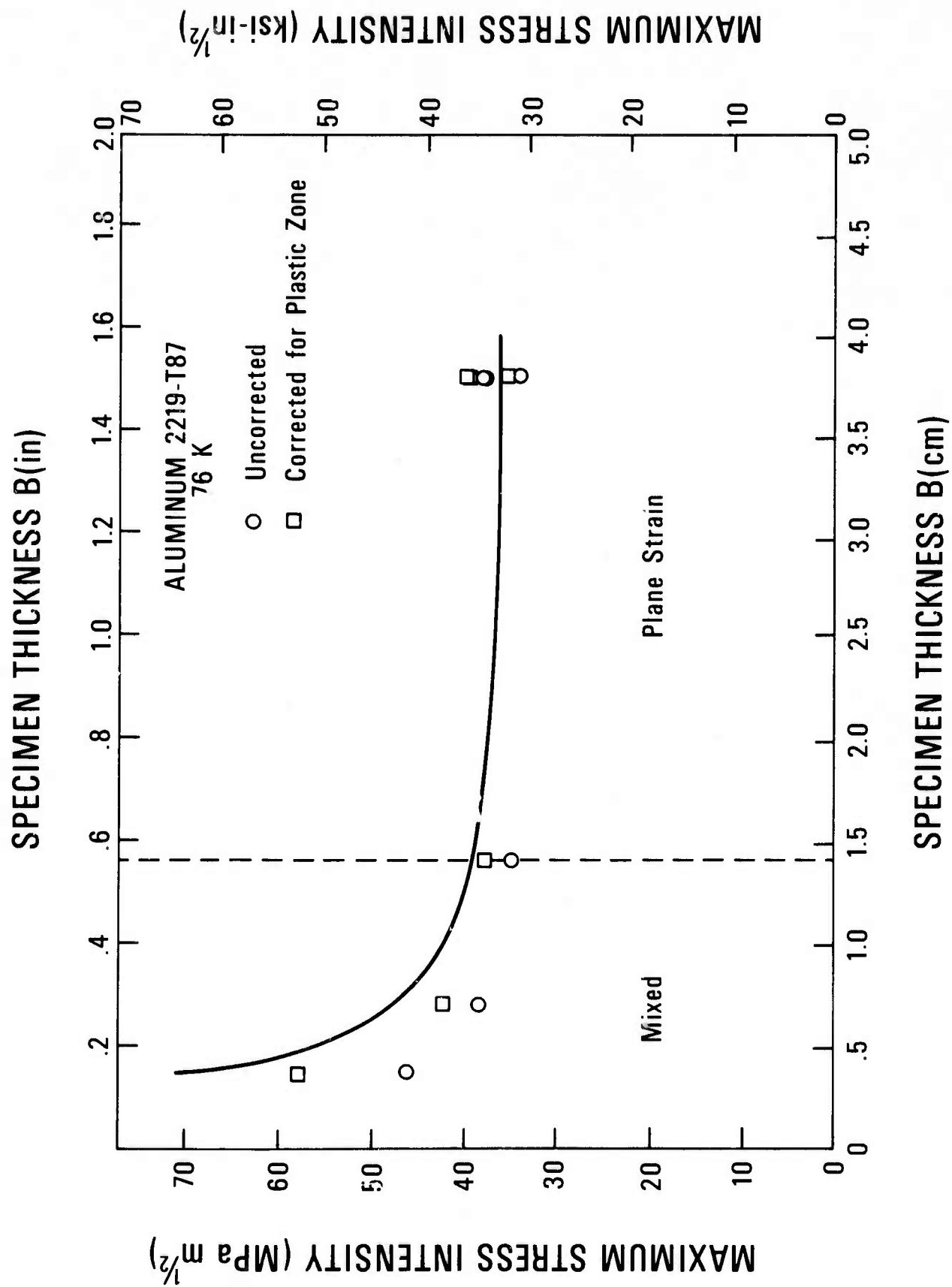


Figure A1. Observed maximum stress intensity versus specimen thickness.

SEMI-ANNUAL REPORT ON MATERIALS RESEARCH IN
SUPPORT OF SUPERCONDUCTING MACHINERY

MAGNETOTHERMAL CONDUCTIVITY

L. L. Sparks

Cryogenics Division
Institute for Basic Standards
National Bureau of Standards
Boulder, Colorado 80302

April 1976

Summary: Magnetothermal Conductivity

The thermal conductivity and effect of a magnetic field on the thermal conductivity of UNS-A91100 in the "0" anneal condition (aluminum 1100 annealed at 350° C for 1 hour) have been determined in the temperature range 5 K to 20 K. A magnetic field typically increases the electronic thermal resistance and thus lowers the total observed thermal conductivity of a metal. For the present aluminum specimen ($RRI = 32.6$) the data indicate that a 6366 kA/m (80 kOe) magnetic field reduces the thermal conductivity by 29% at 5.5 K and by 50% at 20 K. Electrical resistivity data have also been determined and show an increase in resistivity with increasing magnetic field.

Contents: Magnetothermal Conductivity

	Page
1. Introduction	141
2. Procedures	141
2.1 Apparatus	141
2.2 Material	142
3. Results	142
4. Discussion	142
5. References	143
List of Figures	144

MAGNETOTHERMAL CONDUCTIVITY

L. L. Sparks

Cryogenics Division
Institute for Basic Standards
National Bureau of Standards
Boulder, Colorado 80302

1. Introduction

The objective is to determine the effect of magnetic fields on the thermal conductivity of technically important metals. The need for this information arises from the development of rotating machinery operating at cryogenic temperatures. The existing world's literature on magnetothermal conductivity, $\lambda(H)$, is concerned almost exclusively with scientific materials, e.g., very pure materials and single crystals. A complete bibliography of the subject was given by Sparks and Fickett [1].

The materials studied in this program are being used or are candidates for use in superconducting motors and generators. Optimum design of these machines, which must operate at low temperatures while in magnetic fields, requires a detailed knowledge of how the thermal properties of the constituent materials are affected by a magnetic field. The broad material categories of interest include superconductor stabilizing materials such as copper and aluminum, and structural materials such as nickel alloys, stainless steels, and metallic composites.

2. Procedures

2.1 Apparatus

The principal components of the $\lambda(H)$ system are shown schematically in Figure 1. Since the detailed operation of the system has been described in previous reports [1,2] and the details of several system modifications were discussed in [3], only a very brief reiteration of the system and its operation is included here. The specimen chamber, as shown in Figure 1, is evacuated (operating pressure is less than 10^{-4} Pa) and immersed in liquid helium. The liquid helium provides refrigeration to the specimen via the THERMAL LINKS (capitalized terms refer to Figure 1). The specimen is shown mounted with its axis parallel to the axis of the superconducting solenoid which allows the longitudinal field effect to be determined.

The basic operation of the system involves balancing electrical power supplied to three heaters with the heat leak to the liquid helium bath via the THERMAL LINKS. The electrical heaters were wound, one each, on the TEMPERATURE CONTROLLED HEAT SINK (TCHS), the SPECIMEN, and the TEMPERING POST. The power supplied to the TCHS determines the approximate temperature of the specimen; the SPECIMEN HEATER is used to establish a temperature gradient along the specimen; and the TEMPERING POST HEATER is used to reduce the temperature difference between the specimen and the tempering post to less than ± 5 mK. The TEMPERING POST and TCHS heaters are automatically controlled during all tests while a constant current is supplied to the SPECIMEN HEATER. The temperature difference existing along the sample due to the specimen heater current is determined at the two THERMOMETER BLOCKS. The thermal conductivity of the specimen is then computed from a knowledge of the specimen geometry (area/length), the specimen heater power (Q), and the measured temperature difference along the specimen (ΔT). The

relationship of λ to these parameters is given by

$$\lambda = \frac{\dot{Q}}{A \Delta T}. \quad (1)$$

A series of measurements of ΔT and \dot{Q} at various fields ($0 \leq H \leq 6366 \text{ kA/m}$)* and temperatures ($4 < T < 20 \text{ K}$) result in the data presented in this report.

2.2 Materials

One material, UNS-A91100 (aluminum 1100), was tested during this reporting period. The mill analysis in weight percent of the stock used for the $\lambda(H)$ specimen is as follows: Cu = 0.2, Fe = 0.6, Si = 0.1, and the balance is Al. The test specimen is in the "0" condition after being annealed for 1 hour at 350°C in a vacuum of $1.33 \times 10^{-7} \text{ Pa}$ and then furnace cooled. The DP hardness of the annealed specimen is 28 (1 kg load) and its density is $2.818 \times 10^3 \text{ kg/m}^3$ at 294 K. The residual resistance ratio, R_{273K}/R_{4K} , is 32.6, and the ratio of area to length is $4.84 \times 10^{-4} \text{ m}$.

The THERMOMETER BLOCKS and the SPECIMEN HEATER are attached to the specimen by soldering as detailed in [3]. In order to avoid the difficulties involved in soldering to aluminum, thin copper strips were electroplated to the specimen as needed after the specimen was annealed.

3. Results

The thermal conductivity of the present specimen is shown in Figure 2 as a function of temperature with magnetic field as a parameter. The reduction in conductivity from the zero field values caused by a 6366 kA/m (80 kOe) field is 29% at 5 K and 50% at 20 K. The estimated uncertainty of the thermal conductivity data points is $\pm 6\%$ at $T = 4 \text{ K}$ and $\pm 8\%$ at $T = 20 \text{ K}$. Figure 3 presents the relative change in the thermal resistance, $\Delta W/W_{H=0} \equiv (W_H - W_{H=0})/W_{H=0}$, as a function of magnetic field with temperature as a parameter. The electrical resistivity is shown in Figure 4. The estimated uncertainty of the electrical resistivity data points is $\pm 8\%$.

4. Discussion

Attempts to find corroborating data have, to a large extent, been unsuccessful both for the case where $H = 0$ and $H \neq 0$. The literature contains many references to papers dealing with the thermal conductivity of aluminum at zero-magnetic field [4], and several references given in [1] deal with thermal conductivity of aluminum in magnetic fields. With two exceptions, however, the low temperature thermal conductivity of aluminum data pertain to very high purity polycrystalline or single crystal specimens. This, coupled with the fact that thermal and electrical conductivities of most good conductors are extremely dependent on trace impurities and thermal history, makes direct comparison to the present data difficult.

Powell, et al [5] measured the thermal and electrical conductivity of two UNS-A91100 specimens; one was used in the "F" condition (as fabricated)

* The International System of Units (SI) designation for magnetic field strength is ampere per meter, and this unit is used throughout this paper. The more conventional unit of magnetic field strength, the oersted, is also given. Conversion of oersteds to amperes/meter is accomplished by multiplying oersteds by $1000/4\pi$.

and the other in the "0" condition (fully annealed). His results for the "0" specimen were anomalous in that the observed thermal conductivity was even lower than that of the "F" specimen. The RRR for his "0" specimen was around 15 when the expected value for this grade of aluminum is ~ 32 . The behavior of the "0" specimen was attributed to high impurity levels in the stock material. Present results can also be compared with those of de Nobel [6]. In this case the data extend down to only 15 K (a 5 K overlap with the present data) and the material is not well characterized. de Nobel's material was intended to be used in construction of laboratory apparatus (therefore, not of extremely high purity); its conductivity is approximately 5% lower than the present data.

The temperature dependence of the relative change in thermal resistivity, $\Delta W/W_{H=0}$, as shown in Figure 3 is opposite that of the copper specimens tested earlier [7]. This temperature dependence has been observed before [8] for single crystal specimens at lower temperatures. Further study of the present data will be necessary to examine the possible scattering mechanisms responsible for this behavior.

The uncertainty in the electrical resistivity data shown in Figure 4 is high due to the short specimen length and low allowable specimen current (due to small wires). The scatter in the zero field data was considerably higher than the $H \neq 0$ data. These data sets ($H = 0$ and $H \neq 0$) were taken on different days but were otherwise the same. The $H = 0$ curve shown in this figure is from Clark, et al. [9]; their specimen had the same RRR as the present specimen within experimental uncertainty. An analysis of these $\Delta\rho/\rho_{H=0}$ data indicate that the magnetic field effect on the resistivity is only a very weak function of temperature.

In conclusion, the thermal conductivity of aluminum UNS-A91100 in the "0" annealed condition is reduced when a magnetic field is applied. The magnitude of the reduction caused by a 6366 kA/m field is 29% at 5 K and 50% at 20 K. The temperature dependence of $\Delta W/W_{H=0}$ is the inverse of that found for the copper specimens measured previously.

5. References

1. L. L. Sparks and F. R. Fickett; in Materials Research in Support of Superconducting Machinery - I; R. P. Reed, A. F. Clark, E. C. van Reuth (Eds.); Nat. Bur. Stds., Boulder, CO; March 1974; AD780596.
2. L. L. Sparks and F. R. Fickett; in Materials Research in Support of Superconducting Machinery - II; R. P. Reed, A. F. Clark, E. C. van Reuth (Eds.); Nat. Bur. Stds., Boulder, CO; October 1974; ADA004586.
3. L. L. Sparks; in Materials Research in Support of Superconducting Machinery - IV; R. P. Reed, A. F. Clark, E. C. van Reuth (Eds.); Nat. Bur. Stds., Boulder, CO; October 1975; ADA019230.
4. Childs, G. E., Ericks, L. W. and Powell, R. L., Thermal conductivity of solids at room temperature and below, National Bureau of Standards (U.S.), Monogr. 131, 608 pages (September 1973).
5. Powell, R. L., Hall, W. J. and Roder, R. H., Low-temperature transport properties of commercial metals and alloys. II. Aluminums, J. Appl. Phys. 31, No. 3, p. 496 (March 1960).
6. de Nobel, J., Heat conductivity of steels and a few other metals at low temperatures, Physica 17, No. 5, p. 551 (May 1951).
7. L. L. Sparks; in Materials Research in Support of Superconducting Machinery - III; R. P. Reed, A. F. Clark, E. C. van Reuth (Eds.); Nat. Bur. Stds., Boulder, CO; April 1975; ADA012365.

8. Amundsen, T. and Sovik, R. P., Measurements of the thermal magnetoresistance of aluminum, J. Low Temp. Phys. 2, No. 1, 1970.
9. Clark, A. F., Childs, G. E. and Wallace, G. H., Electrical resistivity of some engineering alloys at low temperatures, Cryogenics 10, No. 4, p. 295 (August 1970).

List of Figures

- Figure 1. Magnetothermal conductivity probe and magnet.
- Figure 2. Thermal conductivity of UNS-A91100 "0" as a function of temperature with magnetic field as a parameter.
- Figure 3. Relative change in thermal resistance as a function of magnetic field with temperature as a parameter.
- Figure 4. Electrical resistivity as a function of temperature with magnetic field as a parameter. The dashed line represents $H = 0$ data from Clark, et al. [9].

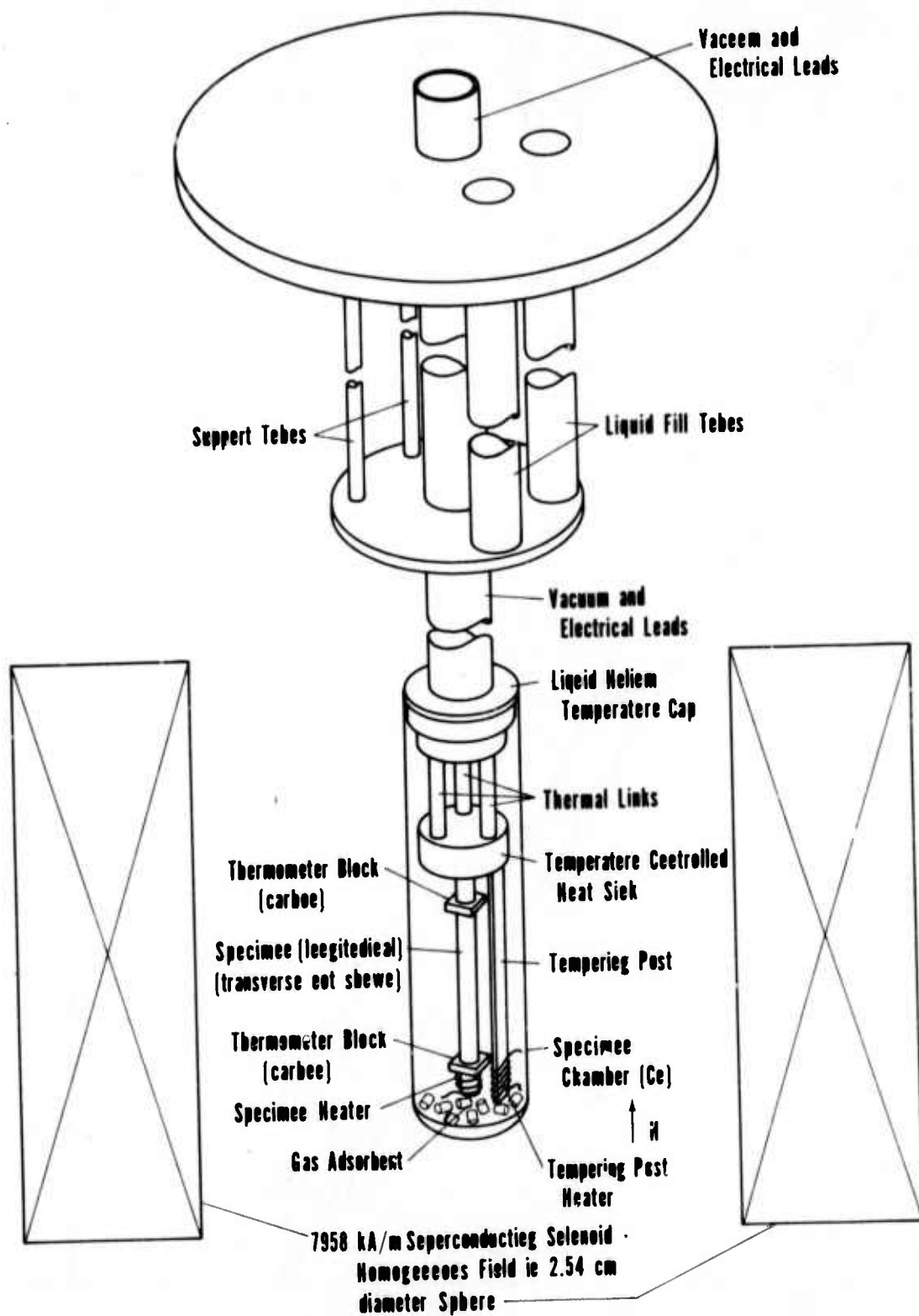


Figure 1. Magnetothermal conductivity probe and magnet.

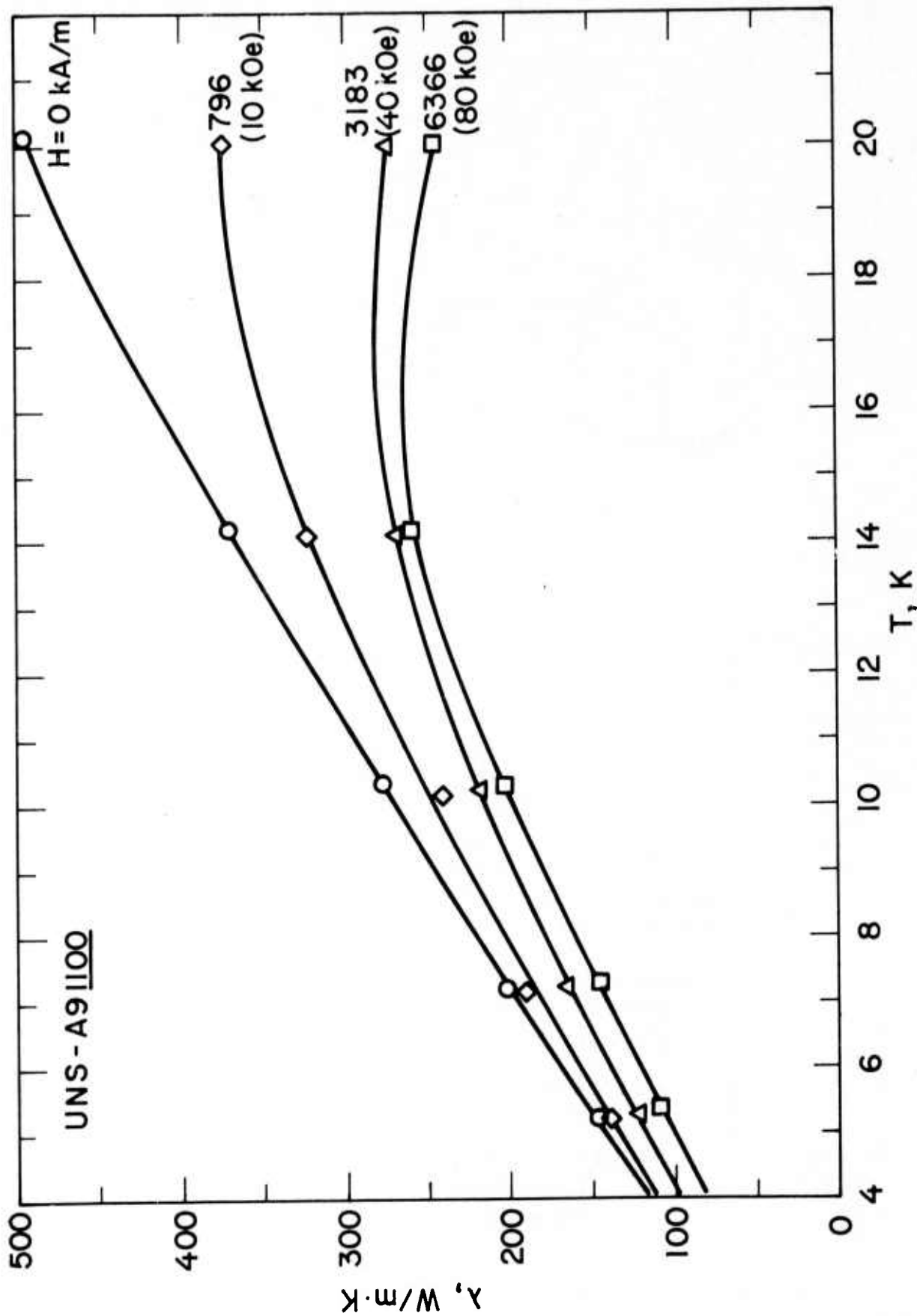


Figure 2. Thermal conductivity of UNS-A91100 "0" as a function of temperature with magnetic field as a parameter.

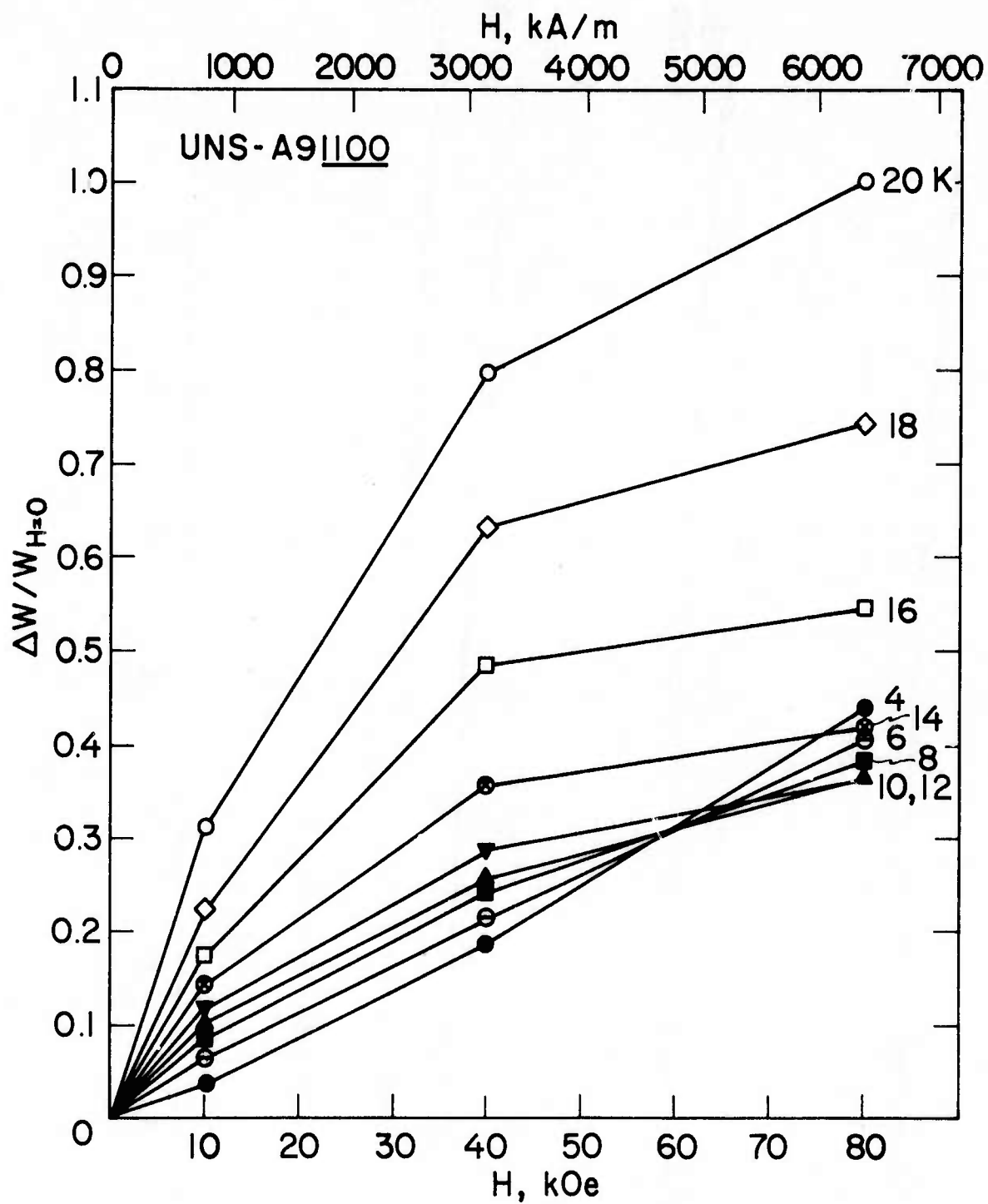


Figure 3. Relative change in thermal resistance as a function of magnetic field with temperature as a parameter.

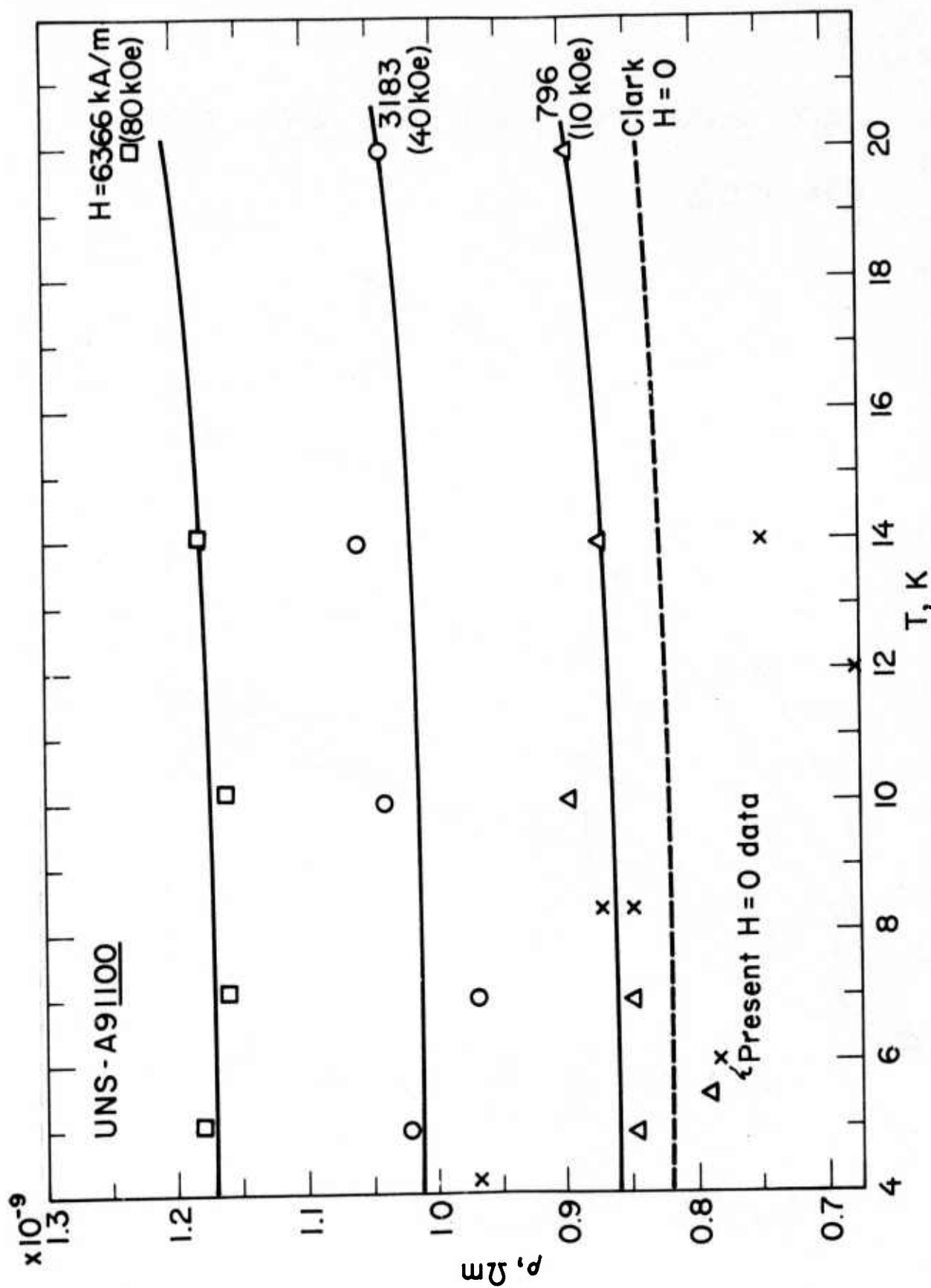


Figure 4. Electrical resistivity as a function of temperature with magnetic field as a parameter. The dashed line represents $H = 0$ data from Clark, et al. [9].

SEMI-ANNUAL REPORT ON MATERIALS RESEARCH
IN SUPPORT OF SUPERCONDUCTING MACHINERY

THERMAL CONDUCTIVITY

J. G. Hust

Cryogenics Division
Institute for Basic Standards
National Bureau of Standards
Boulder, Colorado 80302

April 1976

Summary: Thermal Conductivity

During the current reporting period no thermal conductivity measurements were performed. The final measurements for this program will be performed during the next, and final, reporting period. Measurements are scheduled for the following materials:

Maraging steel 300 (Fe-18Ni-9Co-5Mo)
Carpenter 49 steel (Fe-49Ni)
Boron-Aluminum Composite (longitudinal)
Graphite-Epoxy Composite (longitudinal, transverse)

The final report will contain the results of these measurements and a summary of the thermal conductivities of materials pertinent to this program.

This research was supported by the
Advanced Research Projects Agency of
the Department of Defense and was moni-
tored by the Cryogenics Div., NBS,
Boulder, CO under Contract No. CST-8304
Contract Amount \$402,708.

Sponsored by Advanced Research
Projects Agency ARPA Order No.
2569, Program Code No. 4D10

TITLE: STRUCTURAL MATERIALS FOR CRYOGENIC APPLICATIONS
(Fifth Semi-Annual Technical Report - April 9, 1976)

CONTRACTOR: Westinghouse Electric Corporation
Research and Development Center
Pittsburgh, Pennsylvania 15235

Westinghouse Program Manager: Dr. J. M. Wells (412) 256-3633

Westinghouse Principal Investigators:

Mr. W. A. Logsdon	(412) 256-3652
Dr. R. Kossowsky	(412) 256-3684
Dr. M. R. Daniel	(412) 256-3289
Dr. J. M. Wells	(412) 256-3633

FY 74 Contract Start Date: September 10, 1973

FY 74 Contract Expiration Date: September 9, 1974

FY 75 Contract Start Date: September 10, 1974

FY 75 Contract Expiration Date: September 9, 1975

FY 76 Contract Start Date: September 10, 1975

FY 76 Contract Expiration Date: September 9, 1976

Research Report 76-9D4-CRYMT-R1
Westinghouse Program 9D43-CRYMT
NBS Contract No. CST-8304

STRUCTURAL MATERIALS FOR CRYOGENIC APPLICATIONS

(Fifth Semi-Annual Technical Report)

J. M. Wells, R. Kossowsky, W. A. Logsdon and M. R. Daniel

Westinghouse Electric Corporation
Research and Development Center
Pittsburgh, Pennsylvania 15235

April 9, 1976

The views and conclusions contained in this document are those of the authors and should not be interpreted as necessarily representing official policies, expressed or implied, of the Advanced Research Projects Agency or the U.S. Government.

TABLE OF CONTENTS

	<u>Page</u>
LIST OF FIGURES	i
LIST OF TABLES	viii
1.0 ABSTRACT	1
2.0 INTRODUCTION	3
3.0 INTERPRETIVE SUMMARY	5
3.1 Program Status	5
3.2 Alloy Selection and Utilization	6
3.3 Mechanical and Fracture Mechanics Properties	7
3.4 Effects of Processing	9
3.5 Effects of Metals Joining	10
4.0 WESTINGHOUSE PROGRAM DESCRIPTION	13
4.1 FY 74 Program Summation	14
4.2 FY 75 Program Summation	14
4.3 FY 76 Program Summation	15
5.0 GENERAL CRYOGENIC STRUCTURAL MATERIALS/PROCESSING/ FABRICATION CONSIDERATIONS	17
5.1 Materials Selection Considerations	17
5.1.1 Microstructural Stability in Austenitic Stainless Alloys	17
5.1.2 Martensite in Austenitic Stainless Alloys	19
5.1.3 Delta Ferrite Formation in Austenitic Stainless Steel	24
5.2 Materials Processing Considerations	27
5.2.1 Cold Working and Heat Treatment of Inconel 718	27
5.2.2 Processing of Pyromet 538 (21-6-9) Billet to Plate	29

TABLE OF CONTENTS (CONTINUED)

	<u>Page</u>
5.3 Materials Joining Considerations	31
5.3.1 Current FY 76 Program Weldments	31
5.3.1.1 SMA Weldments in Pyromet 538	31
5.3.1.2 GTA Weldments in Pyromet 538	32
5.3.1.3 GTA Weldments in Armco A-286	33
5.3.2 Varestraint Weldability Testing	34
6.0 FRACTURE MECHANICS	45
6.1 Tensile Results	45
6.2 Dynamic Fracture Toughness	47
6.3 Crack Growth Rate Results	49
7.0 MICROSTRUCTURAL ANALYSIS	57
7.1 Carbide Extraction, Alloys 718 and 706	57
7.2 Recrystallized I-718 (Specimen Codes 67XX, 68XX, 69XX)	61
7.2.1 Summary	62
7.3 Nitronic 33 Deformed Weldment	63
8.0 MAGNETIC MEASUREMENTS	65
ACKNOWLEDGMENTS	69
APPENDIX I - W. A. Logsdon, J. M. Wells and R. Kossowsky, "Fracture Mechanics Properties of Austenitic Stainless Steels for Advanced Cryogenic Applications".	

LIST OF FIGURES

- Figure 3-1 Summary comparison of mechanical strength and ductility values for copper alloys including processing and fabricated joints for RT, 77 K, and 4.2 K.
- Figure 3-2 Summary comparison of mechanical strength and ductility values for AISI 310S and Kromarc 58 stainless steels including processing and welded joints at RT, 77 K and 4.2 K.
- Figure 3-3 Summary comparison of mechanical strength and ductility values for nickel based superalloys, IN X750, 706 and LEA in various processed conditions at RT, 77 K, and 4.2 K.
- Figure 3-3A Summary comparison of mechanical strength and ductility values for Inconel X750 base metal, electron beam and GTA weldments and copper brazement at RT, 77 K and 4.2 K.
- Figure 3-4 Summary comparison of mechanical strength and ductility values for nickel base superalloys Udimet 718 and Inconel 718 in various processed and fabricated conditions at RT, 77 and 4.2 K.
- Figure 3-5 Summary comparison of fracture toughness values at 4.2 K for 310S, Kromarc 58, Inconel X750, Inconel 718, Inconel 706, INCO LEA, and A-286 materials including effects of processing and metals joining.
- Figure 3-6 Effect of processing conditions on yield strength and ultimate tensile strength ratios of OFHC Cu, 310S, Kromarc 58, IN X750, Inconel 718 and Inconel 706 at RT, 77 K and 4.2 K.
- Figure 3-7 Effect of processing conditions on fracture toughness ratio for 310S, Kromarc 58, Inconel X750, and Inconel 706 at 4.2K.
- Figure 3-8 Effect of metals joining conditions on yield strength and ultimate tensile strength ratios for OFHC copper, 310S and K-58 stainless steel at RT, 77 K and 4.2 K.
- Figure 3-9 Effect of metals joining conditions on yield strength and ultimate tensile strength ratios for Inconel X750, Inconel 718 and Inconel 706 at RT, 77 K and 4.2 K.

LIST OF FIGURES (CONTINUED)

- Figure 3-10 Effect of metals joining conditions on fracture toughness ratio for 310S, Kromarc 58 stainless steel, IN X750, IN 718 and IN 706 at 4.2 K.
- Figure 4-1 Westinghouse Program Outline - Structural Materials for Cryogenic Applications.
- Figure 4-2 Westinghouse Program Organization - FY 76.
- Figure 5-1 Calculated temperature ranges for microstructural instability, M_d and M_s in various austenitic stainless steel alloys.
- Figure 5-2 Measured ferrite number (FN) versus FN predicted by the Hull diagram for high manganese stainless steel weldments.
- Figure 5-3 Photomicrographs of Inconel 718 alloy following various processing operations consisting of solution treatment at 1066°C (1950°F), 40% cold work and then treated as shown (X 225).
- Figure 5-4 Photomicrographs comparing the microstructures of Pyromet 538 (21-6-9) material as, I - as received billet, II - 1-1/2 in. thick plate sample from NBS, and III - 3/4 in. thick plate made in Westinghouse FY 76 program (X 225).
- Figure 5-5 Photograph of weld test plates (as-welded) for the Westinghouse FY 76 program, (A) GTAW in Pyromet 538 (21-6-9), (B) SMAW in Pyromet (21-6-9), and (C) GTAW in A-286 material.
- Figure 5-6 Microhardness Survey (A & B), Macrostructure (C) (X6), and microstructure of STQ/SMA Welded Pyromet 538 (21-6-9), Weld Plate No. (1B), (D) through (H), as welded (X 225).
- Figure 5-7 Macro- and microstructural features of FZ-HAZ band of microporosity in SMA Weldment in Pyromet 538.
- Figure 5-8 Microhardness Survey (A & B), Macrostructure (C)(X6), and microstructure of STQ/GTA welded Pyromet 538, Weld Plate No. (1D), (D) through (H), as-welded (X 225).
- Figure 5-9 Sectioning Schematic and microstructure of A-236 forging billet material, (I) Longitudinal Sections and (II) Transverse Sections (X 225).
- Figure 5-10 Macro Fusion Zone hot cracking (A) and heat affected zone microfissuring in A-286 STQA/GTA Weldment No. A.

LIST OF FIGURES (CONTINUED)

- Figure 5-11 Microhardness survey (A&B), Macrostructure (C)(X7), and microstructure of STQA/GTA welded A-286 stainless steel Weld Plate No. 1A, (D) through (H), as welded (X 225).
- Figure 5-12 Microhardness survey (A&B), macrostructure (C)(X6), and microstructure of STQ/GTA welded A-286 stainless steel Weld Plate No. 2C, (D) through (H), as welded (X 225).
- Figure 5-13 The Research Laboratory Vareststraint Tester with the GTA torch in the position for arc initiation. Radius blocks and tested specimens are shown in foreground.
- Figure 5-14 Schematic sketch of the operation of the vareststraint test device.
- Figure 5-15 Schematic representation of the top surface of the weld and the section removed for metallographic examination.
- Figure 5-16 Fusion zone (FZ) cracking observed in longitudinal vareststraint tests of austenitic stainless steels.
- Figure 5-17 Fusion zone (FZ) cracking observed in longitudinal vareststraint test on Alloy A-286.
- Figure 5-18 Heat affected zone (HAZ) cracking observed in longitudinal vareststraint test on Alloy A-286.
- Figure 5-19 Fusion zone (FZ) cracking observed in longitudinal vareststraint test of Alloy 718.
- Figure 5-20 Heat affected zone (HAZ) cracking observed in longitudinal vareststraint tests of Alloy 718.
- Figure 5-21 Comparison of longitudinal vareststraint heat affected zone cracking data for nickel base Alloy 718
- Figure 5-22 Photographs of Vareststraint Test Specimens in AISI 305 stainless steel in the ST (2000°F) Q condition at various augmented strain levels (X10).
- Figure 5-23 Photomacrographs of Vareststraint Test Specimens in Kromarc 58 alloy in (I) Base Metal and (II) Prior Deposited Weldment at various augmented strain levels (X10)
- Figure 5-24 Photomacrographs of vareststraint test specimens in Nitronic 33 alloy in (I) Base Metal and (II) Prior Deposited Weldment (13-20MnCb) at various augmented strain levels (X10)

LIST OF FIGURES (CONTINUED)

- Figure 5-25 Photomacrographs of Varestraint Test Specimens in Pyromet 538 (21Cr-6Ni-9Mn) stainless steel in the (I) as-received billet and (II) ST(2000°F)Q conditions at various augmented strain levels (X10)
- Figure 5-26 Photomacrographs of Varestraint Test Specimens in (I) Armco A-286 and (II) Cameron A-286 alloys in the ST(1800°F)Q and ST (1650°F)Q conditions respectively at augmented strain levels of 0.25% and 2.0% (X10)
- Figure 5-27 Photomacrographs of Varestraint Test Specimens in (I) Armco A-286 and (II) Cameron A-286 alloys, both in the ST(1650°F)QA condition, at augmented strain levels of 0.25% and 2.0% (X10)
- Figure 5-28 Photomacrographs of Varestraint Test Specimens in (I) Armco A-286 and (II) Cameron A-286 alloys in the ST(1800°F)QA condition at augmented strain levels of 0.25% and 2.0% (X10)
- Figure 5-29 Photomacrographs of Varestraint Test Specimens in (I) Udimet 718 and (II) Inconel 718 in the as-received billet condition at various augmented strain levels (X10)
- Figure 5-30 Photomacrographs of Varestraint Test Specimens in (I) Udimet 718 and (II) Inconel 718 alloys in the ST(1800°F) condition at various augmented strain levels (X10)
- Figure 5-31 Photomacrographs of varestraint test specimens in the (I) Udimet 718 and (II) Inconel 718 alloys in the ST(1950°F) condition at various augmented strain levels (X10)
- Figure 5-32 Photomacrographs of Varestraint Test Specimens in Udimet 718 alloy in the (I) ST(1800°F)/DA and (II) ST(1950°F)/DA conditions at various augmented strain levels (X10)
- Figure 6-1 The influence of processing and heat treatment on the strength of Inconel 718 (VIM-VAR)
- Figure 6-2 The influence of processing and heat treatment on the ductility of Inconel 718 (VIM-VAR)
- Figure 6-3 Test record trace for a Udimet 718 Specimen illustrating dynamic loading to a specific displacement
- Figure 6-4 Static and dynamic J resistance curves for Udimet 718
- Figure 6-5 Fatigue crack growth rate properties of Inconel 706 (VIM-EFR)

LIST OF FIGURES(CONTINUED)

- Figure 6-6 Fatigue crack growth rate properties of Inconel 706 (VIM-VAR)
- Figure 6-7 Fatigue crack growth rate properties of Inconel 718 (VIM-VAR)
- Figure 6-8 Fatigue crack growth rate properties of INCO LEA (AAM-VAR)
- Figure 6-9 Comparison of the -452°F (4K) fatigue crack growth rate properties of three superalloys
- Figure 6-10 Comparison of the room temperature fatigue crack growth rate properties of three superalloys
- Figure 6-11 Comparison of the -452 (4K) fatigue crack growth rate properties of superalloys versus stainless steels
- Figure 6-12 Comparison of the room temperature fatigue crack growth rate properties of superalloys versus stainless steels
- Figure 7-1 X-ray powder diffraction data, non-soluble residues (a) alloy 706 VIM-VAR STDA (b) alloy 706 VIM-VAR weld, STDA (c) U718 ST, 1950°F (d) U718 STDA (e) I718 STDA (f) U718 weld, STDA
- Figure 7-2 Non-soluble residue, EDAX analysis
- Figure 7-3 Non-soluble residue, EDAX analysis
- Figure 7-4 Cross sections showing typical grain morphology I-718 (a) group 67XX (b) group 68XX (c) group 69XX
- Figure 7-5 I-718, tensile test specimens 671X (a) longitudinal section, 200X tested at 77K (b) tested at 4.2K. Most of cavities are fracture carbides, see Fig. 7-6
- Figure 7-6 I-718, SEM micrograph (a) of longitudinal section, tensile test specimen 6711, 1000X. Holes seen in Fig. 7-5 are fractured carbides (b-d) energy dispersive x-rays (b) spot 1 (c) spot 2 (d) spot 3
- Figure 7-7 I-718, longitudinal sections, tensile test specimens 681X (a) tested at RT 50X (b) tested at 4.2K, 200X. Slip lines seen clearly in (b)
- Figure 7-8 I-718, longitudinal cross sections, specimen 691X (a) tested at RT 100X (b) tested at 4.2K, 200X. Note severe deformation due to pretest cold reductions. Fractured carbides around cavities are shown in Fig. 7-9

LIST OF FIGURES (CONTINUED)

- Figure 7-9 I-718, SEM micrographs of cavities seen in Figs. 7-7 and 7-8 (a) specimen 6811, 600X (b) specimen 6913, 1200X (c) energy dispersive x-rays of spot 1 Nb rich Mc carbides
- Figure 7-10 I-718 SEM micrographs, fracture surface, tensile specimen 6711 tested at RT (a) 50X (b) 1000X mixed mode of shear and dimpled tensile failure (c) 2000X note secondary cracks in carbides (arrows) (d) 2000X shear facets
- Figure 7-11 I-718, SEM micrographs, fracture surface specimen 6712 tested at 77K (a) typical dimpled structure with carbides (b) shear facet 2000X (c) x-ray of spot A (dots) and spot B (lines). Nb rich Mc carbide in A
- Figure 7-12 I-718, SEM micrograph, 2600X, fracture surface specimen 6712 tested at 77K. Two types of carbides - A Nb rich (Nb, Ti) C (dots, EDAX), B (Nb, 30Ti) C (lines, EDAX)
- Figure 7-13 I-718, SEM micrographs, fracture surface, tensile test specimen 6812 tested at 77K (a) 50X (b) 500X (c) 1000X note dimples and shear facets (d) 2000X large carbide agglomerates and carbides at the bottom of dimples
- Figure 7-14 I-718, SEM micrograph (a) of fracture surface, specimen 6813 tested at 4.2K, 1500X (b) EDAX shear facet, spot 1 (c) EDAX carbides in dimples, spot 2
- Figure 7-15 I-718, SEM micrographs of fracture surface, specimen 6813, tested at 4.2K (a) 200X mixture of dimpled fracture, intergranular and shear fractures (b) dimple detail 500X (c) intergranular detail 1000 (d) shear facets, detail 1400X
- Figure 7-16 I-718, SEM micrographs, fracture surface, tensile specimen 6911, tested at RT (a) 200X (b) dimples and lanes phase sheared particles detail, 500X (c) intergranular and shear facet fracture detail 1000X (d) carbide agglomerations 2000X
- Figure 7-17 I-718, SEM micrographs, fracture surface, specimen 6913, tested at 4.2K (a) 50X (b) shear, dimple detail 500X (c,d) carbides and lanes phases details 2000X
- Figure 7-18 A-286, SEM micrographs, fracture surface tensile specimen tested at 77K (a) 50X (b) 500X intergranular fracture preceded by deformation within the grain (c) detail, 2000X (d) fracture around carbide agglomerations, 2000X

LIST OF FIGURES (CONTINUED)

- Figure 7-19 A-286, SEM micrographs. Fracture surface, tensile specimenTM tested at 4.2K (a) 50X mixed mode of intergranular fracture and cross-granular shear (b) detail 500X (c) detail 2000X
- Figure 7-20 A-286, Fatigue-crack growth specimen, tested at RT. SEM micrographs (a) 100X (b) 500X (c) detail, 2000X (d) 1000X. Fatigue striations along crystallographic direction.
- Figure 7-21 A-286, Fatigue-crack growth specimen, tested at 77K (a) 100X (b) 500X intergranular failure, fatigue striations, tensile fracture (T) and carbides at boundaries (c) 1000X (d) detail 25000X
- Figure 7-22 N-33, SEM micrographs of polished and etched weldment, deformed at RT in bending. Evidence of martensitic transformation S: slip lines, M: martensite (acicular) E: etch pits, a-b: 6800, c-d: 13600
- Figure 8-1 A comparison of the magnetization versus magnetic field for Inconel 718 from the data of Westinghouse and Efferson and Leonard
- Figure 8-2 A comparison of the magnetization versus magnetic field for 310S from the data of Westinghouse and Efferson and Leonard

LIST OF TABLES

TABLE 3-1	STRUCTURAL MATERIALS FOR CRYOGENIC APPLICATIONS, FY 74 WESTINGHOUSE PROGRAM STATUS
TABLE 3-2	STRUCTURAL MATERIALS FOR CRYOGENIC APPLICATIONS, FY 75 WESTINGHOUSE PROGRAM STATUS
TABLE 3-3	STRUCTURAL MATERIALS FOR CRYOGENIC APPLICATIONS, FY 76 WESTINGHOUSE PROGRAM STATUS
TABLE 5-1	CANDIDATE MATERIALS FOR ADVANCED CRYOGENIC STRUCTURAL APPLICATIONS
TABLE 5-2	CHEMICAL COMPOSITION OF MATERIALS IN WESTINGHOUSE FY 76 PROGRAM MATERIALS
TABLE 5-3	DOCUMENTATION DATA FOR WESTINGHOUSE FY 76 PROGRAM MATERIALS
TABLE 5-4	PROCESSING AND HEAT TREATMENT SCHEDULES FOR WESTINGHOUSE FY 76 PROGRAM MATERIALS
TABLE 5-5	MATERIAL HARDNESS AND ASTM GRAIN SIZE MEASUREMENT IN WESTINGHOUSE FY 76 PROGRAM MATERIALS
TABLE 5-6	TEST SPECIMEN IDENTIFICATION SYSTEM
TABLE 5-7	RESULTS OF M_d AND M_s CALCULATIONS FOR SPECIFIC COMPOSITIONS OF AUSTENITIC STAINLESS STEELS
TABLE 5-8	CALCULATED M_d AND M_s RANGES FOR VARIOUS STAINLESS STEELS
TABLE 5-9	COMPARISON OF FERRITE CALCULATIONS WITH HULL METHOD VS. DELONG METHOD FOR HIGH MANGANESE STAINLESS STEELS
TABLE 5-10	RESULTS OF DELTA FERRITE PREDICTIONS IN HIGH MANGANESE STAINLESS STEEL WELDMENTS
TABLE 5-11	SUMMARY TABLE OF WELDING DATA, WESTINGHOUSE FY 76
TABLE 5-12	SUMMARY OF WESTINGHOUSE LONGITUDINAL VARESTRAINT WELDABILITY TESTS ON VARIOUS AUSTENITIC STAINLESS STEELS
TABLE 5-13	SUMMARY OF WESTINGHOUSE LONGITUDINAL VARESTRAINT WELDABILITY TESTS ON ALLOY 718

LIST OF TABLES (CONTINUED)

TABLE 6-1	TENSILE AND NOTCHED TENSILE PROPERTIES OF INCONEL 718 (VIM-VAR) AND UDIMET 718 (VIM-VAR) AT 75°F (297K)
TABLE 6-2	TENSILE AND NOTCHED TENSILE PROPERTIES OF INCONEL 718 (VIM-VAR) AND UDIMET 718 (VIM-VAR) AT -320°F (77K)
TABLE 6-3	TENSILE AND NOTCHED TENSILE PROPERTIES OF INCONEL 718 (VIM-VAR) AND UDIMET 718 (VIM-VAR) AT -452°F (4K)
TABLE 7-1	X-RAY DATA, NON-SOLUBLE RESIDUES
TABLE 8-1	MAGNETIC PROPERTIES OF MATERIALS
TABLE 8-2	COMPARISON OF MAGNETIC PROPERTIES WITH COMPOSITIONS

1.0 ABSTRACT

Interest in the engineering application of superconducting field windings in advanced cryogenic structures and devices has stimulated renewed interest in the mechanical and physical behavior of cryogenic structural support materials. Examples of such advanced cryogenic applications include such prototype devices as superconducting machinery and large s.c. magnets for Magnetohydrodynamic (MHD) and Controlled Thermonuclear Reactor (CTR) Type devices. The prior existing data base for structural materials in such applications was assessed as inadequate for effective materials selection and utilization in a high reliability design. Consequently, a program entitled, "Materials Research For Superconducting Machinery" was initiated by ARPA and NBS in FY 74.

The Westinghouse Research Laboratories (WRL) has been an active participant in the ARPA/NBS program throughout.

The Westinghouse Research Laboratories program has concentrated on three basic tasks, namely: I. The characterization and evaluation of candidate structural alloys, II. The investigation of metals processing considerations on the cryogenic behavior of selected alloys and III. The evaluation of fabricated joints for cryogenic structural applications. The evaluation procedures employed in the WRL program include mechanical and fracture mechanics testing, metallography, fractography and magnetic and electrical resistivity measurements from room temperature to 4K. Emphasis in the focused direction of this effort is placed upon: (A) utilizing modern fracture mechanics technology to evaluate the K_{IC} (J_{IC}) fracture toughness and fatigue crack growth rate (FCGR) of various alloy conditions, (B) evaluating various selected materials/processing and fabrication (MPF) techniques to elucidate the significant effects of MPF on the cryogenic behavior

1.0 ABSTRACT

Interest in the engineering application of superconducting field windings in advanced cryogenic structures and devices has stimulated renewed interest in the mechanical and physical behavior of cryogenic structural support materials. Examples of such advanced cryogenic applications include such prototype devices as superconducting machinery and large s.c. magnets for Magnetohydrodynamic (MHD) and Controlled Thermonuclear Reactor (CTR) Type devices. The prior existing data base for structural materials in such applications was assessed as inadequate for effective materials selection and utilization in a high reliability design. Consequently, a program entitled, "Materials Research For Superconducting Machinery" was initiated by ARPA and NBS in FY 74.

The Westinghouse Research Laboratories (WRL) has been an active participant in the ARPA/NBS program throughout.

The Westinghouse Research Laboratories program has concentrated on three basic tasks, namely: I. The characterization and evaluation of candidate structural alloys, II. The investigation of metals processing considerations on the cryogenic behavior of selected alloys and III. The evaluation of fabricated joints for cryogenic structural applications. The evaluation procedures employed in the WRL program include mechanical and fracture mechanics testing, metallography, fractography and magnetic and electrical resistivity measurements from room temperature to 4K. Emphasis in the focused direction of this effort is placed upon: (A) utilizing modern fracture mechanics technology to evaluate the K_{IC} (J_{IC}) fracture toughness and fatigue crack growth rate (FCGR) of various alloy conditions, (B) evaluating various selected materials/processing and fabrication (MPF) techniques to elucidate the significant effects of MPF on the cryogenic behavior

of these alloys, (C) employment of metallographic and fractographic analysis techniques to characterize the microstructures and fracture surfaces of the tested materials, and (D) evaluating the general and specific structural materials considerations required to establish failure-safe design materials selection and utilization criteria.

During this fifth semi-annual reporting period (October 1975 to April 1976), two additional structural candidate materials were introduced namely: Pyromet 538 (21Cr-6Ni-9Mn) and A-286 stainless steels. Weldments in both these materials have been fabricated and are presently being tested. Tensile and metallographic data on additional processed conditions of Inconel 718 is presented. Dynamic fracture toughness data at 77K is included which reveals no significant differences from the static K_{IC} (J_{IC}) results for Udimet 718 alloy. Fatigue crack growth rate results are included for Inconel 706, 718 and the LEA alloy. Metallographic and fractographic analysis has attributed the low ductility and low fracture toughness of Inconel 718 and 706 weldments to the presence of intergranular (Nb,Ti)C films in the weld fusion zones. Relationships originally derived by Hull for the prediction of delta ferrite and martensite in austenitic stainless steels are presented and evaluated with respect to experimental data available. Results on longitudinal vareststraint weldability tests conducted on both austenitic stainless steels and nickel base 718 superalloy are presented demonstrating considerable hot cracking is experienced in both the FZ and the HAZ of the A-286 and the 718 alloy.

2.0 INTRODUCTION

Work described in this report represents the most recent Westinghouse Research Laboratories contribution to the Advanced Research Project Agency Program entitled "Materials Research for Superconducting Machinery". This program is supported by DOD-ARPA under the direction of Dr. Edward C. vanReuth. Program management is administered by the Cryogenics Division of the National Bureau of Standards with Dr. Richard P. Reed as overall program manager and Dr. Alan F. Clark as contract monitor.

The present Westinghouse Research Laboratories (WRL) program has as its objectives:

- (1) To select, characterize and evaluate candidate structural materials for suitability of use in advanced superconducting machinery.
- (2) To investigate the influence of selected processing and fabrication/joining factors or techniques on the mechanical, fracture mechanics and physical (magnetic and electrical resistivity) properties of candidate structural materials.
- (3) To develop engineering cryogenic mechanical and physical property data of direct usefulness to designers of prototype S.C. machinery.
- (4) To help establish with designers of such systems, more specific criteria for selecting and improving the utilization of structural materials in S.C. machinery prototypes.

Four previous WRL semi-annual technical reports have been issued on this program as follows:

- (a) WRL Report No. 74-9D4-CRYMT-R1, dated March 1, 1974
- (b) WRL Report No. 74-9D4-CRYMT-R2, dated September 9, 1974
- (c) WRL Report No. 75-9D4-CRYMT-R1, dated March 10, 1975
- (d) WRL Report No. 75-9D4-CRYMT-R2, dated October 10, 1975

These Westinghouse reports along with those of the four other participating laboratories, namely, The Battelle Columbus Laboratories, General Electric Research and Development Center, Martin Marietta Aerospace-Denver Division and The National Bureau of Standards-Cryogenic Division, are included in the four corresponding NBS-ARPA overall program semi-annual technical reports, entitled "Materials Research For Superconducting Machinery-I (dated March 1974), -II (dated October 1974), -III (dated March 1974) and -IV (dated October 1975)", respectively. In addition, a "Handbook on Materials for Superconducting Machinery" has been published by the Metals and Ceramics Information Center at Battelle as MCIC-HB-04.

Four technical papers have been written by WRL staff members concerning work mainly accomplished during the Westinghouse FY 74 and FY 75 program. These papers are as follows:

1. Logsdon, W. A., "Cryogenic Fracture Mechanics Properties of Several Manufacturing Process/Heat Treatment Combinations of Inconel X750", *Advances in Cryogenic Engineering*, V. 22, (to be published in 1976).
2. Kossowsky, R., "Microstructure of Inconel X750 Materials For Cryogenic Structural Applications", *Adv. in Cry. Engrg.*, V. 22, (to be published in 1976).
3. Wells, J. M., "Evaluation of Inconel X750 Weldments For Cryogenic Applications", *Adv. in Cry. Engrg.*, V. 22, (to be published in 1976).
4. Logsdon, W. A., Wells, J. M., and Kossowsky, R., "Fracture Mechanics Properties of Austenitic Stainless Steels For Advanced Cryogenic Applications", Westinghouse Scientific Paper 75-9D4-CRYMT-P3, December 31, 1975 (to be published).

The first three papers were presented at the 1975 ICMC Conference at Kingston, Ontario and have been submitted for publication in Vol. 22 of Advances in Cryogenic Engineering.

3.0 INTERPRETIVE SUMMARY

The purpose of this section is to provide for the casual as well as the involved reader both a continuing overall summation of accumulated information developed in the Westinghouse program and a perspective of the significance of such information relative to the design and fabrication of advanced cryogenic machinery.

3.1 Program Status

A testing and evaluation status summary for the Westinghouse FY 74, FY 75 and FY 76 efforts are presented in Tables 3-1, 3-2 and 3-3, respectively.

For the FY 76 effort, all processing and metals joining activities are completed with the exception of three remaining A-286 GTA weldments (Code 91XX) to be fabricated, radiographed and examined. Mechanical tensile testing is completed on the processed 718 base metal conditions Code 67XX, 68XX and 69XX and reported herein. Fracture mechanics tests on these 718 material codes are in progress and will be completed shortly. Mechanical and fracture mechanics specimens have been machined for the SMA and GTA weldments in the Pyromet 538 material (Codes 94XX and 93XX, respectively) and will be tested shortly. Fractographic and additional metallographic analyses have been conducted on both the base metal and weldment conditions in the Inconel 706 and 718 alloys and the Udimet 718 and A-286 base metal materials. Fractographic and further metallographic examination and analyses on the Pyromet 538 and A-286 weldments will be presented in the following report. Magnetic saturation measurements on the A-286 base metal, IN 718 (Code 69XX), Pyromet 538 (21-6-9) base metal and weldments were conducted in this period and are reported herein in Section 8.

Finally, an additional technical paper has been completed entitled "Fracture Mechanics Properties of Austenitic Stainless Steels For Advanced Cryogenic Applications" and is included in this report as Appendix A.

3.2 Alloy Selection and Utilization

Ten different candidate cryogenic structural alloys have been evaluated during the course of the Westinghouse program. Four specific alloys, namely: OFHC Copper, AISI 310S and Kromarc 58 Stainless Steels and Inconel X750 nickel-base superalloy were included in the original FY 74 effort. Subsequently in the FY 75 program, four additional alloys were introduced, namely: PD-135 (a precipitation hardening Cd-Cr-Copper alloy), INCO LEA (an age-hardenable low expansion nickel-base alloy), Inconel 718 and Inconel 706 nickel-base superalloys. In this third and final year (FY 76) effort, two alloys were included, namely: Pyromet 538 (21-6-9) high manganese stainless steel and A-286, an age-hardenable stainless steel.

A particular emphasis has been placed on the characterization and documentation of the starting base materials as well as on the various processing and fabrication conditions to which these materials were subjected. This characterization includes chemical analysis, melting practice and mill processing details when available, heat numbers, microstructural analysis, grain size measurements, and hardness measurements in addition to the physical, mechanical and fracture mechanics property evaluations, and fractographic examination and analyses. Such emphasis on characterization (and complete documentation thereof) is considered essential in a program such as this for two basic reasons, namely:

- The specific physical, mechanical and fracture mechanics property data generated are applicable to the particular materials evaluated herein and may be significantly different from similar data generated elsewhere on material of the same alloy designation, but of different chemical composition, or

product form or size which may differ appreciably in microstructural detail.

- It is highly desirable to understand how such properties, which are required for design and fabrication considerations, are influenced by the actual microstructure and/or composition of a particular alloy. Such information is useful in both materials selection and in assessing the effects of various processing and fabrication operations involved either in the original mill processing of the starting materials or in the actual hardware fabrication of a particular cryogenic device.

Other candidate cryogenic structural materials have been identified (See Table 5-1) which, on the basis of the limited data available, appear worthy of initial screening tests. Modifications of these various alloys should also be considered since their compositions were originally optimized for elevated (rather than cryogenic) temperature service. Furthermore, since various combinations of these alloys are likely to be employed in the same structure or device, the subject of dissimilar metal joint property evaluation for cryogenic service should also be addressed. In addition, a significant effort is still required by materials scientists and engineers in interfacing with the designers and fabricators of advanced cryogenic structures to better establish effective and functional materials selection and utilization criteria.

3.3 Mechanical and Fracture Mechanics Properties

Mechanical property data as obtained from smooth and notched ($K_t = 10$) tensile testing for all candidate materials evaluated to date in this WRL program are graphically summarized in Figs. 3-1 to 3-4. Fracture toughness values evaluated at 4K are summarized in Fig. 3-5 and are coded to reflect either base metal, processing effects or weldment or brazed sample conditions. Much of this summarized data has been reviewed in Section 3 of the previous WRL reports and therefore, the remarks following will pertain primarily to the recently added data.

Figure 3-3 now includes the tensile data on the GTA weldments in Inconel 706 (VIM-VAR) material which were given a post weld solution and double aging treatment, material code 72XX. A comparison of these results reveals that the 0.2% yield strength of the 706 transverse weld specimens was about 94% at RT and 96% at 4K of the corresponding 706 base metal data (condition 71XX). The ultimate tensile strength of these weldments achieved only 38% at RT and 83% at 4K of the base metal UTS values. The notched tensile strength of the 706 weldment was 86% at RT and 83% at 4K of the base metal NTS values. The notched tensile strength to yield strength ratio of the 706 weldments was 1.6 at RT and 1.4 at 4K as opposed to a constant value of 1.8 for the base metal NTS/YS ratio values. Thus, the 706 weldments were slightly more notch sensitive than the corresponding base metal but, notch sensitivity is not considered a significant problem in either.

A significantly lower ductility level expressed as either reduction in area (RA) or total elongation was experienced with the 706 weldments as compared to the 706 base metal from RT to 4K. At 4K, the welds attained only 17% of the RA and 14% of the total elongation values measured for the 706 base metal. These severe losses in the ductility of the weld metal relative to the 706 base metal have been attributed to intergranular (Nb, Ti)C carbide films formed in the weld fusion zone. Such MC films are associated with the Inconel 718 filler wire used in these welds, since no such films are observed in the Inconel 706 base metal. It would be desirable to evaluate GTA weldments made in IN 706 using a matching IN 706 filler wire (instead of the 718 filler wire), although such tests cannot be included in the present Westinghouse FY 76 program.

Figure 3-3A is essentially the same graphical summation of tensile data for the various Electron Beam and GTA Weldment conditions in the Inconel X750 alloy as presented previously as Fig. 3-4.

Figure 3-4 of this report includes tensile test data for Udimet 718 from a separate program (1) as well as Inconel 718 base metal, weld fusion and heat-affected zone and various cold work and re-heat treating conditions. The 0.2% yield strength and the ultimate

tensile strength of the Udimet 718 was quite comparable to that of the Inconel 718 material, both alloys in the STDA condition. The ductility of the Udimet 718 billet material, however, was considerably greater from RT to 4K than that evidenced by the Inconel 718 billet material (Code 64XX). The GTA weldments (Code 65XX) in the Inconel 718 material were made using IN 718 filler wire and demonstrated a further significant reduction in ductility and in notch tensile strength over the IN 718 base metal. The notched tensile strength of the heat-affected zone in the IN 718 weldments (Code 66XX) was greater than or equal to that of the weld fusion zone, but 10 to 20% lower than that of the parent IN 718 base metal.

Figure 3-5 consists of a summary comparison of fracture toughness values at 4K for all materials evaluated to date. No data is shown for the OFHC copper, since valid K_{IC} (J_{IC}) measurements could not be attained with the techniques employed. The OFHC copper is considered of greater fracture toughness than any of the materials tested to date. Fracture toughness tests have been conducted on the PD-135 age hardenable copper alloy, but results are not shown in Figure 3-5 as the elastic constants at 4K are not yet available.

3.4 Effect of Processing

The effects of the various processing operations included in the WRL program on the yield and tensile strength and the fracture toughness properties of several alloys are summarized in Figures 3-6 and 3-7, normalized to their respective base metal conditions. Recent data added to Figure 3-6 includes the various processed conditions of Inconel 718 (Codes 67XX, 68XX and 69XX) and the comparison of the Inconel 706 Vacuum Arc Remelted (VAR) versus the Electroslag Remelted (ESR) materials (Code 71XX/70XX). The most significant effect of the processing operations for these latest additions is for the Inconel 718 material directly aged following cold working which demonstrates an increase of about 20% in 0.2 percent yield strength and 12% in ultimate tensile strength. While not shown in Figure 3-6, this Code

69XX material experienced only a slight decrease (~5%) in the total elongation values as compared to the Code 64XX material. There was little difference between the tensile properties of the VAR and ESR Inconel 706 billet materials.

Figure 3-7 shows the effect of the various processing conditions on the 4K fracture toughness, expressed as a ratio of fracture toughness, normalized with respect to that of the corresponding base metal conditions. For the Inconel 706, the toughness of the VIM-VAR material at 4K was found to be ~10% greater than that of the VIM-ESR billet material. Fracture toughness data for the various processed conditions of Inconel 718 are not yet available.

3.5 Effects of Metals Joining

The effects of various metals joining processes including both brazements and fusion weldments on the yield strength and ultimate tensile strength is presented in Figures 3-8 and 3-9. The fracture locations of the transverse composite weld tensile specimens for these various alloys are indicated. The copper brazed joint in Inconel X750 (Code 38XX) demonstrated a yield strength level equal to and an ultimate tensile strength level below that of the solution treated X750 base metal. Both the yield and ultimate tensile strength of the silver brazed copper joint (Code 13XX) were below that of the OFHC base metal. Both brazed joint conditions failed at the braze interface.

Figure 3-10 presents a graphical comparison of the fracture toughness ratio of joints/base metal at 4K. In certain cases we have observed an increase in the fracture toughness of the weldment over the base metal level. First in the case of GTA weldments in prior cold-worked Kromarc 58 stainless steel where the increased toughness was a result of the elimination of the cold working (hardening). Secondly, in the case of both EB and GTA weldments in various pre- and post-welding heat treatment conditions of the Inconel X750 (MP-1) alloy. In this latter case, the remarkable increase in fracture toughness of

the weldments over the base metal was attributed to the elimination of a continuous brittle carbide film present in the original X750 base metal. Otherwise, the fracture toughness values at 4K of the remaining weldments and of the copper brazed joint in Inconel X750 were below those of their corresponding base metals.

Fatigue Crack Growth Rate (FCGR) data, although not graphically summarized in this section (see Section 6) has revealed the following interesting patterns:

- The FCGR in Kromarc 58, AISI 310S and A-286 stainless steels and Inconel X750, 706, 718 and LEA nickel-base superalloys is significantly greater at room temperature than at 77 or 4K.
- Kromarc 58 stainless steel has the same FCGR at both 77 and 4K in the 30% cold worked condition as for the solution treated and quenched condition. AISI 310S has the same FCGR at both 77 and 4K in the sensitized (STFC) as for the solution treated and quenched condition. Thus, while these respective processing conditions do have a significant effect on the fracture toughness, no processing effect was observed on the FCGR.
- The various heats of Inconel X750 demonstrated significant variations in FCGR as well as in fracture toughness levels. The lowest FCGR was evidenced by the MP-2 designated heat (AAM-VAR) and the highest FCGR was shown by the MP-1 designated heat (AM-VAR). The MP-1 heat showed no apparent difference in FCGR between the solution treated and the age hardened conditions, but such a difference may have existed but was masked by the presence of a brittle carbide film. Support for such speculation is suggested by the results of a higher FCGR in the as-hipped (ST) MP-1 material over the HIP/STDA treated material.

- For the remaining nickel-based superalloys, all in the age hardened condition, the lowest 4K FCGR was evidenced by the Inconel 706 (VIM-VAR) followed by the IN 706 (VIM-ESR), Inconel 718 and finally by the Inco LEA in increasing order.
- Both the GTA welds in Kromarc 58 and the SMA welds in the AISI 310S demonstrated higher FCGR values (above a stress intensity factor of $\sim 35 \text{ ksi}\sqrt{\text{in.}}$) than their corresponding base metals.
- Both the vacuum electron beam and the GTA weldments in the Inconel X750 demonstrated identical fatigue crack growth rates at both 77 and 4K regardless of the pre- or post-weld heat treatments investigated. The FCGR of these weldments was also identical to that of the parent base metal in either the ST or STDA condition at 77 and 4K.

Reference (Section 3)

1. Phase IIB, Program for the Development of a Superconducting Generator, U.S.A.F. Contract F33615-71-C-1591.

TABLE 3-1 STRUCTURAL MATERIALS FOR CRYOGENIC APPLICATIONS

FY74 (C) Program Status As Of March 10, 1975

Material Code	Condition	Chem. Analy.	Metallography		Mag.	Physical Prop.	Processing	Joining	Tensile			Notched Tensile			K _{1C}			J _{1C} (3)		FCGR			Fractography (4)		
			(1)	(2)					R	N	H	R	N	H	R	N	H	R	H	R	N	H	R	N	H
OFHC-Cu 10XX	AR	/1	2/1	1		1			1/1	1/1	1/1	1/1	1/1	1/1	1/2	1/2				1/2	1/3		1/1	3/3	3/3
11XX	SR		2/1	1			1/1		1/1	1/1	1/1	1/1	1/1	1/1	*1/2	1/2				1/2	1/3			5/3	
12XX	GMAW		3/2	1		1		3/2	2/2	2/2	2/2	2/1	2/2	2/2	*1/2	1/2				1/2			1/1	1/1	3/3
13XX	B		3/2	2				2/2	1/2	1/2	1/2	1/1	1/2	1/2	1/2	1/2		4					1/1	1/1	2/2
14XX	S		3/2	2				2/2	1/2	1/2	1/2	1/1	1/2	1/2	1/2	1/2							1/1	1/1	2/2
AISI 310S 20XX	STQ	□/1	2/2	1	2/1	2/1	1/1		1/1	3/2	4/2	1/1	1/2	1/2	*1/1	2/2	2/3	4		1/1	1/2	4/3	1/2	1/3	3/3
21XX	STFC		1/1	1		1	1/1		1/1	1/2	2/2	1/1	1/2	1/2	*1/1	2/2	2/3	5		1/1	2/2	2/3	1/2	1/3	3/3
22XX	SMW	□	2/2		1/1	1/1	2/2	2/2	2/1	2/2	2/2	2/1	2/2	2/2	*1/2	1/3		6		2/2	2/2		1/1	1/3	3/3
Inconel X750 30XX	ST	2/1	3/2	3	2/2	2/2	2/2		1/1	2/2	2/2	1/1	2/2	2/2	*1/1	4/2	2/3	5	4	2/2	1/2	2/3	2/2	2/3	4/4
31XX	STDA		3/2	3	2/1	2/1	2/2		1/1	2/2	2/2	1/1	2/2	2/2	*1/1	4/2	2/3	5		2/2	1/2	4/3	2/2	2/3	2/3
32XX	ST/EBW		2/3	1			3/3	3/3	1/1	1/2	1/2	1/1	1/2	1/2	*1/2	1/2		2		1/1	2/1		1/1	1/2	2/2
33XX	STDA/EBW		2/3	1			3/3	3/3	1/1	1/2	1/2	1/1	1/2	1/2	*1/2	1/2		2		1/1	1/1		1	1	2/2
34XX	EBW/STDA		2/3				3/3	3/3	1/1	1/2	1/2	1/1	1/2	1/2	*1/2	1/2		3		1/2	2/2		1	1	2/2
35XX	ST/GTW		3/3	1			3/3	4/3	1/1	1/2	1/2	1/1	1/2	1/2	*1/2	1/2		6		1/1	2/2		1	1	2/2
36XX	STDA/GTW		3/3	1			3/3	4/3	1/1	1/2	1/2	1/1	1/2	1/2	*1/2	1/2		5		1/1	2/2		1	1	2/2
37XX	GTW/STDA		3/3				3/3	3/3	1/1	1/2	1/2	1/1	1/2	1/2	*1/2	1/2		5		1/1	2/2		1	1	2/2
38XX	B		2/2	2			2/2	2/2	2/2	2/2	2/2	1/1	1/2	1/2	1/2	1/2							1	2/2	2/2
40XX	MP 2/STDA	□/1	2/2	3			2/2		1/1	2/2	2/2	1/1	2/2	2/2	*1/2	1/2		6	1	1	1		1	1	2/2
50XX	MP 3/STDA	□/1	2/2	3			2/2		1/1	2/2	2/2	1/1	2/2	2/2	*1/2	1/2		7	1	1	1		1	1	2/2
60XX	HIP	2/2	2/2	3			5/2		2/1	2/2	2/2	2/1	2/2	2/2	*1/2	1/2		7		2/2	2/2		1/1	2/2	2/2
61XX	HIP/STDA	1	2/2	3	1	1	3/2		2/1	2/2	2/2	2/1	2/2	2/2	*1/2	1/2		6		2/2	2/2		1	1	1/2
Kromarc 58 80XX	STQ	1/1	1/2	2	1/1	1/1	2/2		1/1	2/2	2/2	1/1	2/2	2/2	*1/2	1/3		5		1/2	1/2	2/3	1/2	1/3	2/3
81XX	CW		2/2	2	1/1	1/1	2/2		1/1	2/2	2/2	1/1	2/2	2/2	*1/2	1/3		5		1/2	1/2	2/3	1/2	1/3	2/3
82XX	GTW	1/1	4/2	2	1	1	2/2	2/2	1/1	2/2	2/2	2/1	2/2	2/2	1/2	1/3		6		2/2	2/2		1/1	1/3	2/3
83XX	CW/GTW		1/2		1	1	1/1	1/1	2/1	2/2	2/2	2/1	2/2	2/2	1/2	1/3		6					1	1	2/2
84XX	GTW/CW		1/2		1	1	1/1	1/1	2/1	2/2	2/2	2/1	2/2	2/2	1/2	1/3		6							2/2
85XX	GTW/C W/A N		10/2				3/1	1/1	1/1	1/1	1/1	1/1	1/2	1/2	1/2	1/2		4							2/2
86XX	GTW/C W/A N						1	1/1	1/1	1/1	1/1							5							2/2

Notes: 1 Optical Microscopy

2 Replicate and Transmission Electron Microscopy, X-Ray Dispersive and Microprobe Analysis to be Incorporated as Required

3 Elastic-Plastic (J_{1C}) Testing and Analysis Techniques to be Incorporated Where Linear-Elastic (K_{1C}) Data is Non-Valid

4 Macro and Microfractographic (SEM) Examination Schedule to be Adjusted in Response to Exhibition of Unusual Material Behavior

• Available Specimen Size Invalid for Meaningful K_{1C} Interpretation - Test Eliminated

□ Certified Chemical Analysis from Supplier

■ Ditto-Additional Interstitial Analysis Completed at (C)

→ J_{1C} Tests Substituted for K_{1C}

◇ Solder Joints Not Suitable for Mechanical Tests, Tests Eliminated

TABLE 3-2-STRUCTURAL MATERIALS FOR CRYOGENIC APPLICATIONS

FY 75 (S) Program Status as of April 9, 1976

Material Code	Condition	Chem. Analysis	Metallography		Physical Prop. Mag. Res.	Processing Operations	Plates Joined	Tensile			Notched Tensile			K _{1C} (J _{1C})			FCGR			Fractography		
			(1)	(2)				R	N	H	R	N	H	R	N	H	R	N	H	R	N	H
PD135 Copper 15XX	EXT/PHT	■	2/2		1/1 2/2	2/2		2/2	2/2	2/2	2/2	2/2	2/2	6/6			1/2	1/2		1/1	1/2	2/3
Inconel X750 HIP																						
62XX	GTAW/STDA (FZ)	□	2/2		1/1 1/1	2/2	2/2	*1/2	*1/2	*1/2	*1/2	*1/2	*1/2	*1/6			*1/2			*1/1	*1/1	*1/3
63XX	GTAW/STDA (HAZ)		2/2			2/2	2/2				*1/2	*1/2	*1/2	*1/6			*1/2			*1/1	*1/1	*1/3
Inconel 718																						
64XX	STDA	■	4/4	4	2/2 1/1	2/1		2/2	2/2	2/2	2/2	2/2	2/2	6 5/6	1	1/2	2/2			1/1	2/2	3/3
65XX	ST/GTAW/STDA (FZ)		3/3	4	1/1 1/1	2/2	3/3	2/2	2/2	2/2	2/2	2/2	2/2	2 2/6			1/2			1/1	1/1	3/3
66XX	ST/GTAW/STDA (HAZ)		3/3	4		2/2	3/3				2/2	2/2	2/2	2 2/6			1/2			1/1	1/1	2/3
67XX	ST/CW/AN		2/3			2/3		2/2	2/2	2/2	2/2	2/2	2/2	1/6	1	1	1			2	2	2/2
68XX	ST/CW/AN		2/3			2/3		2/2	2/2	2/2	2/2	2/2	2/2	1/6	1	1	1			2	2	2/2
69XX	ST/CW/AN		2/3			2/3		2/2	2/2	2/2	2/2	2/2	2/2	1/6	1	1	1			2	2	2/2
Inconel 706 (EFR) 70XX (VAR) 71XX (VAR) 72XX	STDA	■	4/4	4	1/1 1/1	1/1		2/2	2/2	2/2	2/2	2/2	2/2	7 5/6	1	2	1/2			1/1	1/1	2/3
	STDA	■	4/4	4	1/1 1/1	1/1		2/2	2/2	2/2	2/2	2/2	2/2	7 7/6	1	1	1/2			1/1	1/1	3/3
	ST/GTAW/STDA		3/3	4	1/1 1	2/2	3/3	2/2	2/2	2/2	2/2	2/2	2/2	4/6			1/2			1/1	1/1	3/3
INCO LEA 73XX 74XX	STA	■	3/3	4	1/1 1/1	2/2		2/2	2/2	2/2	2/2	2/2	2/2	5 5/6	1	1/2	1/2			1/1	1/1	2/3
	ST/GTAW/STA		2/2	3	1/1 1	2/2	2/2	*1/2	1/2	*1/2	*1/2	*1/2	*1/2	*1/6			*1/2			*1/1	*1/1	*1/3
Kromarc 58 87XX	STW/CW/θ	□	1/1			2/2		2/2	2/2	2/2	2/2	2/2	2/2	6/6	1	1	1/2			1/1	1/1	1/3

Notes: (1) Standard optical microscopy

(2) Electron microscopy, microprobe & x-ray dispersive analysis incorporated as required

■ Certified chem. analysis from supplier, additional interstitial gas analysis by (S)

□ Analysis conducted for this material in FY 74 program

(3) Physical property determinations also conducted on five materials (Fe - 9% Ni, Fe - 68% Ni, Fe - 3% Si, AISI 416SS and ARMCO Fe) requested by NBS

* Fracture mechanic testing and fractographic analysis of these specimens indefinitely postponed

FY 76 (S) Program Status as of April 9, 1976

Material Code	Condition	Chem. Analysis	Metallography		Physical Prop. Mag. Res.	Processing Operations	Plates Joined	Tensile			Notched Tensile			K _{1C} (J _{1C})			FCGR			Fractography		
			(1)	(2)				R	N	H	R	N	H	R	N	H	R	N	H	R	N	H
A-286																						
90XX	STQA	■	6		2/2	1/1		2/2	2/2	2/2				5 5	1	1	1			2/2	2/2	2/2
91XX	STQ/GTAW	■	2/2		1/2	2/2	1	1/2	1/2	1/2	1/2	1/2	1/2	1/6	1/1	1/1	1/1			1/2	1/2	1/2
Pyromet 538 (21-6-9 SS)																						
92XX	STQ	■	5/5		4/4	2/2		1/1	1/1	1/1	1/1	1/1	1/1	1/5						1/2	1/2	1/2
93XX	STQ/GTAW	■	2/2		1/2	2/2	2/2	1/2	1/2	1/2	1/2	1/2	1/2	1/6	1/1	1/1	1/1			1/2	1/2	1/2
94XX	STQ/STAW	■	2/2		1/2	2/2	2/2	1/2	1/2	1/2	1/2	1/2	1/2	1/6	1/1	1/1	1/1			1/2	1/2	1/2






Notes: (1) Standard optical microscopy

(2) Electron microscopy, microprobe, x-ray dispersive analysis incorporated as required

■ Certified chemical analysis from supplier, additional interstitial gas analysis by (S)

■ Chemical analysis conducted by (S)

Legend:

-  Notched Ultimate
-  Ultimate Tensile
-  0.2% Yield Strength
-  Reduction in Area
-  Elongation

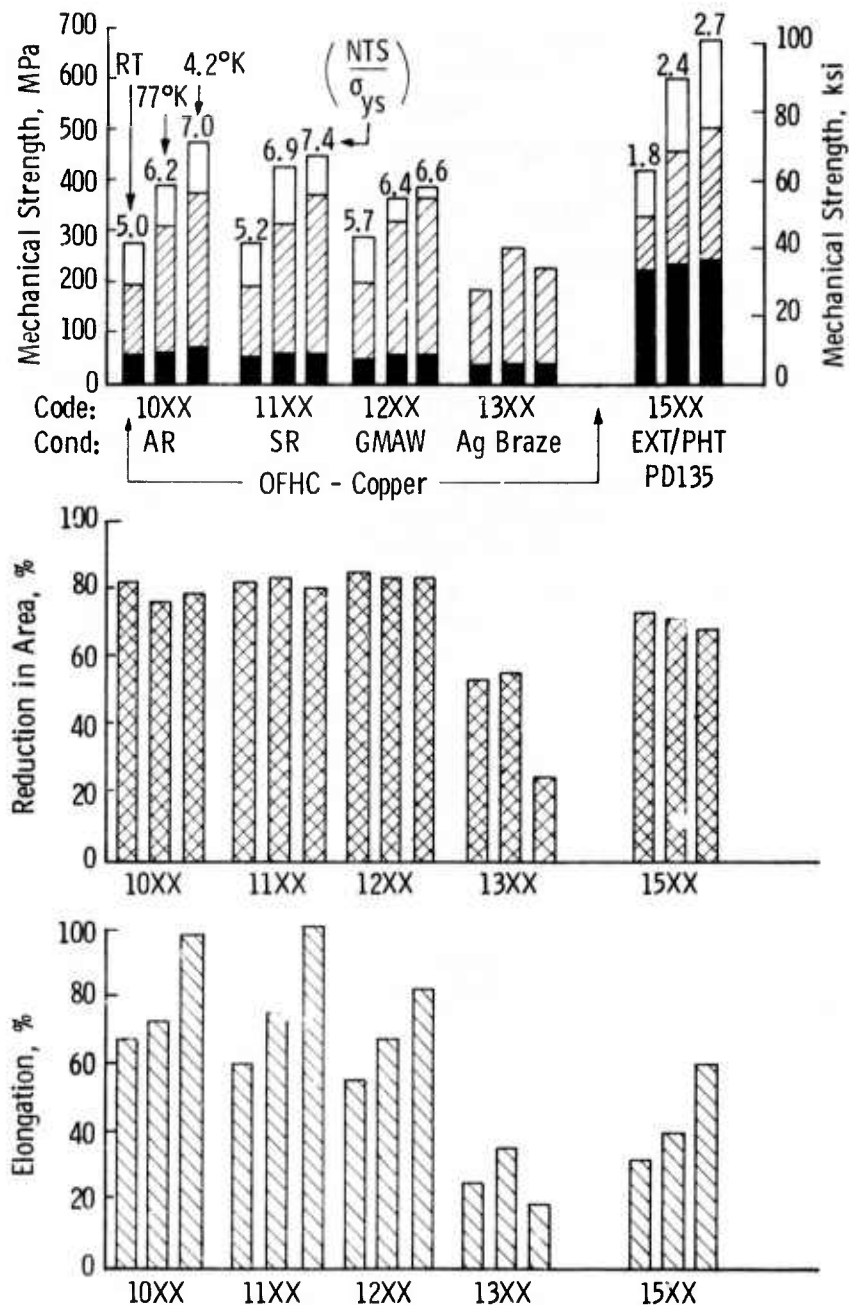


Fig. 3-1—Summary comparison of mechanical strength and ductility values for copper alloys including processing and fabricated joints at RT, 77 K, and 4.2 K

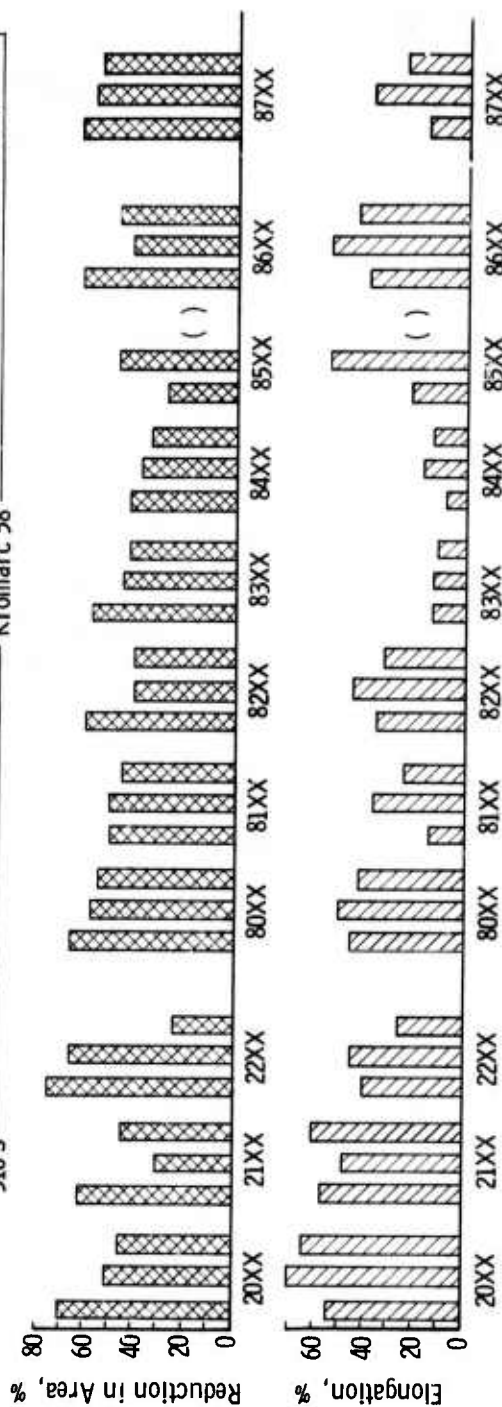
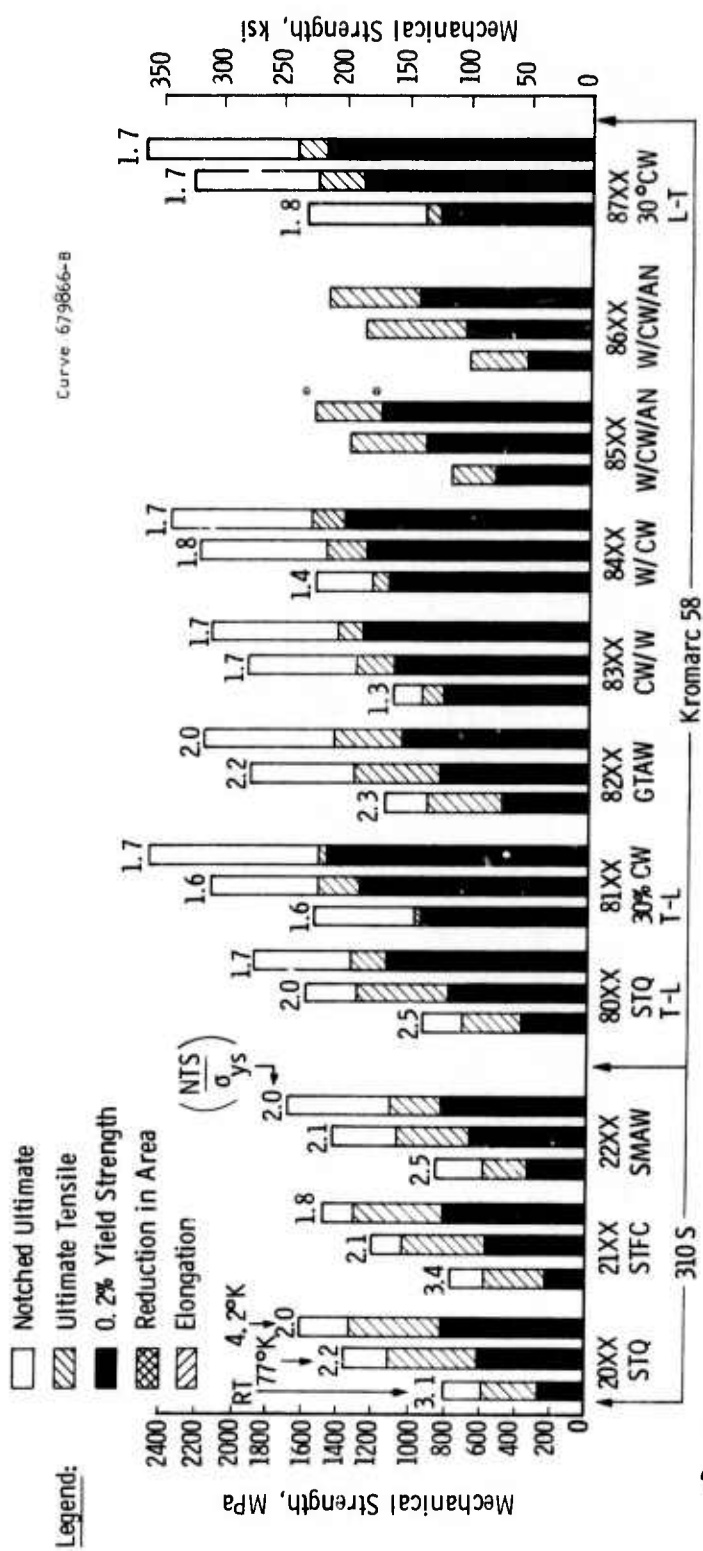


Fig. 3-2—Summary comparison of mechanical strength and ductility values for AISI 310 S and Kromarc 58 stainless steels including processing and welded joints at RT, 77 K and 4.2 K

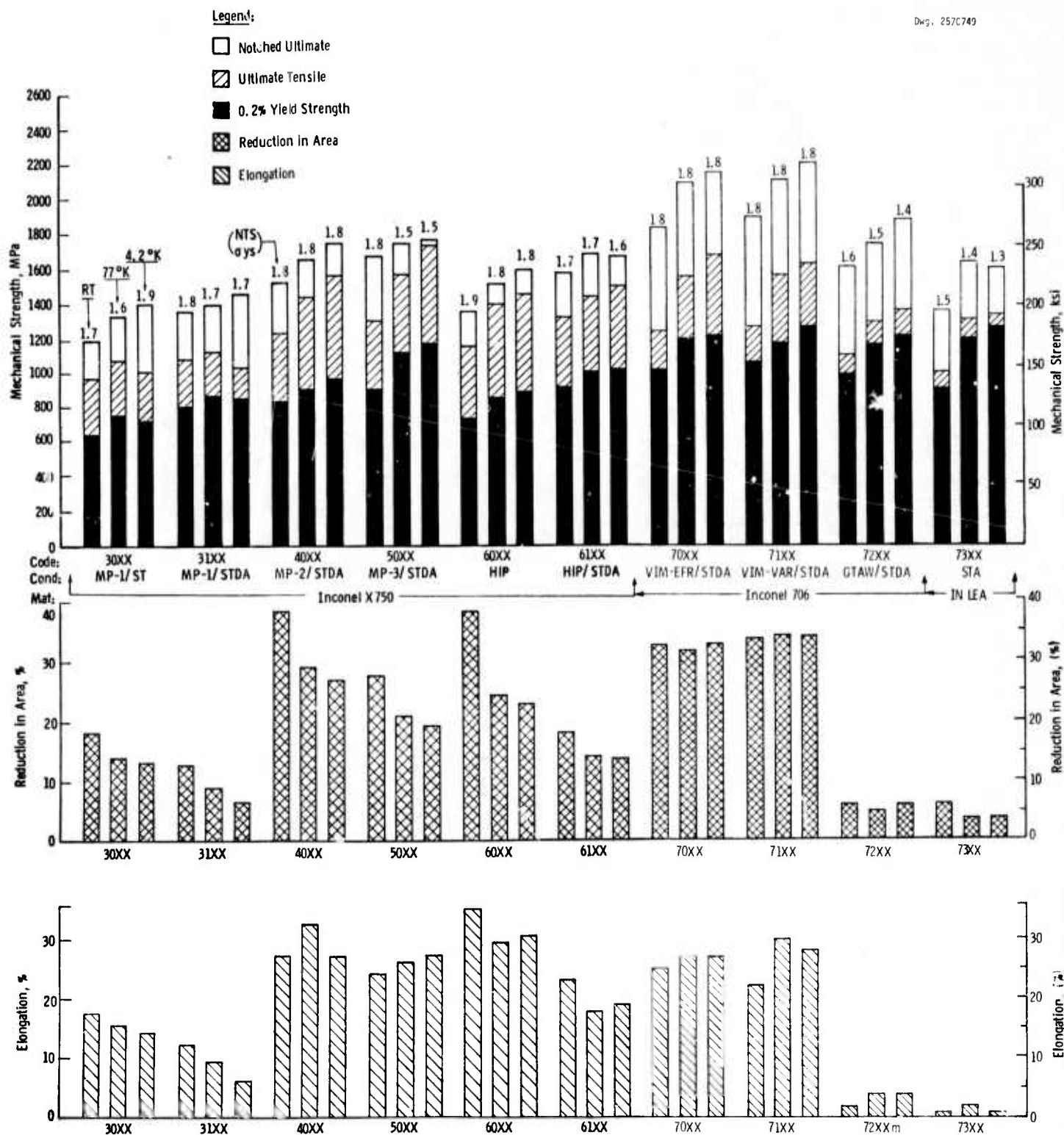


Fig. 3-3 - Summary comparison of mechanical strength and ductility values for nickel based superalloys IN X750, 706 and LEA in various processed conditions at RT, 77K, and 4.2K

Legend:

- Notched Ultimate
- ▨ Ultimate Tensile
- 0.2% Yield Strength
- ▩ Reduction in Area
- ▧ Elongation

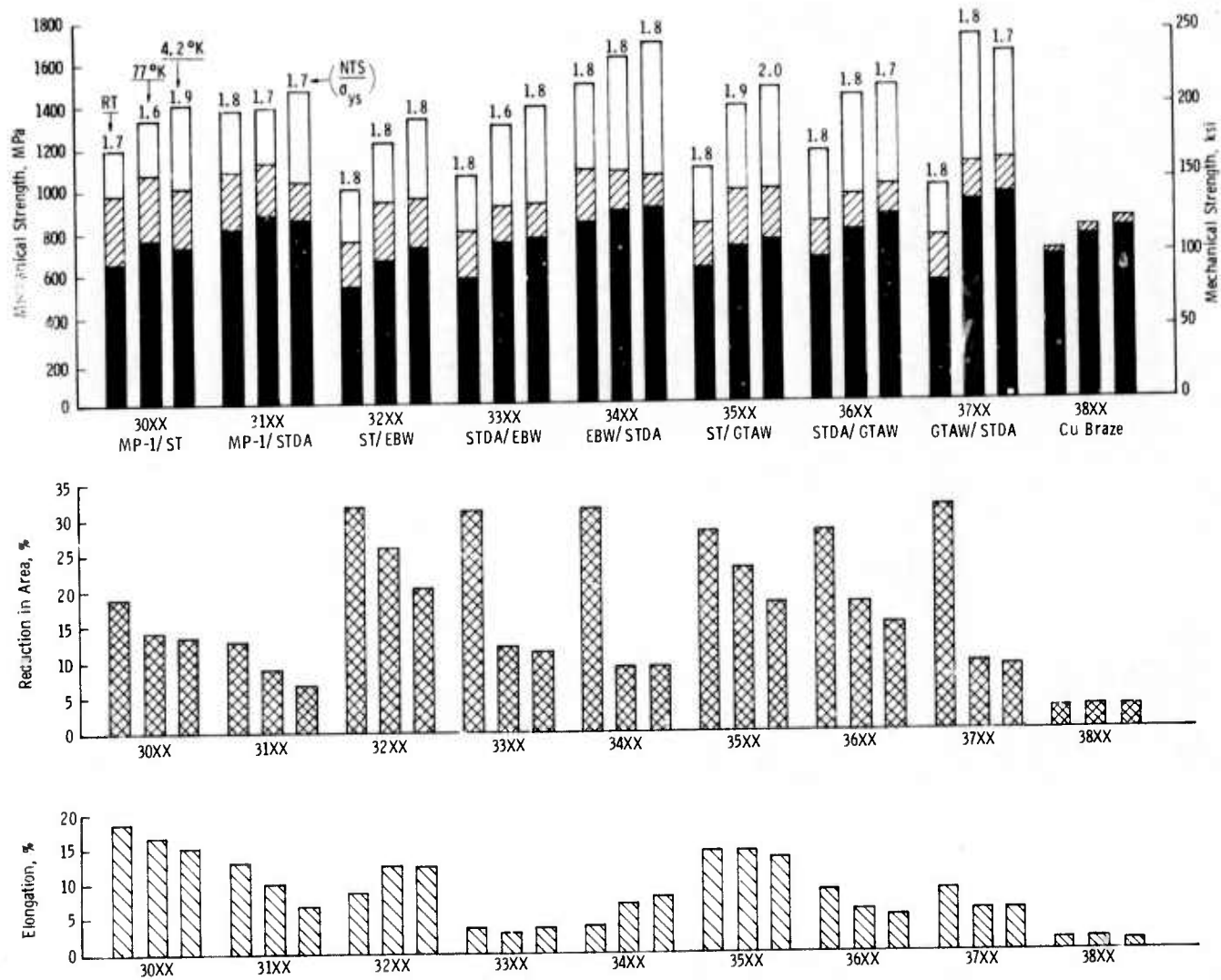


Fig. 3-3A—Summary comparison of mechanical strength and ductility values for Inconel X 750 base metal, electron beam and GTA weldments and copper brazing at RT, 77 K and 4.2 K

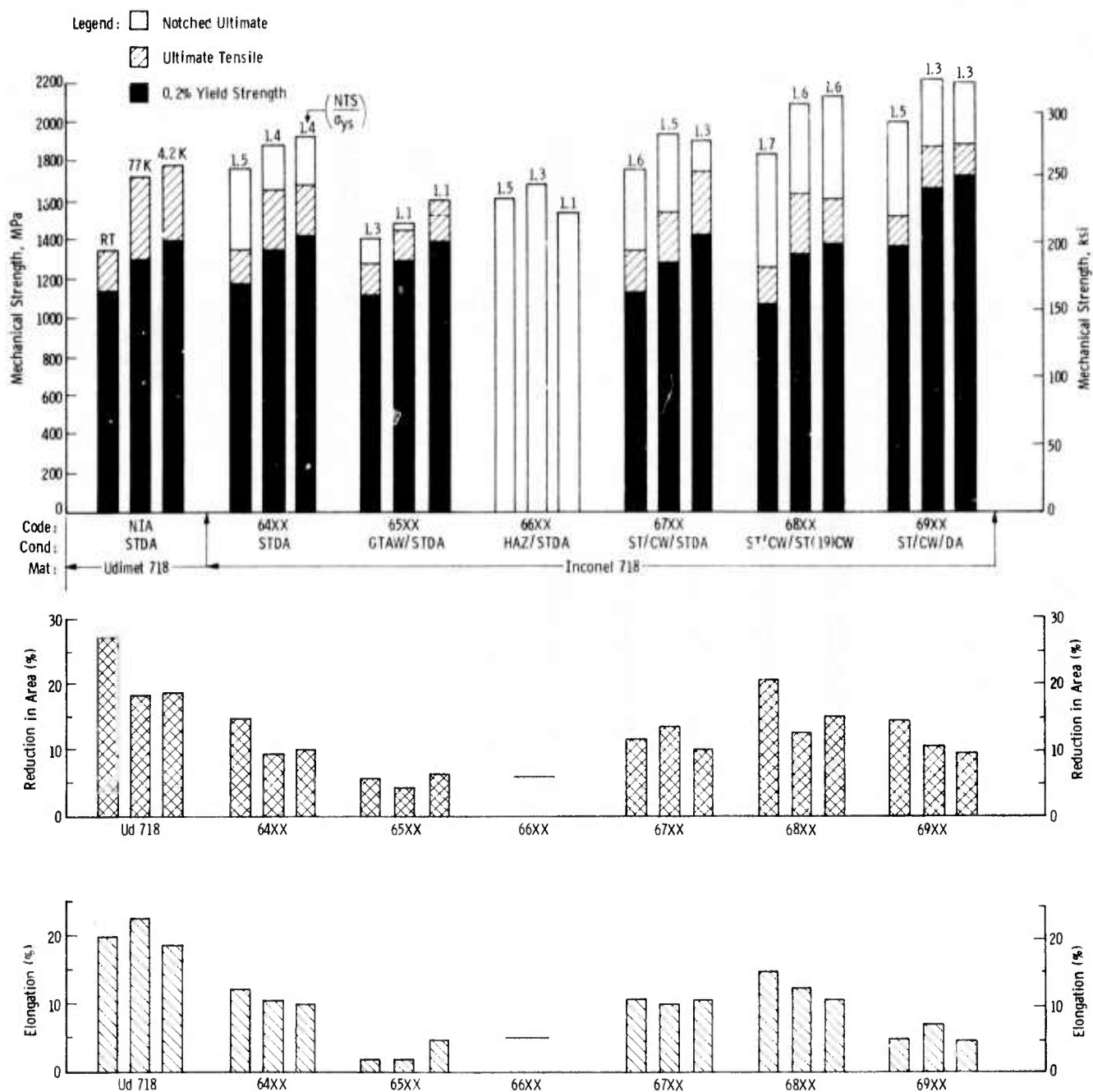


Fig. 3-4—Summary comparison of mechanical strength and ductility values for nickel base superalloys Udmet 718 and Inconel 718 in various processed and fabricated conditions at RT, 77K and 4.2K

Legend:

- Base Metal
- Processing
- Weldment (or Braze)
- Combined Welding and Processing Effects

Dwg. 8508093

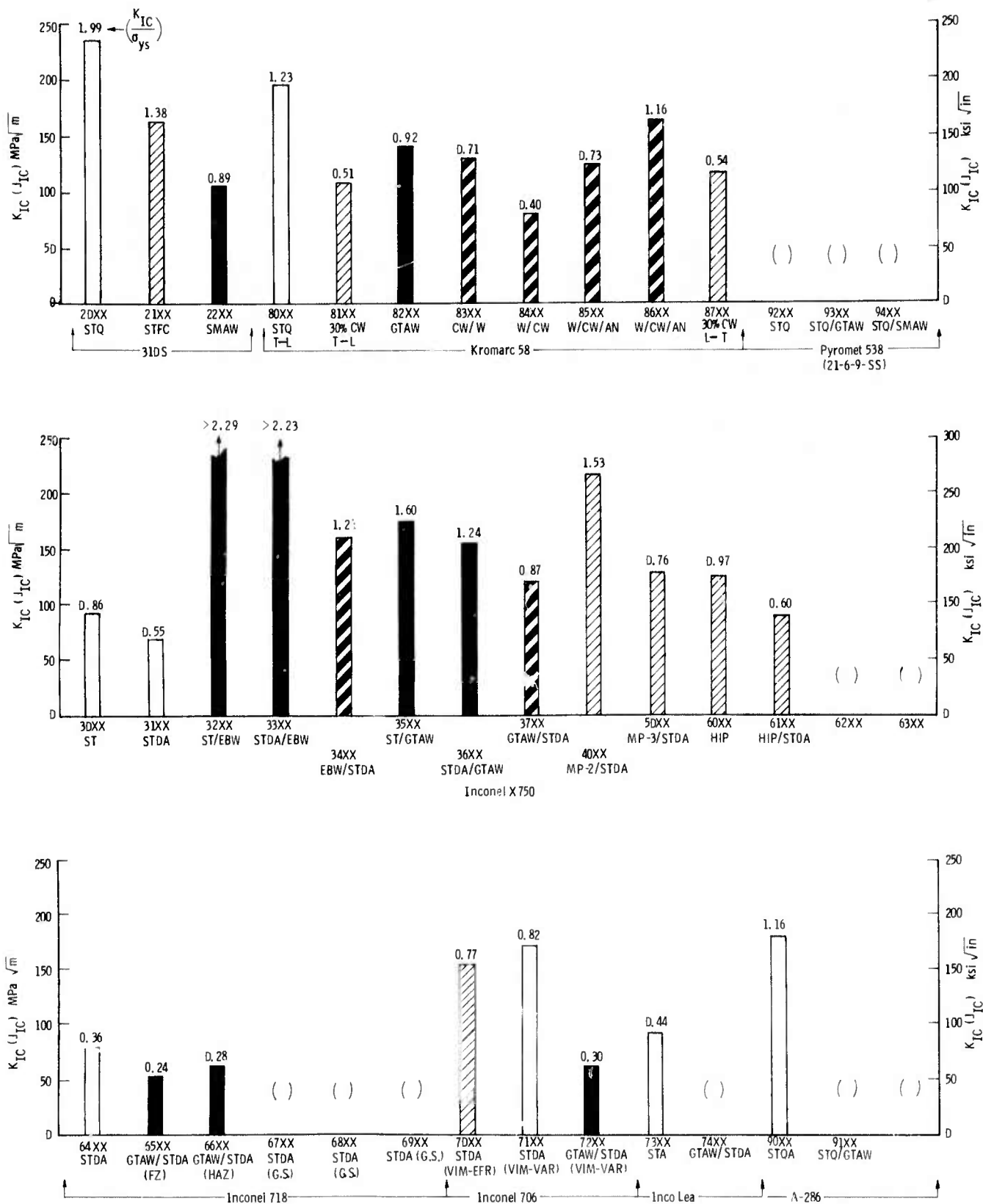


Fig. 3-5—Summary comparison of fracture toughness values at 4.2 K for 31DS, Kromarc 58, Inconel X750, Inconel 718, Inconel 706, Inco Lea, and A-286 materials including effects of processing and metals joining

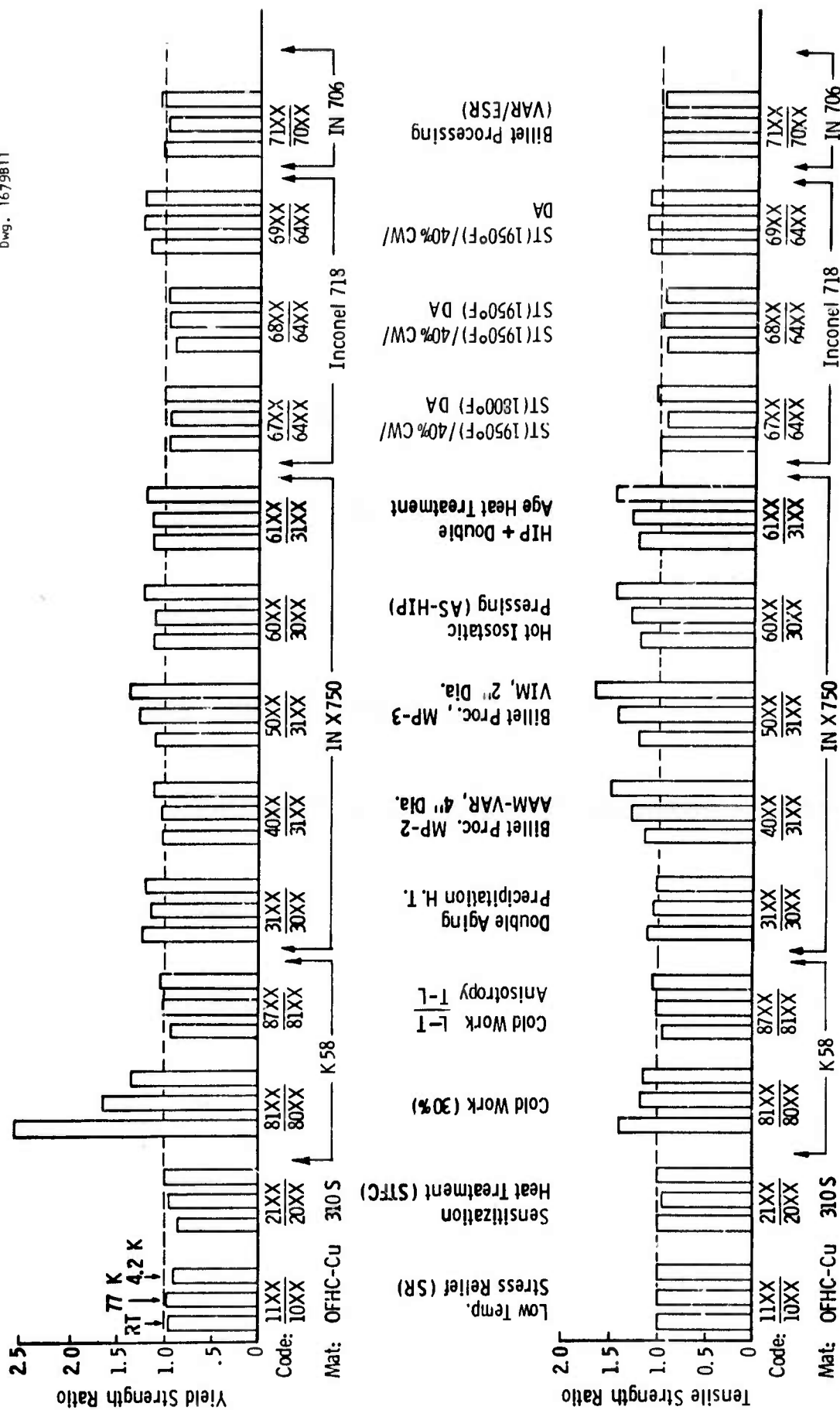


Fig. 3-6—Effect of processing conditions on yield strength and ultimate tensile strength ratios for OFHC Cu, 310 S, Kromarc 58, IN X 750, Inconel 706 at RT, 77 K and 4.2 K

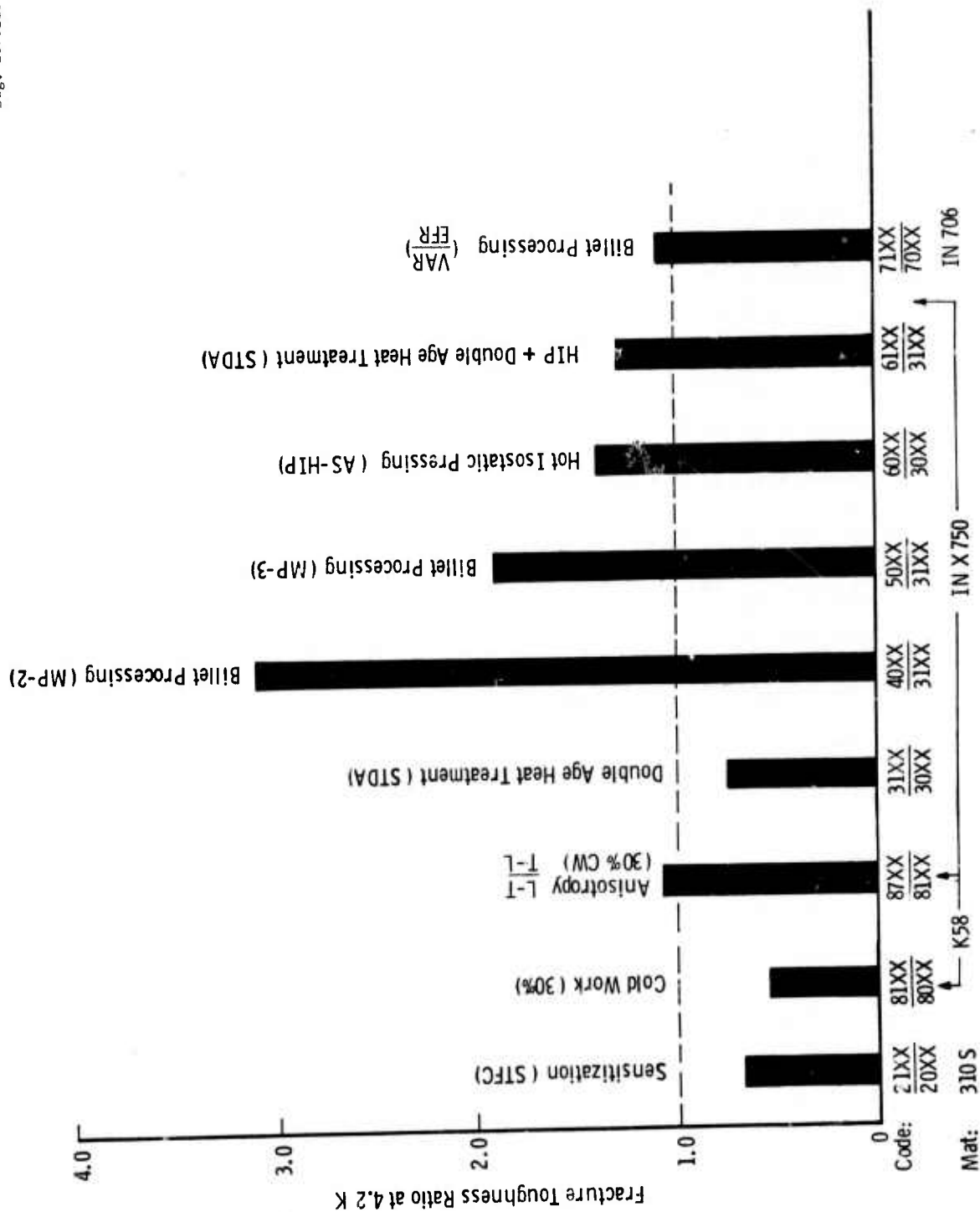


Fig. 3-7—Effect of processing conditions on fracture toughness ratio for 310 S, Kromarc 58, Inconel X 750, and Inconel 706 at 4.2 K

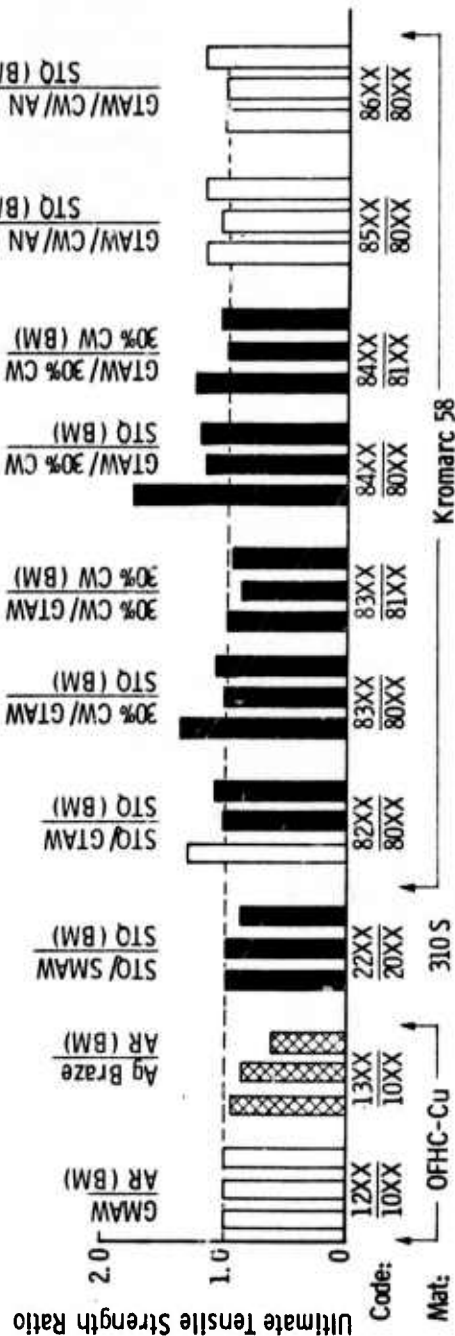
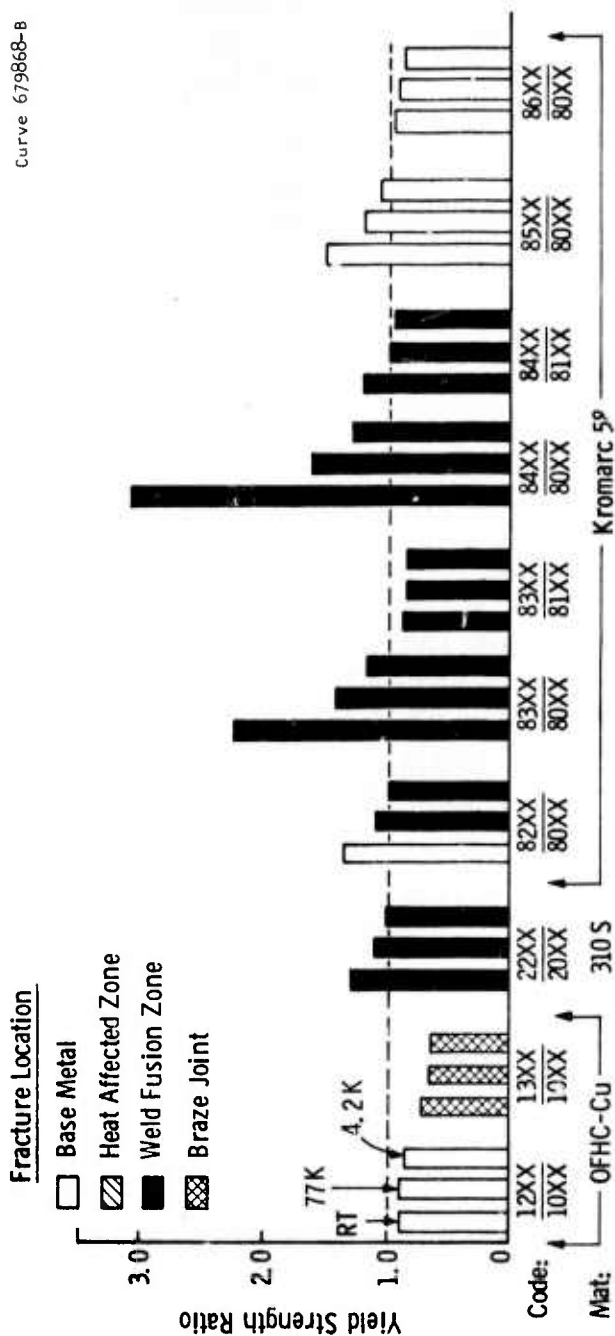


Fig. 3-8— Effect of metals joining conditions on yield strength and ultimate tensile strength ratios for OFHC copper, 310 S and K-58 stainless steel at RT, 77 K and 4.2 K

Code Fracture Location

- Base Metal
 ▨ Heat Affected Zone
 ■ Weld Fusion Zone
 ▩ Braze Joint

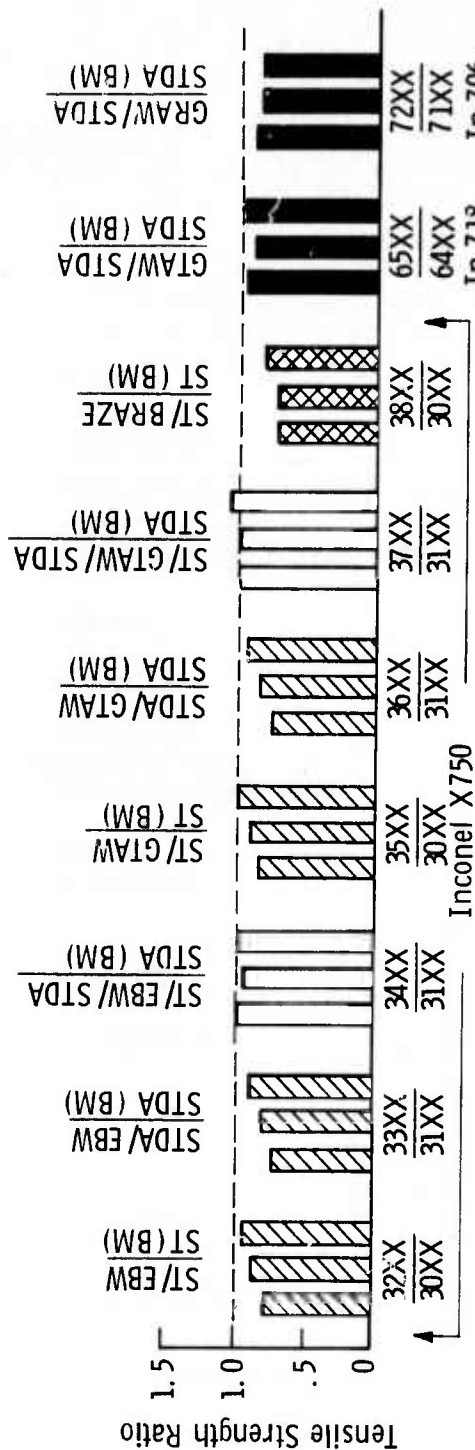
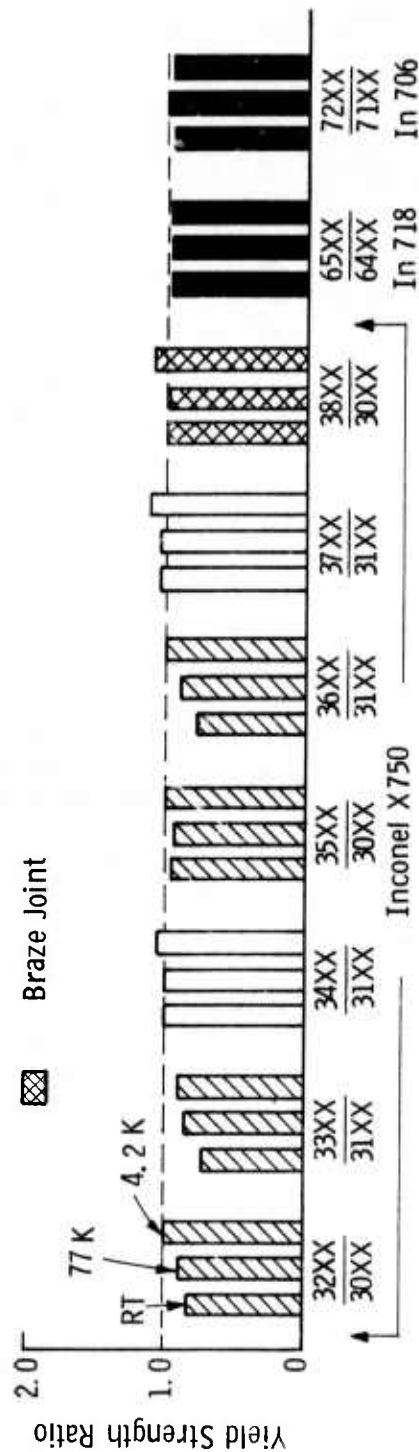


Fig. 3-9—Effect of metals joining conditions on yield strength and ultimate tensile strength ratios for Inconel X 750, Inconel 718 and Inconel 706 at RT, 77 K and 4.2 K

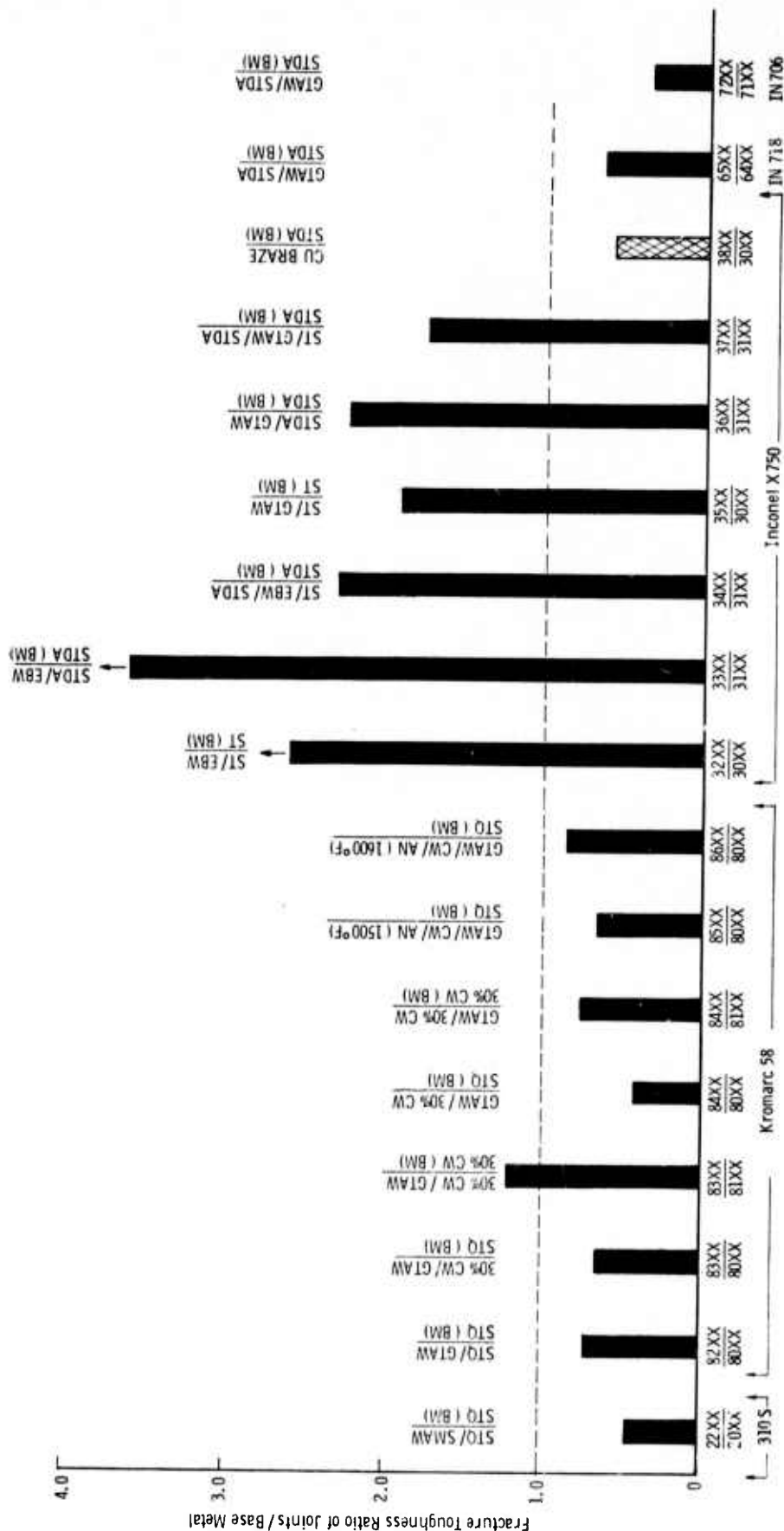


Fig. 3-10—Effect of metals joining conditions on fracture toughness ratio for 310S, Kromarc 58 stainless steel, IN X750, IN 718 and IN 706 at 4.2 K

4.0 WESTINGHOUSE PROGRAM DESCRIPTION

Interest in the engineering application of superconducting field windings in advanced cryogenic structures and devices has stimulated renewed interest in the mechanical and physical behavior of cryogenic structural support materials. Examples of such advanced cryogenic application areas include such prototype devices as superconducting motors and generators and large superconducting magnets for MHD and Tokomak and Mirror Type fusion power devices. The prior existing data base for structural materials in such applications was assessed as inadequate for material selection and utilization in a high reliability design.

This program represents the active participation of the Research Laboratories of the Westinghouse Electric Corporation under Contract CST-8304 in a comprehensive overall program for cryogenic structural materials for s.c. machinery monitored by the Cryogenics Division of the National Bureau of Standards. The overall program is sponsored by the Advanced Research Projects Agency (ARPA) of the Department of Defense. An overall outline for the Westinghouse portion of the ARPA-NBS program is shown schematically in Fig. 4-1. The principal personnel involved are listed in Figs. 4-2 according to their respective functional program responsibility areas.

A brief summation of the candidate materials evaluated, the processing considerations and the metals joining considerations included in each of the three years of the Westinghouse Program is presented below.

4.1 FY 74 Program Summation

- o Candidate Materials Evaluated:

- OFHC Copper
 - AISI 310 S
 - Kromarc 58
 - Inconel X750

- o Processing Considerations:

- Sensitization (STFC) in AISI 310S
 - Melting Practice and Mill Processing in IN X750
 - Hot Isostatic Pressed IN X750
 - Cold Working in Kromarc 58

- o Metals Joining Considerations:

- Gas Metal Arc Weldments in OFHC Copper
 - Silver Brazements in OFHC Copper
 - Solder joints in OFHC Copper
 - Shielded Metal Arc Weldments in AISI 310S
 - Gas Tungsten Arc Weldments in Kromarc 58
 - Electron Beam and Gas Tungsten Arc Weldments in
Inconel X750 with pre- and post-weld heat treatments.

4.2 FY 75 Program Summation

- o Candidate Materials Evaluated:

- PD 135 Copper Alloy
 - Inco Low Expansion Alloy
 - Inconel 706
 - Inconel 718

- o Processing Considerations:

- Melting Practice in IN 706 (ESR vs. VAR)
 - Comparison of Inconel vs. Udimet 718 Alloy
 - Anisotropic CW texture in Kromarc 58

o Metals Joining Considerations:

Copper Brazement in Inconel X750
Gas Tungsten Arc Weldments in HIP X750
Gas Tungsten Arc Weldments in INCO LEA
Gas Tungsten Arc Weldments in IN 706
Gas Tungsten Arc Weldments in IN 718 (FZ & HAZ)

4.3 FY 76 Program Summation

o Candidate Materials Evaluated:

Pyromet 538 (21-6-9)
A-286

o Processing Considerations:

Plate fabrication from Pyromet 538 billet stock
Cold working and recrystallization in IN 718
Comparison of Armco versus Cameron Iron A-286 alloy
Evaluation of predictive expressions for martensite
formation in austenitic stainless steels

o Metals Joining Considerations:

Evaluation of predictive expressions for delta ferrite
formation in austenitic stainless steel weldments
Gas Tungsten Arc Weldments in Pyromet 538
Shielded Metal Arc Weldments in Pyromet 538
Gas Tungsten Arc Weldments in A-286
Varestraint weldability testing for microfissuring
(hot cracking) in various austenitic stainless
steel and nickel-base superalloys.

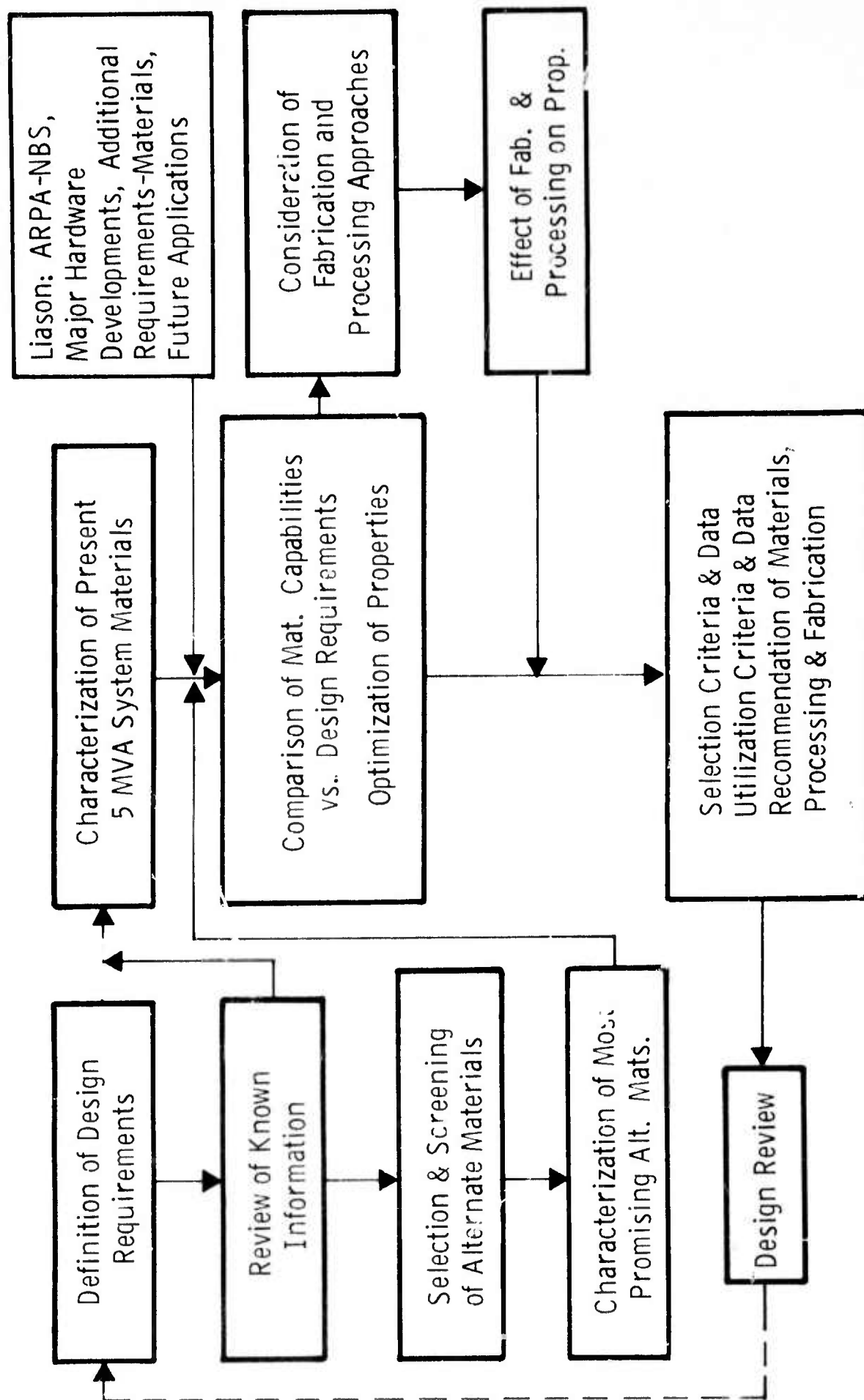


Fig. 4-1 Program Outline - Structural Materials for Cryogenic Applications

EVALUATION OF CRYOGENIC STRUCTURAL MATERIALS, NBS CONTRACT 8304

Functions	Task I	Task II	Task III
	Basic Characterization	Processing Effects	Joint Behavior
Metallurgy, Processing, Joining	•	•	•
Fracture Mechanics	•	•	•
Fractographic & Micro-Structural Analysis	•	•	•
Magnetic Properties	•	•	•

Westinghouse Program Organization

Management

Program Manager - J. M. Wells
 Advisors - G. G. Lessmann
 T. Wessel

Principal Investigators

Materials, Processing, Fabrication - J. M. Wells
 Fracture Mechanics - W. A. Logsdon
 Microstructural Analysis - R. Kossowsky
 Magnetic Properties - M. R. Daniel

Fig. 4-2 Westinghouse Program Organization - FY76

5.0 GENERAL CRYOGENIC STRUCTURAL MATERIALS SELECTION/ PROCESSING/FABRICATION CONSIDERATIONS

The Westinghouse portion of the overall ARPA/NBS program entitled Materials Research For Superconducting Machinery is concerned with the selection and evaluation of several metal alloys in various processed and fabricated forms as cryogenic structural alloys. A listing of the more promising candidate structural alloys for advanced cryogenic structural applications compiled by the present author is included as Table 5-1. Those alloys previously investigated in the Westinghouse program for FY 74 and FY 75 are identified in Table 5-1 by a single and a double asterisk respectively and have been documented in Section 5 of the prior reports of this series (1-4). Those additional alloys included in the present FY 76 program are noted by a tripple asterisk and are documented herein in Table 5- 2 through Table 5- . The material and test specimen identification (Coding) system employed throughout this entire program is presented in Table 5- 6 .

5.1 Materials Selection Considerations

5.1.1 Microstructural Stability in Austenitic Stainless Alloys

Among the general criteria for selection and utilization of structural materials for advanced cryogenic applications is the desirability that a candidate alloy be resistant to microstructural and attendant magnetic transformations. Microstructural transformations can be mechanically deleterious by introducing: (a) weak or low fracture toughness phases, (b) net volume changes and/or dimensional distortions and (c) localized yet appreciable residual stress levels. Structural transformations can also result in significant ferromagnetic behavior in previously paramagnetic materials.

Microstructural transformations will often be accompanied by attendant irreversible magnetic transformations due to the intrinsic differences in various microstructural phases (e.g. austenite in stainless steel is basically paramagnetic but delta ferrite and α' martensite are ferromagnetic). However, magnetic transformations can also occur reversibly in the absence of a microstructural transformation. For example, Inconel 718, while remaining fully austenitic, demonstrates a paramagnetic to ferromagnetic transition at a Curie temperature of $< 77\text{K}$ for the solution treated and $< 160\text{K}$ for age-hardened conditions, respectively (5). Also, 310(S) was reported earlier in this program (2) to demonstrate weak ferromagnetic behavior at 4K while remaining fully austenitic.

Austenitic stainless steels have been and will continue to be, considered as prime candidate materials for advanced cryogenic structural applications, primarily because of the following general characteristics:

- Low ferromagnetic behavior (basically paramagnetic or antiferromagnetic).
- Absence of a sharp ductile-to-brittle transition behavior*.
- Relatively high fracture toughness at cryogenic temperatures.
- Relatively low thermal conductivity.
- Generally acceptable formability, machability and weldability.
- Generally good commercial availability at reasonable cost.

While austenitic stainless steels are generally considered to be fully austenitic and "non-magnetic" (paramagnetic), it is (or should be), nevertheless, quite well known that many austenitic stainless steels are actually neither fully austenitic nor fully paramagnetic, especially in the welded and/or cold worked condition and exposed to cryogenic

* Ductile-to-Brittle transformations in austenitic Cr-Mn-N steels with little or no nickel content have been reported, however (6).

temperatures. In many advanced cryogenic structural applications such as superconducting motors and generators and large superconducting magnets for fusion or MHD power generation devices, the presence of non-austenitic microstructural phases and ferromagnetic behavior may be neither desirable nor tolerable. Consequently, it is useful to briefly review and to further describe the nature and magnitude of such departures from fully austenitic and fully paramagnetic behavior, especially in those specific alloys of interest to designers of advanced cryogenic structural devices.

Three microstructural phases (other than austenite) which may occur in austenitic stainless steels and be a cause of concern are delta (δ) ferrite, epsilon (ϵ) martensite and alpha prime (α') martensite. Two of these phases, namely the δ -ferrite and the α' martensite, have the body centered cubic crystal structure and are ferromagnetic. Analytical means are available to predict the presence and to approximate the amount of the δ -ferrite and α' -martensite phases and are discussed in the following two sections.

5.1.2 Martensite in Austenitic Stainless Alloys

Martensite is a metastable (not a true equilibrium) diffusionless decomposition product of the face centered cubic solid solution austenite phase in rapidly cooled iron-based alloys. The occurrence of martensite is generally suppressed in austenitic stainless steels at room temperature and above by the presence of significant amounts of austenite stabilizing elements such as nickel, manganese and nitrogen. However, martensite can and does form in many plastically deformed austenitic stainless steels at or below a temperature designated as (M_d) or, in some cases when the undeformed austenitic structure is cooled to a sufficiently low temperature (M_s), (see References 6-18).

The presence of martensite in an otherwise austenitic alloy introduces both residual stresses associated with a volume expansion and ferromagnetic behavior, which should be considered in the design of advanced cryogenic structures. While verification test results of the

cryogenic structural and magnetic properties of available specific alloy compositions are often not known during the initial materials selection and conceptual design period, predictive equations are available to assess the stability of stainless alloys.

Expressions for the temperature(s) at which martensite could form with and without deformation assistance (M_d and M_s respectively) in austenitic stainless steels were established by Hull (7). These equations express the M_d and M_s temperature as a function of the alloy composition and are presented below:

$$M_d (^{\circ}\text{F}) = 2520 - 106 (\text{Ni} + \text{Ni equiv. for } M_d) \quad (1)$$

$$M_s (^{\circ}\text{F}) = 2700 - 106 (\text{Ni} + \text{Ni equiv. for } M_s) \quad (2)$$

Basically, Hull found that all elements lowered the M_d and M_s temperatures but that the effectiveness (nickel equivalency) of many elements was approximately only half as large in reducing the M_d as compared to the M_s temperature. The main ramification of this significant difference in the nickel equivalency of a given element on M_d vs M_s is a considerable (and sometimes unappreciated) elevation of the M_d temperature. The relative effectiveness of various elements on lowering both the M_d and M_s were presented in Table 6 of Hull's paper (7). The present author has simply translated these data to nickel equivalents by normalizing with respect to the effect of nickel alone (i.e. numerical division by 106 for both M_d and M_s). The resulting functional equations thus achieved are:

$$\begin{aligned} M_d (^{\circ}\text{F}) = & 2520 - 106 (\text{Ni} + 0.40\text{Cr} + 0.69\text{Mn} + 0.41\text{Mo} + 0.34\text{Si} \\ & + 1.07\text{V} + 0.78\text{Ti} + 0.91\text{Al} + 13.2\text{C} + 5.38\text{N} + 1.11\text{Cb} \\ & + 1.09\text{Ta} + 1.14\text{Cu} + 0.22\text{Co}) \end{aligned} \quad (3)$$

$$\begin{aligned} M_s (^{\circ}\text{F}) = & 2700 - 106 (\text{Ni} + 0.80\text{Cr} + 0.92\text{Mn} + 0.94\text{Mo} + 0.63\text{Si} \\ & + 2.17\text{V} + 3.07\text{Ti} + 5.21\text{Al} + 40.6\text{C} + 54.7\text{N} + 0.86\text{Cb} \\ & + 1.28\text{Ta} + 1.44\text{Cu} + 0.23\text{Co}) \end{aligned} \quad (4)$$

Where the M_d and M_s temperatures are given directly in degrees Fahrenheit and all elements are given in weight percent.

Several austenitic stainless steel alloys of interest to this program have been examined with respect to the structural stability predictions of the above equations. The results of these calculations are presented in Table 5- 7 (actual heat compositions) and Table 5- 8 (specification composition ranges). Certain significant points which are demonstrated by these calculations are as follows:

- For the six specific alloy heat compositions shown in Table 5- 7 , all have a calculated M_s well below that of absolute zero and hence are predicted as being fully stable (i.e. martensite will not form) in the unstrained condition to 4K. Note that while the value of the calculated M_s temperature is below absolute zero and hence represents an imaginary temperature, the magnitude of the negative M_s value provides a further indication of the relative M_s stability of these alloys. Thus the Kromarc 58 alloy indicates the greatest unstrained stability ($M_s \approx -1600K$), followed by the Nitronic 33, A-286, Pyromet 538 (21-6-9), AISI 310S and lastly, by the AISI 305 stainless ($M_s \approx -121K$).
- For these same six specific alloy compositions, a considerable difference exists in the calculated M_d values. The three highest nickel (and nickel equivalent) content alloys (K-58, A-286 and 310(S)) have a calculated $M_d \ll 0 K$ and hence are predicted to be fully structurally stable in the strained condition at 4 K. However, the remaining three lower nickel content alloys (Pyromet 538, Nitronic 33 and AISI 305) have a calculated $M_d \gg 0 K$ and therefore are predicted to be structurally unstable (i.e. martensite will form) in the strained condition at temperature well above 4 K.
- Limited data available on these specific composition alloys is available against which to compare the above predictions. Magnetic and/or metallographic examination (1 - 4) of the Kromarc 58, A-286 and the AISI 310(S) materials indicates the absence of

martensite in both strained and unstrained material (tensile specimens) at 4 K, and thus indicates that both the M_d and the M_s temperatures for these samples are $\ll 4$ K. Magnetic measurements (4) on unstrained Pyromet 538 (21-6-9), and Nitronic 33 at 4 K indicate both these base metal stainless alloys to be antiferromagnetic and thus to have an $M_s \ll 4$ K. However, for strained material, martensite and ferromagnetism have been observed in Pyromet 538 at 77 and 4 K by Tobler and Reed (19). Wells and Kossowsky (20) have observed apparent martensite and ferromagnetism in Nitronic 33 weldments strained at RT (See Section 7, Fig. 7- 22). Thus for the latter two materials, the limited observations to date suggest that their respective M_d temperatures are $\gg 4$ K.

While the preceeding discussion has involved specific alloy heat compositions, it is of further interest to examine the austenitic phase stability (i.e. tendency for $\gamma \rightarrow M$ transformation) over the commercially accepted composition ranges for these and other austenitic iron base alloys. Table 5- 8 indicates the composition ranges for a dozen such alloys and lists the associated ranges of nickel equivalents and instability temperature for the M_d (strained) and M_s (unstrained) conditions respectively. Figure 5- 1 presents this same data in graphical form. While the absolute value of predicted M_d and M_s temperatures may be in significant error (Hull claimed standard errors for the basic M_d and M_s expressions of 69F (124 K) and 88F (158 K) respectively), such calculated values shown provide a reasonable estimate of actual M_d and M_s temperatures and indicate the following significant observations:

- An appreciable temperature range is indicated for the micro-structural instability ($\gamma \rightarrow M$) temperature in austenitic stainless steel for both strained (M_d) and unstrained (M_s) conditions. This temperature range corresponds to the range of calculated nickel equivalence which depends directly on the allowable compositional range in any given stainless steel.

- Austenitic stainless steels considered for cryogenic structural applications may be grouped into three basic classes as follows:

Class A - Alloys which are structurally stable with respect to both M_d and M_s (i.e., M_d and $M_s \ll 0$ K). Such alloys include Kromarc 58, A-286, Incoloy 800 and AISI 310(S).

Class B - Alloys which are structurally stable with respect to M_s but unstable with respect to M_d (i.e., $M_s \ll 0$ K $\ll M_d$). Such alloys include Nitronic 50 (21-6-9), Nitronic 33 and AISI 309(S).

Class C - Alloys which are structurally unstable with respect to M_d (i.e., $M_d \gg 0$ K) and may be either structurally stable or unstable with respect to M_s depending on the exact alloy composition. Such alloys include AISI 304, 305, 316 and 321.

- An estimation of structural stability for any austenitic stainless steel alloy of known composition can be made by simply calculating the total nickel equivalency factors (Ni + Ni equiv.) as given by Eqs. (4) and (5) above. The alloy is likely to be structurally stable with respect to M_d if its respective total nickel equivalency factor is > 28.1 . The alloy is likely to be structurally stable with respect to M_s if its respective total nickel equivalency factor is > 29.8 . Note that separate nickel equivalency equations are employed with respect to M_d and M_s .
- Additional data is available in the open literature (8 - 17) which can be reviewed in terms of the above considerations although only a limited attempt will be made herein to demonstrate the relevancy of these predictive equations. First with respect to unstrained (M_s) instability, Reed and Mikesell (11) reported M_s instability in both 303 and 304 alloys when soaked at 195, 76 and 20 K. The nickel equivalency calculated by the present author for the 304 alloy which Reed and Mikesell employed is equal to 29.8. The corresponding estimate for M_s of -459°F suggest marginal stability with respect

to M_s , whereas the actual 304 composition proved to be definitely unstable. Nachtigal (17) reported no observation of martensite in unstrained 304 cooled to liquid helium. A calculated nickel equivalency of 27.4 ($M_s \approx -204^\circ\text{F}$) suggests that this unstrained 304 alloy should be unstable at 4 K. Nachtigal did not, however, report a nitrogen content for this alloy. A nitrogen content of only 0.043 weight percent would reduce the M_s of the alloy by $\sim 250^\circ\text{F}$ and could thus render the alloy stable ($M_s < -452^\circ\text{F}$) to martensite formation in the unstrained condition. Larbalestier and King (14) have also reported the presence of approximately 5% α' martensite (M_s instability) on cooling to 4.2 K of a British steel equivalent to AISI 321, which is consistent with the M_s instability region for the 321 alloy composition range shown in Fig. 5- of this present report.

Stress induced martensitic transformation (M_d) examples reported in the literature are also consistent with the calculated M_d instability regions shown in Fig. 5- 1 . Reed and Guntner(12, 13) have reported α' martensite formed in 304 stainless strained at 300, 76 and 4 K. Larbalestier and King (14) reported M_d instability at 4 K in tensile specimens of several alloys including 304L, 304N, 309, 316L and 316N but no such M_d instability in 310 and Kromarc 55 alloys. Tobler and Reed have found an M_d instability in Pyromet 538 (21-6-9) at 76 and 4 K. All of which findings are entirely consistent with the predictions of the M_d instability ranges prediction herein in Table 5- 8 and Fig. 5- 1 .

5.1.3 Delta Ferrite Formation in Austenitic Stainless Steel

Delta ferrite (δ) is a body centered cubic metastable solid solution phase, found in otherwise face centered cubic austenitic stainless steels, which basically forms on cooling as small irregular shaped dendritic "stringers" in both weldments and castings. Several recent references (7,21-32) are available in the open literature on the subject of delta ferrite in stainless steel weldments. Delta ferrite is widely accepted as being advantageous in improving the hot cracking (microfissuring)

resistance of weldments in austenitic stainless steels. However, as DeLong (27) has pointed out, the impact toughness at 77 K of ferrite containing austenitic weldments decreases appreciably as the ferrite content of the weld metal increases. Moreover, delta ferrite is also ferromagnetic and thus the magnetic permeability of a stainless steel weldment increases with increasing ferrite content. Thus, high ferrite containing weldments may not be suitable for many cryogenic applications.

Ferrite levels are now conventionally expressed in terms of arbitrary ferrite numbers (FN's) instead of the earlier terminology of percent by volume of ferrite. A numerical conversion table between percent ferrite and the new FN system has been presented by Long and DeLong (26). There is a direct conversion to the FN system by Long and DeLong for ferrite levels up to 6.0 percent, beyond which the respective FN becomes increasingly larger than its corresponding ferrite volume percentage. The determination of ferrite level can be accomplished by four practical techniques, namely:

1. Quantitative metallographic measurement (29).
2. Magnetic Permeability measurement (21,33).
3. Direct Measurement by a Magnetic Ferrite Instrument such as the Severn-Gage or the Magne-Gage (24,26,27).
4. A computational technique based upon calculation of nickel and chromium equivalent values from a known weldment chemical analysis. The FN corresponding to such calculated equivalents is determined from a revision of the Shaeffler constitution diagram for stainless steel weld metal such as developed by DeLong (26) and further modified by Hull (7).

It should be specifically noted, however, that DeLong's formulae (26, 27) for nickel equivalents (effective austenitizers) and chromium equivalents (effective ferritizers) used in combination with the revised DeLong diagram predict a FN which is applicable to standard

AISI 300 series stainless steels (including nitrogen grades), but is not appropriate for use with high manganese containing austenitic stainless steels such as Kromarc 58 (15Cr-22Ni-9Mn), Nitronic 33 (18Cr-3Ni-13Mn), Nitronic 40 (21Cr-6Ni-9Mn) or Nitronic 50 (22Cr-13Ni-5Mn) or with age hardenable stainless alloys such as A-286 (15Cr-25Ni-2Ti-0.3Al). A more appropriate approach to predicting FN's for such high manganese (i.e. Mn > 2.0 wt. percent) containing stainless steels is to calculate the nickel and chromium equivalents according to the formulae derived by Hull (7) and then to use such equivalent values with the Hull revision of the Schaeffler diagram. Calculated values of FN by using both the Hull and the DeLong method are presented in Table 5- 9 for the limited high manganese stainless steel weld data available. When these calculated FN values are compared against the actually measured FN values, it becomes readily obvious that the DeLong diagram drastically underestimates the actual ferrite level of weldments in such high manganese materials.

A further more recent refinement of the Hull approach is an expression which allows the direct numerical estimation of the ferrite number without resorting to a graphical plotting procedure. Such a predictive expression for the direct calculation of the average FN (based upon the average weldment chemical composition) was developed recently by Dr. E. W. Johnson at the Westinghouse Research Laboratory and is as follows:

$$FN = -13.8 - 3.12Ni^* + 2.88Cr^* \quad (5)$$

where

$$Ni^* = Ni + 0.11Mn - 0.0086Mn^2 + 0.41Co + 0.44Cu + 18.4N + 24.5C \quad (6)$$

and

$$Cr^* = Cr + 1.21Mo + 0.48Si + 2.27V + 0.72W + 2.20Ti + 0.14Cb + 0.21Ta + 2.48Al \quad (7)$$

Note: All elements are expressed in weight percent.

A calculation of the FN's for the same weldments included Table 5- 9 is included in Table 5-10 and compared to the FN's obtained graphically from the Hull Diagram and the actually measured FN's obtained via Magne-Gage measurements by Wells and Hagadorn (20) for Nitronic 33 weldments and by Brooks (34) for Nitronic 40 weldments. As expected, the calculated FN's agree quite closely with those interpolated from the Hull Diagram, (See Fig. 5- 2). More importantly, these FN values both agree very well with the measured FN values of Wells and Hagadorn and moderately well with the measured FN values of Brooks. Although only speculation on the present author's part at present, it is possible that the better agreement of the W&H data may be due in part to the fact that the W&H FN measurements were made on actual weldments with a ferrite level ≤ 5 whereas Brook's FN measurements were made on autogeneous weldment (spot-weld) samples of FN up to 13.5. Additional FN measurements in actual weldments with high manganese stainless steels would be highly desirable to further evaluate the accuracy of the Hull method of FN prediction. Nevertheless, the Hull method is obviously preferable to the DeLong Method and provides a reasonably accurate method of predicting the presence and extent of ferromagnetic delta ferrite formation in high manganese stainless steel weldments.

5.2 Materials Processing Considerations

5.2.1 Cold Working and Heat Treatment of Inconel 718

Prior evaluation of the Inconel 718 alloy employed in this program revealed a relatively low ductility behavior for this material(3,4). The cause of such low ductility behavior has been attributed to a pronounced contiguous grain boundary metal carbide network which formed during the original mill processing of the forging billet stock and was not removed by the standard 1800°F (982°C) solution treatment employed in this program with sample codes 64XX, 65XX and 66XX. A later test series of Inconel 718 samples were subjected to an initial solution treatment of 1950°F (1066°C), followed by cold working to approximately

38% reduction in thickness without any intermediate heat treatment and then resolution treated at various secondary solution treatment temperatures from 1650°F (900°C) to 1950°F (1066°C). Photomicrographs, ASTM grain size measurements and hardness test data for these samples was presented in the previous Westinghouse Report (4) as Fig. 5-4 and a discussion of the results was included in Section 5.2.2.

Based upon the results of these earlier tests, three processed conditions were selected for further evaluation of the Inconel 718 alloy, namely:

- o Code 67XX Initial solution treatment at 1950°F (1066°C)
Cold Worked ~ 40%
Secondary Solution Treatment at 1800°F (982°C)
Double Aged at 1325°F (718°C)/1150°F (620°C)
- o Code 68XX Initial solution treatment at 1950°F (1066°C)
Cold Worked ~ 40%
Secondary Solution Treatment at 1950°F (1066°C)
Double Aged at 1325°F (718°C)/1150°F (620°C)
- o Code 69XX Initial solution treatment at 1950°F (1066°C)
Cold Worked ~ 40%
No Secondary Solution Treatment
Double Aged at 1325°F (718°C)/1150°F (620°C)

Photomicrographs representative of the resulting microstructures are shown for these three processed conditions in Fig. 5- 3. Rockwell hardness measurements and ASTM grain size (average) numbers are listed in Table 5- 5 . Little difference was observed in the hardness values between Code 67XX and 68XX although a significant difference in ASTM grain size numbers is apparent, 8.0 vs 2.9 respectively. Code 69XX material which was directly aged following cold working demonstrated the largest hardness value (Rc 44) and an intermediate grain size (~ ASTM No. 5.6). No recrystallization is observed in the Code 69XX material which was directly aged following cold working.

While the effect of grain size alone on the mechanical and fracture mechanics properties of 718 is desirable, such information cannot be isolated from the present material property evaluations because of further microstructural differences other than solely grain size. For a detailed description of such microstructural differences between these three differently processed conditions of Inconel 718, the reader is referred to Section 7 of this report. Both notched and unnotched tensile data have been determined for these three conditions and are presented in Section 6 of this report. Fracture mechanics evaluations on these processed conditions were not completed in time for inclusion in this report and will be presented in the next report of this series.

5.2.2 Processing of Pyromet 538 (21Cr-6Ni-9Mn) Billet to Plate

A high manganese austenitic stainless steel identified by trade name as Pyromet 538 (Carpenter Technology designation) and generically as 21-6-9, was introduced into the ARPA/NBS FY 75 program by NBS (19). Since weldments as well as base metal property evaluations in this material are necessary for effective cryogenic utilization, this material has been included in the Westinghouse FY 76 program.

The material employed for the base metal evaluation by NBS was received in the form of solution treated and water quenched (ST at 2000°F and WQ) plate measuring approximately 20" x 20" x 1.4" (50 cm x 50 cm x 3.6 cm). This material was provided by Dr. P. R. Landon of the Lawrence Livermore Laboratory. The original billet material (Car-Tech Ht. No. 89087) had been hot cross rolled to plate at the Oak Ridge National Laboratory according to the processing schedule reported by Tobler and Reed (19). It was the intention of the present program to use the same plate material for the 21-6-9 weldments as had been evaluated as base metal by NBS. Unfortunately, similar plate material was not available for the weldment studies. However, portions of the original billet material were available and were requested and received from Dr. Landon at LLL. This material consisted of forging billet sections measuring approximately 12 inches (30.5 cm) square by

4 inches (10 cm) thick. The reported chemical composition of the billet material is as shown in Table 5- 2 . Hardness and ASTM average grain size number measurements of the as-received billet material were R_B 84 and ASTM No. 3.5, respectively.

Plate material measuring approximately 3/4" t (1.9 cm) x 4" w (10 cm) x 80" l (203 cm) was formed by forging and subsequent hot rolling (unidirectionally) of original billet sections measuring approximately 4" (10 cm) x 4" (10 cm) x 12" (30.5 cm). The original billet section soaking temperature was 2000°F (1093°C) with four intermediate reheating cycles to the same temperature employed while forging the billet sections into sheet bar measuring approximately 1-3/8" (3.5 cm) x 4" (10 cm) x L. These sections were again reheated to 2000°F and hot rolled to final thickness of 3/4" (1.9 cm) in four flat and one edge pass. The reduction of the billet sections to plate was performed by Braeburn Alloy Steel Co. Subsequent final heat treatment consisting of a 2000°F (1093°C) solution treatment and water quenching was performed at the Westinghouse Research Laboratory. A hardness comparison of this latter WRL 3/4" thick (1.9 cm) plate in the STQ condition with the 1.4" (3.6 cm) plate (also STQ) employed by NBS revealed a slight hardness difference (R_B 89 vs. R_B 84 respectively). ASTM grain size measurements revealed no significant differences (ASTM No. 4.3 vs 4.5 respectively). Photomicrographs showing the respective microstructures of the original billet stock, the NBS plate and the WRL plate are shown in Fig. 5- 4 . No apparently significant differences between the WRL and the NBS plate materials were observed.

5.3 Materials Joining Considerations

5.3.1 Current FY 76 Program Weldments

Metals Joining activities in the FY 76 program effort were concentrated on weldment property evaluation in two materials, namely, Pyromet 538, a 21Cr-6Ni-9Mn stainless steel and on Armco A-286, a precipitation hardening stainless steel. A literature review revealed several prior reference publications concerned with base metal properties of the 21-6-9 type alloy (35-41) and the A-286 alloy (42 - 47). Literature references addressing aspects of weldability and weldment property evaluation were considerably less available for the 21-6-9 type alloy (48 - 50) and for the A-286 alloy (51 - 55). In general, little, if any, reliable information exists concerning the cryogenic mechanical and fracture mechanics behavior of weldments in these materials. Consequently, weldments in the current Westinghouse FY 76 program consisted of gas tungsten arc (GTA) and shielded metal arc (SMA) weldments in Pyromet 538 (21-6-9) stainless steel and GTA weldments in A-286 stainless steel. Photographs showing these weldments are included in Fig. 5- 5 .

5.3.1.1 SMA Weldments in Pyromet 538

Unrestrained butt weldments were made by the manual shielded metal arc welding process in Pyromet 538 (21-6-9) material. Two weldments measuring approximately 11/16" thick (1.75 cm) x 3-5/8" w (9.2 cm) x 16" l (40.6 cm) and identified as weld plates HR-1A and 1B were fabricated according to the welding process conditions listed in Table 5- 11 for material Code 94XX. The weld plate material employed was the 3/4" thick (1.9 cm) Pyromet 538 plate in the STQ condition discussed in Section 5.2.2 above. The filler metal employed was a coated Inconel 182 electrode of highly dissimilar chemical composition (See Table 5- 2) with respect to the base metal. This SMA electrode has reportedly (56) been successfully employed in SMA welding 21-6-9 stainless steel components at LLL.

Radiographs of both weldments revealed no significant defect indications. A microhardness survey taken both through the thickness and across a transverse section of SMA weld HR-1B is shown in Fig. 5- 6 .

An anomalous dark etching band along the entire FZ-HAZ interface is observed in photomicrographs (F) and (G) of this figure. Further examination of this anomalous FZ-HAZ band by optical and scanning electron microscopy reveals that this band consists of a thin band of microporosity in the Pyromet 538 HAZ, as shown in Fig. 5- 7. Although further investigation of this structural anomaly is continuing, the present author speculates that the microporosity is perhaps due to nitrogen bubbles formed from the melted Pyromet 538 base metal immediately adjacent to the original weld plate surface preparations.

Ferrite measurements via the Magne-Gage revealed a Ferrite Number for both these SMA weldments of Zero, i.e. FN=0, as expected with the extremely high (> 60%) nickel content of the Inconel 182 covered electrode. Microstructural examination of the SMA weld fusion zone revealed no evidence of delta ferrite as well.

5.3.1.2 GTA Weldments in Pyromet 538

Two unrestrained butt weldments were also made by the manual gas tungsten arc (GTA) welding process in Pyromet 538 (21-6-9) material. These two weldments, measuring approximately 1-1/16" thick (1.75 cm) x 3-5/8" w (9.2 cm) x 16" l (40.6 cm) and identified as weld plates HR-1C and HR-1D, were fabricated according to the welding process conditions listed in Table 5- 11 for material Cod3 93XX. The weld plate material employed for these GTA weldments was also the 3/4" thick (1.9 cm) Pyromet 538 plate in the STQ condition discussed in Section 5.2.2 above. The filler wire employed with these GTA weldments was a matching 21-6-9 composition (See Table 5- 2) bare wire supplied by Dr. P. R. Landon of LLL.

Radiographs of both these GTA weldments revealed no significant defect indications. A microhardness survey of GTA weldment HR-1D (in transverse section) is shown in Fig. 5- 8 . Photomacro and micrographs of this weldment including FZ, HAZ and BM are also shown. No weld defects were observed. Some microporosity was observed in the FZ/HAZ interface but to a considerably smaller extent than a discussed above for the SMA weldments.

Ferrite measurements via the Magne-Gage revealed in the fusion zone a Ferrite Number for both these GTA weldments as follows:

HR-1C	FN = 5.9 ± 0.8
HR-1D	FN = 7.4 ± 0.9

An appreciable ferrite level was also observed by optical microscopy in the fusion zone of these GTA weldments as well.

5.3.1.3 GTA Weldments in Armco A-286

Three unrestrained butt weldments have been made to date by the manual gas tungsten arc (GTA) welding process in Armco A-286 material. These weldments measure approximately 3/4" thick (1.9 cm) x 3-3/4" wide (9.5 cm) x 5-1/2" long (~ 14 cm). The short length of these weld plates was dictated by the 5-1/2" (~ 14 cm) square dimension of the forged billet cross section. Three additional weldments remain to be fabricated. The weld plate material was obtained as transverse slices from the same Armco A-286 forging billet (Ht. No. 4X0836) used as the source of the base metal material whose properties were also characterized in the STQA condition and reported in the previous WRL report (4). Photomicrographs showing the microstructure of the STQA treated billet base metal are presented for various billet cross section locations are presented in Fig. 5- 9 . An initial weldment (Plate No. A) was fabricated with the weld plate in the solution treated, oil quenched and age hardened condition. Problems were experienced initially as weld fusion zone centerline hot cracking as shown in Fig. 5- 10 . This macrocracking occurred on the starting end of the second filler pass and measured approximately 1 inch (2.5 cm) in length. Successive grinding and rewelding of the second and third weld passes finally eliminated this fusion zone cracking condition. No such cracking was detected in the radiograph (RD No. 76195) of the final completed weldment No. A. Microexamination of transverse sections revealed no indications of such fusion zone cracking but did reveal extensive heat-affected zone microfissuring (hot cracking) as shown in Figs 5- 10 and 5- 11 . It was therefore decided to resolution treat

at 1650°F (900°C) and oil quench all remaining A-286 weld plates and omit the subsequent age hardening treatment. The unaged A-286 weld plates were then welded according to the weld process conditions listed in Table 5- 11 for material Code 92XX. The filler wire employed with these A-286 GTA weldments was a non-matching Inconel 92 composition (See Table 5- 2) bare wire originating from the Huntington Alloys Div. of INCO.

Radiographs of Weld Plates C and E revealed no significant defect indications. A microhardness survey of GTA weldment No. C is shown in Fig. 5- 12 and reflects the anticipated lower base metal hardness ($\sim R_B$ 90) for this STQ material versus the STQA base material hardness ($\sim R_C$ 37) revealed in the hardness traverse of Weld A shown in Fig. 5- 11 . The as-welded fusion zone hardness level ($\sim R_B$ 96) is comparable in both weldments. HAZ microfissuring was observed in both A-286 weldments C and E and is shown in Fig. 5- 12 (arrows).

Ferrite measurements via the Magne-Gage revealed no indication of delta ferrite (FN=0) in the weld fusion zone. No ferrite was anticipated since the dissimilar weld Inconel 92 filler metal has an extremely high nickel content ($\sim 70\%$ Ni) and dilution by the lower but still high nickel content ($\sim 26\%$) base metal would not sufficiently lower the nickel equivalency of these weldments to the level where delta ferrite would occur. Microstructure examination of the weld fusion zone confirmed the absence of any detectable delta ferrite.

5.3.2 Varestraint Weldability Testing

A relatively simple and informative weldability testing procedure known as the longitudinal Varestraint Test was introduced into this program in Section 5.3.2 of the previous WRL report. This Varestraint test was originally developed by Savage and Lundin (57 - 59) to evaluate the relative hot cracking tendency of base materials and of prior deposited weld metal. The most significant feature of the Varestraint (VARIABLE RESTRAINT) test is that it provides an inexpensive, laboratory suitable and reproducible means for augmenting the normal intrinsic weld

metal solidification shrinkage strains and thus simulates the larger shrinkage strains attendant to highly restrained production (hardware) weldments.

The test used herein is essentially the same as developed by Savage and Lundin (S&L) with the exception that the Westinghouse sub-size Varestraint test device shown in Fig. 5- 13 has been designed so as to accept smaller sized (0.125" t x 1.00" w x 6.00" l) sample than that originally employed by S&L (0.250 or 0.500" t x 2.00" w x 12.00" l). Varestraint testing of such sub-sized specimens by Westinghouse has been reported previously for Incoloy 800 by Gold and Lessmann (60), for various refractory metal alloys by Lessmann and Gold (61), for A508 and A533 steels by Grotke (62), and for Nitronic 33, a high manganese stainless steel by Wells and Hagadorn (20).

A schematic sketch of the operation of the Varestraint test device is shown in Fig. 5- 14 . The test conditions for the present tests reported herein were standardized at the following levels:

Arc Voltage	15-16 Volts, DCSP
Arc Current	60-70 amps
Travel Speed	6.35 mm/sec (15 ipm)
GTA Electrode	EWTh-2; 3.2 mm dia., 60° Included Angle with 0.8 mm flat
Electrode Extension	7.9 mm (5/16 inch)
Electrode Standoff	1.6 mm (1/16 inch)
Shield Gas	100% Ar, 1.42 m ³ /hr (50 cfh)
Air Cylinder Pressure	0.55 MPa (80 psig)

Specimens were tested at various levels of upper surface augmented strain over the range of 0.25% to 4.0%. Post test macro-examination at 30X permitted the measurement and recording of the number, location and length of all observed cracks, both in the weld fusion and the heat-affected zone as shown in Fig. 5- 15 . A summary of these crack measurements is presented in Table 5-12 and 5-13 for austenitic stainless steels and nickel base superalloys respectively. A graphical

presentation of the cracking data for the various stainless steel specimens is shown in Fig. 5-16 through 5-18 and for the various conditions of nickel base superalloy 718 in Fig. 19 through 20. Photomicrographs of various specimens at selected augmented strain values are presented in Figs. 5-22 to 5-32.

Certain summary observations from this data of particular interest to the present program are as follows:

- o Fully austenitic stainless steel base metals including Kromarc 58, AISI 305, and A-286 which did not form any delta ferrite when autogeneously welded in the Varestraint test, experienced significant FZ cracking beyond a threshold augmented strain level of 0.25%. Similar results have also been reported for AISI 310S and 316L stainless steels by Arata (63) and for AISI 316 stainless steel by Grotke (62).
- o Austenitic stainless steel base metals which did form delta ferrite when autogeneously welded in the longitudinal varestraint test such as Nitronic 33 and Pyromet 538 high manganese stainless steels, experienced no microfissuring up to augmented strain levels of 4 percent.
- o Prior deposited ferrite-free GTA weldments in fully austenitic Kromarc 58 stainless steel experienced significant FZ microfissuring in Varestraint testing, although less than that observed in the ferrite-free K-58 base metal.
- o Prior deposited ferrite free GTA weldments in Nitronic 33 stainless steel experienced significant FZ microfissuring in Varestraint testing beyond a threshold augmented strain level of 0.25%.
- o In general, little HAZ microfissuring was experienced with these austenitic stainless steel varestraint test specimens. HAZ microfissuring was observed in the ferrite free weldment of Nitronic 33 and in the base metal AISI 305 stainless materials at augmented strain levels of $\epsilon = 2.0\%$ and $\epsilon = 3\%$ respectively.

- o The fully austenitic age hardenable A-286 stainless steel base metal Varestraint test specimens experienced considerable microfissuring in both the fusion zone and the heat-affected zone areas of the autogeneous weld bead regardless of the specific heat treatment condition, at augmented strain levels from 0.25% to 2.0%. The presence of the HAZ microfissuring at the low 0.25% augmented strain level, correlates with the previously described presence (see Section 5.3.1.3) of such HAZ microfissures in unrestrained weldments in A-286.
- o The austenitic nickel-base 718 superalloy Varestraint test specimens also experienced considerable microfissuring in both the fusion zone and the heat-affected zone areas regardless of the specific heat treatment condition. The threshold augmented strain levels for both the Udimet and the Inconel 718 alloys were 0.25% and 0.50% for the FZ and HAZ microfissuring respectively. Figure 5- 21 shows a reasonably good agreement between the graphical comparison of the present Varestraint results in both Udimet 718 and Inconel 718 at both 2.0 and 3.0% augmented strain levels with previously published results of Valdez and Steinman (64) at 2.6% strain level.

Further work is underway on the microstructural examination and characterization of these microfissures in both the FZ and the HAZ in an attempt at improving our understanding of this troublesome phenomenon.

References (Section 5)

1. Lessmann, G. G., Logsdon, W. A., Kossowsky, R., Mathur, M. P. and Wells, J. M., "Structural Materials For Cryogenic Applications - First Semi-Annual Technical Report", Westinghouse Research Report 74-9D4-CRYMT-R1, March 1, 1974 (Unrestricted).
2. Lessmann, G. G., Logsdon, W. A., Kossowsky, R., Mathur, M. P. and Wells, J. M., "Structural Materials For Cryogenic Applications - Second Semi-Annual Technical Report", Westinghouse Research Report 74-9D4-CRYMT-R2, September 9, 1974 (Unrestricted).
3. Wells, J. M., Kossowsky, R., Logsdon, W. A. and Daniel, M. R., "Structural Materials For Cryogenic Applications - Third Semi-Annual Technical Report", Westinghouse Research Report 75-9D4-CRYMT-R1, March 10, 1975 (Unrestricted).
4. Wells, J. M., Kossowsky, R., Logsdon, W. A. and Daniel, M. R., "Structural Materials For Cryogenic Applications - Fourth Semi-Annual Technical Report", Westinghouse Research Report 75-9D4-CRYMT-R2, October 10, 1975 (Unrestricted).
5. Anon., "Inconel 718", Huntington Alloy Products Division, INCO Technical Bulletin 2-68T-39, (1968).
6. Defilippi, J. D., Brickner, K. G. and Gilbert, E. M., "Ductile To Brittle Transition in Austenitic Chromium Manganese Nitrogen Stainless Steels", Trans AIME, V. 245, Oct. 1969, pp. 2141-2148.
7. Hull, F. C., "Delta Ferrite and Martensite Formation in Stainless Steels", Welding Journal, V. 52, No. 5, May 1973, pp. 193s-203s.
8. Reed, R. P., "The Spontaneous Martensitic Transformations in 18%Cr, 8%Ni Steels", Acta Met, V. 10, (1962), p. 865.
9. Reed, R. P., Durholz, R. L., Schramm, R. E., and Patrician, T. L., "Study of Cryogenic Storage Tank Fatigue Life", NBS Technical Note 609, August 1971.

10. Reed, R. P. and Breedis, J. F., "Low Temperature Phase Transformations", ASTM STP No. 387, Behavior of Materials at Cryogenic Temperatures, (1965), pp. 60-132.
11. Reed, R. P. and Mikesell, R. P., "The Stability of Austenitic Stainless Steels at Low Temperatures as Determined by Magnetic Measurements", Proc. of 1958 Conf. on Cryogenic Engineering, ed. K. D. Timmerhaus (1958), pp. 84-100.
12. Reed, R. P. and C. J. Guntner, "Stress-Induced Martensitic Transformations in 18Cr-8Ni Steel", Trans. AIME, V. 230, Dec. 1964, pp. 1713-1720.
13. Guntner, C. J. and Reed, R. P., "The Effect of Experimental Variables Including the Martensitic Transformation on the Low-Temperature Mechanical Properties of Austenitic Stainless Steels", Trans. ASM, V. 55, 1962, pp. 399-419.
14. Larbalestier, D. C. and King, H. W., "Austenitic Stainless Steels at Cryogenic Temperatures, I-Structural Stability and Magnetic Properties", Cryogenics, March 1973, pp. 160-168.
15. Neff, D. V., Mitchell, T. E. and Troiano, A. R., "The Influence of Temperature, Transformation, and Strain Rate on the Ductility Properties of Austenitic Stainless Steels", Trans. ASM, V. 62, (1969), pp. 858-868.
16. Schaller, F. W. and Zackay, V. F., "Low Temperature Embrittlement of Austenitic Cr-Mn-N-Fe Alloys," Trans. ASM, V. 51, (1959), pp. 609-628.
17. Nachtigal, A. J., "Comparison of Tensile Properties of 304L and 310S Stainless Steels in Liquid Helium" NASA Technical Memo TM X-52703, Oct. 1969.
18. Eckenrod, J. J. and Kovach, C. W., "Effects of Manganese on Austenitic Stainless Steels," Met. Engrg. Quart., V. 12, No. 1, Feb. 1972, pp. 5-10.

19. Tobler, R. L. and Reed, R. P., "Tensile and Fracture Behavior of a Nitrogen-Strengthened, Cr-Ni-Mn Stainless Steel at Cryogenic Temperatures," Materials Research for Superconducting Machinery-IV, ARPA/NBS Semi-Annual Tech. Report (Oct. 1975), pp. 131-150.
20. Wells, J. M. and Hagadorn, M. W., "Evaluation of Nitronic 33 Stainless Steel for TFTR Device Application," Westinghouse Research Report 75-8C3-WETWO-R1, (Unrestricted), September 26, 1975.
21. Curtis, G. C. and Sherwin, J., "Magnetic Method for the Estimation of Ferrite in Stainless Steel Welds," Brit. J. Appl. Physics, V. 12, (1961), pp. 344-345.
22. Hull, F. C., "Effect of Delta Ferrite on the Hot Cracking of Stainless Steel," Welding Journal, V. 46, No. 9, Sept. 1967, pp. 399s-409s.
23. Anon., "The Role of Ferrite in Stainless Steel Welds," Welding Engineer, V. 58, No. 2, February 1973, pp. 27-30.
24. DeLong, W. T., "Calibration Procedure for Instruments to Measure the Delta Ferrite Content of Austenitic Stainless Steel Weld Metal," Welding Journal, Vol. 52, No. 2, Feb. 1973, pp. 69s-72s.
25. Freid, H. F. and DeLong, W. T., "Making Sense Out of Ferrite Requirements in Welding Stainless Steels," Metals Progress, Vol. 104, No. 1, June 1973, pp. 73-77.
26. Long, C. J. and DeLong, W. T., "The Ferrite Content of Austenitic Stainless Steel Weld Metal," Welding Journal, V. 52, No. 7, July 1973, pp. 281s-297s.
27. DeLong, W. T., "Ferrite in Austenitic Stainless Steel Weld Metal," Welding Journal, V. 53, No. 7, July 1974, pp. 273s-286s.
28. Anon., "Meet Mr. Ferrite," Teledyne McKay Publication 50-A, (1975).
29. McDougall, P. G., "Measurement of δ -Ferrite in Stainless Steel Welds," Welding Research Abroad, V. XXI, No. 7, August/September 1975, pp. 2-7.

30. Lundin, C. D., DeLong, W. T. and Spond, D. F., "Ferrite-Fissuring Relationships in Austenitic Stainless Steel Weld Metals," Welding Journal, V. 54, No. 8, August 1975, pp. 241S-246S.
31. Anon., "Ferrite Control in Stainless Steel Welds," Metals Progress, V. 108, No. 4, September 1975, pp. 88.
32. Campbell, H. C., "The Ferrite Problem - Is It a Tempest in a Teapot," Welding Journal, V. 54, No. 12, Dec. 1975, pp. 867-871.
33. Anon., "Standard Methods of Test for Permeability of Feebly Magnetic Material," ASTM Standard A342-64.
34. Brooks, J. A., "Weldability of High N, High Mn Austenitic Stainless Steel," Welding Journal, V. 54, No. 6, June 1975, pp. 189S-195S.
35. Douthett, J. A., "Nitronic Family of Nitrogen Bearing Stainless Steels," Metals Progress, August 1975, pp. 50-56.
36. Anon., "Armco 21-6-9," Alloy Digest Sheet SS-125, Dec. 1961.
37. Anon., "Carpenter Pyromet 538," Carpenter Technology Technical Data Sheet (1969).
38. Marlin, C. O., "Low Temperature Properties of Armco 21-6-9 (Cr-Ni-Mn)," NASA NAR 80011 (MSF-18243), (1968).
39. Vandervoort, R. R., "Tensile and Fraction Toughness of Austenitic Stainless Steel 21-6-9 in High Pressure Hydrogen Gas," Met. Engrg. Quart., V. 12, No. 1 (1972), pp. 10-16.
40. Denhard, E. E. and Espy, R. H., "Austenitic Stainless With Unusual Mechanical and Corrosion Properties," Met. Engrg. Quart., V. 12, No. 4, (1972), pp. 18-20.
41. Gaugh, R. R., Denhard, E. E., Jr. and Perry, D. C., "Developing an Austenitic Stainless Steel with Improved Strength and Corrosion Resistance," Met. Engrg. Quart., V. 12, No. 1 (1972), pp. 61-63.
42. Anon., "Armco A-286," Product Data Bulletin LA-8971, Armco Steel Corporation, Advanced Materials Division, August 1971.

43. Anon., "Allegheny A-286," Alloy Digest Sheet SS-4, Engrg. Alloys Digest Inc., N. J., December 1952.
44. Anon., "Unitemp A-286," Product Data Bulletin HT-3020, Universal-Cyclops Specialty Steel Division, (1971).
45. Anon., "Carpenter A-286," Technical Data Sheet, Carpenter Technology Corporation, June 1970.
46. Anon., "Allegheny Ludlum Type A-286," Blue Sheet No. 144, Allegheny Ludlum Steel Corporation, April 1973.
47. Muraca, R. F. and Whittick, J. S., Materials Data Handbook - Stainless Steel A-286, NASA MSF-22797, June 1972.
48. Yushchenko, K. A. and Kabuzan, V. V., "High-Nickel Steels and Alloys for Welded Structures in Cryogenic Engineering (A Survey)," Automatic Welding, V. 27, No. 3, March 1974, pp. 38-44.
49. Bennett, W. S. and Mills, G. S., "GTA Weldability Studies on High Manganese Stainless Steel," Welding Journal, V. 53, No. 12, Dec. 1974, pp. 548S-553S.
50. Bennett, W. S., Hillyer, R. F., Keller, D. L. and Riefenberg, D. H., "Vacuum Brazing Studies on High Manganese Stainless Steel," Welding Journal, V. 53, No. 11, Nov. 1974, pp. 510S-516S.
51. Vagi, J. J., Evans, R. M. and Martin, D. C., "Welding of Precipitation-Hardening Stainless Steels," NASA-SP-5087.
52. Harkins, F. G., "Welding of Age-Hardenable Stainless Steels," Welding Research Council Bulletin No. 103, February 1965.
53. Kaltenhauser, R., "Weldability of Precipitation-Hardening Steels," ASM Metals Engineering Quarterly, V. 9, No. 1, Feb. 1969, pp. 44-57.
54. Brooks, J. A. and Krenzer, R. W., "Progress Toward a More Weldable A-286," Welding Journal, V. 53, No. 6, June 1974, pp. 242S-245S.
55. Brooks, J. A., "Effect of Alloy Modifications on HAZ Cracking of A-286 Stainless Steel," Welding Journal, V. 53, No. 11, November 1974, pp. 517S-523S.

56. Private communication with A. Chargin of LLL on February 20, 1975.
57. Savage, W. F. and Lundin, C. D., "The Varestraint Test," Welding Journal, V. 44, No. 10, October 1965, pp. 433S-442S.
58. Savage, W. F. and Lundin, C. D., "Applicability of the Varestraint Technique to the Study of Weldability," Welding Journal, V. 45, No. 11, November 1966, pp. 499S-503S.
59. Savage, W. F. and Lundin, C. D., "The Evaluation of the Weldability of Structural Alloys with the Varestraint Test," Report No. AFML-TR-68-48, January 1968.
60. Gold, R. E. and Lessmann, G. G., "Varestraint Evaluation of Incoloy 800," Westinghouse Astronuclear Laboratory Report No. XAL-70662-AL, May 1970.
61. Lessmann, G. G. and Gold, R. E., "The Varestraint Test for Refractory Metals," Welding Journal, V. 50, No. 1, January 1971, pp. 1S-8S.
62. Grotke, G. E., "Varestraint Weldability Testing of A508 Class 2 and A533 Grade B, Class 1 Pressure Vessel Steels," Westinghouse Research Report 73-1D4-WELST-R1, (Unrestricted), February 12, 1973.
63. Arata, Y., Matsuda, F. and Saruwarti, S., "Varestraint Test for Solidification Crack Susceptibility in Weld Metal of Austenitic Stainless Steels," Welding Research Abroad, V. XXI, No. 1, January 1975, pp. 2-11.
64. Valdez, P. J. and Steinman, J. B., "Effect of Composition and Thermal Treatments on the Weldability of Nickel-Base 718 Alloy", Effects of Minor Elements on the Weldability of Hi-Nickel Alloys, Proceedings of Welding Research Council Symposium, July 1969, pp. 93-120.

TABLE 5-1 -- CANDIDATE MATERIALS FOR ADVANCED CRYOGENIC STRUCTURAL APPLICATIONS

<u>Trade Name</u>	<u>UNS Designation</u>	<u>Trade Name</u>	<u>UNS Designation</u>
<u>AUSTENITIC STAINLESS STEELS</u>		<u>LOW EXPANSION ALLOYS</u>	
* AISI 310S	S31008	Incoloy 903	
* Kromarc 58	--	** INCO (Unnamed) LEA	
Nitronic 33 (18-3Mn)	S24000		
Nitronic 40 (21-6-9)+	S21900	<u>TITANIUM ALLOYS</u>	
Nitronic 50 (22-13-5)	S20910		
Carpenter 20Cb-3	N08020	Ti-6Al-4V (ELI)	
Carpenter 18-18 Plus	--	Ti-5Al-2.5Sn (ELI)	
<u>IRON BASE SUPERALLOYS</u>			
*** A-286	K66286	<u>ALUMINUM ALLOYS</u>	
W-545	K66545	2014	A92014
Pyromet 860	--	2219	A92219
Discaloy	K66220	5083	A95083
		X2048	
<u>NICKEL BASE SUPERALLOYS</u>			
Inconel 625	N06625	<u>COPPER AND COPPER ALLOYS</u>	
** Inconel 718	N07718	* OFHC-Cu	C10200
** Inconel 706	N09706	Amzirc Cu (CW/HT)	C15000
* Inconel X750 (751)	N07750	Glidcop (Al203-D.S.)	
Hastelloy C-276	N10276	** PD-135 (Cu-Cr-Cd/PHT)	
Pyromet 680	N06002		
Pyromet 102	--		
<u>OTHER SUPERALLOYS</u>			
Haynes 188	R30188		
Multiphase MP35N	R30035		

* Materials characterized in Westinghouse FY 1974 program. ARPA/NBS Contract CST-8034.

** Materials included in Westinghouse FY 1975 Program.

*** Materials included in Westinghouse FY 1976 Program.

+ Also available as Pyromet 538.

TABLE 5-3
DOCUMENTATION DATA FOR WESTINGHOUSE FY76 PROGRAM MATERIALS

<u>Material</u>	<u>Source</u>	<u>Heat No.</u>	<u>Form</u>
A-286	ARMCO Steel	4X0836	5-1/4 inch square forging billet
Pyromet 538 (21-6-9 SS)	Carpenter Technology Corp. (Provided by Lawrence Livermore Labs)	89087	12 inch square forging billet, hot rolled to 3/4" t x 4" w plate by Braeburn Alloy Steel for WRL
Inconel 718	Huntington Alloys-INCO	HT16G6EY	HFFQ round 11-3/8 inch dia. x 12 inch long (VIM/VAR)
Inconel F-92	Huntington Alloys-INCO (via Williams & Co., Inc.)	HT1712MD	Bare filler wire, 0.062 inch diameter x 25 lb spool (AWS, A5.14-69, class ERNICRFE-6)
Inconel E-182	Huntington Alloys-INCO (via Williams & Co., Inc.)	HT5022	Coated Welding Electrode, 0.093 inch diameter x 9 inch length, 10 lbs. (AWS A5.11-69, Class ENICRFE-3)
Inconel E-182	Huntington Alloys-INCO (via Williams & Co., Inc.)	HT4916	Coated Welding Electrode, 0.125 inch diameter x 12 inch length, 20 lbs, (AWS A5.11-69, Class ENICRFE-3)
21-6-9	Carpenter Technology Corp. (Provided by Lawrence Livermore Labs)	82287	Bare filler wire, 0.030 inch diameter x 25 lb spool, (VIM/ESR)

TABLE 5-4
PROCESSING AND HEAT TREATMENT SCHEDULES FOR WESTINGHOUSE FY76 PROGRAM MATERIALS

<u>Material</u>	<u>Code</u>	<u>Condition</u>	<u>Remarks</u>
Inconel 718	67XX	ST/CW/1800ST/DA	ST (1950°F-1 hr-A.C.), cold worked for 40% reduction in thickness and ST (1800°F-1 hr-A.C.), Double Aged 1325°F-8 hrs-F.C. to 1150°F - 8 hrs and A.C.
	68XX	ST/CW/1950ST/DA	ST (1950°F-1 hr-A.C.), cold worked 40%, ST (1950°F-1 hr-A.C.) and DA (1325°F/1150°F)
	69XX	ST/CW/DA	ST (1950°F-1 hr-A.C.), cold worked 40%, Direct Double Age (1325°F/1150°F)
A-286	90XX	STQA	Solution treat at 1650°F-5 hrs - Oil quench, Age at 1325°F-20 hrs-Air cool
Pyromet 538 (21-6-9)	92XX	STQ	Original Billet Section cut in blocks 4" x 4" x 12", preheated to 2000°F - held for 4 hrs and forged to sheet bar 1-3/8" x 4" x L with four intermediate reheat cycles, reheated to 2000°F and hot rolled to 3/4" x 4" w x 80" L in four flat and one edge pass. Final STQ treatment at 2000°F-1 hr-water quench

TABLE 5-5
MATERIAL HARDNESS AND ASTM GRAIN SIZE MEASUREMENTS-WESTINGHOUSE FY76 PROGRAM MATERIALS

<u>Material</u>	<u>Code</u>	<u>Condition</u>	<u>Hardness</u>	<u>Grain Size (ASTM No.)</u>
IN 718 (VIM-VAR)	67XX	ST/40% CW/1800 STDA	Rc 40	8.0
	68XX	ST/40% CW/1950 STDA	Rc 39	2.9
	69XX	ST/40% CW/DA	Rc 44	5.6
A-286	90XX	STQA	Rc 30	4.2
	91XX	STQ/GTAW		
Pyromet 538 (21-6-9)	92XX	STQ	Rb 89	4.3
	93XX	STQ/GTAW	See Figure 5-8	
	94XX	STQ/SMAW	See Figure 5-6	
	--	As received Billet (LLL)	Rb 84	CL 3.5
	--	1-1/2" Plate (NBS/LLL)	Rb 83.5	4.5
	--	3/4" HR Plate (LLL/W)	Rb 96	

TABLE 5-6

TEST SPECIMEN IDENTIFICATION SYSTEM

<u>Material</u>	<u>Condition</u>	<u>Code No.</u>	<u>Specimen ID System</u>
OFHC Copper	As Received, AR Stress Relieved, SR GTAW Braze, B Solder, S	10XX-X 11XX-X 12XX-X 13XX-X 14XX-X	4 Digits + Dash No.
PD 135 Copper	EXT/PHT	15XX-X	Material Condition Test Temperature Replicate
AISI 310S	Sol'n Treated & Quenched, STQ Sensitized, STFC SMAW	20XX-X 21XX-X 22XX-X	X X X X - X
Inconel X750 MP-1 (VIM-VAR)	Solution Treated, ST ST + Double Age, STDA ST/EBW STDA/EBW EBW/STDA ST/GTAW STDA/GTAW GTAW/STDA ST/Cu-Braze STDA	30XX-X 31XX-X 32XX-X 33XX-X 34XX-X 35XX-X 36XX-X 37XX-X 38XX-X 40XX-X	Test (3rd Digit) Smooth Tensile Notched Tensile KIC JIC FCGR
X750, MP-2 (AAM-VAR)		50XX-X	Temperature (4th Digit) Room Temp. (293 K) XXX1 LN2 (77 K) XXX2 LHe (4 K) XXX3
X750, MP-3 (VIM)		60XX-X 61XX-X 62XX-X 63XX-X	
X750, HIP	HIP HIP/STDA HIP/GTAW/STDA (FZ) HIP/GTAW/STDA (HAZ)		

TABLE 5-6 (CONTINUED)

<u>Material</u>	<u>Condition</u>	<u>Code No.</u>
Inconel 718	STDA (VIM-VAR)	64XX-X
	ST/GTAW/STDA (FZ)	65XX-X
	ST/GTAW/STDA (HAZ)	66XX-X
	ST/CW/1800 ST/DA	67XX-X
	ST/CW/1950 ST/DA	68XX-X
	ST/CW/DA	69XX-X
Inconel 706	STDA (VIM-EFR)	70XX-X
	STDA (VIM-VAR)	71XX-X
	Si/GTAW/STDA	72XX-X
Inco LEA	STA	73XX-X
	ST/GTAW/STA	74XX-X
Kromarc 58	STQ	80XX-X
	CW	81XX-X
	STQ/GTAW	82XX-X
	CW/GTAW	83XX-X
	GTAW/CW	84XX-X
	GTAW/CW/(Partially Recrystallized)	85XX-X
	GTAW/CW/(Fully Recrystallized)	86XX-X
	STQ/CW (Anisotropy L-T)	87XX-X
A-286	STQA	90XX-X
	STQ/GTAW	91XX-X
Pyromet 538 (21-6-9)	STQ	92XX-X
	STQ/GTAW	93XX-X
	STQ/SAW	94XX-X

TABLE 5-7 -- RESULTS OF M_d AND M_s CALCULATIONS FOR SPECIFIC COMPOSITIONS OF AUSTENITIC STAINLESS STEELS

M_d ($^{\circ}\text{F}$) = 2520 - 106 (Ni + 0.40Cr + 0.69Mn + 0.41Mo + 0.34Si + 1.07V + 0.78Ti + 0.91Al + 13.2C + 5.38N)					
M_s ($^{\circ}\text{F}$) = 2700 - 106 (Ni + 0.80Cr + 0.92Mn + 0.94Mo + 0.63Si + 2.17V + 3.07Ti + 5.21Al + 40.6C + 54.7N)					
Alloy	Composition	Total Ni Equiv. (M_d)	Calc. M_d $\frac{^{\circ}\text{F}}{\text{K}}$	Total Ni Equiv. (M_s)	Calc. M_s $\frac{^{\circ}\text{F}}{\text{K}}$
Kromarc 58	23.0Ni, 15.5Cr, 9.3Mn, 2.2Mo, 0.05Si, 0.16V, 0.02Al, 0.03C, 0.17N	38.0	-1500 -579	57.0	-3340 -1600
A 286	25.8Ni, 14.9Cr, 1.72Mn, 1.31Mo, 0.57Si, 0.31V, 2.35Ti, 0.15Al, 0.036C	36.4	-1340 -490	51.0	-2700 -1250
AISI 310 S	19.7Ni, 24.4Cr, 1.70Mn, 0.17Mo, 0.74Si, 0.064C, 0.15Cu	31.8	- 853 -219	44.2	-1990 - 851
Pyromet 538 (21-6-9)	7.16Ni, 19.75Cr, 9.46Mn, 0.15Si, 0.019C, 0.28N	23.3	+ 51 +283	47.8	-2370 -1060
Nitronic 33	3.26Ni, 18.09Cr, 13.22Mn, 0.52Si, 0.038C, 0.37N	22.2	+ 167 +348	51.9	-2800 -1300
AISI 305	12.5Ni, 17.4Cr, 1.54Mn, 0.43Si, 0.058C, 0.024N	21.5	+ 241 +389	31.7	- 664 - 121

$$\begin{aligned} M_D \text{ (}^\circ\text{F)} &= 2520 - 106 (\text{Ni} + 0.40\text{Cr} + 0.69\text{Mn} + 0.41\text{Mo} + 0.34\text{Si} + 1.07\text{V} + 0.78\text{Ti} + 0.91\text{Al} + 13.2\text{C} + 5.38\text{N}) \\ M_S \text{ (}^\circ\text{F)} &= 2700 - 106 (\text{Ni} + 0.80\text{Cr} + 0.92\text{Mn} + 0.94\text{Mo} + 0.63\text{Si} + 2.17\text{V} + 3.07\text{Ti} + 5.21\text{Al} + 40.6\text{C} + 54.7\text{N}) \end{aligned}$$

Alloy	Composition Range						Ni Equiv. (d)	M _D		Ni Equiv. (s)	M _S	
								°F	K		°F	K
AISI 304	12.0 8.0	Ni, 20.0 18.0	Cr, 2.0 0.5	Mn, 1.0 0.25	Si, 0.08 0.02	C	22.8 15.9	+106 +835	+314 +719	-874 +177	-231 +353	
AISI 304 (N)	10.5 8.0	Ni, 20.0 18.0	Cr, 2.0 0.5	Mn, 1.0 0.25	Si, 0.08 0.02	C, 0.16 0.10	22.1 16.4	+177 +782	+353 +690	-1680 -406	-662 +29	
AISI 305	13.0 10.0	Ni, 19.0 17.0	Cr, 2.0 0.5	Mn, 1.0 0.25	Si, 0.12 0.04	C	23.9 17.8	-13 +633	+249 +607	-1060 -35	-334 +236	
AISI 309 (S)	15.0 12.0	Ni, 24.0 22.0	Cr, 2.0 0.5	Mn, 1.0 0.25	Si, 0.08 0.02	C	27.4 21.5	-382 +242	+43 +390	-1530 -589	-596 -72	
AISI 310 (S)	22.0 19.0	Ni, 25.0 24.0	Cr, 2.0 0.5	Mn, 1.5 0.4	Si, 0.08 0.02	C	35.3 29.3	-1222 -586	-424 -71	-2470 -1510	-1120 -585	
AISI 316	14.0 10.0	Ni, 18.0 16.0	Cr, 2.0 0.5	Mn, 3.0 2.0	Mo, 1.0 0.25	Si, 0.08 0.02	25.2 17.9	-151 +623	+171 +601	-1210 -67	-418 +218	
AISI 321	12.0 9.0	Ni, 19.0 17.0	Cr, 2.0 0.5	Mn, 1.0 0.25	Ti, 0.41 0.10	C, 0.08 0.02	22.7 16.6	+114 +760	+318 +678	-915 +124	-254 +324	
Nitronic 33 (18-3 Mn)	3.75 2.25	Ni, 19.0 17.0	Cr, 14.5 11.5	Mn, 1.0 0.25	Si, 0.08 0.02	C, 0.40 0.20	24.9 18.4	-119 +570	+144 +572	-3450 -1360	-1660 -515	
Nitronic 40 (21-6-9)	7.50 5.50	Ni, 21.5 19.0	Cr, 10.0 8.0	Mn, 1.0 0.25	Si, 0.08 0.02	C, 0.40 0.15	26.5 19.8	-289 +421	+94 +489	-3630 -1240	-1760 -434	
Kromarc 58	24.0 18.0	Ni, 17.0 14.0	Cr, 3.0 8.0	Mn, 2.75 1.75	Mo, 0.5 0.12	Si, 0.35 0.12	43.5 31.0	-2100 -764	-913 -170	-4440 -2280	-2260 -1010	
A-286	27.0 24.0	Ni, 16.0 13.5	Cr, 2.0 1.0	Mn, 1.75 1.0	Mo, 1.0 0.4	Si, 0.5 0.1	39.5 32.5	-1670 -925	-674 -259	-3350 -1940	-1610 -824	
Incoloy 800	35.0 30.0	Ni, 23.0 19.0	Cr, 1.5 0.4	Mn, 1.0 0.25	Si, 0.75 0.20	Cu, 0.60 0.15	47.9 38.6	-2560 -1570	-1170 -618	-4130 -2410	-2040 -1080	

TABLE 5-9 --COMPARISON OF FERRITE CALCULATIONS WITH HULL METHOD VERSUS DELONG METHOD
FOR HIGH MANGANESE STAINLESS STEELS

DeLong's Formulae for Nickel and Chromium Equivalents (Ref. 26, 27):

1. Ni Equiv. (D) = Ni + 30C + 30N + 0.5 Mn
2. Cr Equiv. (D) = Cr + Mo + 1.5Si + 0.5Cb

Hull's Formulae for Nickel and Chromium Equivalents (Ref.7):

3. Ni Equiv. (H) = Ni + 0.11Mn - 0.0086Mn² + 0.41Co + 0.44Cu + 18.4N + 24.5C
4. Cr Equiv. (H) = Cr + 1.21Mo + 0.48Si + 2.27V + 0.72W + 2.20Ti + 0.14Cb + 0.21Ta + 2.48Al

Base Metal	Weldment	Weld Metal Composition	Hull's Formulae			DeLong's Formulae			Measured FN	References For Data
			Ni*(H)	Cr*(H)	FN(H) (1)	Ni(D)	Cr(D)	FN(D) (2)		
A. N-33 Submerged Arc (with N35W filler)		3.94Ni, 17.8Cr, 12.1Mn, 0.59Si, 0.045C, 0.35N	11.74	18.08	~ 2	21.84	18.69	<<0	2.1	Wells and Hagadorn (20)
B. N-33 Shielded Metal Arc (with N35W filler)		4.54Ni, 17.9Cr, 12.0Mn, 0.36Si, 0.058C, 0.24N	10.46	18.07	~ 5	19.48	18.44	<<0	4.8	"
C. N-33 Gas Tungsten Arc (with N35W filler)		4.37Ni, 17.8Cr, 11.9Mn, 0.40Si, 0.040C, 0.27N	10.41	17.99	~ 5	19.62	18.40	<<0	4.7	"
D. N-33 Gas Tungsten Arc (with 13-20MnCb filler)		12.3Ni, 15.7Cr, 11.2Mn, 0.41Si, 0.051C, 0.21N	17.57	15.90	<<0	25.73	16.32	<<0	0*	"
E. N-40 Gas Tungsten Arc (Autogeneous)		7.12Ni, 20.1Cr, 8.55Mn, 0.19Si, 0.035C, 0.43N	16.20	20.19	<<0	25.34	20.39	<<0	0	Brooks (34)
F. N-40 Gas Tungsten Arc (Autogeneous)		6.72Ni, 21.0Cr, 8.52Mn, 0.25Si, 0.010C, 0.24N	11.69	21.12	~10	18.48	21.38	<<0	5.0	"
G. N-40 Gas Tungsten Arc (Autogeneous)		7.53Ni, 19.9Cr, 8.70Mn, 0.17Si, 0.033C, 0.12N	10.85	19.98	~10	16.47	20.16	<<0	13.5	"

Note (1) FN(H) = Ferrite Number Obtained from Hull's Modification of the Schaeffler Diagram using Hull's Nickel and Chromium Equivalent Formula.

(2) FN(D) = Ferrite Number Obtained from DeLong's Modification of the Schaeffler Diagram using DeLong's Nickel and Chromium Equivalent Formula.

* = Original measurement reported in Ref. was 0.2FN, however the zero calibration of Magne-Gage used was later found to be in error and the corrected reading was found to be ≤ 0 FN.

TABLE 5-10 -- RESULTS OF DELTA FERRITE PREDICTIONS IN HIGH MANGANESE STAINLESS STEEL WELDMENTS

Predictive Formula* For Amount of Ferrite in Austenitic Stainless Steel Weld Metal

$$FN = -13.8 - 3.12 \times Ni^* + 2.88 \times Cr^*$$

Base Metal	Weldment	Ni Equiv. (Ni*)	Cr Equiv. (Cr*)	FN		Reference For Data
				Formula	Diagram Measured	
A. Nitronic 33	Submerged Arc (filler N35W)	11.74	18.08	+ 1.6	~ 2	2.1
B. Nitronic 33	Shielded Metal Arc (filler N35W)	10.46	18.07	+ 5.6	~ 5	4.8
C. Nitronic 33	Gas Tungsten Arc (filler N35W)	10.41	17.99	+ 5.5	~ 5	4.7
D. Nitronic 33	Gas Tungsten Arc (filler 13-20MnCb)	17.57	15.90	- 23	<0	0
E. Nitronic 40	Gas Tungsten Arc (Autogeneous)	16.20	20.19	-6.2	<0	0
F. Nitronic 40	Gas Tungsten Arc (Autogeneous)	11.69	21.12	+11	~ 10	5.0
G. Nitronic 40	Gas Tungsten Arc (Autogeneous)	10.85	19.98	+10	~ 10	13.5
						Brooks (34)
						Wells and Hagadorn (20)
						"
						"
						"
						"

* Formula shown was developed by Dr. E. W. Johnson of the Westinghouse Research Laboratories (unpublished work) based upon Hull's original work (Ref.7).

TABLE 5-11--SUMMARY TABLE OF WELDING DATA (WESTINGHOUSE FY76)

Code	94XX	92XX
Base Metal	Pyromet 538 (21-6-9 SS)	ARMCQ A-286, STQQ
Size	11/16" t x 3-5/8" w x 16" l	3/4" t x 3-3/4" w x 5-1/2" l
Weld Joint	Butt, Double-V, 60° Inc. Angle	Butt, Double-V, 60° Inc. Angle
Process	SMAW - Manual, Flat	GTAW - Manual, Flat
Filler Material	Inconel 182, 1/8" dia x 12" l	Inconel 92 Bare Wire
Current	DCRP - 90/120 amps	DCSP-140/165 amps
Voltage	20 - 26 volts	14-16.5 Volts
Electrode	AWS A.511-69, Cl. ENICRFE-3	EWTh-2, 3/32" dia.
Welding Speed	8 - 12 ipm	2-7 ipm
No. of Passes	18**	18-21
Shielding Gas	N/A	50% Ar/50% He, 20 cfh
Root Backing Gas	N/A	100% Ar, 10 cfh
Root Gap	3/32" approx.	1/16" approx.
Dye Check (DPT)*	Yes	Yes
Radiograph	RD 76145 and RD 76146 (Plate HR-1A) (Plate HR-1B)	RD 76267 (Plate C) RD 76268 (Plate C) RD 76312 (Plate E)

NOTES: * All welds dye checked after root pass ground out and after pass No. 2

** All SMA welds were ground after each pass

*** Filler wire (21-6-9) consisted of three strands of 0.030" dia. @ twist wound together

TABLE 5- 12-- SUMMARY OF WESTINGHOUSE LONGITUDINAL VARESTRAINT WELDABILITY TESTS ON VARIOUS AUSTENITIC STAINLESS STEELS

Material	Condition	Fusion Zone Cracking					Heat Affected Zone Cracking				
		$\epsilon = 0.25$	$\epsilon = 0.5$	$\epsilon = 1.0$	$\epsilon = 2.0$	$\epsilon = 3.0$	$\epsilon = 0.25$	$\epsilon = 0.5$	$\epsilon = 1.0$	$\epsilon = 2.0$	$\epsilon = 3.0$
Kromarc 58 Base Metal	ST (1800°F) WQ	NC	3/0.031	7/0.088	9/0.108	17/0.152	NC	NC	NC	NC	NC
	ST/GTAW	NC	1/0.009	6/0.041	10/0.081	(11/0.122)*	NC	NC	NC	NC	NC
Nitronic 33 Base Metal	ST (2000°F) WQ	NC	NC	NC	NC	NC	NC	NC	NC	NC	NC
	ST/GTAW	NC	4/0.057	6/0.092	11/0.106	13/0.151	NC	NC	NC	3/0.015	7/0.039
AISI 305	ST (2000°F) WQ	NC	6/0.050	7/0.043	10/0.068	20/0.133	NC	NC	NC	NC	1/0.004
Pyromet 538 Base Metal	Billet As-Received	NT	NC	NC	NC	NC*	NT	NC	NC	NC	NC*
	Billet Mat/STQ	NT	NC	NC	NC	NC*	NT	NC	NC	NC	NC*
A-286 Base Metal	ST (1650°F) OQ	NC	8/0.284	10/0.316	9/0.249	NT	4/0.033	9/0.072	16/0.159	22/0.215	NT
	ST(1650°F) OQ/A	NC	9/0.259	6/0.246	9/0.328	NT	5/0.046	15/0.191	11/0.124	26/0.289	NT
Ht. No. 54733	ST (1800°F) OQ/A	1/0.010	8/0.212	10/0.311	9/0.343	NT	4/0.034	12/0.125	16/0.200	22/0.278	NT
Base Metal	ST (1800°F) OQ	1/0.007	6/0.211	6/0.149	6/0.180	NT	NC	9/0.087	20/0.205	30/0.346	NT
	ST (1650°F) OQ/A	1/0.019	10/0.240	13/0.283	13/0.333	NT	4/0.035	12/0.117	18/0.191	23/0.259	NT
Ht. No. 4X0836	ST (1800°F) OQ/A	2/0.017	8/0.242	8/0.230	9/0.273	NT	1/0.005	9/0.099	18/0.205	29/0.337	NT

NOTE: NC - Test Conducted, No Cracking Observed at Indicated Strain Level

NT - Test not Conducted at this Strain Level

* - Data for $\epsilon = 4\%$ Augmented Strain

No. of cracks/total crack length (inches)

TABLE 5-13 -- SUMMARY OF WESTINGHOUSE LONGITUDINAL VARESTRAIN WELDABILITY TESTS ON ALLOY 718

Material	Condition	Fusion Cracking					HAZ Cracking				
		$\epsilon = 1/4$	$\epsilon = 1/2$	$\epsilon = 1.0$	$\epsilon = 2.0$	$\epsilon = 3.0$	$\epsilon = 1/4$	$\epsilon = 1/2$	$\epsilon = 1.0$	$\epsilon = 2.0$	$\epsilon = 3.0$
Udimet 718	As-Received	NC	3/0.51	6/0.091	9/0.172	12/0.191	NC	NC	6/0.034	18/0.134	19/0.123
	ST - 1800°F	NC	3/0.047	9/0.167	11/0.212	8/0.201	NC	NC	8/0.041	9/0.051	16/0.101
	ST - 1950°F	NC	4/0.041	4/0.088	10/0.178	14/0.270	NC	NC	4/0.012	14/0.086	14/0.146
	STD (1800°F)	NC	3/0.057	8/0.192	17/0.245	17/0.294	NC	NC	7/0.054	14/0.079	23/0.165
	STD (1950°F)	NC	3/0.047	6/0.134	15/0.287	14/0.318	NC	NC	5/0.023	15/0.080	24/0.220
Incone1 718	As-Received	NC	5/0.124	9/0.209	10/0.262	13/0.343	NC	NC	4/0.039	21/0.152	31/0.241
	ST - 1800°F	NC	4/0.127	5/0.178	13/0.321	12/0.303	NC	NC	2/0.018	14/0.118	26/0.258
	ST - 1950°F	NC	3/0.065	9/0.143	9/0.181	13/0.219	NC	NC	7/0.039	9/0.062	17/0.122

NOTE: NC = Test Conducted but no cracking observed at indicated augmented stain level.
No. of cracks/total crack length (inches)

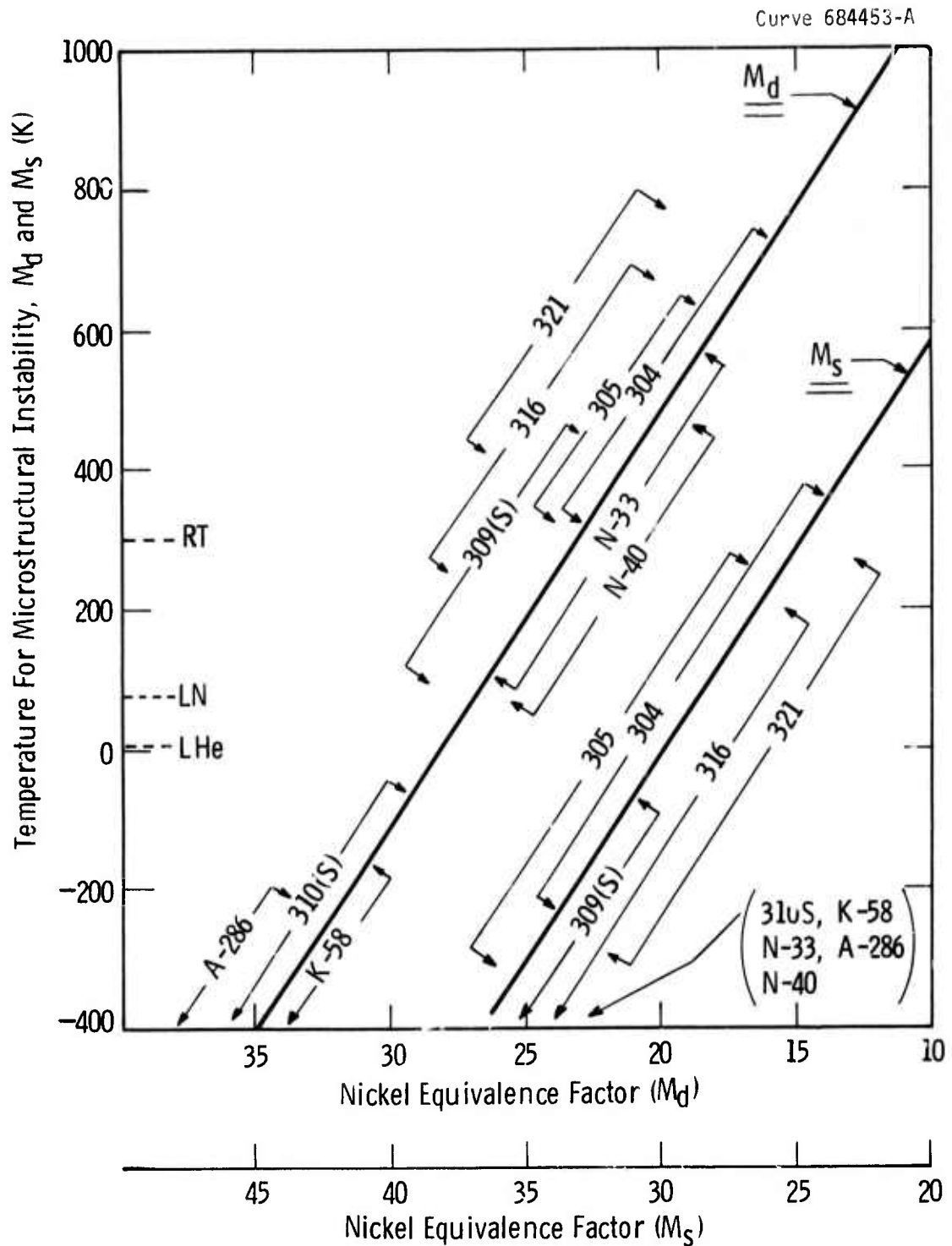


Fig.5-1—Calculated temperature ranges for microstructural instability, M_d and M_s in various austenitic stainless steel alloys

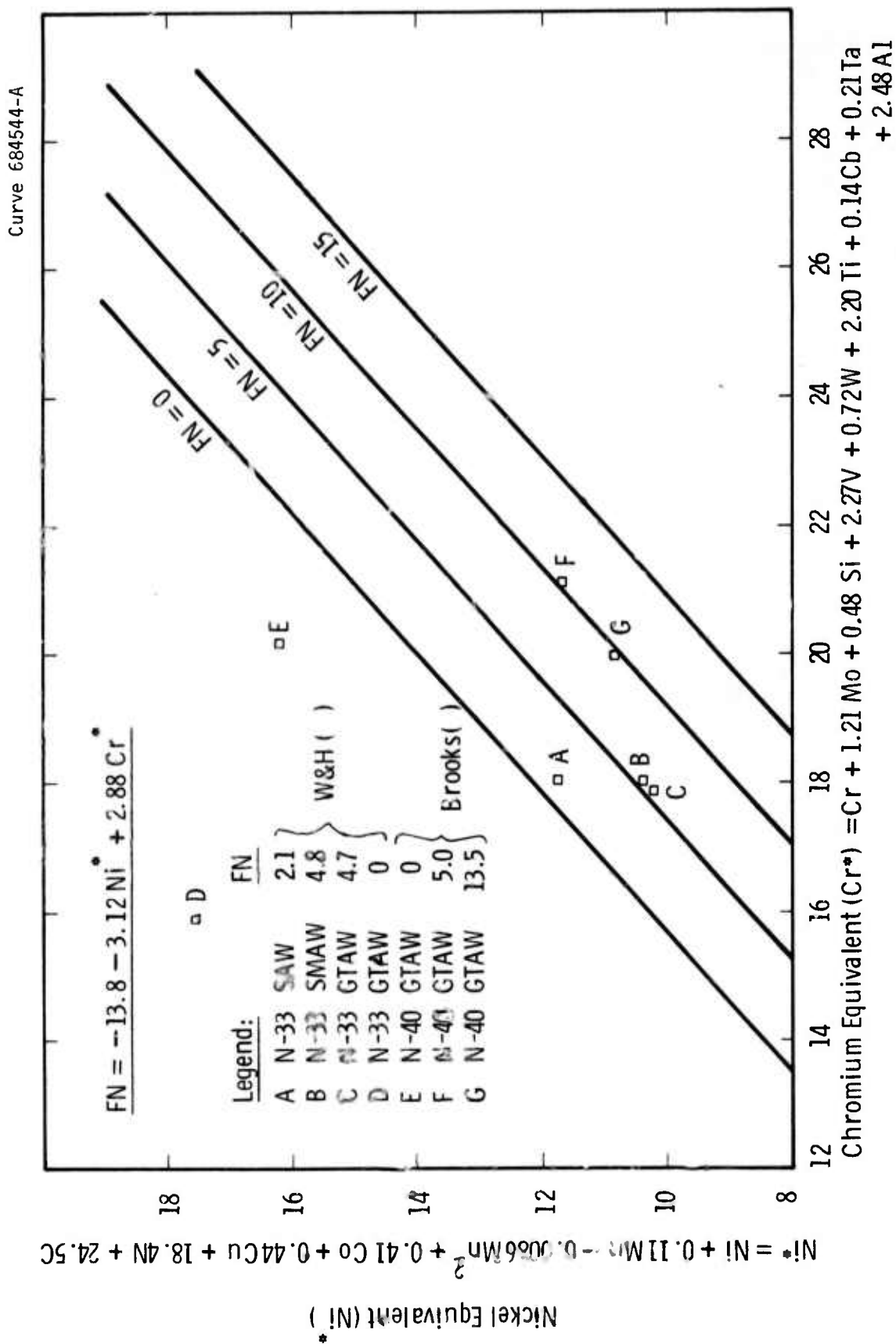
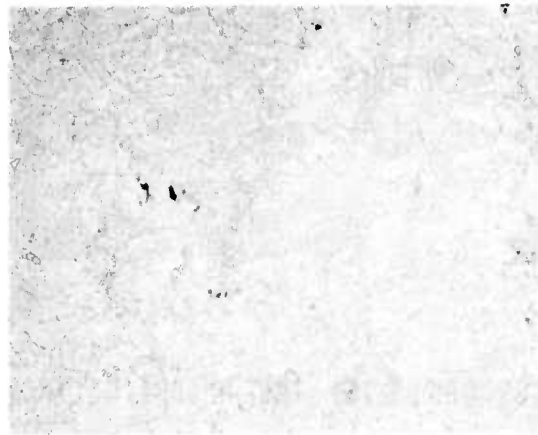


Fig. 5-2 — Measured ferrite number (FN) versus FN predicted by the Hull diagram for high manganese stainless steel weldments

Code 67XX



(A) ST at 980°C (1800°F)
DA at 718°C (1325°F)/620°C
(1150°F)

Code 68XX



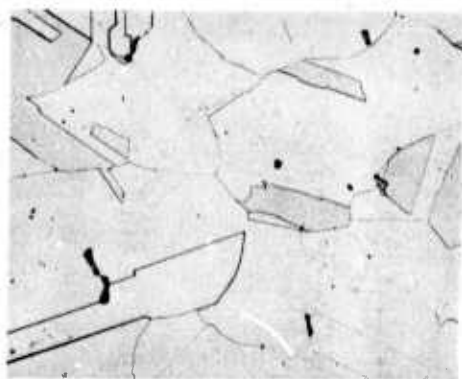
(B) ST at 1066°C (1950°F)
DA at 718°C (1325°F)/620°C
(1150°F)

Code 69XX



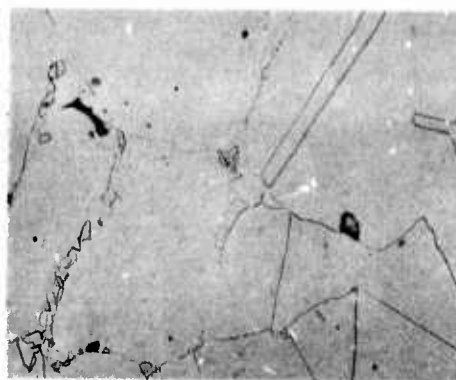
(C) No additional ST
DA at 718°C (1325°F)/620°C
(1150°F)

Figure 5-3 Photomicrographs of Inconel 718 alloy following various processing operations consisting of solution treatment at 1066°C (1950°F), 40% cold work and then treated as shown (X225)



(A) Billet Center Line

I
Original Billet
As Received



(B) Billet Exterior

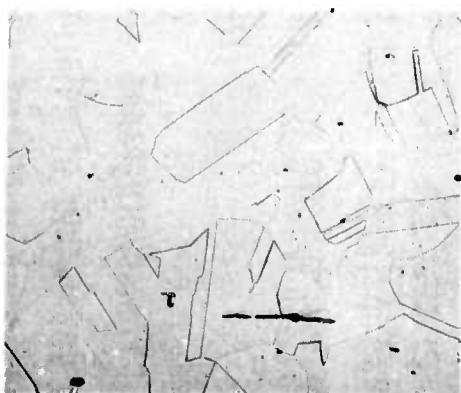


(C) Plate Centerline

II
NBS Plate
STQ

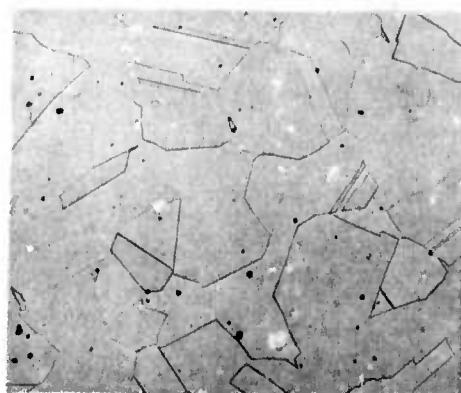


(D) Plate Surface



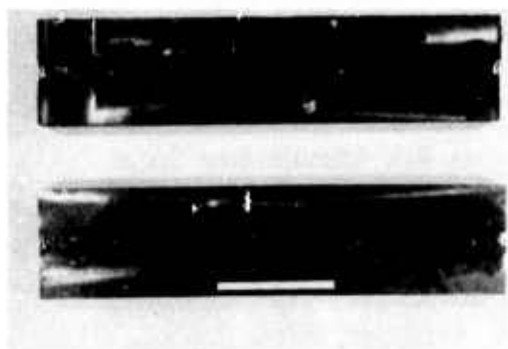
(E) Longitudinal Section

III
Ⓜ Plate
STQ

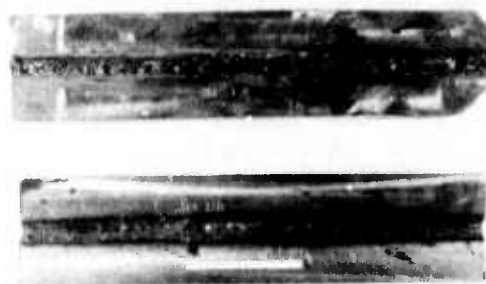


(F) Transverse Section

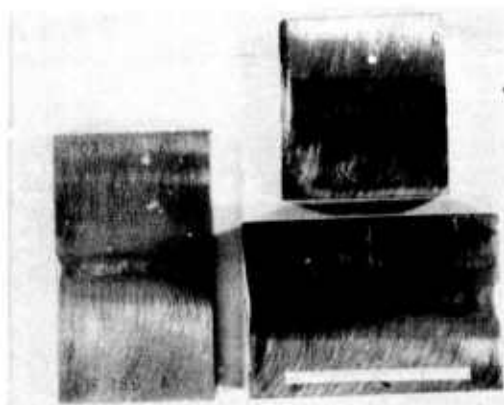
Figure 5-4 Photomicrographs comparing the microstructures of Pyromet 538 (21-6-9) material as, I-as received billet, II-1½ in. thick plate sample from NBS and III-¾ in. thick plate made in Ⓜ FY76 program(X225)



(A) Code 93XX

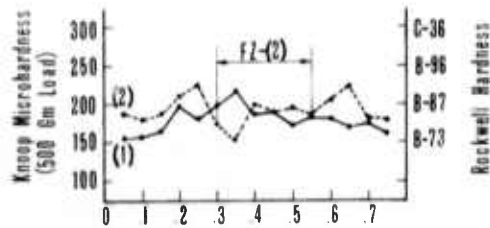


(B) Code 94XX

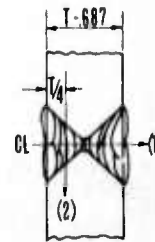


(C) Code 91XX

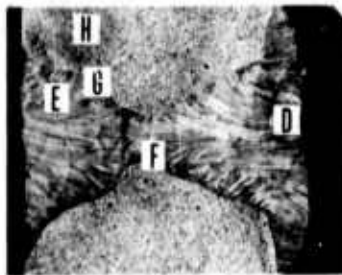
Figure 5-5 Photographs of weld test plates (as welded) for
 ① FY-76 program, (A) GTAW in Pyromet 538 (21-6-9), (B) SMAW in
 Pyromet 538 (21-6-9) and (C) GTAW in A-286 material



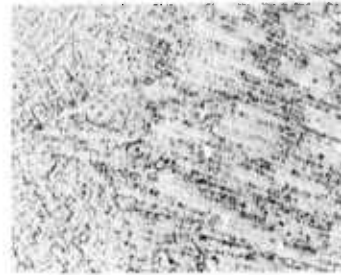
(A) Microhardness Survey



(B) Weld Schematic Cross Section



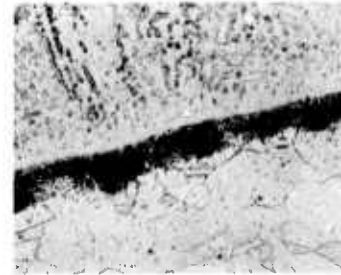
(C) Weld Macro-Section



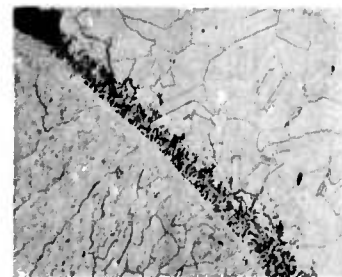
(D) Weld Fusion Zone



(E) Weld Fusion Zone



(F) FZ-HAZ Transition



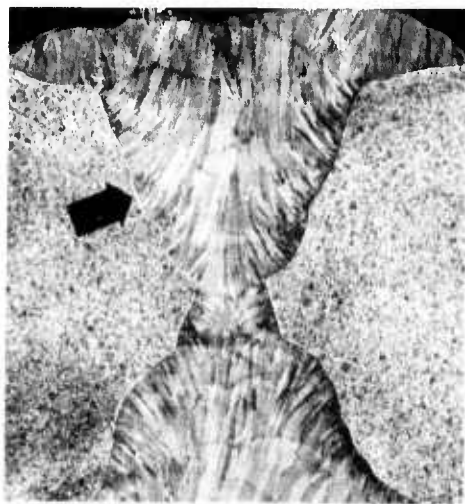
(G) FZ-HAZ Transition



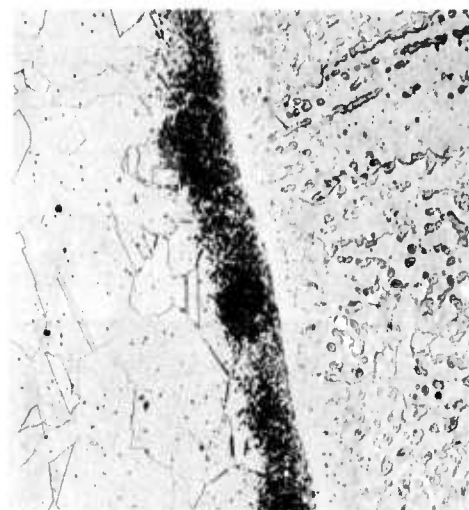
(H) Base Metal

Figure 5-6 Microhardness Survey (A&B), Macrostructure (C) (X6) and Microstructure of ST0/SMA welded Pyromet 538 (21-6-9) (weld plate no. 1B), (D) thru (H) as welded (X225)

SMA Weldment in Pyromet 538



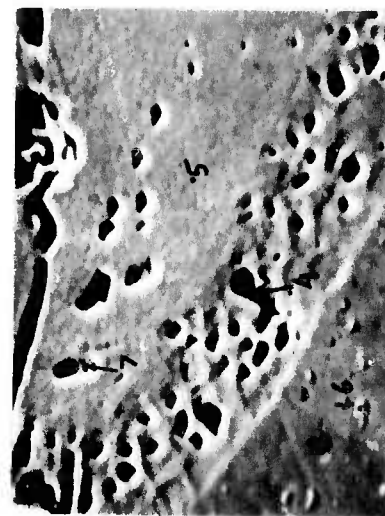
(A) Macrosection (X5)



(B) Optical Microstructure (X225)

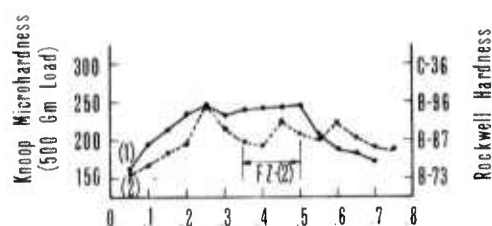


(C) SEM Microstructure (X475)

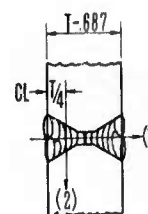


(D) SEM Microstructure (X1900)

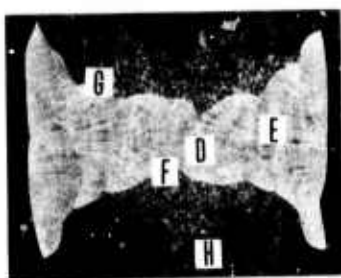
Figure 5-7 Macro and microstructural features of FZ-HAZ band of microporosity in SMA weldment in Pyromet 538



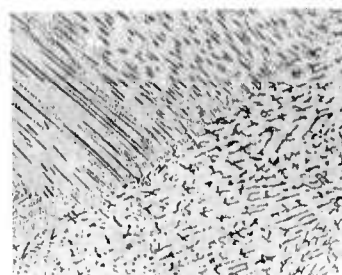
(A) Microhardness Survey



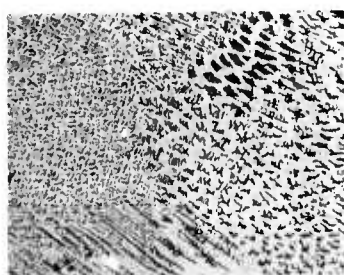
(B) Weld Schematic Cross Section



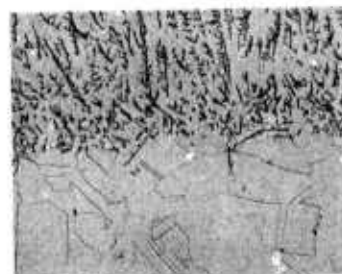
(C) Weld Macro-Section



(D) Weld Fusion Zone



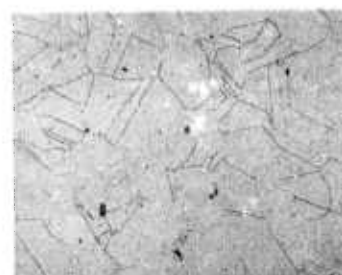
(E) Weld Fusion Zone



(F) FZ-HAZ Transition

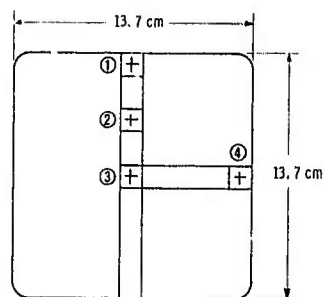


(G) FZ-HA Transition



(H) Base Metal

Figure 5-8 Microhardness Survey (A&B), Macrostructure (C), (X6) and Microstructure of STQ/GTA welded Pyromet 538 (21-6-9) (weld plate no.1D) (D) thru (H) as welded (X225)



(A) Sectioning Schematic for A-286 Forging Billet

I - Longitudinal Section



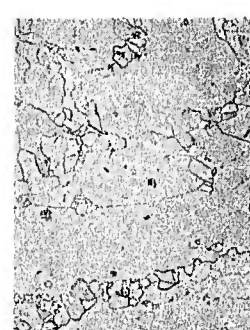
Location 1



Location 2



Location 3

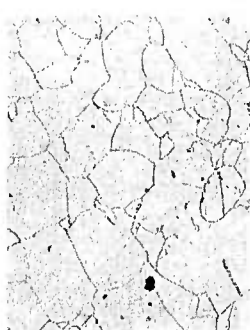


Location 4

II - Transverse Section



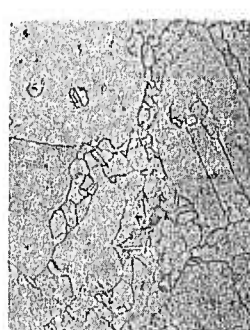
Location 1



Location 2



Location 3



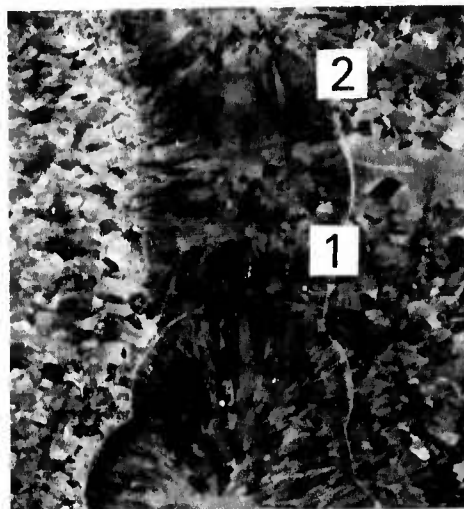
Location 4

Fig. 5-9 - Sectioning Schematic and Microstructure of A-286 Forging Billet Material, (I) Longitudinal Sections and (II) Transverse Sections (X225)

A-286 STQA/GTA Weldment



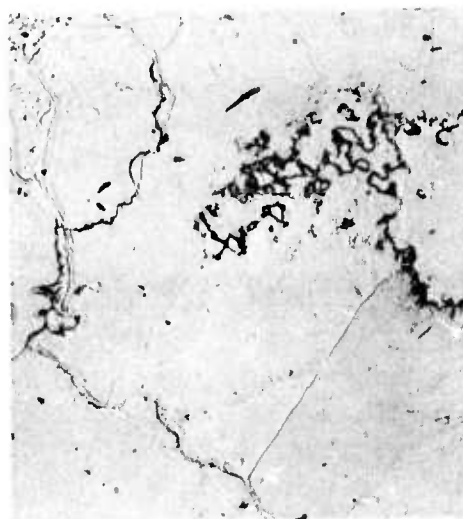
(A) Macroview of FZ Hot Cracking (X5)



(B) Macrosection (transverse) (X7)



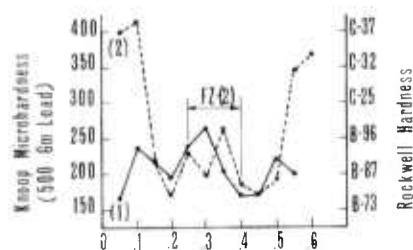
(C) HAZ Microfissuring-1 (X225)



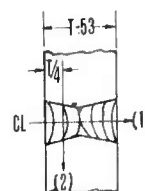
(D) HAZ Microfissuring-2 (X225)

Figure 5-10 Macro Fusion Zone Hot Cracking (A) and Heat Affected Zone Microfissuring in A-286 STQA/GTA Weldment No.A

A-286 SS ST0A/GTAW



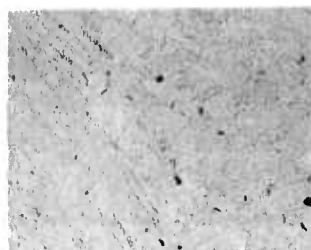
(A) Microhardness Survey



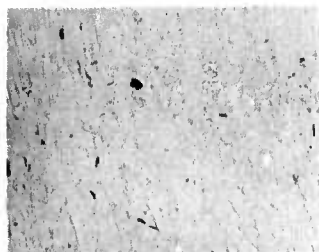
(B) Weld Schematic Cross Section



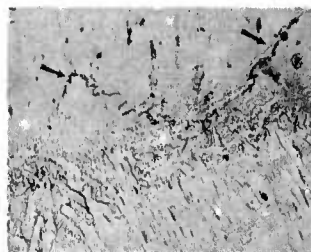
(C) Weld Macro-Section



(D) Weld Fusion Zone



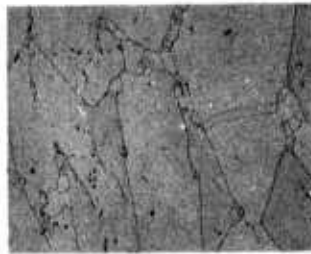
(E) Weld Fusion Zone



(F) FZ-HAZ Transition

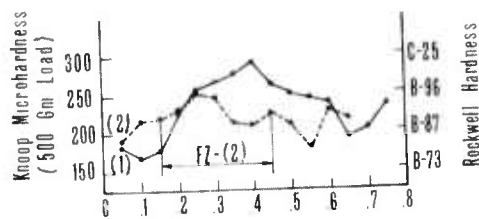


(G) FZ-HAZ Transition

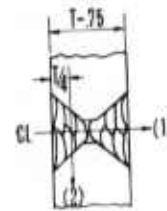


(H) Base Metal

Figure 5-11 Microhardness Survey (A&B), Macrostructure (C),(X7) and Microstructure of ST0A/GTA welded A-286 Stainless Steel (weld plate no.1A)(D)thru(H) as welded (X₂25)



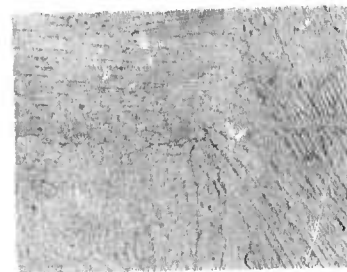
(A) Microhardness Survey



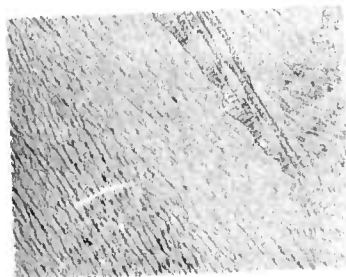
(B) Weld Schematic Cross Section



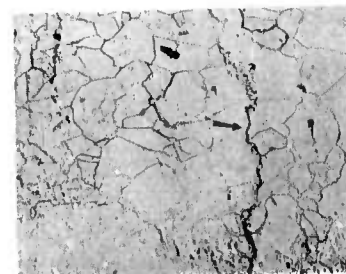
(C) Weld Macro-Section



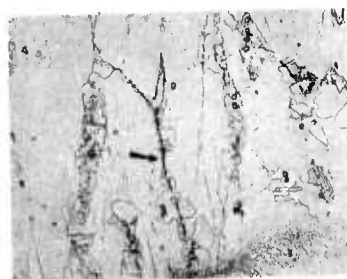
(D) Weld Fusion Zone



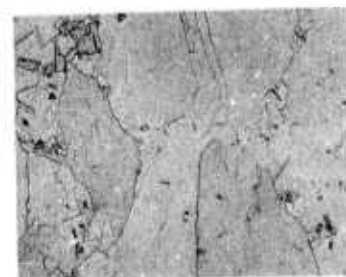
(E) Weld Fusion Zone



(F) FZ-HAZ Transition



(G) FZ-HAZ Transition



(H) Base Metal

Figure 5-12 Microhardness Survey (A&B), Macrostructure (C),(X6) and Microstructure of ST0/GTA welded A-286 Stainless Steel (weld plate no. 2C)(D)thru(H), as welded (x225)

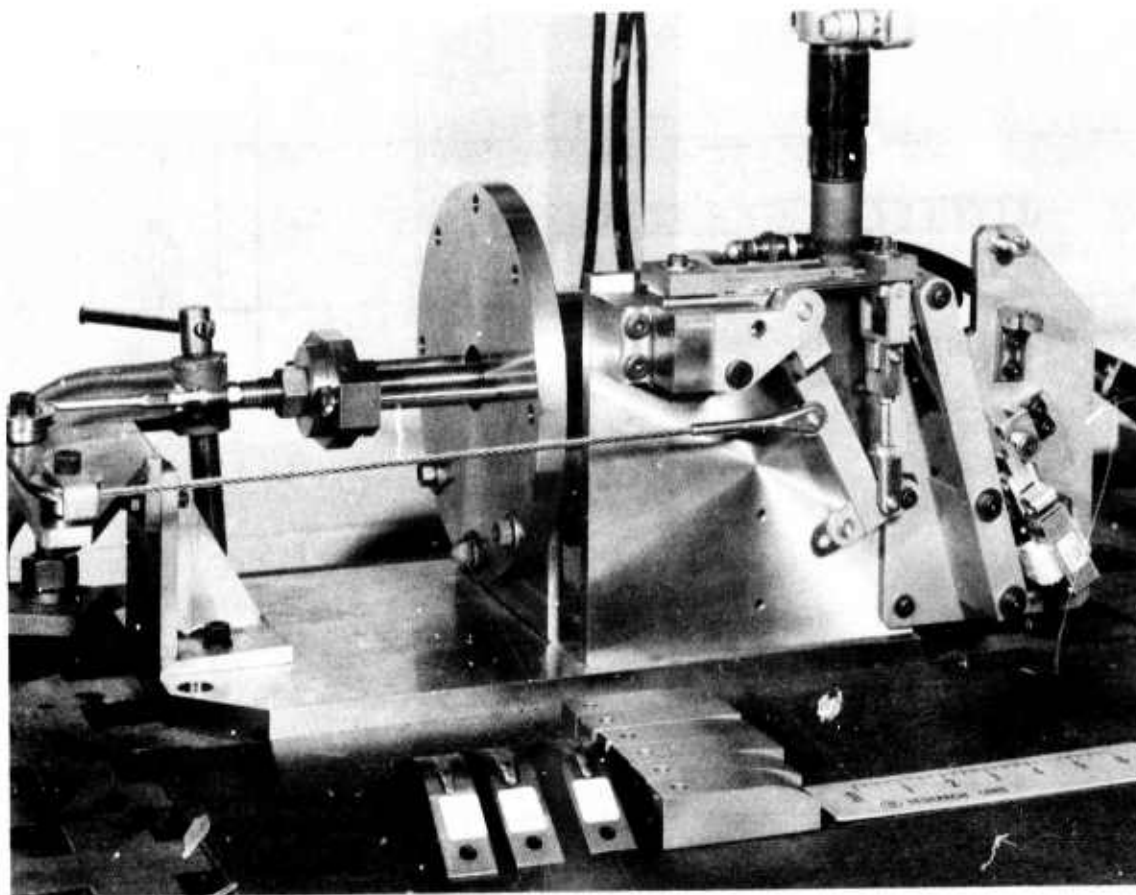


Fig. 5-13—The Research Laboratories Vareststraint Tester with the TIG Torch in the position for arc initiation. Radius blocks and tested specimens are shown in foreground

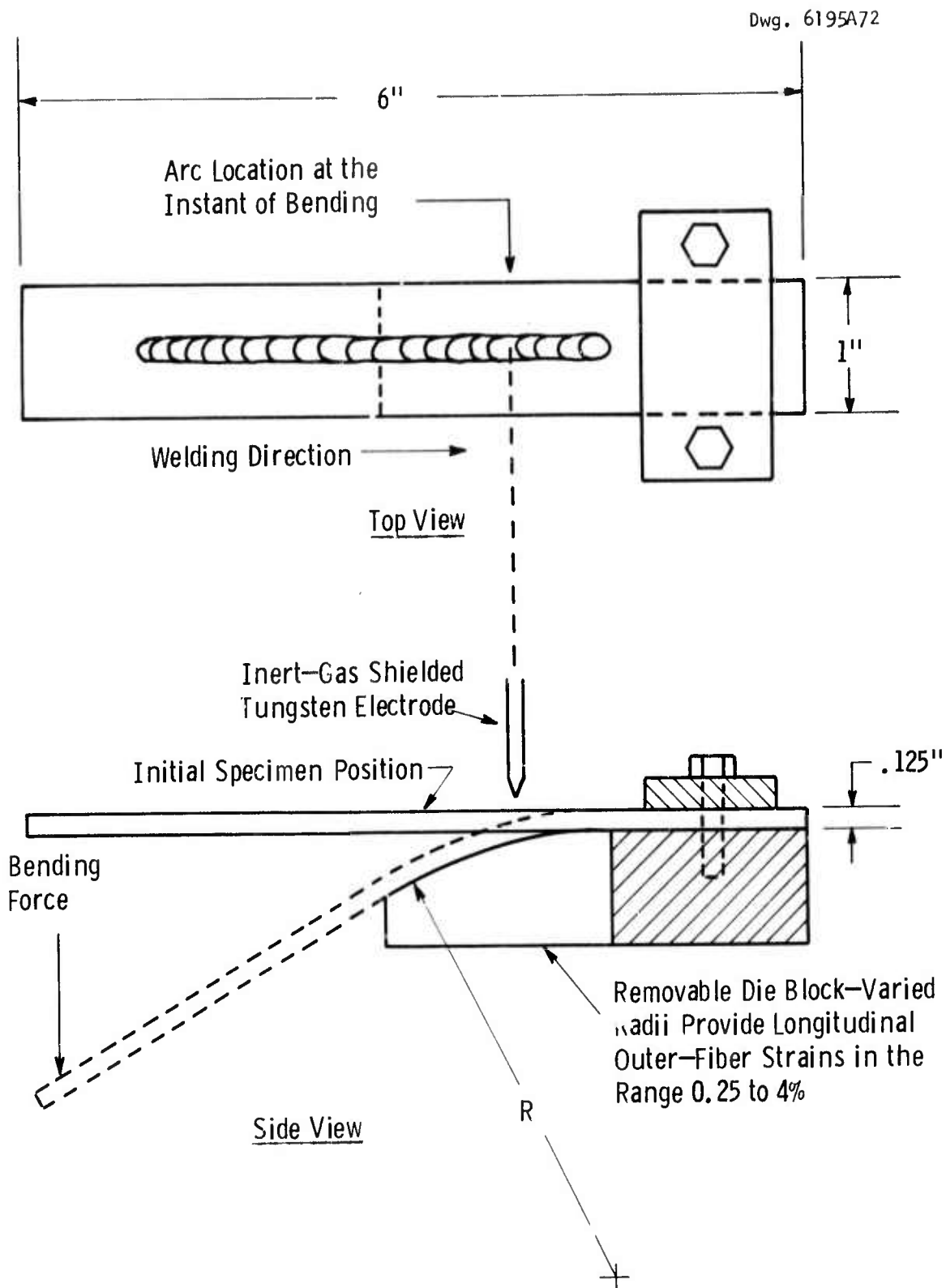


Fig. 5-14 - Schematic sketch of the operation of the varestraint test device

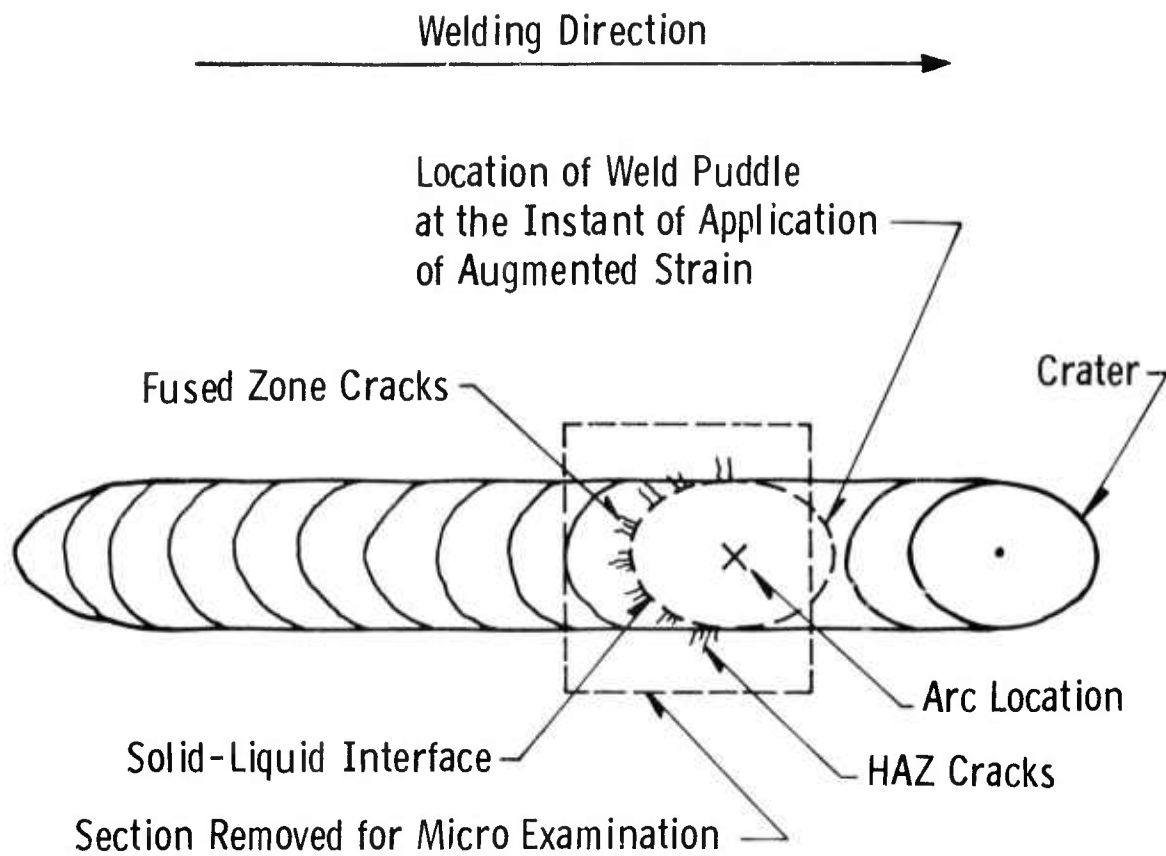


Fig. 5-15—Schematic representation of the top surface of the weld and the section removed for metallographic examination

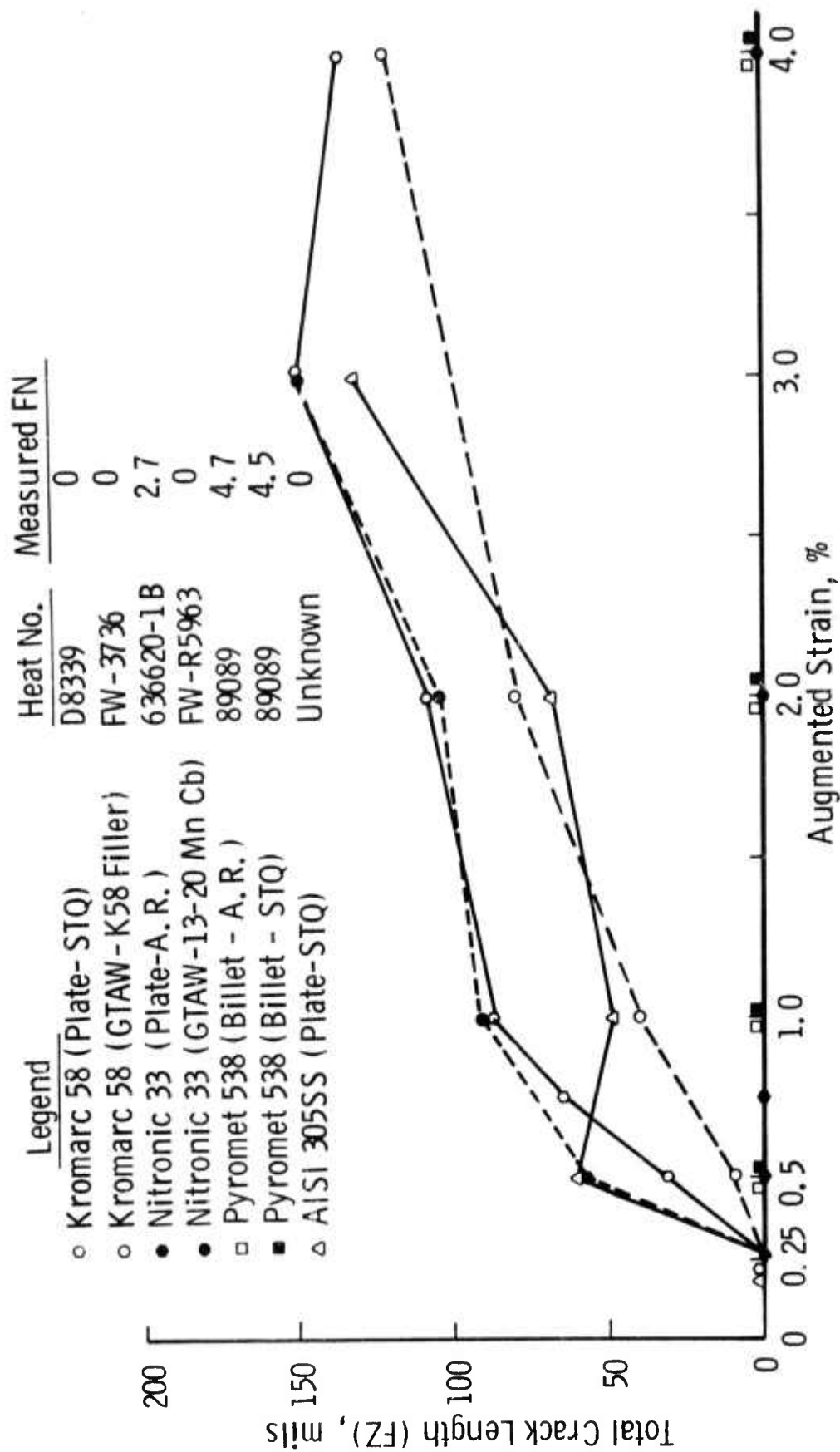


Fig. 5-16-Fusion zone (FZ) cracking observed in longitudinal vareststraint tests of austenitic stainless steels

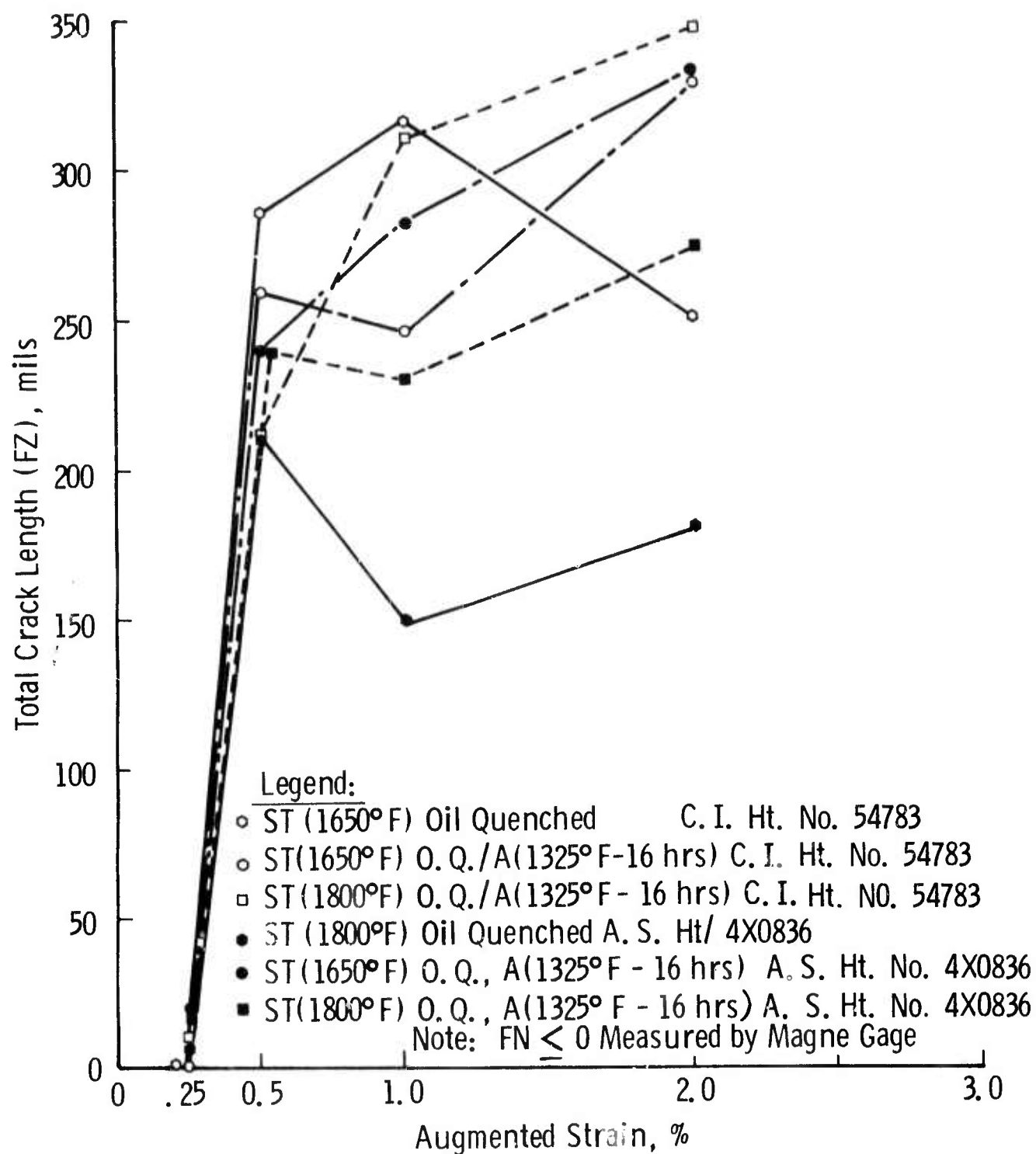


Fig. 5-17 -Fusion zone (FZ) cracking observed in longitudinal vareststraint test on Alloy A-286

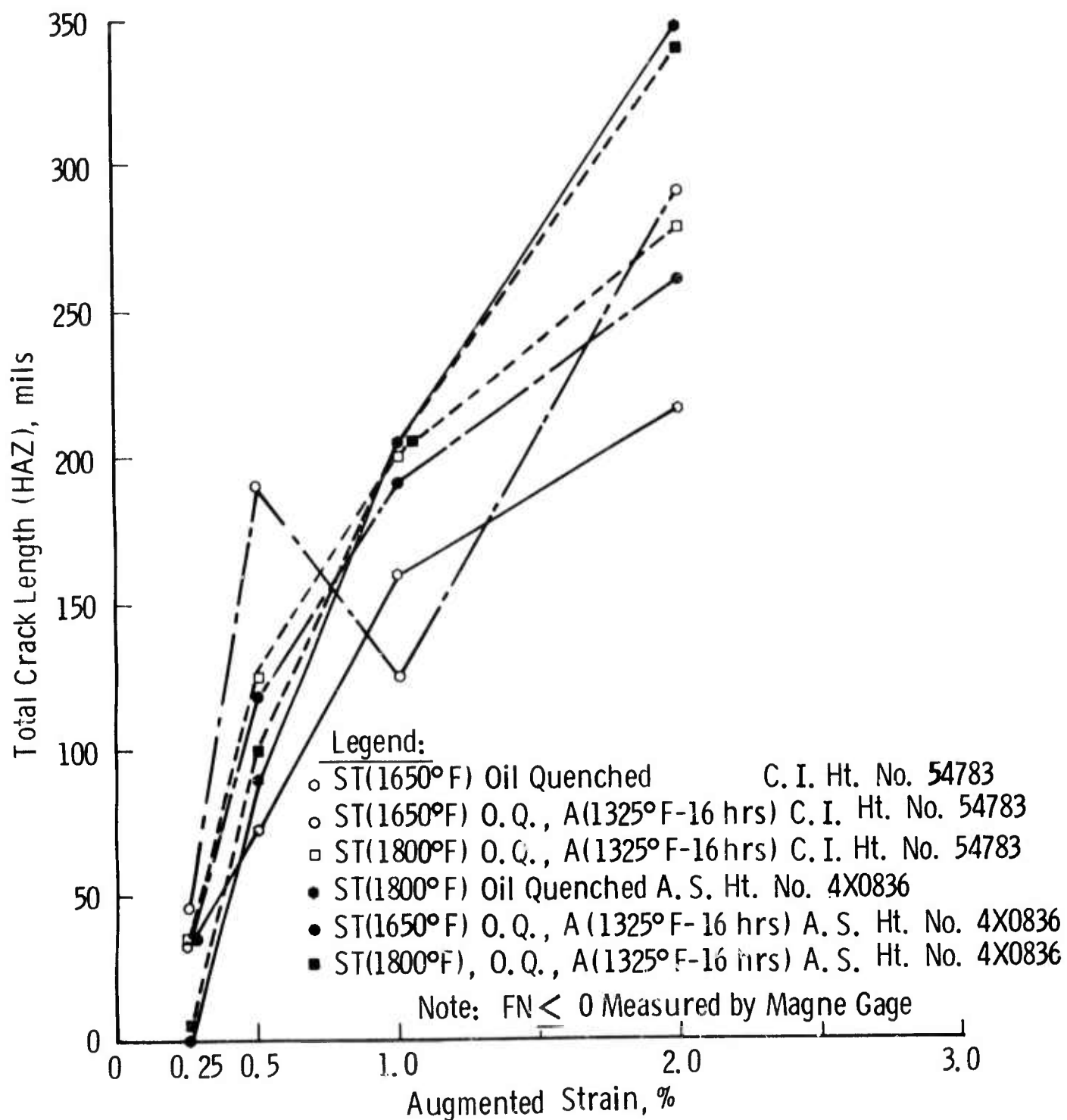


Fig. 5-18—Heat affected zone (HAZ) cracking observed in longitudinal vareststraint test on Alloy A-286

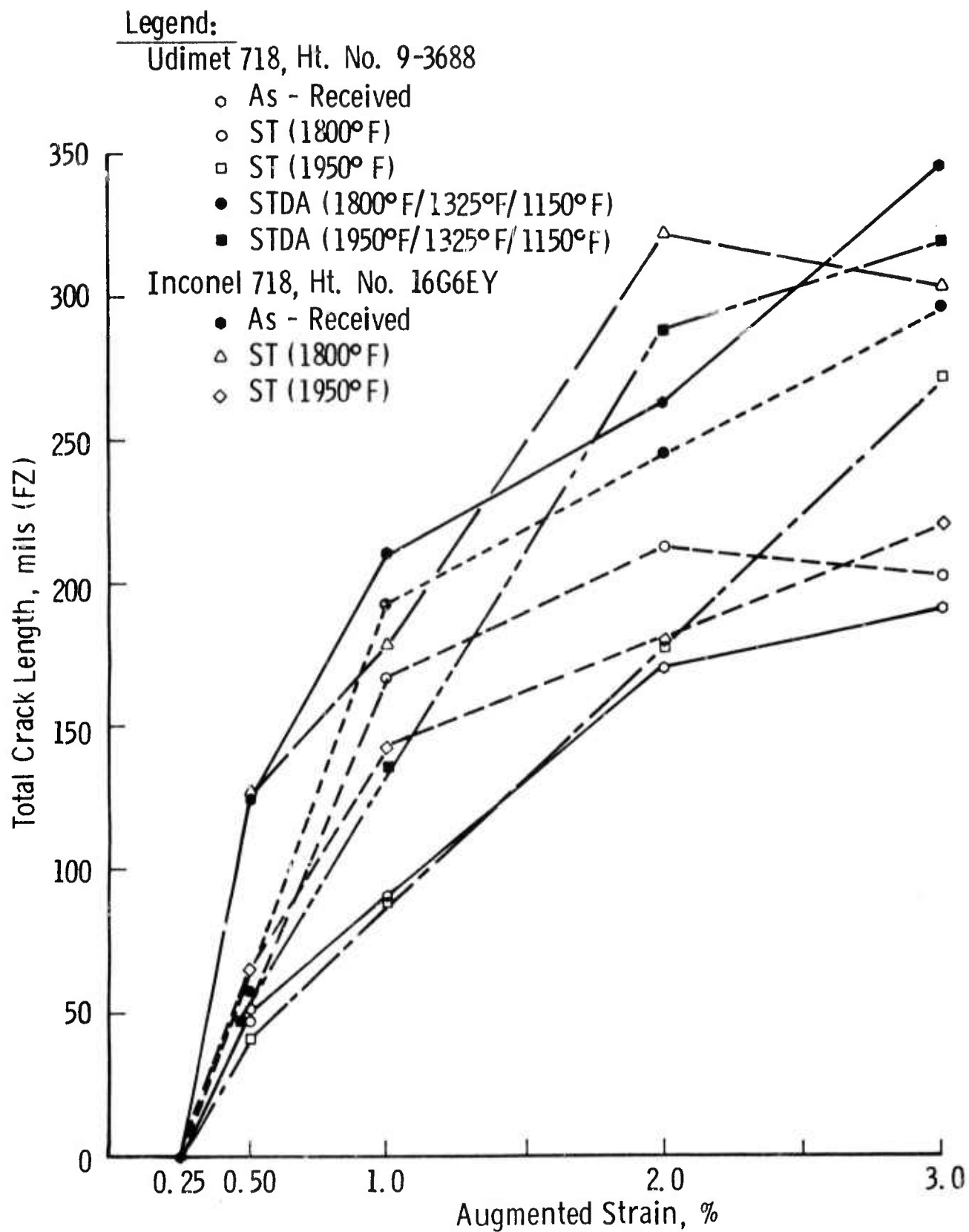


Fig. 5-19-Fusion zone (FZ) cracking observed in longitudinal vareststraint test of Alloy 718

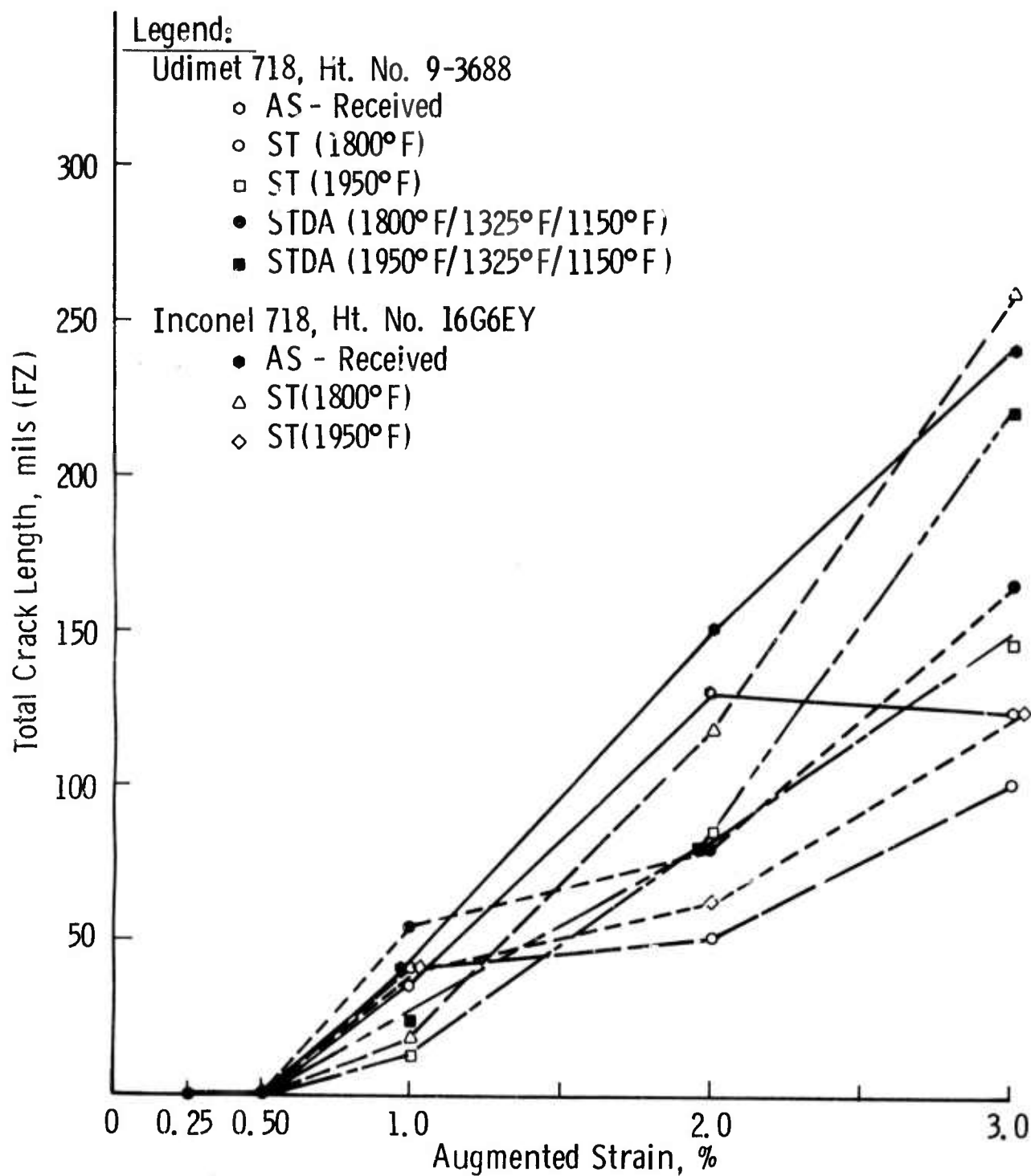


Fig. 5-20—Heat-affected zone (HAZ) cracking observed in longitudinal vareststraint tests of Alloy 718

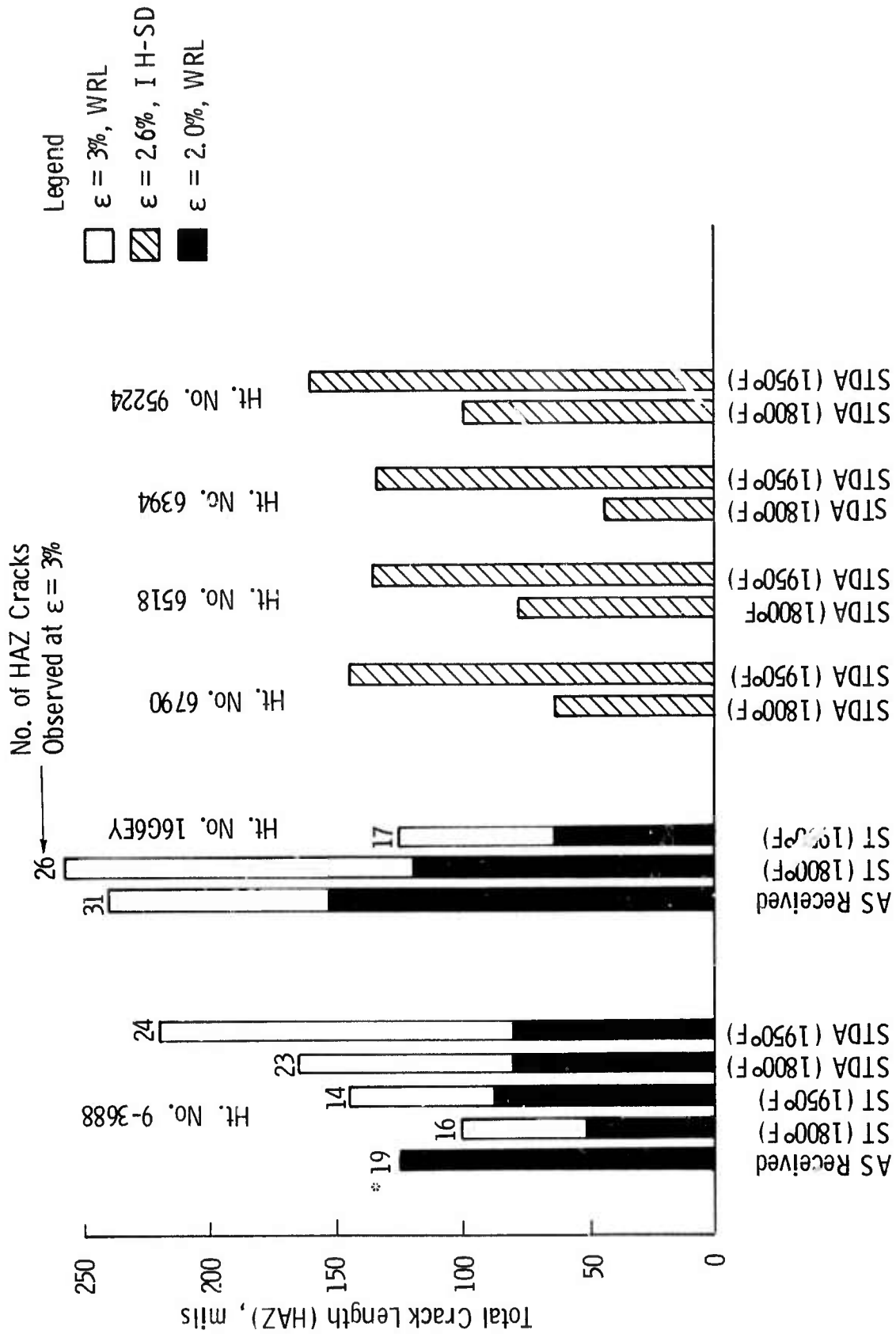
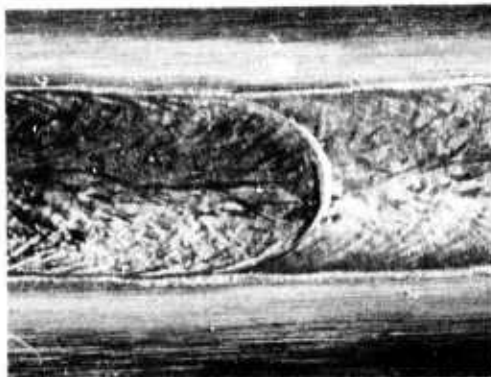
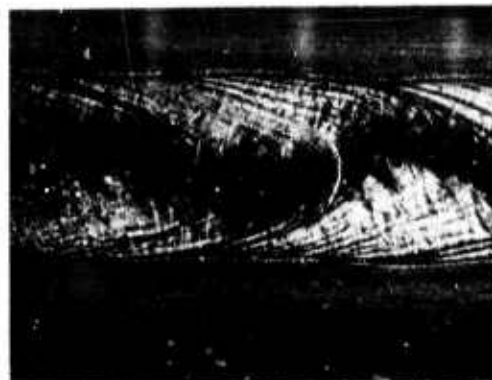


Fig. 5-21—Comparison of longitudinal vareststraint heat affected zone cracking data for nickel base Alloy 718

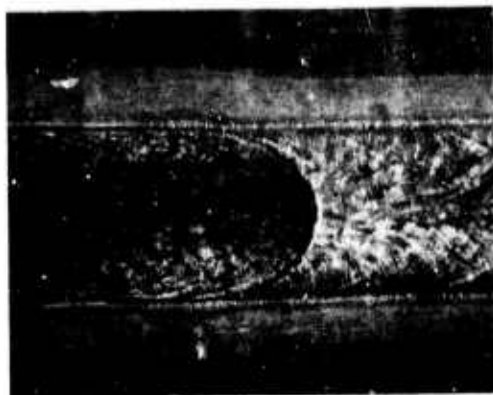
AISI 305 SS- ST0



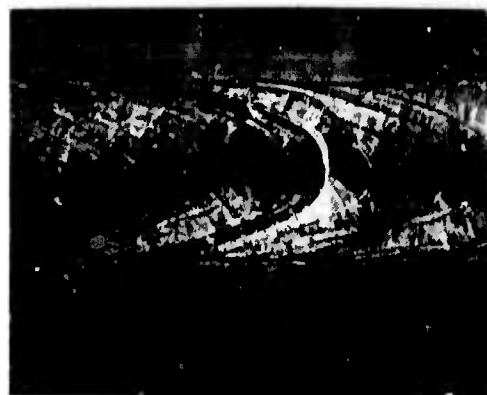
$\epsilon: 0.25\%$, FZ TCL: 0
HAZ TCL: 0



$\epsilon: 0.5$, FZ TCL: 0.060
HAZ TCL: 0



$\epsilon: 2.0\%$, FZ TCL: 0.068
HAZ TCL: 0

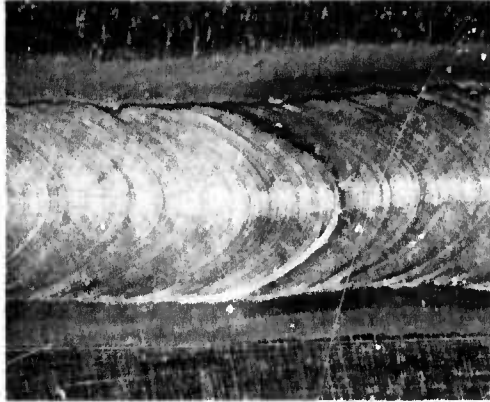


$\epsilon: 3.0\%$, FZ TCL: 0.133
HAZ TCL: 0.004

Figure 5-22 Photomicrographs of Varestraint Test Specimens in AISI 305 Stainless Steel in the ST(2000°F) 0 condition at various augmented strain levels (X10)

Kromarc 58

(I) Base Metal

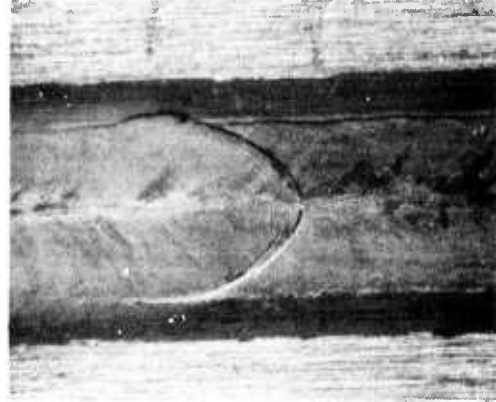


E: 0.50%
FZ TCL: 0.031" HAZ TCL: 0

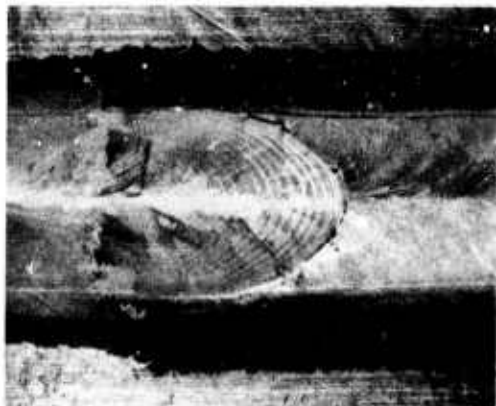


E: 4.0%
FZ TCL: 0.137" HAZ TCL: 0

(II) Prior Deposited Weld



E: 1.0%
FZ TCL: 0.052" HAZ TCL: 0

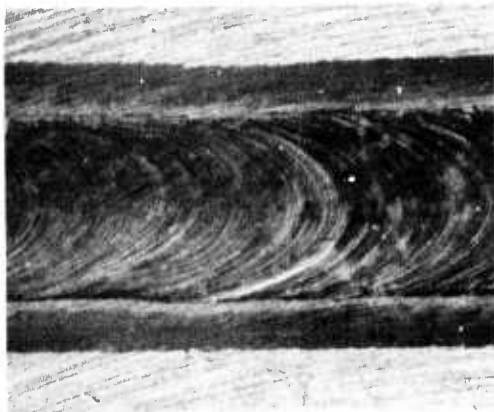


E: 4.0%
FZ TCL: 0.122" HAZ TCL: 0

Figure 5-23 Photomacrographs of Varestraint Test Specimens in Kromarc 58 alloy in (I) Base Metal and (II) Prior Deposited Weldment at various augmented strain levels (X10)

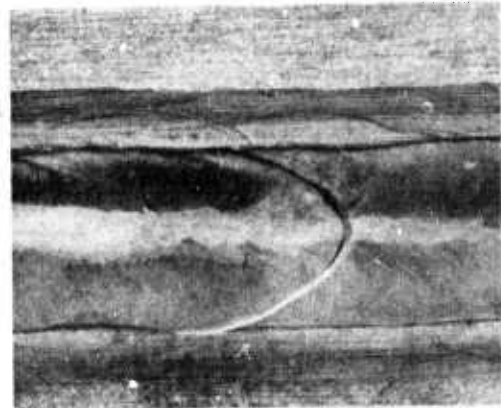
Nitronic 33

(I) Base Metal

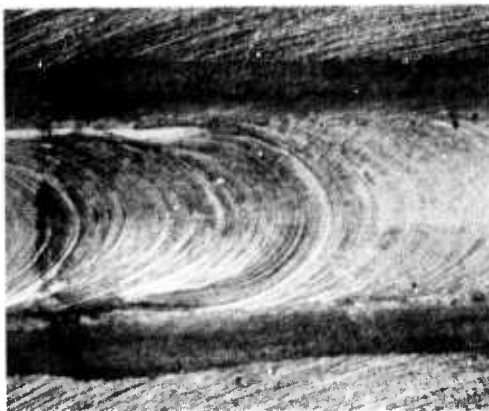


E: 0.75%
FZ TCL: 0 HAZ TCL: 0

(II) Prior Deposited Weld



E: 0.50%
FZ TCL: 0.057' HAZ TCL: 0



E: 4.0%
FZ TCL: 0 HAZ TCL: 0



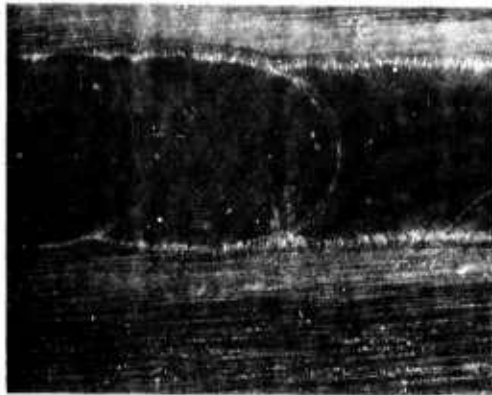
E: 3.0%
FZ TCL: 0.151' HAZ TCL: 0

Figure 5-24 Photomicrographs of Varestraint Test Specimens in Nitronic 33 alloy in (I) Base Metal and (II) Prior Deposited Weldment (13-20 Mn-Cb) at various augmented strain levels (X10)

Pyromet 538 (21-6-9)

(I) As Received Billet

(II) ST(2000°F) 0



E=0.5%

FZ TCL: 0
HAZ TCL: 0

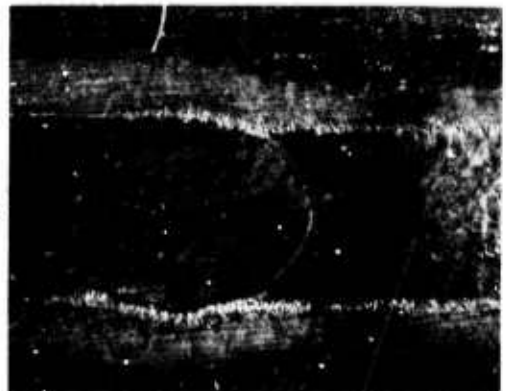


FZ TCL: 0
HAZ TCL: 0



E=4.0%

FZ TCL: 0
HAZ TCL: 0



FZ TCL: 0
HAZ TCL: 0

Figure 5-25 Photomicrographs of Varestraint Test Specimens in Pyromet 538(21Cr-6Ni-9Mn) Stainless Steel in the (I)As received billet and(II) ST(2000°F) 0 conditions at various augmented strain levels (X10)

(I) Armco A-286
ST(1800°F)



E: 0.25%

FZ TCL: 0.007"
HAZ TCL: 0

(II) Cameron A-286
ST(1650°F)



FZ TCL: 0
HAZ TCL: 0.033"



E: 2.0%

FZ TCL: 0.180"
HAZ TCL: 0.346"



FZ TCL: 0.249"
HAZ TCL: 0.215"

Figure 5-26 Photomacrographs of Vareststraint Test Specimens in (I) Armco A-286 and (II) Cameron A-286 alloys in the ST(1800°F) 0 and ST(1650°F) 0 conditions respectively at augmented strain levels of 0.25% and 2.0% (X10)

ST (1650°F) 0A

(I) Armco A-286

(II) Cameron A-286



E:0.25%

FZ TCL:0.019"
HAZ TCL:0.035"



FZ TCL:0
HAZ TCL:0.046"



E:2.0%

FZ TCL:0.333"
HAZ TCL 0.259"



FZ TCL:0.328"
HAZ TCL:0.289"

Figure 5-27 Photomicrographs of Vareststraint Test Specimens in (I) Armco A-286 and (II) Cameron A-286 alloys, both in the ST(1650°F) 0A condition, at augmented strain levels of 0.25% and 2.0% (X10)

ST(1800°F)QA

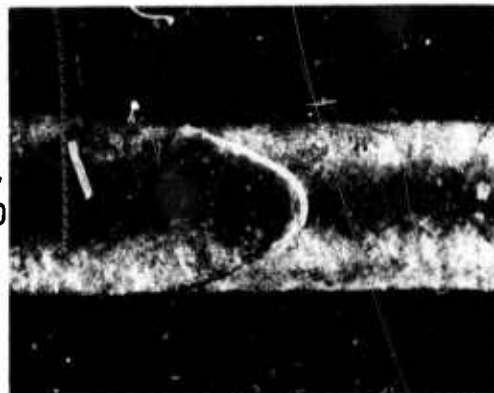
(I) Armco A-286



E:0.25%

FZ TCL:0.017"
HAZ TCL:0.005"

(II) Cameron A-286

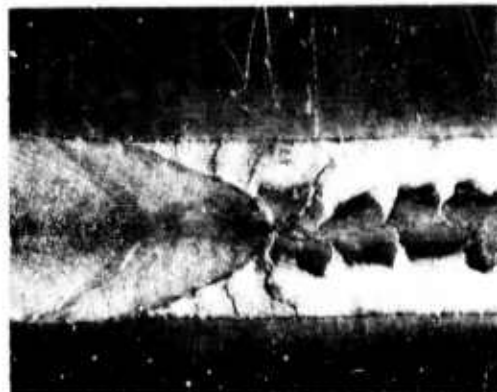


FZ TCL:0.010"
HAZ TCL:0.034"



E:2.0%

FZ TCL:0.273"
HAZ TCL:0.337"



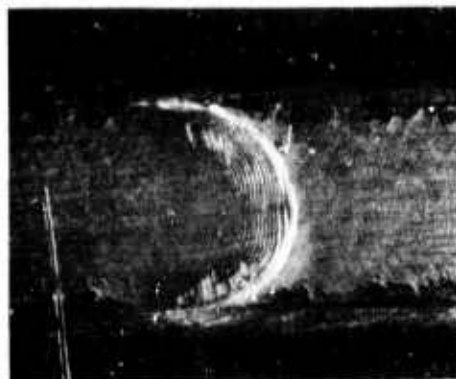
FZ TCL:0.343"
HAZ TCL:0.278"

Figure 5-28 Photomicrographs of Vareststraint Test Specimens in (I) Armco A-286 and (II) Cameron A-286 alloys in the ST (1800°F) QA condition at augmented strain levels of 0.25% and 2.0% (X10)

As Received

(I) Udimet 718

(II) Inconel 718



E:0.25%

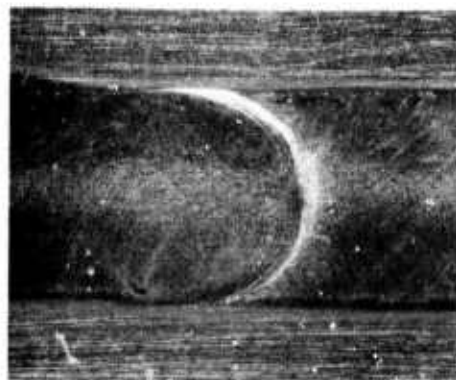
FZ TCL:0

HAZ TCL:0



FZ TCL:0

HAZ TCL:0



E:0.5%

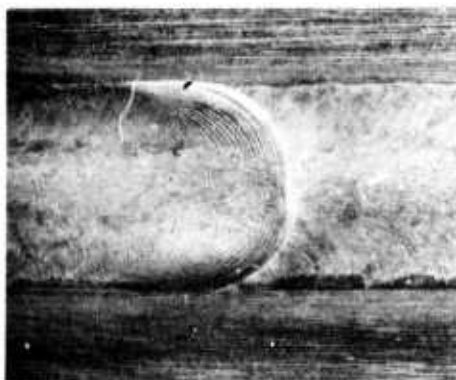
FZ TCL:0.051°

HAZ TCL:0



FZ TCL:0.124°

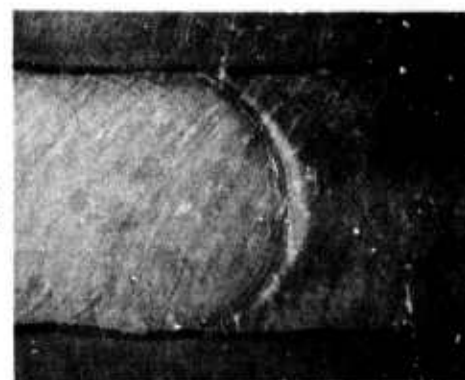
HAZ TCL:0



E:2.0%

FZ TCL:0.172°

HAZ TCL:0.134°



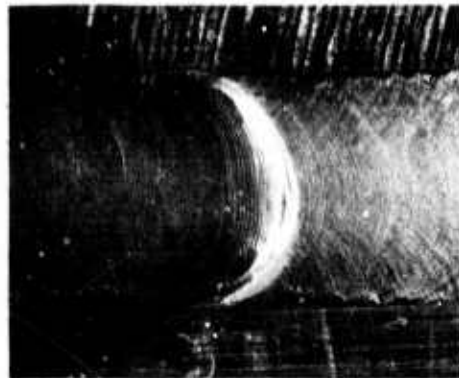
FZ TCL:0.262°

HAZ TCL:0.152°

Figure 5-29 Photomicrographs of Vareststraint Test Specimens in (I) Udimet 718 and (II) Inconel 718 in the as received billet condition at various augmented strain levels (X10)

ST(1800°F)

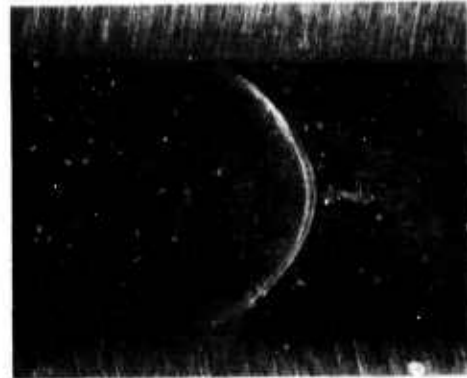
(I) Udimet 718



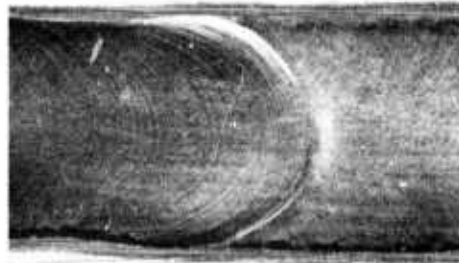
E=0.25%

FZ TCL:0 HAZ TCL: 0

(II) Inconel 718



FZ TCL:0 HAZ TCL: 0



E=0.50%

FZ TCL:0.047° HAZ TCL: 0

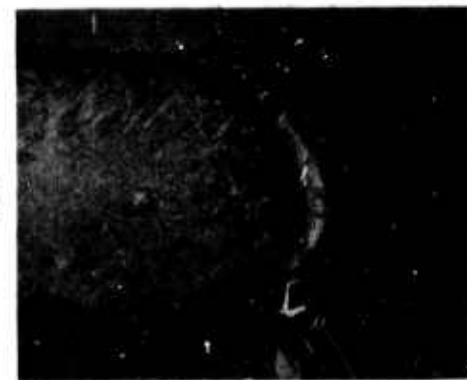


FZ TCL:0.127° HAZ TCL: 0



E=2.0%

FZ TCL:0.212° HAZ TCL:0.051°



FZ TCL:0.321° HAZ TCL:0.118°

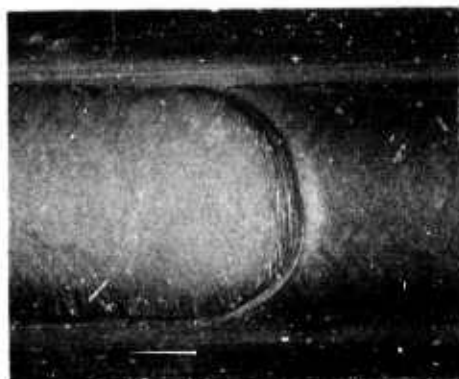
Figure 5-30 Photomicrographs of Varcstraint Test Specimens in (I) Udimet 718 and (II) Inconel 718 alloys in the ST(1800°F) condition at various augmented strain levels (X10)

ST (1950°F)

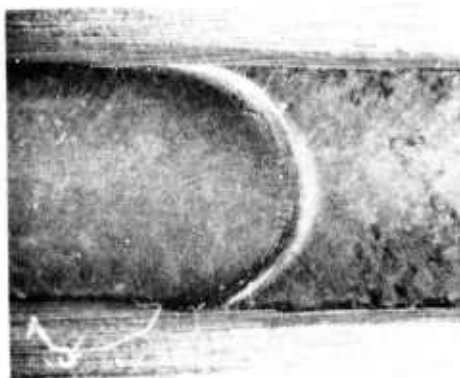
(I) Udimet 718



FZ TCL:0 HAZ TCL:0



FZ TCL:0.041° HAZ TCL:0



FZ TCL:0.178° HAZ TCL:0.086°

(II) Inconel 718



FZ TCL:0 HAZ TCL:0



FZ TCL:0.065° HAZ TCL:0



FZ TCL:0.181° HAZ TCL:0.062°

Figure 5-31 Photomicrographs of Varcstraint Test Specimens in (I) Udimet 718 and (II) Inconel 718 alloys in the ST (1950°F) condition at various augmented strain levels (X10)

Udimet 718 Alloy

(I) ST(1800°F)/DA



E:0.25%

FZ TCL:0 HAZ TCL:0

(II) ST(1950°F)/DA



FZ TCL:0 HAZ TCL:0



E:0.50%

FZ TCL:0.057 HAZ TCL:0



FZ TCL:0.047 HAZ TCL:0



E:2.0%

FZ TCL:0.245 HAZ TCL:0.079



FZ TCL:0.287 HAZ TCL:0.08

Figure 5-32 Photomicrographs of Vareststraint Test Specimens in Udimet 718 alloy in the(I) ST(1800°F)/DA and(II) ST(1950°F)/DA conditions at various augmented strain levels (X10)

6.0 FRACTURE MECHANICS

Introduction

The development of increasingly more cryogenic or superconducting devices and the almost total lack of low temperature fracture mechanics material properties (especially relative to the austenitic materials so ideally suited for low temperature structural applications) has created a strong demand by designers for the material properties required to insure immunity from structural failure of these systems. Naturally, the cryogenic environment has placed severe restrictions on the development of these required material properties, especially those in the area of fracture mechanics technology. Recent advances in fracture mechanics technology, especially in the area of elastic plastic fracture, have now made it possible to determine the required fracture mechanics material properties (specifically fracture toughness and crack growth rate) necessary to permit the application of fracture mechanics technology to structures and components subjected to cryogenic environments, thus insuring their structural performance.

This section of the technical report presents and summarizes the material properties (tensile, static plus dynamic fracture toughness and fatigue crack growth rate) generated throughout the first half of the Westinghouse FY 76 ARPA/NBS program.

6.1 Tensile Results

The Inconel 718 precipitation hardening superalloy evaluated in the Westinghouse program was obtained as an 11 3/8 in. (29 cm) diameter hot finished forging billet, vacuum induction melted-vacuum arc remelted (VIM-VAR). Briefly, it was found that in the as-received conditions, a pronounced contiguous grain boundary network existed at

the stock centerline position while at the 5 1/4 in. (13.3 cm) location such contiguous particles were not observed at the equiaxed matrix grain boundaries but rather at prior "ghost" grain boundaries.⁽¹⁾ The relatively low ductility and fracture toughness demonstrated by this 1800°F (1255 K) solution treated and double aged Inconel 718 were attributed to thin carbide films or an agglomeration of very small carbide particles within the grain boundaries.⁽¹⁾ Carbide chains in the grain boundaries also proved detrimental to the ductility and fracture properties of (VIM-VAR) Inconel X750.^(2,3)

Therefore, it appeared that either a higher solution treatment temperature to dissolve such carbides or a final working treatment followed by a heat treatment to break up this network and recrystallize the entire structure would be necessary to achieve optimum cryogenic material properties with the present Inconel 718 billet material. As a result, the effect of a higher solution treating temperature followed by cold work with a subsequent recrystallization heat treatment in reducing or removing this contiguous carbide grain boundary network as well as to modify the base metal grain size was examined. The various processing and heat treatment details are covered in References 1 and 4. After a 1950°F (1339 K) solution treatment followed by cold working the Inconel 718 was subjected to one of three heat treatment schedules: (a) 1800°F (1255 K) solution treatment and double age; (b) 1950°F (1339 K) solution treatment and double age; and (c) double age. All the tensile and notched tensile properties developed on Inconel 718 are summarized in Tables 6-1 through 6-3 while Figures 6-1 and 6-2 illustrate the influence of processing and heat treatment on the tensile properties of Inconel 718.

Tensile properties of a 10 1/4 in. (26 cm) diameter Udimet 718 billet are also included in Tables 6-1 through 6-3. No contiguous carbide chains were observed at grain boundaries for the Udimet 718 billet centerline location as were observed at the corresponding location in the Inconel 718 billet. Furthermore, no prior ghost boundaries similarly decorated with carbide chains or films were observed.⁽¹⁾

Strength levels, especially yield strength, of the various Inconel 718 materials (with exception of the lone Inconel 718 not subjected to a post cold work solution treatment) are similar. This was expected based on the strength similarity demonstrated between the original carbide containing Inconel 718 and the Udimet 718. The cold worked plus 1800°F (1255 K) solution treated and double aged Inconel 718 demonstrated nearly identical ductility as the original Inconel 718, which was also solution treated at 1800°F (1255 K) and double aged. The cold worked and 1950°F (1339 K) solution treated and double aged Inconel 718, however, demonstrated improved ductility (both reduction in area and elongation) at nearly all test temperatures. This improved ductility was expected since prior microstructural analysis had revealed that the carbide network in the higher solution treated temperature Inconel 718 material was appreciably reduced at the matrix grain boundaries and the ghost boundary network was no longer observed.⁽¹⁾ The Inconel 718 which was not solution treated after cold working typically demonstrated the lowest base metal ductility. Despite these various processing and heat treatment schedules the ductility of Inconel 718 never approached that of the Udimet 718.

6.2 Dynamic Fracture Toughness

Pressure retaining materials for vessels involving nuclear applications must pass minimum dynamic fracture toughness standards.⁽⁵⁾ In detail, for a particular selected material, the adequacy of dynamic fracture toughness must be demonstrated on three heats each of base, weld and heat affected zone (HAZ) material. In other words, the dynamic fracture toughness must lie above a specified minimum K_{IR} reference toughness curve temperature corrected based on drop weight NDT tests and Charpy impact tests.^(5,6)

As a result, a system was developed at Westinghouse to perform dynamic J tests (that is, load a specimen dynamically to a particular deflection, not to failure). Dynamic fracture toughness values

could then be generated with small scale specimens unlike the very thick specimens (8 to 12 in., 20 to 30 cm) previously required to obtain valid K_{Id} values.⁽⁷⁾ All procedures outlined in the J resistance curve test technique⁽⁸⁾ were observed, the only difference being the specimens were loaded dynamically.

Initial dynamic cryogenic J tests were conducted at -320°F (77 K) on Udimet 718, a structurally stable austenitic superalloy. Load versus time, deflection versus time and load versus deflection traces relative to a specific half inch (1.3 cm) thick Udimet 718 compact tension specimen are illustrated in Figure 6-3. Note this specimen reached its final load and deflection in approximately 0.013 sec. Figure 6-4 presents the -320°F (77 K) static and dynamic J resistance curves relative to Udimet 718. Static and dynamic fracture toughness values of Udimet 718 at liquid nitrogen temperature are summarized below.

Udimet 718 Fracture Toughness

Temperature = -320°F (77 K)

	σ_{ys}		J_{IC}		K_{IC}		K_{IC}/σ_{ys}	$(K_{IC}/\sigma_{ys})^2$
	ksi	MPa	in-lb/in ²	MN/m	ksi√in	MPa√m	√in	(in)
Static	187.8	1295	198	.035	82.1	90.0	.44	.19
Dynamic	187.8	1295	178	.031	77.9	86.2	.41	.17

Since dynamic tensile tests were not conducted, the static yield strength was utilized throughout. As was expected the static and dynamic cryogenic fracture toughness values of this structurally stable austenitic superalloy are essentially equivalent.

Future tests will hopefully include dynamic cryogenic fracture toughness tests on a structurally stable austenitic stainless steel (such as Kromarc 58 or A286) plus a structurally unstable austenitic stainless steel (such as Nitronic 40, 21Cr-6Ni-9Mn). While dynamic

loading would not be expected to influence the fracture toughness of the structurally stable austenitic stainless steel, such may not be the case for the structurally unstable stainless steel. (9)

6.3 Crack Growth Rate Results

The test procedures utilized in the development of our cryogenic fatigue crack growth rate data were spelled out in detail in a previous technical report and as such will not be repeated here. (10) It is sufficient to state that all the raw $\log \frac{da}{dN}$ versus $\log \Delta K$ data we developed on each of the materials investigated demonstrated the nearly linear relationship typical of most fatigue crack growth rate data. Since this linear relationship existed, the crack growth rate data was expressed in terms of the generalized fatigue crack growth rate law developed by Paris. (11) This crack growth rate law is expressed as:

$$\frac{da}{dN} = C_0 \Delta K^n$$

where $\frac{da}{dN}$ is the rate of crack growth, C_0 is an intercept constant determined from the $\log \frac{da}{dN}$ versus $\log \Delta K$ plot, n is the slope of the log-log plot and ΔK is the stress intensity factor range.

The fatigue crack growth rate (FCGR) properties of Inconel 706 (VIM-EFR), Inconel 706 (VIM-VAR), Inconel 718 (VIM-VAR) and Inco LEA (AAM-VAR) are illustrated in Figures 6-5 through 6-8, respectively. The growth rate of fatigue cracks in both Inconel 706 materials and in Inco LEA is directly proportional to temperature; that is, the higher the temperature the greater the fatigue crack propagation rate. The growth rate of fatigue cracks in Inconel 718 is also considerably faster at room temperature as opposed to cryogenic temperatures even though no distinction between cryogenic crack growth rates is apparent. In addition, Tobler recently reported both ambient and cryogenic temperature FCGR data on solution treated and double aged Inconel 718. (12)

Tobler's -452°F (4 K) Inconel 718 FCGR data checks very closely with that developed on the Inconel 718 examined under this investigation. Tobler also found higher growth rates at ambient as opposed to cryogenic temperatures although his reported increase in crack growth rate with increasing temperature above -452°F (4 K) was not as great as that found on the Inconel 718 employed in this Westinghouse program. Although not directly applicable, James reported a direct extension of this behavior over the temperature range 75°F (297 K) to 1000°F (811 K) for another Inconel 718^(13,14) and in addition on Inconel 600 over the temperature range 75°F (297 K) to 1200°F (922 K).⁽¹³⁾ Furthermore, higher growth rates at ambient versus cryogenic temperatures were previously observed on an additional superalloy, namely Inconel X750, by both Westinghouse⁽³⁾ and NBS.⁽¹⁵⁾ Finally, this same crack growth rate temperature dependence behavior has been reported on several structurally stable austenitic stainless steels, namely Kromarc 58 and A286 by Westinghouse⁽¹⁶⁾ and AISI 310 S and A286 by NBS.⁽¹⁵⁾ Again, James also observed increasing fatigue crack growth rates with increasing temperature over the temperature range 75°F (297 K) to 1000°F (811 K) for an A286 stainless steel similar to those examined by Westinghouse and NBS.⁽¹⁷⁾ Therefore, a substantial data base exists which indicates that for structurally stable austenitic materials (both superalloys and stainless steels), the growth rate of fatigue cracks at room temperature is faster than at cryogenic temperatures.

Tobler has reported fatigue crack growth rates on a 21Cr-6Ni-9Mn stainless steel faster at -452°F (4 K) than at -320°F (77 K) or room temperature.⁽¹⁸⁾ In addition, the fracture toughness of this stainless steel decreased appreciably with decreasing temperature over the temperature range 75°F (297 K) to -452°F (4 K).⁽¹⁹⁾ During plastic deformation at room temperature this alloy experienced little martensitic phase transformation, but at -320°F (77 K) and -452°F (4 K) it transformed extensively to hcp and bcc martensitic products and is therefore not a structurally stable austenitic stainless steel.⁽¹⁹⁾

Figures 6-9 and 6-10 present a comparison of the liquid helium and room temperature FCGR properties, respectively, of Inconel 706, Inconel 718 and Inco LEA. At -452°F (4 K), the most favorable FCGR properties are associated with the two Inconel 706 materials, especially (VIM-VAR) Inconel 706, followed in order of increasing growth rates by Inconel 718 and Inco LEA. At room temperature, the two Inconel 706 materials again produce superior FCGR properties while Inconel 718 and Inco LEA demonstrate faster and nearly identical growth rates. The room temperature and cryogenic fracture toughness of both Inconel 706 materials also proved superior to that demonstrated by Inconel 718, Inco LEA and most manufacturing process/heat treatment combinations of Inconel X750.⁽³⁾ The superior fracture mechanics material properties of Inconel 706 combined with its improved machinability, formability and reduced cost through the use of lower amounts of expensive alloying elements as compared to Inconel 718, therefore, make Inconel 706 an attractive material for advanced cryogenic structural applications.

A comparison of the liquid helium and room temperature FCGR properties of three superalloys (Inconel 706, Inconel 718 and Inco LEA) versus three stainless steels (Kromarc 58, AISI 310 S and A286) is presented in Figures 6-11 and 6-12, respectively. At both -452°F (4 K) and room temperature the FCGR properties of the three austenitic stainless steels can be bracketed by the FCGR properties relative to (VIM-VAR) Inconel 706 and Inco LEA. In addition, at liquid helium temperature, the FCGR properties of the several manufacturing process/heat treatment combinations of Inconel X750 covered in Reference 3 can also be bracketed in a like manner. At room temperature, the FCGR properties of (AAM-VAR) Inconel X750 are slightly conservative when compared with those of (VIM-VAR) Inconel 706⁽³⁾ and as such barely fall outside the above mentioned scatterband. Nonetheless, the scatterband summarizing the FCGR properties of the various superalloys and stainless steels is not very large regardless of test temperature, indicating that the FCGR properties relative to the majority of structurally stable austenitic materials fall within a relatively narrow scatterband. Therefore, from

a FCGR structural reliability standpoint, structurally stable austenitic materials are adequate for cryogenic structural applications. It is up to the designer to choose the structurally stable austenitic material with the best combination of FCGR, fracture toughness and strength properties plus elastic, thermal and magnetic properties among other considerations such as fabricability for a specific cryogenic structural application.

REFERENCES - SECTION 6

1. Wells, J. M., Logsdon, W. A., Kossowsky, R. and Daniel, M. R., "Structural Materials for Cryogenic Applications, Fourth Semi-annual Technical Report", Westinghouse Research Report 75-9D4-CRYMT-R2, October 1975.
2. Kossowsky, R., "Microstructure of Inconel X750 Materials for Cryogenic Structural Applications", presented at the International Cryogenic Materials Conference, Kingston, Ontario, July 1975.
3. Logsdon, W. A., "Cryogenic Fracture Mechanics Properties of Several Manufacturing Process/Heat Treatment Combinations of Inconel X750", presented at the International Cryogenic Materials Conference, Kingston, Ontario, July 1975.
4. Wells, J. M., Logsdon, W. A., Kossowsky, R. and Daniel, M. R., "Structural Materials for Cryogenic Applications, Third Semi-annual Technical Report", Westinghouse Research Report 75-9D4-CRYMT-R1, March 1975.
5. ASME Boiler and Pressure Vessel Code, Section III - Division I, Subsection NB-2300 and Appendix G, American Society of Mechanical Engineers.
6. PVRC Recommendations on Toughness Requirements for Ferritic Materials, Appendix 1, Derivation of K_{IR} Curve, WRC Bulletin 175, Welding Research Council, August 1972.
7. Shabbits, W. O., "Dynamic Fracture Toughness Properties of Heavy Section A533 Grade B Class I Steel Plate", Heavy Section Steel Technology Program Technical Report No. 13, December 1970.

8. Landes, J. D. and Begley, J. A., "Test Results from J-Integral Studies: An Attempt to Establish a J_{IC} Testing Procedure", Fracture Analysis, ASTM STP 560, American Society for Testing and Materials, 1974, pp. 170-186.
9. Murayama, N., Pense, A. W. and Stout, R. D., "The Fracture Toughness of Cryogenic Steels", presented at the International Cryogenic Materials Conference, Kingston, Ontario, July 1975.
10. Lessmann, G. G., Logsdon, W. A., Kossowsky, R., Mathur, M. P. and Wells, J. M., "Structural Materials for Cryogenic Applications, Second Semi-annual Technical Report", Westinghouse Research Report 74-9D4-CRYMT-R2, September 1974.
11. Paris, P. C., "The Fracture Mechanics Approach to Fatigue", Proc. Tenth Sagamore Army Materials Research Conference, August 1963, Syracuse University Press, 1964.
12. Tobler, R. L., "Low Temperature Effects on the Fracture Behavior of Inconel 718", in Materials Research for Superconducting Machinery V, National Bureau of Standards, April 1976.
13. James, L. A., "The Effect of Temperature Upon the Fatigue - Crack Growth Behavior of Two Nickel-Base Alloys", Journal of Engineering Materials and Technology, Transactions of the American Society of Mechanical Engineers, October 1973, pp. 254-258.
14. James L. A., "Fatigue - Crack Propagation Behavior of Inconel 718", Hanford Engineering Development Laboratory, HEDL-TME 75-80, 1975.
15. Tobler, R. L., Mikesell, R. P., Durcholz, R. L. and Reed, R. P., "Fatigue and Fracture Toughness Testing at Cryogenic Temperatures", in Semi-annual Report on Materials Research in Support of Superconducting Machinery, NBSIR 74-393, National Bureau of Standards, October 1974, pp. 57-121.

16. Logsdon, W. A., Wells, J. M. and Kossowsky, R., "Fracture Mechanics Properties of Austenitic Stainless Steels for Advanced Cryogenic Applications", Westinghouse Scientific Paper 75-9D4-CRYMT-P3, December 1975.
17. James, L. A., "The Effect of Temperature on the Fatigue-Crack Propagation Behavior of A286 Steel", Hanford Engineering Development Laboratory, HEDL-TME 75-82, September 1975.
18. Tobler, R. L., private communication.
19. Tobler, R. L. and Reed, R. P., "Tensile and Fracture Behavior of a Nitrogen Strengthened, Chromium-Nickel-Manganese Stainless Steel At Cryogenic Temperatures", in Semi-annual Report on Materials Research in Support of Superconducting Machinery, NBSIR 75-828, National Bureau of Standards, October 1975, pp 131-150.

TABLE 6-1 - TENSILE AND NOTCHED TENSILE PROPERTIES OF INCONEL 718 (VIM-VAR) AND UDIMET 718 (VIM-VAR) at 75°F (297 K)

Material Condition	Heat Treatment	Yield Strength		Ultimate Strength		Reduction In Area %	Elongation %	NTS		NTS/ σ_{ys} ksi/ksi
		ksi	MPa	ksi	MPa			ksi	MPa	
Inconel 718										
Base	ST (1800°F) DA	168.8	1163.8	195.4	1347.2	14.8	12.0	253.6	1748.5	1.5
GTAW	ST/W/ST (1800°F) DA	158.6	1093.5	182.6	1259.0	5.7	1.7	201.8	1391.4	1.3
HAZ	ST/W/ST (1800°F) DA	-	-	-	-	-	-	232.4	1602.3	1.5
Base	ST/CW/ST (1800°F) DA	162.2	1118.3	193.2	1332.1	11.8	10.8	254.2	1752.6	1.6
Base	ST/CW/ST (1950°F) DA	152.9	1054.2	181.1	1248.6	20.8	14.9	266.5	1837.5	1.7
Base	ST/CW/DA	196.6	1355.5	218.7	1507.9	14.2	4.8	287.9	1985.0	1.5
Udimet 718										
Base	ST (1800°F) DA	163.9	1130.1	194.2	1339.0	27.1	19.7	-	-	-

TABLE 6-2 - TENSILE AND NOTCHED TENSILE PROPERTIES OF INCONEL 718 (VIM-VAR) AND UDIMET 718 (VIM-VAR) AT -320°F (77 K)

Material Condition	Heat Treatment	Yield Strength		Ultimate Strength		Reduction in Area %	Elongation %	NTS		NTS/ σ_{ys} ksi/ksi
		ksi	MPa	ksi	MPa			ksi	MPa	
Inconel 718										
Base	ST (1800°F) DA	194.9	1343.8	237.8	1639.6	9.1	10.1	272.1	1876.1	1.4
GTAW	ST/W/ST (1800°F) DA	185.8	1281.0	208.2	1435.5	4.3	1.8	213.2	1470.0	1.1
HAZ	ST/W/ST (1800°F) DA	-	-	-	-	-	-	243.9	1681.4	1.3
Base	ST/CW/ST (1800°F) DA	184.5	1272.1	222.2	1532.0	13.4	9.9	279.3	1925.7	1.5
Base	ST/CW/ST (1950°F) DA	189.8	1308.6	233.5	1609.9	12.7	12.4	302.3	2084.3	1.6
Base	ST/CW/DA	239.8	1653.4	270.2	1863.0	10.5	7.0	322.8	2225.6	1.3
Udimet 718										
Base	ST (1800°F) DA	187.8	1294.8	248.3	1712.0	13.2	22.8	-	-	-

TABLE 6-3 - TENSILE AND NOTCHED TENSILE PROPERTIES OF INCONEL 718 (VIM-VAR) AND UDIMET 718 (VIM-VAR) at -452°F (4 K)

Material Condition	Heat Treatment	Yield Strength		Ultimate Strength		Reduction in Area %	Elongation %	NTS		NTS/ σ_{ys} ksi/ksi
		ksi	MPa	ksi	MPa			ksi	MPa	
Inconel 718										
Base	ST (1800°F) DA	203.9	1405.8	242.2	1669.9	10.0	9.4	279.5	1927.1	1.4
GTAW	ST/W/ST (1800°F) DA	199.2	1373.4	231.2	1594.1	6.7	4.7	220.5	1520.3	1.1
HAZ	ST/W/ST (1800°F) DA	-	-	-	-	-	-	222.2	1532.0	1.1
Base	ST/CW/ST (1800°F) DA	206.0	1420.3	252.0	1737.5	10.0	10.6	274.5	1892.6	1.3
Base	ST/CW/ST (1950°F) DA	198.5	1368.6	231.0	1592.7	14.8	10.7	309.2	2131.9	1.6
Base	ST/CW/DA	248.7	1714.7	271.8	1874.0	9.5	4.8	319.8	2204.9	1.3
Udimet 718										
Base	ST (1800°F) DA	201.2	1387.2	256.7	1769.9	18.6	18.5	-	-	-

Curve 684623-A

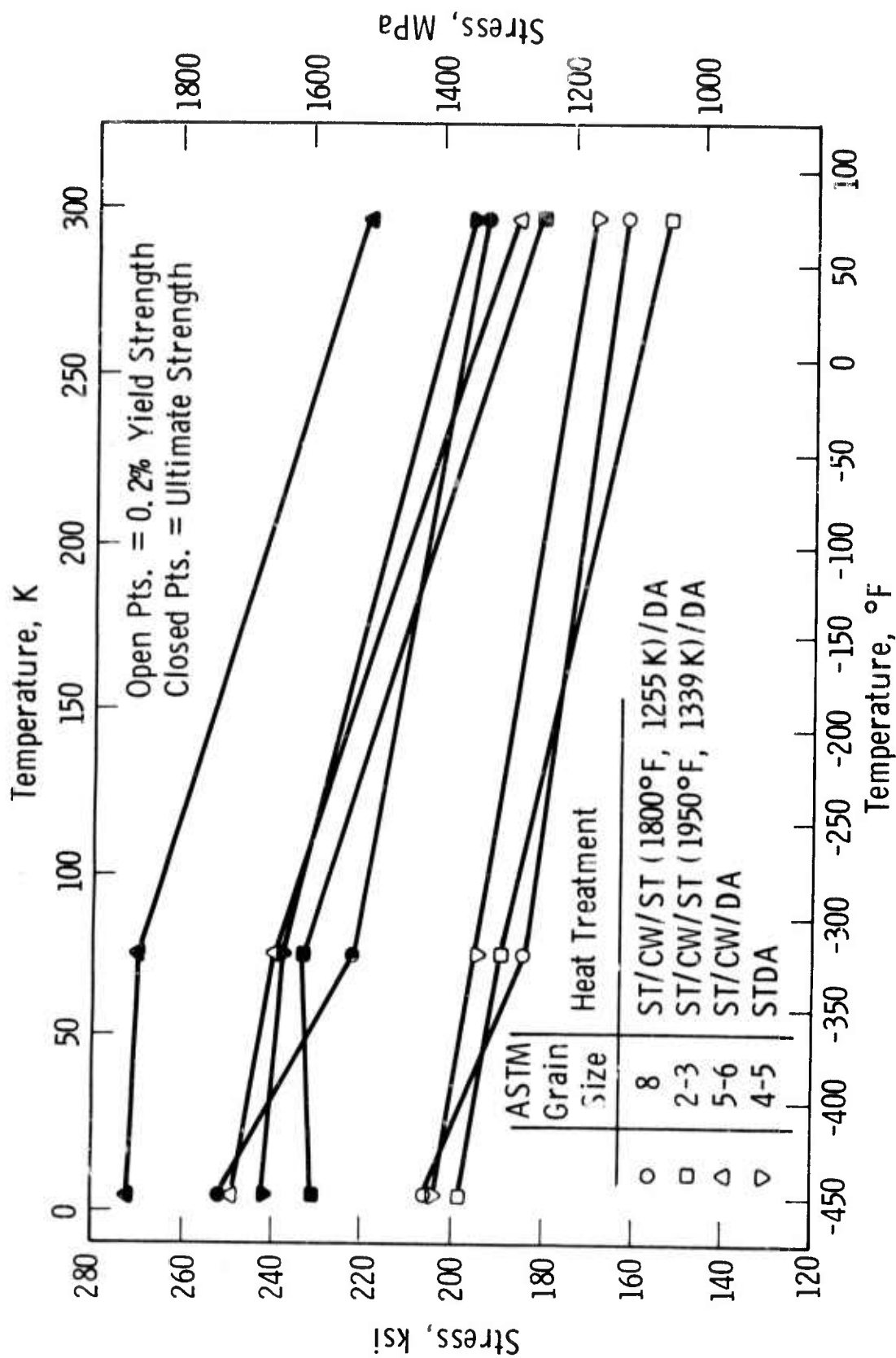


Fig. 6-1— The influence of processing and heat treatment on the strength of Inconel 718 (VIM-VAR)

Curve 684622-A

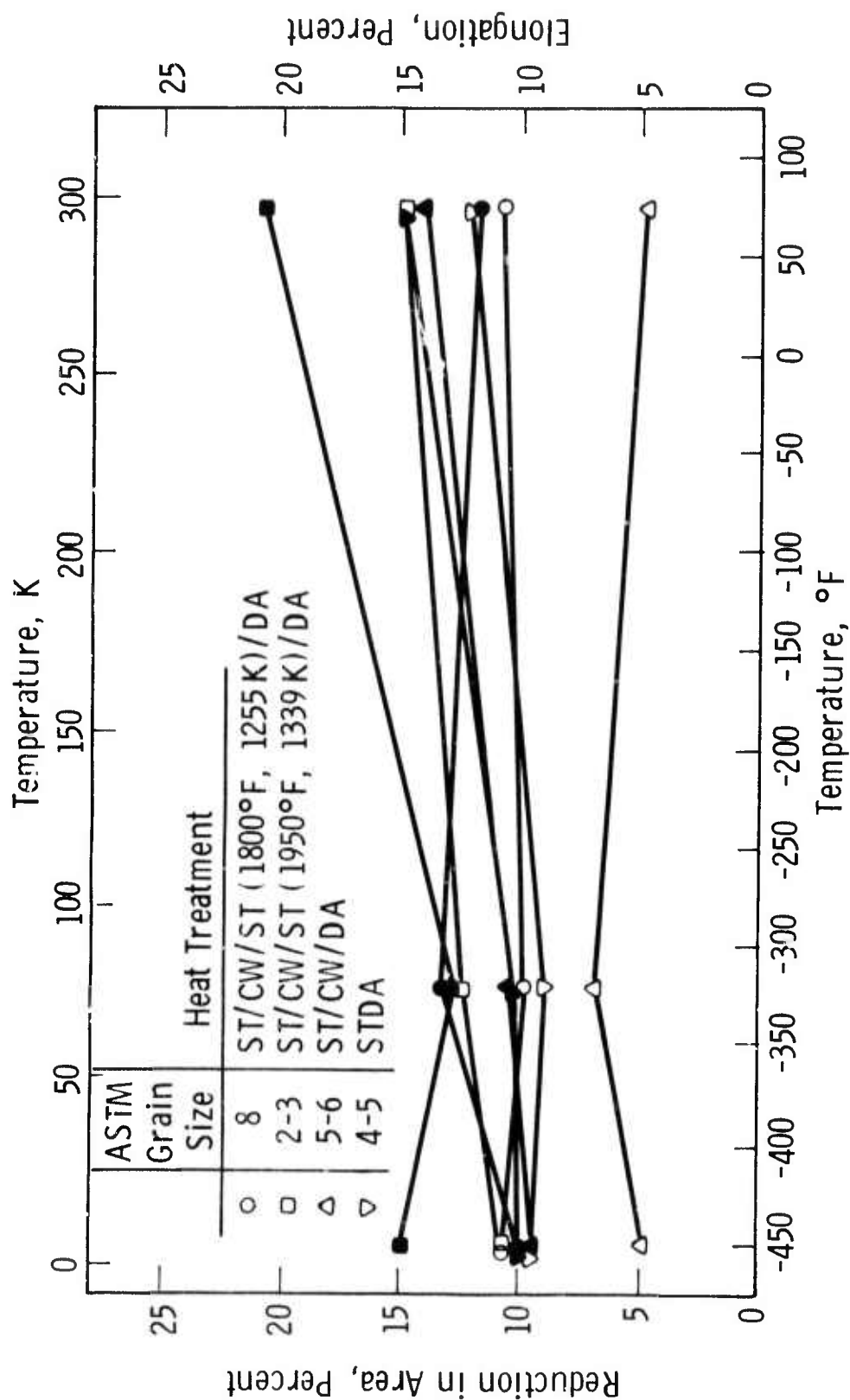
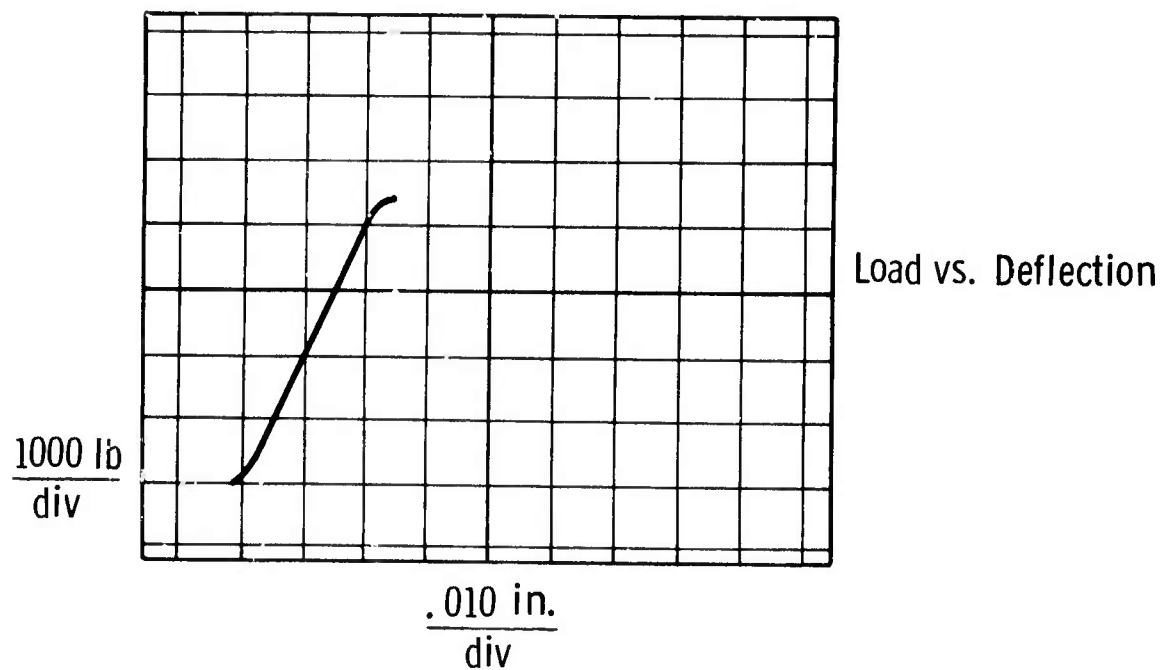
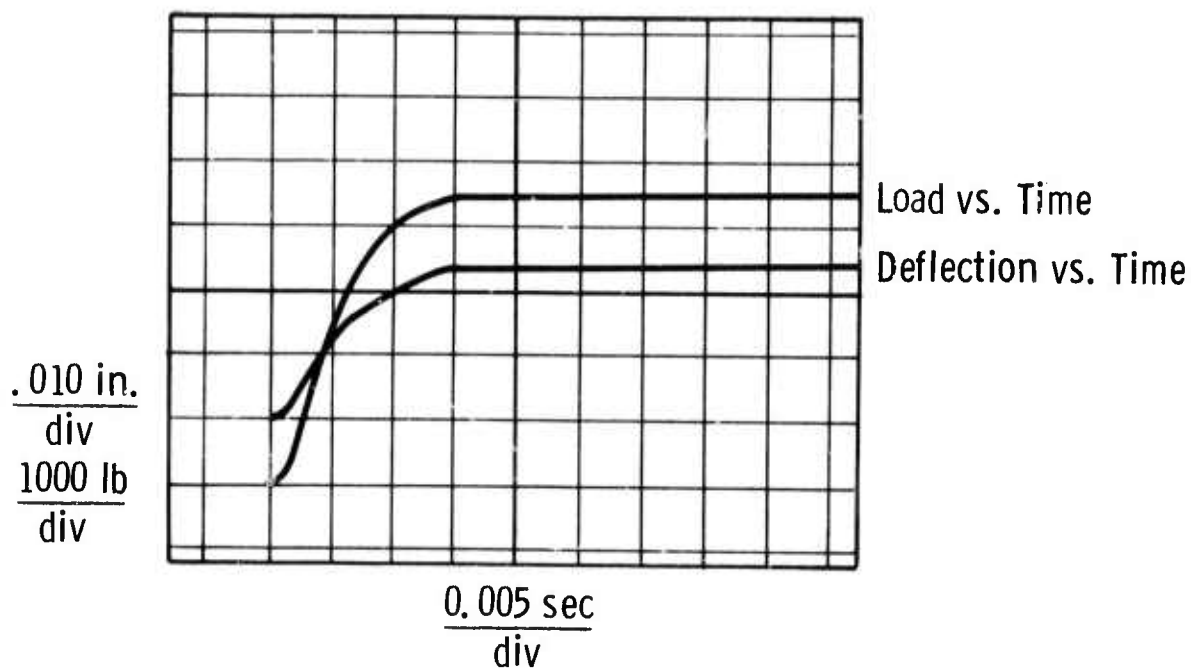


Fig.6-2—The influence of processing and heat treatment on the ductility of Inconel 718 (VIM-VAR)



Temperature = -320°F (77 K)

Fig. 6-3—Test record trace for a Udimet 718 specimen illustrating dynamic loading to a specific displacement

Curve 684624-A

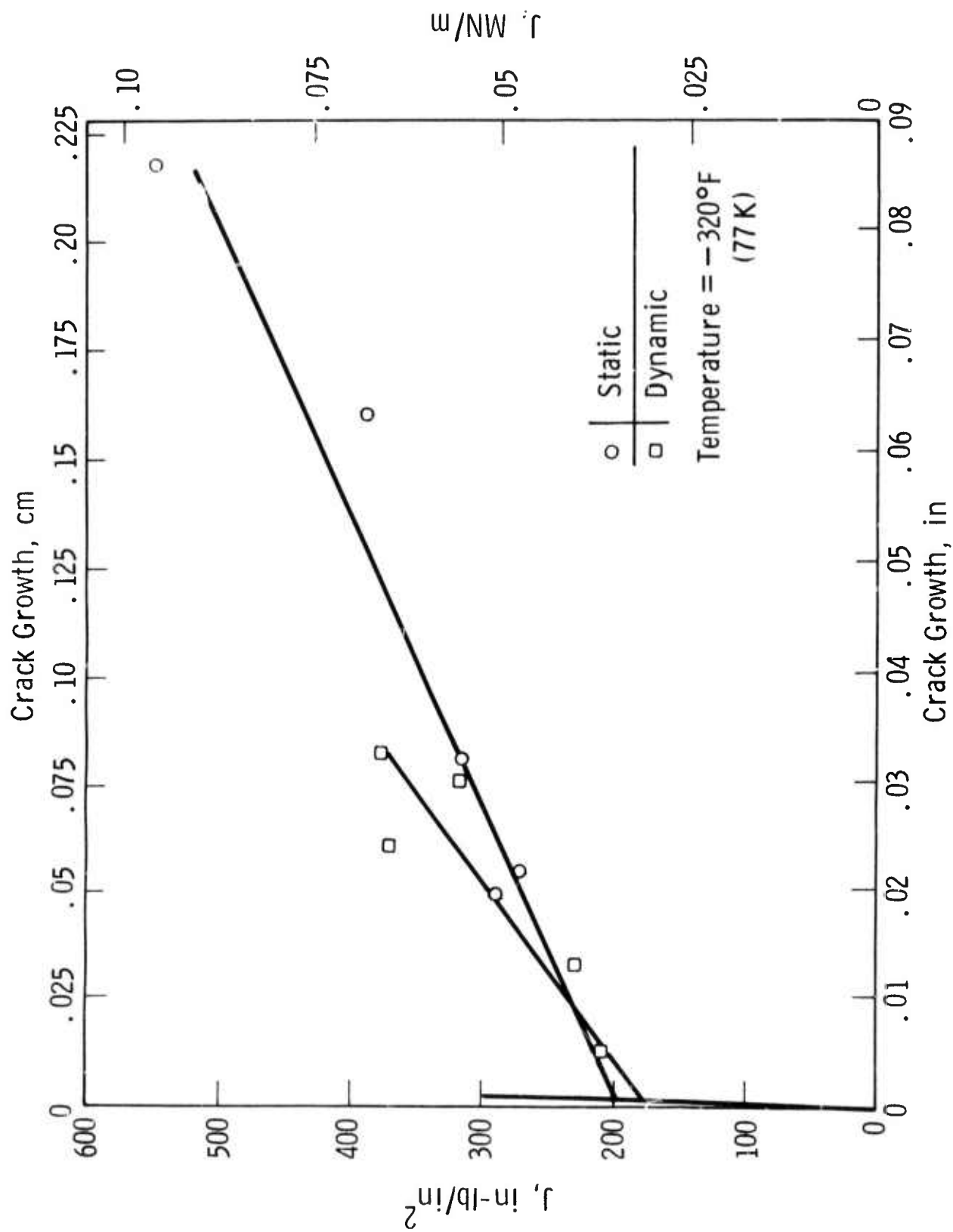


Fig. 6-4—Static and dynamic J resistance curves for Udimet 718

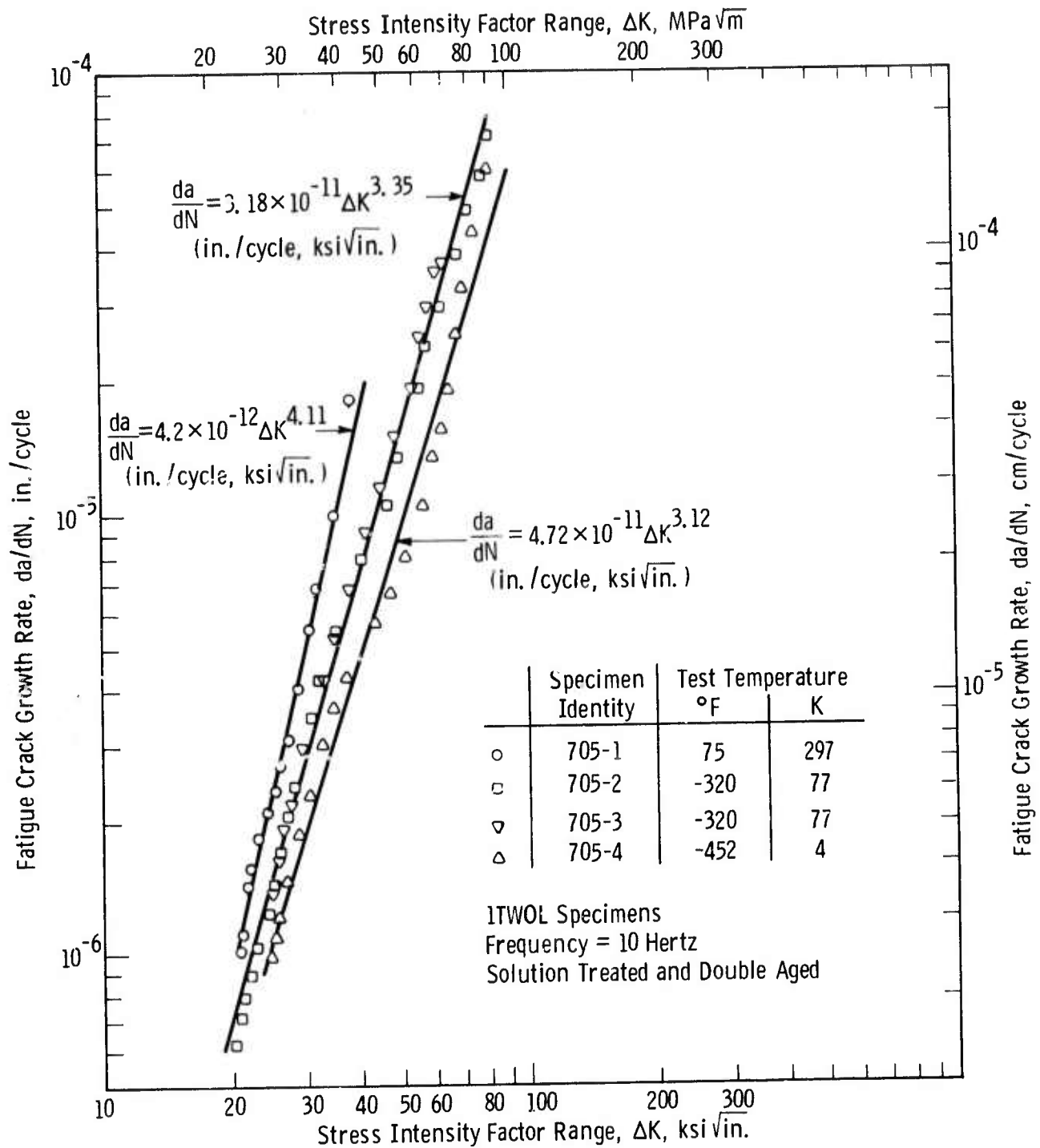


Fig. 6-5 — Fatigue crack growth rate properties of Inconel 706 (VIM-EFR)

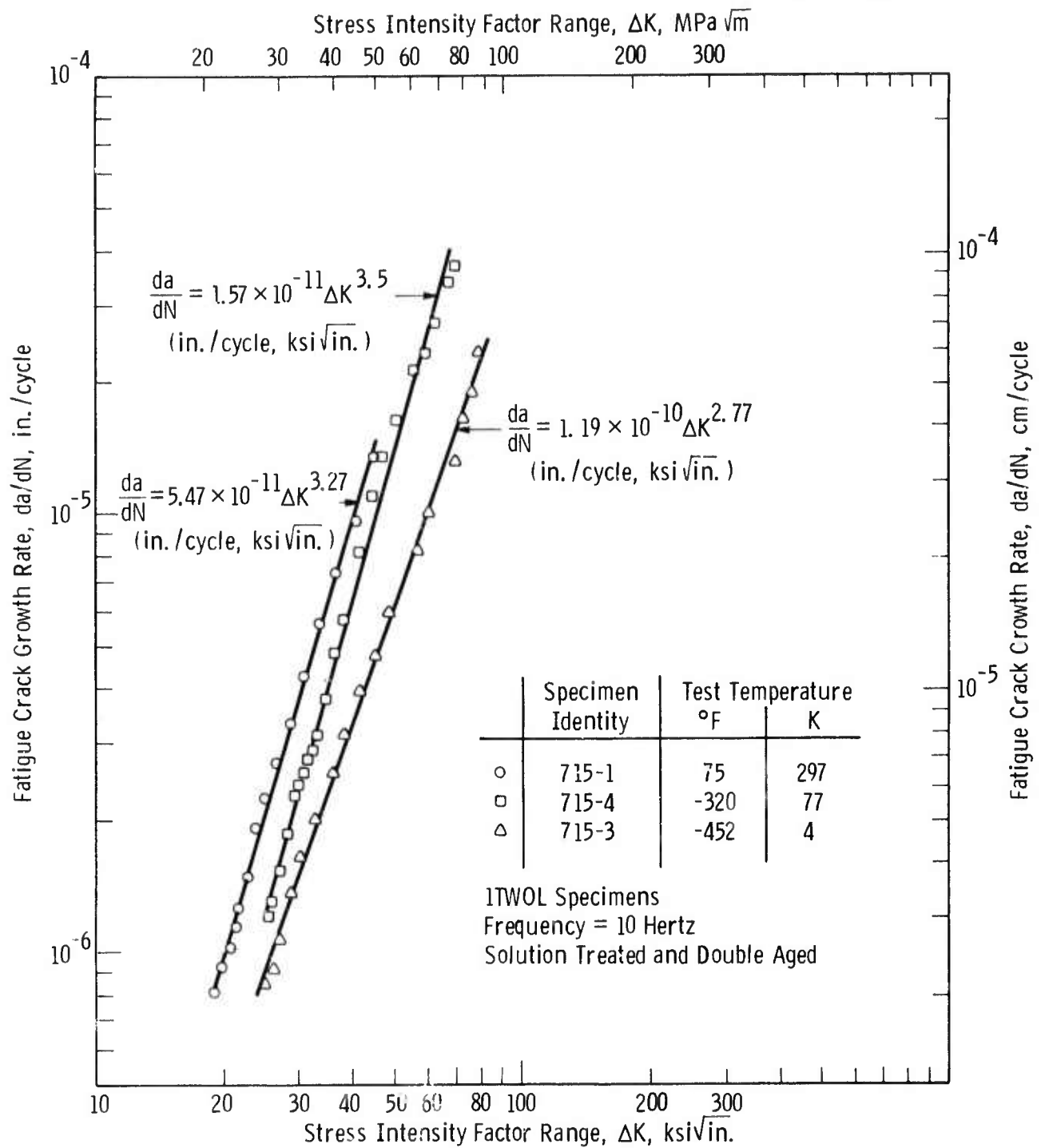


Fig. 6-6—Fatigue crack growth rate properties of Inconel 706 (VIM-VAR)

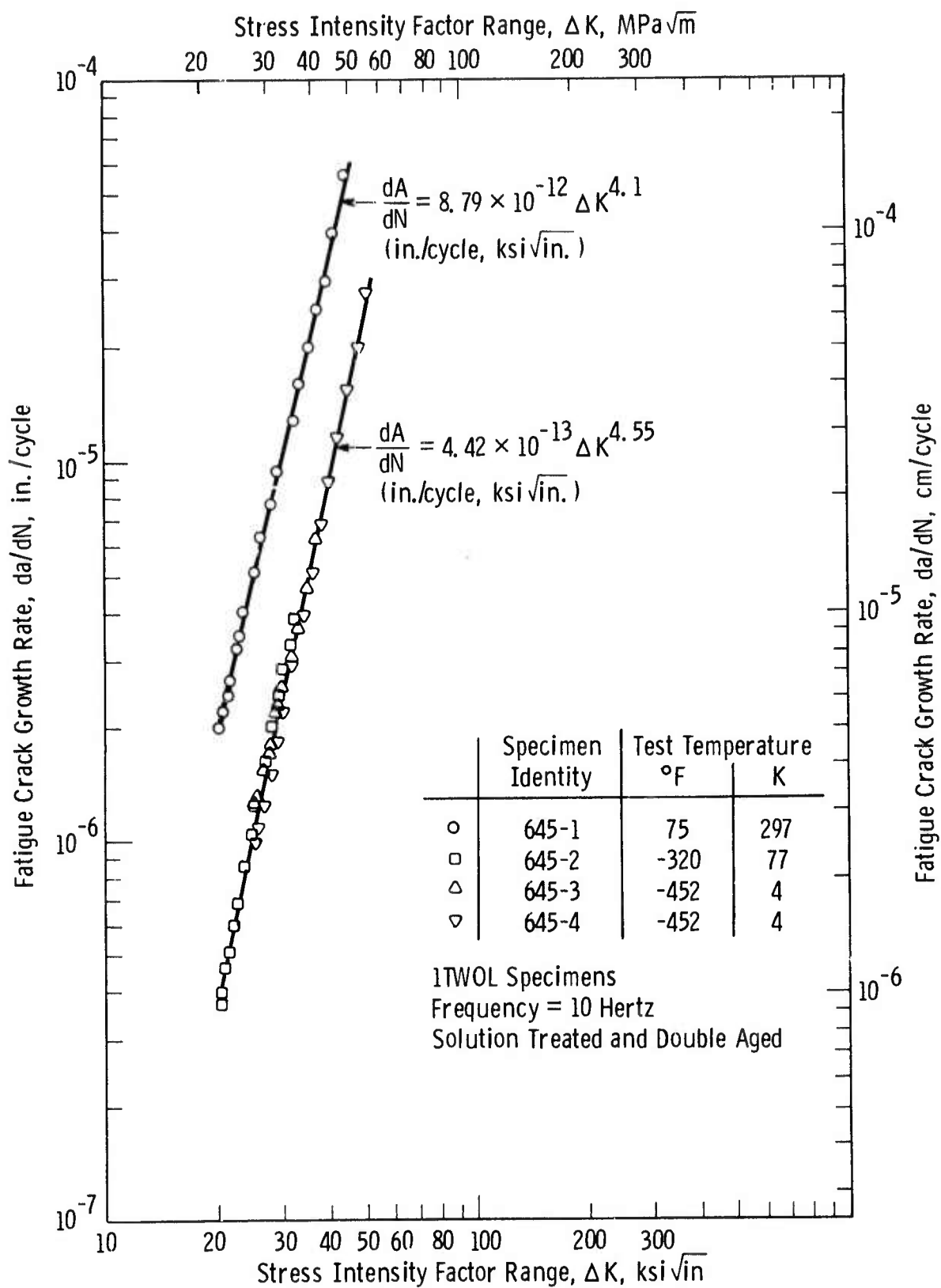


Fig.6-7—Fatigue crack growth rate properties of Inconel 718 (VIM-VAR)

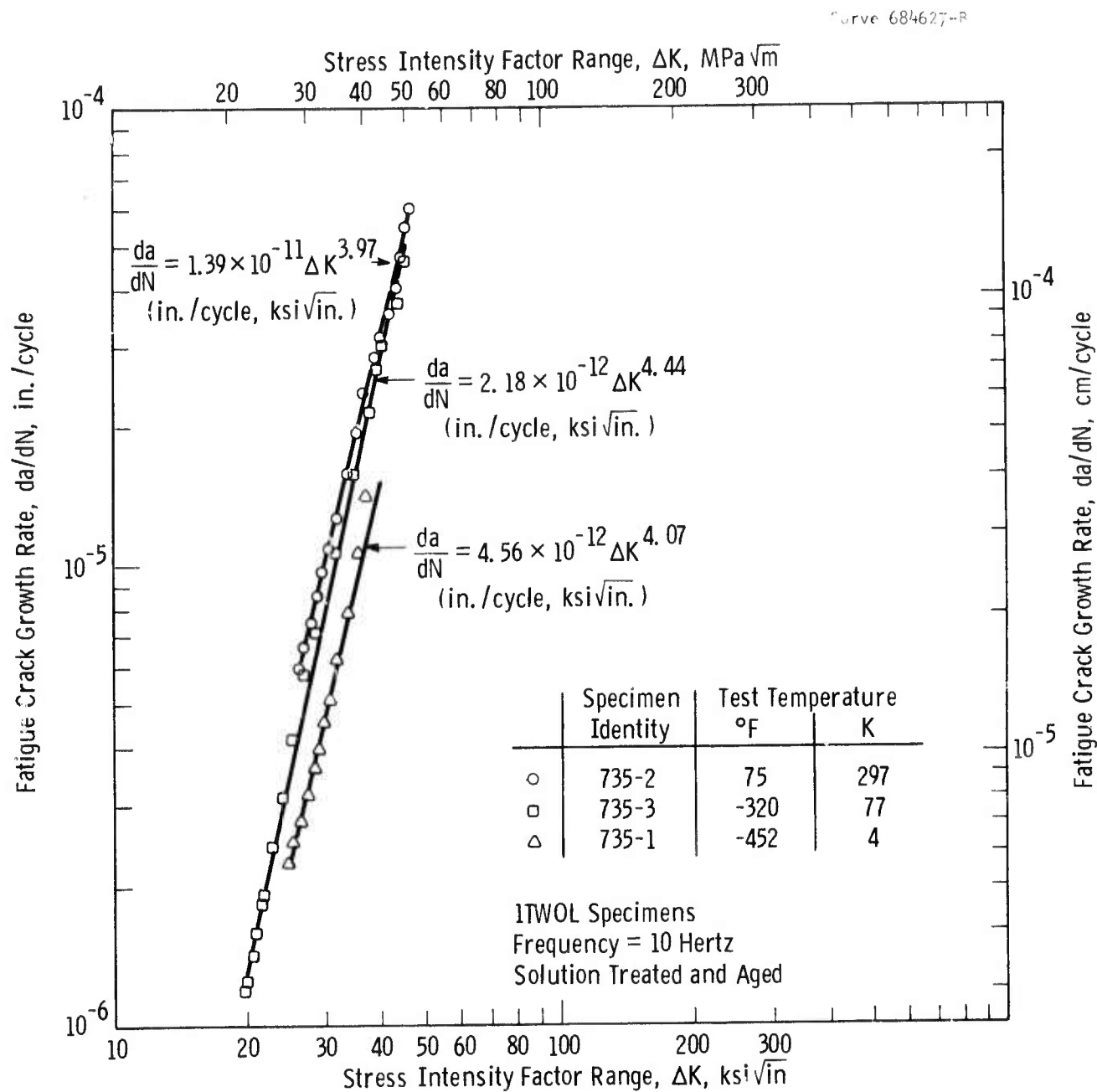


Fig. 6-8 - Fatigue crack growth rate properties of Inco LEA (AAM-VAR)

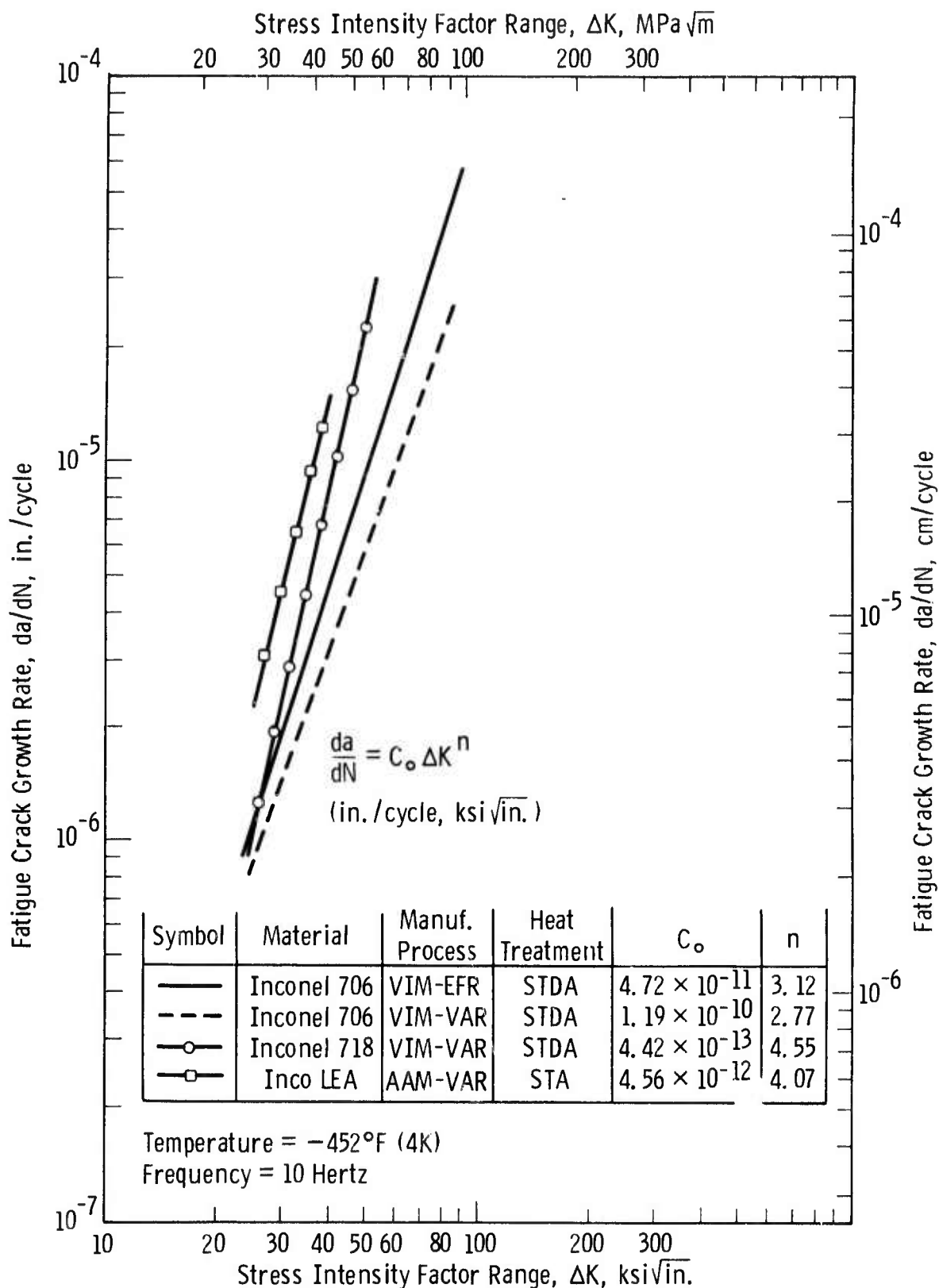


Fig. 6-9—Comparison of the -452°F (4K) fatigue crack growth rate properties of three superalloys

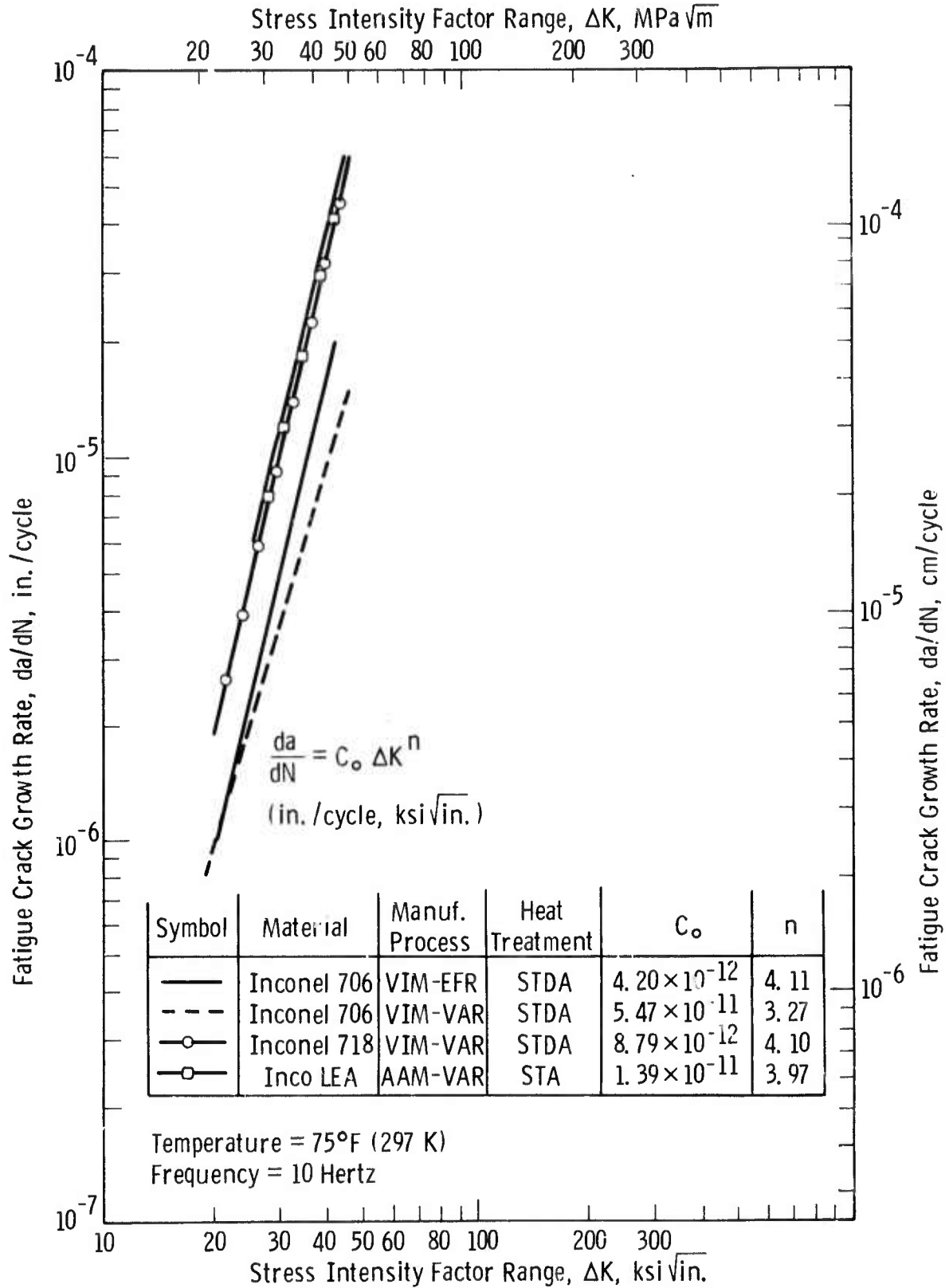


Fig. 6-10— Comparison of the room temperature fatigue crack growth rate properties of three superalloys

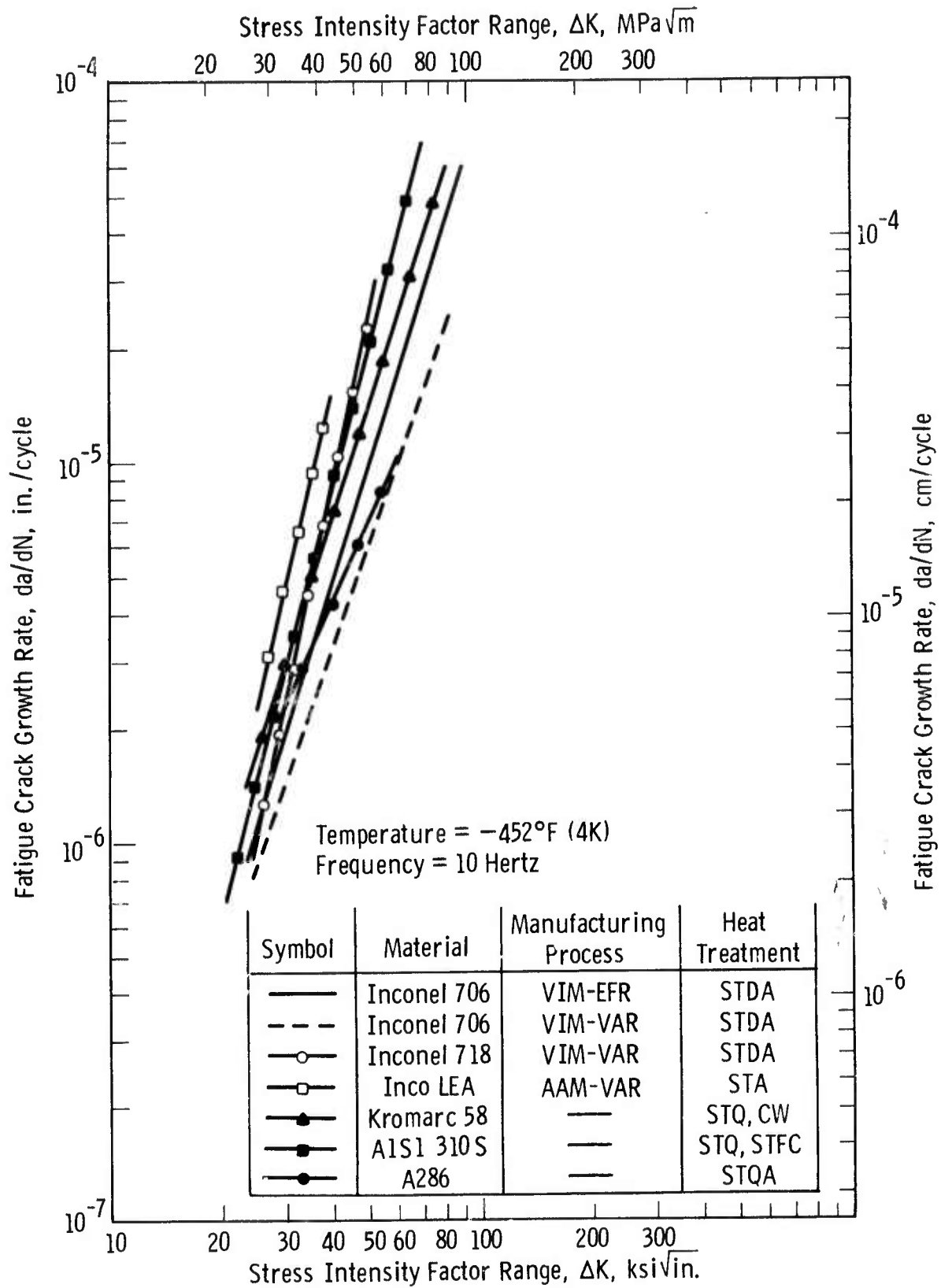


Fig. 6-11 — Comparison of the -452°F (4K) fatigue crack growth rate properties of superalloys versus stainless steels

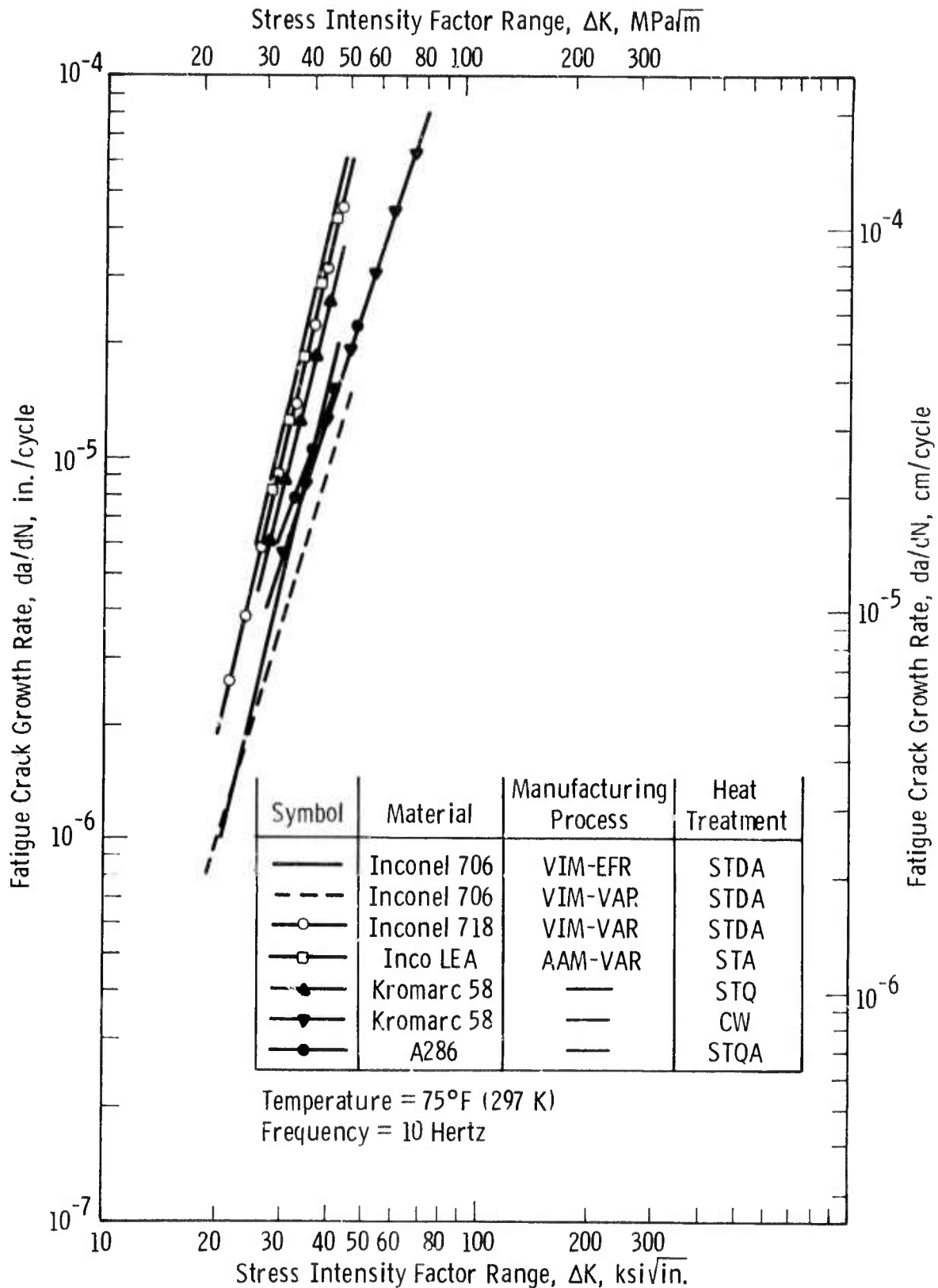


Fig. 6-12 — Comparison of the room temperature fatigue crack growth rate properties of superalloys versus stainless steels

7. MICROSTRUCTURAL ANALYSIS

The purpose of this phase of the work is two-fold: (a) examine the microstructures of tested specimens to determine the cause and mode of failure, (b) correlate the microstructural features with mechanical test data to establish failure mechanisms and effects of processing variables. With this knowledge at hand, one is able to identify critical areas in processing, material use, and performance realization. In this report, we conclude the discussion on base metal and weldments of alloys 718 and 706 which were discussed in the previous report.¹ We then present results on the effect of cold reduction-aging schemes on structure and properties in alloy 718. Results are presented in terms of light microscopy, scanning electron microscopy with energy dispersive x-ray data, and x-ray powder diffraction of carbide-extraction residues.

7.1 Carbide Extraction, Alloys 718 and 706

The "carbide extraction" method is designed to collect all phases present in the alloy that are not related structurally to the matrix. The matrix and the coherent phases such as the coherent phase γ' and γ'' are dissolved electrolytically following the procedure below:

- a. A piece of material 1 cm x 1 cm x 3 mm thick is prepared and electropolished to remove all surface contamination.
- b. The piece is carefully weighed.
- c. The metal is electropolished for eight hours at a current density of 60 mA/cm² with an electrolyte mixture of

0.9 gal methanol

0.1 gal HCl (conc)

67 g tartaric acid

- d. The acid liquid is filtered through 0.25 μm "millipore" filter which has been previously weighed.
- e. The weight of the solid residue is recorded and the weight loss of the original metal is also recorded.
- f. The solid residues are analyzed by powder x-ray diffraction to determine phases.

Examples of x-ray diffraction data are shown in Fig. 7-1. The "weld" specimens were machined entirely from the weld fusion zone. This figure shows the simple pattern of f.c.c. MC-carbides, Figs. 7-1a and c, and the very complex pattern where a multitude of phases are analyzed, such as MC carbides, δ and Laves phases (Figs. 7-1e and f).

All the findings are summarized in Table 7-1. These data shall now be discussed.

Alloys 718 and 706 belong to class II nickel-iron Nb containing superalloys.² These materials derive their primary strengthening from a combination of γ' (f.c.c. (Ni_3Al , Ti)) and γ'' (BCT Ni_3Nb) precipitation within the grain. Other common phases in this class of alloys^{2,3} are η (hcp, Ni_3Ti), δ (orthorhombic Ni_3Nb), and MC carbides (Ti ; Nb ; C). The MC carbides precipitate immediately after casting and usually remain unchanged. Thermomechanical treatment may result in redissolution and fragmentation of the carbides. The η and δ phases appear, usually, after prolonged exposure to elevated temperature and result from transformations, respectively, of γ' and γ'' . The solvus temperatures for the δ phase are⁴ slightly above 1800°F (982 °C) for alloy 718 and about 1650°F (907 °C) for alloy 706.

The first two lines in Table 7-1 reveal a significant difference between alloys U-718 and I-718*, in that the volume fraction of MC carbides

*U-718: Udimet alloy 718, special metals

I-718: Inconel alloy 718, Huntington alloys

in I-718 is quite higher in comparison to U-718. The higher content of non-soluble residues is maintained in alloy I-718 after the usual solution (982°C) and double-age treatment. Note, however, that lowering the solutioning temperature to 1800°F (982°C) maintains the δ phase in U-718 but results in Laves and silicide phase in alloy I-718.

There is no difference in phase content between the two processing variations of alloy 706. In fact, for all practical purposes, 706-VIM-VAR and 706-VIM-EFR appear microstructurally as two identical materials where the only phase present in the residue after the STDA treatment is the MC carbides. This is also confirmed by the comparable mechanical test data.¹

The data for the weld fusion zone show a marked increase in the content of non-soluble residue. All phases are detected in the fusion zones of both I-718 and I-706 weldments. It has to be mentioned here that I-718 filler wire was used to produce the weldments in alloy 706 as well. The data reflect, therefore, the characteristics of a 718 weld metal rather than that of alloy 706. The effect of the increase in volume fraction of all phases is reflected in the mechanical test data.¹ All transverse weldment test specimens broke in the fusion zone displaying slightly lower strengths, significantly lower ductilities, and severe reduction in fracture toughness.

The x-ray diffraction data in Table 7-1 are confirmed by energy dispersive x-ray analysis of the residues, shown in Figs. 7-2 and 7-3. The data in these figures reveal information about the elemental content of the residues. Fig. 7-2a shows only three elements in the residue of U-718 after the normal STDA treatment; Nb and Ti are tied in the MC carbides, while the high Ni content is related to the δ (Ni_3Nb) phase. I-718, solutioned at the high temperatures (Fig. 7-2b) shows Nb and Ti only, in agreement with the identification of MC carbides only (Table 7-1).

The data in Fig. 7-3 confirms the multitude of phases in I-718. Note the low Ti content after the STDA treatment. This indicates that the MC carbides are very rich in Nb. Also note the Si content, as compared to U-718 (Fig. 7-2).

The differences in phase content between alloys I-718 and I-706 are in agreement with their chemistry. Alloy I-718 contains twice as much Nb as alloy I-706. This will account for higher content of MC carbides.

The more significant information revealed by the data in Table 7-1 are the differences between the two heats of alloy 718, i.e., U-718 compared to I-718. It should be noted here that the differences in volume fraction and nature of the residual phases are reflected in the mechanical test data.¹ Alloy U-718 exhibited twice the fracture toughness and ductility at all temperatures when compared to alloy I-718. On the other hand, yield strengths at all temperatures were the same for both alloys. This indicates that the intrinsic strength of the alloys, which is derived from precipitations of γ' and γ'' is not affected by carbides and other phases. Ductility and fracture toughness, on the other hand, are strongly affected by carbides and particularly by the Laves phases, which tend to precipitate in the grain boundaries. It is significant, therefore, that we try to establish the possible source for the higher content of Laves phases in alloy I-718.

Chemistry of the alloys is given in Tables 5-8 to 5-10 of Reference 1. The only apparent significant difference in chemistry between alloys U-718 and I-718 is in the Si content; less than 0.1% Si in U-718 and 0.3% Si in I-718. The silicide phase of the type $\text{Ni}_2\text{Co}_3\text{Si}$ is the major source for Si precipitations; Fe and Cr can substitute for Co in this phase. It is, thus, conceivable that the small, but finite, difference in Si content is the source of the formation of silicide phase in alloy I-718.

It is of interest to note that the effect of Si on the formation of extraneous phases was previously observed by Kossowsky et. al. in Fe-30Ni-10Cr, γ' strengthened alloys.⁵ Lowering the Si content from

0.9% to 0.1% decreased the volume fraction of Si containing phases from 0.7 to less than 0.2 weight pct.

7.2 Recrystallized I-718 (specimens code 67XX, 68XX, 69XX)

These tests were designed originally to define the effect of grain size on structural variations and mechanical strength of I-718 (see Section 5). Briefly, three groups of specimens were examined: (a) specimens from group 67XX were initially solution annealed at 1950°F (1066°C), cold rolled, then given the standard 1800°F (982°C) solution anneal and double age (STDA); (b) specimens from group 68XX were given the same sequence of thermal-mechanical treatment with the solution temperature after cold work increased to 1950°F (1066°C), followed by double-aging treatment; (c) group 69XX was given solution anneal at 1950°F (1066°C), cold rolled and then directly doubled aged.

Grain size of the various groups of specimens were:

67XX - non-uniform distribution, average 15 μm

68XX - generally uniform distribution, average 95 μm

69XX - elongated, non-uniform distribution, ranging in width 20-50 μm , length 100-300 μm .

Examples of the typical grain morphologies are shown in Fig. 7-4. The structure of specimen 6700 and 6800 exhibit recrystallized morphologies, while the structure of specimen 6900 is that of a heavily worked material.

Micrographs of failed tensile test specimens are shown in Figs. 7-5 through 7-17. First, we examine light micrographs of longitudinal sections through the fractured ends, Figs. 7-5 through 7-9. All three sets of light micrographs (Figs. 7-5, 7-7, 7-8) reflect a similar mode of failure, i.e., a mixture of intergranular cracking and cross-granular shear. Large cracks are associated with agglomerations of particles as seen clearly in Fig. 7-7. These cracks were examined in more detail by scanning electron microscopy and shown in Figs. 7-6 and 7-9. Both micrographs show Nb rich and Ti rich MC carbides around the holes. Since all specimens were cold worked prior to testing, we suggest that the carbide

agglomerations were broken and cracked during processing. The voids are already observed in cross-sections, away from the deformed gauge section areas (Fig. 7-4). During tensile testing, the voids continue to open under stress. We propose, however, that these voids did not contribute significantly to weakening of the structure. The tensile test data (Fig. 6-) indicate very similar yield strengths for the cold worked specimens 67XX and 68XX and the standard base metal specimens 69XX.

Figs. 7-10 through 7-17 illustrate the modes of failure of the three groups of specimens in SEM micrographs of fractured surfaces. A close examination of all the micrographs supports the conclusions drawn from the light micrograph, i.e., that there are no significant differences in the modes of failure of all three groups of specimens at all three test temperatures. The x-ray analysis in Fig. 7-11, for example, corroborates the identification of carbides on the fractured surface and the general alloy composition of the cross-granular shear facets. The two types of carbides identified around the large voids (Fig. 7-9) are present around some voids which are found on the fracture surface. This is illustrated in Fig. 7-12.

The high magnification details of the dimpled part of the fracture surface indicate that small particles are located at the bottom of each dimple, see Figs. 7-13 and 7-14.

The mixed mode of failure is illustrated clearly in the large grain size specimens in Figs. 7-15 and 7-16. The combination of inter-granular cracking, cross-granular shear and the limited ductility (shallow dimples) can be observed in Fig. 7-15.

7.2.1 Summary

Examination of the tensile test data (Figs. 6-1 and 6-2) and the various micrographs illustrated above indicate that there is virtually no grain size dependence of strength for the range of grain sizes obtained between specimens 67XX and 68XX. Recrystallization has

taken place upon solution annealing after the cold work step. This is evident in specimens of group 67XX which were solution annealed after cold work at 1800°F (982°C). Solution annealing at 1950°F (1066°C) after cold work results in a significant grain growth. Although there is an order of magnitude increase in grain size from specimen 67XX to 68XX, the yield strength data do not indicate any particular trend. There is, however, a small increase in ductility at room temperature for the large grain size specimens.

The increase in yield strength in specimens of group 69XX (not solution annealed after cold work) illustrate the effect of residual cold work. This also indicates that the secondary solution treatment at either 1800°F (982°C) or 1950°F (1066°C) is sufficient to relieve all deformation imparted to the specimens during the cold reduction step.

I-718 fails by a combination of cross-granular shear and intergranular cracking. The ductility is further limited by particles within the grains as illustrated by the shallow dimpled structure. The large agglomeration of carbides within the grain is lower in alloy 706 and, hence, the occurrence of large agglomeration, Fig. 7-18d, was not as prevalent as in alloy 718.

The crystallographic orientation of fatigue striations are clearly demonstrated in Figs. 7-20 and 7-21. Branching and secondary cracking of grain boundaries are depicted in Figs. 7-21c and 7-21d.

7.3 N-33 Deformed Weldment

Fig. 7-22 shows polished sections of a weldment deformed at room temperature in bending (see Section 5 of this report). Although the information in this micrograph is limited, it supports the magnetic data which showed a small, by finite amount, of ferromagnetism. Since alloy N-33 is austenitic in the undeformed state, it was postulated (Section 5.1.2) that localized martensitic transformations may have been induced by deformation. Slip bands and acicular martensitic plates can be recognized on the polished and heavily etched surface, Fig. 7-22.

7.4 References

1. J. M. Wells, W. A. Logsdon, R. Kossowsky and W. R. Daniel, "Structural Materials for Cryogenic Applications," Fourth Semi-Annual Report, November 1975, p. 7-53.
2. D. R. Muzyka in "Superalloys", Sims and Hagel, eds., John Wiley and Sons, New York, 1972, p. 133.
3. R. F. Decker and C. T. Sims, Ibid., p. 52.
4. D. R. Muzyka, Met. Eng. Q. 11 (1971), p. 12.
5. R. Kossowsky and M. L. Bleiberg, Alloy Development Program, National LMFBFR Program, Limited Distribution Reports.

TABLE 7-1-X-RAY DATA, NON SOLUBLE RESIDUES

Material			Non Soluble Residue			
Designation	Condition	Treatment	wt% Residue	MC (Nb, Ti) C	δ Ni ₃ Nb	Laves: Fe ₂ Ti or Ni ₂ CO ₃ Si
U718-AF-4C	Base Metal	ST 1950°F	0.23	maj	—	—
I-718	Base Metal	ST 1950°F	1.13	maj	—	—
U718-AF-4C	Base Metal	STDA*	1.14	maj	maj	—
I-718	Base Metal	STDA	1.58	maj**	—	maj
I-706 VIM-VA R	Base Metal	STDA	0.50	maj	—	—
I-706 VIM-EFR	Base Metal	STDA	0.49	maj	—	—
I-718	Weld-fusion Zone	WELD+STDA	2.72	maj	maj	maj
I-706	Weld-fusion Zone	WELD+STDA	2.41	maj	maj	maj

* STDA: ST 1800°F + 1325°F/8 hr, FC to 1150°F/8 hr, AC

** MC, Nb rich in 718, less Nb in 706

*** 718 Filler Wire

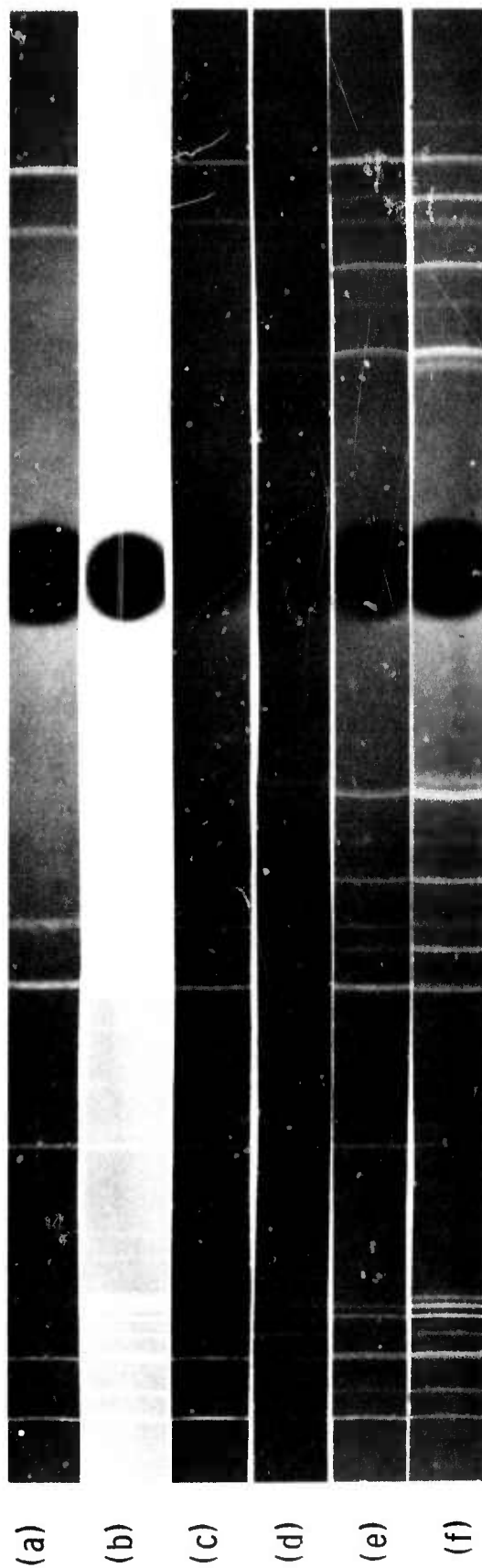


Fig. 7-1 - X-ray powder diffraction data, non-soluble residues (a) alloy 706 VIM-VAR STDA (b) alloy 706 VIM-VAR weld, STDA (c) U718 ST, 1950°F (d) U718 STDA (e) U718 STDA (f) U718 weld, STDA

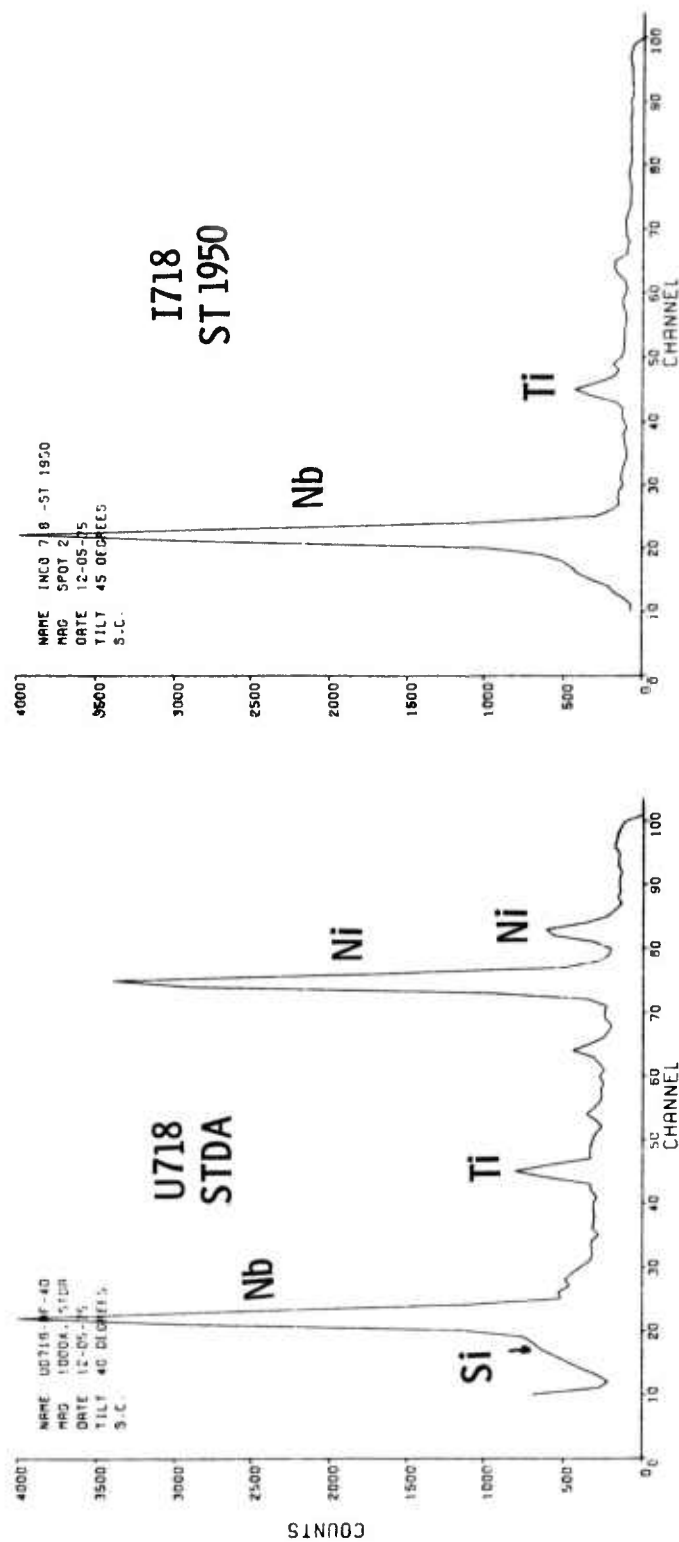


Fig. 7-2 -- Non-soluble residue, EDAX analysis

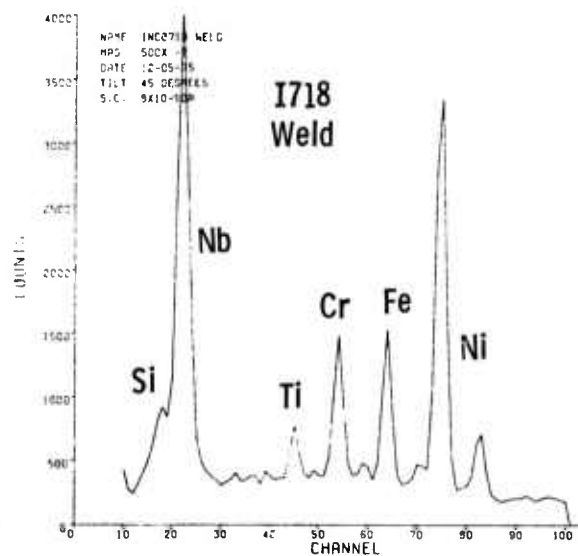
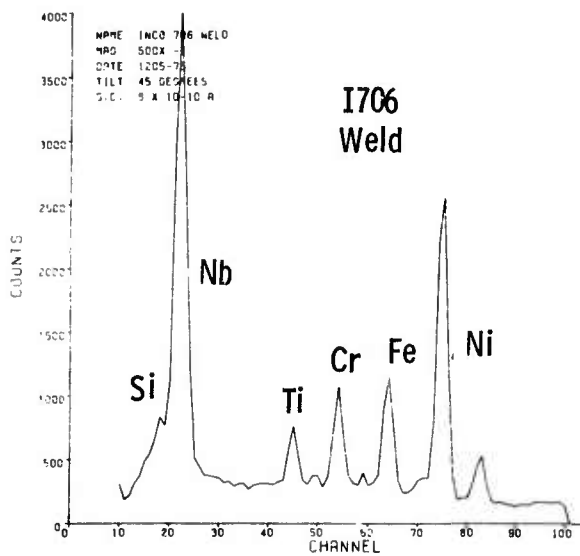
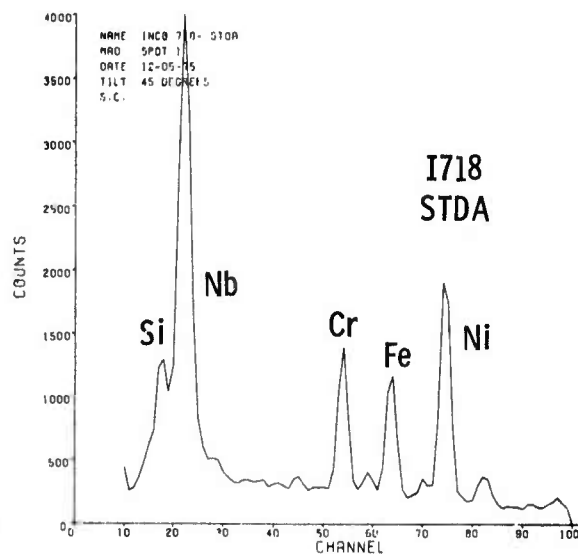
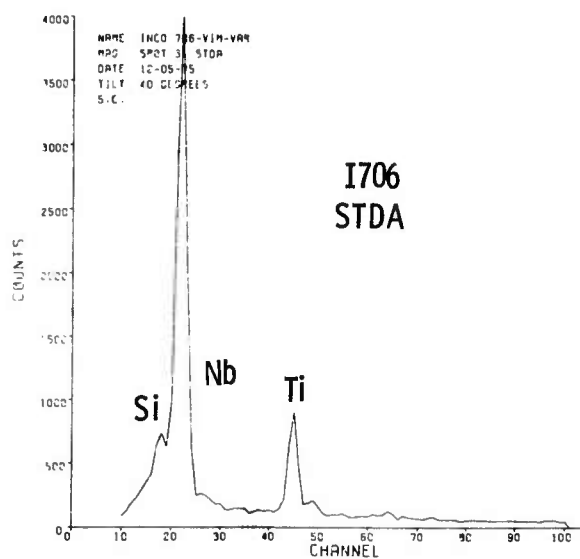
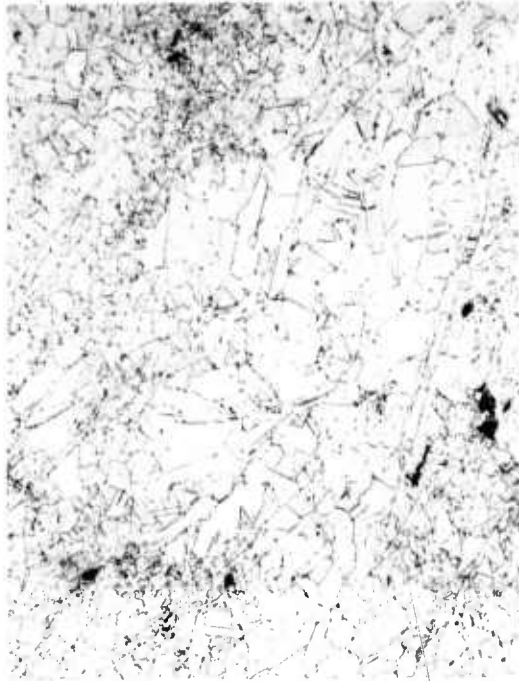
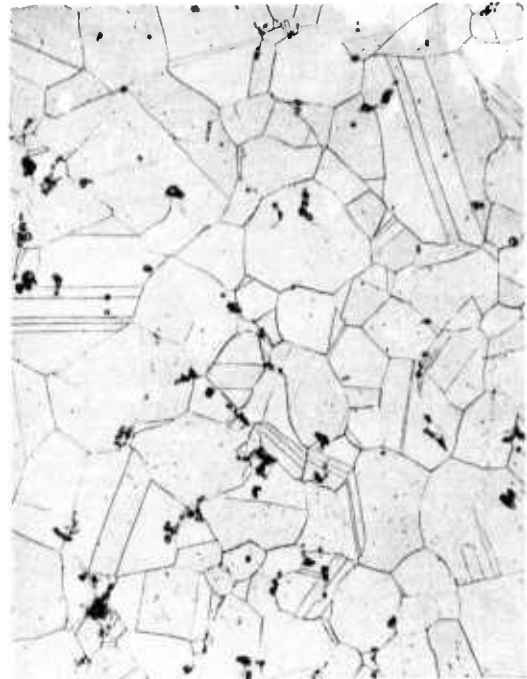


Fig. 7-3 — Non-soluble residue, EDAX analysis



(a) 200X

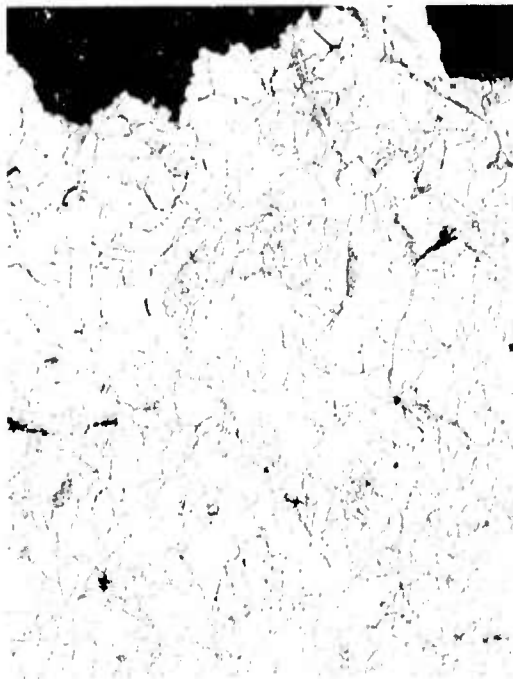


(b) 100X

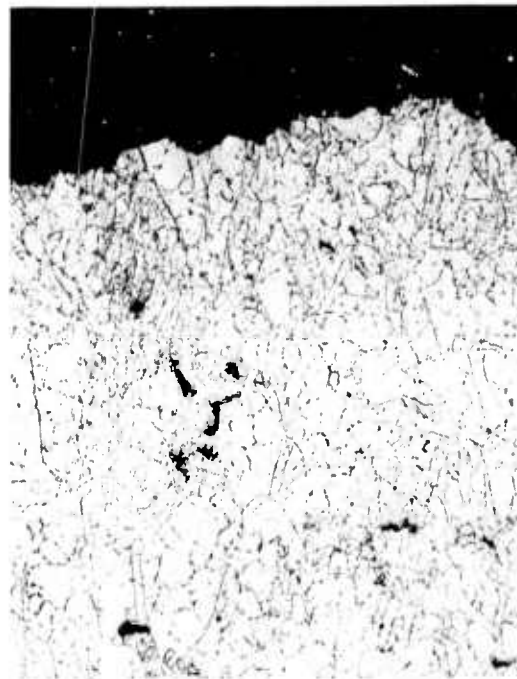


(c) 100X

Fig. 7-4 — Cross sections showing typical grain morphology
I-718 (a) group 67XX (b) group 68XX (c) group 69XX



(a)



(b)

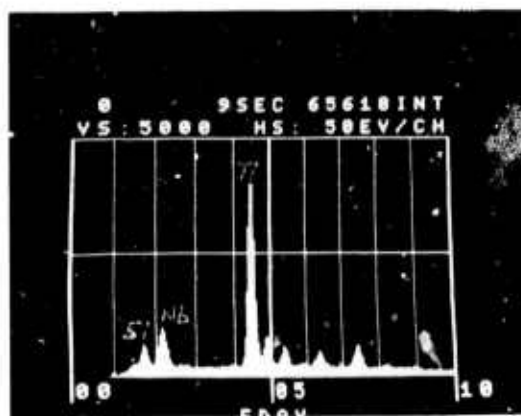
Fig. 7-5 — I-718, tensile test specimens 671X (a) longitudinal section, 200X tested at 77°K (b) tested at 4.2°K. Most of cavities are fracture carbides, see Fig. 6



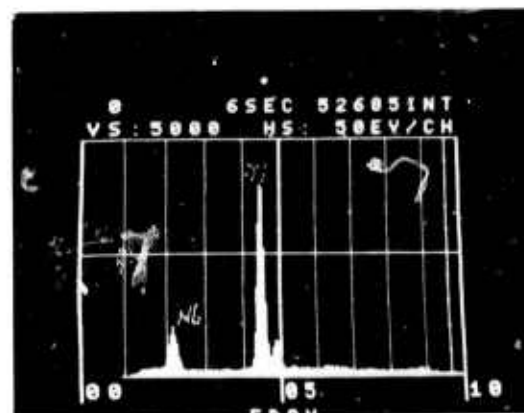
(a)



(b)



(c)



(d)

Fig. 7-6 — I-718, SEM micrograph (a) of longitudinal section, tensile test specimen G711, 1000X. Holes seen in Fig. 5 are fractured carbides (b-d) energy dispersive x-rays (b) spot 1 (c) spot 2 (d) spot 3

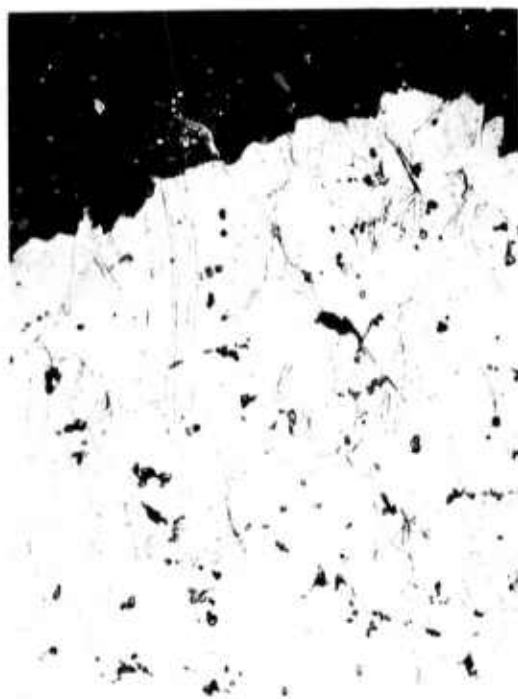


(a)

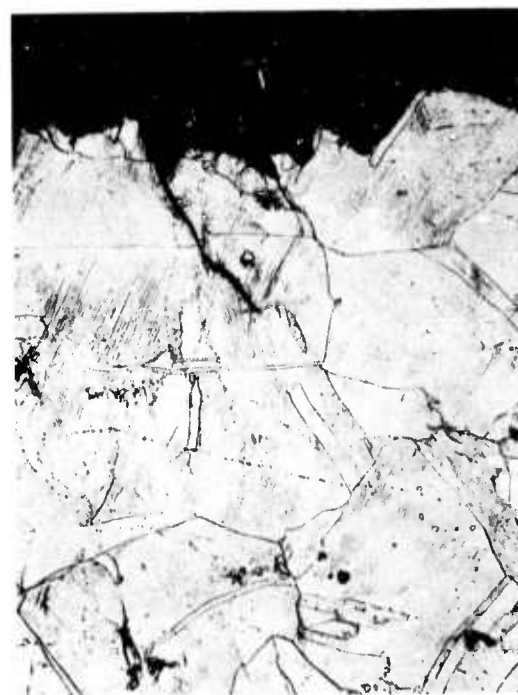


(b)

Fig. 7-7 - I-718, longitudinal sections, tensile test specimens 681X (a) tested at R.T. 50X (b) tested at 4.2°K, 200X. Slip lines seen clearly in (b)



(a)



(b)

Fig. 7-8 — I-718, longitudinal cross sections, specimen 691X (a) tested at R. T. 100X (b) tested at 4.2° K, 200X. Note severe deformation due to pretest cold reductions. Fractured carbides around cavities are shown in Fig. 7-9

(a)



(b)



(c)

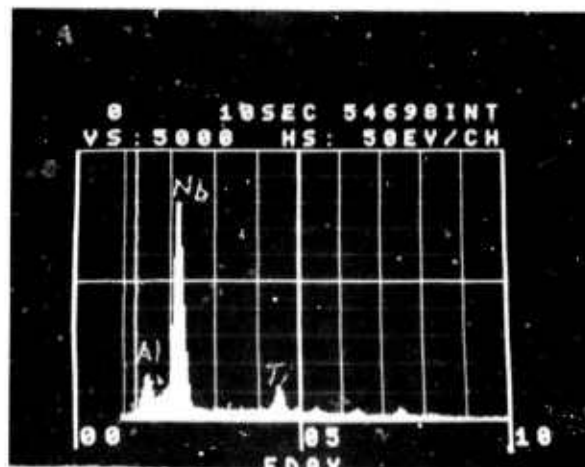
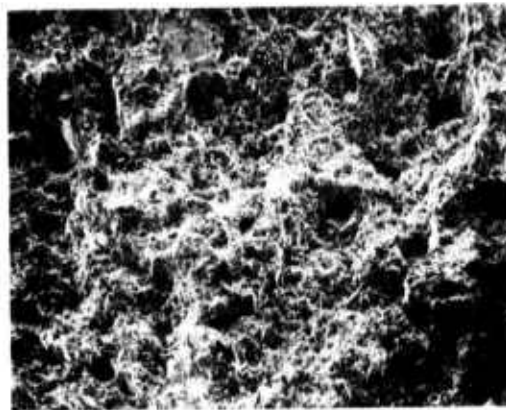
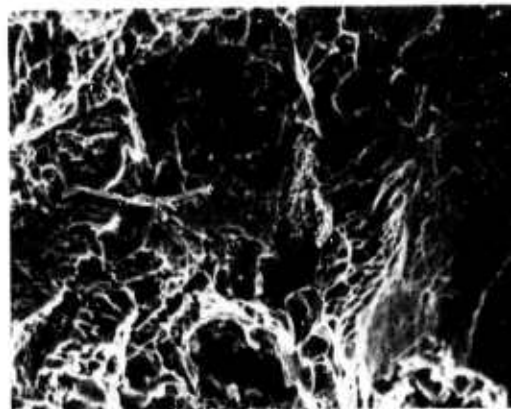


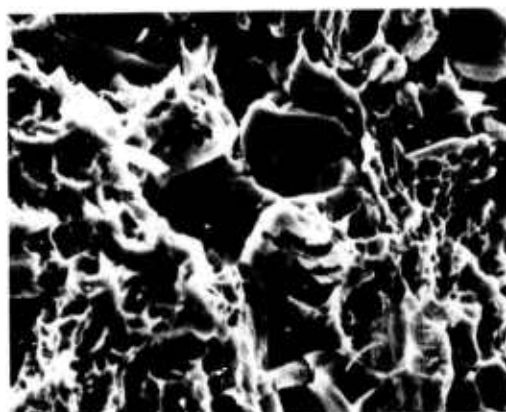
Fig. 7-9 - I-718, SEM micrographs of cavities seen in Figs. 7-7 and 7-8 (a) specimen 6811, 600X (b) specimen 6913, 1200X (c) energy dispersive x-rays of spot 1 Nb rich Mc carbides



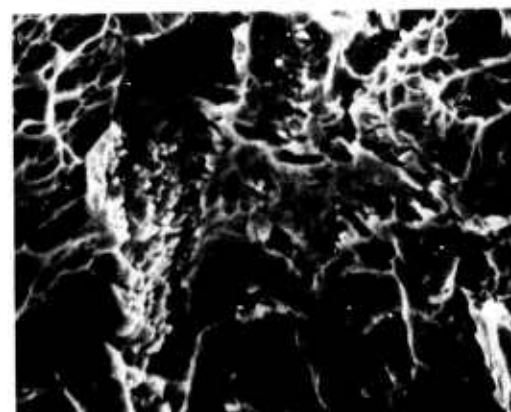
(a)



(b)



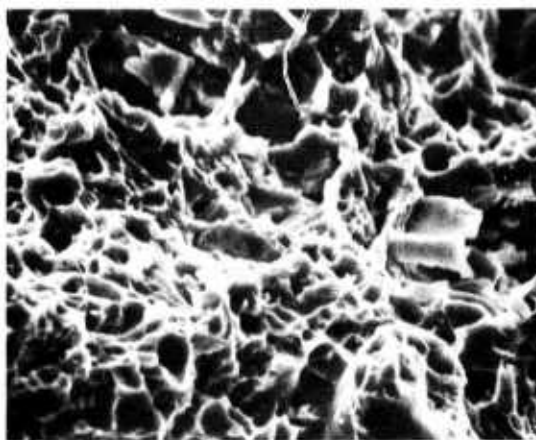
(c)



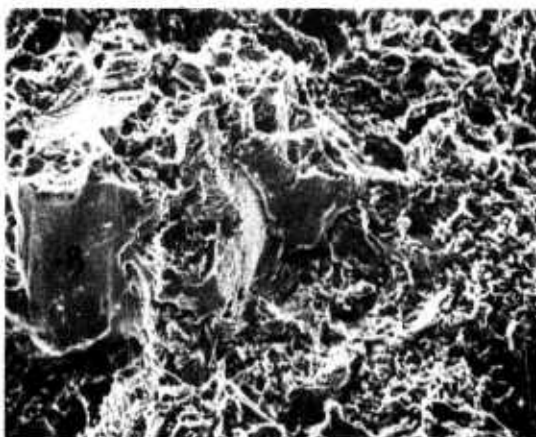
(d)

Fig. 7-10— I-718 SEM micrographs, fracture surface, tensile specimen 6711 tested at R. T. (a) 50X (b) 1000X mixed mode of shear and dimpled tensile failure (c) 2000X note secondary cracks in carbides (arrows) (d) 2000X shear facets

(a)



(b)



(c)

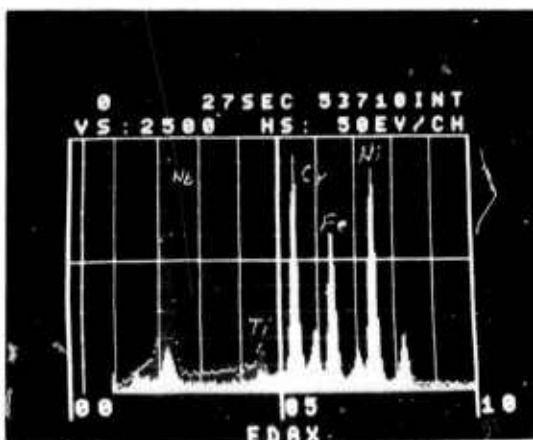
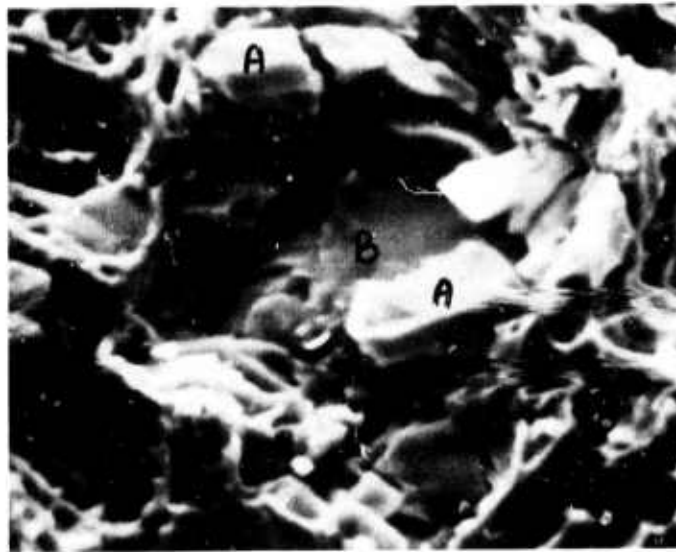
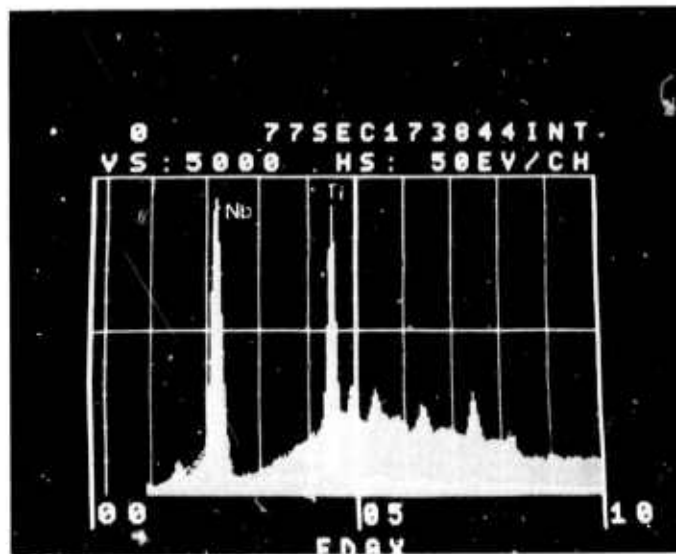


Fig. 7-11 - I-718, SEM micrographs, fracture surface specimen 6712 tested at 77°K (a) typical dimpled structure with carbides (b) shear facet 2000 X (c) x-ray of spot A (dots) and spot B (lines). Nb rich Mc carbide in A

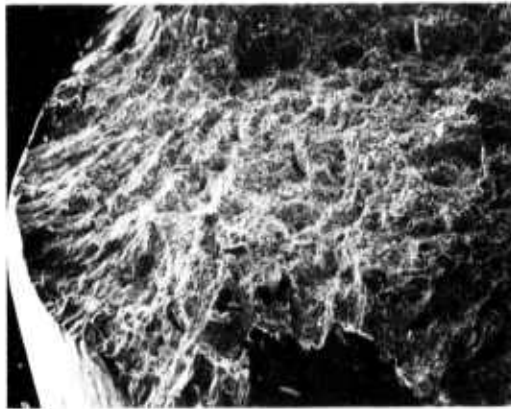


(a)

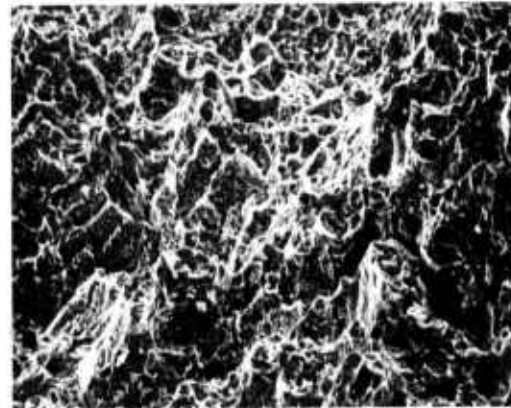


(b)

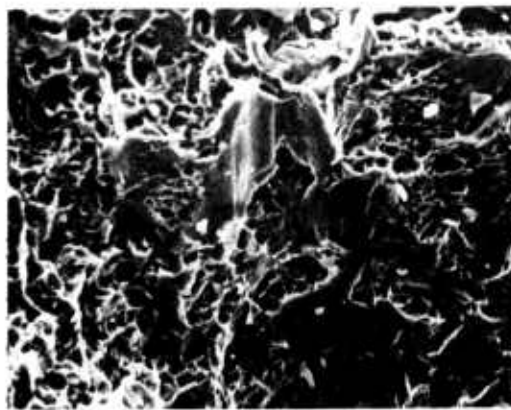
Fig. 7-12 - I-718, SEM micrograph, 2600X, fracture surface specimen 6712 tested at 77°K. Two types of carbides - A Nb rich (Nb, Ti) C (dots, EDAX), B (Nb, 30Ti) C (lines, EDAX)



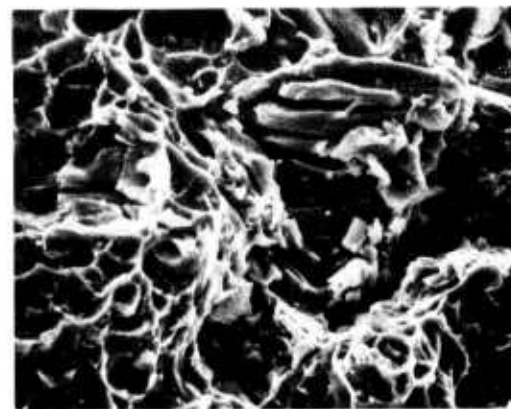
(a)



(b)



(c)



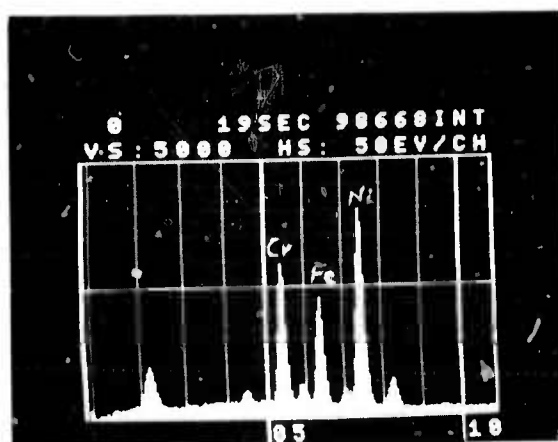
(d)

Fig. 7-13 — I-718, SEM micrographs, fracture surface, tensile test specimen 6812 tested at 77°K (a) 50X (b) 500X (c) 1000X note dimples and shear facets (d) 2000X large carbide agglomerates and carbides at the bottom of dimples

(a)



(b)



(c)

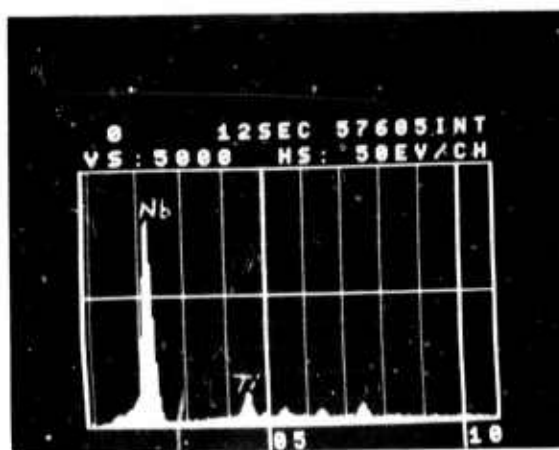
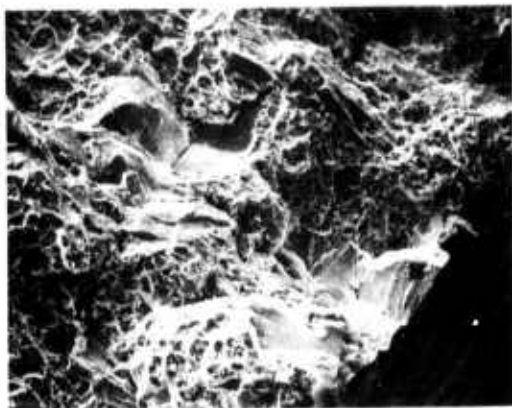
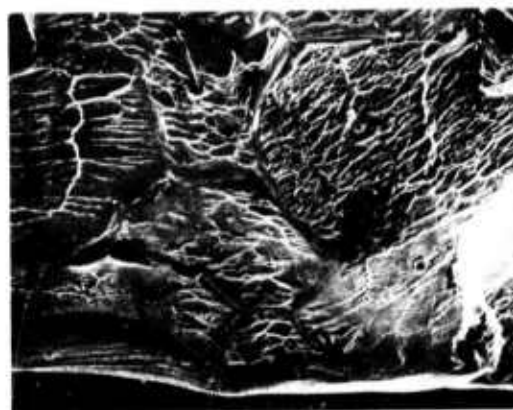


Fig 7-14 — I-718, SEM micrograph (a) of fracture surface, specimen 6813 tested at 4.2°K, 1500X (b) EDAX shear facet, spot 1 (c) EDAX carbides in dimples, spot 2



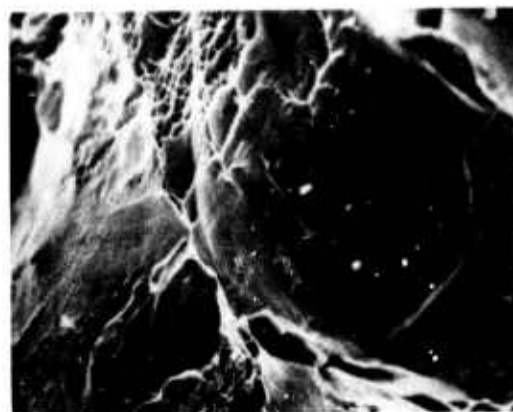
(a)



(b)

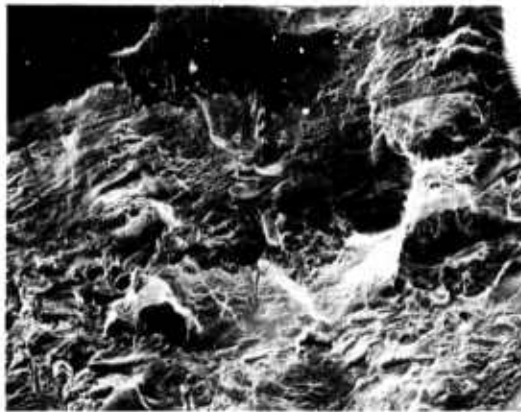


(c)

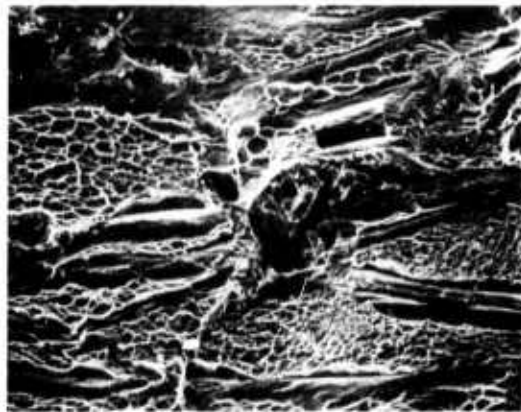


(d)

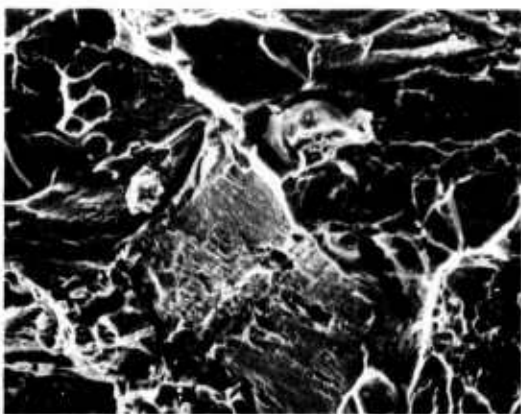
Fig. 7-15 - I-718, SEM micrographs of fracture surface, specimen 6813, tested at 4.2°K
 (a) 200X mixture of dimpled fracture, intergranular and shear fractures (b) dimple
 detail 500X (c) intergranular detail 1000 (d) shear facets, detail 1400X



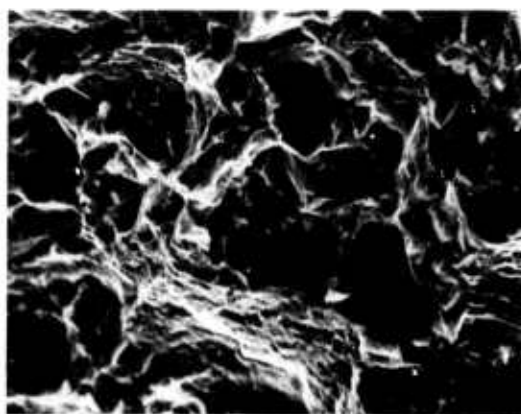
(a)



(b)

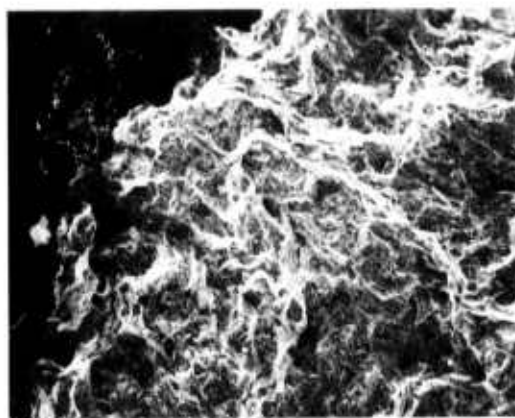


(c)

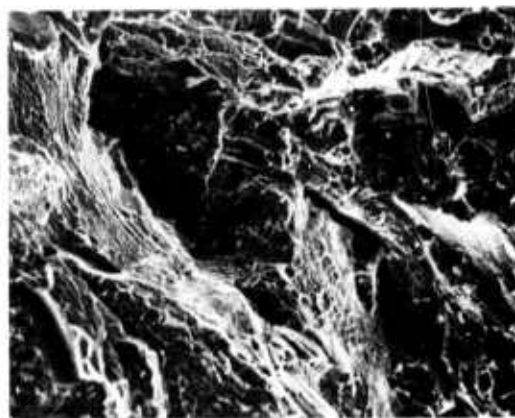


(d)

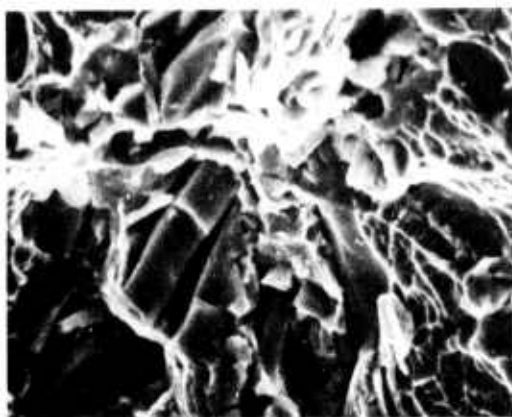
Fig. 7-16 — I-718, SEM micrographs, fracture surface, tensile specimen 6911, tested at R. T. (a) 200X (b) dimples and lanes phase sheared particles detail, 500X (c) intergranular and shear facet fracture detail 1000X (d) carbide agglomerations 2000X



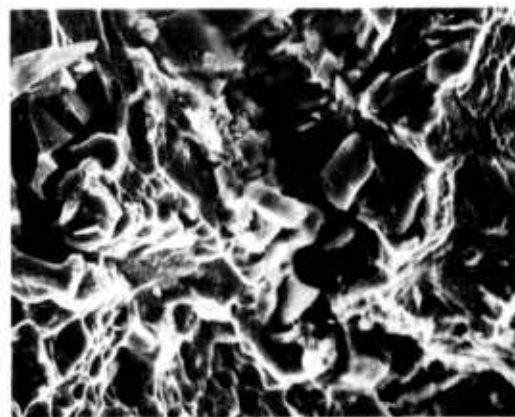
(a)



(b)

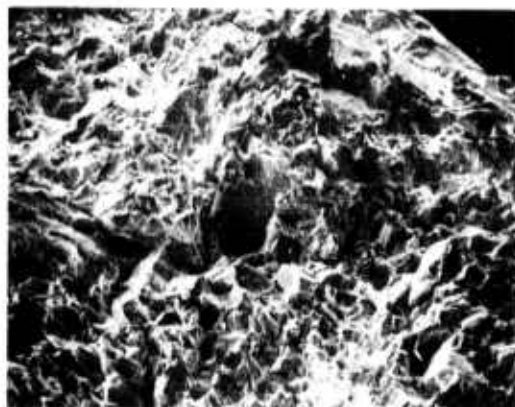


(c)

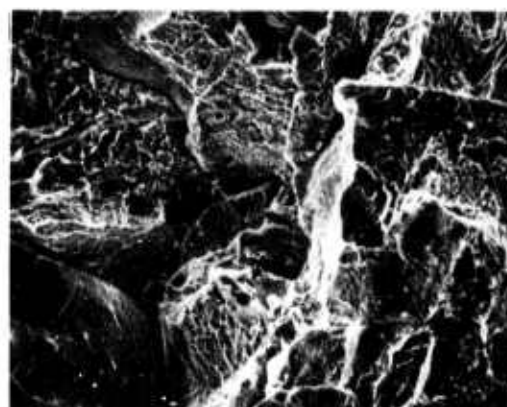


(d)

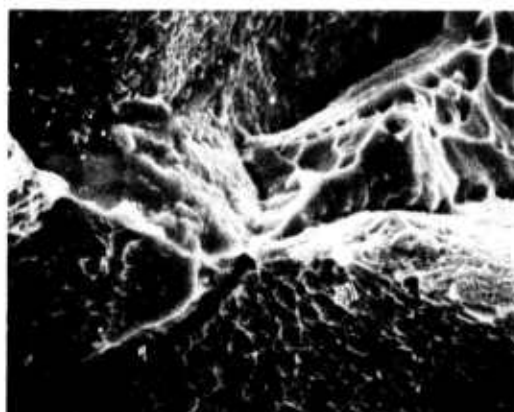
Fig. 7-17 - I-718, SEM micrographs, fracture surface, specimen 6913, tested at 4.2°K (a) 50X (b) shear, dimple detail 500X (c,d) carbides and lath phases details 2000X



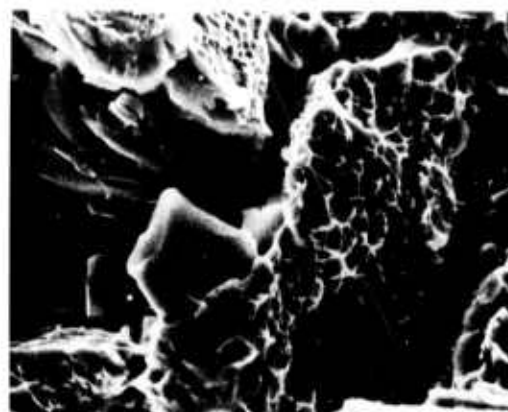
(a)



(b)

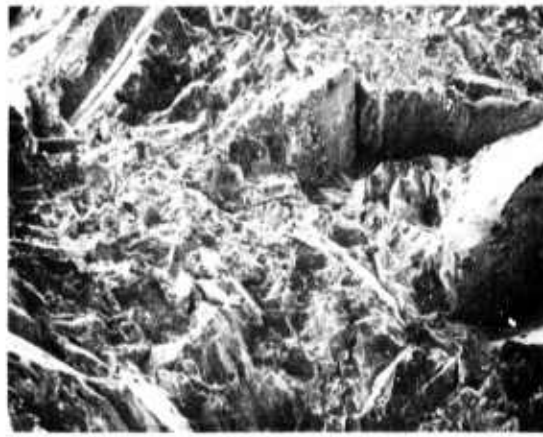


(c)

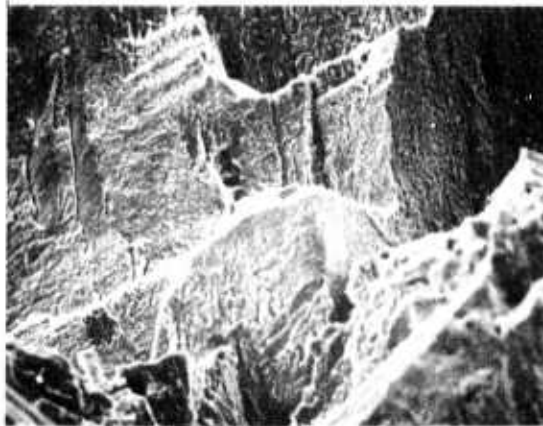


(d)

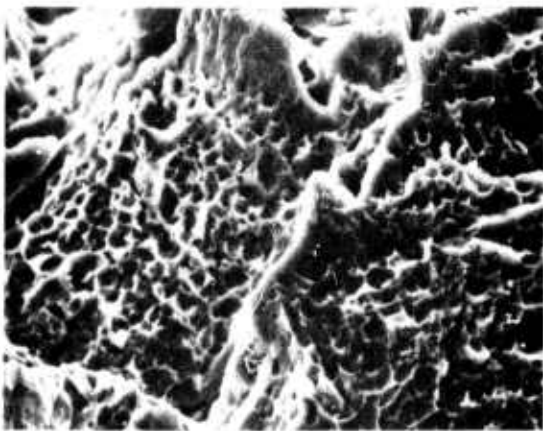
Fig. 7-18— A-286, SEM micrographs, fracture surface tensile specimen tested at 77°K (a) 50X (b) 500X intergranular fracture preceded by deformation within the grain (c) detail, 2000X (d) fracture around carbide agglomerations, 2000X



(a)

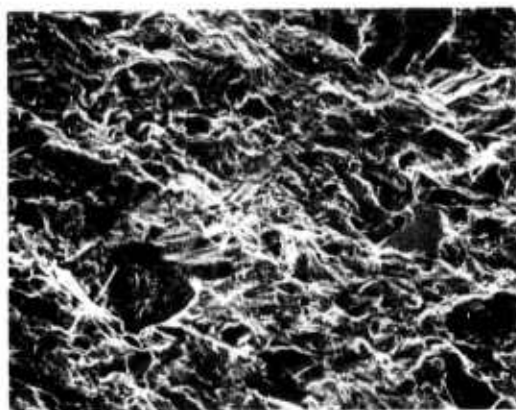


(b)

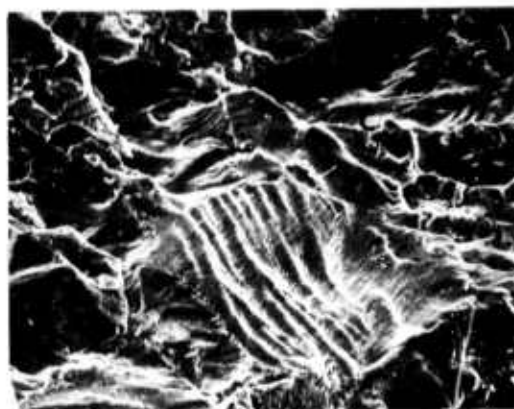


(c)

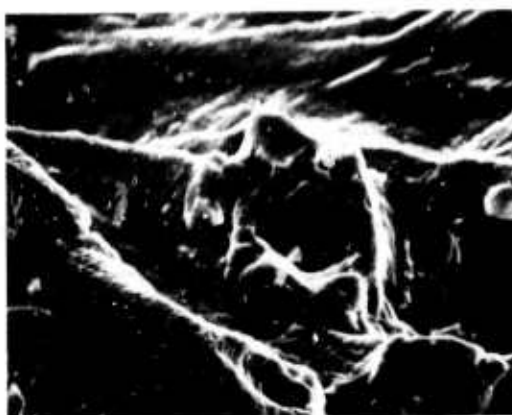
Fig. 7-19 — A-286, SEM micrographs. Fracture surface, tensile specimen tested at 4.2°K (a) 50X mixed mode of intergranular fracture and cross-granular shear (b) detail 500X (c) detail 2000X



(a)



(b)

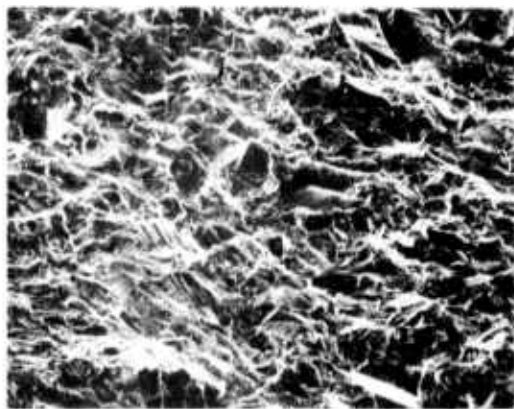


(c)

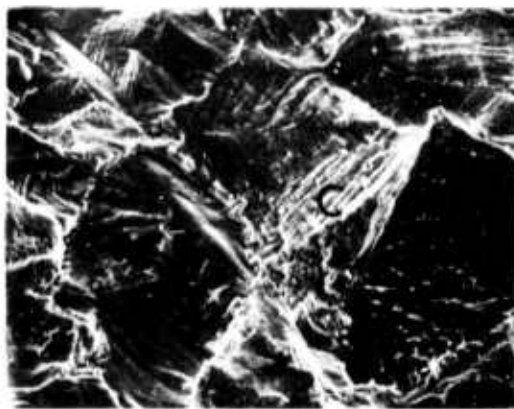


(d)

FIG. 7-20— A-286, Fatigue-crack growth specimen, tested at R. T. SEM micrographs (a) 100X (b) 500X (c) detail, 2000X (d) 1000X. Fatigue striations along crystallographic direction



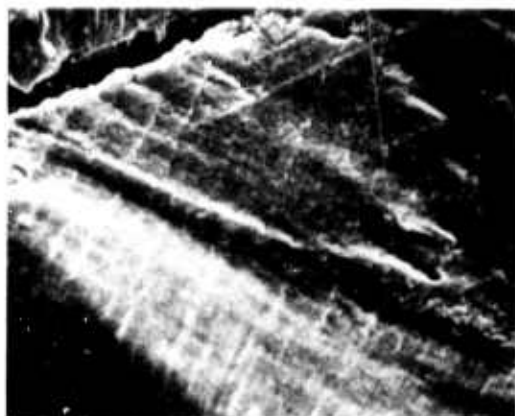
(a)



(b)



(c)

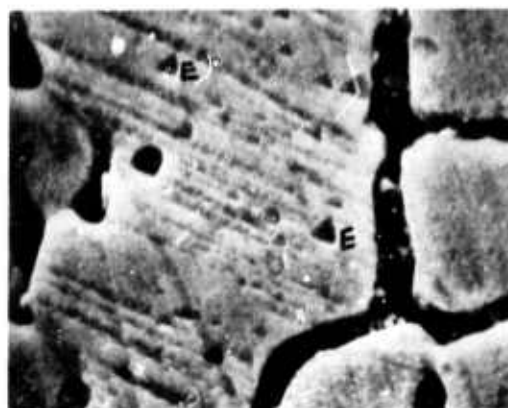


(d)

Fig. 7-21— A-286, Fatigue-crack growth specimen, tested at 77° K (a) 100 X (b) 500 X intergranular failure, fatigue striations, tensile fracture (T) and carbides at boundaries (c) 1000 X (d) detail 25000 X



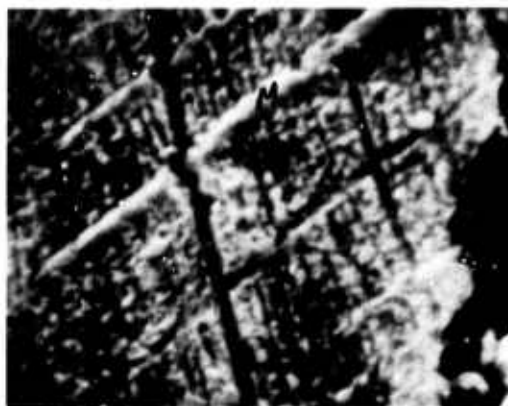
(a)



(b)



(c)



(d)

Fig. 7-22—N-33, SEM micrographs of polished and etched weldment, deformed at R. T. in bending. Evidence of martensitic transformation S: slip lines, M: martensite (accicular) E: etch pits, a-b: 6800, c-d: 13600

8.0 MAGNETIC MEASUREMENTS

The magnetic measurements conducted in this portion of the Westinghouse FY76 program are reported herein. A discussion of the type and extent of these has already been given in the previous Westinghouse report 75-9D4-CRYMT-R2⁽²⁾ (hereafter referred to as R2). Attention is here confined to giving the results on the two alloys A-286 and 21-6-9. Additionally some results on 310SS and Inconel 718 are compared with the work of Efferson and Leonard⁽¹⁾ (E and L).

Table 8.1 sets out the magnetic condition and strengths of the A-286 and 21-6-9. A listing of the various ferromagnetic designation is given in R2.

Table 8.2 compares the magnetic composition of the alloys with their magnetic state at 4.2 K. Excepting the 21-6-9 SMAW and GTAW materials the transition from ferromagnetism to antiferromagnetism is determined by the Mn content. Based on the results contained in R2 the 21-6-9 is expected to be antiferromagnetic with a 9.5% Mn content and A-286 to be ferromagnetic with only 1.7% Mn. The above transition from ferromagnetism to antiferromagnetism would be expected to occur with a composition having ~5% Mn. In contrast, Cr is seen not to have so noticeable an effect on the magnetic state. The weldments 21-6-9 SMAW and GTAW are presumably acquiring their ferromagnetic condition from the filler metal. The absence of any measureable temperature variation in the

ferromagnetism up to 78 K suggests these weldments are likely to be still ferromagnetic at room temperature. In contrast to this the drop in magnetic moment of the A-286 at 78 K to around 300 G is likely to give a paramagnetic state up at room temperature. The magnetic effects of strain on A-286 are not large. The strained sample was taken from the immediate vicinity of a fracture zone of a tensile specimen. Strain produces a small but measureable decrease in the magnetic moment.

Efferson and Leonard⁽¹⁾ have reported magnetic measurements on a number of materials including Inconel 718 and 310SS. For interest and comparison we show in Figures 1 and 2 a comparison of their data and Westinghouse data at 4.2 K on the magnetization versus magnetizing field. We inferred from the report of E and L that their material was solution annealed (SA) base metal. The Westinghouse data on 718 (CW/DA) compares well with the E and L data and is close to the Westinghouse 718 (STDA) data. In the case of 310SS the heat treatments STFC and STQ cause an increase of magnetic moment over the SA heat treatment of E and L. In summary the Westinghouse and E and L data are comparable and where differences exist they probably result from the different heat treatments given to the materials.

Electrical resistivity measurements were not performed on any material in this report. Past experience has shown that electrical resistivity of these stainless steels and superalloys is insensitive to heat treatments and shows little variation with temperature. To within 20% they show a typical resistivity of 100 $\mu\Omega\text{cm}$.

REFERENCES

1. K.R. Efferson and W.J. Leonard, "Magnetic Properties of Some Structural Materials Used in Cryogenic Applications," Oak Ridge National Laboratory, Report ORNL-4150 (Sept. 1967).
2. J.M. Wells, W.A. Logsdon, R. Kossowsky, and Michael R. Daniel, "Structural Materials for Cryogenic Applications," Westinghouse Research Laboratories Report 75-9D4-CRYMT-R2 (Oct. 1975).

Table 8.1. Magnetic Properties of Materials

Material	Condition	Magnetic Condition	Saturation Induction(G)		
			4.2 K	20 K	78 K
A286	Strained	Weakly Ferromagnetic	985	890	318
A286	Unstrained	Weakly Ferromagnetic	1005	919	345
Inconel 718	CW/DA	Weakly Ferromagnetic	990	890	360
21-6-9	As Received	Antiferromagnetic	--	--	--
21-6-9	HR/STWQ	Antiferromagnetic	--	--	--
21-6-9	SMAW	Weakly Ferromagnetic	1240	1240	970
21-6-9	GTAW	Feebly Ferromagnetic	470	470	470

Table 8.2. Comparison of Magnetic Properties
with Composition

Material	Nominal Composition (wt%)				Magnetic Condition at 4.2 K	Induction at 4.2 K(G)
	Mn	Cr	Ni	Fe		
A286	1.7	14.9	25.8	53	Weakly Ferromagnetic	1000
21-6-9	9.5	19.7	7.2	63.2	Antiferromagnetic	--

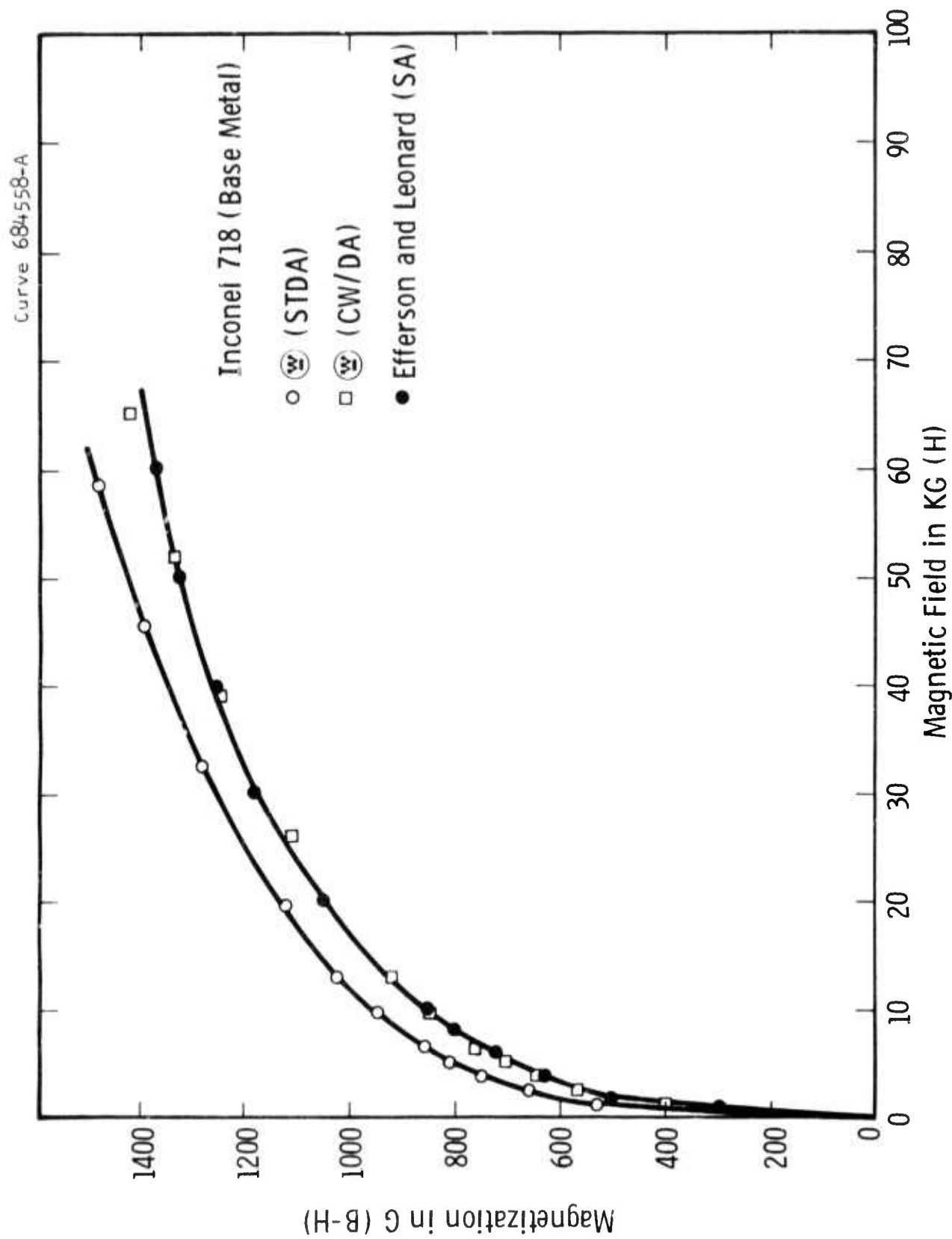


Fig. 1—A comparison of the magnetization versus magnetic field for Inconel 718 from the data of (STDA) and Efferson and Leonard

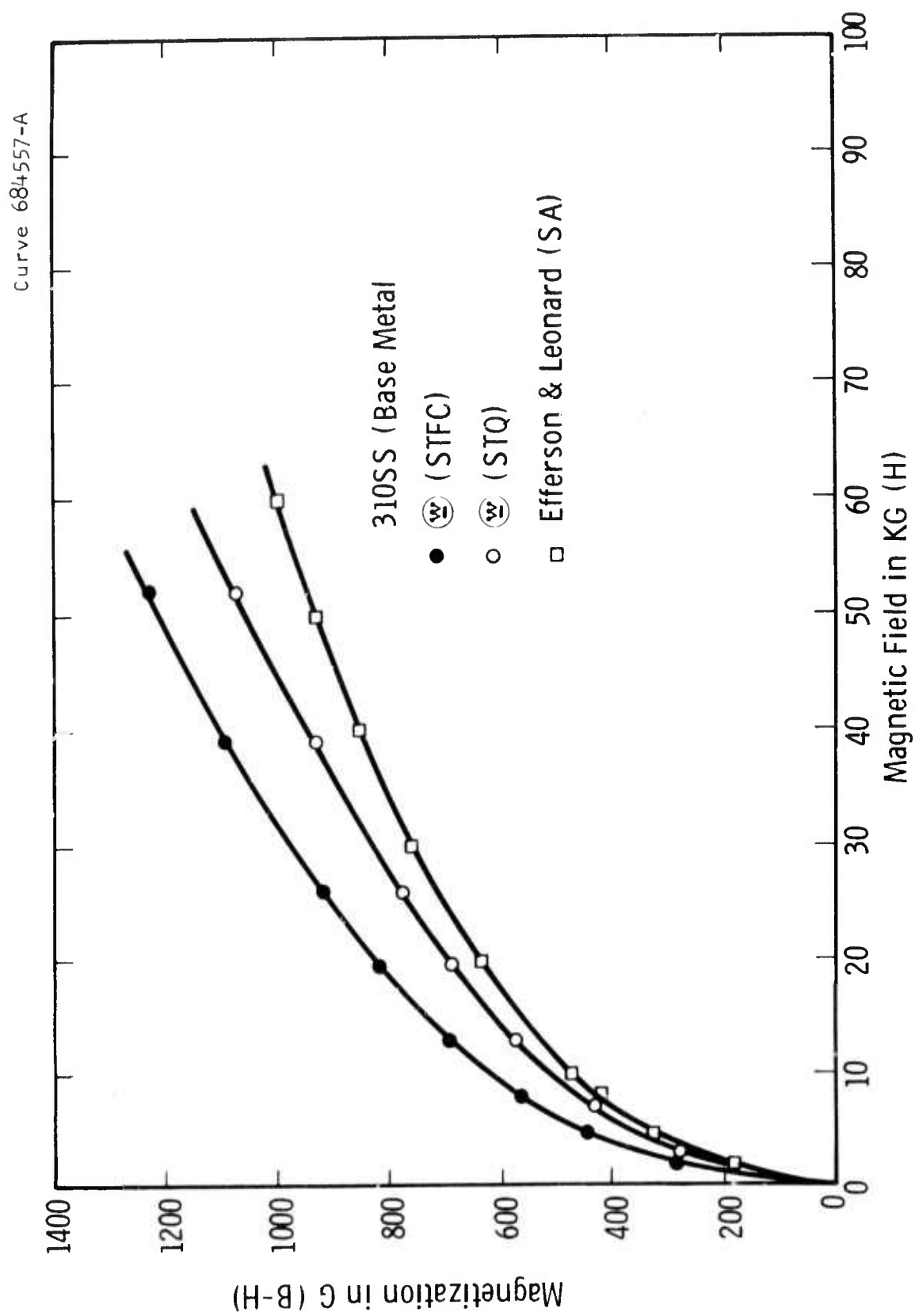


Fig. 2—A comparison of the magnetization versus magnetic field for 310SS from the data of \bar{w} and Efferson and Leonard

ACKNOWLEDGMENT

The authors wish to gratefully acknowledge the following Westinghouse personnel for their respective advice, contributions, and cooperation and encouragement in the conduct of this work:

Dr. J. H. Parker, Jr.	E. T. Wessel
J. L. McCabria	W. A. Pryle
D. C. Litz	D. R. Young
G. D. Cooper	R. R. Hovan
G. G. Lessmann	A. R. Petrush
G. E. Grotke	W. H. Halligan
J. E. Smith	R. C. Brown
W. R. Kuba	M. J. Airgood

In addition, special acknowledgement is extended to:

- (1) The Huntington Alloys Product Division of the International Nickel Company, for providing the Low Expansion Alloy.
- (2) To the Phelps Dodge Copper Products Company for providing the PD-135 Copper Alloy at no charge to the program.
- (3) The USAF/APL Contract F33615-71-C-1591, under which support the data for the Udimet 718 and Cameron Iron A-286 materials were obtained.
- (4) Dr. P. R. Landon of the Lawrence Livermore Laboratory for providing the Pyromet 538 billet material.

Scientific Paper 75-9D4-CRYMT-P3
Proprietary Class: Unrestricted

December 31, 1975

FRACTURE MECHANICS PROPERTIES OF
AUSTENITIC STAINLESS STEELS FOR ADVANCED CRYOGENIC APPLICATIONS

W. A. Logsdon, J. M. Wells, and R. Kossowsky
Westinghouse Research Laboratories
Pittsburgh, Pennsylvania 15235

ABSTRACT

The rise of cryogenic and/or superconducting devices as modern and efficient energy sources has inspired development of the low temperature mechanical and fracture mechanics properties of three structurally stable austenitic stainless steels. These stainless steels included solution treated and quenched (annealed) plus cold worked Kromarc 58, solution treated and quenched (annealed) plus sensitized AISI 310 S and solution treated, quenched and aged A286. Because of their excellent cryogenic fracture toughness properties, both heat treatments of AISI 310 S and solution treated and quenched Kromarc 58 are especially attractive in structural applications where large critical flaw sizes are preferred. Due to superior fatigue crack growth rate properties, A286 is particularly appealing in low temperature structural applications requiring high cyclic lifetimes. Cold worked Kromarc 58 is best utilized in cryogenic structural applications where yield strengths in excess of 200 ksi (1379 MPa) are desired.

INTRODUCTION

The advent and necessity of increasingly more cryogenic and/or superconducting devices⁽¹⁻⁵⁾ in our energy conscious economy has created a strong demand by designers for the material properties necessary to insure immunity from structural failure of these systems. Thus far the most popular candidate materials for structural applications below -320°F (77 K) are austenitic stainless steels and superalloys,⁽¹⁻³⁾ many of which were basically developed for high temperature applications. Recently, a few ferritic based materials were produced which demonstrated good cryogenic fracture toughness properties.⁽⁶⁻⁹⁾ These ferritic based materials are not commercially available, however, and should be regarded as experimental in nature. Obviously, the vast majority of materials suitable for cryogenic structural applications are still inadequately characterized for full confidence in potentially high risk low temperature application areas where fail safe performance is required.

As a result, both mechanical and fracture mechanics material properties of three austenitic stainless steels presently employed in cryogenic structural applications were determined. These stainless steels included solution treated and quenched (annealed) plus cold worked Kromarc 58, solution treated and quenched (annealed) plus solution treated and furnace cooled (sensitized) AISI 310 and solution treated, quenched and aged A286. Tensile, notched tensile, elastic plastic fracture toughness and fatigue crack growth rate tests were

performed at temperatures down to -452°F (4 K). A basic, parametric linear elastic fracture mechanics analysis was also included to assist in grading, selecting and utilizing these materials for future advanced cryogenic structural applications.

MATERIALS

The austenitic stainless steels explored included Kromarc 58,^{*} AISI 310 S and A286. Chemical compositions, heat treatments and processing schedules relative to these materials are presented in Table 1. Starting form for both the Kromarc 58 and AISI 310 S were plates with respective thicknesses of 1.0 in. (2.54 cm) and 0.625 in. (1.6 cm) while the A286 was received as a 5.5 in. (14 cm) square forging. Kromarc 58, a wrought version of the cast Kromarc 55 stainless steel formally utilized in large cryogenic bubble chambers,⁽¹⁰⁾ was examined in both the solution treated and quenched (STQ) plus cold worked (CW) conditions. Kromarc 58, a fully austenitic stainless steel, is normally^{*} not hardenable by thermal treatment and as such proved an excellent material with which to evaluate the influence of cold work on strength and fracture properties at cryogenic temperatures. Initial one-inch thick plates of Kromarc 58 were cold rolled to a thirty percent reduction in thickness. Reductions were made in approximately 0.02 in. (0.05 cm) increments with no intermediate anneals employed. No evidence of cracking was detected during or subsequent to the cold rolling operations.

* Kromarc 58 is a registered trademark of the Westinghouse Electric Corporation.

* While not normally considered hardenable by heat treatment, Hull⁽¹¹⁾ has reported a substantial hardness increase (~ 70 points DPH) obtained in cold worked material followed by aging for 4 hrs at 600° to 1000°F (589 to 811 K).

A common question regarding cold working is whether an anisotropic texture exists in the as cold-rolled plate sufficient to cause an appreciable degradation of mechanical or fracture properties under specific orientations of load application. To determine specifically the nature and extent of any such texturing, a series of automatic x-ray pole figures were conducted essentially according to the ASTM Standard Method for Preparing Quantitative Pole Figures of Metals (E 81-63). Details of the pole figure analysis are available through Ref. 12. It is sufficient to state that a fairly complex deformation texture does develop in a nitrogen strengthened austenitic stainless steel parallel to the rolling direction after approximately thirty percent cold work. Furthermore, the character of this deformation did alter through the thickness of the Kromarc 58 plate. Effects of texturing were studied by conducting mechanical, fracture and fatigue crack growth rate tests on specimens loaded either normal or parallel to the plate rolling direction (orientations T-L and L-T per ASTM E399-74, respectively).

AISI 310 S, a low carbon (0.08 C max.) version of AISI 310 stainless steel (0.25 C max.) has been structurally utilized in a 5 MVA Westinghouse superconducting generator.⁽¹⁾ AISI 310 S was studied in both the STQ and solution treated and furnace cooled (STFC, sensitized) conditions. Since sensitizing (slow cooling) has a similar influence on base material properties as welding, the sensitizing heat treatment provided an estimate of the expected degradation in fracture mechanics properties in the heat affected zones of weldments.

A286 stainless is a precipitation hardenable austenitic alloy often referred to as ASTM A453 and sometimes designated AISI 660. This alloy can be strengthened via heat treatment and was analyzed in the solution treated, quenched and aged (STQA) condition. A286 has also been structurally utilized in cryogenic environments.

EXPERIMENTAL PROCEDURES

Fracture Toughness

The well documented linear elastic (K_{Ic}) fracture criterion with its inherent plane strain specimen size limitation cannot produce valid fracture toughness results (per the ASTM Test for Plane Strain Fracture Toughness of Metallic Materials, E399-74) on tough austenitic stainless steels unless specimens of very large thickness are employed, which in turn are not representative of the cross-sectional thicknesses found in actual cryogenic structures. Furthermore, if a failure should occur, proper design of cryogenic structures or components would cause these structures or components to fail plastically (elastic plastic fracture) as opposed to catastrophically (linear elastic fracture). Therefore, the fracture toughness of Kromarc 58, AISI 310 S and A286 was obtained via the elastic plastic (J_{Ic}) fracture criterion^(13,14) and associated resistance curve test technique.⁽¹⁵⁾

A thorough description of the resistance curve test technique is given in Ref. 15. Briefly, the testing procedure is to: (a) load a deeply notched fatigue precracked compact specimen of ASTM E399-74 design to a predetermined J level in the region where crack extension is anticipated; (b) unload and heat tint the specimen to mark the crack; (c) pull the specimen apart and measure crack extension (Δa) from the exposed fracture surface. J is calculated from the load-displacement record and specimen dimensions using the approximation of Rice, et al.⁽¹⁶⁾ The result of a test series is plotted as J versus Δa .

In the majority of J tests, some measurable deformation at the crack tip precedes material separation. Apparent crack extension therefore includes a contribution due to deformation in addition to actual material separation.

To account for apparent crack extension due to deformation, the straight line given by the equation $J = 2\sigma_f \Delta a$ was plotted on each J versus Δa graph, where σ_f is a flow stress midway between the material's yield and ultimate stresses. The intersection of the J versus Δa curve and the straight line of slope $2\sigma_f$ represents the initial point of material separation and as such is the critical value of J (J_{Ic}). Corresponding K_{Ic} values were calculated from the relationship between elastic plastic and linear elastic fracture mechanics parameters. (13,17)

All fracture toughness tests were conducted on 0.5 in. (1.27 cm) thick compact tension (CT) specimens, except for the 1.0 in. (2.54 cm) thick A286 specimens tested at room temperature. The tests were performed on a servo-hydraulic test machine using stroke control at a ram rate of 0.005 in./sec. (0.127 m/sec). All fracture toughness specimens were precracked at room temperature in accordance with ASTM E399 requirements on maximum fatigue stress intensity. Displacement was measured with a hermetically sealed linear variable differential transformer (LVDT) attached to the specimen front face and immersed along with the specimen in the cryogen.

Crack Growth Rate

All fatigue crack growth rate tests were conducted on half inch (1.27 cm) thick wedge open loading (WOL) geometry compact tension specimens which were precracked at room temperature in accordance with

ASTM E399 requirements on maximum fatigue stress intensity. These tests were performed on a universal hydraulic fatigue machine under sinusoidal tension loading. The maximum alternating load (ΔP) was maintained constant throughout each individual test. Test frequency equalled 10 Hertz. Since crack growth rates can be influenced by abrupt temperature changes, the crack growth rate was allowed to stabilize before data were accepted as valid.

Instantaneous crack length was determined by first measuring specimen crack opening displacement with an LVDT attached to the specimen front face and finally transforming this crack opening displacement value via specimen compliance into crack length. Specimen compliance was determined from a test procedure originally developed by Novak and Rolfe.⁽¹⁸⁾ Growth rates were established by means of a computerized curve-fitting analysis of the crack length versus number of elapsed cycles data.⁽¹⁹⁾

Compact tension (CT) and WOL specimen orientations according to the Crack Plane Orientation Identification Code per ASTM Test Method E399-74 are included in Table 3.

RESULTS

Tensile

Smooth-bar uniaxial tensile tests were conducted to determine the 0.2 percent offset yield strength, ultimate strength, reduction in area and elongation of Kromarc 58, AISI 310 S and A286 stainless steels. Tensile specimen geometry was 0.20 in. (0.51 cm) diameter with a 1.00 in. (2.54 cm) gauge length. All tensile as well as notched tensile specimens were oriented so their loading directions matched those of the corresponding CT and WOL specimens. For the most part, each tensile data point is the average of two tensile tests.

The tensile properties of STQ and cold worked Kromarc 58 are presented in Fig. 1. Cold working Kromarc 58 produced a substantial increase in yield and ultimate strengths, especially at room temperature, combined with a moderate drop in area reduction and a substantial decrease in elongation. Yield and ultimate strengths of Kromarc 58 were essentially independent of specimen orientation although cold worked Kromarc 58 specimens loaded parallel to the rolling direction realized moderately superior area reductions and slightly greater elongations at all test temperatures.

Figure 2 illustrates the tensile properties of STQ and sensitized AISI 310 S. Compared with Kromarc 58 and A286 the 310 S demonstrated the largest temperature dependence of both yield and ultimate strength. Sensitizing 310 S produced an insignificant strength

decrease, although, except for room temperature elongation, the ductility of sensitized 310 S is inferior to that of STQ 310 S. The ductility displayed by 310 S is substantial even at cryogenic temperatures, however, and is comparable with that of Kromarc 58.

The -452°F (4 K) values of yield strength, ultimate strength and elongation developed at Westinghouse on AISI 310 S compare quite closely with those published by Nachtigall.⁽²⁰⁾ In addition, our strength values are slightly greater than those reported by Tobler, et al. at all three test temperatures.⁽²¹⁾

The tensile properties of STQA A286 are illustrated in Fig. 3. Unlike Kromarc 58 and 310 S, the yield and ultimate strengths of A286 increased only moderately with decreasing temperature. A common criticism of many austenitic materials concerns their strength retention with increasing temperatures. Clearly, the moderate temperature dependence of both the yield and ultimate strengths demonstrated by A286 gives this material a decided advantage when compared with either STQ Kromarc 58 or STQ and sensitized 310 S. Whereas the strength superiority of A286 is modest at best at liquid helium temperature, its strength advantage increases significantly as temperature increases toward ambient. The ductility of A286 is relatively constant with temperature and, although comparable with that reported for Inconel X750⁽²²⁾ and Inconel 706,⁽²³⁾ is well below that demonstrated by Kromarc 58 and 310 S.

A major area of concern in dealing with austenitic stainless steels for structural applications at cryogenic temperatures (especially the 300 series) is their ability to remain stable relative to martensitic transformation when repeatedly cooled to cryogenic temperatures,

plastically strained or subjected to sensitizing heat treatments. For example, Guntner and Reed reported that the martensitic transformation in austenitic stainless steels can produce a wide range of mechanical properties, depending on the test variables and the initial alloy condition.⁽²⁴⁾ Fortunately, several studies which examined the structural and magnetic stability of austenitic stainless steels have been completed.⁽²⁴⁻²⁷⁾ It is interesting to note that Larbalestier and King investigated the structural and magnetic properties of fifteen austenitic stainless steels and found that only the high alloy 310 and Kromarc 55 steels remained fully austenitic after deformation to rupture at -452°F (4 K).⁽²⁷⁾ To conclude, no austenite to martensite structural transformations were observed by the authors on the Kromarc 58, AISI 310 S or A286 stainless steels included in the present work.

Notched Tensile

Notched tensile tests serve to screen the notch toughness of materials in terms of a comparison parameter defined as the ratio of notched tensile fracture strength to the unnotched tensile yield strength of a particular material for a specific notch-acuity. Increasing values of the ratio above 1.0 are considered to indicate increasing ability of the material for plastic deformation at the notch tip. Stated alternatively, increasing values of the ratio above 1.0 can be utilized as a measure of the material's resistance to catastrophic brittle fracture.

In all cases the root radius at the bottom of a particular test specimen's sharp V-notch was adjusted to yield a stress concentration factor (K_t) equivalent to 10. It should be pointed out that the notched tensile fracture strength was calculated by dividing the maximum load

experienced by a test specimen, or in a few cases where the load dropped slightly before failure dividing the fracture load, by its original as opposed to final cross sectional area. This was largely due to the great difficulty in accurately measuring the extremely small change in test section diameter (hence cross-sectional area) experienced by the test specimen.

The notched tensile properties of Kromarc 58 and AISI 310 S stainless steels are summarized on Table 2. No notched tensile tests were performed on A286. For the two materials investigated regardless of heat treatment, processing or test temperature, the ratio of notched tensile fracture strength to tensile yield strength was always greater than one, the minimum value equaling 1.6.

Fracture Toughness

The fracture toughness values of Kromarc 58, AISI 310 S and A286 stainless steels are summarized in Table 3 while the associated resistance curves are illustrated in Figs. 4 through 6, respectively. For comparison purposes, the ratios $\frac{K_{Ic}}{\sigma_{ys}}$ and $\left(\frac{K_{Ic}}{\sigma_{ys}}\right)^2$ are also included in Table 3. Typically the material with the highest $\frac{K_{Ic}}{\sigma_{ys}}$ ratio is the toughest material for a given application. (28) The plane strain crack size factor $\left(\frac{K_{Ic}}{\sigma_{ys}}\right)^2$ provides a measure of toughness that accounts in a single parameter for the interactions of K_{Ic} and strength on crack size tolerance. (29,30)* Stated alternatively, when conducting a parametric

*The crack size factor is not related to critical crack size at a stress equal to the yield strength but only under small-scale yielding, that is, at applied stresses appreciably below the yield strength. (29,30)

fracture mechanics analysis (that is, the applied stress is considered a fixed percentage of the particular material's yield strength), the critical defect size for failure in one cycle of loading will be proportional to the crack size factor.⁽²⁸⁾

While cryogenic structural applications certainly exist where a yield strength in excess of 200 ksi (1379 MPa) is desirable and cold worked Kromarc 58 is an ideal choice, to obtain the 35 percent strength increase which resulted from cold working the Kromarc 58 necessitated an even larger sacrifice (42 percent decrease) in fracture toughness. Also, cold worked Kromarc 58 was the only stainless steel to yield a crack size factor less than one. Fortunately, at this level of cold work (30 percent) the Kromarc 58 does not contain an especially weak fracture plane. The -452°F (4 K) fracture toughness for the T-L and L-T orientations varies by only $8.7 \text{ ksi}\sqrt{\text{in.}}$ ($9.6 \text{ MPa}\sqrt{\text{m}}$). The corresponding difference in yield strength equals just 2.4 ksi (16.5 MPa).

Of the three stainless steels investigated, STQ AISI 310 S produced the greatest fracture toughness and largest crack size factor in combination with its moderate yield strength. The -452°F (4 K) fracture toughness value for STQ 310 S is slightly higher than that reported by Tobler, et al.⁽²¹⁾ on commercial annealed 310 S at -320°F (77 K). Sensitizing the 310 S produced a significant decrease (31 percent) in liquid helium temperature fracture toughness although the corresponding strength levels remained unchanged. Even so, the crack size factor for sensitized 310 S is still greater than those which represent Kromarc 58 and A286.

Recall, the sensitizing heat treatment was employed to provide an estimate of the expected degradation in fracture mechanics properties in the heat affected zones of weldments. It is interesting to note that tests at -452°F (4 K) on non post weld heat treated AISI 310 S shielded metal arc welds^(12,31) produced a weld fusion zone fracture toughness of $106.5 \text{ ksi}\sqrt{\text{in.}}$ ($117.9 \text{ MPa}\sqrt{\text{m}}$), which was 35 percent below that of sensitized 310 S.

Both the A286 stainless steel liquid helium temperature fracture toughness and crack size factor, although quite attractive from a fracture mechanics structural reliability standpoint, surpass only those relative to cold worked Kromarc 58. Also, the fracture toughness of A286 is 11 percent less at room temperature than at liquid helium temperature. This trend toward slightly decreasing fracture toughness with increasing temperature was further exemplified by additional J tests at 400°F (477 K) and 800°F (700 K).⁽³²⁾

Reed, et al.⁽³³⁾ obtained fracture toughness values ranging from $107 \text{ ksi}\sqrt{\text{in.}}$ ($118 \text{ MPa}\sqrt{\text{m}}$) to $114 \text{ ksi}\sqrt{\text{in.}}$ ($126 \text{ MPa}\sqrt{\text{m}}$) over the temperature range -452°F (4 K) to 75°F (297 K) on an A286 stainless steel of almost identical chemical composition and heat treatment. Although Reed's fracture toughness and yield strength values were significantly below the Westinghouse values regardless of temperature, Reed's specimens were machined in the T-S orientation while our specimens were oriented in the L-T direction. Although this variation in material properties may be attributed to material structural differences, most likely the two distinct specimen orientations accounted for the large variation in mechanical and fracture toughness properties.

Despite this large variation in material properties, both steels demonstrated a moderate insensitivity of fracture toughness to temperature over the temperature range -452°F (4 K) to 75°F (297 K). This behavior is typical of structurally stable austenitic materials whereby the fracture toughness essentially remains constant with temperature. (12,21-23,33)

Crack Growth Rate

The fatigue crack growth rate (FCGR) data generated on Kromarc 58, AISI 310 S and A286 stainless steels are presented in Figs. 7 through 9, respectively. The raw $\log \frac{da}{dN}$ versus $\log \Delta K$ data relative to each of these materials demonstrated the nearly linear relationship typical of most FCGR data. Since this linear relationship existed, the crack growth rate data was stated in terms of the generalized fatigue crack growth rate law developed by Paris. (34) This crack growth rate law is expressed as:

$$\frac{da}{dN} = C_0 \Delta K^n \quad (1)$$

where $\frac{da}{dN}$ is the rate of crack growth, C_0 is an intercept constant determined from the $\log \frac{da}{dN}$ versus $\log \Delta K$ plot, n is the slope of the log-log plot and ΔK is the stress intensity factor range.

The cryogenic fatigue crack growth rate properties of Kromarc 58 are independent of whether the Kromarc 58 was solution treated and quenched or cold worked. This is quite unlike its yield strength and fracture toughness properties, which respectively increased 35 percent and decreased 42 percent at -452°F (4 K) when cold worked. At room temperature, however, the growth rate of fatigue cracks is faster in STQ as opposed to cold worked Kromarc 58. Also, for both conditions of Kromarc 58 there is no measurable difference in growth rates between -320°F (77 K) and -452°F (4 K).

Furthermore, the room temperature and cryogenic FCGR properties of cold worked Kromarc 58 are independent of specimen orientation. Therefore, Kromarc 58 can be cold worked without creating specially oriented planes with exceptionally low resistance to catastrophic fracture or fatigue crack propagation.

Finally, the growth rate of fatigue cracks in Kromarc 58 at room temperature is significantly greater than at cryogenic temperatures regardless of test specimen orientation or whether the Kromarc 58 was solution treated and quenched or cold worked. This behavior is further substantiated by the data of Fig. 9, which reveals that the growth rate of fatigue cracks in A286 is directly proportional to temperature; that is, the higher the temperature the greater the fatigue crack propagation rate. James has reported a direct extension of this behavior over the temperature range 75°F (297 K) to 1000°F (811 K) on a similar A286 stainless steel.⁽³⁵⁾ Furthermore, higher growth rates at ambient as opposed to cryogenic temperatures were previously observed by Westinghouse on Inconel X750^(12, 22) and on AISI 310 S,⁽²¹⁾ A286^(21, 33) and Inconel X750⁽²¹⁾ by the National Bureau of Standards Cryogenic Division. Therefore, a general trend previously reported applicable to structurally stable austenitic materials has been varified whereby the growth rate of fatigue cracks at room temperature is substantially greater than at cryogenic temperatures.

Tobler has reported fatigue crack growth rates on a 21-6-9 stainless steel faster at -452°F (4 K) than at -320°F (77 K) or room temperature.⁽³⁶⁾ In addition, the fracture toughness of this stainless steel decreased tremendously with decreasing temperature over the

temperature range 75°F (297 K) to -452°F (4 K).⁽³⁷⁾ During plastic deformation at room temperature this alloy experienced little martensitic phase transformation, but at -320°F (77 K) and -452°F (4 K) it transformed extensively to hcp and bcc martensitic products and is therefore not a structurally stable austenitic stainless steel.⁽³⁷⁾

The FCGR properties of AISI 310 S are, like its strength properties, independent of heat treatment (see Fig. 8). Also, there is no measurable difference in growth rates between -320°F (77 K) and -452°F (4 K) for this material.

The cryogenic FCGR properties developed through this investigation on 310 S compared closely with those published by Tobler, et al. on a commercial annealed 310 S.^(21, 38) Although this work contains no room temperature FCGR data on 310 S, Tobler reported room temperature growth rates on 310 S significantly faster than those at cryogenic temperatures.⁽²¹⁾

A comparison of the room and liquid helium temperature FCGR properties of Kromarc 58, AISI 310 S and A286 is presented in Fig. 10. At -452°F (4 K), the most favorable FCGR properties are associated with A286, followed in order of increasing growth rates by Kromarc 58 and 310 S. At room temperature, the FCGR properties of cold worked Kromarc 58 and STQA A286 are essentially identical while the fastest growth rate is demonstrated by STQ Kromarc 58.

DISCUSSION - EXAMPLE PROBLEM

To more appropriately grade, select and utilize these austenitic stainless steels for structural service in cryogenic environments a basic linear elastic fracture mechanics analysis was conducted employing the -452°F (4 K) mechanical and fracture mechanics data developed through this investigation. Each material was proposed for a structural application where the applied nominal and cyclic stresses were assumed equivalent to 75 percent of the particular material's yield strength ($\sigma/\sigma_{ys} = 0.75$).

The defect geometry considered was a 10 to 1 length to depth ratio elliptical surface crack oriented with the major crack plane perpendicular to a uniform tension stress field. The pertinent stress intensity expression for this configuration is⁽³⁹⁾

$$K_I^2 = \frac{1.21 a \pi \sigma^2}{Q} \quad (2)$$

where K_I = nominal stress intensity factor
a = surface crack depth
 σ = applied nominal stress
Q = flaw shape parameter (from Fig. 11).

The flaw shape parameter (Q) permits evaluation of defect severity by accounting for surface or internal defects with various length to depth ratios. The flaw shape parameter Q is obtained from Fig. 11, which also illustrates prototype surface and internal defects and the necessary

dimensions required for obtaining length to depth ratios. For the case of a 10 to 1 length to depth ratio elliptical surface defect where σ/σ_y equals 0.75, Q equals 0.98.

The initial step in conducting a fracture mechanics analysis is to calculate the critical flaw sizes necessary to cause failure of our hypothetical stainless steel structures in one cycle of loading when subjected to a liquid helium environment at applied stress levels equivalent to 75 percent of the appropriate material's yield strength. If the terms in Eq. 2 are rearranged and K_I and "a" are respectively set equal to K_{Ic} and a_{cr} , the following critical flaw size expression is obtained

$$a_{cr} = \frac{K_{Ic}^2 Q}{1.21 \pi \sigma^2} \quad (3)$$

Substituting the appropriate values of applied stress (see Table 4), K_{Ic} (see Table 3) and Q (0.98) into the above expression yields the critical flaw sizes presented in Table 4.

By combining these critical flaw sizes with the -452°F (4 K) fatigue crack growth rate properties of Kromarc 58, AISI 310 S and A286 it is possible to compute the number of elapsed cycles (start up-shut down cycles) for an existing subcritical flaw to grow to failure. Wilson has developed a generalized cyclic life expression which readily determines the number of cycles required for an existing defect to grow to the critical flaw size.⁽²⁸⁾ This expression is presented below

$$N = \frac{2}{(n-2)C_o M^{n/2} \Delta\sigma^n} \left[\frac{1}{a_i^{(n-2)/2}} - \frac{1}{a_{cr}^{(n-2)/2}} \right] \text{ for } n \neq 2 \quad (4)$$

$$N = \frac{1}{C_o M \Delta\sigma^2} \ln \frac{a_{cr}}{a_i} \text{ for } n = 2$$

where N = number of cycles to failure

n = slope of the log (da/dN) vs log ΔK curve

C_o = intercept constant from log (da/dN) vs log ΔK curve

a_i = initial flaw size

a_{cr} = critical flaw size

$\Delta\sigma$ = alternating stress range

M = flaw shape and geometry parameter [for surface defects,

$$M = (1.21 \pi/Q)].$$

The above expression is applicable to those loading situations where the relationship between applied load, flaw size and stress intensity factor has the form of $K_I = \sigma(Ma)^{1/2}$. In addition, it is assumed that the cyclic stress range ($\Delta\sigma$) remains constant throughout the component life and that the mean stress does not influence the results.

Solving this expression for N at the various cyclic stress ranges of interest and for a_i values ranging from the minimum detectable flaw size to the appropriate critical flaw size develops cyclic life curves which relate the maximum initial allowable flaw size to the number of cycles required to cause failure at different stress levels.

The resulting cyclic life curves for hypothetical structures manufactured from Kromarc 58, AISI 310 S and A286 stainless steels are presented in Fig. 12. These cyclic life curves represent the most convenient form of presenting fatigue life information because either: (a) the total life can readily be determined from a knowledge of the defect size known or assumed to be present at the start of life or; (b) the initial allowable flaw sizes can be ascertained based on a desired cyclic structural lifetime. For example, initial allowable flaw sizes based on structural lifetimes of 1000 and 100 cycles of alternating applied stress are included in Table 4.

If cyclic lifetimes greater than 650 cycles of alternating applied stress are desired for our hypothetical stainless steel structures, the superior -452°F (4 K) FCGR properties of A286 make this material the logical choice from a fracture mechanics structural reliability standpoint. For cyclic lifetimes less than 150 cycles, however, the superior cryogenic fracture toughness properties of both heat treatments of AISI 310 S plus STQ Kromarc 58 make these materials more desirable than A286. Obviously, cold worked Kromarc 58 is best utilized when a yield strength level in excess of 200 ksi (1370 MPa) is required. Naturally, any techniques employed to inspect our hypothetical stainless steel structures must be capable of locating and defining some defect smaller than the specified initial allowable flaw size, the exact size of which depends on the safety factors desired. Therefore, it is up to the designer to input whatever safety factors (margins of error) he desires for a specific application.

CONCLUSIONS

1. Solution treated and quenched (annealed) plus cold worked Kromarc 58, solution treated and quenched (annealed) plus sensitized AISI 310 S and solution treated, quenched and aged A286 stainless steels all demonstrated good low temperature mechanical, fracture toughness and fatigue crack growth rate properties and as a result are well suited to cryogenic structural applications requiring service at cryogenic temperatures.
2. Both heat treatments of AISI 310 S and STQ Kromarc 58 are especially attractive in structural applications where large critical flaw sizes as opposed to high cyclic lifetimes are preferred because of their excellent cryogenic fracture toughness properties.
3. Due to superior fatigue crack growth rate properties, A286 is particularly appealing in low temperature structural applications requiring high cyclic lifetimes.
4. Cold worked Kromarc 58 is best utilized in low temperature structural applications where yield strengths in excess of 200 ksi (1379 MPa) are desired.
5. Cryogenic and ambient fatigue crack growth rate tests on Kromarc 58 and A286 further verified a general trend previously reported applicable to structurally stable austenitic materials whereby the growth rate of fatigue cracks at room temperature is substantially greater than at cryogenic temperatures.

6. Kromarc 58 can be cold worked (30 percent) without creating specially oriented planes with exceptionally low resistance to catastrophic fracture or fatigue crack propagation.
7. Sensitizing AISI 310 S produced a 31 percent decrease in cryogenic fracture toughness although the low temperature strength and fatigue crack growth rate properties were unchanged.

ACKNOWLEDGEMENTS

The authors gratefully acknowledge Messrs. W. H. Prvle, D. R. Young, R. R. Hovan, A. R. Petrush, W. H. Halligan and R. C. Brown for their contributions to the experimental phases of this investigation.

This work was supported in part by National Bureau of Standards (NBS) Contract CST-8304. The views and conclusions contained in this document are those of the authors and should not be interpreted as necessarily representing the official policies, either expressed or implied, of the Advanced Research Projects Agency or the United States Government.

REFERENCES

1. Mole, C. J. and Sterrett, C. C., "A Superconducting Machine for Central Station Power Generation," Proceedings of the American Power Conference, Vol. 35, 1973, pp. 1035-1047.
2. Blaugher, R. D., Fagan, T. J., Parker, J. H., Jr., Wells, J. M. and McCabria, J. L., "A High Speed Superconducting Generator," Proc. Intl. Cryogenic Engineering Conference, 1974, Kyoto, Japan (to be published).
3. Parker, J. H., Jr., Blaugher, R. D., Patterson, A., Vecchio, P. D. and McCabria, J. L., "A High Speed Superconducting Rotor," Westinghouse Scientific Paper 74-8J2-SCGEN-P2, October 1974.
4. Kirtley, J. L., Jr., Smith, J. L., Jr., Thullen, P. and Woodson, H. H., "MIT-EEI Program on Large Superconducting Machines," Proc. IEEE, Vol. 61, No. 1, January 1973, pp. 112-115.
5. Smith, J. L., Jr., Kirtley, J. L., Jr. and Thullen, P., "Superconducting Rotating Machines," IEEE Trans. on Magnetism, MAG-11, No. 2, March 1975.
6. Jin, S., Morris, J. W., Jr. and Zackay, V. F., "An Iron-Nickel-Titanium Alloy with Outstanding Toughness at Cryogenic Temperatures," Univ. of California, Berkeley, Report MSE 73-2, July 1973.
7. Jin, S., Whitaker, B., Morris, J. W., Jr. and Zackay, V. F., "Cryogenic Toughness Through Microstructure Control in an Iron-Nickel-Titanium Alloy," Properties of Materials for Liquefied Natural Gas Tankage, ASTM STP 579, American Society for Testing and Materials, 1975, pp. 348-360.

8. Schanfein, M. J., Yokota, M. J., Zackay, V. F., Parker, E. R. and Morris, J. W., Jr., "Cryogenic Properties of Iron-Manganese and Iron-Manganese-Chromium Alloys," Properties of Materials for Liquefied Natural Gas Tankage, ASTM STP 579, American Society for Testing and Materials, 1975, pp. 361-377.
9. Jin, S., Hwang, S. K. and Morris, J. W., Jr., "Comparative Fracture Toughness Testing of Cryogenic Alloys at Liquid Helium Temperature," University of California, Berkeley, Technical Report No. 5, ONR Contract No. N00014-69-A-0200-1062, NR031-762, August 1974.
10. Goodzeit, C. L., "Evaluation of Stainless Steel Casting Alloys for Cryogenic Service in the 80-Inch Liquid-Hydrogen Bubble Chamber," Advances in Cryogenic Engineering, Vol. 10, Paper A-3, 1965, pp. 26-36.
11. Hull, F. C., "Cryogenic Tensile Properties of Cold Rolled Kromarc 58 Stainless Steel Sheet," Westinghouse Research Report 67-1D6-KROMA-R1, May 1967.
12. Wells, J. M., Logsdon, W. A., Kossowsky, R. and Daniel, M. R., "Structural Materials for Cryogenic Applications, Third Semi-annual Technical Report," Westinghouse Research Report 75-9D4-CRYMT-R1, March 1975.
13. Begley, J. A. and Landes, J. D., "The J Integral as a Fracture Criterion," Fracture Toughness, Proceedings of the 1971 National Symposium on Fracture Mechanics, Part II, ASTM STP 514, American Society for Testing and Materials, 1972, pp. 1-20.

14. Landes, J. D. and Begley, J. A., "The Effect of Specimen Geometry on J_{Ic} ," Fracture Toughness, Proceedings of the 1971 National Symposium on Fracture Mechanics, Part II, ASTM STP 514, American Society for Testing and Materials, 1972, pp. 24-39.
15. Landes, J. D. and Begley, J. A., "Test Results from J-Integral Studies: An Attempt to Establish a J_{Ic} Testing Procedure," Fracture Analysis, ASTM STP 560, American Society for Testing and Materials, 1974, pp. 170-186.
16. Rice, J. R., Paris, P. C. and Merkle, J. G., "Some Further Results of J-Integral Analysis and Estimates," Progress in Flaw Growth and Fracture Toughness Testing, ASTM STP 536, American Society for Testing and Materials, 1973, pp. 231-245.
17. Begley, J. A., Landes, J. D. and Wessel, E. T., "Fracture Mechanics, A Practical Tool for Preventing Failures," Presented at the Third International Conference on Fracture, München, Germany, April 1973.
18. Novak, S. R. and Rolfe, S. T., "Modified WOL Specimen for K_{Isc} Environmental Testing," Journal of Materials, JMLSA, Vol. 4, No. 3, September 1969, pp. 701-728.
19. Federowicz, A. J. and Powell, B. A., "A Computer Program to Obtain a Min-Max Regression Model by Linear Programming," Unpublished Westinghouse Research data.
20. Nachtigall, A. J., "Comparison of Tensile Properties of 304 L and 310 S Stainless Steels in Liquid Helium," NASA Technical Memo TM-X-52703, October 1969.

21. Tobler, R. L., Mikesell, R. P., Durcholz, R. L. and Reed, R. P.,
"Fatigue and Fracture Toughness Testing at Cryogenic Temperatures,"
in Semi-annual Report on Materials Research in Support of Super-
conducting Machinery, NBSIR 74-393, National Bureau of Standards,
October 1974, pp. 57-121.
22. Logsdon, W. A., "Cryogenic Fracture Mechanics Properties of Several
Manufacturing Process/Heat Treatment Combinations of Inconel X750,"
Presented at the International Cryogenic Materials Conference,
Kingston, Ontario, July 1975.
23. Wells, J. M., Logsdon, W. A., Kossowsky, R. and Daniel, M. R.,
"Structural Materials for Cryogenic Applications, Fourth Semi-annual
Technical Report," Westinghouse Research Report 75-9D4-CRYMT-R2,
October 1975.
24. Guntner, C. J. and Reed, R. P., "The Effect of Experimental Variables
Including the Martensitic Transformation on Low Temperature Mechanical
Properties of Austenitic Stainless Steels," Transactions of the ASM,
Vol. 55, 1962, pp. 399-419.
25. Watson, J. F. and Christian, J. L., "A Study of Austenite Decomposition
at Cryogenic Temperatures," Transactions of the Metallurgical Society
of AIME, Vol. 224, October 1962, pp. 998-1005.
26. Bhandarkar, D., Zackay, V. F. and Parker, E. R., "Stability and
Mechanical Properties of Some Metastable Austenitic Steels,"
Metallurgical Transactions, Vol. 3, October 1972, pp. 2619-2631.

27. Larbalestier, D. C. and King, H. W., "Austenitic Stainless Steels at Cryogenic Temperatures: 1 - Structural Stability and Magnetic Properties," Cryogenics, Vol. 13, March 1973, pp. 160-168.
28. Wessel, E. T., Clark, W. G. and Wilson, W. K., "Engineering Methods for the Design and Selection of Materials Against Fracture," U. S. Army Tank-Automotive Center Report AD No. 801005, June 1966.
29. Brown, W. F., Jr. and Srawley, J. E., "Commentary on Present Practice," Review of Developments in Plane Strain Fracture Toughness Testing, ASTM STP 463, American Society for Testing and Materials, 1970, pp. 216-248.
30. Vishnevsky, C. and Steigerwald, E. A., "Plane Strain Fracture Toughness of Some Cryogenic Materials at Room and Subzero Temperatures," Fracture Toughness Testing at Cryogenic Temperatures, ASTM STP 496, American Society for Testing and Materials, 1971, pp. 3-26.
31. Wells, J. M., Logsdon, W. A. and Kossowsky, R., "Evaluation of Austenitic Stainless Steel Weldments for Advanced Cryogenic Applications," Westinghouse Research data, to be published.
32. Sheinker, A. A. and Logsdon, W. A., "Mechanical Properties and Fracture Toughness of Four Pressurized Water Reactor Structural Alloys," Unpublished Westinghouse Research data, 1975.
33. Reed, R. P., Tobler, R. L. and Mikesell, R. P., "The Fracture Toughness and Fatigue Crack Growth Rate of an Fe-Ni-Cr Superalloy at 298, 76, and 4 K," Presented at the International Cryogenic Materials Conference, Kingston, Ontario, July 1975.

34. Paris, P. C., "The Fracture Mechanics Approach to Fatigue," Proc. Tenth Sagamore Army Materials Research Conference, August 1963, Syracuse University Press, 1964.
35. James, L. A., "The Effect of Temperature on the Fatigue-Crack Propagation Behavior of A286 Steel," Hanford Engineering Development Laboratory, HEDL-TME 75-82, September 1975.
36. Tobler, R. L., private communication.
37. Tobler, R. L. and Reed, R. P., "Tensile and Fracture Behavior of a Nitrogen-Strengthened, Chromium-Nickel-Manganese Stainless Steel at Cryogenic Temperatures," in Semi-annual Report on Materials Research in Support of Superconducting Machinery, NBSIR 75-828, National Bureau of Standards, October 1975, pp. 131-150.
38. Tobler, R. L. and Reed, R. P., "Fatigue Crack Growth Rates of Structural Alloys at Four Kelvin," Presented at the International Cryogenic Materials Conference, Kingston, Ontario, July 1975.
39. Irwin, G. R., "Crack Extension Force for a Part-Through Crack in a Plate," Journal of Applied Mechanics, Vol. 29, Transactions ASME, Vol. 84, Series E, December 1962.

TABLE 1 - CHEMICAL COMPOSITIONS, HEAT TREATMENT and PROCESSING DETAILS FOR KROMARC 58, AISI 310 S AND A286 STAINLESS STEELS

Material	C	Mn	P	S	Si	Ni	Cr	Mo	V	Al	Ti	Cu	N	B	Zr
Kromarc 58	.030	9.30	.005	.005	.65	23.0	15.5	2.2	.16	.02	---	---	.17	.016	.008
AISI 310 S	.053	1.70	.027	.011	.48	20.8	25.0	.21	---	---	---	.14	---	---	---
A286 (ASTM A453)	.036	1.72	.017	.0025	.57	25.8	14.9	1.31	.31	.15	2.35	---	---	---	---

Heat Treatment* and Processing Details

<u>Material</u>	<u>Heat Treatment and Processing Designation</u>	<u>Details</u>
Kromarc 58	STQ	1800°F (1255 K) - 1 hr - Water Quench
Kromarc 58	CW	Cold Work ~ 30% Reduction in Thickness
AISI 310 S	STQ	2000°F (1366 K) - 1 hr - Water Quench
AISI 310 S	STFC	2000°F (1366 K) - 1 hr - Furnace Cool to 800°F (700 K); min; then Air Cool
A286 (ASTM A453)	STQA	1650°F (1172 K) - 5 hr - Oil Quench: t _{1/2} en Age at 1325°F (991 K), hold 20 hr and Air Cool

TABLE 2 - HARDNESS, GRAIN SIZE AND NOTCHED TENSILE PROPERTIES OF KROMARC 58, AISI 310 S AND A286 STAINLESS STEELS

Material	Heat Treatment	Hardness	Grain Size (ASTM No.)	Notched Tensile Properties											
				75°F (297 K)				-320°F (77 K)				-452°F (4 K)			
				σ_{ys} ksi	σ_{ys} MPa	NTS ksi	NTS MPa	σ_{ys} ksi	σ_{ys} MPa	NTS ksi	NTS MPa	σ_{ys} ksi	σ_{ys} MPa	NTS ksi	NTS MPa
Kromarc 58	STQ	88.0 Rb	5.5	53.8	370.9	134.6	928.0	114.3	788.1	228.9	1578.2	158.7	1094.2	272.3	1877.4
Kromarc 58	CW	33.0 Rc	9.5	137.3	946.7	223.5	1541.0	186.8	1287.9	308.4	2126.3	213.4	1471.3	356.2	2455.9
AISI 310 S	STQ	73.0 Rb	4.6	37.9	261.3	115.8	798.4	87.6	604.0	196.5	1354.8	118.5	817.0	231.8	1598.2
AISI 310 S	STFC	67.3 Rb	5.0	32.8	226.1	110.6	762.6	83.2	573.6	173.8	1198.3	118.5	817.0	213.5	1472.0
A286* (ASTM A453)	STQA	32.3 Rc	4.0												

* No notched tensile tests conducted on A286.

TABLE 3 - FRACTURE TOUGHNESS PROPERTIES OF KROMARC 58, AISI 310 S AND A286 STAINLESS STEELS

Material	Heat Treatment	ASTM E399 Orientation	Test Temperature		Yield Strength		J _{Ic}		K _{Ic}		K _{Ic} ² (σ_{ys}) _{vs}	
			°F	K	ksi	MPa	in.-lb in. ²	MN m	ksi/in.	MPa√m	$\frac{K_{Ic}}{\sigma_{ys}}$ √in.	in.
Kromarc 58	STQ	T-L	-452	4	158.7	1094.2	1250	0.219	195.4	216.3	1.23	1.52
Kromarc 58	CW	T-L	-452	4	213.4	1471.3	388	0.068	108.8	120.4	0.51	0.26
Kromarc 58	CW	L-T	-452	4	215.8	1487.9	452	0.079	117.5	130.1	0.54	0.30
AISI 310 S	STQ	T-L	-452	4	118.5	817.0	1600	0.280	236.3	261.6	1.99	3.98
AISI 310 S	STFC	T-L	-452	4	118.5	817.0	765	0.134	163.4	180.9	1.38	1.90
A286 (ASTM A453)	STQA	L-T	-452	4	140.5	968.7	815	0.143	162.8	180.2	1.16	1.34
A286 (ASTM A453)	STQA	L-T	75	297	119.3	822.5	692	0.121	145.6	161.2	1.22	1.49

TABLE 4 - CRITICAL AND INITIAL ALLOWABLE FLAW SIZES FOR KROMARC 58, AISI 310 S and A286 STAINLESS STEELS AT
-452°F (4 K)

Material	Heat Treatment	Applied Stress Level $\sigma/\sigma_{ys} = 0.75$		Critical Flaw Size		Initial Allowable Flaw Size (1000 cycles)		Initial Allowable Flaw Size (100 cycles)	
		ksi	MPa	Depth in.	Length cm	Depth in.	Length cm	Depth in.	Length cm
Kromarc 58	STQ	119.0	820.5	0.70	1.78	0.30	0.76	0.62	1.57
Kromarc 58	CW	161.0	1110.1	0.13	0.33	0.06	0.15	0.12	0.30
AISI 310 S	STQ	88.9	612.9	1.82	4.62	0.41	1.04	1.38	3.51
AISI 310 S	STQ	88.9	612.9	0.87	2.21	0.32	0.81	0.75	1.90
A286 (ASTM A453)	STQA	105.4	726.7	0.62	1.57	0.55	1.40	0.61	1.55

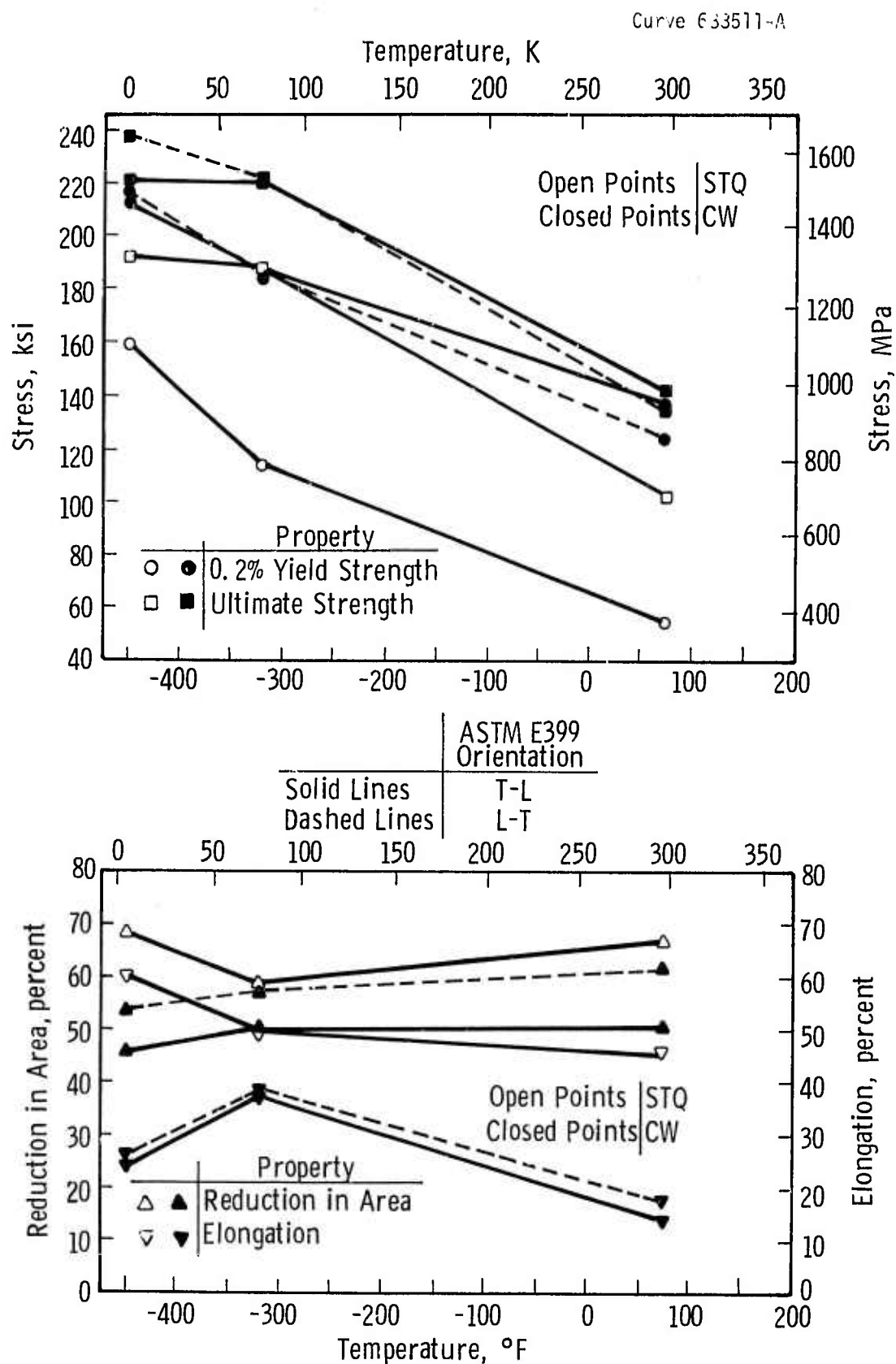


Fig. 1—Tensile properties of Kromarc 58 stainless steel

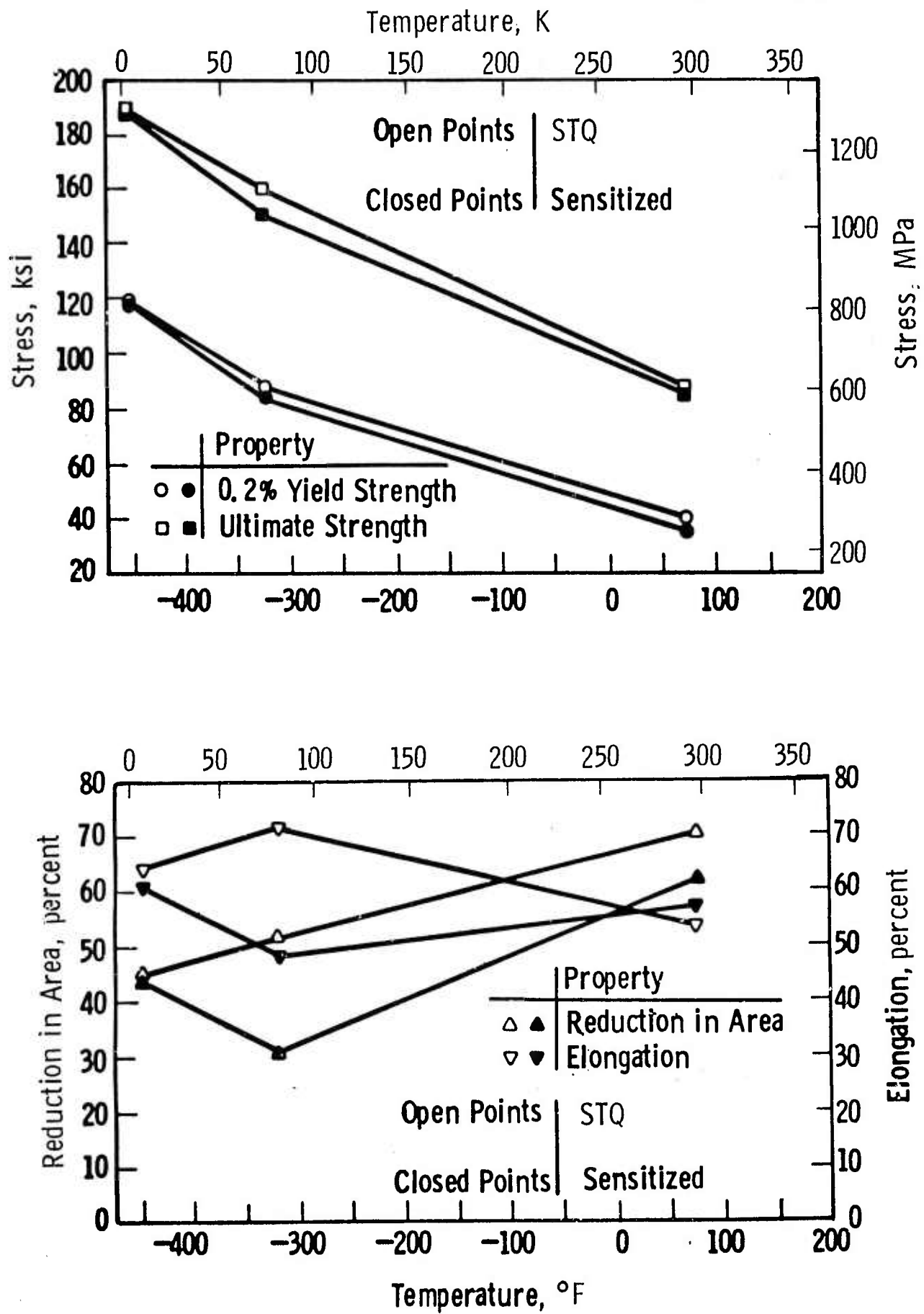


Fig. 2—Tensile properties of AISI 310 S stainless steel

Curve 682165-A

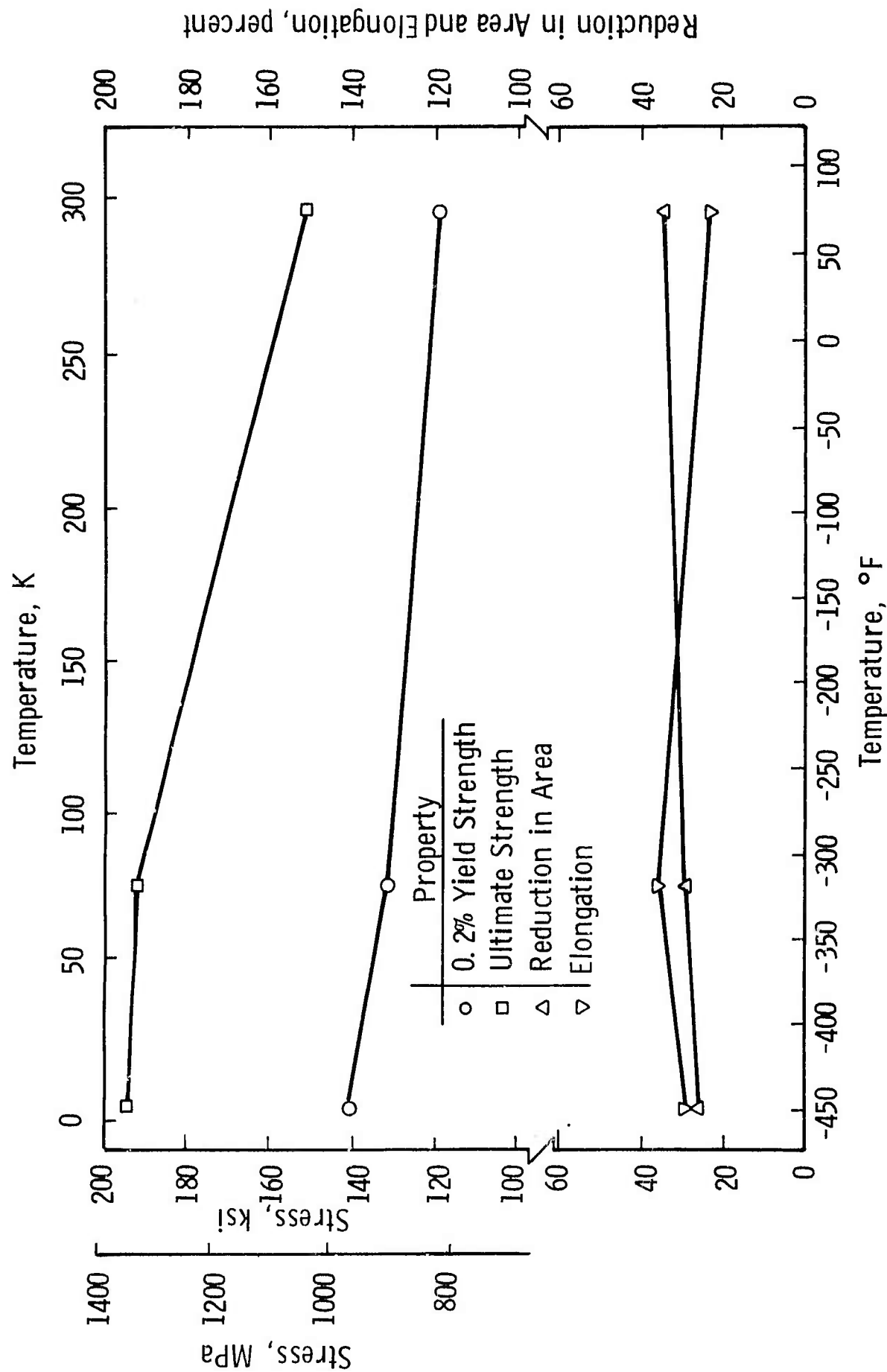


Fig. 3—Tensile properties of A286 stainless steel

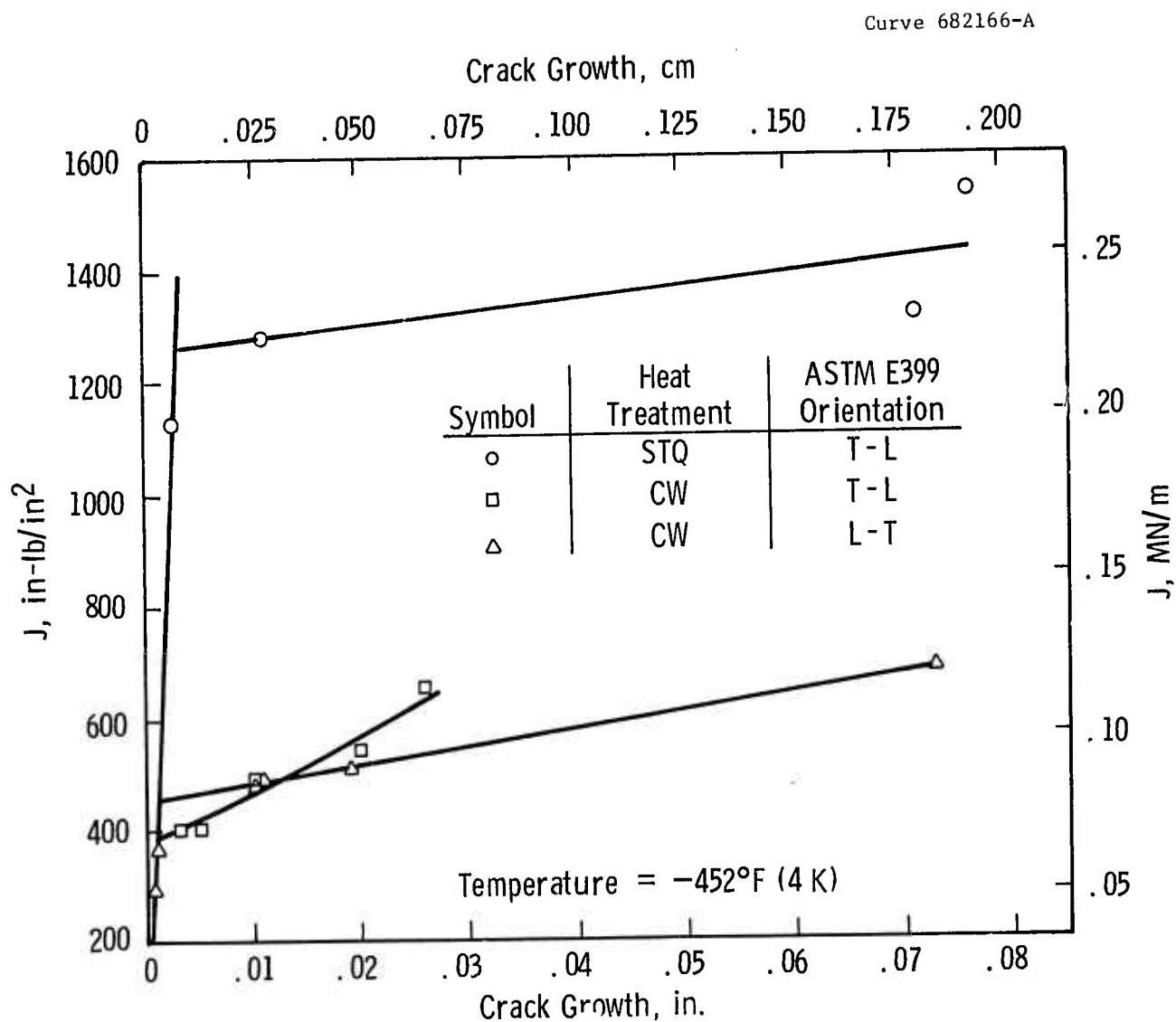


Fig. 4 -J resistance curves for Kromarc 58 stainless steel

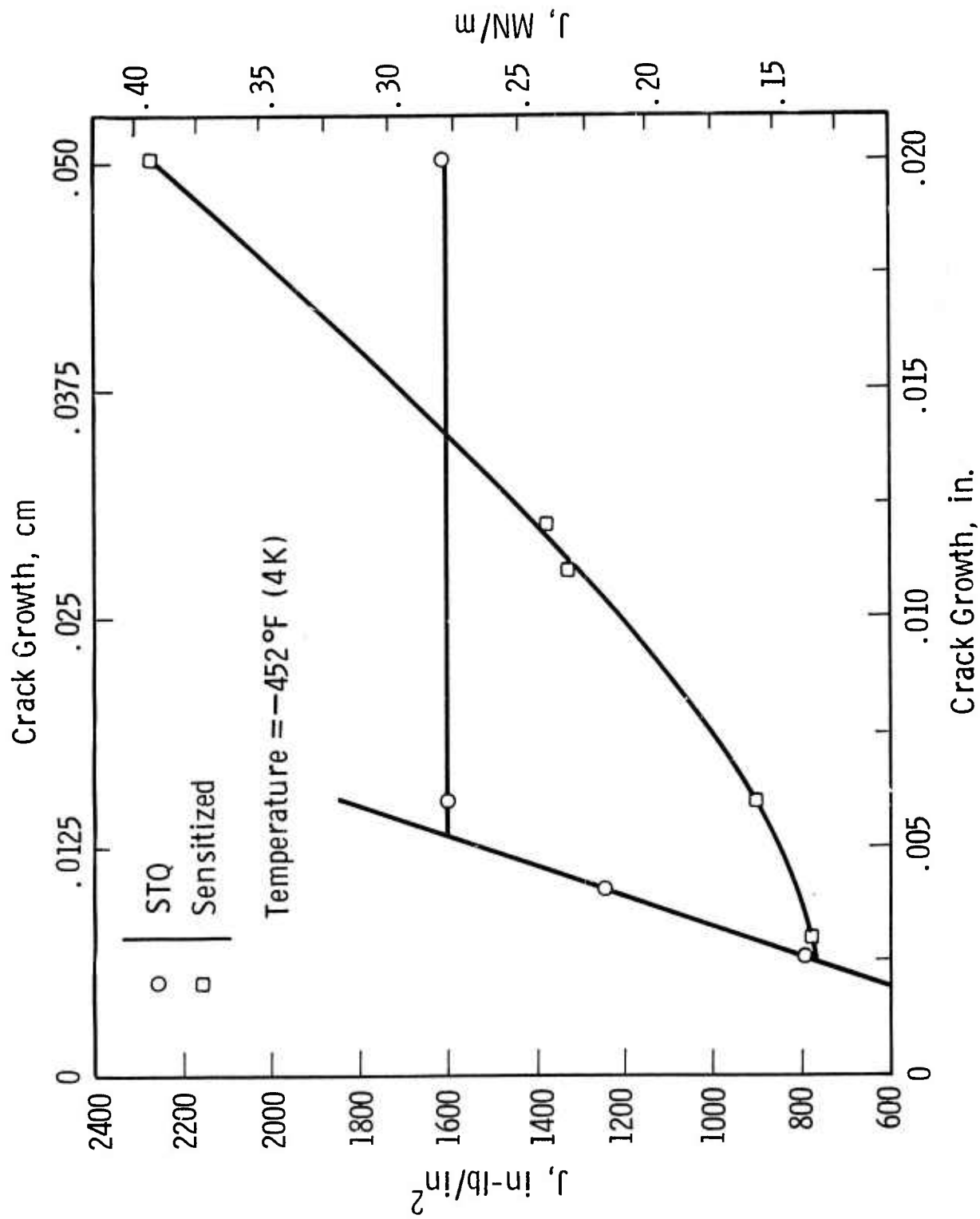


Fig. 5 -J resistance curves for AISI 310 S stainless steel

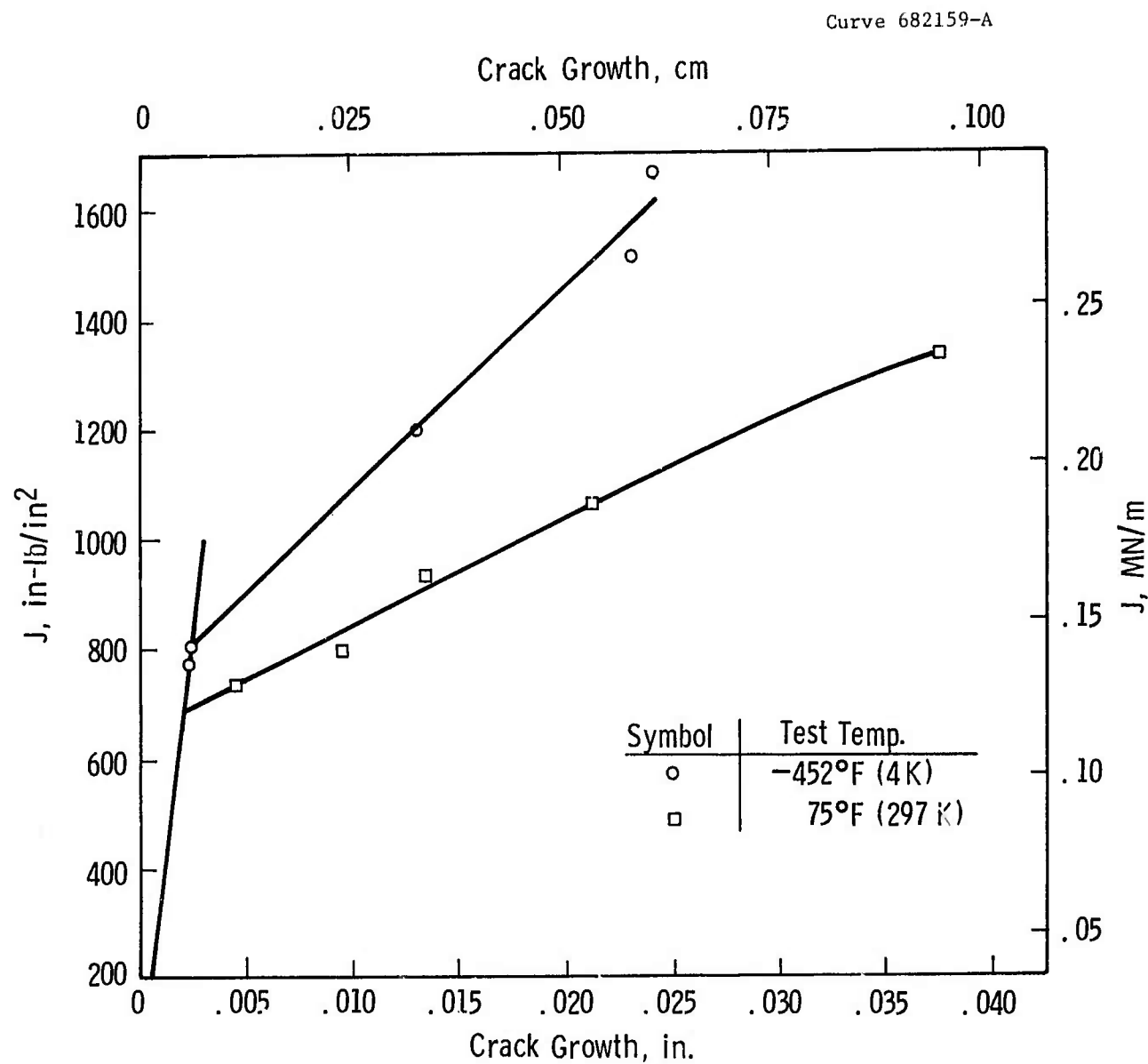


Fig. 6—J resistance curves for A286 stainless steel

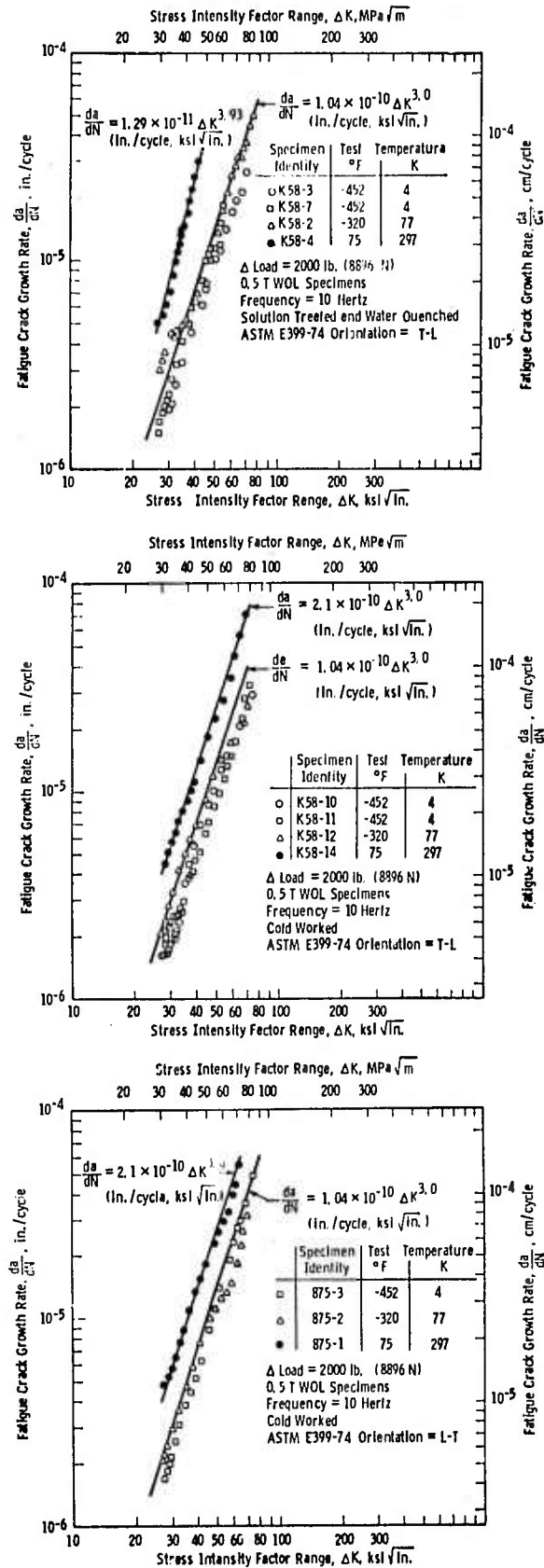


Fig. 7 — Fatigue crack growth rate properties of Kromarc 58 stainless steel

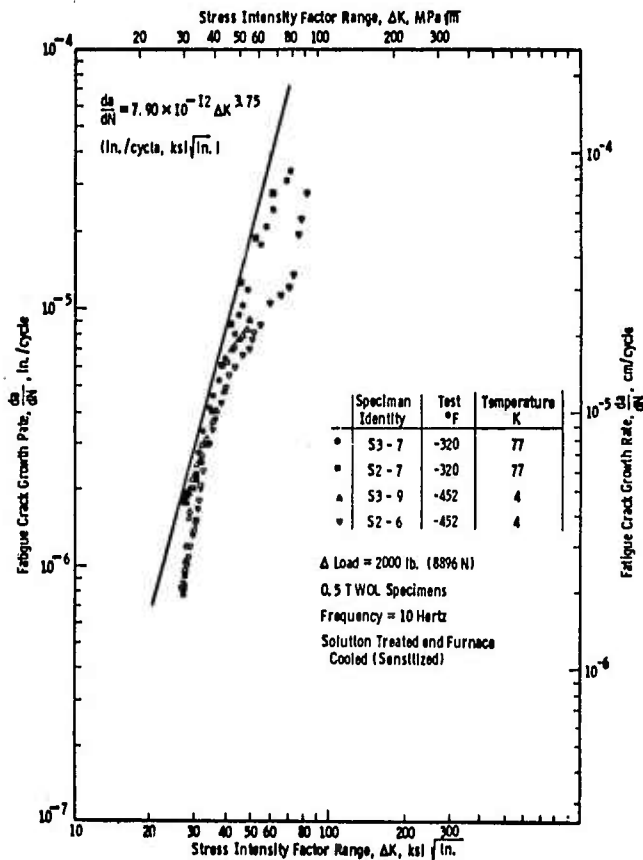
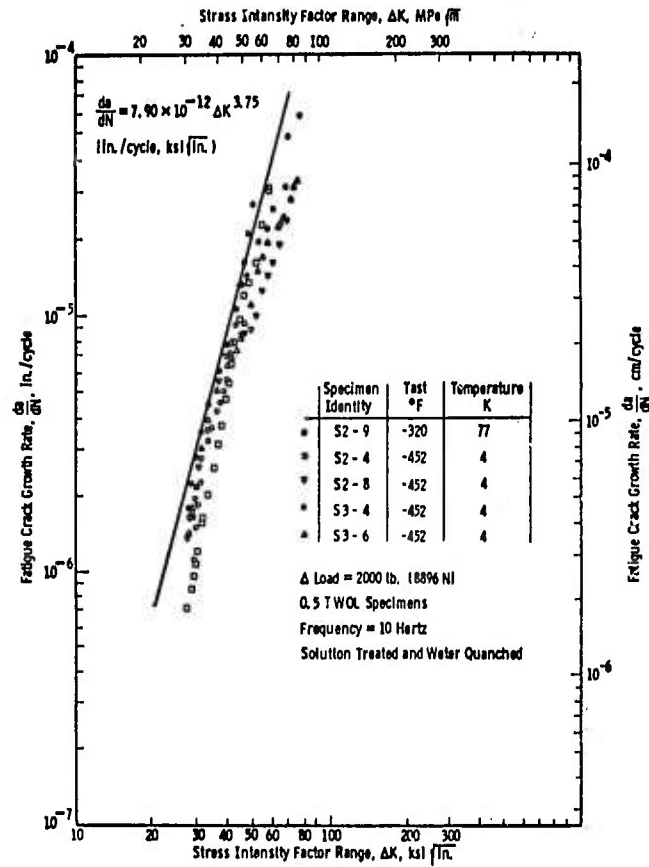


Fig. 8—Fatigue crack growth rate properties of AISI 310 S stainless steel

Curve 682293-A

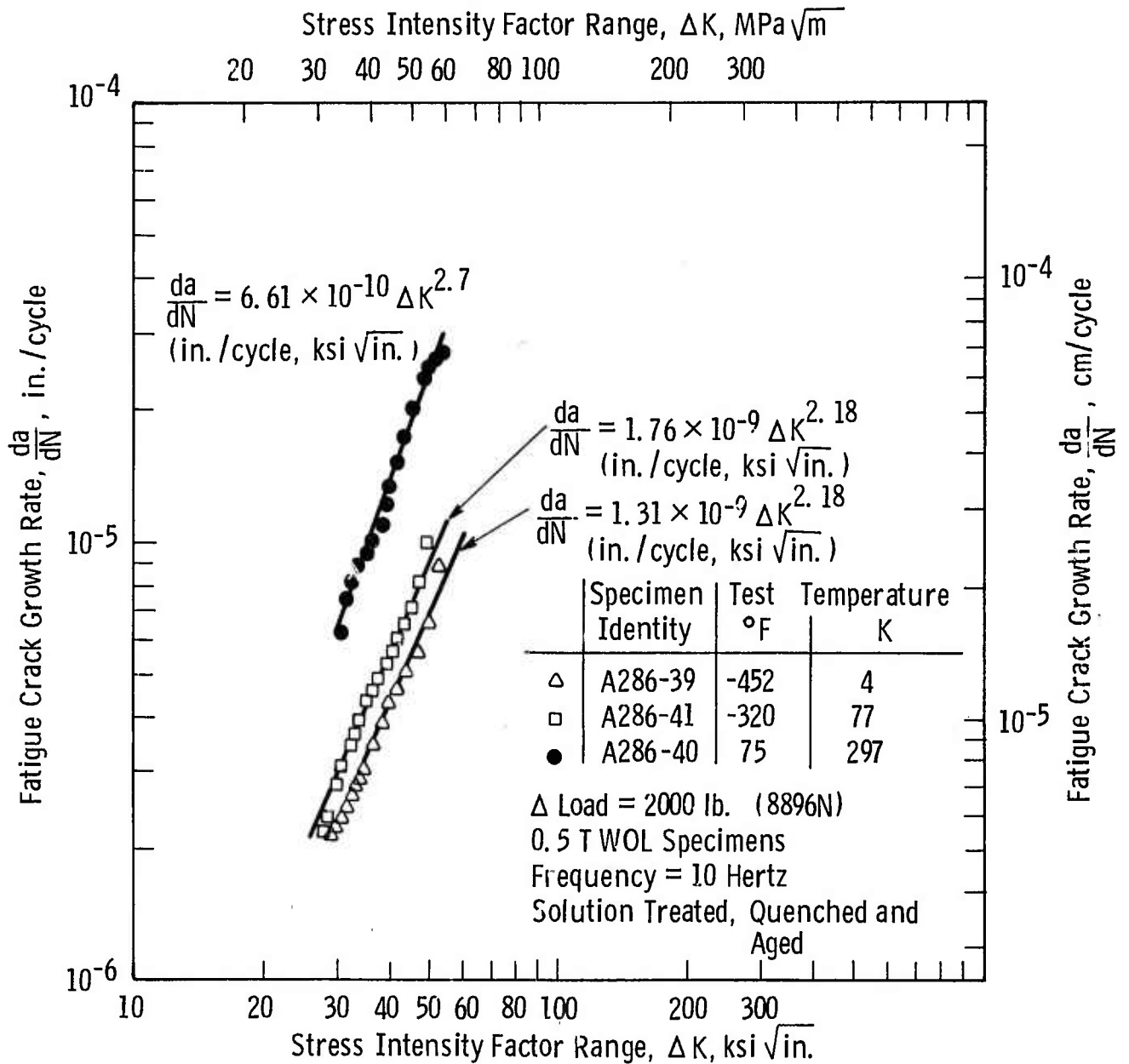


Fig. 9 - Fatigue crack growth rate properties of A286 stainless steel

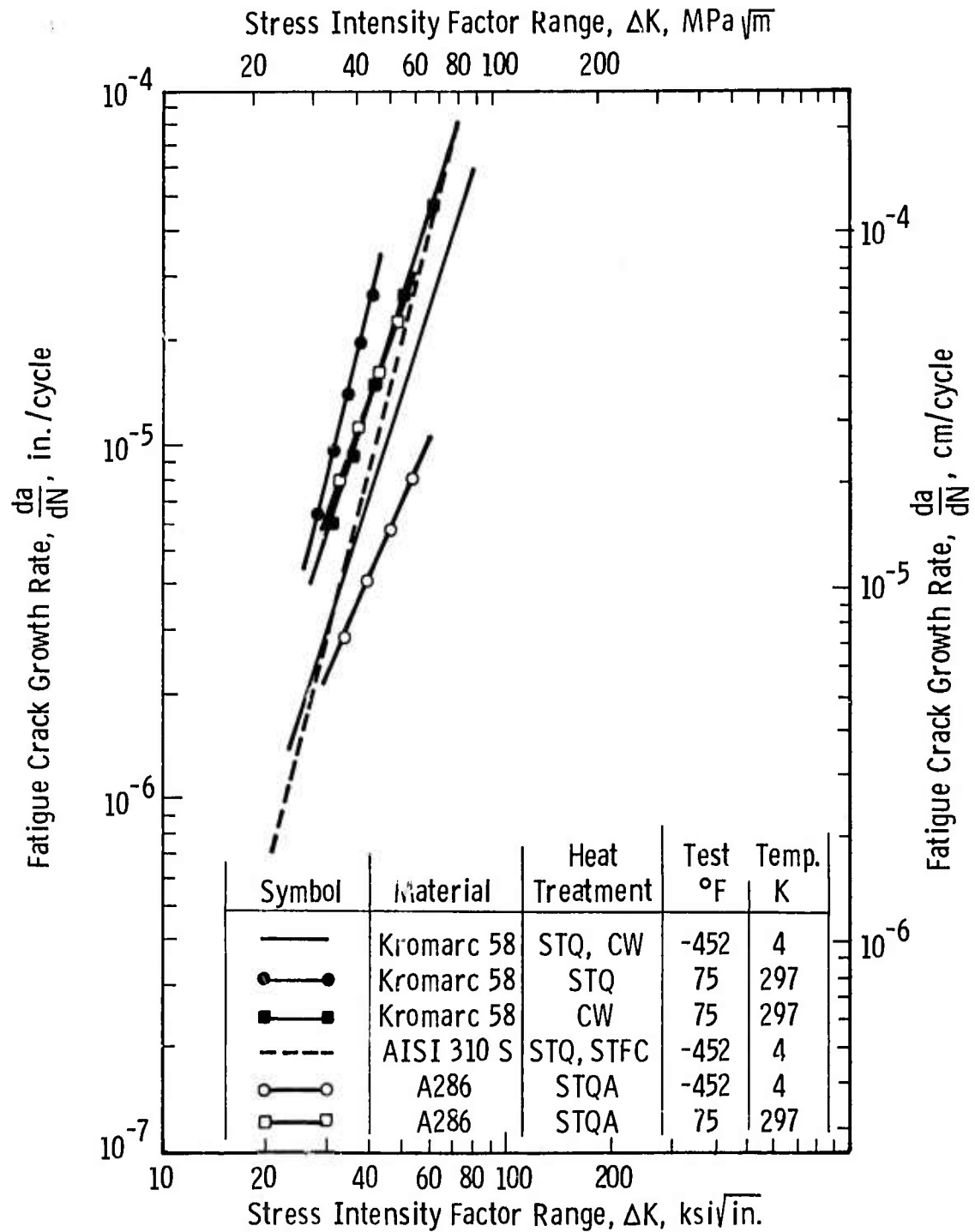


Fig. 10—Comparison of the room temperature and -452°F (4K) fatigue crack growth rate properties of Kromarc 58, AISI 310 S and A286 stainless steels

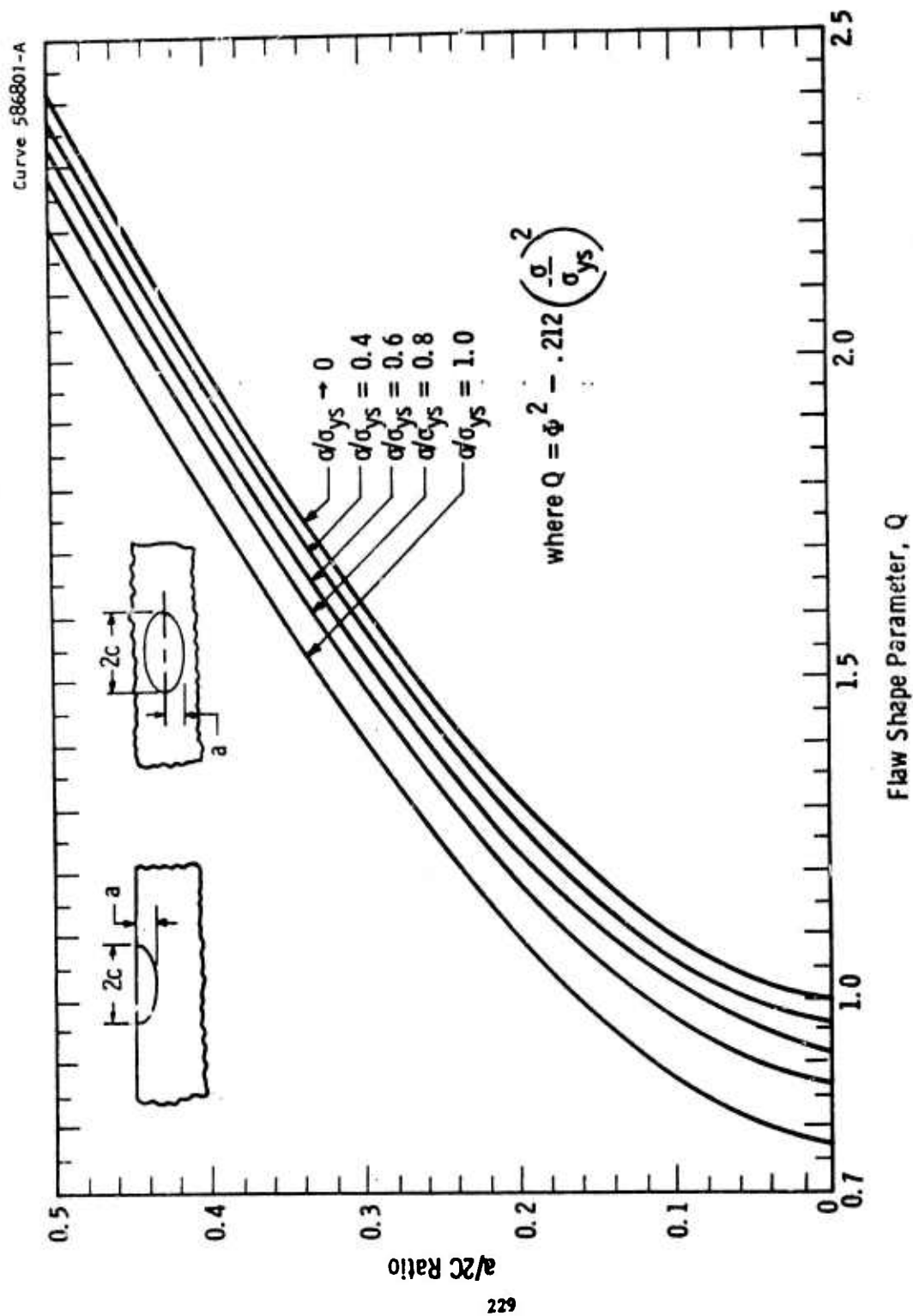


Fig. 11 —Flaw shape parameter curves for surface and internal cracks

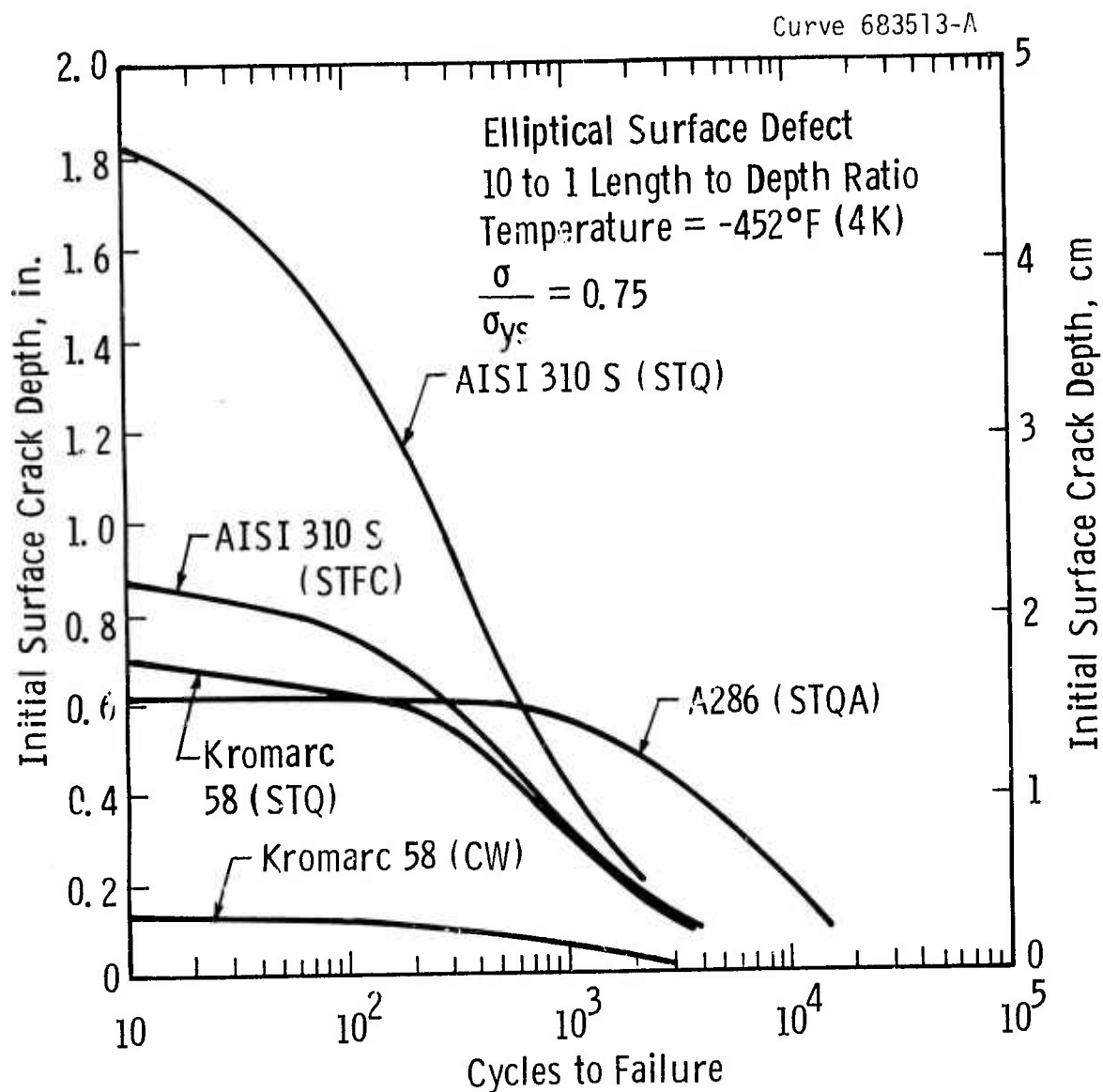


Fig. 12—Cyclic life curves for Kromarc 58, AISI 310 S and A286 stainless steels